AIR-GAPS VIA THERMALLY DECOMPOSABLE POLYMERS AND THEIR APPLICATION TO COMPLIANT WAFER LEVEL PACKAGING (CWLP)

A Dissertation
Presented to
The Academic Faculty

by

Hollie Anne Kelleher

In Partial Fulfillment
Of the Requirements for the Degree
Doctor of Philosophy in Chemical Engineering

Georgia Institute of Technology

December 2004

AIR-GAPS VIA THERMALLY DECOMPOSABLE POLYMERS AND THEIR APPLICATION TO COMPLIANT WAFER LEVEL PACKAGING (CWLP)

Approved by:

Dr. Paul A. Kohl, Co-Chair	Dr. Sue Ann Bidstrup Allen, Co-Chair
Dr. Kevin P. Martin	Dr. J. Carson Meredith
Dr. F. Joseph Schork	Dr. Suresh K. Sitaraman

Date Approved: December 6, 2004

ACKNOWLEDGEMENTS

I would like to thank and acknowledge several people that have helped and encouraged me throughout my academic career. I express my deepest thanks to my advisors, Dr. Sue Ann Bidstrup Allen and Dr. Paul Kohl, for giving me the opportunity to work in their group, and thus giving me the wonderful learning and growing experience during my years at Georgia Tech. They truly inspired me to think creatively and taught me the value of not giving up.

I would also like to thank several other Georgia Tech faculty members: my committee of Dr. Kevin Martin, Dr. Carson Meredith, Dr. Joseph Schork, and Dr. Suresh Sitaraman; also, a special thanks to Dr. James Meindl, Dr. Dennis Hess, and Dr. Cliff Henderson, for their advice, expertise, use of equipment, and general interest in my career.

Thanks to PROMERUS, LLC., and especially Jeff Krotine, Larry Rhodes, Rob Shick, and Ed Elce, for providing me with the materials and expertise required to make this project a success.

A very special thanks goes to Dr. Muhannad S. Bakir, who has been my colleague and friend and whose contributions to this project are immeasurable. The opportunities and recognition this project has received would not have been possible without his research and collaboration on Sea of Leads. My career would not be the same without Muhannad and I owe him many thanks for always believing in me.

Special thanks also go to all the wonderful post-docs I've had the opportunity to work with and whom have made countless contributions to this work, especially Dr. Joseph Paul Jayachandran for his work on photosensitive polycarbonates, Dr. Xhaoqin Wu for his work on photosensitive polynorbornenes, Dr. Dhananjay Bhusari, and Dr. Hongshi Zhen. Also a special thanks to Chris Timmons for performing XPS experiments, Gary Gray for his contributions with CoventorWare modeling, and all the past and present members of the Kohl/Bidstrup research group.

Most importantly, my love and endless thanks goes to my family for their love and support. Thank you to my husband, Matthew, whose patience, motivation, love, and support allowed me to reach my goals. Without my mother Sue and my father William, I would not have learned the meaning of working hard to reach your goals. A special thanks also to my sister, Carrie, who motivated me to succeed through her example.

TABLE OF CONTENTS

ACKNOWLEDGEMENTS.....iii

LIST OF TABLES.....xiv

LIST OF FIGURES.....xix

SUMMARY..... xlii

CHAPTER 1: INTRODUCTION..... 1

CHAPTER 2: BACKGROUND 10

2.1 Overview of Air-gap Fabrication Techniques 10

2.2 Sea of Leads Compliant Wafer Level Packaging 15

CHAPTER 3: EXPERIMENTAL TECHNIQUES, MATERIALS, AND EQUIPMENT..... 20

3.1 General Process of the Fabrication of Air-gaps Using Sacrificial Polymers 20

3.2 Sacrificial Polymer Chemistry..... 25

3.2.1 Polynorbornenes 27

3.2.2 Polycarbonates 31

3.3 Encapsulating Materials..... 34

3.4 Analysis Methods and Procedures 35

3.4.1 Thermogravimetric Analysis (TGA) 35

3.4.2 X-ray Photoelectron Spectroscopy (XPS) 38

3.4.3 Atomic Force Microscopy (AFM) 39

3.4.4 Ellipsometry 40

3.4.5 Goniometry 40

3.4.6 Scanning Electron Microscopy (SEM) 41

3.4.7 Nanoindentation 43

3.4.8 Application of the analysis techniques in subsequent chapters 45

CHAPTER 4: THERMAL DECOMPOSITION OF SACRIFICIAL POLYMERS 46

4.1 Kinetic Parameters From Thermogravimetric Analysis 47

4.1.1 Integral method to determine kinetic parameters from dynamic TGA 49

4.1.2 Differential method to determine kinetic parameters from isothermal TGA .. 51

4.1.3 Residue factor 52

4.2 Thermal Decomposition of Polynorbornene Sacrificial Materials 52

4.2.1 Dynamic TGA results of various composition and molecular weight PNB 53

4.2.2 Discussion of the TGA results for various molecular weight and composition PNB 61

4.3 Thermal Decomposition of Polycarbonate Sacrificial Materials 67

4.3.1 Dynamic TGA results of various composition polycarbonates 68

4.3.2 TGA results of polycarbonate decomposition in nitrogen and air atmospheres 71

4.3.3 Kinetic parameters for the decomposition of PPC in nitrogen and air 79

4.3.4 Residual surfaces of decomposed polycarbonate films 83

4.3.5 Decomposition results from the addition of a photoacid generator to polycarbonates 85

4.3.6 Discussion of the decomposition of polycarbonate sacrificial materials 90

4.4 Summary of Conclusions on Thermal Decomposition..... 94

CHAPTER 5: POLYNORBORNENE AIR-GAP FABRICATION AND RESULTS 97

5.1 Experimental Details Relevant to Air-gap Fabrication With PNB Sacrificial Material..... 98

5.1.1 Deposition of PNB sacrificial materials 98

5.1.2 Hard mask and photolithography..... 100

5.1.3 PNB dry etching..... 102

5.1.4 Deposition of encapsulating materials 102

5.1.5 Decomposition of PNB sacrificial material..... 104

5.2 Optimization of the Air-gap Fabrication Process 106

5.2.1 The effect of curing temperature on PNB decomposition..... 106

5.2.2 Variation of hard mask materials 107

5.2.3 PNB RIE etching results 109

5.3 Air-gaps Fabricated With PNB and SiO_2 or SiN_x Encapsulation 115

5.3.1 Results of air-gaps encapsulated in inorganic glasses 115

5.3.2 Discussion of air-gaps encapsulated in glass 118

5.4 Air-gaps Fabricated With PNB and Polymer Encapsulation 121

5.4.1 Polyimides 122

5.4.2 Ultradel 7501 polyimide encapsulated air-channels 124

5.4.3 DuPont Pyralin PI-2611 and PI-2734 encapsulated air-channels 129

5.4.4 Air-gaps encapsulated with other polyimides 134

5.4.5 Air-gaps overcoated with structurally different polymers 140

5.4.6 Discussion of polymer overcoated air-gaps 147

5.5 Overcoming Thermal and Mechanical Problems With Overcoat Materials 151

5.5.1 Experimental details relevant to Section 5.5 152

5.5.2 Results of air-gaps with two-layer overcoats 152

5.5.3 Discussion of two-layer overcoated air-gaps 160

5.6 Air-gaps Integrated With Metal Features 162

5.7 Air-gaps Fabricated With Other Composition PNB 166

5.7.1 Polynorbornenes with varying CTE values 166

5.7.2 Photosensitive polynorbornene 171

5.8 Summary of Conclusions on the Fabrication of Air-gaps With PNB Sacrificial Material 174

CHAPTER 6: POLYCARBONATE AIR-GAP FABRICATION AND RESULTS 176

6.1 Experimental Details Relevant to Air-gap Fabrication With PC Sacrificial Material 177

6.1.1 Deposition of PC sacrificial materials 177

6.1.2 Patterning of non-photosensitive polycarbonate sacrificial materials 178

6.1.3 Patterning of photosensitive polycarbonate sacrificial materials 184

6.1.4 Deposition of encapsulating material and decomposition 186

6.2 Air-gap Fabrication With Non-photosensitive PC and SiO_2 Encapsulation 188

6.2.1 Results of air-gaps fabricated with PC encapsulated in SiO2 188

6.2.2 Discussion of SiO2 encapsulated air-gaps 190

6.3 Air-gap Fabrication Using Non-photosensitive PC and Polymer Encapsulation ... 195

6.3.1 Results of air-gaps fabricated with PC encapsulated in thermoplastic polymers 195

6.3.2 Results of air-gaps fabricated with PC encapsulated by thermoset polymers 197

6.3.3 Results of air-gaps fabricated with PC encapsulated in higher-cure temperature polymers 198

6.3.4 Discussion of air-gaps fabricated from non-photosensitive PC encapsulated in polymer 207

6.4 Air-gaps Fabricated With Photosensitive Polycarbonates 208

6.5 Discussion of Air-gaps Fabricated Using Polycarbonate Sacrificial Materials 212

CHAPTER 7: IN-SITU DECOMPOSITION OF POLYNORBORNENE IN AIR-GAPS 217

7.1 Experimental Details Relevant to Chapter 7 218

7.1.1 TGA sample preparation and procedure 218

7.1.2 XPS sample preparation and procedure 224

7.1.3 Air-gap fabrication details of samples for the decomposition of PNB at a constant rate of conversion 225

7.2 Thermogravimetric Analysis Results for Unencapsulated and Encapsulated PNB 226

7.2.1 Dynamic TGA results of unencapsulated PNB in the presence of metals 226

7.2.2 Dynamic TGA results of unencapsulated PNB and PNB encapsulated by PI-2611 227

7.2.3 Isothermal TGA results of unencapsulated PNB and PNB encapsulated in PI-2611 237

7.3 Kinetic Parameters for the Decomposition of Encapsulated and Unencapsulated PNB 238

7.3.1 Kinetic parameters for the decomposition of unencapsulated PNB and PNB encapsulated in PI-2611 from dynamic TGA data 242

7.3.2 Kinetic parameters for the decomposition of unencapsulated PNB and PNB encapsulated in PI-2611 from isothermal TGA data 243

7.3.3 Discussion of the TGA results for the decomposition of unencapsulated PNB and PNB encapsulated by PI-2611 244

7.4 Analysis of Surfaces Following the Decomposition of Unencapsulated and Encapsulated PNB Sacrificial Material..... 250

7.4.1 X-ray photoelectron spectroscopy (XPS) of residual surfaces 250

7.4.2 Goniometry results of residual surfaces..... 255

7.5 Optimization and Discussion of PNB Decomposition..... 257

7.5.1 Analysis of the time of decomposition from the reaction kinetic parameters 258

7.6 The Effect of Area, Volume, and Rate of Decomposition on Air-gap Formation 261

7.6.1 Pressure inside the air-gap during isothermal decomposition 264

7.6.2 Air-gaps with identical overcoat area and thickness, but different PNB thickness..... 269

7.6.3 Constant rate of conversion decomposition..... 270

7.6.4 Results of air-gaps fabricated at a constant rate of conversion..... 271

CHAPTER 8: AIR-GAPS IN SEA OF LEADS WAFER LEVEL PACKAGING TECHNOLOGY 283

8.1 Experimental Process Details for SoL Fabrication With Embedded Air-gaps 286

8.2 Discussion of Results and Critical Issues for the Integration of Air-gaps into SoL 295

8.2.1 Metal compatibility in SoL processing 295

8.2.2 Lithography on non-planar surfaces 301

8.2.3 Yield and uniformity of air-gaps in SoL 304

CHAPTER 9: MECHANICAL PERFORMANCE OF AIR-GAPS 309

9.1 Experimental Methods Specific to Chapter 9 309

9.1.1 Fabrication details of air-gaps for mechanical testing 309

9.1.2 Experimental details of nanoindentation 313

9.2 Mechanical Properties From Nanoindentation 315

9.3 Nanoindentation Results for Polyimide Overcoat Films 319

9.4 Mechanical Performance Sample Fabrication Results 320

9.5 Air-gap Indentation Results and Discussion 328

9.5.1 Repeatability of the force-displacement behavior of air-gaps 330

9.5.2 The effect of experimental parameters on air-gap force-displacement curves. 333

9.5.3 The effect of nanoindenter tip geometry on air-gap force-displacement results 341

9.5.4 The effect of air-gap and overcoat geometry and properties on air-gap force-displacement results 347

9.6 Modeling of Air-gap z-axis Mechanical Movement With CoventorWare 352

9.7 Design Considerations for Air-gap Out-of-plane Compliance 359

APPENDIX A: SUPPORTING DATA FOR THE CALCULATION OF KINETIC PARAMETERS FROM TGA DATA 363

A.1 Kinetic Parameters From Dynamic and Isothermal TGA Data for PPC Decomposed in Air and Nitrogen 365

A.2 Kinetic Parameters From Dynamic and Isothermal TGA Data in Nitrogen for Unencapsulated and PNB Encapsulated by PI-2611 392

APPENDIX B: SPIN-SPEED CURVES FOR SACRIFICIAL POLYMERS..... 433

APPENDIX C: SPIN-SPEED CURVES AND PROCESSING CONDITIONS FOR ENCAPSULATING POLYMERS 442

REFERENCES 449

LIST OF TABLES

Table 1: Select future cost-performance packaging requirements as outlined by the 2001 ITRS [42]. 15

Table 2: The composition and weight-average molecular weight of polynorbornene sacrificial materials used in this research. 30

Table 3: Encapsulating materials used in this research along with select properties [52-68]. 36

Table 4: Dynamic TGA results for various compositions and molecular weights of polynorbornene sacrificial materials. Results are for a constant heating rate of 10^{o}C/min in a nitrogen atmosphere (<50 ppm O_2). 60

Table 5: Comparison of the decomposition for various polycarbonates from dynamic TGA at 10^{o}C/min. 70

Table 6: Properties of the dynamic TGA decomposition of PPC performed at various heating rates in: (1) nitrogen; and (2) air. 74

Table 7: Properties of the isothermal TGA decomposition of PPC performed at various isothermal hold temperatures in: (1) nitrogen; and (2) air. 78

Table 8: Residue factors from the dynamic TGA decomposition of PPC performed at various ramp rates in: (1) nitrogen; and (2) air. 81

Table 9: Residue factors from the isothermal TGA decomposition of PPC performed at various temperatures in: (1) nitrogen; and (2) air. 82

Table 10: Kinetic parameters for the decomposition of PPC in nitrogen and air from dynamic and isothermal TGA data. 82

Table 11: Contact angle of silicon before and after decomposition of PEC and PPC films at 300^{o}C in various environments 85

Table 12: Comparison of 50% weight loss temperatures from dynamic TGA at 1 ^{o}C/min for various polycarbonates decomposed by photo-induced acid catalyzed decomposition (PIAD), thermal-induced acid catalyzed decomposition (TIAD) and thermal decomposition (TG). 89

Table 13: Polynorbornene polymer/solvent compositions used for spin-coating and air-cavity fabrication. 99

Table 14: Various polynorbornene RIE etch conditions. 103

Table 15: Deposition conditions for SiO_2 and SiN_x overcoat materials. 105

Table 16: Various Lindberg furnace decomposition programs used with PNB sacrificial material. 105

Table 17: Thickness and refractive index values for PNB films before and after curing at temperatures of 300^{o}C, 325^{o}C, and 350^{o}C. 108

Table 18: Commercial polyimides used as encapsulating materials and their properties [52-54, 58-62]. 123

Table 19: Summary of results for air-gaps fabricated using SiO_2 as a mechanical support layer with overcoat materials PI-2771, PI-2555, HD4000, and PBO CRC-8650. (Thin refers to a SiO_2 layer ~5000 Å and thick refers to a SiO_2 layer ~2 µm thick). 154

Table 20: Effective Modulus for two-layer overcoats of SiO_2 and polymer. The modulus for SiO_2 is 73 GPa. 163

Table 21: Compositions of the various polycarbonate sacrificial polymer solutions. 178

Table 22: Decomposition conditions for various polycarbonate/encapsulant combinations. 187

Table 23: Dynamic TGA samples containing unencapsulated PNB sacrificial material and PNB encapsulated in polyimide PI-2611 220

Table 24: Dynamic TGA samples containing unencapsulated PNB sacrificial material on various TGA pan surfaces. 221

Table 25: Isothermal TGA samples containing unencapsulated PNB sacrificial material and PNB encapsulated in polyimide PI-2611. 221

Table 26: Dynamic TGA characteristics for the decomposition of PNB using various sample pans at a heating rate of 10^{o}C/min in nitrogen. 229

Table 27: Comparison of the dynamic TGA at various points in the decomposition reaction for unencapsulated PNB and PNB encapsulated in polyimide PI-2611 ... 234

Table 28: Isothermal TGA characteristics for unencapsulated PNB and PNB encapsulated in polyimide PI-2611 241

Table 29: Residue factors from the dynamic TGA decomposition of PPC performed at various ramp rates in: (1) nitrogen; and (2) air 245

Table 30: Residue factors from the isothermal TGA decomposition of PNB at 400^{o}C and 425^{o}C: (1) unencapsulated; and (2) encapsulated in polyimide PI-2611. 246

Table 31: Kinetic parameters for the thermal decomposition reaction of unencapsulated PNB and PNB encapsulated in PI-2611 from dynamic and isothermal TGA data. 247

Table 32: Kinetic parameters determined by Wedlake [69] for the decomposition of 90/10 butyl/TES PNB in nitrogen. 249

Table 33: Atomic composition of residual surfaces following the decomposition of unencapsulated PNB and PNB encapsulated in either PECVD deposited SiO_2 or polyimide PI-2611..... 251

Table 34: Contact Angle measurements of residual surfaces following the decomposition of unencapsulated PNB and PNB encapsulated in either SiO_2 or polyimide PI-2611. 256

Table 35: Geometries and initial and final weight values for various PNB structures decomposed to 95 and 99 percent conversion. 260

Table 36: Estimated time of reaction for the thermal decomposition of unencapsulated PNB and PNB encapsulated in PI-2611..... 260

Table 37: Typical values for the variables in equation 7.13, based on a square air-gap with dimensions of 190 μm ×190 μm, formed from 10 μm thick sacrificial PNB, decomposed isothermally at 425°C to a reaction conversion of 95%..... 268

Table 38: Experimental furnace programs for the constant rate of conversion decomposition of PNB. 276

Table 39: Air-gap height following decomposition at a constant rate of conversion, as measured by profilometry and SEM. 279

Table 40: Processing conditions for the fabrication of SoL prototype packages. 298

Table 41: Processing details for the fabrication of samples for mechanical analysis..... 311

Table 42: Air-gap geometries and dimensions for mechanical performance analysis. .. 312

Table 43: Indentations and elastic modulus calculation results from polymer overcoat films containing no air-gaps..... 321

Table 44: Air-gap height for air-gaps on samples MECH-1 through MECH-4, measured by contact profilometry. 325

Table 45: Compliance for selected geometry air-gaps from various depth indentations. 351

Table 46: Maximum stress and displacements predicted by CoventorWare for a 190 × 190 μm square air-gap or 190 μm diameter circular air-gap with various overcoat properties..... 357

Table A.1: Activation Energy (kJ/mol) at various values of conversion for the decomposition of PPC in nitrogen and air.....370

Table A.2: The reaction order and pre-exponential constant for the decomposition of PPC in nitrogen and air at various heating rates.....371

Table A.3: The reaction order and reaction constant for the decomposition of PPC in nitrogen and air at various isothermal temperatures.....372

Table A.4: Activation energy (kJ/mol) at various values of conversion for the decomposition of unencapsulated PNB, based on instantaneous and average dynamic heating rates.....395

Table A.5: Activation energy (kJ/mol) at various values of conversion for the decomposition of PNB encapsulated by PI-2611 in nitrogen, based on instantaneous and average dynamic heating rates.....395

Table A.6: Linear coefficients and the best fit parameter, R^2, for the linear function used to determine RF.....396

Table A.7: Reaction orders and pre-exponential constants calculated from dynamic TGA for unencapsulated PNB.....397

Table A.8: Reaction orders and pre-exponential constants calculated from dynamic TGA for PNB encapsulated by PI-2611.....398

Table A.9: Reaction orders and rate constants for the decomposition of unencapsulated PNB and PNB encapsulated by PI-2611 from isothermal TGA.....399

Table C.1: Processing conditions for polymers used as overcoat materials to sacrificial polymers.....443

LIST OF FIGURES

Figure 1: Process flow diagram showing the steps involved in (a) conventional packaging technology and (b) wafer level packaging technology. 6

Figure 2: A cross-sectional schematic of a SoL packaged chip. 3-D movement is achieved through the combination of a flexible metal lead with an air-gap embedded in a flexible overcoat polymer. Contact or attachment is made through a solder ball placed at the end of the lead. (Figure taken from reference [25])..... 9

Figure 3: Air-gap formed from poor step coverage of PECVD deposited oxide between narrowly spaced metal lines. This figure shows a phosphorous doped SiO_2 layer deposited into a 0.32 μm space between Cu lines. (Figure taken from reference [3]). 11

Figure 4: Schematic of the SoL fabrication process: (a) the wafer following back-end processing and bond pad formation; (b) the wafer is spin-coated with a complaint polymer; (c) the first masking step patterns and etches vias in the compliant polymer; (d) the second masking step forms electroplated Cu or Au leads; (e) the third masking step provides the end of the leads with solder bumps. (Figure taken from reference [24]). 19

Figure 5: SEM image of a fabricated SoL chip containing 12,000 leads/cm^2. The chip contains short (~60 μm length) leads distributed on an 80 μm x 80 μm square lattice at the chip center, and longer (~120 μm length) leads distributed on an 80 μm x 160 μm rectangular lattice at the chip periphery. (Figure taken from reference [25]) ... 19

Figure 6: Process flow for the fabrication of air-gaps: (a) substrate; (b) spin-coating of sacrificial polymer; (c) deposition of hard mask; (d) photolithography and etching of hard mask (see details in Figure 7); (e) plasma etching of sacrificial polymer; (f) stripping of photoresist and hard mask; (g) deposition of encapsulating material; (h) thermal decomposition of the sacrificial polymer to produce air-gaps. 21

Figure 7: Process details for lithography and patterning of a hard mask: (a) substrate coated with a layer of sacrificial polymer and a hard mask material (SiO_2 or metal); (b) spin-coat photoresist onto hard mask surface; (c) expose photoresist to light through a mask containing clear and opaque regions; develop the photoresist to (d) remove exposed photoresist areas for a positive-tone resist material and (e) remove

unexposed areas for a negative-tone resist material; (f, g) remove hard mask in areas no longer protected by resist through wet-chemical or plasma etching. 22

Figure 8: General structure of polynorbornene. 27

Figure 9: Dynamic TGA thermogram for a typical polynorbornene, obtained at a heating rate of 10°C/min. 28

Figure 10: Various R-groups attached to the polynorbornene backbone: (a) Butyl; (b) Methyl Acetate; (c) Triethoxysilyl (TES); (d) Cyclolacrylate. 28

Figure 11: General chemical structure of a polycarbonate. 32

Figure 12: Structure of specific polycarbonate sacrificial materials investigated in this research. 32

Figure 13: Schematic of measurement of contact angle, α 42

Figure 14: Dynamic TGA thermograms of PNB-1 (90/10 butyl/triethoxysilyl PNB) at heating rates of 1, 5, and 10°C/min. 48

Figure 15: Dynamic TGA curves for PNB-2 (90/10 butyl/TES PNB), PNB-7 (50/50 norbornene/TES PNB), and PNB-14 (80/10/10 butyl/TES/cyclolacrylate PNB) obtained at a heating rate of 10°C/min in nitrogen. 56

Figure 16: Dynamic TGA curves for PNB-5 (methyl acetate PNB), PNB-6 (90/10 methyl acetate/TES PNB), PNB-10 (90/10 methyl acetate/cyclolacrylate PNB) and PNB-11 (80/10/10 methyl acetate/TES/cyclolacrylate PNB) obtained at a heating rate of 10°C/min in nitrogen. 57

Figure 17: Dynamic TGA curves for two compositions of butyl/cyclolacrylate polynorbornene: PNB-8 (90/10 butyl/cyclolacrylate PNB); and PNB-9 (80/20 butyl cyclolacrylate PNB) obtained at a heating rate of 10°C/min in nitrogen. 58

Figure 18: Dynamic TGA curves for three molecular weights of 80/10/10 methyl acetate/triethoxysilyl/cyclolacrylate polynorbornene obtained at a heating rate of 10°C/min in nitrogen. 59

Figure 19: Dynamic TGA thermograms obtained at a heating rate of 10°C/min for (a) PNB-5, methyl acetate homopolymer; (b) PNB-6, 90/10 methyl acetate/TES copolymer; (c) PNB-10, 90/10 methyl acetate/cyclolacrylate copolymer; and (d) PNB-12, 80/10/10 methyl acetate/ triethoxysilyl/cyclolacrylate terpolymer. 63

Figure 20: Dynamic TGA thermogram ramping 10°C/min in a nitrogen atmosphere for various polycarbonate sacrificial materials. 70

Figure 21: Dynamic TGA thermograms for PPC obtained at heating rates of 10, 5, 2, 1, and 0.5°C/min in (a) nitrogen and (b) air (40% relative humidity). 73

Figure 22: Comparison of dynamic TGA curves for the decomposition of PPC performed at heating rates of 0.5, 2, and 10°C/min in nitrogen and air environments. 75

Figure 23: Isothermal TGA thermograms for the decomposition of PPC at various hold temperatures in (a) nitrogen and (b) air (40% relative humidity). 77

Figure 24: Chemical structure of photo-acid generators used to catalyze polycarbonate decomposition. 88

Figure 25: Dynamic TGA thermogram performed at 1°C/min for: (a) PPC only; (b) PPC + 5 wt% PAG with no UV exposure; and (c) PPC + 5 wt% PAG + 1J/cm^2 UV exposure (240 nm). 88

Figure 26: Dynamic TGA curves ramping 10°C/min showing the effect of curing temperature on the decomposition of 90/10 butyl/triethoxysilyl polynorbornene. Samples were cured by ramping 5°C/min to the final temperature and held for 1 hour in nitrogen. 108

Figure 27: SEM image showing cracks in the top surface of a 140 µm wide patterned PNB line after removal of the Cr hard mask. 110

Figure 28: SEM micrographs of a 35 µm wide and 5 µm tall PNB feature etched using RIE conditions PNB-ETCH1 with (a) the 1 µm thick SiO_2 hard mask remaining, and (b) after removal of the hard mask. 111

Figure 29: SEM micrograph of the end portion of a 140 µm wide and 12 µm tall PNB feature etched using RIE conditions PNB-ETCH2 and a 2000 Å Al hard mask... 114

Figure 30: SEM micrograph of a 190 μm diameter circle etched into a 30 μm thick PNB film using recipe PNB-ETCH3. The Al hard mask is remaining on the sample... 114

Figure 31: Air-channel structures fabricated from 2 μm thick PNB sacrificial material features encapsulated in (a) SiO_2 and (b) SiN_x. 116

Figure 32: (a) Example of poor step coverage with PECVD SiO_2 and (b) the resulting damage to the overcoat upon cleaving of the sample. 119

Figure 33: Multilevel air-channels encapsulated in SiO_2. (a) two layers of air-channels fabricated with an offset (b) directly stacked air-channels 120

Figure 34: SEM image of 70 μm wide and 4 μm thick PNB pattern encapsulated with Ultradel 7501, before decomposition of the sacrificial material. 127

Figure 35: SEM images of (a) 35 μm wide and 9 μm tall air-channels with 15 μm spacing, and (b) a 140 μm wide and 5 μm tall air-channel with 70 μm spacing between channels, encapsulated in Amoco Ultradel 7501. At the smaller spacing size between air-channels shown in (a) the overcoat fills into the spaces and planarization occurs. 128

Figure 36: SEM image of a portion of a large air-gap 8 μm in height, 1 cm in width, and 1 cm in length encapsulated in Amoco Ultradel 7501. 129

Figure 37: 190 μm wide x 1 cm long air-gap fabricated with PI-2611 overcoat polyimide. 131

Figure 38: 190 μm wide x 1 cm long air-gap fabricated with PI-2734 overcoat polyimide. 131

Figure 39: 12 μm wide and 3 μm tall air-channels fabricated with PI-2734 overcoat polyimide 132

Figure 40: 140 μm wide air-gaps fabricated from a 3.6 μm thick PNB film and overcoated with 3 μm thick PI-2734. (a) Sample with laser-ablated vent holes and (b) sample with completely enclosed air-gap structures. 132

Figure 41: SEM cross-sectional image of 70 µm wide air-channels following the decomposition of 3.75 µm PNB overcoated with PI-2540 overcoat polyimide. 136

Figure 42: SEM images of following the decomposition of 5 µm PNB overcoated with PI-2771 overcoat polyimide and channel width of (a) 140 µm (b) 70 µm (c) 35 µm and (d) 15 µm. 137

Figure 43: SEM cross-sectional images following the decomposition of 5 µm PNB overcoated with PI-2555 overcoat polyimide and channel width of (a) 70 µm and (b) 15 µm. 139

Figure 44: SEM images following the completion of the air-gap fabrication process with Sumitomo Bakelite CRC-8650 PBO overcoat material. (a) Cross-sectional view showing an area with original PNB film 70 µm wide and 5 µm thick. (b) Cross-sectional view of an area with original PNB film 140 µm wide and 5 µm thick. .. 141

Figure 45: SEM images following the completion of the air-gap fabrication process with FLARE (Honeywell) overcoat material. (a) Cross-sectional view showing an area with original PNB film 35 µm wide and 3.9 µm thick. (b) Top surface perspective view of an area with original PNB film 70 µm wide and 3.9 µm thick. 142

Figure 46: Corner of a 35 µm wide PNB feature overcoated with FLARE. 144

Figure 47: SEM images following the completion of the air-gap fabrication process with 2 µm thick Parylene-N overcoat material. (a) Cross-sectional view showing an area with original PNB film 70 µm wide and 3.6 µm thick following a 1.5 hour decomposition at 400^{o}C. (b) Cross-sectional view showing an area with original PNB film 15 µm wide and 3.6 µm thick following a 2 hour decomposition at 375^{o}C. 146

Figure 48: SEM images of air-gaps overcoated with 5000 Å SiO_2 and 9 µm PI-2771. The with of the air-gaps shown are: (a) 15 µm; (b) 35 µm; (c) 70 µm; and (d) 140 µm. 155

Figure 49: SEM cross-sectional image of a 35 µm air-gap overcoated with 5000 Å SiO_2 and 4 µm PI-2555..... 155

Figure 50: SEM images of air-gaps (a) 35 μm wide, and (b) 70 μm wide, overcoated with 5000 Å SiO_2 and 10 μm PBO-8650. 156

Figure 51: SEM cross-sectional images of air-gaps overcoated with PI-2771 and SiO_2. Dimensions are: (a) width:140 μm, overcoat: 9 μm PI-2771 and 5000 Å SiO_2; (b) width: 35 μm, overcoat:9 μm PI-2771 and 5000 Å SiO_2; (c) width: 140 μm, overcoat: 9 μm PI-2771 and 2 μm SiO_2; and (d) width: 15 μm, overcoat:9 μm PI-2771 and 2 μm SiO_2. 158

Figure 52: SEM cross-sectional images of a 140 μm wide (a) collapsed channel and (b) air-gap, overcoated with 10 μm PBO CRC-8650 and 2 μm SiO_2. 159

Figure 53: SEM image of two air-gaps 4 μm in height and 70 μm in width with an electroplated Cu line between them and overcoated with Ultradel 7501 polyimide. 165

Figure 54: Air-channels fabricated between copper lines that are insulated from the air-channel and overcoated with Ultradel 7501 Polyimide 165

Figure 55: SEM image of a 70 μm wide air-channel fabricated with PNB-8 (norbornene/triethoxysilyl norbornene copolymer) and overcoated with PECVD SiO_2 deposited at 275°C. 169

Figure 56: SEM images of 4 μm tall air-gaps and (a) 15 μm wide, and (b) 35 μm wide, fabricated with methyl acetate polynorbornene (PNB-5) and overcoated with SiO_2 deposited at 300°C. 170

Figure 57: SEM image of 15 μm wide air-channels fabricated from solution PNB- 8-S2 (90/10 butyl/cyclolacrylate norbornene copolymer with photoinitiator) and overcoated with 9 μm Ultradel 7501 polyimide. The PNB features were patterned via non-photosensitive processing. 173

Figure 58: SEM image of a 105 μm wide air-channel fabricated from solution PNB- 8-S2 (90/10 butyl/cyclolacrylate norbornene copolymer with photo-initiator) and overcoated with 2 μm PECVD SiO_2. The PNB features were patterned photosensitive processing. 173

Figure 59: Optical microscope image showing the top surface of 140 μm wide PEC features following RIE etching and Ti/Au hard mask removal. 181

Figure 60: (a) Top-surface and (b) cross-sectional SEM images of patterns formed in a 5.4 μm thick PPC sacrificial layer, following RIE etching and Ti hard mask removal. 182

Figure 61: (a) Top-surface and (b) cross-sectional SEM images of patterns formed in a 5.3 μm thick PPC sacrificial layer, following RIE etching and Cr hard mask removal. 182

Figure 62: Optical microscope image of 70 μm wide PNC features following RIE etching and Al hard mask removal. Poor adhesion results in an irregular pattern and wrinkling of the features. 183

Figure 63: (a) Cross-sectional and (b) top-surface SEM images of features patterned into a 6.8 μm thick PNC film following RIE etching and Al hard mask removal. 183

Figure 64: Fabrication process flow for the fabrication of air-gaps using photosensitive polycarbonate sacrificial materials. 185

Figure 65: Optical microscope image of a pattern formed from a solution of 12 wt% PPC in anisole with 5 wt% DPI-TPFPB based on dry polymer. Mask dimensions are lines = 70 μm, and spaces = 35 μm. 185

Figure 66: SEM images of (a) 25 μm wide and (b) 130 μm wide air-channels fabricated from a 4.8 μm thick PEC sacrificial layer and overcoated with PECVD SiO_2 deposited at 200°C. The original mask dimensions are 35 μm and 140 μm. 191

Figure 67: SEM images of air-channels fabricated from an 8.0 μm thick PCC overcoated with PECVD SiO_2 deposited at 200 °C. The features on the mask had width dimensions of: (a) 140 μm; (b) 70 μm; (c) 35 μm; and (d) 15 μm. The resulting channels are about 10 μm less in width from undercutting during RIE etching. 192

Figure 68: SEM images of air-channels fabricated from a 6.8 μm thick PNC sacrificial layer and overcoated with PECVD SiO_2 deposited at 200°C. The features on the mask had width dimensions of: (a) 70 μm; and (b) 35 μm. The resulting dimensions are smaller from undercutting during RIE etching. 193

Figure 69: SEM images of air-channels fabricated from a 4.9 μm thick PEC sacrificial layer overcoated with Avatrel 2000P dielectric polymer. The width of the air-channels on the mask are: (a) 35 μm; and (b) 140 μm wide. The overcoat collapsed into the channel in (b). 199

Figure 70: SEM images of air-channels fabricated from a 5.3 μm thick PPC sacrificial layer and overcoated with Cyclotene 3022-57 BCB. Air-channels were fabricated from PPC patterned into channels using a mask with features (a) 140 μm wide and (b) 70 μm wide. 200

Figure 71: SEM image of a 140 μm wide microchannel fabricated from a 1.5 μm thick layer of PEC sacrificial material and overcoated with LMB-7081 epoxy. 201

Figure 72: SEM images showing the resulting structures from the decomposition of 5.3 μm thick PCC patterned into 35 μm wide air-channels and overcoated with polyimide PI-2771..... 205

Figure 73: SEM image showing the resulting structures from the decomposition of 5.3 μm thick PCC patterned into 140 μm wide air-channels and overcoated with polyimide PI-2771..... 206

Figure 74: Cross-sectional SEM image showing the resulting structures from the decomposition of 5.3 μm thick PCC patterned into 140 μm wide air-channels and overcoated with PBO CRC-8250. 206

Figure 75: SEM image showing the resulting structures from the decomposition of 5.3 μm thick PCC patterned into 70 μm wide air-channels and overcoated with PBO CRC-8650. 207

Figure 76: Micrograph of a 70 μm wide air-channel fabricated from 5 μm photo-patterned PPC overcoated with 7800 Å PECVD SiO_2 deposited at 100°C. 211

Figure 77: SEM image of a 70 μm wide air-channel fabricated using a 5.45 μm thick photo-patterned PPC encapsulated in 8 μm Avatrel 2000P dielectric polymer. 211

Figure 78: SEM micrograph showing two air-channels fabricated with photosensitive PCC sacrificial material and overcoated with PECVD SiO_2. 212

Figure 79: Dynamic thermograms for the decomposition of unencapsulated PNB sacrificial material using TGA sample pans coated with various materials at a heating rate of 10°C/min in nitrogen. 228

Figure 80: Dynamic TGA at a heating rate of 3°C/min for unencapsulated PNB with and without a 1 hour hold at 350°C. 230

Figure 81: Dynamic TGA at heating rates of 1, 3, and 10°C/min for polyimide PI-2611 following a 1 hour cure at 350°C. 230

Figure 82: Dynamic thermogram obtained at a heating rate of 1°C/min for unencapsulated PNB and PNB encapsulated in PI-2611, following 1 hour at 350°C. 232

Figure 83: Dynamic thermogram obtained at a heating rate of 3°C/min for unencapsulated PNB and PNB encapsulated in PI-2611, following 1 hour at 350°C. 232

Figure 84: Dynamic thermogram obtained at a heating rate of 10°C/min for unencapsulated PNB and PNB encapsulated in PI-2611, following 1 hour at 350°C. 233

Figure 85: Thermogram from isothermal TGA at a hold temperature 400°C for unencapsulated PNB with and without a 1 hour hold at 350°C. 239

Figure 86: Weight percentage as a function of time for PI-2611 held for 300 min at (a) 400°C and (b) 425°C; PI-2611 following a 1 hour hold at 350°C 239

Figure 87: Isothermal thermograms of unencapsulated PNB and PNB encapsulated in polyimide PI-2611 at hold temperatures of (a) 400°C and (b) 425°C. 240

Figure 88: Calculated and experimental time/temperature profiles for the decomposition of PNB at a constant rate of conversion of 5 %/min. 273

Figure 89: Calculated and experimental time/temperature profiles for the decomposition of PNB at a constant rate of conversion of 2 %/min. 273

Figure 90: Calculated and experimental time/temperature profiles for the decomposition of PNB at a constant rate of conversion of 1 %/min. 274

Figure 91: Calculated and experimental time/temperature profiles for the decomposition of PNB at a constant rate of conversion of 0.5 %/min. 274

Figure 92: Calculated and experimental time/temperature profiles for the decomposition of PNB at a constant rate of conversion of 0.1 %/min. 275

Figure 93: SEM images of air-channels decomposed at a rate of 0.1 % conversion/min from original PNB thickness of (a) 10 µm (b) 20 µm and (c) 30 µm 280

Figure 94: SEM images of air-channels decomposed at a rate of 1 % conversion/min from original PNB thickness of (a) 10 µm (b, c) 20 µm and (d, e) 30 µm 281

Figure 95: SEM images of air-channels decomposed at a rate of 5 % conversion/min from original PNB thickness of (a) 10 µm (b) 20 µm and (c) 30 µm. 282

Figure 96: SEM image demonstrating the s-shape of an Au electroplated lead designed for lateral compliance in SoL packaging technology. 285

Figure 97: Diagram demonstrating how SoL CWLP allows simultaneous contact to all I/O across a wafer through z-axis (out-of-plane) compliance. 285

Figure 98: Schematic showing the top view and side view of an SoL interconnect with (a) a rectangular air-gap and (b) a dome-shaped air-gap. 286

Figure 99: Schematic of the fabrication process sequence for SoL with an embedded air-gap: (a) chip fabrication is complete; the die-pads are exposed; (b) the sacrificial polymer film is applied and patterned; (c) the overcoat polymer is deposited and encapsulates the sacrificial polymer layer; (d) the sacrificial material is thermally decomposed to form air-gaps; (e) vias are etched in the overcoat polymer to expose the die pads; (f) the compliant leads are electroplated; (g) the chip solder bumps are fabricated. 287

Figure 100: SEM images of (a) flat and (b) dome-shaped air-gaps for SoL, following decomposition of the sacrificial polymer (step (d) in Figure 99) 292

Figure 101: SEM images of (a) the top surface and (b) a cross-section of vias etched into 10 µm thick PI-2611 overcoat polyimide layer. 293

Figure 102: SEM image of a SoL package containing 1000 leads/cm^2, fabricated with Ultradel 7501 polyimide and embedded air-gaps under each lead. 296

Figure 103: SEM image of a SoL I/O structure with an embedded air-gap. The structure was fabricated using PNB sacrificial polymer, Ultradel 7501 overcoat polyimide, and electroplated Cu leads. 296

Figure 104: SEM image of a SoL package containing 3000 leads/cm^2, fabricated with polyimide PI-2611 and air-gaps under each electroplated Au lead. 297

Figure 105: SEM image of a SoL I/O structure with an embedded air-gap. The structure was fabricated using PNB sacrificial polymer, overcoat polyimide PI-2611, and Au electroplated leads. 297

Figure 106: Photoresist electroplating mold for SoL lead fabrication on an air-gap with a maximum height of 30 µm. 305

Figure 107: Leads with enlarged contact pads due to overplating of Au in the photoresist mold for lead electroplating. 306

Figure 108: Poorly formed leads on air-gaps due to incomplete development of the photoresist mold for lead electroplating. 306

Figure 109: Optical microscope photograph of the top surface of air-gaps for SoL. The red arrow indicates the path for a profilometry scan across the center of a row of air-gaps. 307

Figure 110: Profilometry scan performed across the center of a row of air-gaps to measure height uniformity. 308

Figure 111: SEM images of various shape air-gaps from sample MECH-1 overcoated with 2.4 µm thick PI-2734. The various shapes shown are: (a) rectangle1: 190 x 590 µm and (b) circle 1: 190 µm diameter. 323

Figure 112: SEM images of various shape air-gaps from sample MECH-2 overcoated with 7.4 µm thick PI-2734. The various shapes shown are: (a) circle 1:190 µm diameter; ellipse1 190 × 225 µm; and rectangle 2: 190 × 9940 µm; (b) a cross sectional image of rectangle 1: 190 × 590 µm; (c) rectangle 1: 190 × 590 µm; and (d) circle 1: 190 µm diameter. 323

Figure 113 SEM images of the various shape air-gaps from sample MECH-3 overcoated with 7.4 μm thick PI-2734. The various shapes include: (a) circle 1: 190 μm diameter; (b) rectangle 1: 190 × 590 μm; (c) square 1: 190 × 190 μm; and (d) a cross sectional image of rectangle 2: 190 × 9940 μm. 324

Figure 114: SEM images of the various shape air-gaps from sample MECH-4 overcoated with PI-2611. The various shapes include: (a) circle 1: 190 μm diameter; (b) rectangle 2: 190 × 9940 μm; (c) square 1: 190 × 190 μm; and (d) a cross sectional image of rectangle 1: 190 ×590 μm. 325

Figure 115: 3-D surface profile of a 190 μm dia. circular air-gap on sample MECH-1.326

Figure 116: 3-D surface profile of a 190 μm dia. circular air-gap on sample MECH-2.326

Figure 117: 3-D surface profile of a 190 μm dia. circular air-gap on sample MECH-3.327

Figure 118: 3-D surface profile of a 190 μm dia. circular air-gap on sample MECH-4.327

Figure 119: Linear force-displacement curve for an air-gap on MECH-2 with dimensions of Rectangle-1 (190 × 590 μm). The indent was performed with a 200 μm tip at a rate of 2000 nm/s, and a 5 s hold at maximum displacement. 329

Figure 120: Force-displacement curves for three MECH-1 air-gaps with dimensions of Rectangle 1 (190 × 590 μm) indented with a 50 μm conical tip to a depth of 20 μm at a displacement rate of 2000 nm/s and a 5 s hold at maximum displacement. 331

Figure 121: Force-displacement curves for five MECH-1 air-gaps with dimensions of Rectangle 1 (190 × 590 μm) indented with a 200 μm spherical tip to a depth of 10 μm at a displacement rate of 1000 nm/s and a 5 s hold at maximum displacement. 331

Figure 122: Force-displacement curves for two MECH-2 air-gaps with dimensions of Rectangle 1 (190 × 590 μm) indented with a 200 μm spherical tip to a depth of 10 μm at a displacement rate of 1000 nm/s and a 5 s hold at maximum displacement. 332

Figure 123: Force-displacement curves for MECH-4 air-gaps with dimensions of Rectangle 1 (190 × 590 μm) indented 20 μm with a 20 μm radius conical tip at displacement rates of 10000, 2000, and 1000 nm/s. 334

Figure 124: Force-displacement curves for MECH-4 air-gaps with dimensions of Rectangle 2 (190 × 9940 μm) indented 20 μm with a 20 μm radius conical tip at a displacement rates of 2000 nm/s. Hold times at maximum displacement were 5 and 60 s. 334

Figure 125: Force-displacement curves for MECH-1 air-gaps with dimensions of Rectangle 1 (190 × 590 μm) indented with a 200 μm radius spherical tip to maximum displacements of 10, 20, and 30 μm. The displacement rate varies to create a 10 s load and unload, with a 5 s hold at maximum displacement. 336

Figure 126: Force-displacement curves for MECH-3 air-gaps with dimensions of Rectangle 1 (190 × 590 μm) indented with a 50 μm radius conical tip to maximum displacements of 10, 20, and 30 μm. The displacement rate varies to create a 10 s load and unload, with a 5 s hold at maximum displacement. 336

Figure 127: Force-displacement curves for MECH-4 air-gaps with dimensions of Rectangle 1 (190 × 590 μm) indented with a 20 μm conical tip to maximum displacements of 10, 20, and 30 μm. The displacement rate varied to create a 10 s load and unload, with a 5 s hold at maximum displacement. 339

Figure 128: Optical images of a MECH-1, Rectangle-1 air-gap (190 × 590 μm) (a) before indentation, and (b) after a 30 μm indentation with a 200 μm spherical tip..... 340

Figure 129: Optical images of a MECH-4, Rectangle-1 air-gap (190 × 590 μm) (a) before indentation, and (b) after a 30 μm indentation with a 200 μm spherical tip..... 340

Figure 130: Force-displacement curves for MECH-3 air-gaps with dimensions of Rectangle-1 indented with a 20 μm conical tip and a 50 μm conical tip. The displacement rate is 1000 nm/s to a maximum displacement of 10 μm and a 5 s hold at maximum displacement. 343

Figure 131: Force-displacement curves for MECH-1 air-gaps with dimensions of Rectangle-1 indented with a 50 μm radius conical tip and a 200 μm spherical tip. The displacement rate is 1000 nm/s to a maximum displacement of 10 μm and a 5 s hold at maximum displacement. 343

Figure 132: Force-displacement curves for MECH-1 air-gaps with dimensions of Rectangle-1 indented with a 50 μm radius conical tip and a 200 μm spherical tip. The displacement rate is 3000 nm/s to a maximum displacement of 30 μm and a 5 s hold at maximum displacement. 344

Figure 133: Force-displacement curves for MECH-2 air-gaps with dimensions of Square-1 indented with a 50 μm conical tip and a 200 μm spherical tip. The displacement rate is 2500 nm/s to a maximum displacement of 25 μm and a 5 s hold at maximum displacement. 344

Figure 134: Force-displacement curves for MECH-4 air-gaps with dimensions of Square-1 indented with a 20 μm conical tip and a 200 μm spherical tip. The displacement rate is 1000 nm/s to a maximum displacement of 10 μm and a 5 s hold at maximum displacement. 345

Figure 135: Force-displacement curves from MECH-2 air-gaps with dimensions of Square-1 indented with a 50 μm conical tip and a 200 μm spherical tip. The displacement rate is 2500 nm/s to a maximum displacement of 25 μm and a 5 s hold at maximum displacement. 345

Figure 136: Comparison of force-displacement curves for MECH-4 air-gaps with and without a hole. The air-gaps have dimensions of Circle-1 (190 μm dia.). The indentation is performed with a 200 μm spherical tip, a displacement rate of 1000 nm/s to a maximum displacement of 10 μm, and a 5 s hold at maximum displacement. 346

Figure 137: Comparison of force-displacement curves for Rectangle-1 air-gaps (190 × 590 μm) which vary in PI-2734 overcoat thickness. The indentation is performed with a 200 μm radius spherical tip, a displacement rate of 1000 nm/s to a maximum displacement of 10 μm, and a 5 s hold at maximum displacement. 349

Figure 138: Comparison of force-displacement curves for air-gaps with different overcoat material properties. The Rectangle-1 air-gaps (190 × 590 μm) are from samples MECH-2 and MECH-4. 349

Figure 139: Comparison of force-displacement curves for differently shaped air-gaps from sample MECH-4, indented to 10 μm with a 200 μm radius spherical tip. The indentation parameters are a displacement rate of 1000 nm/s, and a 5 s hold at maximum displacement. 350

Figure 140: Bottom view of a 190 × 190 μm square air-gap model created using CoventorWare. 354

Figure 141: Top view of the displacement magnitude as a function of position for a 140 MPa pressure force applied to a 20 × 20 μm square area in the center of a 190 × 190 μm square air-gap. 355

Figure 142: Bottom view of mises stress as a function of position for a 140 MPa pressure force applied to a 20 × 20 μm square area in the center of a 190 × 190 μm square air-gap 356

Figure 143: Comparison between experimental data and the CoventorWare model results for square and circular air-gaps from sample MECH-2..... 358

Figure 144: Maximum z-axis displacement as a function of overcoat thickness for a 140 MPa pressure force applied to a 20 × 20 μm square at the center of a 190 × 190 μm square or a 190 μm diameter circle air-gap. 358

Figure 145: Design space for maximum compliance and maximum deflection of air-gaps, limited by fabrication capability. 362

Figure A.1: Analysis plot to determine the activation energy for the decomposition of PPC in nitrogen from dynamic TGA.....369

Figure A.2: Analysis plot to determine the activation energy for the decomposition of PPC in air from dynamic TGA.....380

Figure A.3: dW/dt as a function of W for the decomposition of PPC in nitrogen at various heating rates.....373

Figure A.4: dW/dt as a function of W for the decomposition of PPC in air at various heating rates.....374

Figure A.5: dW/dt corrected for temperature as a function of W for the decomposition of PPC in nitrogen at various heating rates.....375

Figure A.6: dW/dt corrected for temperature as a function of W for the decomposition of PPC in air at various heating rates.....376

Figure A.7: The determination of RF for the decomposition of PPC in nitrogen at constant heating rates of 0.5, 1, 2, 5, and 10^{o}C/min.....377

Figure A.8: The determination of RF for the decomposition of PPC in air at constant heating rates of 0.5, 1, 2, 5, and 10^{o}C/min.....378

Figure A.9: The determination of n and A from dynamic TGA at 0.5^{o}C/min for the decomposition of PPC in nitrogen.....379

Figure A.10: The determination of n and A from dynamic TGA at 1^{o}C/min for the decomposition of PPC in nitrogen.....379

Figure A.11: The determination of n and A from dynamic TGA at 2^{o}C/min for the decomposition of PPC in nitrogen.....380

Figure A.12: The determination of n and A from dynamic TGA at 5^{o}C/min for the decomposition of PPC in nitrogen.....380

Figure A.13: The determination of n and A from dynamic TGA at 10^{o}C/min for the decomposition of PPC in nitrogen.....381

Figure A.14: The determination of n and A from dynamic TGA at 0.5^{o}C/min for the decomposition of PPC in air.....381

Figure A.15: The determination of n and A from dynamic TGA at 1^{o}C/min for the decomposition of PPC in air.....382

Figure A.16: The determination of n and A from dynamic TGA at 2^{o}C/min for the decomposition of PPC in air.....382

Figure A.17: The determination of n and A from dynamic TGA at 5^{o}C/min for the decomposition of PPC in air.....383

Figure A.18: The determination of n and A from dynamic TGA at 10^{o}C/min for the decomposition of PPC in air.....383

Figure A.19: Plot of ln(dW/dt) as a function of ln(W) to determine the uncorrected reaction order for the decomposition of PPC in nitrogen at various isothermal temperatures.....384

Figure A.20: Plot of ln(dW/dt) as a function of ln(W) to determine the uncorrected reaction order for the decomposition of PPC in air at various isothermal temperatures.....384

Figure A.21: dW/dt as a function of W for the decomposition of PPC in nitrogen at various isothermal temperatures.....385

Figure A.22: dW/dt as a function of W for the decomposition of PPC in air at various isothermal temperatures.....386

Figure A.23: The determination of RF for the decomposition of PPC in nitrogen at isothermal temperatures.....387

Figure A.24: The determination of RF for the decomposition of PPC in air at isothermal temperatures.....388

Figure A.25: Plot of ln(dW/dt) as a function of ln(W-RF) to determine the reaction order and the reaction rate constant corrected with RF, for the decomposition of PPC in nitrogen at various isothermal temperatures.....389

Figure A.26: Plot of ln(dW/dt) as a function of ln(W-RF) to determine the reaction order and reaction rate constant corrected with RF, for the decomposition of PPC in air at various isothermal temperatures.....390

Figure A.27: The determination of E_a and A from isothermal TGA data of the decomposition of PPC at various temperatures in nitrogen.....391

Figure A.28: The determination of E_a and A from isothermal TGA data of the decomposition of PPC at various temperatures in air.....391

Figure A.29: Analysis plot to determine the activation energy for the decomposition of unencapsulated PNB in nitrogen, using instantantaneous heating rate values.....400

Figure A.30: Analysis plot to determine the activation energy for the decomposition of unencapsulated PNB in nitrogen, using the overall average heating rate values.....400

Figure A.31: Analysis plot to determine the activation energy for the decomposition of PNB encapsulated by polyimide PI-2611 in nitrogen, using instantaneous heating rate values.....401

Figure A.32: Analysis plot to determine the activation energy for the decomposition of PNB encapsulated by polyimide PI-2611 in nitrogen, using the overall average heating rate values…….....401

Figure A.33: dW/dt as a function of W for the decomposition of unencapsulated PNB in a nitrogen atmosphere at heating rates of 1, 3, and 10^{o}C/min.....402

Figure A.34: dW/dt as a function of W for the decomposition of PNB encapsulated by PI-2611 and in a nitrogen atmosphere at heating rates of 1, 3, and 10^{o}C/min.....403

Figure A.35: dW/dt corrected for temperature as a function of W for the decomposition of unencapsulated PNB in a nitrogen atmosphere at heating rates of 1, 3, and 10^{o}C/min.....404

Figure A.36: *d*W/*d*t corrected for temperature as a function of W for the decomposition of PNB encapsulated by PI-2611 and decomposed in a nitrogen atmosphere at heating rates of 1, 3, and 10°C/min.....405

Figure A.37: The determination of RF for the constant heating rate decomposition of unencapsulated PNB in nitrogen using instantaneous heating rate values.....406

Figure A.38: The determination of RF for the constant heating rate decomposition of PNB encapsulated by PI-2611 using overall average heating rate values.....407

Figure A.39: The determination of RF for the constant heating rate decomposition at 1 and 10°C/min of PNB encapsulated by PI-2611 using instantaneous heating rate values.....408

Figure A.40: The determination of RF for the constant heating rate decomposition at 3°C/min of PNB encapsulated by PI-2611 using instantaneous heating rate values.....409

Figure A.41: The determination of RF for the constant heating rate decomposition at 1 and 10°C/min of PNB encapsulated by PI-2611 using overall average heating rate values.....410

Figure A.42: The determination of RF for the constant heating rate decomposition at 3°C/min of PNB encapsulated by PI-2611 using overall average heating rate values.....411

Figure A.43: The determination of n and A from sample S-CD10-1, dynamic TGA of unencapsulated PNB at a constant heating rate of 10°C/min in nitrogen.....412

Figure A.44: The determination of n and A from sample S-CD3-1, dynamic TGA of unencapsulated PNB at a constant heating rate of 3°C/min in nitrogen.....412

Figure A.45: The determination of n and A from sample S-CD3-2, dynamic TGA of unencapsulated PNB at a constant heating rate of 3°C/min in nitrogen.....413

Figure A.46: The determination of n and A from sample S-CD3-3, dynamic TGA of unencapsulated PNB at a constant heating rate of 3°C/min in nitrogen.....413

Figure A.47: The determination of n and A from sample S-CD1-1, dynamic TGA of unencapsulated PNB at a constant heating rate of 1°C/min in nitrogen.....414

Figure A.48: The determination of n and *k* from the average PNB weight of sample SP-CD10-1, dynamic TGA of PNB encapsulated by PI-2611 at a constant heating rate of 10°C/min in nitrogen.....414

Figure A.49: The determination of n and *k* from the lower limit on PNB weight of sample SP-CD10-1, dynamic TGA of PNB encapsulated by PI-2611 at a constant heating rate of 10°C/min in nitrogen.....415

Figure A.50: The determination of n and *k* from the upper limit on PNB weight of sample SP-CD10-1, dynamic TGA of PNB encapsulated by PI-2611 at a constant heating rate of 10°C/min in nitrogen.....415

Figure A.51: The determination of n and *k* from the average PNB weight of sample SP-CD3-1, dynamic TGA of PNB encapsulated by PI-2611 at a constant heating rate of 3°C/min in nitrogen.....416

Figure A.52: The determination of n and *k* from the lower limit on PNB weight of sample SP-CD3-1, dynamic TGA of PNB encapsulated by PI-2611 at a constant heating rate of 3°C/min in nitrogen.....416

Figure A.53: The determination of n and *k* from the upper limit on PNB weight of sample SP-CD3-1, dynamic TGA of PNB encapsulated by PI-2611 at a constant heating rate of 3°C/min in nitrogen.....417

Figure A.54: The determination of n and *k* from the average PNB weight of sample SP-CD3-2, dynamic TGA of PNB encapsulated by PI-2611 at a constant heating rate of 3°C/min in nitrogen.....417

Figure A.55: The determination of n and *k* from the lower limit on PNB weight of sample SP-CD3-2, dynamic TGA of PNB encapsulated by PI-2611 at a constant heating rate of 3°C/min in nitrogen.....418

Figure A.56: The determination of n and *k* from the upper limit on PNB weight of sample SP-CD3-2, dynamic TGA of PNB encapsulated by PI-2611 at a constant heating rate of 3°C/min in nitrogen.....418

Figure A.57: The determination of n and *k* from the average PNB weight of sample SP-CD3-3, dynamic TGA of PNB encapsulated by PI-2611 at a constant heating rate of 3°C/min in nitrogen.....419

Figure A.58: The determination of n and *k* from the lower limit on PNB weight of sample SP-CD3-3, dynamic TGA of PNB encapsulated by PI-2611 at a constant heating rate of 3°C/min in nitrogen.....419

Figure A.59: The determination of n and *k* from the upper limit on PNB weight of sample SP-CD3-3, dynamic TGA of PNB encapsulated by PI-2611 at a constant heating rate of 3°C/min in nitrogen.....420

Figure A.60: The determination of n and *k* from the average PNB weight of sample SP-CD1-1, dynamic TGA of PNB encapsulated by PI-2611 at a constant heating rate of 1°C/min in nitrogen.....420

Figure A.61: The determination of n and *k* from the lower limit on PNB weight of sample SP-CD1-1, dynamic TGA of PNB encapsulated by PI-2611 at a constant heating rate of 1°C/min in nitrogen.....421

Figure A.62: The determination of n and *k* from the upper limit on PNB weight of sample SP-CD1-1, dynamic TGA of PNB encapsulated by PI-2611 at a constant heating rate of 1°C/min in nitrogen.....421

Figure A.63: *d*W/*d*t as a function of W for the decomposition of unencapsulated PNB in a nitrogen atmosphere at isothermal temperatures of 400°C and 425°C.....422

Figure A.64: *d*W/*d*t as a function of W for the decomposition of PNB encapsulated by polyimide PI-2611 at isothermal temperatures of 400°C and 425°C.....423

Figure A.65: The determination of RF for the decomposition of unencapsulated PNB in nitrogen at an isothermal temperature of 400°C.....424

Figure A.66: The determination of RF for the decomposition of unencapsulated PNB in nitrogen at an isothermal temperature of 425°C.....425

Figure A.67: Plot of ln(*d*W/*d*t) as a function of ln(W) or ln(W-RF) to determine the reaction order and reaction rate constant for the isothermal decomposition of unencapsulated PNB in nitrogen at 400°C.....426

Figure A.68: Plot of ln(*d*W/*d*t) as a function of ln(W) or ln(W-RF) to determine the reaction order and reaction rate constant for the isothermal decomposition of unencapsulated PNB in nitrogen at 425°C.....427

Figure A.69: The determination of RF for the decomposition of PNB encapsulated by PI-2611 in nitrogen at a constant temperature of 400°C.....428

Figure A.70: The determination of RF for the decomposition of PNB encapsulated by PI-2611 in nitrogen at a constant temperature of 425°C.....429

Figure A.71: Plot of ln(*d*W/*d*t) as a function of ln(W) or ln(W-RF) to determine the reaction order and reaction rate constant for the isothermal decomposition of PNB encapsulated by PI-2611 in nitrogen at 400°C.....430

Figure A.72: Plot of ln(*d*W/*d*t) as a function of ln(W) or ln(W-RF) to determine the reaction order and reaction rate constant for the isothermal decomposition of PNB encapsulated by PI-2611 in nitrogen at 425°C.....431

Figure A.73: The determination of E_a and A from isothermal TGA data of the decomposition of (1) unencapsulated PNB and (2) PNB encapsulated by PI-2611 at temperatures of 400°C and 425°C.....432

Figure B.1: Spin-speed curve for solution PNB-1-S1: 22.04 wt% 90/10 butyl/ triethoxysilyl polynorbornene (MW = 283K) in mesitylene. Softbaking conditions are a 120°C hotplate bake for 5 min.....434

Figure B.2: Spin-speed curves for solutions of PNB-2: 90/10 butyl/triethoxysilyl polynorbornene (MW = 182K) in mesitylene. PNB-2-S1 is 30.80 wt% polymer and solution PNB-2-S2 is 20.0 wt% polymer. Softbaking conditions are a 120°C hotplate bake for 5 min. 434

Figure B.3: Spin-speed curve for solution PNB-3-S1: 21.40 wt% 90/10 butyl/ triethoxysilyl polynorbornene (MW = 355K) in mesitylene. Softbaking conditions are a 120°C hotplate bake for 5 min.....435

Figure B.4: Spin-speed curve for solution PNB-4-S1: 9.80 wt% methyl acetate polynorbornene (MW = 261K) in anisole. Softbaking conditions are a 100°C hotplate bake for 3 min.....435

Figure B.5: Spin-speed curves for solutions of PNB-5: methylacetate polynorbornene (MW = 325K). PNB-5-S1 is 14.93 wt% polymer in anisole and solution PNB-5-S2 is 9.85 wt% polymer in toluene. Softbaking conditions are a 100°C hotplate bake for 3 min.....436

Figure B.6: Spin-speed curves for solutions of PNB-6: 90/10 methyl acetate/ triethoxysilyl polynorbornene (MW = 183K). PNB-6-S1 is 9.95 wt% polymer in anisole and solution PNB-6-S2 is 14.93 wt% polymer in toluene. Softbaking conditions are a 100°C hotplate bake for 3 min.....436

Figure B.7: Spin-speed curve for solution PNB-7-S1: 9.80 wt% 50/50 polynorbornene/triethoxysilyl polynorbornene (MW = 412K) in mesitylene. Softbaking conditions are a 120°C hotplate bake for 3 min.....437

Figure B.8: Spin-speed curves for solutions of PNB-8: 90/10 butyl/cyclolacrylate polynorbornene (MW = 300K) in mesitylene. PNB-8-S1 is 9.95 wt% polymer and solution PNB-8-S2 is 15.90 wt% polymer. Softbaking conditions are a 120°C hotplate bake for 3 min.....437

Figure B.9: Spin-speed curve for solution PNB-9-S1: 16.40 wt% 80/20 butyl/cyclolacrylate polynorbornene (MW = 213K) in trichloroethane. Softbaking conditions are a 100°C hotplate bake for 3 min.....438

Figure C.8: Softbaked film thickness as a function of spin speed for Promerus Avatrel 2000P Dielectric Polymer (45 wt.% solids).....448

SUMMARY

Air-gaps or air-channels formed in a thin encapsulating film have numerous applications in the microsystems industry including: a mechanism to reduce the dielectric constant of an interlayer dielectric; a critical component for micro- and nano-fluidic devices; and a building block in micromachining and the fabrication of micro-electro-mechanical devices. While significant advancements have been made in recent years for the design and fabrication of air-gaps and air-channels, more effort is required to improve the techniques currently used to fabricate these structures. Many of the current air-gap fabrication processes require extremely complex processing, have poor control over the air-gap geometry, are not compatible with a wide variety of devices and materials, and cannot be extended to usage in all applications. The research presented here has two main objectives: (1) the development and investigation of a new air-gap fabrication method capable for use in all applications; and (2) the integration of air-gaps into a specific application: air-gaps for use in a compliant wafer level packaging technology.

Chapter 1 communicates the need for air-gaps and the objectives of the research in detail. Chapter 2 summarizes the current state of air-gap technology. Also included in Chapter 2 is a brief description of integrated-circuit packaging requirements for the future. Details of the compliant wafer level packaging technology are presented along with a description of how air-gaps may fit into this technology to meet those future requirements.

The specific details of the research begin in Chapter 3 with a general description of the process flow developed for the fabrication of air-gaps via thermally decomposable

sacrificial polymers. The chemistry and the properties of the various materials, and the analytical equipment and procedures used in the research are introduced. Chapter 4 discusses the thermal decomposition of sacrificial materials, and how changes in the chemistry affect the decomposition. The results of kinetic analysis via thermogravimetric experiments, and surface characterization following the decomposition are presented.

The focus of Chapters 5 and 6 is the description of the specific procedures and the results of air-gaps formed using thermally decomposable sacrificial polymers. Various materials are selected as potential candidates to form air-gaps based on their thermal and mechanical properties. Each of these materials is then investigated to link properties of the materials with success or failure in the air-gap fabrication process. Chapters 4, 5, and 6 build a foundation for the information presented in Chapter 7, which discusses the decomposition process of a sacrificial material encapsulated in a dielectric, and optimization using kinetic parameters of the overall decomposition reaction.

Chapter 8 targets the integration of air-gaps into Sea of Leads compliant wafer level packaging technology. The design concept of three-dimensionally compliant packaging technology is followed by the details of the fabrication process developed in order to integrate air-gaps into the compliant package. The critical issues resulting from the addition of air-gaps into the process are then discussed. The goals of Chapter 9 are: (1) to evaluate factors influencing the z-axis mechanical performance of the air-gaps; and (2) determine the feasibility of achieving the necessary z-axis compliance through the incorporation of air-gaps in SoL I/O technology. The model calculations combined with the known limitations of fabrication are applied to provide a design space for maximum out-of-plane mechanical movement and the compliance of the air-gaps.

CHAPTER 1

INTRODUCTION

Air-gaps or air-channels formed in a thin encapsulating film have numerous applications in the microsystems industry. The formation of air-gaps was originally proposed as a means to reduce the dielectric constant (κ) of an interlayer dielectric material for electronic devices [1-3]. However, applications of air-gaps have also been realized in microelectronics packaging, microfluidic devices, and micro electro-mechanical systems (MEMS). Various microfluidic and MEMS devices have been disclosed in the recent years that offer the potential to improve our way of life significantly by impacting the medical, pharmaceutical, environmental, electrical, and chemical technologies [4-8]. Improvements or novel methods to fabricate the air-channels or air-gaps in these devices could considerably advance these technologies.

An exponential increase in the performance and productivity of silicon technology over the past four decades has produced a need for ultra-low dielectric constant materials. As transistor and feature size on integrated circuits (IC's) continues to shrink, the number and density of interconnect wiring levels must increase. Consequently, the delay caused by resistance (R) in the metal wiring and capacitance (C) between these metal lines becomes an ever-increasing problem. One way to reduce this RC delay is by reducing the resistivity of the metal used to form the interconnects. Aluminum was the standard material used by industry until 1998. At that time, a switch to copper as the standard metal occurred. Since copper is the lowest resistivity metal, there are no alternate metal

systems to produce large changes in resistance. Another way to reduce RC delay is by lowering the effective dielectric constant of the inter-level dielectric material. Several classes of low-κ materials are currently under investigation, including fluorinated inorganics, porous silicas and polymers, and several organic materials. However, many of these materials pose significant challenges to reliability, mechanical stability, and integration. As an alternative, air or vacuum (κ = 1.0), can dramatically reduce signal delay and crosstalk between adjacent metal interconnects, allowing increased processing speed of devices. Several approaches have been demonstrated to fabricate sub-micron air-gaps between metal lines for electrical isolation [1-3, 9-15]. Modeling and electrical testing have shown air-gaps to provide a possible reduction in parasitic capacitance of 40-50% from a solid intralevel dielectric material, such as SiO_2 [1-2, 14].

Air-gaps or air-channels are also a critical component for micro- and nano-fluidic devices. Once air channels are fabricated, they are filled with fluids to function as mixers, heating or cooling systems, miniature chemical and biological reactors, high-resolution liquid crystal displays, or chromatographs for separations. The use of microelectronics processing equipment has spread far from silicon chip fabrication into the areas of machining, chemistry, and biology [4-8, 16]. The focus has shifted to the development of microscale total analysis systems (μTAS), which are miniature and often disposable systems designed to perform specialized analytical functions [16]. The miniaturization of these systems may facilitate more portable equipment, eliminate the large use of reagents, widen sensitivity, and also increase throughput by the integration of a large number of miniature systems on a single chip [16]. The dimensions of these systems range from 1 to 100 μm, well within the current technologies available in microsystems fabrication.

Air-gaps also have abundant utility in micromachining and MEMS devices. Miniature devices, such as actuators, sensors, pumps, nozzles, and valves, often contain moving parts that are released from the substrate or chambers containing air or fluids. Air-gap fabrication techniques have found widespread use as a release mechanism to form membranes and beams used in actuators, switches, and valves. Micro air-cavities can also be used as a mechanical means to mitigate problems due to excess thermal expansion or to increase the effective compliance of a material. Photoresist or other sacrificial materials are often used as a mold or release mechanism to fabricate the air-gaps in these MEMS devices.

Many of the current air-gap fabrication processes require extremely complex processing, have poor control over the air-gap geometry, are not compatible with a wide variety of devices and materials, and cannot be extended to usage in microfluidic devices and MEMS applications. One objective of this research was to develop and investigate a new air-gap fabrication method capable for use in all of these applications. This work was initiated by Zhao and Kohl at the Georgia Institute of Technology [9-12]. A model of the effective dielectric constant achieved using an air-gap as the intralevel dielectric and another material as the interlevel dielectric has previously been performed [10]. In a simple demonstration, polynorbornene sacrificial material was then used to fabricate sub-micron air-gaps as an ultra low-κ material between Cu interconnections with a SiO_2 capping layer [9-12]. This research goes well beyond these previous studies by focusing on the development and critical understanding of the processes and materials needed to form air-gaps. This work was not limited to polynorbornene, but also other polymeric sacrificial materials which are removed by thermal decomposition at a variety of

temperatures. The first goal was to develop an air-gap fabrication process which provides several important aspects as advantages over other currently existing processes including:

1. The ability to make completely enclosed air-gap structures with no fill holes or wet chemicals required;
2. A process performed entirely with semiconductor CMOS compatible techniques;
3. Excellent control over the air-gap geometry through lithography and photosensitivity;
4. Solvent and temperature compatibility with a wide range of substrates, encapsulating materials, and processing conditions;
5. Easy integration of metals and devices;
6. The ability to selectively alter the properties of the residual surface inside the air-cavity as hydrophobic or hydrophilic.

These criteria are key to widespread applications of this air-gap fabrication process throughout microelectronics, microfluidic devices, and MEMS structures. Following extensive characterization of the air-gap fabrication processing, the air-gap geometry and processing conditions can be selected and optimized for any particular application and desired structure.

The second goal of the research was to focus on a specific application: air-gaps for use in a compliant wafer level packaging (CWLP) technology. In this application, the air-gaps are embedded in a flexible polymer layer as a means to enhance the mechanical flexibility of metal interconnections between a silicon chip and a substrate or printed wiring board (PWB). This mechanical compliance is needed to accommodate the

mechanical strains that result from coefficient of thermal expansion (CTE) mismatches of parts and from warpage and bending of components (chips and boards).

Packaging of IC's is necessary to provide power and protection to the chip through reliable electrical and mechanical connection between the IC and the board. In conventional packaging of IC's, the final processing step performed while dice are in wafer form, is the fabrication of vias through a passivation layer to expose metal contact pads on the dice. A simplified process flow for conventional packing technology is shown in Figure 1 (a). Each individual die, while still part of the wafer, undergoes wafer-sort to identify known good die (KGD), after which wafer sawing and singulation are performed. The KGDs are then shipped to a packaging foundry where they are individually placed in temporary packages for burn-in. The dice that pass this first test are then individually packaged into permanent packages and retested for functionality. The chips that pass the second test are finally ready to be assembled to the PWB. Figure 1 (b) outlines the steps involved in the wafer-level packaging (WLP) approach. In WLP, all dice are fully packaged, tested, burned-in, and identified as functional while in wafer form. The dice are then singulated and are immediately ready for final system assembly. The WLP approach not only shrinks the package to the size of the die allowing smaller and lighter products, but also offers significant savings in cost and throughput, including elimination of an entire testing step.

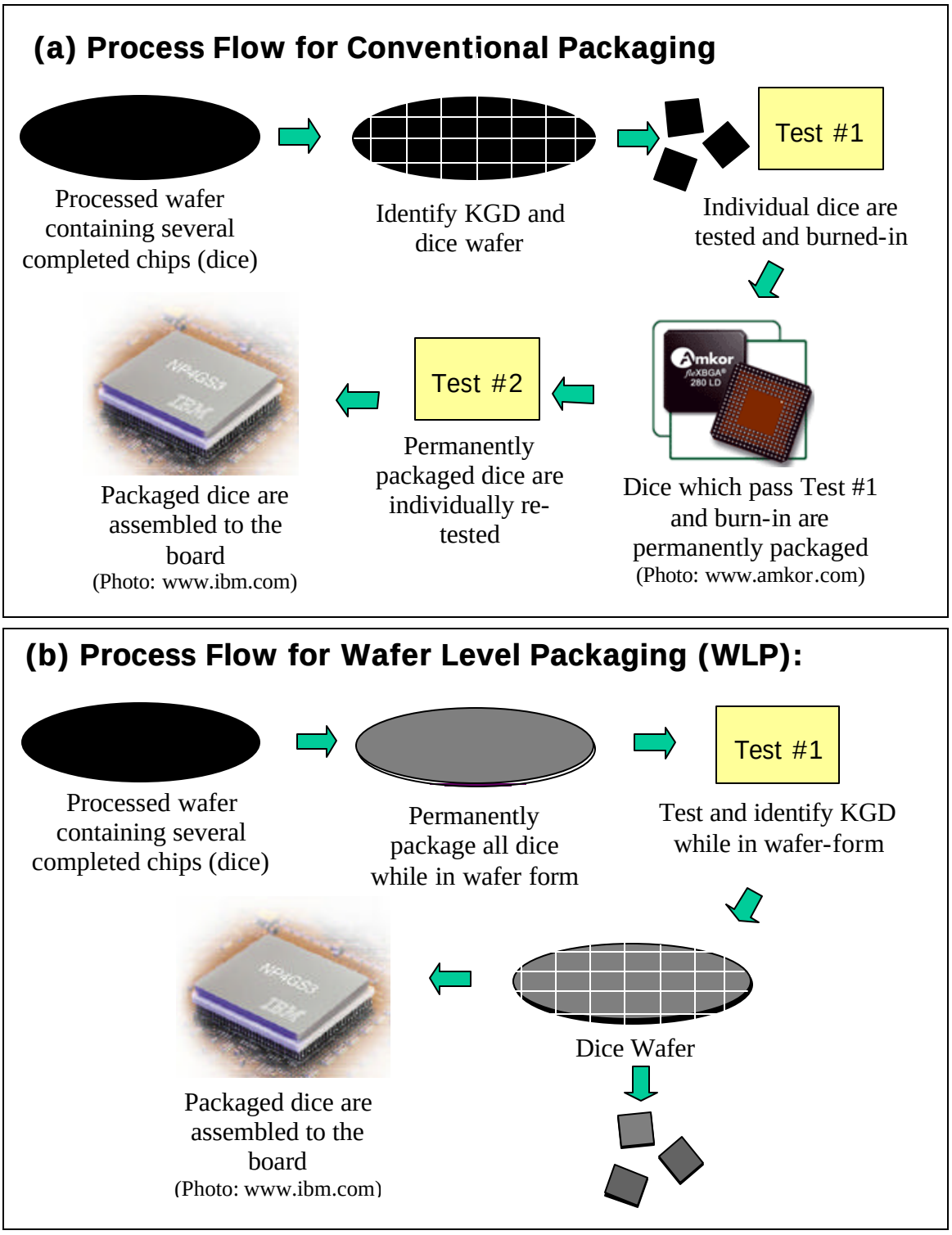

Figure 1: Process flow diagram showing the steps involved in (a) conventional packaging technology and (b) wafer level packaging technology.

The need for the mechanical flexibility (hence CWLP, not WLP) arises indirectly from the simultaneous improvement in density of transistors and performance, which are direct results of shrinking the size of the transistor. Although the transistors are shrinking, the wires connecting the transistors do not improve with the shrinking dimensions. Longer wires and more wiring levels at a smaller pitch are necessary to interconnect the large number of transistors. In fact, the interconnect response time is a very significant problem, in addition to the processing issues associated with increased wiring levels and longer wire lengths. The number of chip input/output (I/O) interconnects to the substrate also increases with chip functionality. A WLP with an area-array format of I/O that bond directly to the substrate provides a means to take advantage of chip real estate while minimizing wire length. However, the I/O must be able to withstand large stresses incurred from temperature cycling due to CTE mismatch between the silicon die (CTE = 3 ppm/^{o}C) and the organic board (CTE ~15 to17 ppm/^{o}C). In the case of solder as the attachment mechanism, the solder balls must be sufficiently large to prevent failure, or an underfill material must be dispensed between the chip and board as a stress buffer layer. Traditionally, packaging technologies have been relatively inexpensive and simple compared to the IC processing. However, the need for increased performance requires increasingly complex processing and expensive underfills. Packaging must remain cost effective in order to maintain the present trends in systems costs. No packaging technology has yet been able to satisfy simultaneously these performance and cost requirements. However, improvement in electrical performance (short wires) and reduction in the cost of packages both can be achieved through a reduction in the number of packaging levels and the elimination of underfill. Wafer-scale

packaging and direct chip-on-board mounting, where the interconnections themselves are compliant and can function as stress buffers, is a clear trend in that direction.

Sea of Leads (SoL), a novel ultra high-density compliant wafer-level I/O packaging technology, has been proposed [17-25]. In this CWLP scheme, a series of monolithic wafer-level process steps follow back-end-of-the-line processing, to provide the dice with high-density chip-to-module interconnections capable of moving in three dimensions. This approach extends the economic benefits of wafer-level processing to include batch fabrication of compliant high performance I/O interconnects and wafer level testing. A schematic showing a cross-section of the SoL interconnection design is depicted in Figure 2. The metal leads are designed to be flexible in the x-y direction (in the plane of the chip). Dice with SoL I/O interconnects may be mounted on substrates with significantly higher coefficients of thermal expansion without the need for underfill due to the x-y compliant nature of the metal lead. Z-axis compliance may be achieved through the use of a thick compliant polymer layer or an embedded air-gap, which can compress to allow reliable electrical contact between non-planar wafer and probe card surfaces during assembly, and wafer-level testing and burn-in. The air-gaps must be fabricated underneath the metal leads and thus must be fabricated via a method compatible with the CMOS devices on the chip, and also which can be integrated with the lead processing and solder bumping technology. This research specifically focuses on the integration of the air-gaps into SoL, following the development and characterization of the air-gap fabrication process. The objective was to fabricate and optimize air-gaps in complete SoL packages, as well as experimentally and predicatively evaluate the z-axis compliance provided by the air-gap. 3-D compliant SoL leads

containing an embedded air-gap not only may potentially revolutionize conventional packaging technology, but also have the ability to facilitate wafer-level testing through the use of air-gaps and flexible metal probes on a test probe card.

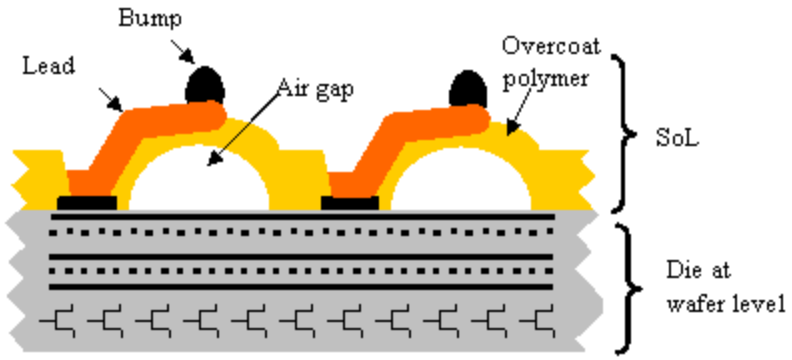

Figure 2: A cross-sectional schematic of a SoL packaged chip. 3-D movement is achieved through the combination of a flexible metal lead with an air-gap embedded in a flexible overcoat polymer. Contact or attachment is made through a solder ball placed at the end of the lead. (Figure taken from reference [25]).

CHAPTER 2

BACKGROUND

The fabrication of air-gap structures has been the focus of a multitude of studies found in literature [1-3, 9-16, 21, 24-39]. This chapter contains a summary of the various fabrication approaches, with a discussion on advantages and disadvantages of each of these approaches. Also included in this chapter is a brief description of packaging requirements for the future. Details of the Sea of Leads CWLP technology are presented along with a description of how air-gaps may fit into this technology to meet those future requirements.

2.1 Overview of Air-gap Fabrication Techniques

The fabrication of air-gaps or microchannels has been explored using several different approaches. Three dominant methods currently exist for forming air-gaps or air-channels in an encapsulating medium. The first approach, mainly for ultra low-K applications, is through plasma enhanced chemical vapor deposition (PECVD) of silicon dioxide over closely spaced lines or narrow etched vias [1-3, 14-15]. Figure 3 depicts an air-gap fabricated by Anand et al. [3] via this PECVD method. Poor step coverage of the oxide into the spaces allows air-cavities to form between the lines. Unfortunately, this process is limited to encapsulation by PECVD deposited materials on very small or high-aspect ratio structures. The air-gap structures are completely enclosed, but the geometry

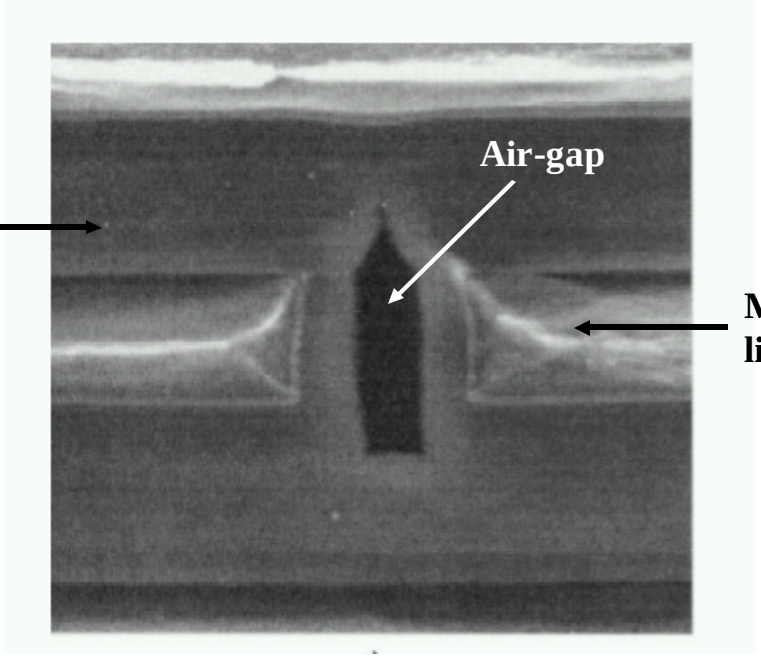

Figure 3: Air-gap formed from poor step coverage of PECVD deposited oxide between narrowly spaced metal lines. This figure shows a phosphorous doped SiO_2 layer deposited into a 0.32 μm space between Cu lines. (Figure taken from reference [3]).

of the gaps cannot be controlled to high accuracy and often extend above or below the metal lines. These geometry constraints limit the applications of this process. Multilevel microfluidic device networks are difficult to fabricate.

The second approach to create air-gaps or air-channels is to physically pattern grooves or channels into a material such as glass, silicon, or poly(dimethylsiloxane) (PDMS), then bond this surface to another flat or patterned surface. The most prevalent method of fabrication using this approach involves bonding layers of ultra-flat glasses to one another, each glass layer containing the patterned channels already etched into it, to form the required complex three-dimensional network [26]. There are several severe limitations with this material system and layering process. First, the bonding of glass

plates together leads to an obvious source of defects and low device yield [26]. The requirement that the layers be extremely flat (for proper bonding) eliminates the ability to build onto structures that have surface topography. An additional limitation to the bonding technique is that the construction of metal lines and other structures in the glass layers is very difficult. This limits complex systems with integrated electrical and non-electrical processes and components.

PDMS offers some advantage over glass bonding because it is less expensive, more robust, and conformal to the substrate due to its elastic properties [16, 27]. A master tool, typically fabricated from metal, is used as a master mold to cast replicas in PDMS. PDMS layers are then easily bonded to one another or to glass, silicon, silicon dioxide, silicon nitride and select polymers through oxidation of the PDMS surface and contact force. PDMS offers some surface property alteration because the oxidized PDMS surfaces are hydrophilic, but the surfaces return to a hydrophobic state over time [28]. PDMS molding is a fast and inexpensive process, but the PDMS cannot be bonded to some surfaces, including polyimide and metals. In addition, the PDMS cannot withstand high temperature processing, and as with glass, limits integration of metals and devices.

The third approach to forming air-cavities or air-channels involves the use of a sacrificial material, which acts as a placeholder during processing, that is etched or thermally decomposed leaving a void in the space once occupied. Sacrificial materials may be: metallic, such as titanium, aluminum, copper, and chromium; inorganic, such as poly-Si, phosphoric glass, silicon nitride, and silicon dioxide; or polymeric in nature [29-41]. Wet-chemical or plasma etching is required to subsequently remove many of these sacrificial materials, which requires fill holes or inlets to be incorporated into the

design. The removal of the sacrificial material through liquid extraction is inexpensive and easy, but limits the use in small or encapsulated spaces. The etch distance that can be attained by wet chemicals is limited by diffusion [35]. Wet chemicals can also cause stiction, or adhesion of surfaces, due to capillary forces in the tiny spaces.

Many of the sacrificial materials also are limited to specific applications due to temperature or solubility constraints, and lack compatibility with standard CMOS processing. Metallic sacrificial materials often require costly and time consuming deposition, show poor film uniformity, have poor adhesion to many materials, are not directly photosensitive, and require strong acids to remove the sacrificial metal [36]. Bell et al. [37] have investigated the use of porous silicon as a sacrificial material, which requires anodic electrochemical etching in hydrofluoric acid (HF) to create the porosity and dilute hydroxide solutions at room temperature to dissolve the sacrificial layer. This process works well for devices in silicon, but is not selective to either silicon dioxide or photoresist, which minimizes compatibility with other materials used in the devices. Silicon nitride and silicon dioxide sacrificial layers are also removed by hydrofluoric acid solutions and are limited in their deposition thickness to a few microns [31]. Sacrificial layers based on novolac photoresists are easily spin-coated and photo-patterned, followed by removal through dissolution in acetone or other solvents. The maximum processing temperature for using novolac photoresist as a sacrificial material is 110^{o}C, eliminating the use of high-temperature deposited oxide or polymers requiring a high-temperature cure as encapsulating materials [38]. Polyimides which can withstand processing temperatures > 400^{o}C have been utilized as sacrificial layers which are subsequently removed by an oxygen plasma or piranha etch [39-41]. This processing again requires

holes to remove the sacrificial material, and poor etch selectivity eliminates the use of other polymers as encapsulating materials or parts of the structure. Suh et al. [35] have developed dendritic hyperbranched polymers of phenylacetylene as sacrificial materials. These materials require an oxygen environment and temperatures in excess of 500^{o}C for decomposition, again excluding them from use with many other materials. Vapor-deposited polyoxymethylene has also been demonstrated as a feasible sacrificial material for fabricating air-gaps [32]. The onset decomposition temperature for this material is below 250^{o}C, which is compatible with many encapsulating materials, but not higher temperature curing materials, such as polyimide. Recently, polycarbonate which is patterned by electron-beam lithography has been used as a thermally decomposable sacrificial material [32]; although, this material also cannot withstand temperatures above 250^{o}C.

While significant advancements have been made in recent years in the design and fabrication of air-gaps and air-channels, more effort is required to improve the techniques currently used to fabricate these structures. Many of the studies mentioned above have been applied to only one air-gap geometry or have been demonstrated for a specific application with one encapsulating material or in one device. Hence, very few studies in the past considered the fabrication process in detail for many types of applications.

This work focuses on the fundamental understanding of the processing involved to produce air-gap structures, and developing the processing for wide applicability. From that understanding, the types of devices that can be built and any limitations on the air-channel structures or materials can be determined.

2.2 Sea of Leads Compliant Wafer Level Packaging

Chapter 1 introduced the ever-increasing need for advanced silicon packaging technology and the promise of CWLP as a key enabling technology. The 2001 International Technology Roadmap for Semiconductors (ITRS) addresses the industrial need for high performance and low cost packaging solutions [42]. According to the ITRS, existing packaging technologies are incapable of addressing the cost, performance, functionality, heat removal, and size requirements of future generation of semiconductor ICs, and therefore a novel packaging solution is required. Some of the packaging requirements for cost-performance electronics as outlined by the ITRS are listed in Table 1 [42]. The number of required I/O increases substantially as the power and performance speed required by the chip increase.

Table 1: Select future cost-performance packaging requirements as outlined by the 2001 ITRS [42].

Generation	**2003**	**2006**	**2016**
Node	100 nm	70 nm	22 nm
Power (W)	81	98	158
Performance (GHz)	3	5.6	19
Pin count	500-1450	550-1936	1300-4700
I/O Pitch (μm)	160	130	70

Wafer level packaging has seen a clear trend of interest by the packaging community in order to meet future requirements outlined by the ITRS. Companies including Chip Scale Inc., Flip Chip Technologies, FormFactor, Amkor, Fujitsu, Sandia National Laboratories, Shell Case, Toshiba, Tessera Inc., and others have developed or reported wafer level packages [43]. Despite the chip scale size, these WLPs must still meet the traditional requirements of reliable electrical and mechanical connection.

Current packages are permanently attached to the chip through various bonding methods including gold wire bonding, Tape Automated Bond (TAB) bonding, eutectic flip chip, high temperature flip chip, C4 bump with eutectic flip chip, gold-to-gold thermo-compression, gold stud bump and conductive adhesives. The packaged chip is then connected to pads on the system board and encapsulated with an epoxy underfill. The underfill is used to absorb the thermo-mechanical stress resulting from the CTE mismatch between the system board and the silicon chip. Underfill materials require long processing time and make reworking of the parts extremely difficult once the underfill is applied. These two factors make underfill a costly solution. Thick layers of a compliant polymer, such as polyimide or benzocyclobutene (BCB), are often used as additional stress buffer or pad redistribution layers. One alternative approach to these bonding techniques and use of underfill is to introduce mechanical compliance directly into the connection layer between the die and the substrate. Compliant leads are designed to physically expand and contract during the temperature cycling to absorb the thermo-mechanical stress.

Sea of Leads (SoL) CLWP technology utilizes this compliant lead approach and aggressively addresses the packaging requirements outlined by the ITRS until 2016 [23].

SoL is designed to have an area array I/O distribution and a smaller I/O pitch then other leading packages. I/Os are an abundant resource, allowing additional pins to be used for simplifying testing, or as heat transfer paths from the IC to the package to the board [44]. SoL CWLP potentially provides compliance both parallel and perpendicular to the plane of the IC. Vertical compliance (perpendicular to the plane of the IC) is necessary to make reliable contact to all leads for wafer level testing and burn-in. Vertical motion of the leads is also required to account for non-planarity of the chip, board, or test probe cards, and twisting type strains the chip may encounter during assembly or use. The vertical compliance requirements of interconnects are dependent on the application and the critical stress limit of the intralevel dielectric material utilized in the wiring levels on the IC. Porous materials, which are being investigated to meet the effective dielectric constant requirement of 2.3 to 2.7 by 2007, are often mechanically fragile. Assuming the critical yield stress of the intralevel dielectric is approximately 2 to 3 MPa, the vertical compliance requirement is between 5-10 mm/N.

Horizontal motion of I/Os is required to account for strains caused by CTE mismatch between the IC and the PWB or substrate. Larger movements, and thus larger leads, are required as the mismatch between the parts increases. More spatial mismatch occurs at the edge of the die, thus the leads at the edge of the die must be more compliant. The approximate required value of relative displacement at the edge of a 3 mm x 3 mm chip under an effective CTE mismatch of 15 ppm/^{o}C during temperature cycling is 20 µm [19]. The lateral compliance is also a function of usage conditions and the mechanical properties of the intralevel dielectric on the IC. As the die size or the temperature difference increases, more stress will be applied to the intralevel dielectric passivation

layers. Assuming a critical stress of around 2 to 3 MPa for this dielectric material, a CTE mismatch of 15 ppm/^{o}C, and a temperature difference of 300 K, a lateral compliance greater than 10 mm/N is required for the leads at the edge of the IC.

The electrical and in-plane mechanical design and performance of the leads in SoL CWLP, as well as optimization of the fabrication (excluding air-gap fabrication) of SoL packaging, has been studied and reported by M. Bakir [19-25]. The process sequence for the fabrication of compliant leads with solder ball attachments is schematically depicted in Figure 4. In this scheme, a thick layer of compliant polymer underneath the leads provides compliance in the out-of-plane direction. A SEM image of a SoL package fabricated using the process sequence in Figure 4 is shown in Figure 5. The design of the leads for increasing lateral compliance from the chip center to the edge is demonstrated. SoL packages have been fabricated with a density of 12,000 leads/cm^2 [25]. The processing for via, lead, and solder ball formation has been optimized and discussed in detail elsewhere [23]. Integration of air-gap fabrication into this technology, and the process details and results of SoL CWLP with embedded air-gaps will be discussed in Chapter 8. Chapter 9 includes the results and discussion of the mechanical performance and compliance of air-gaps through modeling and experimental nanoindentation studies.

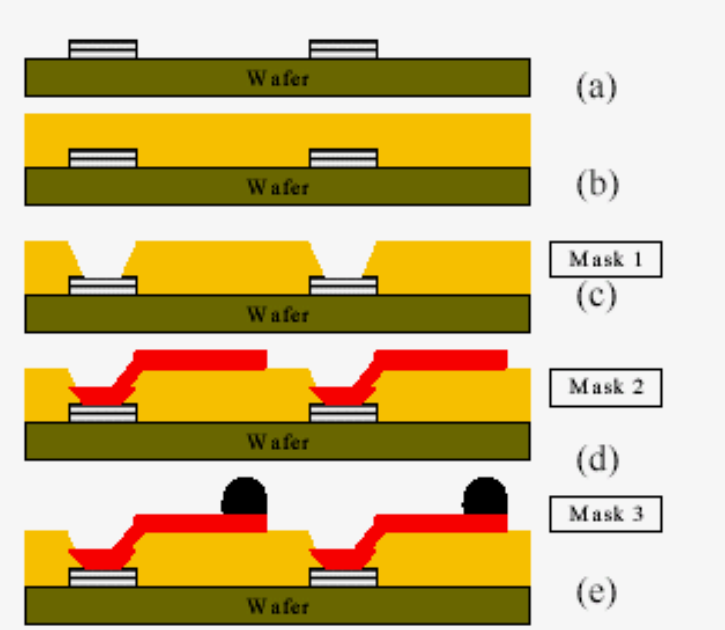

Figure 4: Schematic of the SoL fabrication process: (a) the wafer following back-end processing and bond pad formation; (b) the wafer is spin-coated with a complaint polymer; (c) the first masking step patterns and etches vias in the compliant polymer; (d) the second masking step forms electroplated Cu or Au leads; (e) the third masking step provides the end of the leads with solder bumps. (Figure taken from reference [24]).

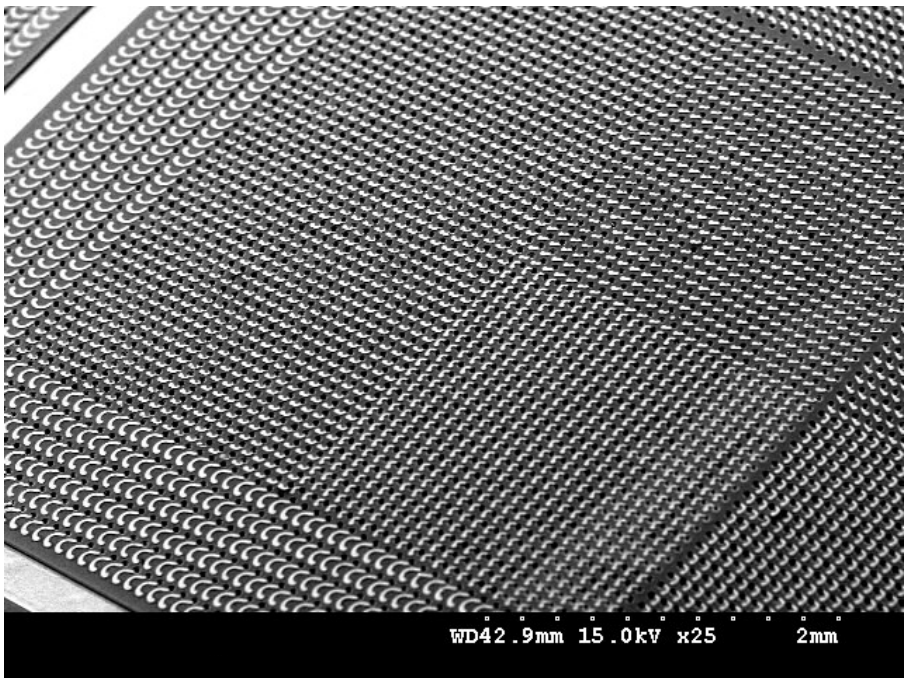

Figure 5: SEM image of a fabricated SoL chip containing 12,000 leads/cm^2. The chip contains short (~60 µm length) leads distributed on an 80 µm x 80 µm square lattice at the chip center, and longer (~120 µm length) leads distributed on an 80 µm x 160 µm rectangular lattice at the chip periphery. (Figure taken from reference [25]).

CHAPTER 3

EXPERIMENTAL TECHNIQUES, MATERIALS, AND EQUIPMENT

The purpose of this chapter is threefold: (1) to outline the process flow developed for the fabrication of air-gaps via thermally decomposable sacrificial polymers; (2) to introduce the chemistry and the properties of various polymers and materials used in this research; and (3) to describe the analytical equipment and procedures used for evaluation of fabrication results, as well as for analysis of thermal, chemical, and mechanical properties. In section 3.1, the fabrication process flow is briefly described to introduce the terminology and methodology which were developed. The specific details of the air-gap fabrication process, including microelectronics fabrication equipment, procedures, and results are discussed in Chapter 5 and Chapter 6. In addition, several of the subsequent results chapters contain a section with experimental details relevant to the experiments and discussion in the chapter.

3.1 General Process of the Fabrication of Air-gaps Using Sacrificial Polymers

The general procedure developed as part of this research for the fabrication of air-channel structures via thermally decomposable sacrificial materials is depicted in Figure 6. The process begins with a substrate onto which the air-cavities will be fabricated. The substrate, which is shown in Figure 6 (a), may consist of a variety of materials, including silicon, glasses, other semiconductors, or organic PWB materials. The requirements of

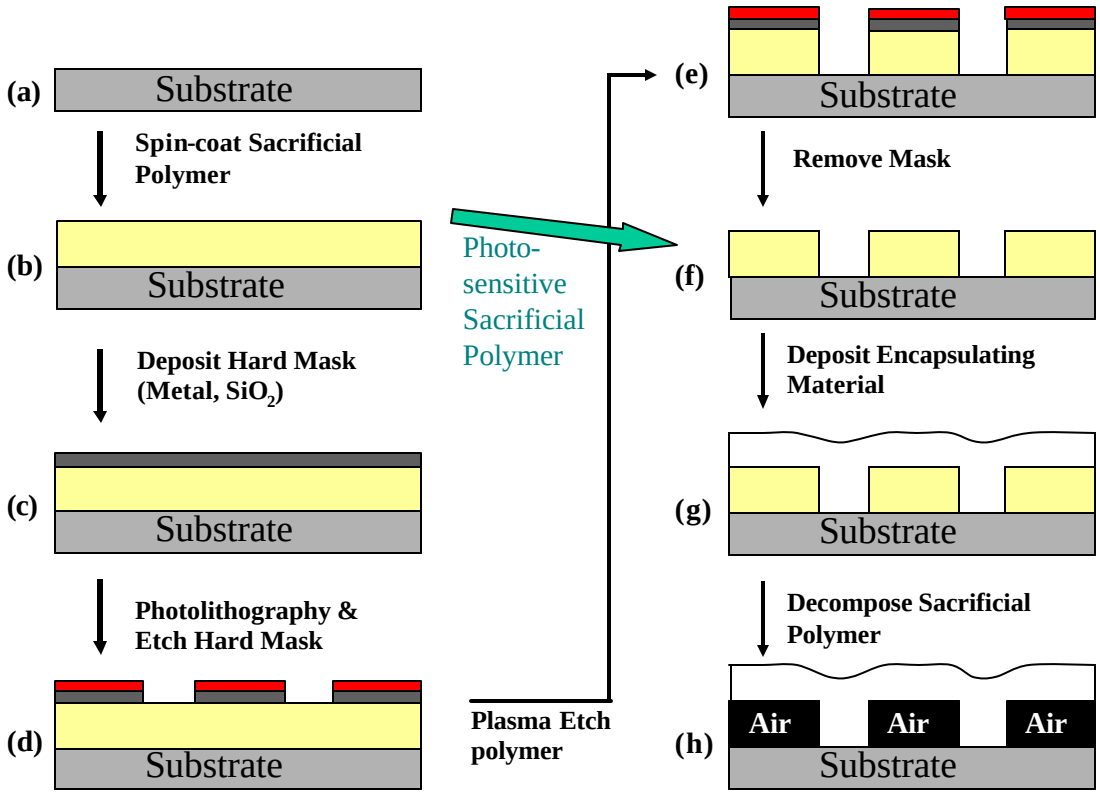

Figure 6: Process flow for the fabrication of air-gaps: (a) substrate; (b) spin-coating of sacrificial polymer; (c) deposition of hard mask; (d) photolithography and etching of hard mask (see details in Figure 7); (e) plasma etching of sacrificial polymer; (f) stripping of photoresist and hard mask; (g) deposition of encapsulating material; (h) thermal decomposition of the sacrificial polymer to produce air-gaps.

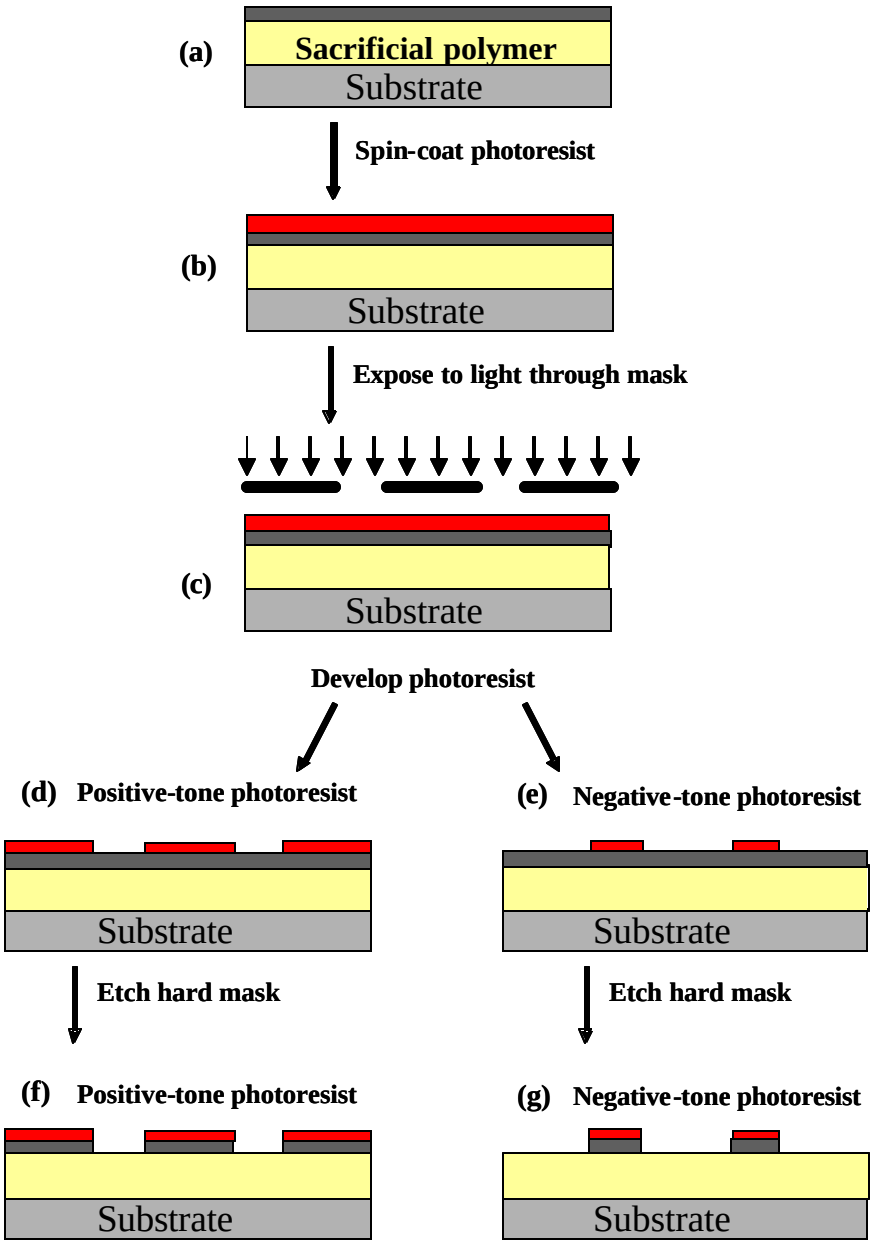

Figure 7: Process details for lithography and patterning of a hard mask: (a) substrate coated with a layer of sacrificial polymer and a hard mask material (SiO_2 or metal); (b) spin-coat photoresist onto hard mask surface; (c) expose photoresist to light through a mask containing clear and opaque regions; develop the photoresist to (d) remove exposed photoresist areas for a positive-tone resist material and (e) remove unexposed areas for a negative-tone resist material; (f, g) remove hard mask in areas no longer protected by resist through wet-chemical or plasma etching.

the substrate include resistance to the solvent(s) in the sacrificial polymer, good adhesion to the sacrificial polymer, and thermal stability to withstand the decomposition temperature of the sacrificial polymer. Various substrates were used in this research, including bare 4" <100> silicon wafers, and wafers coated and patterned with one or more materials including: SiO_2, SiN_x, Ti/Cu/Ti, Ti/Au, Pt, Cr, Al, and polyimide.

The first step in the fabrication of air-gaps is to uniformly apply the sacrificial polymer through a method such as spin-coating or doctor-blading to blanket-coat a thin film across the substrate, as shown in Figure 6 (b). The thickness of the polymer film (i.e. ultimately the height of the air-channel) is controlled by both the weight fraction of the polymer in solution as well as the spin speed or height setting of the doctor-blading tool. Following film deposition, the sacrificial polymer film is patterned into the desired shape of the air-gaps or air-channels. Many of the sacrificial materials are not directly photosensitive and therefore a hard mask and photolithography is required to selectively remove portions of the sacrificial layer. As depicted in Figure 6 (c) either SiO_2 or a metal is deposited to serve as a hard mask. The patterning is first performed in the hard mask layer followed by a subsequent transfer of the pattern to the underlying sacrificial polymer layer.

Lithography and either wet-chemical or plasma etching of the hard mask is performed to form the desired pattern in the hard mask (Figure 6 (d)). The steps involved in the lithography and etching process are outlined in Figure 7. Figure 7 (a) depicts a substrate with deposited layers of sacrificial polymer and a hard mask as previously described in Figure 6 (c). Photoresist, which is a photosensitive polymer, is spin-coated onto the surface of the hard mask material as in Figure 7 (b). In Figure 7 (c) the

photoresist is selectively exposed to ultraviolet light (typically 365 nm) through a mask consisting of both transparent and opaque regions. Wet-chemical developing follows the exposure. If a positive-tone resist is used, only the exposed regions become highly soluble in the developer solution and are removed as in Figure 7 (d). In the case of a negative-tone resist system, the exposed areas remain when the resist film is developed (Figure 7 (e)). Following developing, the pattern is transferred into the hard mask layer through wet-chemical or dry plasma etching, as shown in Figure 7 (f, g).

Once lithography and hard mask etching is complete, the exposed sacrificial polymer areas are removed through dry plasma etching (Figure 6 (e)). Any remaining photoresist and hard mask are then removed, leaving only a patterned polymer film on the substrate (Figure 6 (f)). If the sacrificial polymer is directly photosensitive, it may be directly patterned by exposure through a mask after spin-coating and developing. If the polymer is positive-tone, the exposed areas are removed after developing and if it is negative-tone, the exposed areas remain. This eliminates steps (c), (d), (e), in Figure 6.

Patterning of the sacrificial material is followed by blanket coating the encapsulating material (such as SiO_2, SiN_x or other low-κ polymer) as in Figure 6 (g). This is performed using vapor deposition, spin-coating, or doctor-blading. After encapsulating the patterned sacrificial polymer, it is decomposed in a horizontal tube furnace by holding at the decomposition temperature of the sacrificial polymer for a predetermined amount of time (Figure 6 (h)). The decomposition products exit the system, leaving a virtually residue-free hollow structure.

3.2 Sacrificial Polymer Chemistry

The sacrificial material requires specific properties in order to form air-cavities via thermal decomposition. Some of the requirements for the sacrificial material follow:

1. The sacrificial material must have adequate adhesion with substrates such as Si, SiO_2, polymers, and metals;
2. Chemical processing and the use of solvents (following application of the sacrificial polymer) should not swell, remove, or degrade the sacrificial material;
3. Complete decomposition of the sacrificial material should occur in a narrow and useful temperature range with little or no solid remaining residue;
4. The decomposition products should be able to permeate through the overcoat layer;
5. The decomposition temperature must be compatible with subsequent processing and other materials in the structure.

The decomposition temperature of the sacrificial polymer limits the choice the substrates and overcoat materials that may be used with the process. The target decomposition temperature of the sacrificial material is one at which the encapsulating material is already fully cured and resistant to degradation, flow, or deformation. The substrate material must also be able to withstand the decomposition temperature without degradation. For example, epoxy-based printed wiring boards decompose at temperatures slightly above 200^{o}C. Therefore, a sacrificial material that thermally decomposes at 400^{o}C would be of little use on epoxy board. On the other hand, many polyimides require a temperature of 350^{o}C to completely react and cure. A sacrificial material that thermally decomposes at 400^{o}C allows the polyimide to be fully cured

before decomposition begins. Different materials and processes therefore require different sacrificial materials. To cover a wide range of applications, this research has targeted three approximate decomposition temperatures for sacrificial materials: 200°C, 300°C, and 400°C. Sacrificial materials that decompose around 200°C or lower are for use with PWBs or board-like applications with epoxies and other low-temperature curing materials. Sacrificial materials that decompose around 300°C target encapsulating materials that cure around 250°C, including benzocyclobutene (BCB) and some polyimides. One specific application of this 300°C material would be for chip-to-module interconnections, where the decomposition temperature is at the temperature in which solder reflows. Sacrificial materials that decompose around 400°C are best suited for IC, MEMS, and interconnect applications, where there is frequent use of high temperature deposition and curing materials such as metals, SiO_2, SiN_x, and polyimides.

The focus of this research is on both polynorbornenes and polycarbonates as potential sacrificial materials for air-gap fabrication. Polynorbornenes thermally decompose around 400°C and fill the need for a higher temperature decomposing sacrificial polymer. The polycarbonates have been investigated as possible lower-temperature candidates. Aliphatic polycarbonates are known to thermally decompose at temperatures between 200 to 350°C [45-46]. In addition, the decomposition temperature of a polycarbonate can be reduced through acid-catalyzation of the decomposition reaction. The details of each polymer's chemistry are discussed in sections 3.2.1 and 3.2.2 of this chapter.

3.2.1 Polynorbornenes

One sacrificial polymer used in this study is a functionalized polynorbornene (PNB). Polynorbornenes were synthesized and provided by Promerus, LLC (Brecksville, OH) according to proprietary methods. Figure 8 shows the rigid polycyclic backbone structure of the norbornene chain. The 'R' groups attached to the rigid polymer backbone can be tailored to impart desired properties to the polymer and achieve some specific purposes, including adhesion with the substrate, photosensitivity, and mechanical or thermal properties [47-49]; and also to render the inner surface of the resultant cavity either hydrophilic or hydrophilic. Norbornene based polymers show little weight loss before 370^{o}C, a clean and steep decomposition around 425^{o}C, and a residual weight of less than 2%. A dynamic thermogravimetric analysis (TGA) thermogram of a typical polynorbornene, performed at a heating rate of 10^{o}C/min, is shown in Figure 9. Figure 9 demonstrates that as temperature is increased, little weight is lost until approximately 370^{o}C. Following the onset of decomposition, the weight of the material steeply drops until a fraction of a percentage remains. Further details of the decomposition of polynorbornene are discussed in subsequent chapters.

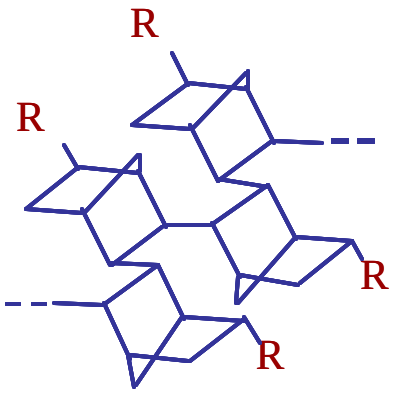

Figure 8: General structure of polynorbornene.

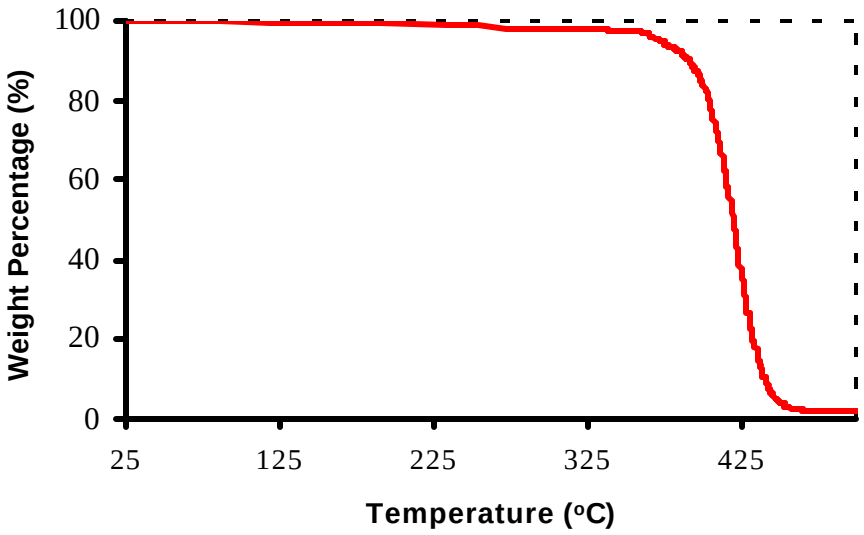

Figure 9: Dynamic TGA thermogram for a typical polynorbornene, obtained at a heating rate of 10°C/min.

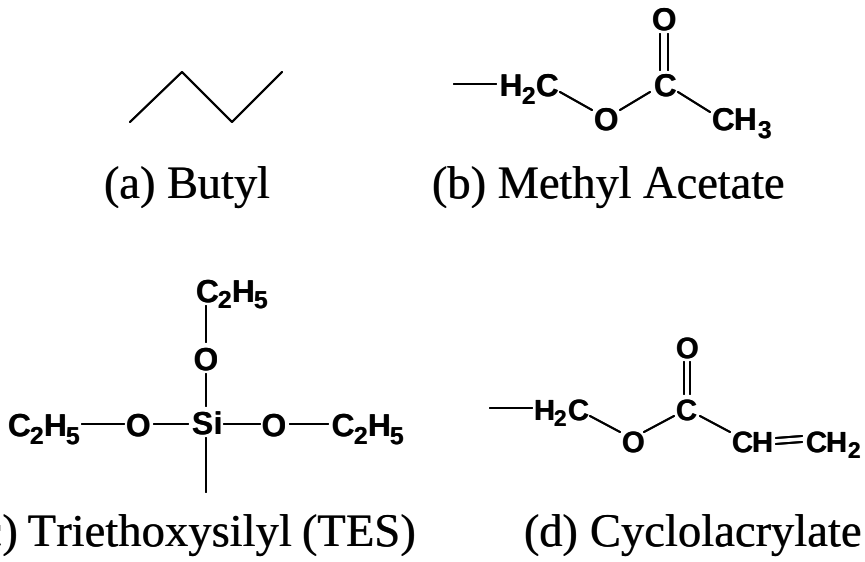

Figure 10: Various R-groups attached to the polynorbornene backbone: (a) Butyl; (b) Methyl Acetate; (c) Triethoxysilyl (TES); (d) Cyclolacrylate.

The molecular weight of the norbornene polymer can be controlled to a high degree of accuracy by regulating the amount of chain transfer agent used in the polymerization. In order to meet specific application requirements, the molecular weight may range from ten thousand to one million atomic mass units (amu). Copolymers or terpolymers are created through stoichiometry control of the reacted monomer and are used to combine properties from the various functional groups. The functional groups included in this study include straight chain alkyl, triethoxysilyl (TES), methyl acetate, and cyclolacrylate. The structures of the functional groups are shown in Figure 10. Table 2 provides the functional group composition in mole percentage and the weight-average molecular weight for each polynorbornene polymer used in this work.

One specific polymer used in a majority of this research is polybutylnorbornene with 10 weight percentage of the polymer functionalized with TES side groups. Polynorbornenes PNB-1 through PNB-3 listed in Table 2 contain this functional group combination. The 90/10 butyl/TES polymer was used extensively for air-gap fabrication because of its clean decomposition properties and solvent resistance when compared with other polynorbornenes. In addition, the TES groups provide excellent adhesion to metals (Cu, Au, Ag, Al, Ta, W, Ti) and oxides [47]. This is a highly desirable property for forming air-channels because many organic adhesion promoters may leave solid decomposition products and residues in the air-channels upon high temperature decomposition. The thermal decomposition and processing characteristics of the 90/10 butyl/TES polymer and many other PNB polymer compositions are discussed in detail in Chapter 4 and Chapter 7.

Table 2: The composition and weight-average molecular weight of polynorbornene sacrificial materials used in this research.

Polymer #	**Composition***	**Molecular Weight, M_w**
PNB-1	90/10 butyl/triethoxysilyl copolymer	283,000
PNB-2	90/10 butyl/triethoxysilyl copolymer	182,000
PNB-3	90/10 butyl/triethoxysilyl copolymer	355,000
PNB-4	methyl acetate homopolymer	261,000
PNB-5	methyl acetate homopolymer	325,000
PNB-6	90/10 methyl acetate/triethoxysilyl copolymer	183,000
PNB-7	50/50 norbornene/triethoxysilyl copolymer	412,000
PNB-8	90/10 butyl/cyclolacrylate copolymer	300,000
PNB-9	80/20 butyl/cyclolacrylate copolymer	213,000
PNB-10	90/10 methyl acetate/cyclolacrylate copolymer	274,000
PNB-11	80/10/10 methyl acetate/triethoxysilyl/cyclolacrylate	256,000
PNB-12	80/10/10 methyl acetate/triethoxysilyl/cyclolacrylate	123,000
PNB-13	80/10/10 methyl acetate/triethoxysilyl/cyclolacrylate	84,000
PNB-14	80/10/10 butyl/triethoxysilyl/cyclolacrylate	674,000
PNB-15	80/10/10 butyl/triethoxysilyl/cyclolacrylate	343,000
PNB-16	80/10/10 butyl/triethoxysilyl/cyclolacrylate	278,000
PNB-17	80/10/10 butyl/triethoxysilyl/cyclolacrylate	213,000
PNB-18	80/10/10 butyl/triethoxysilyl/cyclolacrylate	160,000
PNB-19	80/10/10 butyl/triethoxysilyl/cyclolacrylate	105,000

*side group compositions given in mole percentage

3.2.2 Polycarbonates

The second group of polymers investigated as sacrificial materials in this research is polycarbonates. The general structure of a polycarbonate is shown in Figure 11. Groups in or attached to the polycarbonate backbone may be tailored to achieve desired properties such as decomposition temperature, glass transition temperature (T_g), or adhesion. The specific polycarbonates used in this research include poly(ethylene carbonate) (PEC), poly(propylene carbonate) (PPC), poly(cyclohexene carbonate) (PCC), and poly(norbornene carbonate) (PNC). The structures of these polymers are shown in Figure 12. PPC with a weight-average molecular weight of 50,000 was obtained from Aldrich Chemical Company. PEC with a number-average molecular weight of 50,000 was obtained from Q-PAC polymers and the structure was confirmed by Fourier transform infrared spectroscopy (FT-IR) and nuclear magnetic resonance (NMR) spectroscopy. PCC and PNC were synthesized by B. Tsuie and H. Zhen at Promerus, LLC. (Brecksville, OH) according to the procedures described in following paragraphs.

Polycarbonates are characterized by clean decomposition in either a nitrogen or air environment. An increase in the functional group chain length present in the polymer backbone corresponds with an increase in the decomposition temperature of the polycarbonate. The decomposition and processing characteristics of the polycarbonates are discussed in detail in Chapter 4 and Chapter 6.

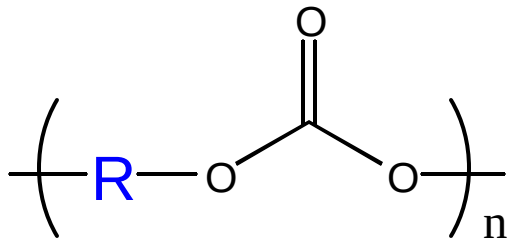

Figure 11: General chemical structure of a polycarbonate.

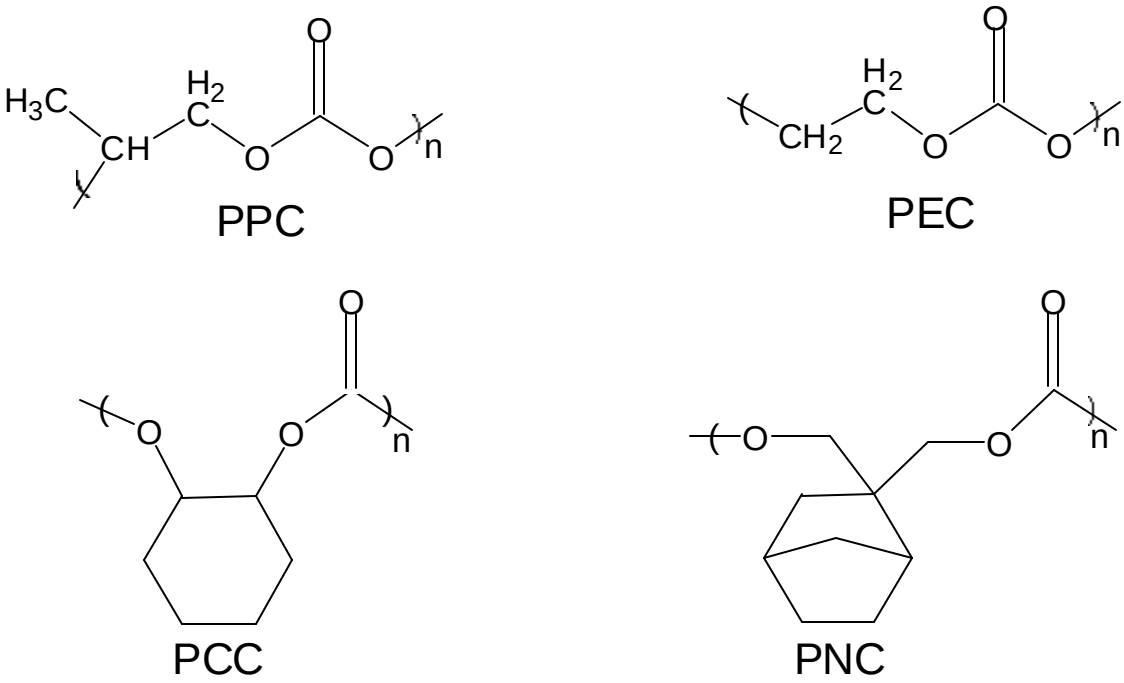

Figure 12: Structure of specific polycarbonate sacrificial materials investigated in this research.

Synthesis of poly(cyclohexene carbonate) (PCC):

The catalyst $[(2,6\text{-Difluorophenoxide})_2Zn]_2(THF)_2$ used for the polymerization reactions was prepared following a literature report [50]. 1.0 g of this Zn catalyst was mixed with 175.0 g of cyclohexene oxide under nitrogen. The mixture was then transferred to a 500 mol stainless steel pressure reactor and CO_2 was introduced to a pressure of 780 psi. The reaction mixture was heated to 80°C for 48 hr. The product was diluted in tetrahydrafuran (THF) and precipitated in methanol. The polymer was then collected by filtration and dried under vacuum at 80°C for 24 hr to yield 128 g. The polymer structure was verified by proton NMR and IR spectroscopy. Size exclusion chromatography (SEC) (THF, polystyrene standard) gave a weight average molecular weight of 125,000 (polydispersity index, PDI = 6.6). Differential scanning calorimetry (DSC) analysis determined that the glass transition temperature (T_g) was 115°C.

Synthesis of poly(norbornene carbonate) (PNC):

The precursor, spiro[bicyclo[2,2,1]hept-5-ene-2,5'-[1,3]dioxan]-2'-one was prepared according to a literature procedure [51]. Preparation of the precursor was followed by hydrogenation under a H_2 pressure of 70 psi in the presence of $[(COD)Ir(PMe_3)(Pyridine)]PF_6$ as a catalyst. The product was purified by recrystalization from methylcyclohexane and the structure was confirmed by proton NMR. In a nitrogen atmosphere, 0.5 mL of secondary butyl lithium (1.3 M in cyclohexane) was added to 15 g of the precursor, spiro[bicyclo[2,2,1]heptane-2,5'-[1,3]dioxan]-2'-one, in 200 mL of toluene at 0°C. After addition, the reaction mixture was slowly warmed to ambient temperature and stirred overnight. The polymer product was precipitated into methanol and dried under vacuum to yield 11.0g. The structure was

verified by proton NMR and size exclusion chromatography gave a weight average molecular weight of 51,000.

3.3 Encapsulating Materials

In order to form air-gaps or air-channels, the encapsulating material must also exhibit certain characteristics. These characteristics are listed below:

1. The cure or deposition temperature of the encapsulating material must be compatible with the decomposition temperature of the sacrificial material;
2. The encapsulating material must have a glass transition temperature (T_g) higher than the decomposition temperature of the sacrificial material to prevent it from flowing and filling in the cavities during decomposition;
3. The encapsulating material requires adequate mechanical strength to span the air-cavity without sagging or expanding during decomposition of the sacrificial material;
4. Sufficient permeability to the decomposition products is required for formation of the air-cavity without distortion or rupture during the decomposition process;
5. The encapsulating material also needs to provide adequate step coverage over the patterned sacrificial film.

Table 3 lists the various encapsulating materials used in this research and select thermal and mechanical properties of these materials including: the maximum temperature required for curing or deposition; the coefficient of thermal expansion (CTE); the Young's modulus; and the percent elongation. The specific details of the chemistry of each of these materials, the fabrication processing conditions, and the results of the fabrication with each material are discussed in Chapters 5 and 6.

3.4 Analysis Methods and Procedures

3.4.1 Thermogravimetric Analysis (TGA)

Thermogravimetric analysis (TGA) was used to study the thermal decomposition of the polymeric sacrificial materials. These experiments were performed using a Seiko TG/DTA 320 thermogravimetric analyzer under various conditions. The instrument uses a counterbalanced beam system to monitor the changes in weight of a sample, with respect to an inert reference pan, as a function of temperature and time. The microbalance of this tool is capable of detecting weight changes ± 10 μg. Sample pans either consist of Al or Pt, depending on the temperature range of the experiment. Experiments which exceed 550^{o}C require the use of Pt sample pans.

TGA sample preparation for the sacrificial polymers occurred as follows. The polycarbonate sacrificial polymers were each available as dry polymer samples. Many of the various compositions of polynorbornene polymer samples were also available as dry polymer; some were provided as polymer dissolved in a solvent. For dry polymer samples, the sample pan was first cleaned by rinsing with acetone, methanol, isopropanol, and deionized water, followed by blowing dry with nitrogen. 10 to 20 mg of the dry polymer was then placed into the pan. For polymer samples in solvent, the empty sample pan weight was determined immediately following cleaning. The microbalance on the TGA was used to determine this weight to the nearest 0.001 mg. A syringe was used to dispense the polymer solution dropwise into the sample pan. A bake step followed each drop dispense by placing the sample pan on a 120^{o}C hotplate for 5 min. A total of 1 to 5 drops was used for each sample in order to attain a weight of 2 to 20 mg.

Table 3: Encapsulating materials used in this research along with select properties [52-68].

Encapsulating Material	**Max. Temp. for Cure or Deposition**	**T_g (^oC)**	**CTE (PPM/^oC)**	**Young's Modulus (GPa)**	**Elong-ation (%)**
• Polyimides:					
Amoco Ultradel 7501	350^{o}C for 0.5 hour	> 400	24	3.5	7.6 [52]
DuPont Pyralin PI-2611	350^{o}C for 1 hour	360	5	8.5	60
DuPont Pyralin PI-2734	350^{o}C for 1 hour	> 350	16	4.7	>10
DuPont Pyralin PI-2731	350^{o}C for 1 hour	> 350	16	4.7	>10
DuPont Pyralin PI-2771	350^{o}C for 1 hour	294	42	2.7	45
DuPont Pyralin PI-2540	350^{o}C for 1 hour	> 400	20	1.4	40
DuPont Pyralin PI-2555/2556	350^{o}C for 1 hour	325	40	2.5	10
Hitachi HD4000	350^{o}C for 1 hour	350	35	3.5	45
Dow Corning/Toray PWDC-1000	300-320^{o}C for 1 hour	290	32	3.0	60
• PECVD Silicon Dioxide	Deposit at 100-350^{o}C	N/A	0.5	50-75	
• PECVD Silicon Nitride	Deposit at 100-350^{o}C	N/A	1-3	150-380	
• Honeywell FLARE^{TM} poly (arylene ether)	250^{o}C for 0.33 hour	> 400	55	4.9	
• Sumitomo Bakelite PBO CRC-8650 (poly benzoxazole)	320^{o}C for 0.5 hour	295	51	2.5	65
• Parylene-N	Deposit at 150^{o}C	420	690	2.4	30
• Ciba-Geigy LMB 7081 Epoxy	165^{o}C for 1 hour	130		3.3	
• Dow CYCLOTENE^{TM} 3022-57 (bisbenzocyclobutene)	250^{o}C for 1 hour	375	52	2.0 ± 0.2	6 ± 2.5
•Avatrel 2000P Dielectric Polymer	200^{o}C for 1 hour	330	83	0.5	20

Some samples were cured in a Lindberg horizontal tube furnace following the recommended polymer cure schedule prior to running the TGA. The weight of the pan was determined while empty. The polymer was then dispensed into the pan and cured. The sample weight was determined by subtracting the previously measured empty pan weight from the total weight of the pan including the cured polymer.

TGA experiments were also performed on encapsulated sacrificial polymer. The encapsulated samples were prepared using a sacrificial polymer/solvent solution. First, the empty pan weight was initially determined following cleaning. A syringe was used to place a small drop of sacrificial polymer in the center of the pan. The sacrificial polymer was then cured and its weight determined. Encapsulation occurred by either dispensing another polymer on top of the sacrificial material, or depositing SiO_2 using PECVD.

Dynamic TGA experiments consisted of a constant heating-rate ramp to a final temperature of 530°C. A dynamic TGA ramped at a heating rate of 10°C/min was performed on all sacrificial polymers. From this TGA thermogram, the temperature for 5% weight loss is reported as the onset temperature for decomposition and the temperature for 50% weight loss is the reported decomposition temperature (T_d). In addition, the percent weight remaining at 500°C for PNB and at 350 to 400°C for PC was used to compare residual weight from the decomposition. Isothermal TGA experiments were performed by ramping quickly to the desired isothermal temperature and holding for a period of 1 to 6 hours. Isothermal experiments consisted of a 20°C/min ramp to 110°C, a 10 min dwell to remove moisture, then a 100°C/min ramp to the desired hold temperature. During the dynamic and isothermal experiments, the polymer weight, instantaneous weight loss, temperature, and time were recorded.

Polynorbornenes have been shown to undergo degradation at lower temperatures and with higher residual material through oxidation [69]. Therefore, all TGA experiments for polynorbornenes were run in an ambient nitrogen environment. TGA analysis of the polycarbonates was performed in both nitrogen and air environments. A nitrogen environment was achieved by purging the TGA with 99.998% pure nitrogen at a rate of 100 sccm throughout the experiment. An oil bubbler was attached to the exit stream to prevent the backflow of air. The oxygen level was measured at the outlet from the TGA using an Alpha Omega Instruments Series 3000 Trace Oxygen Analyzer. At the purge rate of 100 sccm the oxygen concentration was below 100 ppm for all experiments. Experiments performed in air were open to the atmosphere under no gas flow.

3.4.2 X-ray Photoelectron Spectroscopy (XPS)

X-ray photoelectron spectroscopy (XPS) was used to determine the elemental composition of residual material remaining after decomposition of the sacrificial polymers. The fabrication details for preparation of XPS samples are discussed in the relevant chapters. XPS measurements were completed on a Physical Electronics model 1600 XPS system using an aluminum K_a source and toroidal monochrometer. The analyzer is a hemispherical electron analyzer. All analyses were setup with a 0.8 mm spot size and 45^o take-off angle. The penetration depth into the samples was approximately 75Å. Base pressure is typically less than 10^{-9} Torr and analysis was performed at a working pressure of 4×10^{-9} Torr. A scan was performed through all binding energies, and the atomic percentages were calculated from the area under each peak.

3.4.3 Atomic Force Microscopy (AFM)

Thickness of the resultant residual films was analyzed by atomic force microscopy (AFM) using a Nanoscope IIIa from Digital Instruments, Inc. This instrument was operated in contact mode using flexible silicon cantilevers to prevent the tip from breaking by sticking in crevices. The procedure for determining residual thickness by AFM analysis is as follows:

1. Spin-coat a blanket film of sacrificial polymer cast from solution onto a gold-coated silicon substrate;
2. Pattern the sacrificial film using a mask with large circles and squares or remove a portion of the film with a razor blade to create a step;
3. Measure the non-decomposed film thickness using a Tencor Alphastep profilometer and mark the measured step area with a scribe;
4. Decompose the sacrificial film either on a hotplate or in a Lindberg horizontal tube furnace using the required decomposition time-temperature profile;
5. Mount the sample onto the AFM stage and position the tip over the marked step created by the patterned features. Align and focus the tip, and focus on the surface of the residue;
6. Set the scan area (typically a rectangular area with each side between 20 to 100 μm) and the scan rate (0.5 to 2.0 Hz) and engage the tip with the surface.
7. Modify the deflection set-point (contact force), integral gain, and proportional gain to achieve a high-resolution image;
8. Capture the image then analyze the step height (thickness) of the residual material across the measured step feature.

3.4.4 Ellipsometry

Thickness measurements of transparent polymer complete surface films were analyzed using a J. A. Woolam M-2000 multi-wavelength variable angle spectroscopic ellipsometer. The steps in performing the analysis are as follows:

1. Input a model which describes the materials and number of transparent layers on your sample. Estimate the thickness and refractive index values for each layer;
2. Mount the sample on the vacuum stage. Use the alignment detector to adjust the leveling and the height of the sample to produce the maximum reflected light intensity;
3. Adjust the scan parameters including the desired number of scans, the positions of the scans across the sample, the wavelength range (400 to 1000 nm), the step size between data points (in nm), the range of reflection angles (10^o to 90^o) , and the step size between angles. Then run the scan;
4. View the results which include film thickness, refractive index, and the mean squared error between the model fit and the experimental data;
5. Adjust the model parameters and re-fit the experimental data until the mean square error (MSE) is minimized. Confirm the parameters make sense and the refractive index decreases with increasing wavelength.

3.4.5 Goniometry

Goniometry, or contact angle measurement, was utilized to determine the nature of the resultant surface following decomposition. The angle deionized and distilled water makes with the surface indicates whether it is hydrophobic or hydrophilic. Contact angle

measurements were obtained immediately after film decomposition through use of a video contact angle 2500XE system (AST products). The procedure for preparing and measuring samples is as follows:

1. Prepare full-surface films of the sacrificial polymers by spin-coating the polymer in solution onto 4" diameter silicon wafers;
2. Decompose the full-surface films either by baking on a hotplate or in a Lindberg horizontal quartz tube furnace with nitrogen or dry air flowing at a rate of 1.5 L/min. Backstreaming of air was prevented by an oil bubbler on the exit tube from the furnace;
3. Mount the sample onto the sample stage;
4. Dispense a 1 μL drop of deionized and distilled water onto the sample surface;
5. Capture the image of the water drop on the surface of the film by video photography;
6. Measure both the right and left angles between the sample surface and the tangent line to the droplet as shown in Figure 13.

When the droplet takes a spherical shape, the angle is large, indicating the surface is hydrophobic. A large angle ($>90^o$) typically characterizes the surface as hydrophobic. When the droplet spreads out on the surface ($<90^o$) the surface is characterized as hydrophilic.

3.4.6 Scanning Electron Microscopy (SEM)

Scanning electron microscopy (SEM) was utilized to visually inspect samples containing air-gaps and microchannels at various stages of the processing. Cross-sections

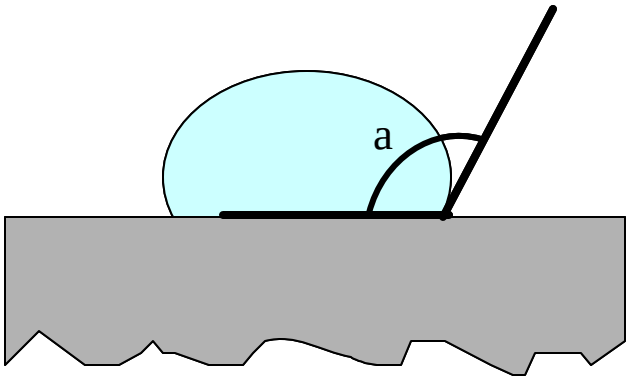

Figure 13: Schematic of measurement of contact angle, α.

of the air-gaps were examined following completion of fabrication, and also samples prior to and following nanoindentation experiments. A Hitachi 3500H Scanning Electron Microscope (SEM) was used to perform sample imagine. To prepare cross-sections, the samples were submerged in liquid nitrogen for 2 to 3 minutes. Immediately following removal the liquid nitrogen, a diamond scribe was used to break the sample along the desired cross-sectional plane. The procedure for sample imaging using the SEM is as follows:

1. Mount the sample on an Al SEM sample stub mount using two-sided conductive carbon or copper tape;
2. Sputter-coat the sample with a thin Au layer for sample conductivity. Sputtering was performed using an Ernest Fullum sputter-coating system at 100 mA current for 30 to 60 sec;
3. Vent the SEM sample chamber, load the sample, and pump down the system.
4. Set the electron acceleration voltage (typically 10 to 30 kV) and raster scan speed (slow, medium, fast);

5. Focus on the sample, locate the area for imaging, and increase the magnification to the desired value, using the course focus to maintain a clear image. Once the sample location and desired magnification is reached, adjust the fine focus, brightness, contrast, and stigmation to achieve the best-resolution image;
6. Set the raster scan speed to slow then capture and save the SEM image;
7. Calibrate the software on-screen measurement tool using the measurement bar given on the image by the SEM. Then, measure the size of features on the image.

3.4.7 Nanoindentation

The force-deflection mechanical behavior of the fabricated air-gaps was characterized using a Triboindenter (Hysitron, Minneapolis, MN). This tool operated with one of two load heads: a high-force head and a low-force head. The high-force head is capable of applying vertical loads up to 1.5 N with a resolution of approximately 200 μN, and can measure vertical deflections up to 96 μm. The low-force head can apply both vertical and lateral loads up to 9mN, and can measure vertical deflections up to 9.6 μm and lateral deflections of 8 μm. The resolution of the x-y movement of the stage is 50 nm. The indenter can be operated in load-control mode or displacement-control mode. In load control mode, a specific load function containing a ramp rate and a peak load is specified. In displacement control mode, a displacement function is specified with a ramp rate and a maximum displacement. In either case, the load and displacement are continuously monitored throughout the experiment.

Several geometries of diamond indenter tips are available for use with each head. In this research, only the high-force head was used with 3 various tips: 200 μm radius

spherical tip; a 50 μm conical tip; and a 20 μm conical tip. The preparation of samples for nanoindentation is discussed in detail in Chapter 9, along with specifics of the experimentation. The general procedure for performing nanoindentation experiments follows:

1. Mount the sample on the magnetic stage using steel clips or tape to hold the sample firmly in position;
2. Define the boundaries and the safety height of the sample via the software provided with the tool;
3. Calibrate the indenter software: determine the calibration spring constants by performing an air-indent, and calibrate the optics by performing a single indent on aluminum;
4. Using the optics, identify the location on the sample where the indent is to be performed;
5. Set up either the load function (for load-control) or the displacement function (for displacement control). The function consists of a ramp rate and a peak load or displacement. The unloading ramp rate is automatically set the same as the loading ramp rate;
6. Perform a quick approach to quickly determine the approximate sample height on the stage;
7. Perform the indent in the location indicated by the optics position;
8. The force/displacement data is automatically recorded throughout the indent.

3.4.8 Application of the analysis techniques in subsequent chapters

The analysis techniques described previously are selected to provide information in three main categories: (1) thermal decomposition analysis; (2) air-gap fabrication results analysis; and (3) mechanical property analysis. Chapter 4 provides results and discussion particularly relating to the thermal decomposition analysis of each sacrificial material. TGA and goniometry are the primary techniques used to characterize the decomposition of the sacrificial materials. Chapter 7 provides a more in-depth analysis of the thermal decomposition of PNB, by considering how encapsulation affects the reaction. TGA, goniometry, XPS, and AFM are the methods applied to perform the analysis. The process flow for the fabrication of air-gaps was described and depicted in section 3.1 of this chapter. The process flow is re-visited in Chapters 5 and 6, which discusses each process step in detail for PNB and PC sacrificial materials, respectively. Various encapsulating materials are also examined for use in the fabrication of air-gaps. SEM is the main technique used to analyze the fabrication results. Additionally, SEM is used to analyze the integration of air-gaps into SoL packaging technology in Chapter 8. The results from the mechanical analysis tool, nanoindentation, are discussed in Chapter 9.

CHAPTER 4

THERMAL DECOMPOSITION OF SACRIFICIAL POLYMERS

The desired properties of sacrificial materials and the chemistry of the polynorbornene (PNB) and polycarbonate (PC) sacrificial materials used in this research were presented in Chapter 3. One of key requirements of the sacrificial materials is decomposition in a narrow and useful temperature range with little or no residue. In this chapter, the results and analysis of the decomposition of PNBs and PCs, and the characteristics of the remaining surface after decomposition are presented. The object is to identify factors that may influence the decomposition of the sacrificial materials in order to choose the optimum materials for the fabrication of air-gaps.

Section 4.1 of this chapter explains the analysis procedure for extracting kinetic parameters from thermogravimetric analysis (TGA) data. Section 4.2 discusses the thermal decomposition of PNB sacrificial materials with various functional side groups attached to the polymer backbone, and how the side groups affect the decomposition of the polymers. Section 4.3 presents the decomposition studies of the polycarbonate sacrificial materials with various groups contained in or attached to the polycarbonate backbone. The PNB sacrificial materials oxidize and char when oxygen is present in the atmosphere during decomposition. However, the effect of oxygen present during the decomposition of polycarbonates is examined. The results of kinetic analysis via TGA experiments, and surface characterization for the overall decomposition reaction of PC in nitrogen and air are presented. Section 4.4 summarizes the conclusions of the chapter.

4.1 Kinetic Parameters From Thermogravimetric Analysis

The use of thermogravimetric analysis to study the kinetics governing the decomposition of polymeric materials, including polynorbornene, has been studied and documented [69-71, 73]. TGA data collected while varying a single parameter, such as heating rate or isothermal hold temperature, not only reveals qualitative information about the decomposition reaction, but also provides data for calculation of the kinetic parameters governing the reaction. Flynn [71] describes the method most commonly used to quantitatively analyze TGA data. The decomposition process is described in terms of fractional conversion (α), time (t), and temperature (T), as described in equation 4.1.

$$\frac{da}{dt} = f(a)k(T) \qquad \text{Eq. (4.1)}$$

In equation 4.1, $f(a)$ and $k(T)$ represent independent functions of fractional conversion and temperature. An important assumption is that variables including gas flow rate, pressure, and sample geometry are included in $k(T)$, or do not affect the rate of reaction. In addition, the mechanism of the reaction, indicated by the shape of thermogravimetric TG curve (the weight loss as a function of temperature or time), should not change with a change in heating rate or isothermal temperature. Figure 14 shows dynamic TG curves for PNB-1 (90/10 butyl/TES PNB, Table 2, Section 3.2.1, page 30) at heating rates of 1, 5, and 10^{o}C/min. The shape of the TGA curves in Figure 14 is typical for polynorbornenes. Each curve shows a single, smooth drop in weight with the constant rate of increase in temperature. Increasing or decreasing the heating rate causes the curve to shift on the temperature axis with no change in the qualitative shape of the curve. This

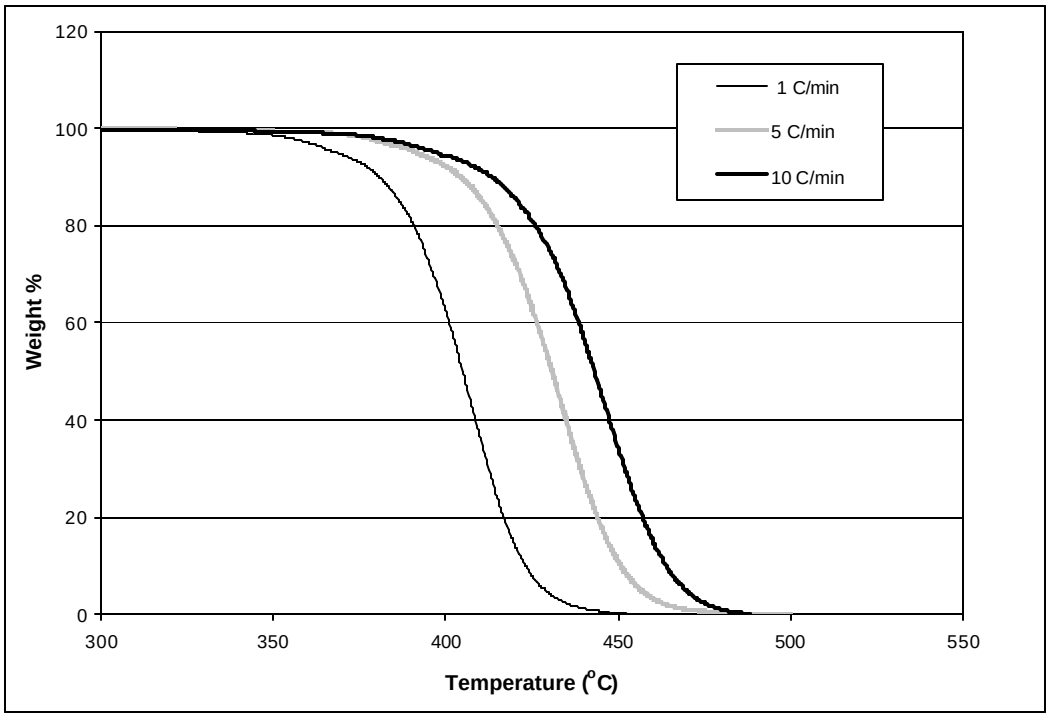

Figure 14: Dynamic TGA thermograms of PNB-1 (90/10 butyl/triethoxysilyl PNB) at heating rates of 1, 5, and 10°C/min.

indicates that the mechanism of the reaction is consistent over the various heating rates, and therefore the form of equation 4.1 applies.

The most commonly used kinetic model for a polymer decomposition [72] uses a power law function for $f(\alpha)$, ($f(\alpha) = (1-\alpha)^n$), and $k(T)$ follows an Arrhenius function dependence with temperature. Substituting these expressions into equation 4.1 yields the following:

$$\frac{da}{dt} = A \exp(-\frac{E_a}{RT})(1-a)^n \qquad \text{Eq. (4.2)}$$

In equation 4.2, n is the reaction order, E_a is activation energy, A is the pre-exponential constant, and R is the universal gas constant in appropriate units. Equation 4.2 may be

fitted with a single set of data. However, techniques which use several sets of data points produce far more confidence in the fit parameters. A differental or integral method is used to mainpulate equation 4.2 to a form where the known variables from multiple sets of TGA data can be used to solve for the kinetic parameters n, E_a, and A. It is important to note that polymeric decompositions can involve many reaction steps and can follow a complicated mechanism that changes with conversion. This model considers only the "overall" kinetic parameters for the decomposition reaction of the form described by Wedlake [69]:

$$A\ (solid) \rightarrow B\ (solid) + C\ (gas) \qquad \text{Eq. (4.3)}$$

4.1.1 Integral method to determine kinetic parameters from dynamic TGA

The integral method developed by Ozawa [73] utilizes data obtained from dynamic TGA experiments at several constant heating rates to obtain the overall kinetic reaction parameters. One major advantage of this technique is that no prior knowledge of the reaction order is needed. Equation 4.2 assumes that $f(\alpha)$ and $k(T)$ are completely independent functions. When these are separable functions, equation 4.2 can be integrated from the initial time, t_o, to obtain equation 4.4:

$$-\int_0^a \frac{da}{f(a)} = A\int_{t_0}^{t} \exp\left(\frac{-E_a}{RT}\right)dt \qquad \text{Eq. (4.4)}$$

When the rate of heating ($ß$) is constant, equation 4.4 can be modified to:

$$-\int_0^a \frac{da}{f(a)} = \frac{A}{b}\int_0^{T} \exp\left(\frac{-E_a}{RT}\right)dT \qquad \text{Eq. (4.5)}$$

The rate of the reaction is very low at low temperatures, so the integral limits of temperature can be approximated as 0 to T. An integral approximation is made for the right side of equation 4.5 to yield the following equation:

$$-\int_0^a \frac{da}{f(a)} = \frac{A}{b} * \frac{RT^2}{E_a} \exp\left(\frac{-E_a}{RT}\right) \qquad \text{Eq. (4.6)}$$

A plot of conversion as a function of temperature at various heating rates yields a set of curves with a different value of T at the same fractional conversion. Therefore, at any given fractional conversion, the left side of equation 4.6 must be constant, due to the fact that $f(\alpha)$ was not considered a function of temperature. Equation 4.6 at any given value of conversion after some manipulation becomes:

$$\log \frac{b}{T^2} = -\left(\frac{E_a}{2.3RT}\right) + \text{const.} \qquad \text{Eq. (4.7)}$$

A plot of $\log(ß/T^2)$ as the ordinate and 1/T as the abscissa for any specific conversion at several heating rates results in a straight line from which the activation energy (E_a) can be determined from the slope. Following the determiniation of the activation energy, the reaction order and pre-exponential constant can be determined from the non-integrated overall rate expression, equation 4.2. Equation 4.8 is equation 4.2 in terms of weight (W) instead of conversion .

$$\frac{dW}{dt} = A \exp\left(\frac{-E_a}{RT}\right) W^n \qquad \text{Eq. (4.8)}$$

Conversion is defined as follows:

$$a = \frac{W_0 - W}{W_0 - W_f} \qquad \text{Eq. (4.9)}$$

W_o is the weight of the unreacted sample, and W_f is the final weight when the reaction is complete. In equation 4.8, W_f is assumed to be zero, or the reaction has gone to completion. Dividing both sides of equation 4.8 by the Arrhenius expression for k(T), and taking the natural logarithm of both sides yields:

$$\ln \frac{-\frac{dW}{d\,\mathrm{t}}}{\exp(\frac{-E_a}{RT})} = n \ln W + \ln A \qquad \text{Eq. (4.10)}$$

The reaction order and pre-exponential constant are determined from the best linear fit to a plot of the left side of equation 4.10 as a function of ln(W). The slope of the line is the reaction order, n, and the inverse natural log of the y-axis intercept is A.

4.1.2 Differential method to determine kinetic parameters from isothermal TGA

The determination of kinetic parameters from isothermal TGA is simpler in that it does not require integration of equation 4.2. Equation 4.8 described the kinetic expression for the overall decomposition reaction, equation 4.2, in terms of weight. Describing k(T) simply as the rate constant, k, instead of the Arrhenius expression and taking the natural logarithm of both sides of equation 4.8 gives:

$$\ln(\frac{-dW}{dt}) = \mathrm{n} * \ln \mathrm{W} + \ln k \qquad \text{Eq. (4.11)}$$

The best fit line to a plot of the left side expression of equation 4.11 as a function of ln(W) provides the order of the reaction from the slope, and the rate constant from inverse natural log of the y-axis intercept. The activation energy is determined directly from the Arrhenius expression for k(T):

$$k(T) = A \exp(-\frac{E_a}{RT}) \qquad \text{Eq. (4.12)}$$

A plot of the natural logarithm of the rate constant, ln(k), as a function of inverse absolute temperature, (1/T), produces a line with the slope equal to the activation energy divided by the universal gas constant, R. The inverse natural log of the y-axis intercept yields the pre-exponential constant, A.

4.1.3 Residue factor

A correction called the residue factor (RF) is often needed to provide accurate kinetic parameters. If equation 4.8 correctly describes the thermogravimetric data, the curve from a plot of (dW/dt) as a function of W should pass through the origin. However, many samples do not fully decompose to zero weight during the TGA experiment. The residue factor represents this residue, or the mass of inert material in the sample. The residue factor is computed by plotting (dW/dt)/(exp(-E_a/RT)) as a function of W at high conversions. The data is then linearly extrapolated to find the x-intercept, or the RF. The RF represents the mass present when dW/dt reaches zero. A plot of the true amount of weight which can react, given by (W-RF), is then used to calculate the kinetic parameters.

4.2 Thermal Decomposition of Polynorbornene Sacrificial Materials

This section examines the thermal decomposition of polynorbornene sacrificial materials. A complete list of polynorbornenes investigated in this research was presented as Table 2 (Chapter 3, Section 3.2.1, page 30). The polynorbornenes vary in both side group composition and molecular weight, and were selected as sacrificial polymer

candidates based on desirable properties of their attached side groups. As described previously, triethoxysilyl (TES) groups increase adhesion between the polynorbornene and many substrate materials. Variations in the side groups also affect the thermal expansion coefficient (CTE) of the polynorbornene, such as methyl acetate polynorbornene with a CTE of 75 ppm/^{o}C, as compared to 90/10 butyl/TES polynorbornene with a CTE of 127 ppm/^{o}C [74]. Cyclolacrylate groups react in the presence of a free-radical generator and crosslink the polynorbornene to change its solubility in organic solvents. This allows the material to be directly patterned by selectively crosslinking the areas to remain on the sample.

In additional to the thermal decomposition characteristics, excellent processing capability is another important criterion of a sacrificial material. Variations in side group composition may improve or change the thin film processing characteristics of the polymer, and is discussed in Chapter 5. The best choice for a polynorbornene sacrificial material possesses both processability and desirable decomposition characteristics. This section includes results and discusses the thermal decomposition of the various polynorbornenes.

4.2.1 Dynamic TGA results of various composition and molecular weight PNB

Dynamic TGA was performed on at least one molecular weight of each of the various side-group composition polymers listed in Table 2, using a constant heating rate of 10^{o}C/min from 25 to 530^{o}C under nitrogen. Representative TG curves for these polymers are shown in Figures 15 through 17. Figure 15 includes the TG curves for polymers containing TES side groups: PNB-2 (90/10 butyl/TES PNB), PNB-7 (50/50 norbornene/ TES norbornene copolymer) and PNB-14 (80/10/10 butyl/TES/

cyclolacrylate PNB). Figure 16 includes TG curves for polymers containing the methyl acetate substituent: PNB-5 (methyl acetate PNB); PNB-6 (90/10 methyl acetate/TES PNB); PNB-10 (90/10 methyl acetate/cyclolacrylate PNB); and PNB-11 (80/10/10 methyl acetate/TES/cyclolacrylate PNB). Figure 17 shows the TG curves for two compositions of butyl/cyclolacrylate polynorbornene: PNB-8 (90/10 butyl/cyclolacrylate PNB), and PNB-9 (80/20 butyl/cyclolacrylate PNB). Figure 15 to 17 show that all PNB compositions are represented by a smooth TGA thermogram curve with a single drop in weight loss beginning at a temperature over 350°C. The decomposition temperature, T_d, of each polymer composition varies between 429 and 454°C. The T_d is defined as the temperature at which one-half of the original sample weight remains.

The effect of composition on the PNB decomposition is examined by sub-dividing the PNB polymers into two groups. Each polynorbornene used in this research, excluding PNB-7, contains either butyl or methyl acetate side groups as the main constituent side group attached to the polymer backbone. The first group consists of the "butyl" polymers (PNB-1, PNB-2, PNB-8, PNB-9, and PNB-14 to PNB-19), and the second group consists of the "methyl acetate" polymers (PNB-4 to PNB-6, and PNB-10 to PNB-13). Table 4 provides a comparison of the 5% weight loss temperature, the T_d (50% weight loss temperature), and the remaining weight percentage at 500°C from the dynamic TGA data obtained at 10°C/min for the various PNB compositions. The results show several differences in the TGA data from the two polymer groups. The thermal stability (indicated by the onset of decomposition, or 5% weight loss) of the methyl acetate polymers is notably lower than those containing the butyl side group. Each of the butyl polymers begin to decompose at temperatures above 386°C, while the methyl

acetate polymers begin to decompose at temperatures lower than 375°C. In comparison, PNB-7, which is a copolymer containing 50 mol% polynorbornene with no attached side group and 50 mol% triethoxysilyl polynorbornene displays the highest thermal stability under these TGA conditions, with an onset of decomposition at 413°C.

The values for the 50% weight loss temperature, T_d, in Table 4 show the temperature difference between the two polymer groups becomes much smaller when the decomposition reaches 50% conversion. For example, the temperature difference between the 5% weight loss temperatures of 90/10 butyl/TES PNB and 90/10 methyl acetate/TES PNB is 18.6°C. When the decomposition reaches the T_d, the difference in temperature is reduced to 7.2°C. A second example is the difference in temperature between the T_d of the terpolymer 80/10/10 butyl/TES/cyclolacrylate PNB and the terpolymer 80/10/10 methyl acetate/TES/cyclolacrylate PNB. At 5% weight loss, the temperature difference is 39.3°C, and reduces to 8.2°C at 50% weight loss. The percentage of remaining weight at 500°C again shows differences between each of the polymers. The value of the percent remaining weight at 500°C is used as a comparison of residual material from the polymer decomposition. The values range from 1.5% to 16.6% for the various PNB materials.

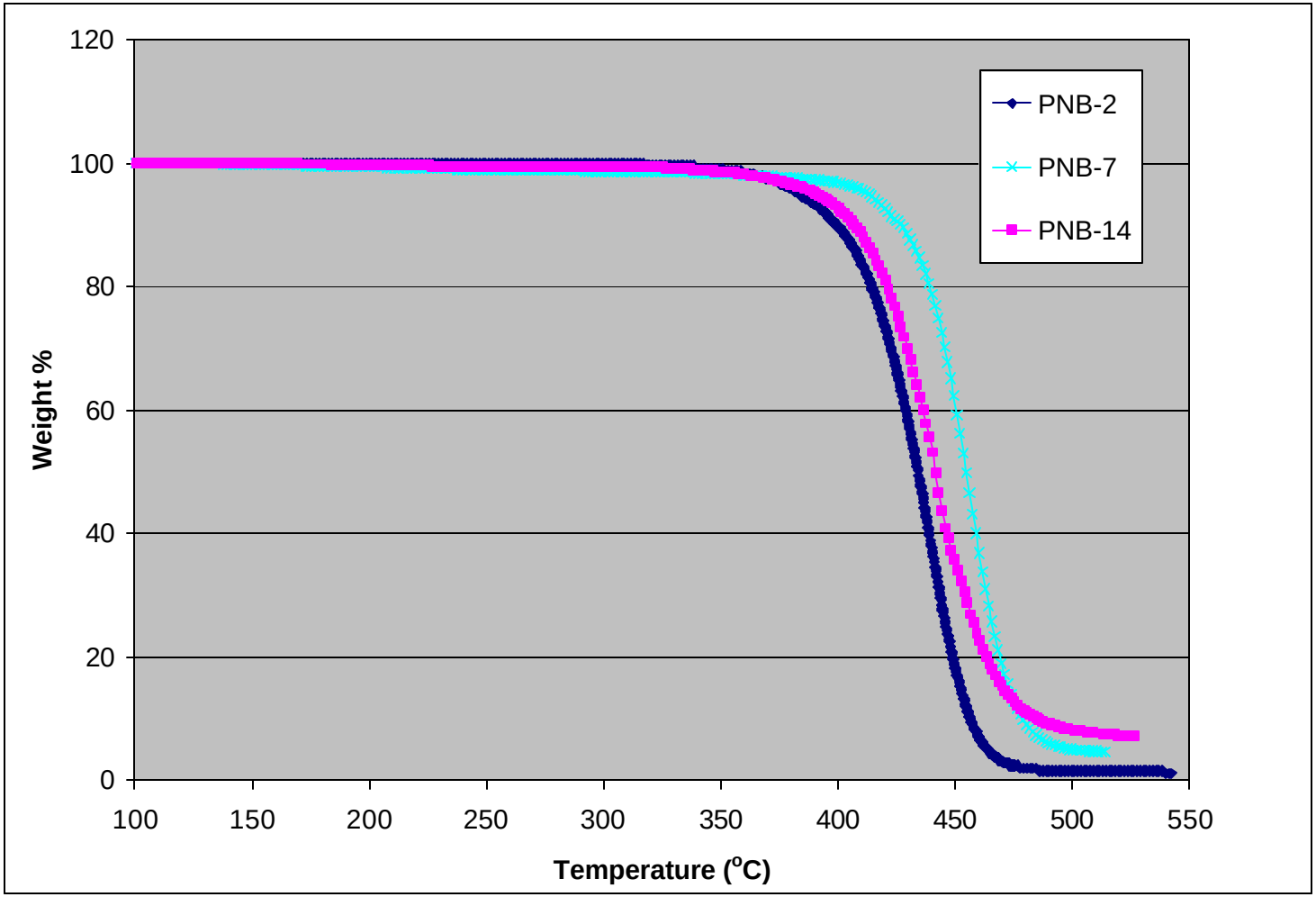

Figure 15: Dynamic TGA curves for PNB-2 (90/10 butyl/TES PNB), PNB-7 (50/50 norbornene/TES PNB), and PNB-14 (80/10/10 butyl/TES/cyclolacrylate PNB) obtained at a heating rate of 10°C/min in nitrogen.

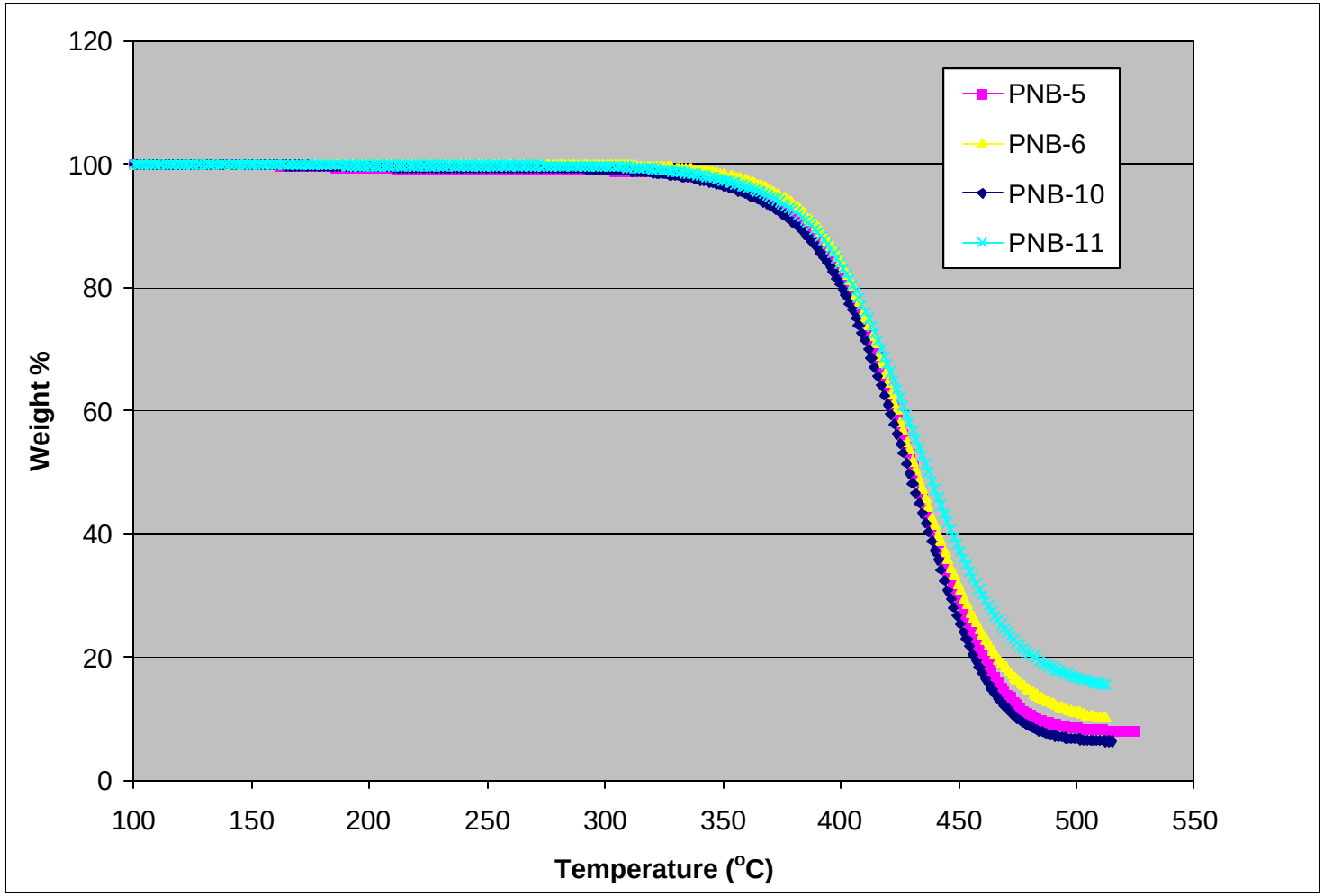

Figure 16: Dynamic TGA curves for PNB-5 (methyl acetate PNB), PNB-6 (90/10 methyl acetate/TES PNB), PNB-10 (90/10 methyl acetate/cyclolacrylate PNB) and PNB-11 (80/10/10 methyl acetate/TES/cyclolacrylate PNB) obtained at a heating rate of 10°C/min in nitrogen.

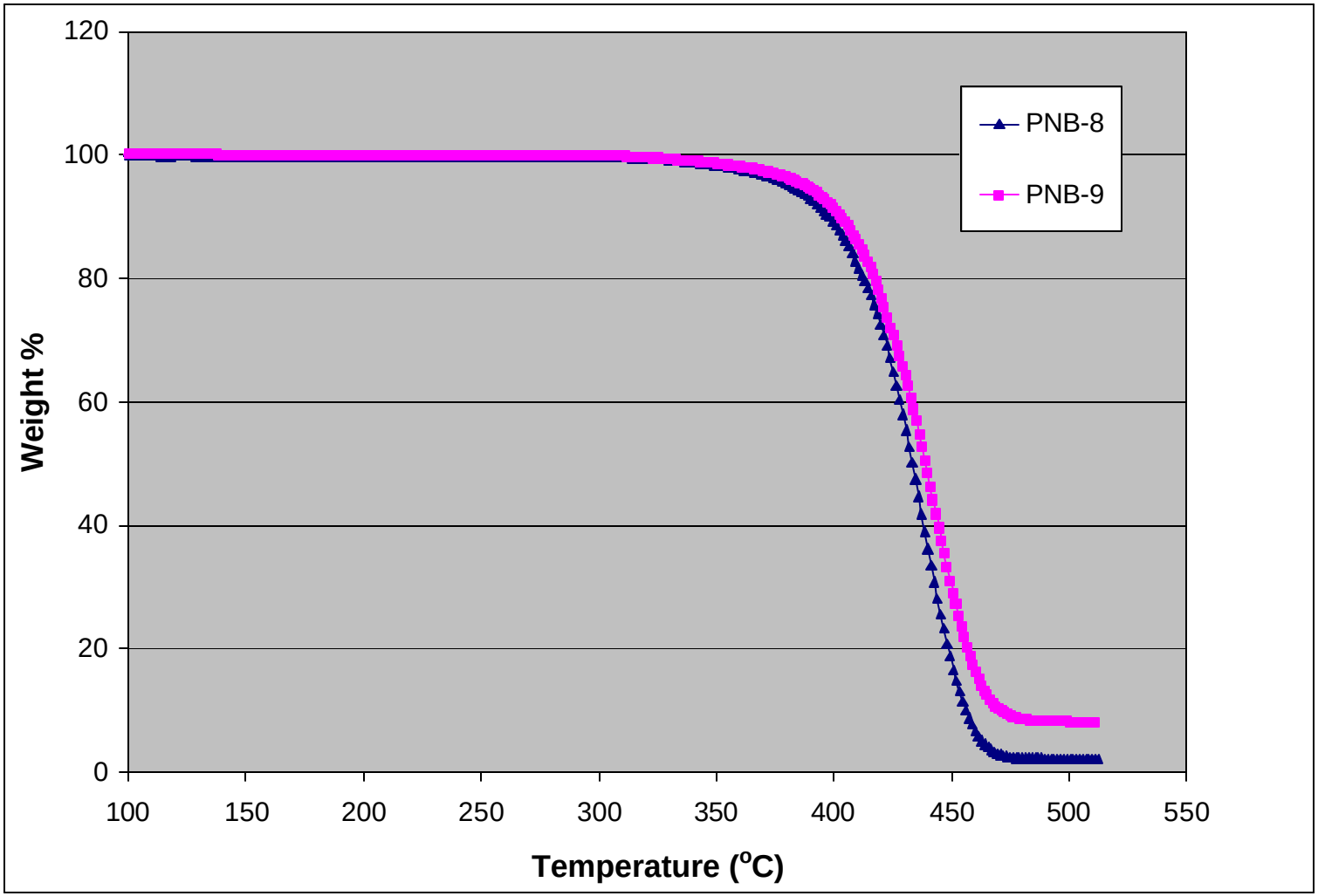

Figure 17: Dynamic TGA curves for two compositions of butyl/cyclolacrylate polynorbornene: PNB-8 (90/10 butyl/cyclolacrylate PNB); and PNB-9 (80/20 butyl cyclolacrylate PNB) obtained at a heating rate of 10°C/min in nitrogen.

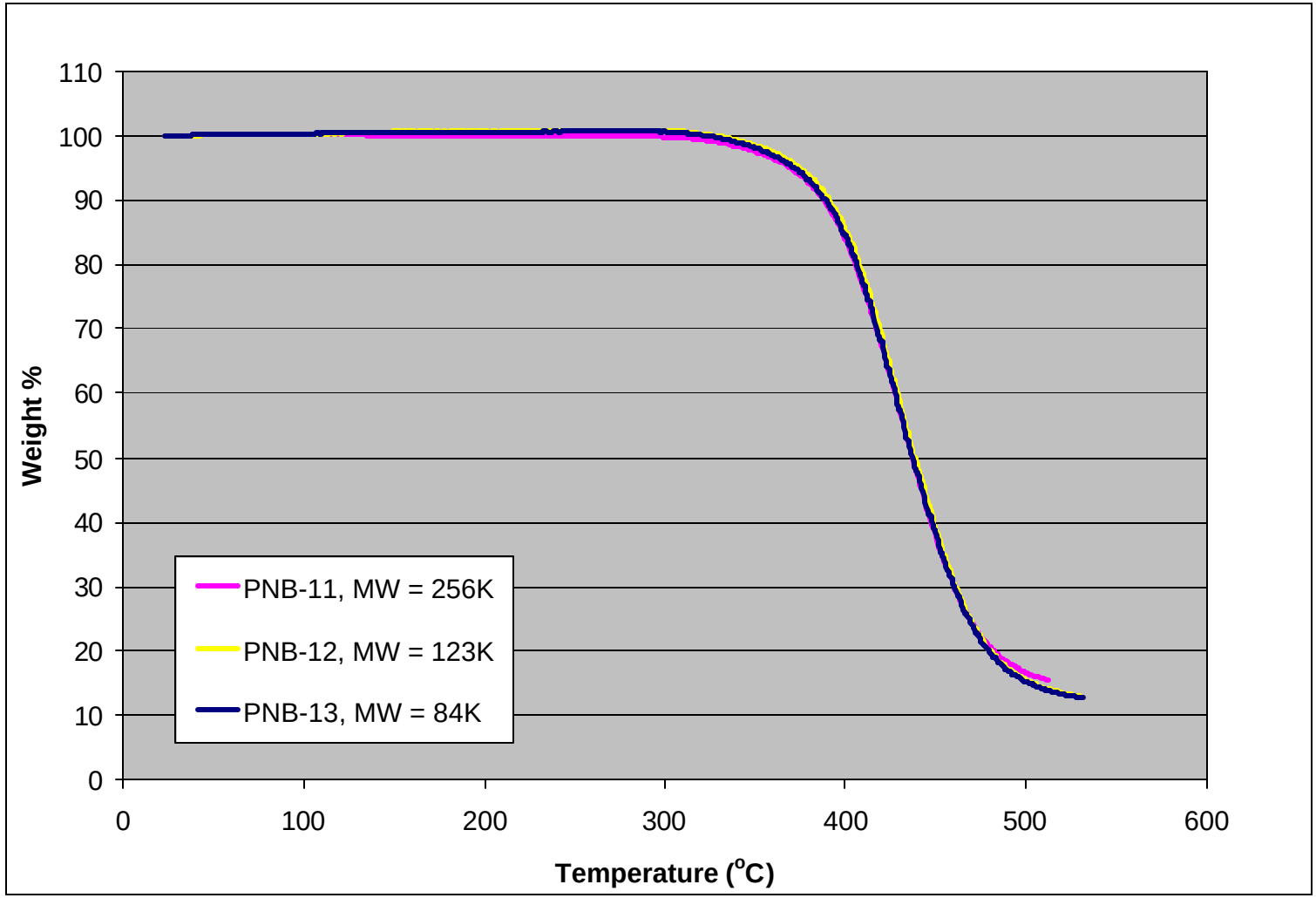

Figure 18: Dynamic TGA curves for three molecular weights of 80/10/10 methyl acetate/triethoxysilyl/cyclolacrylate polynorbornene obtained at a heating rate of 10°C/min in nitrogen.

Table 4: Dynamic TGA results for various compositions and molecular weights of polynorbornene sacrificial materials. Results are for a constant heating rate of 10°C/min in a nitrogen atmosphere (<50 ppm O_2).

Polymer #	Composition	Molecular Weight	Temperature for 5% Weight Loss (°C)	Temperature for 50% Weight Loss, T_d (°C)	Remaining polymer at 500°C
PNB-1	90/10 butyl/triethoxysilyl copolymer	283,000	393.4	439.7	1.6%
PNB-2	90/10 butyl/triethoxysilyl copolymer	182,000	389.3	434.1	1.5%
PNB-4	methyl acetate homopolymer	261,000	371.9	431.0	8.2%
PNB-5	methyl acetate homopolymer	325,000	368.9	431.2	8.4%
PNB-6	90/10 methyl acetate/triethoxysilyl copolymer	183,000	374.8	432.5	11.2%
PNB-7	norbornene/triethoxysilyl copolymer	412,000	413.2	454.2	4.9%
PNB-8	90/10 butyl/cyclolacrylate copolymer	300,000	386.3	436.0	2.2%
PNB-9	80/20 butyl/cyclolacrylate copolymer	213,000	397.8	439.0	8.2%
PNB-10	90/10 methyl acetate/cyclolacrylate copolymer	274,000	362.2	429.1	6.7%
PNB-11	80/10/10 methyl acetate/triethoxysilyl/cyclolacrylate	256,000	369.2	437.3	16.6%
PNB-12	80/10/10 methyl acetate/triethoxysilyl/cyclolacrylate	123,000	374.7	438.4	15.3%
PNB-13	80/10/10 methyl acetate/triethoxysilyl/cyclolacrylate	84,000	371.9	437.0	15.1%
PNB-14	80/10/10 butyl/triethoxysilyl/cyclolacrylate	674,000	401.5	442.1	8.3%
PNB-15	80/10/10 butyl/triethoxysilyl/cyclolacrylate	343,000	392.0	442.0	6.0%
PNB-16	80/10/10 butyl/triethoxysilyl/cyclolacrylate	278,000	392.2	442.3	7.2%
PNB-17	80/10/10 butyl/triethoxysilyl/cyclolacrylate	213,000	391.7	437.8	4.9%
PNB-18	80/10/10 butyl/triethoxysilyl/cyclolacrylate	160,000	394.7	439.7	5.8%
PNB-19	80/10/10 butyl/triethoxysilyl/cyclolacrylate	105,000	390.7	437.0	7.2%

4.2.2 Discussion of the TGA results for various molecular weight and composition PNB

The shape of the dynamic TG curves for polynorbornene show three desirable decomposition characteristics for a sacrificial material. The first is the material shows no weight loss up to a temperature around 370^{o}C. This allows processing following PNB deposition at temperatures up to 370^{o}C, such as sputtering, evaporation, PECVD deposition, or curing of other materials, with negligible loss of the sacrificial material. The second characteristic is the temperature range over which decomposition occurs. As discussed in Chapter 3, sacrificial materials are desired which decompose at: (a) 200^{o}C; (b) 300^{o}C; and (c) 400^{o}C. Polynorbornene is an ideal candidate for a 400^{o}C decomposition temperature sacrificial material for use with polyimides, inorganic glasses, and other materials which cure near 350^{o}C. The third characteristic of the TG curve is the remaining residual material at 500^{o}C. A clean decomposition with little or no residue is desirable. The dynamic TG curves show the decomposition reaction for several of the polynorbornene compositions proceeds nearly to zero remaining weight by 500^{o}C.

The dynamic TGA experiments were designed to investigate the effect of molecular weight and composition on the thermal decomposition of PNB. Figure 18 superimposes on one set of axes the dynamic TG thermograms (heating rate = 10^{o}C/min) of three different molecular weight 80/10/10 methyl acetate/TES/cyclolacrylate norbornene terpolymers. The decomposition curves in Figure 18 are nearly identical, regardless of molecular weight. Similar results are seen for the other polynorbornene compositions. Therefore, the molecular weight of the polymer in the range of the sacrificial materials investigated (84,000 to 674,000) was shown to cause negligible differences in the polymer decomposition.

Previously, Wedlake [69] presented TGA data on the thermal stability and decomposition of some polynorbornenes, including homopolymers of methyl polynorbornene, butyl polynorbornene, hexyl polynorbornene, and the 90/10 butyl/TES norbornene copolymer. Using dynamic TGA at the same rate of 10°C/min under nitrogen, Wedlake [69] reports each of the homopolymers and the 90/10 Bu/TES PNB show a 5% weight loss temperature of around 395 to 400°C. The polymers in Table 4 with the main side-group substituent as an alkyl group (butyl) begin to decompose at temperatures near, but in a slightly expanded range between 386 to 405°C. On the other hand, the change of the main side group constituent from an alkyl to an acetate group causes a significant drop in the temperature for 5% weight loss. The methyl acetate polymers begin to decompose in an entirely different temperature range between 362 to 375°C.

The dynamic TGA data obtained by Wedlake [69] also showed the thermal stability of alkyl polynorbornene homopolymers minimally increased as the length of the alkyl side group was increased from methyl to butyl to hexyl. At the same TGA heating rate of 10°C/min in nitrogen, the 90/10 Bu/TES polymer showed a slightly higher thermal stability than all three homopolymers until about 40% conversion. After 40% conversion, the TG curve of the copolymer began to almost identically resemble the TG thermogram of the butyl homopolymer until the completion of the experiment at 500°C [69]. TES and/or cyclolacrylate side group components in the copolymers and terpolymers also induce a slight variance from the onset decomposition temperature of the butyl and methyl acetate homopolymers. Figure 19 shows the reaction portion of the dynamic TGA thermograms for four different methyl acetate polymers: (a) PNB-5,

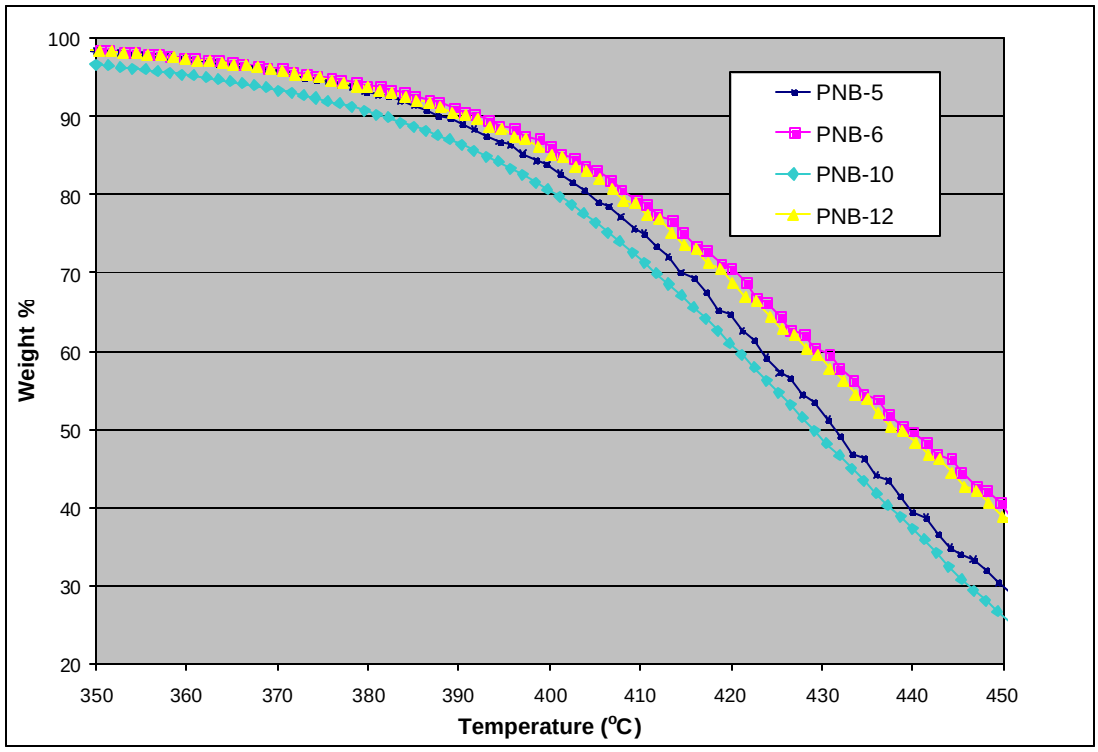

Figure 19: Dynamic TGA thermograms obtained at a heating rate of 10°C/min for (a) PNB-5, methyl acetate homopolymer; (b) PNB-6, 90/10 methyl acetate/TES copolymer; (c) PNB-10, 90/10 methyl acetate/cyclolacrylate copolymer; and (d) PNB-12, 80/10/10 methyl acetate/ triethoxysilyl/cyclolacrylate terpolymer.

methyl acetate homopolymer; (b) PNB-6, 90/10 methyl acetate/TES copolymer; (c) PNB-10, 90/10 methyl acetate/cyclolacrylate copolymer; and (d) PNB-12, 80/10/10 methyl acetate/TES/cyclolacrylate terpolymer. Comparison of the curves for PNB-5 and PNB-6 in Figure 19 shows the addition of 10 mol% TES groups to the methyl acetate polymer slightly increases the temperature for 5% weight loss. This is consistent with the results reported for the 90/10 butyl/TES copolymer. However, the addition of the TES groups to the methyl acetate polymer shifts the entire TG thermogram to higher temperature, not only the initial portion of the curve from 0 to 40% conversion, as reported for the butyl polymer. Figure 19 also shows the addition of 10 mol %

cyclolacrylate groups to the methyl acetate homopolymer slightly decreases the temperature for 5% weight loss. The difference between 5% weight loss temperatures for the homopolymer, PNB-5, and the 90/10 methyl acetate/cyclolacrylate copolymer, PNB-10, is 6.7°C. However, by 20% conversion, the temperature difference between these two polymers is < 3°C, and remains small. The addition of cyclolacrylate groups to the butyl polymers produces no change in the thermal stability. The addition of both 10 mol% TES groups and 10 mol% cyclolacrylate groups to both polymers results in thermal stability equivalent to the polymers containing only 10 mol% TES. For example, the TG curve for the terpolymer, PNB-12, in Figure 19 follows the TG curve for PNB-6, the 90/10 methyl acetate/TES copolymer. However, significant differences in the weight percentages remaining at 500°C exist between the terpolymers and copolymers.

Generally, in glassy polymers, the T_g and thermal stability directly correlate with increasing chain stiffness of the polymer [72, 75-77]. However, bulky side groups, branching, or crosslinks can influence the mobility of the polymer molecules or change intermolecular forces, resulting in either a positive or negative effect on T_g and T_d [72]. A change which increases the mobility of the molecules tends to decrease the thermal stability of the polymer. Branching or bulky side groups often decrease the thermal stability due to decreased packing density of the molecules or an increase in the number or type of thermally liable end groups [72]. The larger free volume from steric hindrance provides more chain mobility, and thus less thermal stability. The methyl acetate polynorbornene polymers contain many more bulky side groups, and thus likely contain more free volume than the butyl polymers. In addition, the methyl acetate groups have greater mobility due to free bond rotation about the oxygen in the ester linkages in these

side-groups. Both factors increase mobility and significantly contribute to less thermal stability. In fact, the polymers with methyl acetate groups as the main side-group substituent initially degrade at an average temperature of 25^{o}C lower than the butyl containing polymers.

Following the same argument, as the length of the alkyl group attached to the PNB increases, or bulky TES groups are added to the polymer, the packing density and the thermal stability of the polymers is expected to decrease. However, Wedlake's [69] experimental TGA data show the opposite effect. The increase in thermal stability of these polymers as the length of the alkyl side group increased was significantly smaller than the change between the butyl and methyl acetate polymers. Therefore, the change in length of the alkyl group must not significantly contribute to free volume differences or the effect is exceeded by some other mechanism.

Mass spectroscopy was performed by Wedlake [69] and revealed the polynorbornenes all decomposed in a similar manner, irrespective of the side-groups attached to the backbone. The main degradation products included monomers, dimers, trimers and tetramers, intact side groups, and fragments of these species including cyclopentenyl and cyclopentadiene. From this mass spectroscopy and TGA data, Wedlake [69] describes the decomposition of the alkyl polynorbornene homopolymers, as well as the 90/10 butyl/TES PNB, as depropagation until about 40% conversion, where chain transfer reactions then dominate the mechanism. Therefore, during the initial depropagation reaction period, the main degradation product is monomer units as the polymer chain unzips. In order for the reaction to continue, a radical must be able to continuously find the next reaction site from the chain end before termination. The

termination process is diffusion controlled. If radicals are prohibited from movement, they are more likely to recombine and terminate the reaction [78]. This effect is increased when the polymer is in a solid or melt form. At atmospheric pressure, only monomer units and smaller fragments are volatile. As the length of an alkyl side group increases, the radical mobility to the next reaction site is more likely to be blocked and the reaction terminates. This effect may account for the small differences in thermal stability as the alkyl side group length is increased. The TES side groups also may block radical diffusion, but their main contribution to an increase in thermal stability comes from a resonance effect [69]. The free volume effect from the methyl acetate and cyclolacrylate groups apparently overcomes any steric hindrance of radical diffusion. The chemistry of these groups also contributes to a decrease in thermal stability. The ester groups begin to undergo intermolecular ester exchange reactions between 360 to 365^{o}C [78]. The ether linkages in the methyl acetate and cyclolacrylate groups also are more thermally liable and require less energy to break than the C-C bonds between rings in the backbone. Therefore, they may act as end-groups or sites to initiate the depolymerization and transfer reactions throughout the decomposition temperature. Once the conversion exceeds 40%, transfer reactions become dominant and diffusion is no longer controlling the reaction. The increased mobility of polymer chains and reaction sites may account for the smaller temperature differences between the polymer compositions at 50% conversion.

The values for residual material remaining in the TGA at 500^{o}C were listed in Table 4 in this chapter for the various PNB compositions. Each of the methyl acetate polymers leaves a significantly higher amount of residue than its butyl counterpart. For

example, PNB-1 (90/10 butyl/TES copolymer) has a residual value of 1.6 % weight while PNB-6 (90/10 methyl acetate/TES copolymer) leaves 11.2 % remaining weight. The methyl acetate copolymers and terpolymers show even higher values of residual weight than the methyl acetate homopolymer. The residual material therefore is dependent on the amount and type of side groups attached to the polymer backbone. The cleanest decomposing materials are the PNB-2 (90/10 butyl/TES copolymer) and PNB-8 (90/10 butyl/ cyclolacrylate copolymer), with residual values of 1.5% and 2.2%, respectively. A monomer ring unit with an attached butyl group has a greater ability to volatilize and leave the system than a ring containing a bulky side group. Mass spectrometry data also showed that intact side groups volatilize from the system [69]. Side groups which are broken from the main polymer chain often react together [79]. The exact interaction and reactions between side groups is beyond the scope of this work. However, the bulkier TES, cyclolacrylate, and methyl acetate groups likely produce larger and less volatile species than the butyl groups. In addition, the decomposition reaction may not proceed to completion for the copolymer and terpolymer compositions if the non-volatile products do not further decompose, or hinder diffusion of the volatile species from the system.

4.3 Thermal Decomposition of Polycarbonate Sacrificial Materials

The polycarbonates introduced in Chapter 3 (Figure 12, Section 3.2.2, pg. 32) have been investigated for use as sacrificial materials with lower decomposition temperatures than polynorbornene sacrificial materials. The lower decomposition temperatures advance the use of the sacrificial polymer air-gap formation process to incorporate materials which cannot be exposed to temperatures > 400^{o}C. As described in Chapter 3, the target decomposition temperatures for polycarbonate sacrificial materials

are 200°C and 300°C. Extensive literature of previous investigations on the thermal decomposition of aliphatic and aromatic polycarbonates exists, and the temperatures and mechanisms for decomposition are well-known [45-46, 80-83]. The previous applications of poly-carbonates include electron beam photoresists, electron-beam patternable sacrificial layers for nanofluidic devices, sacrificial ceramic binding agents, and UV-biodegradable materials [33-34, 46]. The goal of this research is to innovatively use polycarbonates as sacrificial materials specifically in the air-gap fabrication process. As with PNB sacrificial materials, the polycarbonates must have acceptable processing capabilities and the necessary decomposition characteristics required for air-gap formation. This section specifically discusses the concepts and evaluates the decomposition of the polycarbonate materials. One proposed scheme is to change the chemistry of the polymers and allow the decomposition temperature to be modified over a desired temperature range. However, as with the PNB sacrificial materials, the decomposition is only part of the necessary requirements of a sacrificial material. The processing characteristics of poly-carbonates are another key factor and are discussed in Chapter 6.

4.3.1 Dynamic TGA results of various composition polycarbonates

Dynamic TGA was performed on each of the polycarbonates described in Chapter 3: polyethylene carbonate (PEC); polypropylene carbonate (PPC); polycyclohexene carbonate (PCC); and polynorbornene carbonate (PNC). Figure 20 shows the dynamic TGA thermograms for each of these polycarbonates obtained at a heating rate of 10°C/min in nitrogen-purged environment. Similar to polynorbornenes, the polycarbonates show desirable decomposition characteristics for a sacrificial material.

Figure 20 indicates that each of these polycarbonate materials shows a single drop in weight loss as temperature is ramped at a constant rate. The PEC and PPC are ideal materials for decomposition at temperatures in the range of 200 to 280^{o}C, and PCC and PNC are ideal for decomposition at temperatures between 280 to 350^{o}C. PEC and PPC, show negligible weight loss at temperatures up to 200^{o}C, followed by a steep decline in weight as the temperature is further increased. Therefore, additional processing can be performed up to 200^{o}C on samples containing PEC or PPC, without loss of the sacrificial material. PCC and PNC can resist higher temperatures of 275^{o}C and 300^{o}C, respectively. In addition, each polycarbonate cleanly decomposes in nitrogen. The dynamic TGA results show less than 0.5% residual material remaining at 400^{o}C for each of the polymers.

As with the polynorbornenes, various functional groups in or attached to the polycarbonate backbone may be tailored to achieve desired properties such as decomposition temperature (T_d), glass transition temperature (T_g), or adhesion. Figure 20 demonstrates how variation in the functional group incorporated into chemistry of the polycarbonate backbone shifts the decomposition temperature of the polymer, as well as produces slightly different decomposition profiles for the polycarbonates. Table 5 compares the T_g, the 5% weight loss temperature, the T_d, and the percentage of weight remaining at 400^{o}C for the data in Figure 20. An increase in the length of an alkyl chain in the polycarbonate backbone corresponds to an increase in both the T_g and T_d. For example, the T_d for PEC is 208^{o}C and the T_d for PPC is 261^{o}C. Therefore, one additional methyl group pendant to the carbon atoms in the backbone changes the decomposition temperature over 50^{o}C. In Table 5, the values for weight percentage at 400^{o}C also

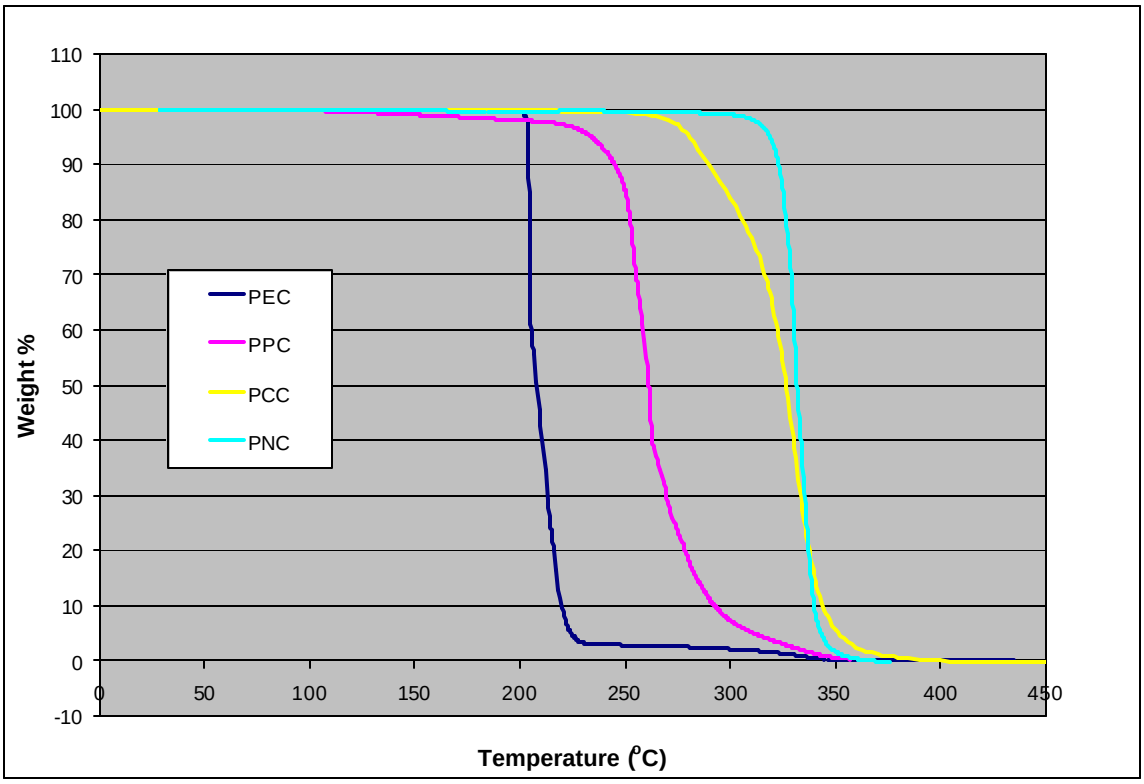

Figure 20: Dynamic TGA thermogram ramping 10°C/min in a nitrogen atmosphere for various polycarbonate sacrificial materials.

Table 5: Comparison of the decomposition for various polycarbonates from dynamic TGA at 10°C/min.

Polycarbonate	**Glass Transition T_g (°C)** [74,84]	**T for 5% Weight Loss (°C)**	**T for 50% Weight Loss (°C)**	**Weight percent at 400°C**
PEC	5	203.8	208.0	0.07%
PPC	30	234.0	261.3	0.32%
PCC	66	280.6	326.8	0.009%
PNC	115	319.1	331.9	-0.16%

indicate the carbonates in this research completely decompose in nitrogen. The negative value of weight for PNC is effectively 0%, and is a result of the tolerance limits of the TGA (± 10 μg).

4.3.2 TGA results of polycarbonate decomposition in nitrogen and air atmospheres

The effects of heating rate and the presence of oxygen on the decomposition of a polycarbonate were investigated by performing dynamic and isothermal TGA on PPC in: (1) air, and (2) nitrogen. Figures 21 (a) and (b) contain the dynamic TGA results for PPC in nitrogen and ambient air, respectively, at ramp rates of 10, 5, 2, 1, and 0.5°C/min. As the temperature ramp rate is increased, the TGA curve shifts on the x-axis to higher temperatures. However, the shape of the curve is constant for each environment as the ramp rate is changed. The consistency of the shape indicates that the reaction mechanism is not changed by an increase in heating rate. At a higher ramp rate, less time is spent at each temperature, which decreases the value of the conversion at each temperature.

Table 6 compares values from the thermogram curves in Figure 21 at various points during the decomposition. At the lowest heating rate of 0.5°C/min, the onset of decomposition (5% weight loss temperature) for PPC is 177.3°C in nitrogen and 182.4°C in air. These values indicate that oxygen in the environment does not significantly affect the temperature at which the reaction begins. The difference in the onset temperatures is small enough to derive from variation in the actual average heating rate provided by the TGA from experiment to experiment. However, a comparison of the shapes of the curves in Figure 21 (a) to those in Figure 21 (b), indicate a significant variation at high

conversion due to the presence of oxygen. A small foot begins at approximately 5% weight remaining on the curves in nitrogen, and is absent from the curves in air.

A difference between decomposition in each environment can be further recognized in Figure 22, which directly compares the dynamic TGA curves in both environments at ramp rates of 0.5, 2, and 10°C/min on a single set of axes. At each heating rate, decomposition begins at approximately the same temperature in both nitrogen and air. However, the decomposition in air follows a substantially different path after the onset of decomposition. At the slowest ramp rate of 0.5°C/min, decomposition to less than 5% remaining weight occurs for PPC in air at approximately 250°C. The same extent of conversion does not occur for PPC in nitrogen until about 300°C. Therefore, a higher temperature or more time is required to complete decomposition of the final 5% remaining weight in nitrogen. In addition, the shape of the curves in air and nitrogen in Figure 22 become more similar as the heating rate is increased. The foot at 5% remaining weight disappears completely from the data taken at 10°C/min in nitrogen. At higher temperatures, either the oxygen has less of an effect on the reaction, or its effect is overshadowed by faster decomposition due to the higher temperature. When the TGA reaches 350°C, the polymers are fully decomposed in both environments at each heating rate. The values of percentage weight remaining at 350°C following the dynamic TGA at each ramp rate are reported in Table 6. Again, the negative values of weight percentage are a result of experimental tolerance limits of the TGA.

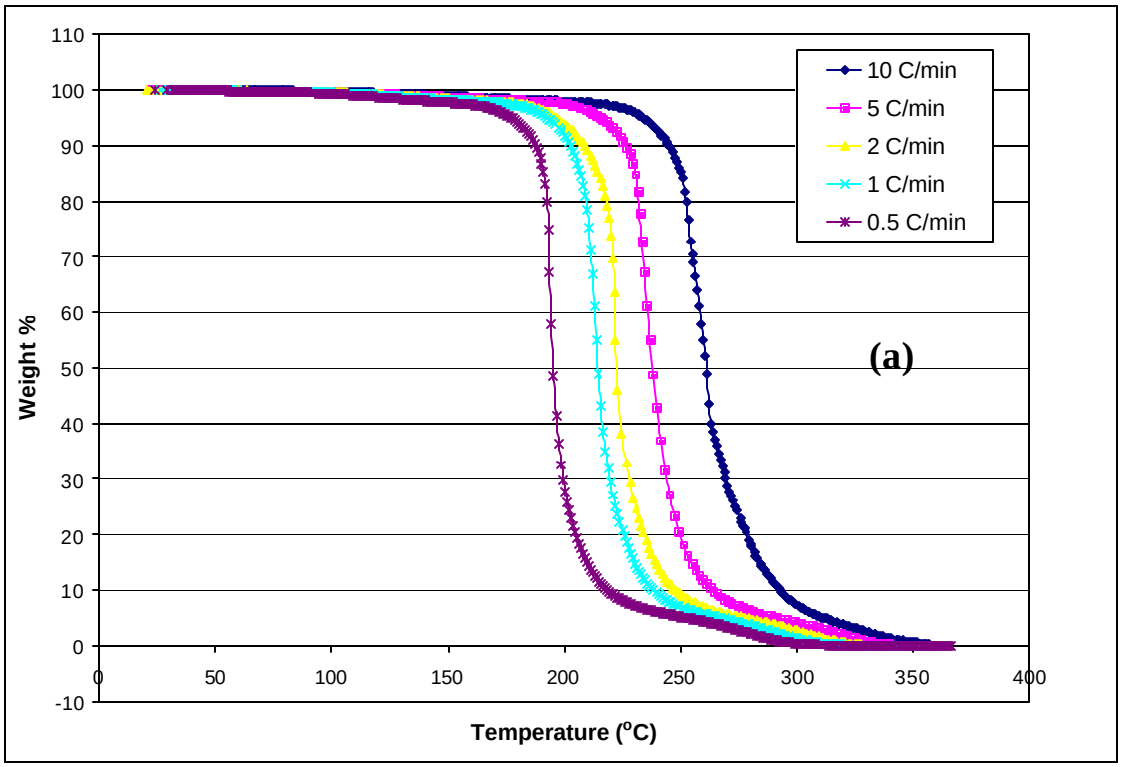

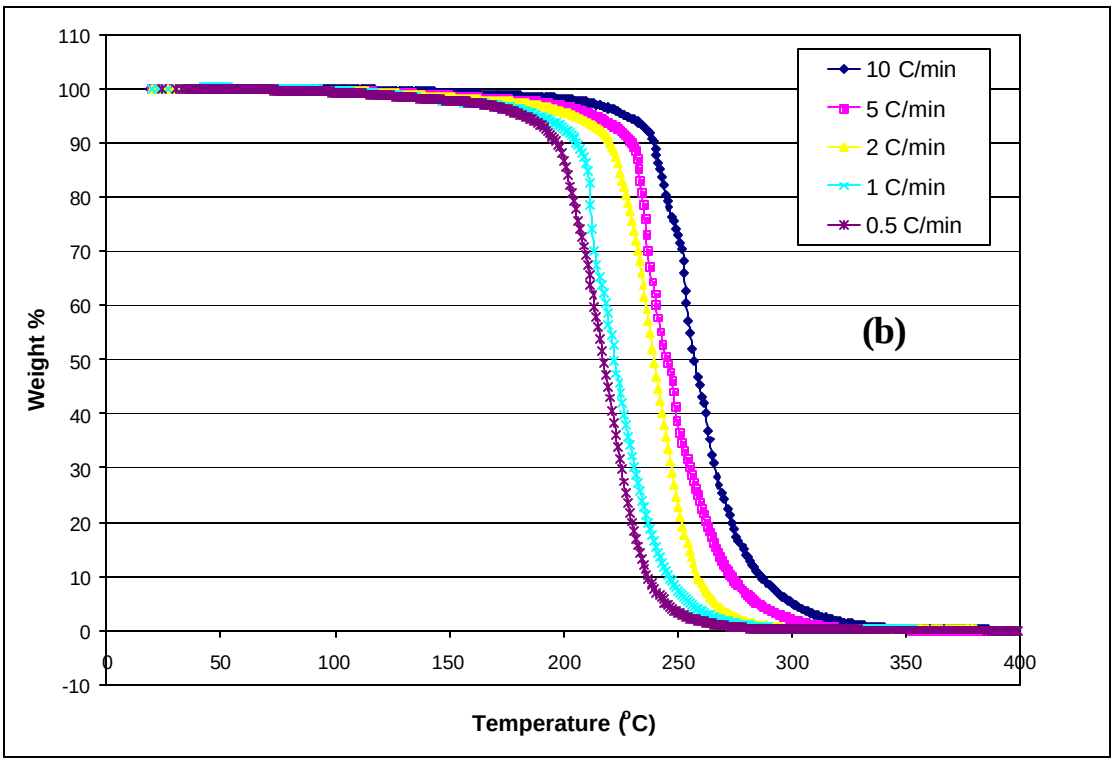

Figure 21: Dynamic TGA thermograms for PPC obtained at heating rates of 10, 5, 2, 1, and 0.5°C/min in (a) nitrogen and (b) air (40% relative humidity).

Table 6: Properties of the dynamic TGA decomposition of PPC performed at various heating rates in: (1) nitrogen; and (2) air.

	Set Heating Rate (^{o}C/min)	**Average Measured Heating Rate (^{o}C/min)**	**T for 5% Weight Loss (^{o}C)**	**T for 50% Weight Loss (^{o}C)**	**Range for 10-90% Conversion (^{o}C)**	**Weight Percent at 350^{o}C**
PPC in Nitrogen	0.5	0.48	177.3	195.2	187.5 - 218.7	-0.04%
	1	0.95	192.9	214.4	202.6 - 238.4	-0.08%
	2	2.37	196.9	222.6	208.7 - 248.1	-0.15%
	5	4.77	215.8	238.0	226.3 - 264.0	0.07%
	10	9.98	234.0	261.3	245.1 - 292.7	0.59%
PPC in Air	0.5	0.51	182.4	217.4	197.3 - 236.9	0.08%
	1	1.03	188.6	222.1	205.9 - 245.9	0.11%
	2	2.05	204.7	239.4	220.6 - 258.7	0.14%
	5	5.17	213.2	245.0	229.9 - 273.4	0.11%
	10	10.45	227.3	257.1	239.4 - 286.2	0.28%

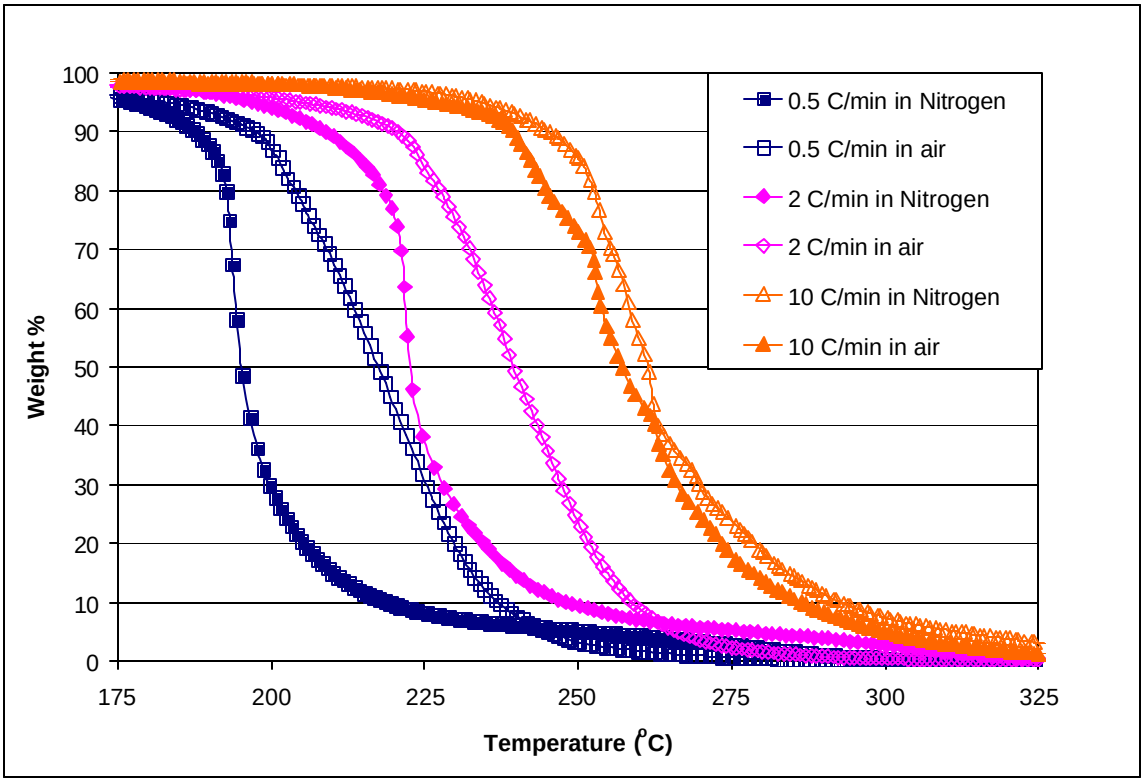

Figure 22: Comparison of dynamic TGA curves for the decomposition of PPC performed at heating rates of 0.5, 2, and 10°C/min in nitrogen and air environments.

The dynamic TGA data are useful in detecting the temperature for the onset of decomposition, the number of weight loss steps in the decomposition, the temperature range over which decomposition occurs, and the remaining residual material. However, the dynamic TGA data do not necessarily indicate the optimum or lowest temperature required for complete decomposition of the polymer. Isothermal TGA data is the second piece of information needed to indicate how complete the decomposition reaction reaches at a particular and constant temperature. Figures 23 (a) and (b) contain isothermal TGA curves showing the remaining weight of PPC as a function of time, at various isothermal temperatures. The data in Figure 23 (a) was taken in a nitrogen-purged environment and

the data in Figure 23 (b) was obtained in air. Although the TGA program set points were often identical, the required flow of nitrogen into the TGA resulted in cooling of the sample. Therefore, the isothermal temperatures varied for the experiments in each environment. Table 7 compares the actual isothermal temperatures of the samples, to the set point temperatures. In addition, the time scale on the x-axes in Figure 23 is not the absolute time required for decomposition, but rather relative time for comparison of the various temperatures. All isothermal TGA programs included a 10°C/min ramp to 100°C, a hold for 5 min, then a ramp to the isothermal temperature at a rate of 100°C/min. Note that the data taken in the first few minutes after the onset of the decomposition is not at the true isothermal temperature, due to delay in the temperature control system.

The isothermal TGA curves in Figure 23 shift on the x-axis to lower times as the isothermal temperature increases. This indicates the PPC decomposition reaction proceeds at a faster rate as the temperature is increased in both air and nitrogen, as expected from the Arrhenius expression for the rate constant. Table 7 compares various points of the decomposition reaction at the various isothermal temperatures. As the temperature increases, the time required for 50% conversion decreases. However, the time required for 50% conversion does not show a dependence on the environment. For example, the decomposition of PPC at an isothermal temperature of 292.4°C in nitrogen, and 292.5°C in air requires 18.2 and 18.6 min, respectively. This difference is time is not significant. As the reaction proceeds to higher conversions, the environment begins to impact the PPC decomposition. After 60 min at a temperature of approximately 270°C, >3% weight remains in nitrogen, and <1% weight remains in air. In addition, in order for the reaction to reach 95% conversion after 1 hour, the temperature must be above

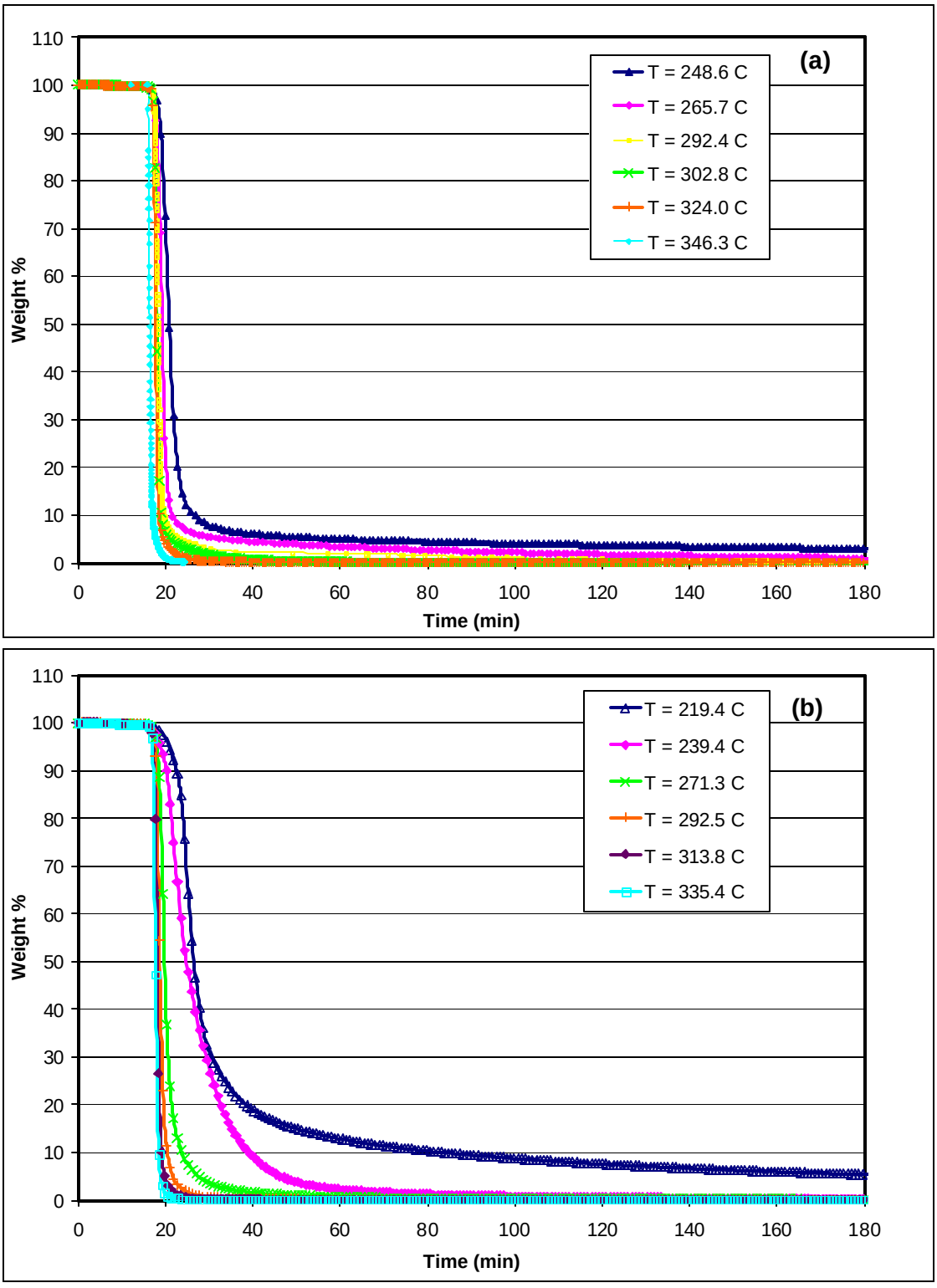

Figure 23: Isothermal TGA thermograms for the decomposition of PPC at various hold temperatures in (a) nitrogen and (b) air (40% relative humidity).

Table 7: Properties of the isothermal TGA decomposition of PPC performed at various isothermal hold temperatures in: (1) nitrogen; and (2) air.

	TGA Temp. Set Point (^oC)	**Actual Isothermal Temp. (^oC)**	**Time for 50% Weight Loss (min)**	**Weight Percentage after 60 min**	**Weight Percentage after 120 min**
PPC in Nitrogen	260	248.6	20.8	5.04%	3.75%
	280	265.7	19.2	3.36%	1.72%
	300	292.4	18.2	1.71%	0.25%
	320	302.8	17.9	0.19%	0.00%
	340	324.0	17.7	0.08%	0.05%
	360	346.3	16.5	0.07%	0.03%
PPC in Air	230	219.4	26.5	12.80%	7.59%
	250	239.4	24.8	2.24%	0.62%
	280	271.3	19.8	0.67%	0.22%
	300	292.5	18.6	0.15%	0.07%
	320	313.8	18.0	0.14%	0.09%
	340	335.4	17.6	0.14%	0.11%

250°C in nitrogen and 220°C in air. The reaction proceeds to a higher conversion after one hour in air at either a lower temperature, or in less time. However, as temperature increases, the PPC decomposes cleanly and within a reasonable time in both nitrogen and air environments.

4.3.3 Kinetic parameters for the decomposition of PPC in nitrogen and air

Variations in the shapes of the dynamic TGA curves for PPC decomposition in nitrogen and air indicate possible differences in the overall decomposition reaction mechanisms. Calculation of the kinetic parameters for the overall decomposition reaction may further reveal these differences. Therefore, the dynamic and isothermal TGA data for PPC were used to calculate the kinetic parameters for decomposition in ambient air and nitrogen atmospheres. In order for the validity of the calculations, the decomposition mechanism is assumed to follow nth-order reaction kinetics with an Arrhenius rate constant, represented previously by equation 4.8.

$$\frac{dW}{dt} = A\exp\left(\frac{-E_a}{RT}\right)W^n \qquad \text{(Eq. 4.8)}$$

The Ozawa method described in Section 4.1 is utilized to calculate the kinetic parameters in ambient air and nitrogen from the dynamic TGA data. As described in Section 4.1, equation 4.8 is represented in terms of conversion, and then integrated to obtain equation 4.7.

$$\log\frac{b}{T^2} = -\left(\frac{E_a}{2.3RT}\right) + \text{const.} \qquad \text{Eq. (4.7)}$$

A plot of log (β/T^2) vs. 1/T is constructed from the data in air and nitrogen at conversions of 10, 20, 30, 40, 50, 55, 60, 65, 70, 75, 80, 85, and 90 percent. These plots for PPC

decomposition in nitrogen and air are included as Figure A.1 and Figure A.2 in Appendix A. The heating rate (β) used in the calculations is the average heating rate determined from the change in temperature and time (dT/dt) between each pair of data points. The average heating rate values are listed in Table 8. Activation energy values are determined from the slope of the least squares best fit line through the five data points at each conversion. An average activation energy is then calculated from the values at each conversion, and used to determine the residue factor (RF) at each heating rate, also included in Table 8. Details of the activation energy and residue factor determinations are included in Appendix A. The RF values for the decomposition of PPC in nitrogen are approximately 8 percent of the original mass of the sample. This correlates to the percentage weight remaining at the initial portion of the foot at the bottom of the TG curves. The kinetic parameters calculated by this method apply to the governing kinetics dominating the first 92% conversion, or the majority of the decomposition reaction. Once the residue factor is known, a reaction order (n) and a pre-exponential constant (A) are determined at each heating rate using equation 4.10.

$$\ln \frac{-\frac{dW}{dt}}{\exp(\frac{-E_a}{RT})} = n \ln W + \ln A \qquad \text{Eq. (4.10)}$$

The slope of the best-fit line to the curve produced by a plot of $\ln((-dW/dt)/(\exp(-E_a/RT)))$ as a function of ln(W) yields n. However, in the case where non-reactive weight remains, the parameters are corrected by plotting $\ln((-dW/dt)/(\exp(-E_a/RT)))$ as a function of ln(W-RF). The pre-exponential constant, A, is determined from the inverse natural log of the y-axis intercept. The plots and the values of n and A at each heating rate before

and after the RF correction are included in Appendix A. A summary of the resulting average kinetic parameters and one standard deviation from the dynamic TGA data are reported in Table 10.

Table 8: Residue factors from the dynamic TGA decomposition of PPC performed at various ramp rates in: (1) nitrogen; and (2) air.

	Actual Heating Rate (^{o}C/min)	**Residue Factor (mg)**	**Initial Sample Mass (mg)**	**RF as a Percentage of Initial Mass**
PPC in Nitrogen	0.47± 0.06	1185	14.30	8.29%
	0.94 ± 0.08	1029	12.81	8.03%
	2.38 ± 0.34	795	10.07	7.89%
	4.77 ± 0.62	1176	14.47	8.13%
	10.13 ± 2.30	1277	17.04	7.49%
PPC in Air	0.51 ± 0.04	666	13.72	4.85%
	1.03 ± 0.11	661	12.00	5.51%
	2.07 ± 0.13	588	14.81	3.97%
	05.20 ± 0.53	655	8.379	7.82%
	10.70 ± 1.55	758	9.092	8.34%

Table 9: Residue factors from the isothermal TGA decomposition of PPC performed at various temperatures in: (1) nitrogen; and (2) air.

	Isothermal Temperature (^{o}C)	Residue Factor (mg)	Initial Sample Mass (mg)	RF as a Percentage of Initial Mass
PPC in Nitrogen	248.6	870	15.24	5.71%
	265.7	682	13.04	5.23%
	292.4	684	14.67	4.66%
	302.8	480	12.85	3.74%
	324.0	415	15.76	2.63%
	346.3	410	12.11	3.39%
PPC in Air	219.4	807	11.67	6.92%
	239.4	214	12.30	1.74%
	271.3	1029	18.39	5.60%
	292.5	454	14.71	3.09%
	313.8	409	15.36	2.66%
	335.4	214	14.37	1.49%

Table 10: Kinetic parameters for the decomposition of PPC in nitrogen and air from dynamic and isothermal TGA data.

	Activation Energy, E_a (kJ/mol)	Reaction order, n	Pre-exponential Constant, A
PPC decomposed in nitrogen – dynamic data	93.21 ± 2.08	1.297 ± 0.101	$1.371 \times 10^{8} \pm 9.448 \times 10^{7}$
PPC decomposed in nitrogen – isothermal data	111.8	1.403 ± 0.137	1.31×10^{9}
PPC decomposed in air – dynamic data	114.2 ± 6.5	1.148 ± 0.063	$2.449 \times 10^{13} \pm 7.868 \times 10^{12}$
PPC decomposed in air – isothermal data	153.9	1.198 ± 0.262	5.126×10^{13}

As a comparison, the kinetic parameters in nitrogen and air were also calculated using a differential method with the isothermal TGA data, as described in Section 4.1.2. The natural log function is applied to both sides of the overall weight loss rate expression to yield equation 4.11.

$$\ln \frac{d\mathrm{W}}{d\mathrm{t}} = \ln k + \mathrm{n} \ln \mathrm{W} \qquad \text{Eq. (4.11)}$$

A plot of ln dW/dt as a function of ln W yields a line with a slope of n, and a y-axis intercept of ln k. However, similar to the dynamic data, the isothermal data must be adjusted with the correction factor, RF. Details on the calculation of the RF for the isothermal data are provided in Appendix A. The RF values at each temperature are provided in Table 9. Once the RF is known, a corrected n and k are found from a plot of ln(dW/dt) as a function of ln(W-RF) for each isothermal temperature. The Arrhenius equation (Eq. 4.12) is then used to calculate values of E_a and A from the k determined at each temperature. Appendix A includes details on the calculation of all kinetic parameters. A summary of the calculated kinetic parameters for the isothermal decomposition of PPC in both environments is given in Table 10.

4.3.4 Residual surfaces of decomposed polycarbonate films

The surface properties following the decomposition of the sacrificial material are of significant importance, especially if a gas or liquid is to flow through the channel, or moisture absorption of the structure is critical. The resulting surface following decomposition of PNB materials has been previously reported as hydrophobic. Silicon wafers were used to characterize the surface following the decomposition of full surface films of the PEC and PPC polycarbonates in dry air, ambient air (74% relative humidity),

and nitrogen at 300°C. The contact angle of de-ionized and distilled water on the resulting silicon surface was measured immediately after decomposition and cooling to room temperature. The contact angle measurements are included in Table 11. A bare silicon control sample with no polymer film was exposed only to the heat treatment in each environment. Before heat treatment, the native oxide layer was not removed prior to measurement, and the surface had a hydrophilic nature. The resulting surface of the control sample remains hydrophilic following heat treatment in each environment. However, the contact angle slightly increases following heat treatment in dry or ambient air, and more than doubles from 25° to 60° following heat treatment in nitrogen. The surfaces following decomposition of PEC films are similar to the control sample. The surfaces following decomposition of PPC also remain hydrophilic, but consistently have contact angle values approximately 20° to 25° higher in each environment than either the control or PEC samples.

The decomposition environment and polymer film impact the wetting properties of the remaining silicon surface. The surface properties may in fact be affected by small amounts of residual organic components on the surface. The organic products formed from the decomposition have a hydrophobic nature. If any remain on the surface, they may contribute to an increase in the contact angle. Residue may be a factor from experimental conditions. The increase in contact angle on the control sample from heat treatment in nitrogen may simply result from contamination by organic compounds in the furnace from prior polymer decompositions. Oxygen readily reacts with organic compounds, and may help scavenge the contaminants from the surface when present, resulting in no increase in the contact angle for the heat treatments in air. The dynamic

TGA data provided in Table 5 show that a higher amount of residue remains at 400°C for PPC than PEC. In addition, the isothermal TGA data for PPC in Table 7 established that 0.25% weight remains after 2 hours in nitrogen at 292.4°C, and 0.07% weight remains after 2 hours at 292.5°C in ambient air. The higher decomposition temperature of PPC (260 to 280°C [97]) provides a greater sensitivity to small temperature differences around 300°C. If the nitrogen or air flow provides temperature gradients <300°C throughout the tube furnace, a minimal amount of material may remain on the surface – increasing the contact angle.

Table 11: Contact angle of silicon before and after decomposition of PEC and PPC films at 300°C in various environments

	Contact Angle of Deionized and Distilled Water with the Surface (degrees)			
Surface	**Before Heat Treatment**	**Dry Air**	**Ambient Air (74% RH)**	**Dry Nitrogen**
Control Sample (no polycarbonate)	$25^o \pm 2^o$	$35^o \pm 1^o$	$33^o \pm 1^o$	$60^o \pm 3^o$
Si and decomposed PEC	--	$33^o \pm 1^o$	$27^o \pm 2^o$	$62^o \pm 2^o$
Si and decomposed PPC	--	$58^o \pm 1^o$	$44^o \pm 1^o$	$79^o \pm 1^o$

4.3.5 Decomposition results from the addition of a photoacid generator to polycarbonates

Polycarbonate sacrificial materials have been shown to thermally degrade at temperatures between 180 to 350°C. The introduction of a photo-acid generator (PAG), such as a diphenyliodonium or triphenylsulphonium salt, into a polycarbonate results in a

UV sensitive material [85]. Frechet et al. [85-86] report the acid-catalyzed thermolytic decomposition of polycarbonates using photoactive triarylsulphonium salts and have demonstrated photo-patterning using these materials. Narang and Attarwala [87] synthesized a variety of polycarbonates incorporating tertiary diols and used them as photoresist materials for deep UV and mid UV microlithography in the presence of diaryliodonium and triarylsulphonium salts. Upon irradiation to UV light, the triphenylsulphonium or diphenyliodonium salt undergoes a photolysis reaction. The organic cation of the PAG decomposes and a strong Brϕnsted acid is generated [88]. The protonic acid catalyzes the degradation of polycarbonate in the subsequent process at a lower temperature than the acid-free polymer.

Acid catalyzed decomposition of the four polycarbonates has been studied via TGA as a way to alter the decomposition temperature of the sacrificial material. Figure 24 shows the structures of the different PAGs investigated in this research. These include the commercially available PAGs (4-methylphenyl)[4-(1-methypropyl)phenyl] iodonium-tetrakis(pentafluorophenyl)borate (DPI-TPFPB), tris(4-(1,1-dimethylethyl) phenyl sulfonium-tetrakis(pentafluorophenyl)borate (TTBPS-TPFPB), and tris[4-(1,1-di-methylethyl)phenyl] sulfonium-hexafluorophosphate (TTBPS-HFP). A dynamic TGA at a heating rate of 1^{o}C/min in nitrogen was performed on each of the polycarbonate mixtures containing 5 weight percent PAG (based on dry polymer only), following solvent removal. The polymer formulations containing the PAG salts were either irradiated with UV light (240nm), or were given no UV exposure. Figure 25 compares the TGA thermograms for: (a) PPC alone; (b) PPC containing 5 weight % DPI-TPFPB and no UV exposure; and (c) PPC containing 5 weight % DPI-TPFPB following 1 J/cm^2

UV exposure. The temperature for onset of decomposition (5% weight loss) and the T_d (50% weight loss) for PPC alone (curve (a) in Figure 25) are 195°C and 214°C, respectively. The addition of a PAG decreases both the onset temperature and the T_d, with or without UV exposure. Without UV exposure (curve (b)), the onset temperature is 140°C, and the T_d is 193°C. The UV exposure (curve (c)) further reduces the onset temperature to 92°C, and the T_d to 110°C. The decomposition behavior of the PPC without PAG but exposed to UV irradiation is identical to that of the non-UV irradiated PPC. Therefore, the exposure has no effect on the polymer alone. The decomposition of each PAG is lower than the decomposition temperature of each PC. Therefore, when the PAG is not UV irradiated, acid is still produced once the temperature reaches the decomposition temperature of the PAG. The curve (b) in Figure 25 has a hump in the middle, or a two step decomposition. During the first portion of the curve, the PAG begins to decompose. This is followed by small decline in the rate of weight loss until enough PAG is present and a temperature is reached to catalyze the polymer decomposition. At 350°C, the weight percentage remaining is 0.37% for PPC alone, 0.12% for the non-UV exposed PPC + PAG, and 1.79% for the UV irradiated PPC + PAG. The photo-induced decomposition leaves slightly more residue than the thermally activated PAG decomposition, or thermolytic decomposition of PPC.

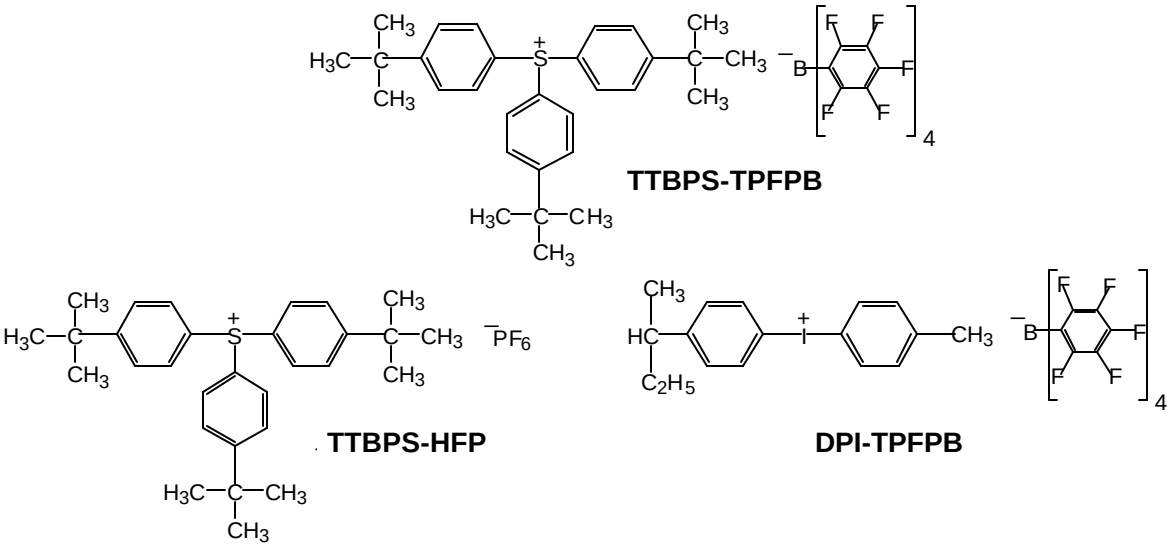

Figure 24: Chemical structure of photo-acid generators used to catalyze polycarbonate decomposition.

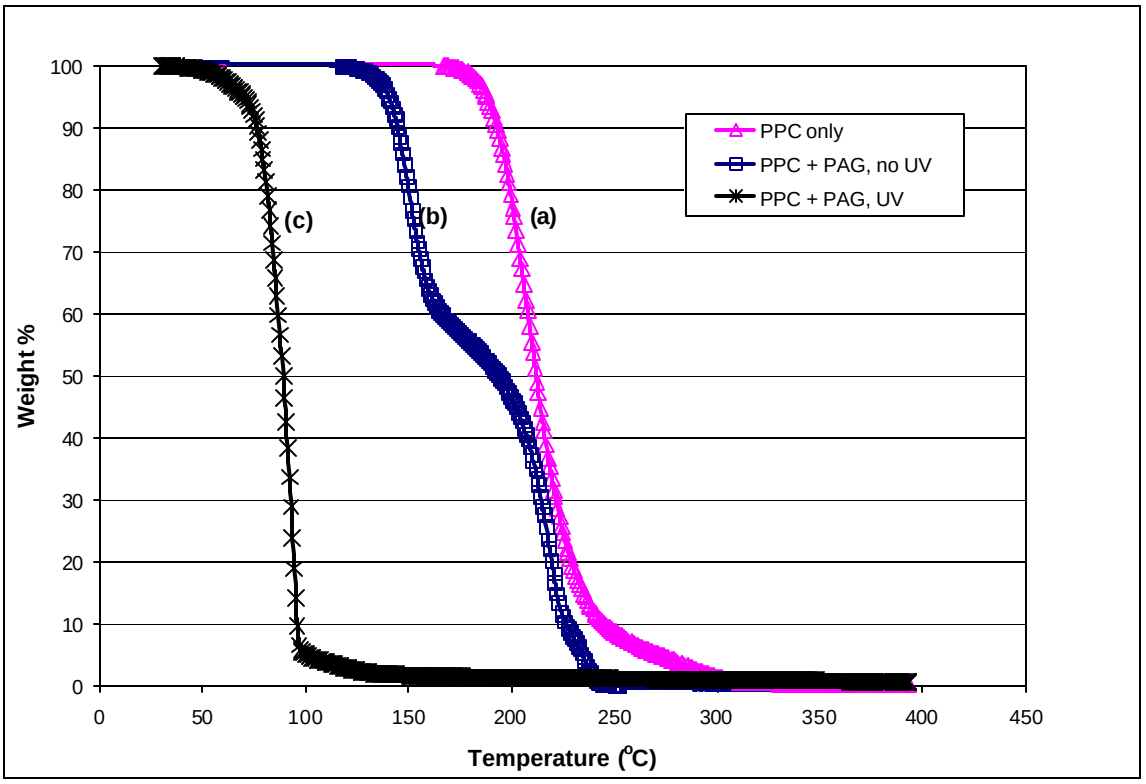

Figure 25: Dynamic TGA thermogram performed at 1°C/min for: (a) PPC only; (b) PPC + 5 wt% PAG with no UV exposure; and (c) PPC + 5 wt% PAG + 1J/cm^2 UV exposure (240 nm).

Table 12: Comparison of 50% weight loss temperatures from dynamic TGA at 1 ^{o}C/min for various polycarbonates decomposed by photo-induced acid catalyzed decomposition (PIAD), thermal-induced acid catalyzed decomposition (TIAD) and thermal decomposition (TG).

Polycarbonate & Weight % in Solution*	**Solvent**	**PAG**	**PIAD T_d (^{o}C)**	**TIAD T_d (^{o}C)**	**PC alone (no PAG) T_d (^{o}C)**
10% PEC	Propylene carbonate	DPI-TPFPB	114 ± 2	189 ± 2	182 ± 2
10% PEC	Propylene carbonate	TTBPS-HFP	117 ± 2	184 ± 2	182 ± 2
12% PPC	Anisole	DPI-TPFPB	102 ± 2	180 ± 2	212 ± 2
20% PPC	Anisole	TTBPS-TPFPB	125 ± 2	214 ± 2	212 ± 2
12% PCC	Anisole	DPI-TPFPB	177 ± 2	199 ± 2	270 ± 2
35% PCC	Anisole	TTBPS-TPFPB	191 ± 2	252 ± 2	270 ± 2
12% PNC	Anisole	DPI-TPFPB	207 ± 2	194 ± 2	305 ± 2
50% PNC	Anisole	TTBPS-TPFPB	196 ± 2	291 ± 2	304 ± 2
*Each solution contains 5 wt% PAG, based on the polymer weight only					

.

Similar experiments were performed on other polycarbonate/PAG combinations and the results are shown in Table 12. Each formulation contained 5 weight % PAG based on the polymer weight only. In Table 12, the thermal decomposition temperature of the polymer with PAG and UV exposure is less than the decomposition temperature of the non-exposed PAG or the polycarbonate alone. In each case, the T_d for the thermally induced acid-catalyzed decomposition (TIAD) is higher than the T_d when the PAG is photolytically activated (PIAD).

4.3.6 Discussion of the decomposition of polycarbonate sacrificial materials

The polycarbonate decomposition results identify the polymers as suitable lower decomposition temperature sacrificial materials. One important aspect of the polycarbonates is that PPC indicates the materials decompose readily in both nitrogen and air environments, without significant changes in the overall decomposition reaction. Although the reaction order for decomposition in nitrogen is slightly higher than the reaction order for decomposition in air, the calculated kinetic parameters show the reaction as first order in either environment. The higher values for the reaction order for decomposition of PPC in nitrogen are a result from the foot seen at the bottom of the TG curves at the lower ramping rates. The activation energies calculated using the dynamic data are less than those calculated using the isothermal data. However, in either case, the decomposition in air consistently has a lower activation energy. This indicates that oxygen provides some utility in the decomposition. In addition, the residual surface following decomposition in air is more hydrophilic than the surface decomposed in nitrogen. The oxygen may act as a carbon scavenger or react with the decomposition products to provide easier removal of the decomposed polymer. Also, polycarbonates

may provide an advantage over polynorbornene for encapsulating materials which require processing in oxygen for curing or deposition.

Another extremely important aspect of the polycarbonates is the ability to modify the decomposition temperature through alteration of the carbonate chemical structure, or by adding a photo-acid to the polymer. Table 5 shows that an increase in the length of the alkyl group in the polycarbonate backbone increases the thermal decomposition temperature of the polymer. This increase in T_d with an increase in alkyl chain length is explained by the decomposition reaction and products. Inoue et al. [45] have reported the synthesis and thermal degradation of PEC and PPC carbon dioxide-epoxide copolymers, and have proposed a thermal degradation mechanism. Monomer units unzip from the polycarbonate chain and form cyclic carbonates, followed by removal of CO_2 and the formation of epoxide. The degradation products of PEC are CO_2 and ethylene oxide, and those for PPC are CO_2 and propylene oxide. The vaporization and degradation temperatures of the carbonate formed from the monomer increase as the size of the alkyl group is increased, thus increasing the degradation temperature of the polymer. A cyclic group or phenyl-containing group in the polycarbonate backbone significantly increases the T_d. In Table 5, PNC shows the highest thermal stability with a T_d of 332^{o}C. The ring structures require more energy for thermal breakdown than an alkyl group due to radical stabilization. In fact, the decomposition thermograms of some carbonates containing phenyl rings, such as bisphenol-A carbonate, contain multiple TGA weight loss peaks at several different temperatures, or may not reach complete conversion of the original mass until temperatures over 500^{o}C.

In addition to the increase in the alkyl length of the group in the polycarbonate backbone, the decomposition temperature can be modified through thermal or photolytic activation of an acid catalyst. The acid catalyst decreases the decomposition temperature of the polycarbonate. Of significance is that the decomposition characteristics are maintained when the decomposition temperature is altered. The dynamic TGA curves for the polycarbonate/PAG mixtures maintain no weight loss to a certain temperature, followed by a steep decline in weight, and have an extremely small amount of residual weight. Table 12 compares the T_d (50% weight loss) for photo-induced acid catalyzed decomposition (PIAD) of the polycarbonates, thermally induced acid catalyzed decomposition (TIAD) of the polycarbonates (polycarbonate and PAG mixture without UV exposure), and thermal decomposition of the polycarbonates alone. In all cases, the PIAD decomposition occurs at a lower temperature than the other conditions.

It has been reported [88] that UV exposure or heat causes the cation part of the PAG salt to decompose and produce a proton, which pairs with the complex anion to form a protic acid. For the catalysts DPI-TPFPB and TTBPS-TPFPB the acid produced is fluorinated arylborate acid. The anion of the PAG TTPBS-HFP produces fluorinated phosphate acid. The carbonyl oxygen in the polycarbonate is protonated by either protic acid, which leads to the formation of unstable transition states, followed by product formation [89]. The products from PPC have been reported [89] as acetone, carbon dioxide, and cyclic propylene carbonate, which breaks down into carbon dioxide and propylene oxide. The decomposition products remain the same for both TIAD and PIAD, and are similar to the products formed from the un-assisted thermal decomposition of the polycarbonates.

It is clear from Table 12 that the introduction of a PAG significantly lowers the decomposition temperature of the polycarbonate, using either photolytic or thermolytic decomposition of the PAG. However, the choice of PAG has some influence on the decomposition temperature. TGA was performed on each of the four polycarbonates using two PAGs with each polycarbonate. The first two rows in Table 12 present the T_d results for PEC with either DPI-TPFPB or TTBPS-HFP. Although the acid produced is different, the decomposition temperatures are the same using either PAG. Also, no reduction in the decomposition temperature of PEC is achieved by TIAD, since the polymer decomposition begins before the decomposition temperature of the PAG. The decompositions of the other polycarbonates(e.g. PPC, PCC, and PNC) were studied using DPI-TPFPB and TTBPS-TPFPB. Although the concentration of polymer in solution differs, the PAG:PC ratio always is 1:20. The acid produced by the two PAGs is the same. The different PAGs produce similar decomposition temperatures by PIAD and TIAD for PNC. However, the polymers PPC and PCC have a higher T_d for both PIAD and TIAD, when catalyzed with the PAG TTBPS-TPFPB. In the case of PIAD, the same exposure dose may produce different acid concentrations using the two PAGs. The geometry or thickness of the sample may bring about absorption of the UV light by the polymer, and decrease the amount of acid produced. If the concentration of the acid produced is not enough to saturate the polymer decomposition reaction, a temperature difference occurs at the same conversion. The decomposition temperatures of the two PAGs are approximately 110^oC and 180^oC. Since the DPI-TPFPB decomposition begins sooner, a higher concentration of acid may be present at the beginning of polymer decomposition with DPI-TPFPB. This also may contribute to a lower temperature at the

same conversion. In the case of PNC, the thermal decomposition temperature of the polymer is above 300°C. The acid-catalyzed reaction with either PAG may have reached a high enough conversion at the temperature where the onset of acid-assisted polymer decomposition occurs.

4.4 Summary of Conclusions on Thermal Decomposition

The thermal decomposition of many different polymeric sacrificial materials has been investigated and discussed in this chapter. The goal of this portion of the research was to discover sacrificial materials whose decomposition temperatures are compatible with a wide range of temperatures and curing materials, while also decomposing cleanly in a reasonable time frame. The TGA studies on polynorbornenes and polycarbonates have identified polymers at the three desired decomposition temperatures: 200°C, 300°C, and 400°C, in addition to other temperatures. The polynorbornenes have utility for temperatures at or near 400°C. The polycarbonates provide a solution as lower-temperature sacrificial materials with decomposition temperatures from as low as 100°C (for the photo-induced acid-catalyzed decomposition) to 350°C (non-photosensitive PNC). The polycarbonates also are compatible with materials that require curing in air. This wide range of decomposition temperature sacrificial materials offers solutions for many applications. In addition, simple changes in the backbone of the polymer, or adding a photo-reactive component can allow the exact decomposition temperature requirement to be pinpointed.

The results for PNB allow elimination of many of the polynorbornene compositions as potential sacrificial materials. The terpolymers containing both TES and

cyclolacrylate groups, and each of the methyl acetate containing polymers all had very high residual values at 500°C. In most applications for air-gaps, residual material is not tolerated. For example, if the application is to form air-gaps as a low-κ material in IC's, residue can be detrimental, especially if it diffuses or conducts electrical current. However, some applications of the sacrificial polymer may tolerate residue in exchange for properties desired of the sacrificial material. Air-gaps fabricated primarily for mechanical movement may tolerate some residue inside the cavity. Also, if the surface properties of the residue can be selectively modified, such as for hydrophobicity, the residue may be beneficial.

The dynamic TGA results do not necessarily indicate the percentage of material which will remain inside a fabricated cavity. The air-cavities are fabricated using a decomposition process with a much slower temperature ramp and an isothermal hold. Time, temperature, and the volume of material all influence the conversion of the reaction. Isothermal TGA performed by Wedlake [69] have demonstrated the decomposition of 90/10 Bu/TES PNB at temperatures as low as 374°C with residual material <2% weight. The kinetics are extremely useful for determining the process parameters to be used in the actual formation of air-gaps. For example, a PNB which decomposes to < 5% of the original weight at 500°C during a 10°C/min dynamic TGA may decompose to <1% residue when isothermally held at 425°C for 2 hours.

A sacrificial material must also have good processing characteristics for the air-gap fabrication process. Therefore, several of these materials are still investigated for their ability to fabricate of air-gaps regardless of high residual weight values. The fabrication results with the various PNB compositions are discussed in Chapter 5.

However, the 90/10 butyl/TES polynorbornene showed excellent thermal stability, clean decomposition, excellent solvent resistance, and good adhesion to substrates. Therefore, this material was used extensively for fabrication, and its decomposition is investigated and discussed in more detail in Chapter 7. The fabrication results with PC sacrificial materials are discussed in Chapter 6. The ability to actually form air-cavities from that sacrificial polymer requires specific properties for the sacrificial material, in addition to the decomposition temperature and characteristics. This includes film formation properties, surface roughness, adhesion, solvent resistance, plasma etching characteristics, metal adhesion to the polymer, etc. Only when the fabrication process is investigated and optimized can the actual utility of a sacrificial material be realized.

CHAPTER 5

POLYNORBORNENE AIR-GAP FABRICATION AND RESULTS

In this chapter, the specific procedures and results of the fabrication of air-gaps formed using polynorbornene (PNB) sacrificial materials are discussed. Various overcoat materials are selected as potential candidates to form air-gaps with PNB sacrificial material based on their thermal and mechanical properties. Each of these materials is then investigated to link properties of the overcoat material with success or failure in the air-gap fabrication process.

The general process flow which was developed for the fabrication of air-gaps was first introduced by Figure 6 (Chapter 3, pg. 21). In this chapter, section 5.1 discusses the specific equipment and experimental details relevant to each particular step of this fabrication process. Several of these processing steps were optimized and the details are discussed in Section 5.2. Sections 5.3 and 5.4 cover the inorganic and organic materials selected as encapsulating materials, and the results of complete air-gaps fabricated using these encapsulating materials. A discussion of how problems with overcoat materials may be solved is presented in Section 5.5. Section 5.6 briefly describes a novel method developed to form air-gaps between metal features.

Sections 5.2 to 5.6 in this chapter describe fabrication using only the polynorbornene sacrificial material composition containing 90 mole percent butyl and 10 mole percent triethoxysilyl (TES) substituent groups (PNB-1 through PNB-3 in Table 2,

section 3.2.1, pg. 30). The thermal decomposition analysis discussed in Chapter 4 indicated that this particular composition of PNB sacrificial material was the overall best candidate for the 400^{o}C temperature air-gap fabrication process, among the materials studied. Fabrication has also been investigated with other compositions of polynorbornene sacrificial materials and the details are discussed in section 5.7. Section 5.8 discusses conclusions on the PNB air-gap fabrication process.

5.1 Experimental Details Relevant to Air-gap Fabrication With PNB Sacrificial Material

5.1.1 Deposition of PNB sacrificial materials

As described in section 3.1 and shown in Figure 6 (b), (Chapter 3, Section 3.1, pg. 21), the air-gap fabrication process begins with deposition of the sacrificial material onto a substrate by a method such as spin-coating or doctor blading. The thickness of the sacrificial polymer film after curing influences the height of the air-gap. To apply the sacrificial PNB polymers, the dry polymers were dissolved into organic solvents, and filtered through 0.2 μm Teflon syringe filter discs. The compositions of the various polynorbornene solutions used throughout this research are shown in Table 13. Films were spin-coated onto 4" <100> silicon wafers using a CEE 100CB spin-coater at speeds from 500-6000 RPM to achieve a thickness between 0.4 to 50 μm. Each spin-coating process consisted of two steps: a 500 RPM spin for 5 s to spread the polymer solution, followed by a 30 s spin at the final speed. After spin-coating, the PNB films were softbaked by heating on a hotplate between 100^{o}C to 120^{o}C for 3 to 5 min to evaporate the solvent. Spin-speed curves showing the thickness after softbaking as a function of spin speed for the polynorbornene solutions in Table 13 are included in Appendix B.

Table 13: Polynorbornene polymer/solvent compositions used for spin-coating and air-cavity fabrication.

Solution #	Polymer Alkyl Group Composition	Molecular Weight	Solvent	wt. polymer/ wt. solution
PNB-1-S1	90/10 butyl/triethoxysilyl copolymer	283,000	mesitylene	22.04%
PNB-1-S2	90/10 butyl/triethoxysilyl copolymer	283,000	mesitylene	6.00%
PNB-2-S1	90/10 butyl/triethoxysilyl copolymer	182,000	mesitylene	30.80%
PNB-2-S2	90/10 butyl/triethoxysilyl copolymer	182,000	mesitylene	20.00%
PNB-3-S1	90/10 butyl/triethoxysilyl copolymer	355,000	mesitylene	21.40%
PNB-4-S1	methyl acetate homopolymer	261,000	anisole	9.80%
PNB-5-S1	methyl acetate homopolymer	325,000	anisole	14.93%
PNB-5-S2	methyl acetate homopolymer	325,000	toluene	9.85%
PNB-6-S1	90/10 methyl acetate/triethoxysilyl copolymer	183,000	anisole	9.95%
PNB-6-S2	90/10 methyl acetate/triethoxysilyl copolymer	183,000	toluene	14.93%
PNB-7-S1	50/50 norbornene/triethoxysilyl copolymer	412,000	mesitylene	9.80%
PNB-8-S1	90/10 butyl/cyclolacrylate copolymer	300,000	mesitylene	9.95%
PNB-8-S2	90/10 butyl/cyclolacrylate copolymer with 4 wt%/polymer photoinitiator	300,000	mesitylene	15.90%
PNB-9-S1	80/20 butyl/cyclolacrylate copolymer	213,000	trichloroethane	16.40%
PNB-10-S1	90/10 methyl acetate/cyclolacrylate copolymer	274,000	anisole	10.40%
PNB-11-S1	80/10/10 methyl acetate/triethoxysilyl/cyclolacrylate terpolymer	256,000	cyclohexanone	9.99%
PNB-17-S1	80/10/10 butyl/triethoxysilyl/cyclolacrylate terpolymer	213,000	mesitylene	10.83%

An additional heating step or "curing" is required for samples fabricated with PNB compositions containing the triethoxysilyl (TES) moiety on the polymer backbone. Many polymers, in general, require a curing step to produce the fully polymerized polymer film. The PNB "cure" differs from a regular cure because a reaction does not occur to produce a change in the polymer backbone. The polymer is already in a fully polymerized state when spin-coated onto the substrate. The additional curing step rather removes residual solvent from the film and promotes the reaction of the triethoxysilyl groups with the substrate surface to aid in adhesion. The cure is performed in a N_2 purged tube furnace ramped at 5°C/min to a temperature between 200°C and 350°C, and held at that temperature for a period of 1 to 2 hr. Shrinkage in film thickness due to curing ranged from 0.36 to 2.98 percent, with an average of 1.37 ± 0.74 percent.

5.1.2 Hard mask and photolithography

Figure 6 and Figure 7 in Chapter 3 (Section 3.1, pgs. 21-22) depicted the process developed to pattern non-photosensitive PNB polymers through the deposition and patterning of a hard mask, followed by dry etching of the PNB film. A hard mask is required because the plasma chemistry used to etch the polynorbornene is not selective to the polymeric photoresist used to define patterns on the samples. Various materials were investigated as possible hard mask materials including SiO_2, Cr, and Al. SiO_2 was deposited by plasma enhanced chemical vapor deposition (PECVD) at 200°C using a gas mixture of N_2O and SiH_4 diluted in N_2. Typical PECVD conditions using an STS PECVD were: chamber pressure = 550 mTorr; gas flow rates = 1400 sccm N_2O, and 400 sccm of 2%SiH_4 in N_2; RF frequency = 380 KHz and RF power = 50W. Typical conditions using a Plasmatherm PECVD with an 11" electrode were: chamber pressure =

600 mTorr; gas flow rates = 900 sccm N_2O, and 400 sccm of 2% SiH_4 in N_2; and DC power = 35 W. Mask oxide thickness ranged from 0.5 to 1.0 μm, depending on the thickness of the PNB. Aluminum and chromium masks were deposited using a CVC DC sputtering system at room temperature. The aluminum deposition rate was 4.0 Å/s, and that of chromium was 1 Å/s.

All hard masks were patterned by a standard photolithography method using a positive photoresist (Shipley Microposit 1813 or 1827) and exposing it to UV radiation (365 nm) for a total dose of 150 mJ. The resist was developed in Shipley Microposit 319 or 354 developer for 50 to 120 s to remove the resist in the exposed areas. This was followed by wet-chemical or plasma etching of the hard mask material. SiO_2 was removed at a rate of 250 nm/min in 6:1 buffered oxide etch (BOE) solution diluted to 10:1 in deionized water. Cr was etched using Mantek Co. CR-7S Chromium etchant. Aluminum was etched in two different ways. Wet-chemical etching of Al was performed using Type A PAN (phosphoric acid/ acetic acid/ nitric acid) etch heated to 50^{o}C at a rate of 100 Å/s. The Al on samples containing other materials that are susceptible to the acids in PAN etch (i.e. Cu, some polymers) was etched using reactive ion etching (RIE). The RIE etch conditions using a Plasmatherm RIE were: gas flow rates = 30 sccm BCl_3, 10 sccm Cl_2, and 3 sccm $CHCl_3$; chamber pressure = 40 mTorr; DC power = 125W; and temperature = 35^{o}C. The typical etch rate of sputtered Al under these conditions is approximately 350 Å/min. Following etch of the hard mask, the remaining photoresist was removed by rinsing (in the given order) with acetone, methanol, isopropanol, and deionized water, following by drying with N_2.

Several mask patterns were used in the fabrication of air-gaps. Air-channels were fabricated using a clear-field mask pattern containing four different size line/space patterns: 140 μm wide channels with 60 μm spacing, 70 μm wide channels with 30 μm spacing, 35 μm wide channels with 15 μm spacing, and 15 μm wide channels with 5 μm spacing. A second mask pattern was used to fabricate large air-cavities in the shapes of circles and squares ranging from 2 mm to 1 cm in width. A third mask pattern contained air-gaps in various geometry shapes for compliance testing, mechanical analysis, and decomposition analysis. The dimensions of the features on this mask are described in Chapter 7. Two additional mask patterns were created for Sea of Leads Packaging technology with air-gap densities of 1000/cm^2 and 3000/cm^2. Further details of the Sea of Leads air-gap patterns will be discussed in Chapter 8.

5.1.3 PNB dry etching

The next processing step in air-gap formation is to etch away the PNB in the areas where the hard mask has been removed. This was performed using RIE. Three different etch programs were used to etch the 90/10 Bu/TES PNB. The parameters for each set along with the average etch rate and one standard deviation are shown in Table 14.

5.1.4 Deposition of encapsulating materials

A complete list of all encapsulating materials used in this research was provided previously as Table 3 (Chapter 3, pg. 36). The encapsulating materials selected for use with PNB were chosen based on a promising ability to withstand the 425^{o}C decomposition temperature of the sacrificial material. These encapsulating materials

Table 14: Various polynorbornene RIE etch conditions.

Recipe / Parameter	PNB-ETCH1	PNB-ETCH2	PNB-ETCH3
Pressure (mTorr)	**300**	**250**	**250**
Power (W)	**400**	**400**	**300**
Temp (^{o}C)	**35**	**35**	**35**
CHF_3 (sccm)	**5**	**5**	**5**
O_2 (sccm)	**15**	**15**	**45**
Ar (sccm)	**40**	**30**	**0**
Etch rate (mm/min)	**0.207 ± 0.081**	**0.363 ± 0.120**	**0.414 ± 0.060**

include: Ultradel 7501 polyimide (Amoco); Pyralin (DuPont) polyimides PI-2611, PI-2731, PI-2734, PI-2771, PI-2540, and PI-2555; HD4000 polyimide (Hitachi); FLARE^{TM} poly(arylene ether) (Honeywell); polybenzoxazole (PBO) CRC-8650 (Sumitomo-Bakelite); Parylene-N (Paratronix); and PECVD deposited SiO_2 and SiN_x. The other encapsulating materials previously listed in Table 3 are for use with lower-temperature polycarbonate sacrificial materials and will be discussed subsequently in Chapter 6.

The inorganic glasses, SiO_2 and SiN_x, were deposited using PECVD. The polymers were spin-coated or doctorbladed with appropriate conditions to achieve various overcoat thickness from 0.1 to 30 μm. Parylene-N is deposited by chemical vapor-deposition, and the details are discussed in Section 5.4.5. PECVD deposition parameters for SiO_2 and SiN_x overcoat materials, and the deposition rate at these conditions, using either a Plasmatherm or an STS PECVD are listed in Table 15. Spin-

speed curves and processing details for each of the respective polymer overcoat solutions are given in Appendix B.

5.1.5 Decomposition of PNB sacrificial material

Decomposition of PNB sacrificial material was performed at a maximum temperature of 425°C using a nitrogen-purged Lindberg horizontal tube furnace. Samples encapsulated with SiO_2 or SiN_x were decomposed by ramping 5°C/min to 350°C, followed by a 1°C/min ramp to 425°C and holding at 425°C for 1 to 2 hours. In samples encapsulated with polymers requiring a cure, the encapsulate was cured and the sacrificial polymer was decomposed in one furnace cycle. The cure schedules recommended by the manufacturers for the overcoat polymers was succeeded with a 1°C/min ramp to 425°C and holding at 425°C for 1 to 3 hours. For example, polyimide coated samples were ramped 3°C/min to 350°C, held for 1 hour to cure the polyimide, followed by a 1°C/min ramp to 425°C and holding for 1 to 2 hours to decompose the PNB sacrificial material. Other samples were performed using slow decomposition profiles. These decomposition profiles are summarized in Table 16.

Table 15: Deposition conditions for SiO_2 and SiN_x overcoat materials.

Material	**SiO_2**	**SiO_2**	**SiN_x**	**SiN_x**
PECVD Tool	Plasmatherm PECVD	STS PECVD	Plasmatherm PECVD	STS PECVD
Gas Flow Rates	900 sccm N_20 400 sccm 2% SiH_4 in N_2	1420 sccm N_20 400 sccm 2% SiH_4 in N_2	5 sccm NH_3 200 sccm 2% SiH_4 in N_2 900 sccm N_2	20 sccm NH_3 2000 sccm 2% SiH_4 in N_2
Pressure	600 mTorr	550 mTorr	900 mTorr	550 mTorr
Power	35 W DC	50 W RF at 380 kHz	30 W DC	60 W RF at 380 kHz
Temperature	200 ^oC	200 ^oC	230 ^oC	230 C
Deposition Rate	364 Å/min	467 Å/min	214 Å/min	380 Å/min

Table 16: Various Lindberg furnace decomposition programs used with PNB sacrificial material.

	Furnace Program				
Step	**A**	**B**	**C**	**D**	**E**
1	3 ^oC/min to 350 ^oC, hold 1.0 hr	3 ^oC/min to 350 ^oC, hold 1 hr	3 ^oC/min to 150 ^oC, hold 0.5 hr	5 ^oC/min to 370 ^oC, no hold	3 ^oC/min to 150 ^oC, hold 0.5 hr
2	1 ^oC/min to 405 ^oC, hold 0.5 hr	1 ^oC/min to 378 ^oC, hold 1.5 hr	3 ^oC/min to 320 ^oC, hold 0.5 hr	1 ^oC/min to 380 ^oC, hold 1 hr	3 ^oC/min to 250 ^oC, hold 0.5 hr
3	1 ^oC/min to 425 ^oC, hold 0.5 hr	1 ^oC/min to 385 ^oC, hold 1.5 hr	3 ^oC/min to 375 ^oC, no hold	1 ^oC/min to 385 ^oC, hold 1 hr	3 ^oC/min to 300 ^oC, hold 0.5 hr
4	step to 25 ^oC	1 ^oC/min to 395 ^oC, hold 1.5 hr	1 ^oC/min to 425 ^oC, hold 0.5 hr	1 ^oC/min to 390 ^oC, hold 1 hr	1 ^oC/min to 400 ^oC, hold 1 hr
5		1 ^oC/min to 405 ^oC, hold 1.5 hr	step to 25 ^oC	1 ^oC/min to 395 ^oC, hold 1 hr	step to 25 ^oC
6		1 ^oC/min to 415 ^oC, hold 1.5 hr		1 ^oC/min to 400 ^oC, hold 1 hr	
7		1 ^oC/min to 425 ^oC, hold 3 hr		step to 25 ^oC	
8		step to 25 ^oC			

5.2 Optimization of the Air-gap Fabrication Process

The previous section described the experimental processing conditions and equipment used for each step of the air-gap fabrication process. This section describes the results from variations in many of the experimental process parameters. From these results, the overall fabrication process was optimized for various size and shape air-gap structures.

5.2.1 The effect of curing temperature on PNB decomposition

The effect of the cure temperature on the decomposition of PNB was investigated using 500 nm thick PNB films formed from solution PNB-1-S2 (90/10 butyl/TES norbornene). These films were cured for 1 hour at temperatures of 300°C, 325°C, and 350°C. Figure 26 shows dynamic thermogravimetric analysis (TGA) curves performed at a ramp rate of 10°C/min for the PNB samples cured at each temperature. The TGA curves for the samples baked at 325°C and 350°C (the blue and yellow curves) are identical. However, the onset for decomposition of the sample cured at 300°C occurs at approximately 20°C before the other two samples.

Ellipsometry was performed at three points on each sample before and after curing to investigate thickness loss during the cure. The ellipsometry results are shown in Table 17. The sample cured at 300°C showed an average thickness loss of only 90 Å (~2% of the original film thickness) and only a slight increase in the refractive index after curing. The samples baked at 325°C and 350°C lost average thicknesses of 700 Å and 1900 Å, respectively. The non-uniformity in thickness loss seen in all samples was a result of temperature non-uniformity in the curing tube due to nitrogen flow. However, the clear trend was that the thickness loss increased simultaneously with an increase in

the curing temperature. Dynamic TGA data of PNB presented by Wedlake [69] using a ramp rate of 0.5°C/min shows that by 300°C, 2 wt% of the original sample mass has been removed. Wedlake also used mass spectrometry to show that decomposition began with the evolution of low molecular weight products. The intensity of the peaks from these low molecular weight emitted species increased with either a temperature increase or an increase in heating rate. The film cured at 300°C contains some of these low molecular weight products. The evolution of these products during the TGA experiment creates the difference seen in the onset of decomposition between the film cured at 300°C, and those cured at the higher temperatures.

5.2.2 Variation of hard mask materials

As described in Section 5.1, a hard mask is required to etch PNB sacrificial materials since the plasma chemistry used to etch the PNB is not selective to polymeric photoresist used to define patterns on the samples. The various materials investigated as possible hard mask materials included SiO_2, Cr, and Al. SiO_2 hard mask was found to etch at a rate of 300 to 400 Å/min in the plasma chemistry used to etch the PNB. This required a very thick oxide layer to pattern layers of PNB thicker than 10 μm. Deposition of a thick oxide is time consuming. In addition, SiO_2 etches anisotropically, which decreases the feature size from the original mask dimensions. Therefore, metals were chosen as a hard mask to pattern PNB greater than 10 μm thick. Metals provide much higher selectivity than SiO_2 to PNB during the PNB plasma etch.

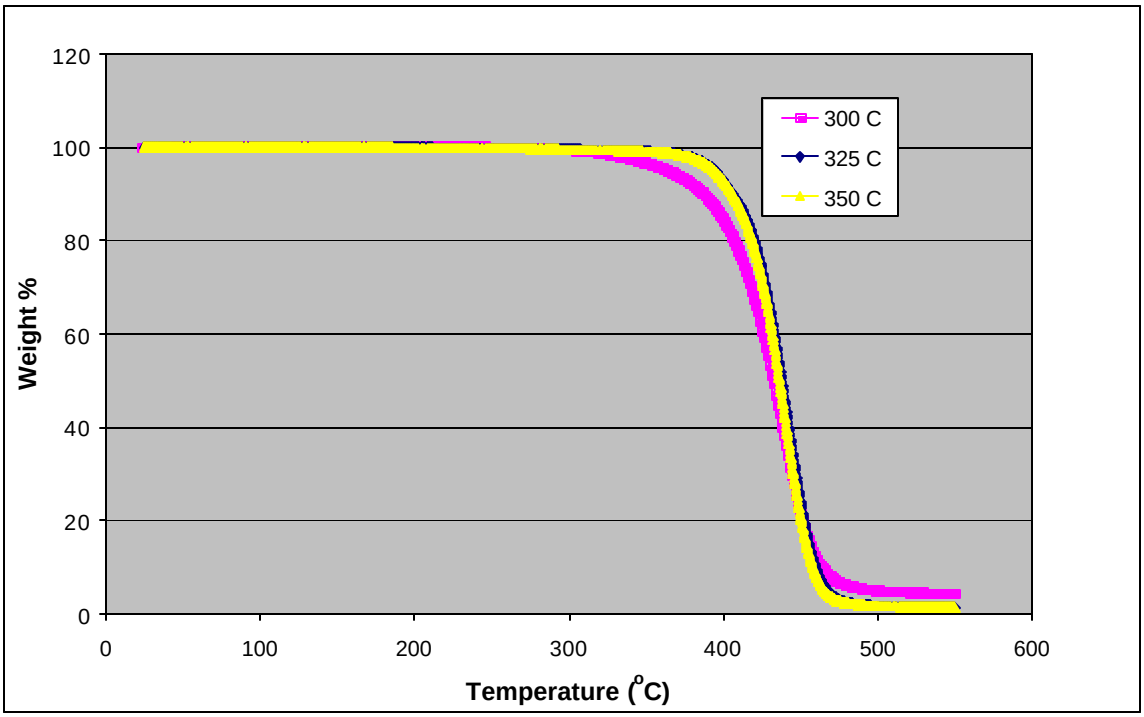

Figure 26: Dynamic TGA curves ramping 10°C/min showing the effect of curing temperature on the decomposition of 90/10 butyl/triethoxysilyl polynorbornene. Samples were cured by ramping 5°C/min to the final temperature and held for 1 hour in nitrogen.

Table 17: Thickness and refractive index values for PNB films before and after curing at temperatures of 300°C, 325°C, and 350°C.

Sample #	Thickness (Å) Before Curing	Refractive Index, n Before Curing	Thickness (Å) After Curing	Refractive Index, n After Curing	Thickness Change (Å)
T300-1	4973.3	1.5048	4922.9	1.5068	50.4
T300-2	4873.3	1.5052	4809.3	1.5065	64
T300-3	4857.8	1.5055	4703.4	1.5087	154.4
T325-1	4867.3	1.5064	4710.5	1.5094	156.8
T325-2	4825.7	1.5058	4232.0	1.5175	593.7
T325-3	4863.9	1.5057	3464.3	1.5245	1399.6
T350-1	4840.2	1.5052	4537.7	1.5103	302.5
T350-2	4844.1	1.5055	3214.7	1.531	1629.4
T350-3	4856.0	1.5053	1100*	N/A*	3756.0
* Film had about 50% non-uniformity and could not get an accurate measurement					

Both SiO_2 and Al showed excellent pattern transfer when used as hard masks, with no changes to the underlying PNB film. Although Chromium also showed good selectivity to the RIE polymer etch, the inherent high stress of sputtered Cr caused problems with processing. After sputter deposition of the Cr, cracks were observed throughout the metal film. The cracking transcended into the top portion of the PNB film and was present upon removal of the mask. Figure 27 is an SEM image showing these cracks in the top portion of the PNB film following Cr mask removal. The Al mask did not cause this cracking in the PNB and was determined to be a better choice for patterning thick layers of PNB.

5.2.3 PNB RIE etching results

The various PNB etch conditions used to pattern PNB films were listed in Table 14 in Section 5.1 of this chapter. PNB-ETCH1 is a set of process conditions for etching polynorbornene based polymers developed by Zhao and Kohl [90]. The oxygen component of the etch gas is necessary to chemically attack carbon and hydrogen species, while the CHF_3 component is necessary to remove the Si containing groups attached to the polymer backbone. Ar is added to the etch chemistry as a physical bombarder and etcher. Figure 28 (a) is a cross-sectional SEM micrograph of a 35 µm wide and 5 µm tall PNB feature formed using solution PNB-1-S1 and etched using RIE conditions PNB-ETCH1, before removal of the SiO_2 hard mask. Figure 28 (b) shows a cross-section of the same sample after SiO_2 removal. As seen from these images, a great amount of undercutting of the mask occurred, and the resultant sidewall angle was $< 90^o$. It is very important to have control over the sidewall angle and undercutting of the etched polymer

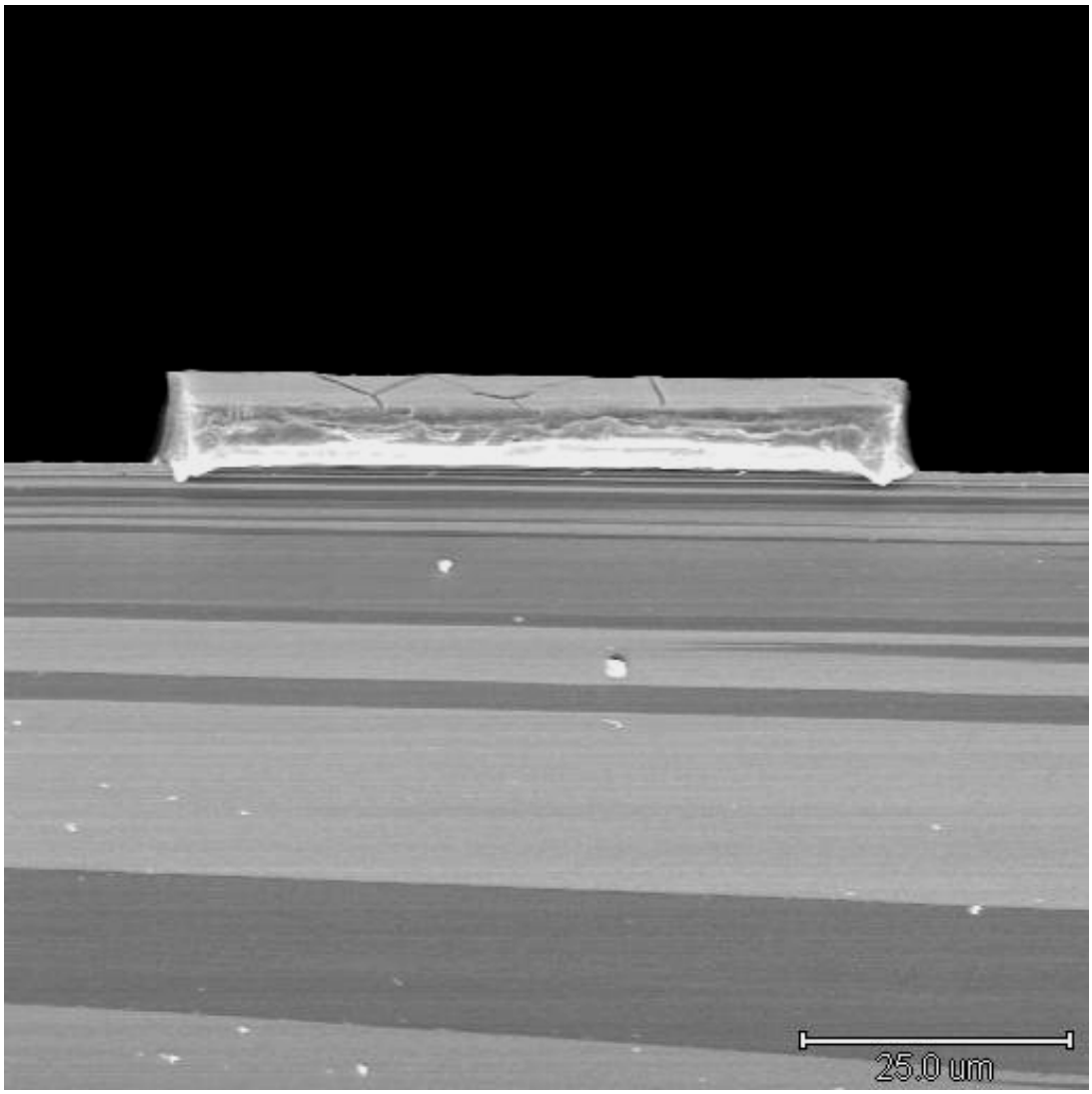

Figure 27: SEM image showing cracks in the top surface of a 140 μm wide patterned PNB line after removal of the Cr hard mask.

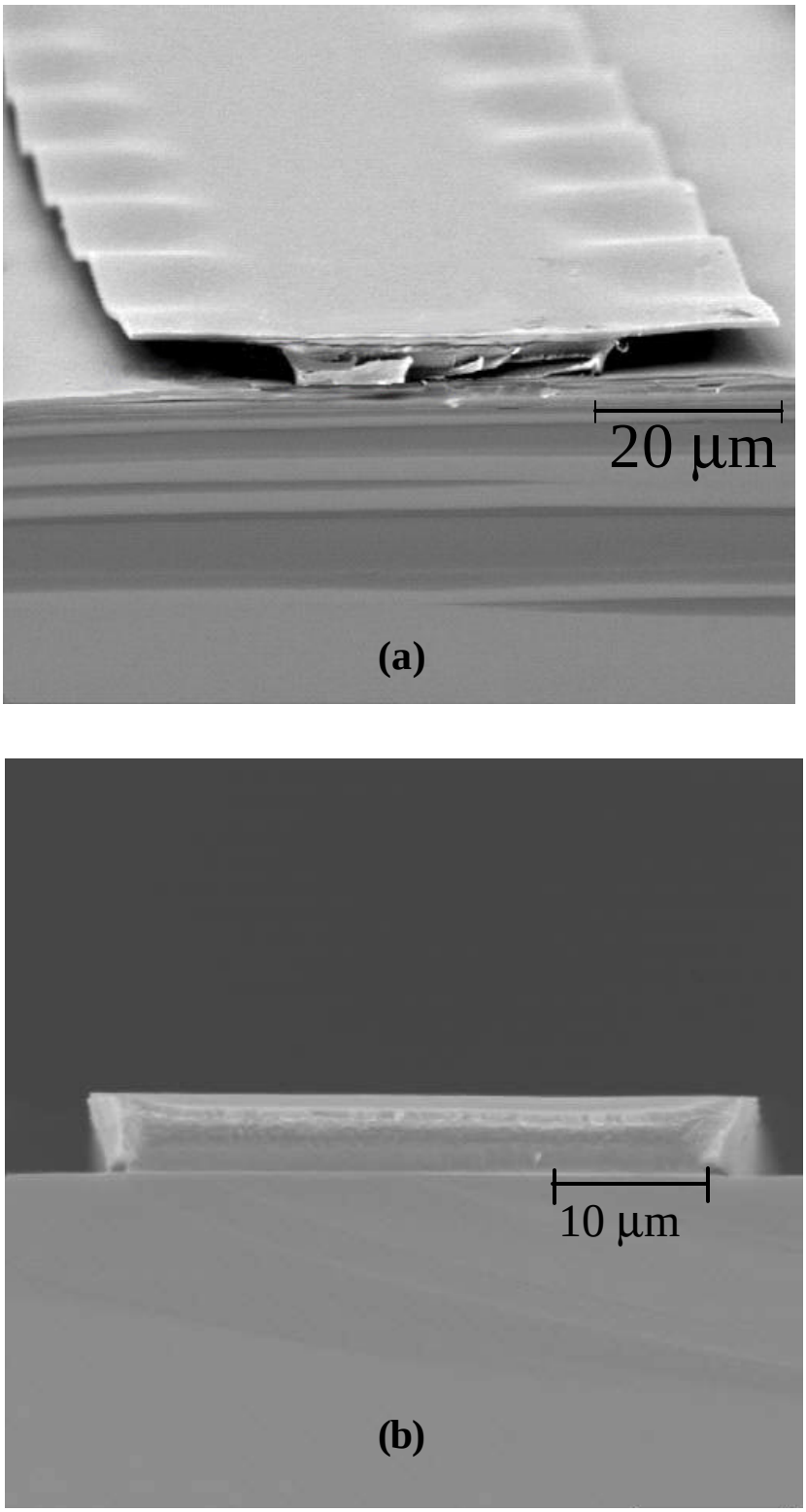

Figure 28: SEM micrographs of a 35 μm wide and 5 μm tall PNB feature etched using RIE conditions PNB-ETCH1 with (a) the 1 μm thick SiO_2 hard mask remaining, and (b) after removal of the hard mask.

film. A 90^o angle or an angle $>90^o$ is important for adequate step coverage of the overcoat material over the sacrificial material, or for electroplating of a metal in between the sacrificial material. A side wall angle $>90^o$ may also be important for microchannel design, to reduce turbulence caused by corners in the channel. Therefore, undercutting needs to be controlled in order for accurate feature size transfer from the mask to the patterned film. A reduction in the pressure of the RIE process typically leads to a straighter sidewall angle (closer to 90^o) [91]. Therefore, the etch process PNB-ETCH2 was developed, with the same parameters as PNB-ETCH1, except a reduction in the pressure from 300 to 250 mTorr and a reduction in Ar flow from 40 to 30 sccm. The total Ar flow was reduced to decrease physical sputtering across the sample, which may help increase the amount of sidewall passivation formed on the sample during etching. The sidewall passivation reduces undercutting by protecting the sidewall during the process. Figure 29 shows a cross-sectional SEM image of the end-portion of a 140 μm wide and 12 μm tall PNB feature etched using an Al hard mask and etch recipe PNB-ETCH2. As seen from the image, the change in process parameters led to a reduction in the undercutting, and increased the sidewall angle closer to 90^o.

After using the PNB-ETCH2 process to etch a 20 μm thick PNB film masked with 2000 Å of Al, profilometry showed the features changed from 20 μm tall uniform features to non-uniform features 12-16 μm in height. Much of the Al was observed to have eroded away. Al could only be removed in the PNB-ETCH2 chemistry by the physical sputtering of it away by Ar. Therefore, either the Ar had to be removed from the process, or a thicker Al hard mask layer was needed. The physical sputtering of Al could lead to other problems, such as the formation of residue in the etched areas. Therefore,

the best solution was to remove Ar from the etch gas chemistry. The third set of RIE conditions, PNB-ETCH3, consisted of only O_2 and CHF_3, with no Ar in the etch gas chemistry. The oxygen gas flow was increased to keep the total volume flow rate of gas the same. PNB-ETCH3 was used to etch PNB films 20 to 50 μm in height, with no noticeable loss in feature height or uniformity. In addition, good sidewall angle and little to no undercutting was achieved, although some roughening of the sidewall did occur. Figure 30 is a SEM image of a 190 μm diameter circle etched into a 30 μm thick PNB film. The Al hard mask is remaining on the sample.

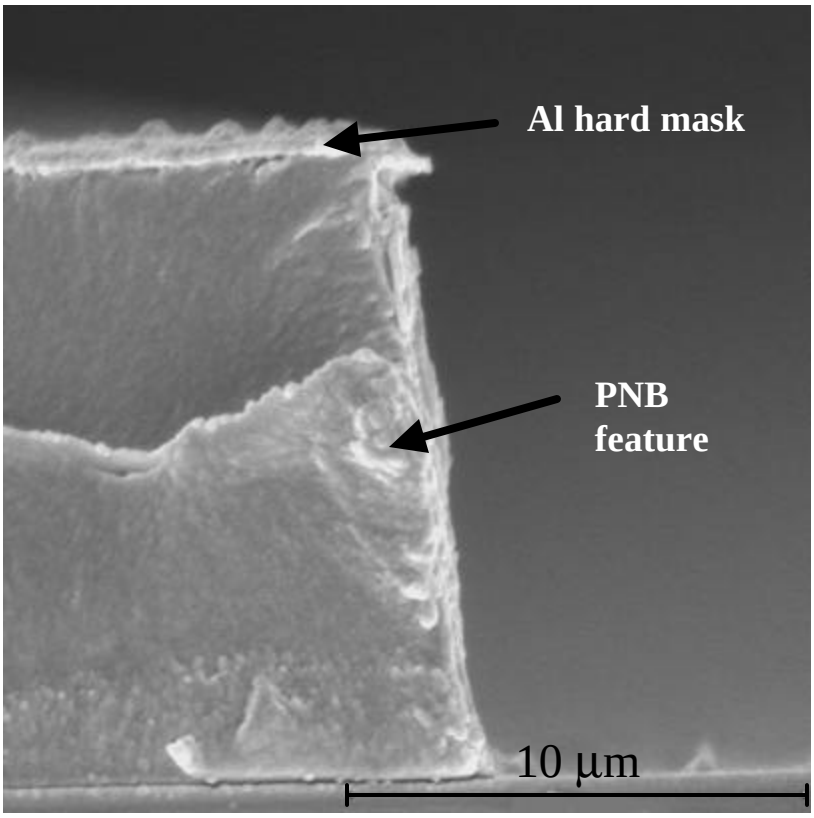

Figure 29: SEM micrograph of the end portion of a 140 μm wide and 12 μm tall PNB feature etched using RIE conditions PNB-ETCH2 and a 2000 Å Al hard mask

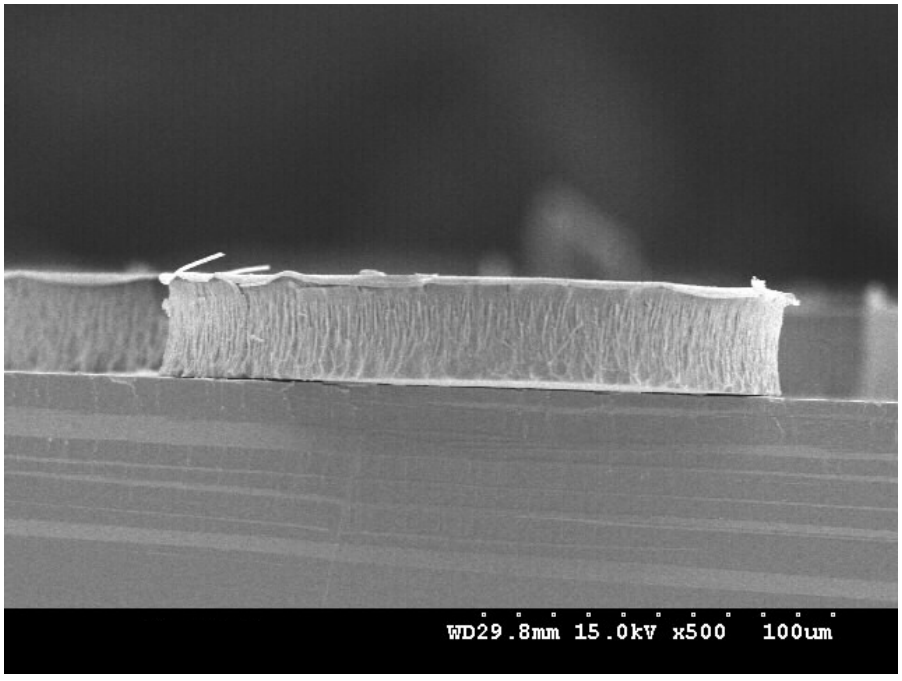

Figure 30: SEM micrograph of a 190 μm diameter circle etched into a 30 μm thick PNB film using recipe PNB-ETCH3. The Al hard mask is remaining on the sample.

5.3 Air-gaps Fabricated With PNB and SiO_2 or SiN_x Encapsulation

5.3.1 Results of air-gaps encapsulated in inorganic glasses

SiO_2 and SiN_x were investigated as encapsulating materials with PNB based on: (1) high thermal stability; (2) high mechanical strength; and (3) widespread interest in these two materials by the microelectronics community as low dielectric constant inter- and intra-level materials when combined with air. The hypothesis was that these overcoat materials would be compatible with the fabrication process and could be used to form air-gaps in a variety of sizes and dimensions. Figure 31 (a) and (b) show scanning electron micrographs of cross-sectioned air-channel structures formed from 2 μm thick PNB sacrificial material features encapsulated in SiO_2 and SiN_x respectively. The resulting air-channels shown in these pictures are the same rectangular shape as the patterned PNB before decomposition. Deformation or distortion of the encapsulating layer does not occur. Residual PNB material is not seen in the air-cavities that were sealed during the decomposition. Both SiO_2 and SiN_x have adequate permeability to the gaseous products formed at elevated temperatures and can withstand any pressure formed inside the cavity during the decomposition.

One of the pertinent processing issues with SiO_2 and SiN_x air-channels was found to be the temperature for deposition of the encapsulating layers. The SiO_2 and SiN_x PECVD deposition was limited to 200°C and 230°C respectively. Above these temperatures, the overcoat material severely cracked. The most important factor limiting the deposition temperature of both SiO_2 and SiN_x films is the mismatch between the coefficient of thermal expansion of PNB (CTE = 127 ppm/°C) and SiO_2 (CTE = 0.6 to 0.9 ppm/°C) or SiN_x (CTE = 1.0 to 2.2 ppm/°C). Due to this mismatch, the overcoat

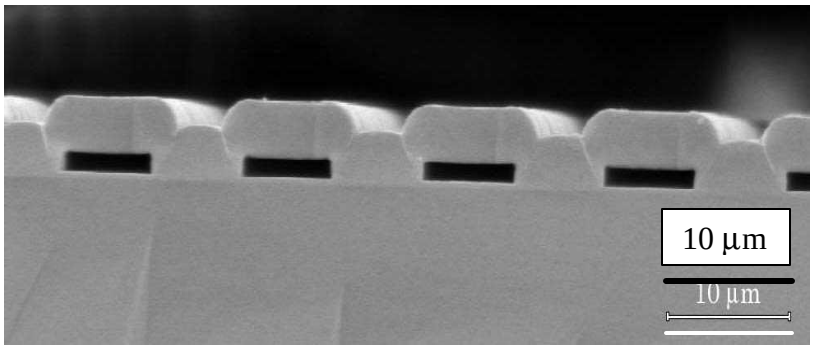

(a)

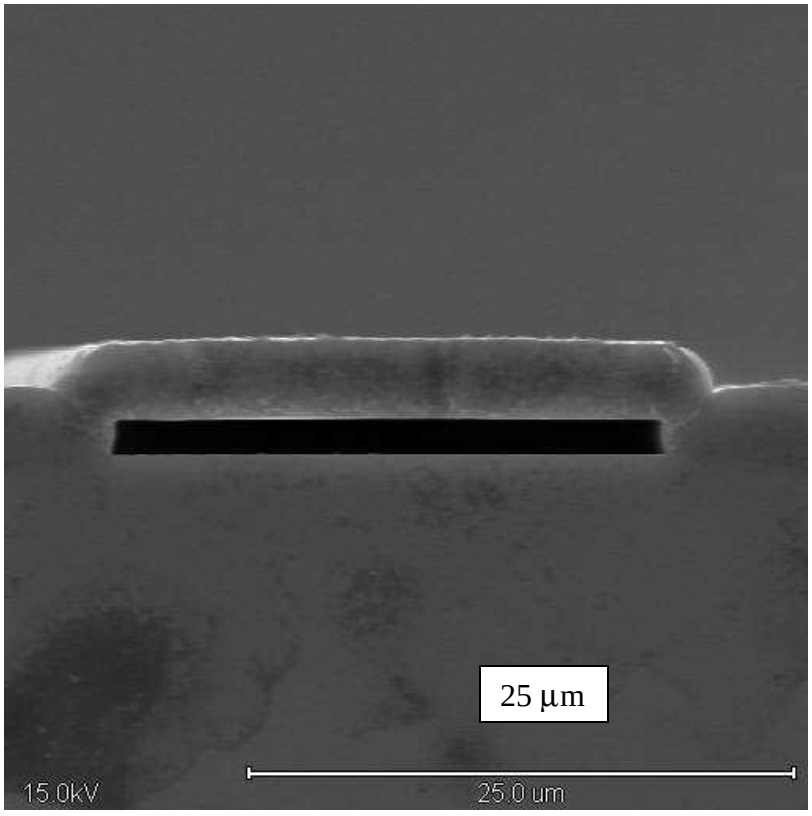

(b)

Figure 31: Air-channel structures fabricated from 2 µm thick PNB sacrificial material features encapsulated in (a) SiO_2 and (b) SiN_x.

films crack from stress developed between the substrate and the film during cooling from the deposition temperature.

Good mechanical strength of the air-channel was found over a range of dimensions. However, the step coverage at the corners of PNB by the encapsulating material became critical as the thickness of the PNB features was increased. Figure 32 shows an example of poor step coverage over 5 μm thick PNB features, which was more critical for SiO_2 than for SiN_x. As can be seen from Figure 32 (a), a clear boundary is formed in the SiO_2 between the horizontal and vertical faces of the coating around the feature. This boundary is also seen in Figures 31 (a) and (b), although not as severe. Although the air-channels in Figure 31 and Figure 32 (a) remain intact, this boundary is the weakest point in the air-channel structure and cleavage often occurs along this plane during decomposition or post-decomposition handling, as can be seen in Figure 32 (b). The step coverage issue is dependent on the air-gap geometry and the PECVD deposition conditions. The step coverage becomes a greater concern when the PNB film thickness is large, or the space between PNB features is small. SiN_x yields satisfactory step coverage over a rather broad range of growth parameters whereas SiO_2 coating suffers from inferior step coverage over a large range of parameters. Step coverage of PECVD SiO_2 has been shown to be dependent on the deposition rate and residence time of the deposition gases [92]. Standard recipes were used in the deposition of the encapsulating SiO_2 in these experiments. The process was not optimized for deposition over the PNB features. Therefore, the step-coverage problem with SiO_2 may be mitigated by varying the PECVD source gas or deposition conditions for a given size structure.

Multi-layered air-channel structures have also been fabricated. Figure 33 (a) and (b) show SEM images of cross-sectioned structures with two levels of air-channels. The multi-level structures were processed by two approaches: i) the first level was completely processed including decomposition of the PNB and then the second level was formed and decomposed separately; ii) the first level PNB was patterned and blanket coated with SiO_2, then the second level was fabricated and both levels were decomposed simultaneously. Both these approaches have been found to work equally well. In the first approach, the mechanical strength of the first level has to be adequate to withstand the processing of the second level on top. In the second approach, diffusion of the decomposition products through the overcoat material has to be adequate to allow such diffusion through multiple layers of overcoat. In actual practice, the choice of approach would be dictated by the number of layers to be processed, the thickness of the encapsulating materials, and other processing conditions.

5.3.2 Discussion of air-gaps encapsulated in glass

Air-gaps have been successfully fabricated with SiO_2 and SiN_x overcoat materials as predicted. The glasses are thermally resistant, with sufficient permeability and mechanical strength to endure the decomposition of PNB. The limiting factor for air-channel dimensions of SiO_2 and SiN_x structures has been found to be the length of the unsupported span of the overcoat layer (i.e. width of the air-channel). In practice, air-channels as wide as 140 μm and up to 10 μm in height are readily fabricated. There appears to be no limitation on the minimum width or maximum length limits of the air-gaps due to the PNB sacrificial material. The minimum size of air-gaps is determined by

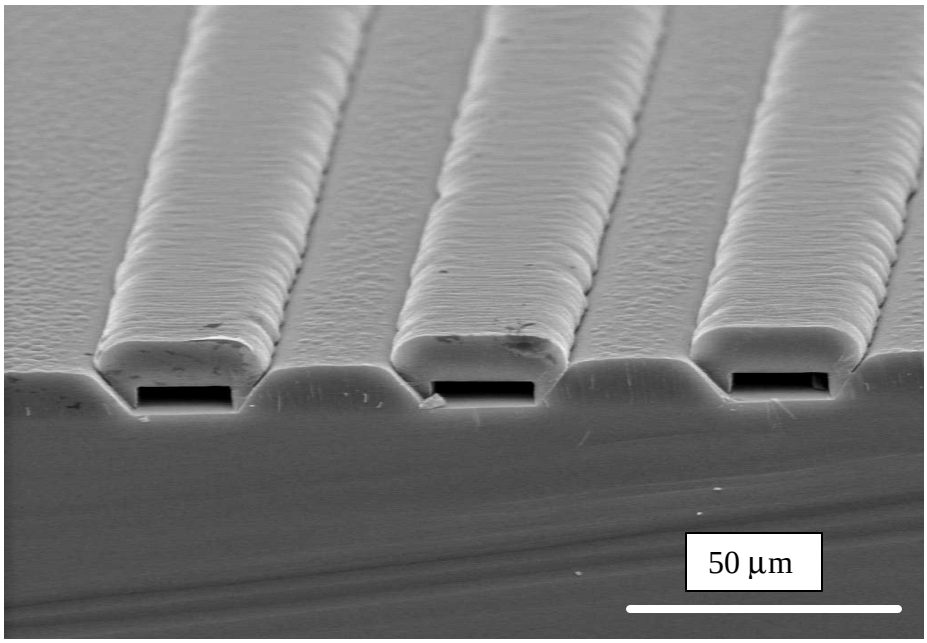

(a)

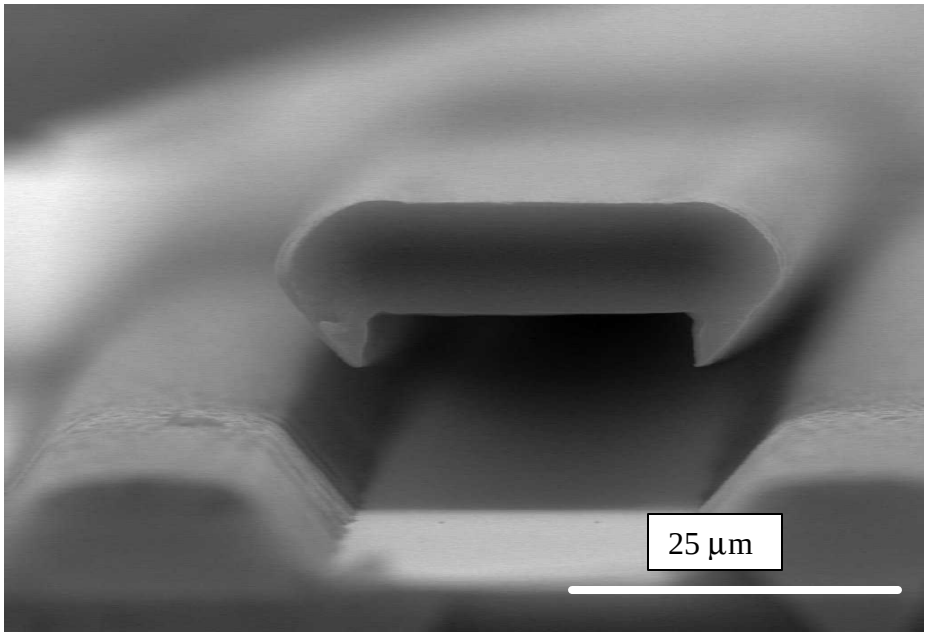

(b)

Figure 32: (a) Example of poor step coverage with PECVD SiO_2 and (b) the resulting damage to the overcoat upon cleaving of the sample.

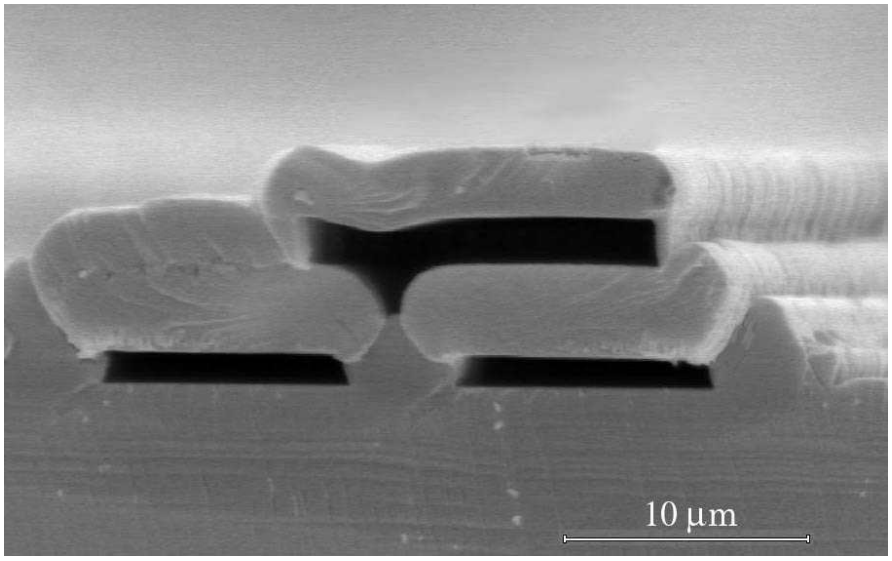

(a)

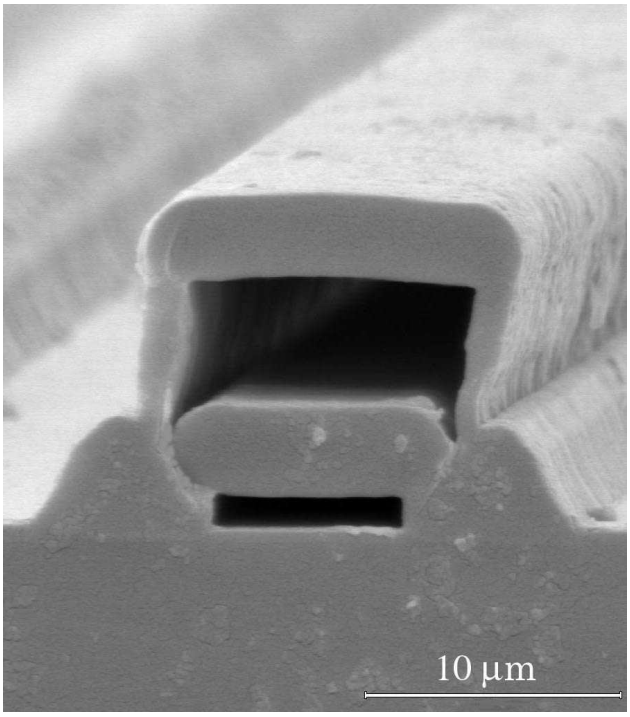

(b)

Figure 33: Multilevel air-channels encapsulated in SiO_2. (a) two layers of air-channels fabricated with an offset (b) directly stacked air-channels

the ability to pattern and etch the small features. Zhou et. al. [10] has demonstrated 0.28 μm wide air-channels. Overcoat thicknesses of 1 to 15 μm (SiO_2 and SiN_x) have been found to be possible without deformations. Thicker overcoats had greater mechanical strength, but are less permeable and may have higher stress.

The other limitation for glass overcoated air-gaps is the stress and step coverage of the overcoat film. The step coverage was discussed in the previous section, and could possibly be eliminated by varying the glass deposition parameters. Stress may be an intrinsic part of the overcoat film from the deposition, or generated at interfaces due to mismatch in CTE between the overcoat and PNB. These stresses can play an important role in the structural deformation of the overcoat. The stress in the SiO_2 film can be seen in Figure 28 (a) on page 111. Figure 28 (a) shows an example of corrugation of the hard mask SiO_2 layer when a portion of the underlying PNB was removed due to undercutting during the polymer etch. In the areas where PNB is present, the strain in the glass was contained. The encapsulating SiO_2 layer is expected to behave similarly. The combined stresses in the film may limit the size of structures that may be fabricated. If the span across both dimensions of the air-gap is large, the stress may cause the overcoat to curve or break when released from the surface.

5.4 Air-gaps Fabricated With PNB and Polymer Encapsulation

Air-channels encapsulated in polymer have several applications including: microchannels for microfluidics; a means to reduce the effective dielectric constant of the polymer; and a means to enhance mechanically flexibility by providing a reduction in the modulus of the encapsulating polymer. Many polymers exist that may be possible

candidates to form air-gaps. However, select overcoat materials were chosen based on: i) applications or interest in the microelectronics industry; ii) curing temperature (below the temperature at which PNB starts to decompose); and iii) thermal stability measured by the glass transition temperature (around 400^{o}C to withstand PNB decomposition). Polyimides are a good choice for an overcoat with PNB sacrificial material because they display high glass transition temperature, high thermal stability, low dielectric constant, low modulus, low moisture adsorption, and relatively low stress. The mechanical properties of polyimides also vary with the linkage groups in the backbone. The other polymers chosen include the high-temperature curing polymers poly(arylene ether), polybenzoxazole (PBO), and parylene-N. This section discusses the results and limitations of air-gaps encapsulated in these polymeric materials. The variation in properties between the polymers and between the polymers and glasses can indicate which properties are necessary for success or failure in forming air-gaps.

5.4.1 Polyimides

The term polyimide refers to a polymer formed from a diamine and a dianhydride which undergoes a condensation reaction to form a heterocyclic polyimide repeat linkage in the backbone of the polymer. The choice of the diamine and dianhydride molecules used to form the polyimide affects the chain stiffness of the polymer, which in turn influences properties of the cured material such as thermal stability, permeability and permselectivity, and mechanical properties. The chemistry and properties of each of the polyimide encapsulating materials investigated in this research are shown in Table 18. The various dianhydride precursors of the polyimides include: biphenyl dianhydride

Table 18: Commercial polyimides used as encapsulating materials and their properties [52-54, 58-62].

Polyimide	Precursor Chemistry	Backbone Rigidity	Tensile Strength	Elastic Modulus	Elong-ation(%)	Film Stress (MPa)	Tg (^{o}C)	Td (^{o}C)	CTE (ppm/^{o}C)	Dielectric Constant
Ultradel 7501	Pre-imidized	semi-flexible	50.6 MPa	3.5 GPa	7.6	108	>400	490	24	2.8
PI-2611	BPDA/PPD	rigid rod	340 MPa	8.3 GPa	25	2	>400	620	3	2.9
PI-2734	BPDA/PPD	rigid rod	178 MPa	4.7 GPa	>10	18	>350	620	16	2.9
PI-2540	PMDA/ODA	semi-flexible	103 MPa	1.4 GPa	40	16	>400	580	20	3.5
PI-2771	PMDA/ODA	semi-flexible	130 MPa	2.7 GPa	45	N/A	294	500	42	3.0
PI-2555	BTDA/ODA/MPD	flexible	132 MPa	2.4 GPa	15	36	>320	550	40	3.3
HD4000	proprietary	semi-flexible	200 MPa	3.5 GPa	45	~30	350	N/A	35	3.2

(BPDA); pyromellitic dianhydride (PMDA); and 3,3',4,4'-benzophenone tetracarboxylic dianhydride (BTDA). The diamine precursors include: p-phenylene diamine (PPD); 4-4'-oxydianiline (ODA); and m-phenylene diamine (MPD). The thermal stability of the cured polymer is known to increase with increasing chain stiffness. The trend followed for chain stiffness would be BTDA<PMDA<BPDA for the dianhydrides and ODA<MPD<PPD for the diamines [54]. The polyimides with the stiffest backbone and highest thermal stability therefore are PI-2611 and PI-2734, which are formed from the precursors of BPDA/PPD. Ultradel 7501 is slightly different from the other polyimides in that the imide ring in the polyimide backbone is already formed. The exact chemistry of Ultradel 7501 polymer has not been disclosed; however, it is known that the polymer backbone is based on a benzophenonetetracarboxylic acid dianhydride (BTDA and 6FDA (2,2-bis(3,4-decarboxyphenyl) hexafluoropropane dianhydride)) system [93]. These three polymers; PI-2611, PI-2734, and Ultradel 7501; have been extensively investigated in the fabrication of air-gaps to determine sizes and shapes which can be formed. The results are discussed in the following sections 5.4.2 through 5.4.5. The remaining portion of section 5.4 discusses results using polyimides and other polymers as encapsulating materials.

5.4.2 Ultradel 7501 polyimide encapsulated air-channels

Ultradel 7501 is a preimidized negative-tone photosensitive polyimide with a dielectric constant of 2.8 and a glass transition temperature greater than 400^{o}C. This polymer is cured between 200 to 350^{o}C and is characterized by low shrinkage. The low shrinkage occurs because the cure reaction does not include formation of the imide ring through a condensation reaction, and thus no water is lost from the film. Therefore, this

polymer allowed a study of the formation of air-gaps independent of any overcoat curing reaction. A main focus of the study using Ultradel 7501 was to determine limitations of the air-channel size and shape with a polymeric overcoat material. Variables investigated for the formation of air gaps using Ultradel 7501 included PNB thickness (height of the air-channel), width and length of the air-channel, and thickness of overcoat material. Solutions PNB-1-S1 and PNB-2-S1 (see Table 13, pg. 99) were applied at a range of spin speeds to achieve PNB thickness from 4 to 12 μm. Ultradel 7501 thickness ranged from 0.1 to 28 μm. Figure 34 shows a 4 μm thick patterned PNB film following encapsulation with Ultradel 7501, but before decomposition. Figure 34 demonstrates that encapsulation does not affect the shape of the PNB features. The features are rectangular with a flat top surface after both patterning and encapsulation. Figures 35 (a) and (b) and Figure 36 show SEM images of air-channels fabricated with 7501 overcoat. Figure 35 (a) shows 35 μm wide air-channels with 15 μm spacing. With this geometry of cavities, the overcoat polymer is able to fill in the spaces between the cavities and planarize the surface. Figure 35 (b) shows an air-channel 140 μm wide with 60 μm spacing. As the spacing between the air-channels is increased, the planarity decreases. The planarization achieved depends on both the flow properties of the overcoat material and the dimensions of the air-channels. Various shapes were seen with the 140 μm wide air-channels. Sometimes the overcoat sagged slightly in the middle as in Figure 35 (b). This is a result from either cross-sectioning the sample or from softening of the overcoat during the decomposition, which will be discussed in detail in the following sections.

The limiting factor of air-channels encapsulated in Ultradel 7501 was found to be overcoat thickness. Problems occurred with very thin polymeric overcoats (< 1 μm)

spanning distances as small as 10 μm. During decomposition either the thin overcoat film collapsed filling in the cavity, or the overcoat ruptured and cracked. These problems were not observed with thicker overcoats. The minimum thickness of Ultradel 7501 to maintain mechanical stability across features was experimentally determined to be ~1 μm. However, as the span across the channel decreases to a single micron or the sub-micron scale, it is likely that a thinner polymer overcoat layer may be used. Smaller features were not tested due to limitations in equipment. As with the air-gaps encapsulated in glass, the minimum width depends on the ability to pattern the PNB into fine patterns. While the glass-overcoated air-gaps were limited by the length of the unsupported span, no limit was found on the maximum width of Ultradel 7501 coated channels. Air-channels were readily fabricated with Ultradel 7501 overcoat up to 1 cm in width x 1 cm in length. Figure 36 shows an SEM image of a portion of an air-gap that is a 1cm x 1 cm square. Air-gaps fabricated with SiO_2 and SiN_x overcoats had a 1 cm dimension in length, but the maximum width only reached approximately 200 μm. The critical difference using Ultradel 7501 overcoat was the ability to form both wide and long air-gaps. The glass overcoat layers were found to sag or break over such large gaps. The height of fabricated air-gaps was limited by the ability to spin-coat the PNB solutions. Viscosity limited the spin-coated thickness of PNB to a maximum of ~35 μm. Alternative methods such as doctor blading, screen printing, multi-layer coating, or melt dispensing the sacrificial material may increase the maximum thickness or height of air-channels that can be fabricated.

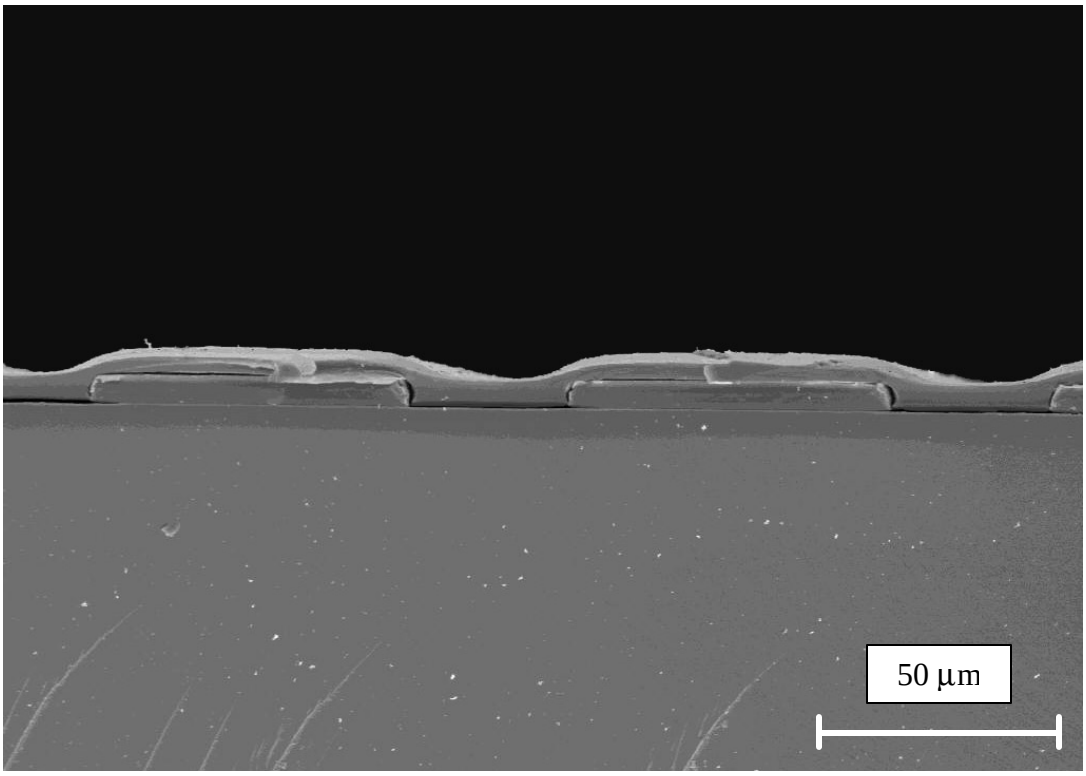

Figure 34: SEM image of 70 µm wide and 4 µm thick PNB pattern encapsulated with Ultradel 7501, before decomposition of the sacrificial material.

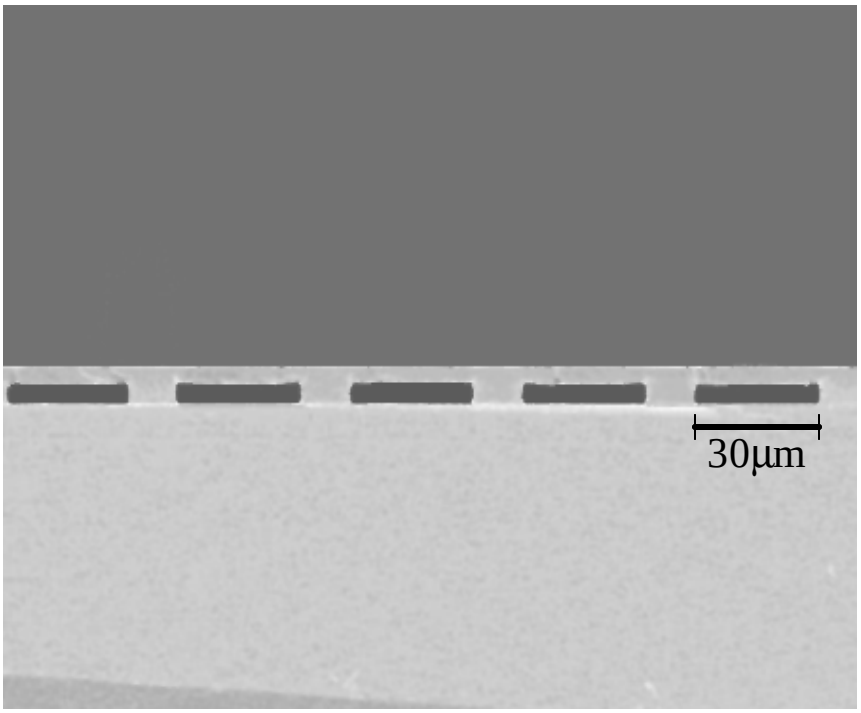

(a)

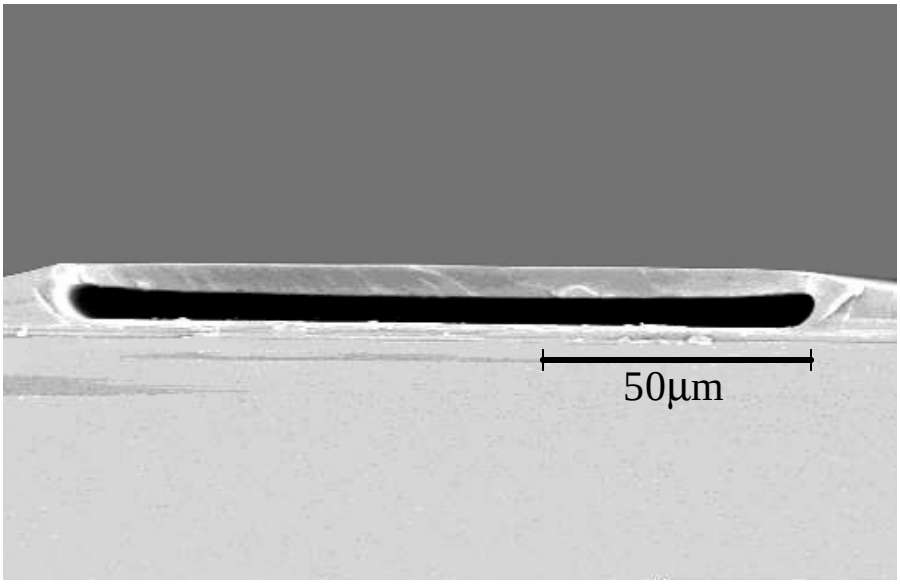

(b)

Figure 35: SEM images of (a) 35 μm wide and 9 μm tall air-channels with 15 μm spacing, and (b) a 140 μm wide and 5 μm tall air-channel with 70 μm spacing between channels, encapsulated in Amoco Ultradel 7501. At the smaller spacing size between air-channels shown in (a) the overcoat fills into the spaces and planarization occurs.

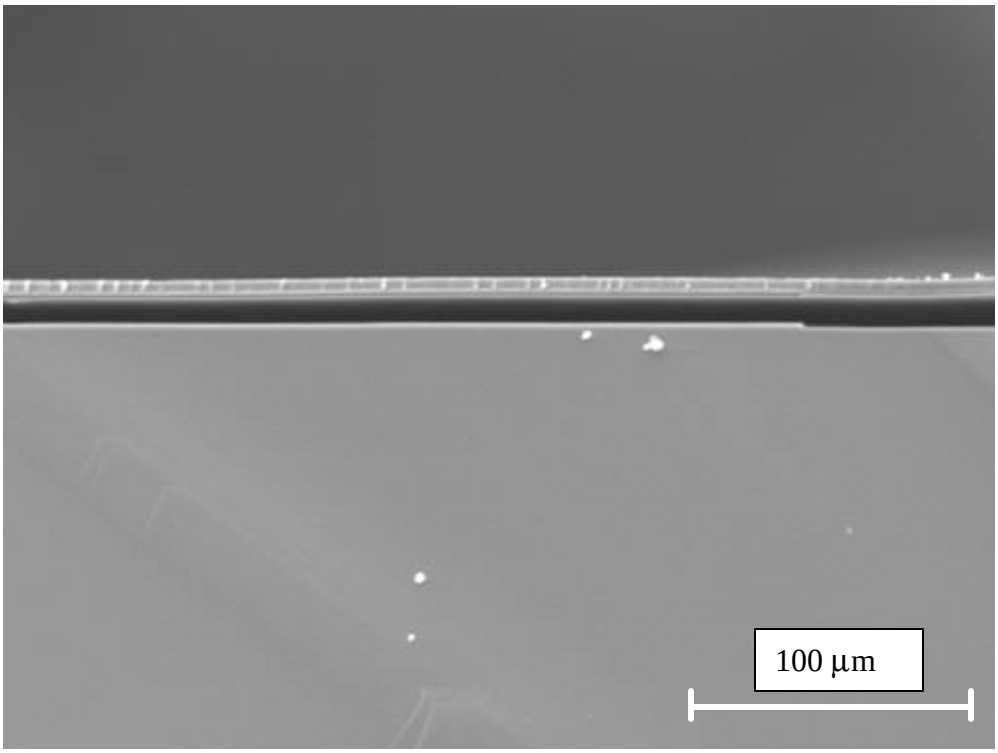

Figure 36: SEM image of a portion of a large air-gap 8 µm in height, 1 cm in width, and 1 cm in length encapsulated in Amoco Ultradel 7501.

5.4.3 DuPont Pyralin PI-2611 and PI-2734 encapsulated air-channels

DuPont Pyralin PI-2611 and PI-2734 are both rigid-rod polyimides which have high thermal stability. PI-2611 is a low CTE polyimide based on polyamic acid chemistry while PI-2734 is a photosensitive polyamic ester. Both polymers are cured between 350 to 400^{o}C, have a dielectric constant of 2.9, and have a glass transition temperature greater than 350^{o}C. These polymers have very similar thermal properties, but different mechanical properties. The elastic modulus and tensile strength of PI-2611 are approximately double the values for PI-2734.

Air-gaps have been fabricated with PI-2611 and PI-2734 using sacrificial PNB layers 4 to 30 µm in thickness, and overcoat layers between 3 and 15 µm. The resulting

air-gaps from both polymers have dimensions up to 50 μm in height. Figure 37 shows a 190 μm wide and 1 cm long air-channel fabricated with PI-2611 overcoat. Before overcoating and decomposing the PNB film, the feature was rectangular with a flat top surface of a uniform thickness of 10.6 μm, similar to Figure 34. The curvature in the top of the air-channel appears following the decomposition process. The resulting height of the air-gap in Figure 37 measures approximately 50 μm. The overcoat polymer at the top of the air-gap overhangs at the edge of the cross-section and flares out near the sides, which is a result of the cleaving process. The high tensile strength and elongation of PI-2611 make it very difficult to cross-section without distortion at the edge. The true height of the air-gap is measured from the background. This sample was decomposed fairly quickly using decomposition profile A, as described in Table 16 (page 105). The resulting air-gap is 5 times taller in the center than the original sacrificial film.

Similar results were obtained for air-gaps overcoated with PI-2734. Figure 38 shows a cross-section of a 190 μm x 1 cm long air-channel overcoated with PI-2734. The original sacrificial material thickness in this case was 29.5 μm, and the height after decomposition is 43.1 μm at the center. The air-gaps were formed using decomposition profile B in Table 16 (page 105). Profile B is a slow program with many intermediate holds at several temperatures. Figure 39 shows 12 μm wide air-channels overcoated with PI-2734 and decomposed rapidly using profile A. The original PNB film thickness was 3.6 μm. The smaller features remain flat after decomposition.

Dome air-gap structures were realized when investigating PI-2611 and PI-2734 as overcoat materials. They were also observed with Ultradel 7501 overcoat when PNB

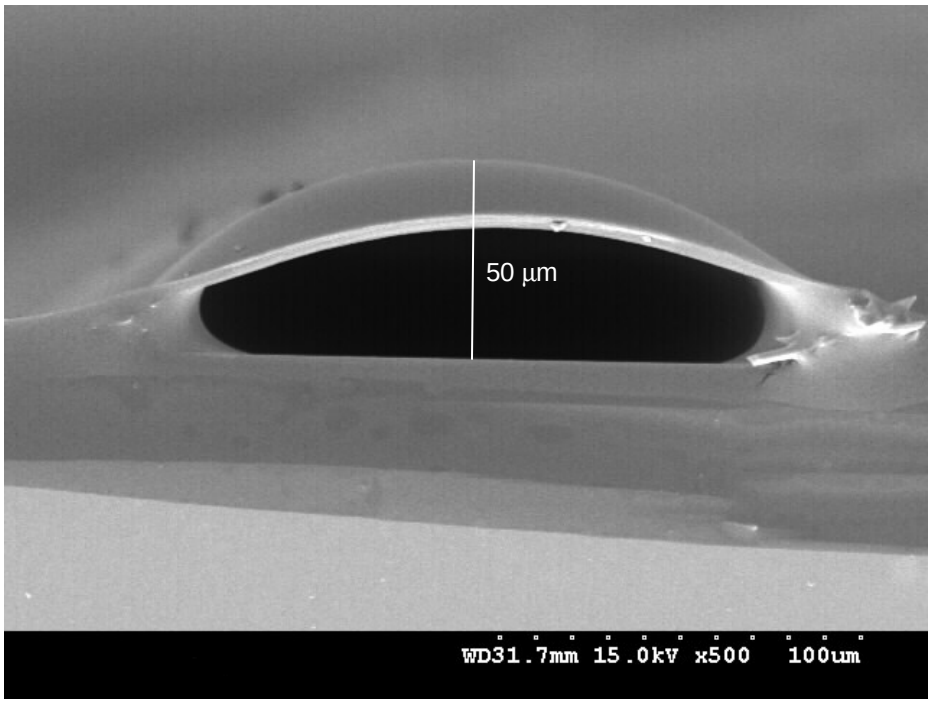

Figure 37: 190 µm wide x 1 cm long air-gap fabricated with PI-2611 overcoat polyimide.

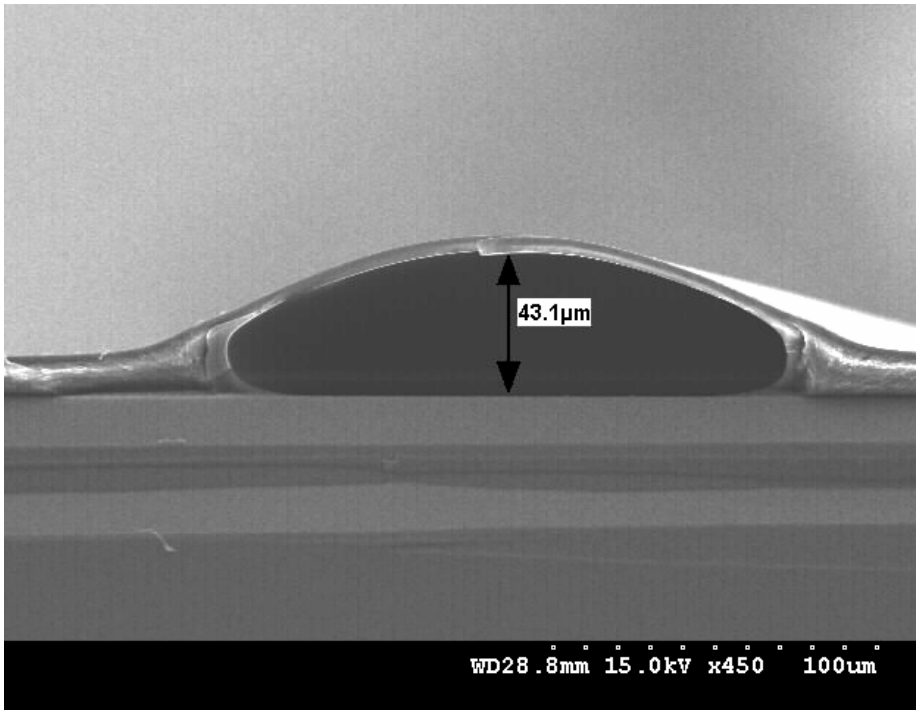

Figure 38: 190 µm wide x 1 cm long air-gap fabricated with PI-2734 overcoat polyimide.

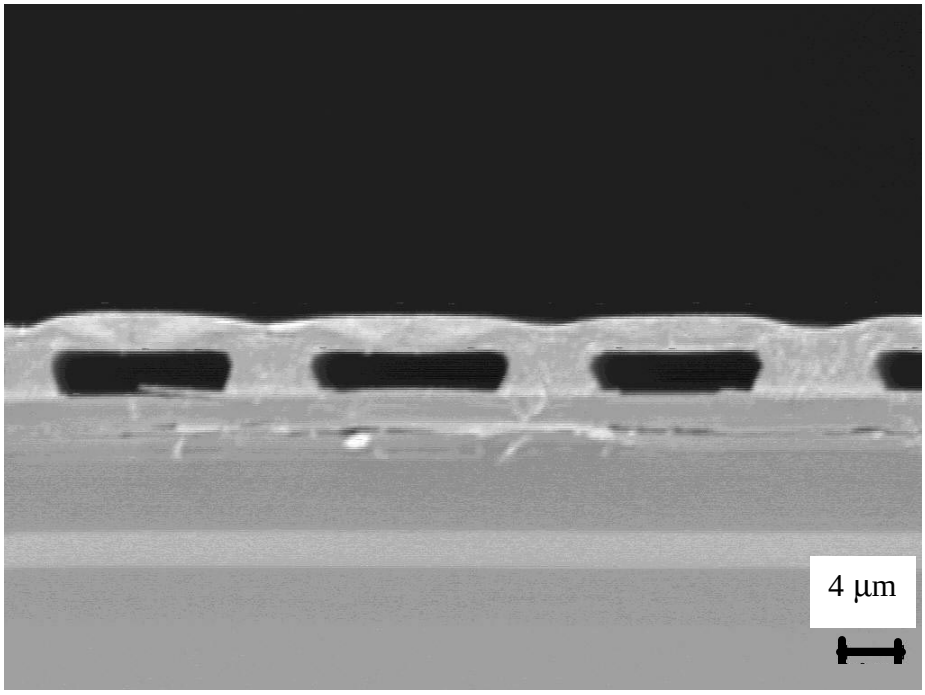

Figure 39: 12 μm wide and 3 μm tall air-channels fabricated with PI-2734 overcoat polyimide

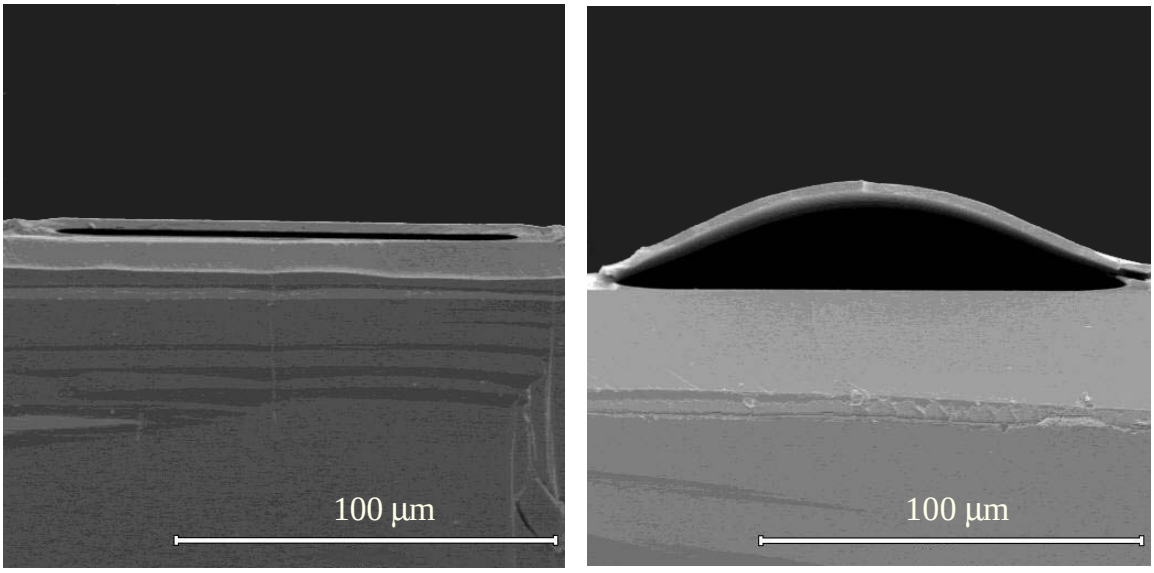

Figure 40: 140 μm wide air-gaps fabricated from a 3.6 μm thick PNB film and overcoated with 3 μm thick PI-2734. (a) Sample with laser-ablated vent holes and (b) sample with completely enclosed air-gap structures.

thickness was > 8 μm or the feature area was large. The cause of the air-gap dome shape was hypothesized to result from pressure build-up inside the air-cavity by either a fast reaction rate of the PNB to volatiles, or low permeability to the decomposition products. To investigate this hypothesis, a sample was prepared consisting of PNB features 4 μm in height. The sample was broken into six smaller samples and the encapsulating material was applied as follows: two samples with 4 μm thick Ultradel 7501; two samples with 4 μm thick PI-2611; and two samples with 3 μm thick PI-2734. A laser ablation tool was used to make a hole or "vent" in the overcoat directly on the features in three samples (one sample of each overcoat). All six samples were decomposed in a Lindberg tube furnace ramped at 5°C/min to 350°C, held for one hour to fully cure the overcoat material, then ramped 1°C/min to 425°C and held for 1.5 hours to decompose the sacrificial material. All three samples with no holes or vents yielded dome-shaped air-gap structures. All three samples with holes yielded flat or rectangular air-gaps. Figure 40 shows SEM micrographs of the pair of samples overcoated with PI-2734 following decomposition: (a) with laser holes and (b) with completely enclosed air-gap structures. The vent in the sample in Figure 40 (a) allows a means for quick removal of the decomposition gases from the cavity, and the cavity retains the shape of the sacrificial film. When the air-cavity is sealed, as in Figure 40 (b), the products can only be removed by diffusion through the overcoat material. Pressure would build if the gaseous products were initially produced at a faster rate than diffusion out of the film. Since only completely sealed cavities result in dome shaped structures, it is concluded that the dome shape originates from this pressure in the cavity.

The overcoat is frozen in the dome-shaped position, even when the cavity returns to atmospheric pressure. The air-gaps maintain their shape even when cross-sectioned down the center of the air-cavity. A slow decomposition profile results in flat air-cavities for some overcoat materials and PNB thicknesses, but not in all cases. The permeability of the overcoat material to the decomposition produces also impacts the resulting structure. In addition, since the decomposition temperature is near the T_g of these polymers, the overcoat material may be slightly deforming due to a loss of mechanical properties. The overcoat must flow some during the decomposition, because the air-cavities have rounded, not rectangular edges, as seen in the air-cavity in Figure 35(b).

5.4.4 Air-gaps encapsulated with other polyimides

Several other polyimides were investigated as encapsulating materials with PNB sacrificial material. These include DuPont Pyralin polyimides PI-2540, PI-2555, PI-2556, and PI-2771, and Hitachi HD4000 polyimide. These polymers are constructed from precursors that allow more flexibility in the backbone, compared to the rigid-rod backbone and highly thermally stable PI-2611 and PI-2734.

The various polyimides were deposited as the overcoat on Unity 400 samples with film thicknesses between 3.75-5.49 μm and patterned with the multi-sized line/space mask pattern. Each of the polyimide chemistries listed above was spin-coated as the encapsulating material according to the conditions in Appendix C. A commercial adhesion promoter, VM-652 (DuPont) was spin-coated at 3000 RPM for 30 s on several of the samples. Each of the polyimides requires a cure at 350°C for 1 hour. Decompositions were performed in the Lindberg tube furnace by ramping 3°C/min to

350°C, holding 1 hour, ramping 1°C/min to 425°C, holding 0.5 hour, ramping 1°C/min to 425°C, and holding for 0.5 hour in nitrogen.

PI-2540 is a semi-flexible backbone polyimide with a T_g above 400°C. The structure of this polymer provides high thermal stability, similar to PI-2611 and PI-2734. However, the increased flexibility in the backbone allows for a lower tensile strength and lower elastic modulus than the other polyimides. Figure 41 shows a cross-sectional SEM image of two 70 μm wide air-channels 3.75 μm in height and encapsulated with polyimide PI-2540. The polyimide film peeled up in the area of the right channel in the image, when the sample was cross-sectioned. Although this sample exhibited low yield, many air-gaps were produced with this polyimide with a width of 140 μm, 70 μm, 35 μm and 15 μm. The lower tensile strength and mechanical properties of this polyimide did not have an effect on the feasibility to form of air-gaps with PI-2540.

PI-2771 is composed of the same precursors as PI-2540, yet contains components to create photosensitivity. The resulting polymer is less thermally stable than the previous described polyimides. The T_g of this polymer is reported as 294°C [61]. Figures 42 (a) through (d) show SEM cross-sections of 5 μm tall PNB features overcoated with PI-2771 and decomposed. The dimensions of the PNB features include: (a) 140 μm in width with 60 μm spacing; (b) 70 μm in width with 30 μm spacing; (c) 35 μm in width with 15 μm spacing; and (d) 15 μm in width with 5 μm spacing. Only the smallest width features produced air-channels, as shown in Figure 42 (d). The overcoat material sagged or flowed into the channel for the other size features. Some remaining sacrificial material is seen in the corners of the channels in Figures 42 (a), (b), and (c) from incomplete decomposition. The overcoat follows the exact shape of the remaining

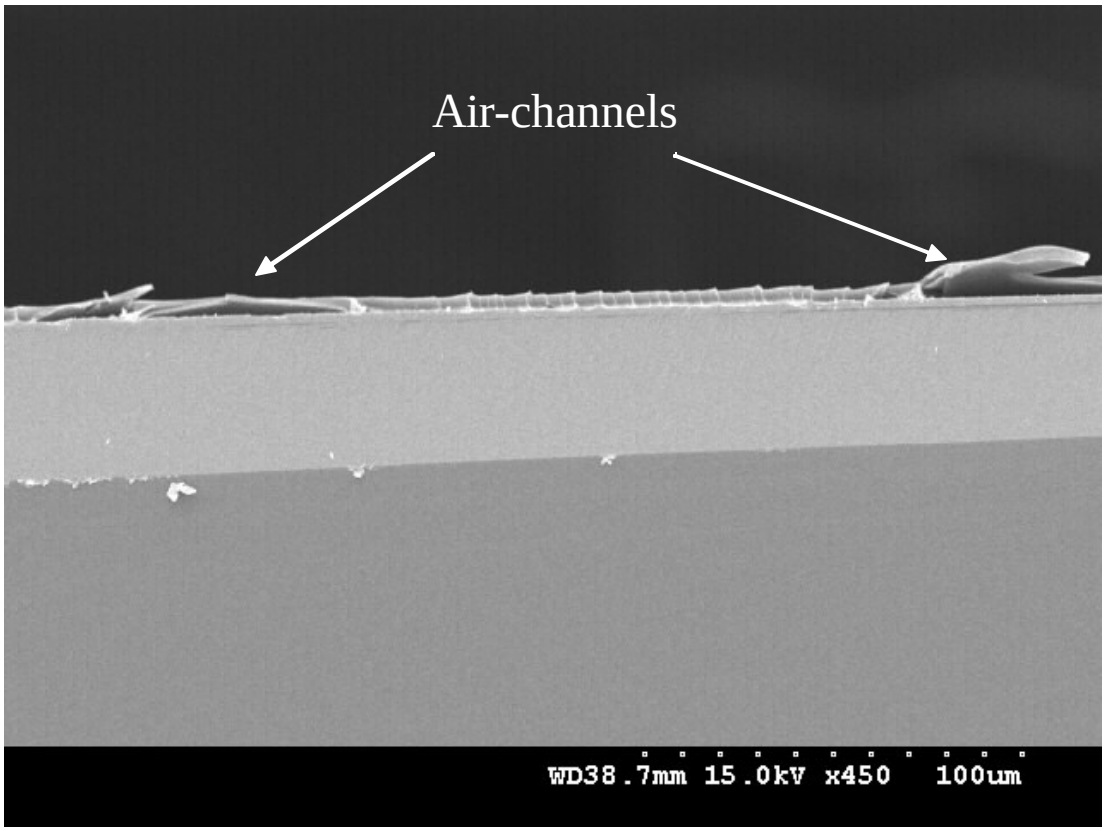

Figure 41: SEM cross-sectional image of 70 μm wide air-channels following the decomposition of 3.75 μm PNB overcoated with PI-2540 overcoat polyimide.

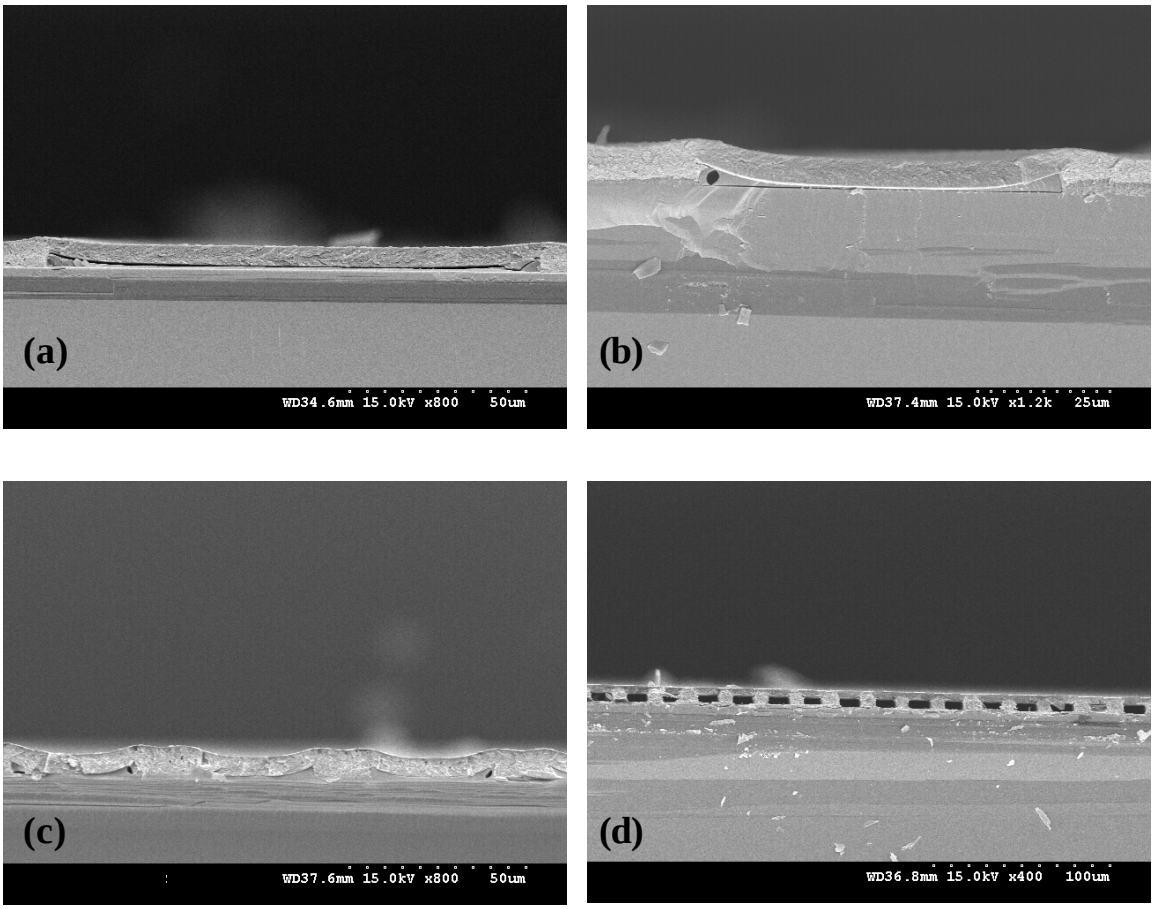

Figure 42: SEM images of following the decomposition of 5 µm PNB overcoated with PI-2771 overcoat polyimide and channel width of (a) 140 µm (b) 70 µm (c) 35 µm and (d) 15 µm.

sacrificial material. The samples are decomposed in the vertical position, so the weight of the overcoat material is not causing it to sag into the channel. Instead, this profile may be a result of the combination of softening of this overcoat material at the T_g of 294^{o}C plus surface tension between the overcoat and the liquid-state sacrificial material. At the elevated temperature, the polyimide does not possess sufficient mechanical stability across the air-cavity to hold its position, is overcome by the surface tension forces, and is pulled down into the cavity. The chemistry of the polyimide HD4000 (Hitachi) is proprietary. However, the thermal and mechanical properties of this polymer closely match the properties of PI-2771. Identical results are seen with HD4000 as with PI-2771 as an overcoat material, though pictures are not included in this thesis.

The final polyimide investigated as an overcoat material is PI-2555. This polyimide has a flexible backbone and similar mechanical and thermal properties to PI-2771. However, PI-2555 contains no photoactive components. Figures 43 (a) and (b) show SEM cross-sectional images following the decomposition of (a) 70 μm wide and (b) 15 μm wide PNB features overcoated with polyimide PI-2555. The polyimide film delaminated some during cross-sectioning of the samples. However, the shape of the overcoat material is still clearly seen in the images. Figure 43 (a) shows that the overcoat material is again pulled down or sags into the channel for the 70 μm wide features. As with the samples overcoated with PI-2771, some undecomposed sacrificial material remains in the corners of the 70 μm wide channel. This was also seen with the 35 μm and 140 μm wide channels. Successful air-gaps were achieved from the 15 μm wide features, although slight curvature is seen in the overcoat layer spanning across the air-gap. The PI-2555 results are almost identical to PI-2771 and HD4000.

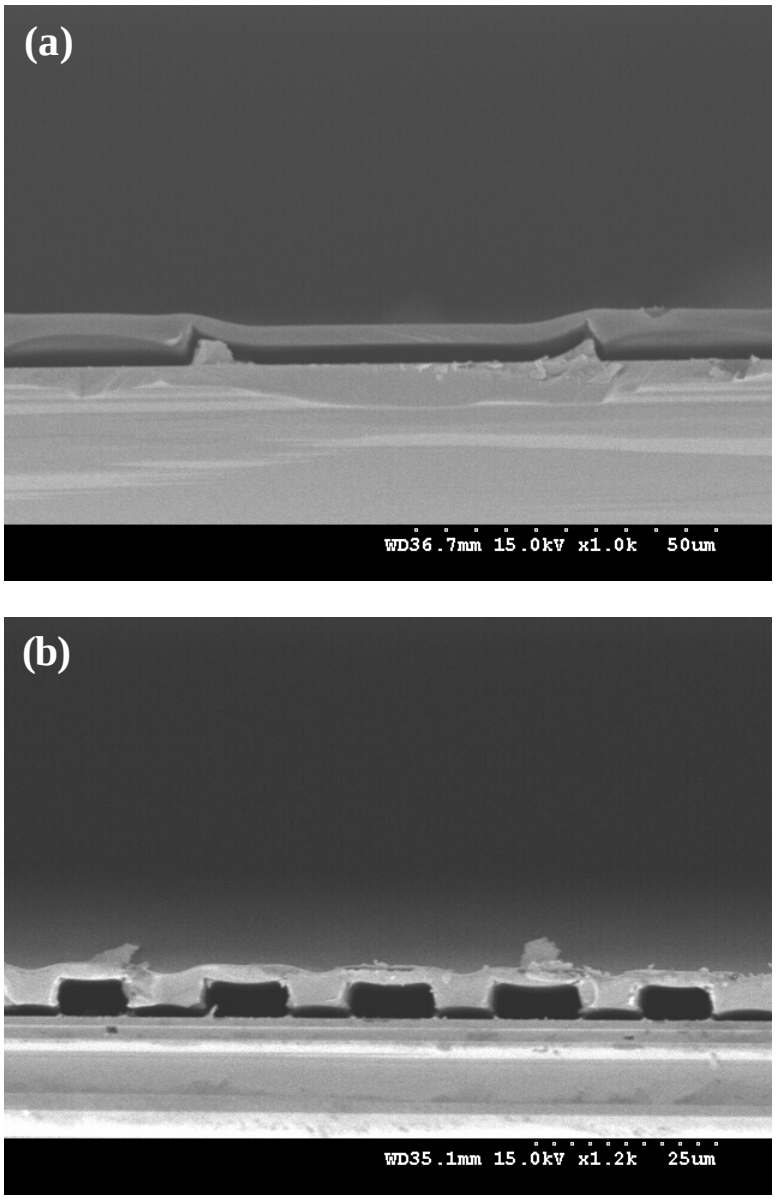

Figure 43: SEM cross-sectional images following the decomposition of 5 μm PNB overcoated with PI-2555 overcoat polyimide and channel width of (a) 70 μm and (b) 15 μm.

5.4.5 Air-gaps overcoated with structurally different polymers

PBO CRC-8650 is a rigid rod polymer formed from a dicarboxylic acid and bisaminophenol. The curing condensation reaction for PBO occurs at temperatures >300^{o}C. The resulting structure and mechanical properties are very similar to polyimide. The cured polymer film has high thermal stability and chemical resistance, and is characterized by a low dielectric constant and low moisture uptake. PBO was spin-coated onto PNB patterned films to yield a thickness of ~10 μm after curing. The decomposition was performed with program C, as described in Table 16 (page 105). As with the polyimides, the PBO material is cured and then decomposed in one furnace program. The PBO film turned to a dark brown color after the decomposition, indicating possible oxidation or decomposition of the film. Figure 44 shows cross-sectional SEM images of PBO overcoated PNB channels 5 μm thick and (a) 70 μm wide and (b) 140 μm wide, following the decomposition. As seen in Figure 44 (a) and (b), the overcoat has completely filled into the air-channel. The T_g of PBO is reported as 295^{o}C [66]. This material will soften and perhaps even flow during the decomposition, similar to the less thermally stable polyimides.

Honeywell FLARE ^{TM} poly(arylene ether) is another candidate for a low-κ inter-level dielectric material. This material has excellent gap fill capability, a dielectric constant of 2.8, good adhesion properties, and low moisture absorption [94]. The backbone structure of this polymer is very different from the polyimides and PBO, but also has high thermal stability (T_g >400^{o}C [65]). The use of this material investigated the ability to make air-gaps with a completely different polymer overcoat system. The low viscosity of the material only allows spin-coating of the polymer less than 2 μm

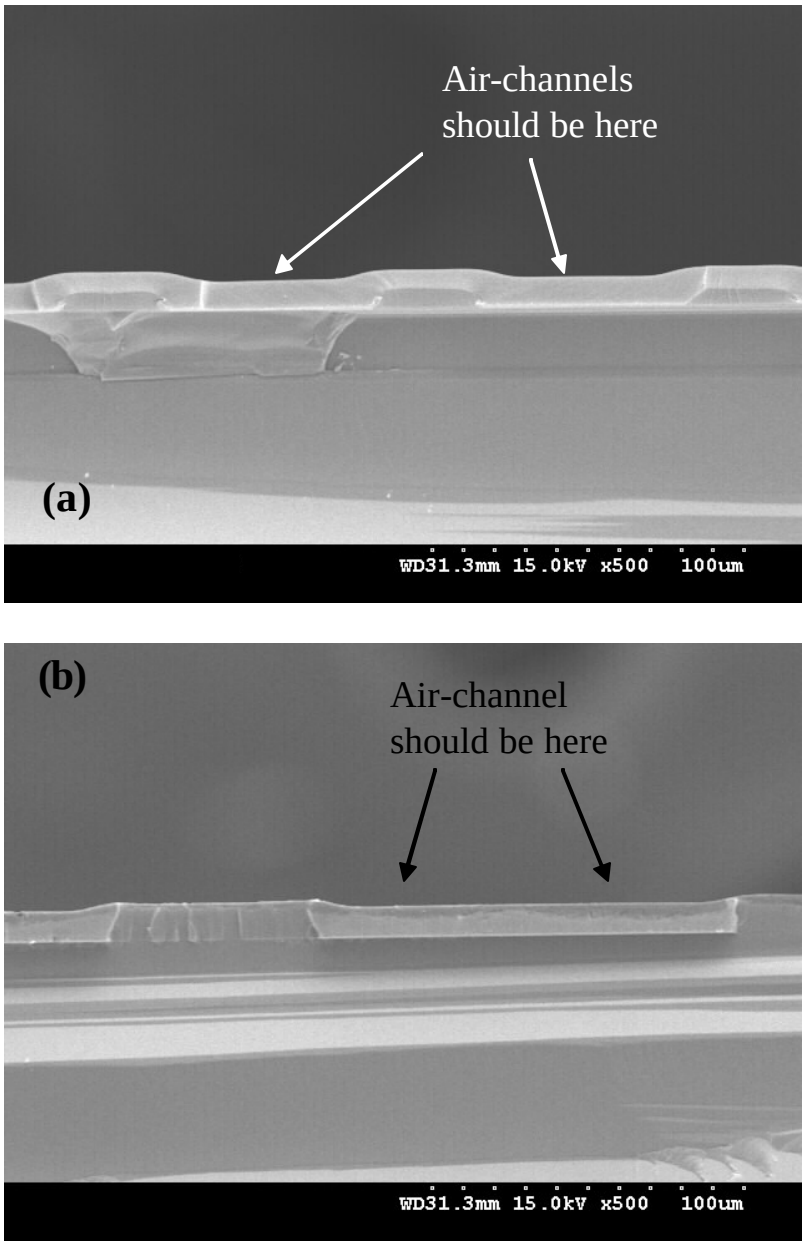

Figure 44: SEM images following the completion of the air-gap fabrication process with Sumitomo Bakelite CRC-8650 PBO overcoat material. (a) Cross-sectional view showing an area with original PNB film 70 μm wide and 5 μm thick. (b) Cross-sectional view of an area with original PNB film 140 μm wide and 5 μm thick.

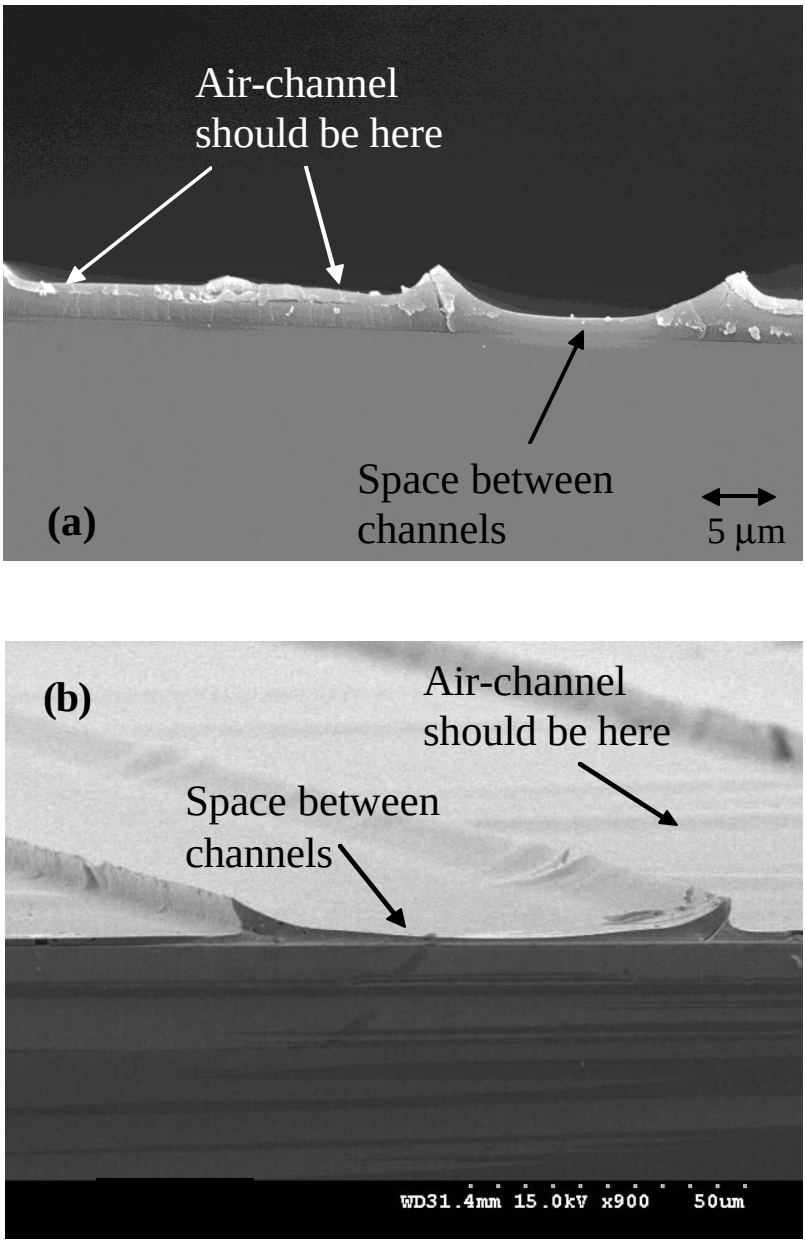

Figure 45: SEM images following the completion of the air-gap fabrication process with FLARE (Honeywell) overcoat material. (a) Cross-sectional view showing an area with original PNB film 35 μm wide and 3.9 μm thick. (b) Top surface perspective view of an area with original PNB film 70 μm wide and 3.9 μm thick.

thick. Two decomposition programs were used. A fast decomposition was performed by ramping 5°C/min to 350°C, holding for 1 hour, followed by a 1°C/min ramp to 400°C, and holding for 1 hour. A slow decomposition was also used, following program D in Table 16 (page 105). The different decomposition programs produced no visual differences in the samples. Figures 45 (a) and (b) are SEM images showing two different views following decomposition of PNB air-channels. Figure 45 (a) is a cross-sectional image following decomposition of a PNB film patterned into channels 35 μm wide and 3.9 μm in thickness, with a spacing of 15 μm. Figure 45 (b) is a perspective image of the top surface following the decomposition of PNB patterned into a channel 70 μm wide and 3.9 μm thick, with a spacing of 30 μm. These images clearly show that the FLARE has collapsed or flowed into the area once occupied by the PNB sacrificial material. The polymer which covered the sides of the structures is clearly visible and indicated by the thicker polymer ridges. Figure 46 shows an enlarged image of one of the corners of the 35 μm wide structures. The decomposition was performed at 400°C for 1 hour, which resulted in incomplete removal of the PNB. Figure 46 demonstrates that FLARE planarizes the surface. The thickness in the spaces between the channels is much greater than on the top of the channels, causing poor step coverage at the sides of the PNB. Such a thin overcoat can easily be overcome by the surface tension forces. A crack in the FLARE at the top right corner also can clearly be seen in Figure 46. Once the film is cracked at this corner, or softens, it loses mechanical stability and is easily pulled down into the channel.

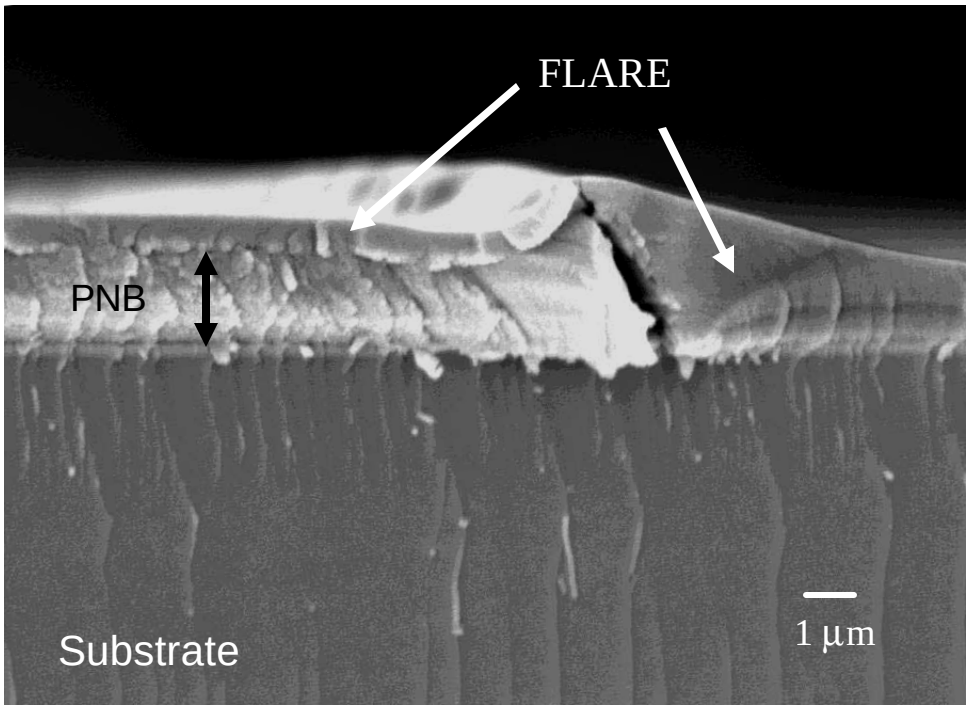

Figure 46: Corner of a 35 µm wide PNB feature overcoated with FLARE.

Parylene-N (poly- para-xylene) is a vapor-deposited conformal coating polymeric material. Parylene-N is widely used in MEMS devices as a conformal coating or a passivation layer due to its high solvent resistance. The solid parylene-N dimer is sublimed to a vapor and pyrolized to form the polymer in vapor form, followed by cooling to deposit the polymer on the sample surface. Parylene-N was deposited using a Paratronix Parylene 2010 Labcoater with a 12 in. diameter chamber and a power of 110 V (AC) at 60 Hz and 15 A. Deposition conditions were as follows: vapor heater set-point = 150^{o}C; pressure = base + 55 mTorr; pyrolysis set point = 650^{o}C; and tube heater temperature = 140^{o}C. The thickness of the produced film is dependent on the weight of solid dimer loaded into the system. Under the conditions listed, 5 g of dimer resulted in a 2.0 µm thick film. The decomposition of parylene-overcoated air-gap structures was not

performed at temperatures above 400°C, since the glass transition temperature is reported as 400°C [55]. Decomposition conditions included a 5°C/min ramp to 350°C, no hold at 350°C, then a 1°C/min ramp to either 375°C or 400°C, and holding for 1.5 hours in nitrogen. A SEM cross-sectional image of a 70 µm wide air-gap structure following decomposition at 400°C is shown in Figure 47 (a). This image shows collapse of the overcoat material. One difference in the parylene-N overcoated sample as opposed to other overcoats that collapsed is the folds seen in the overcoat layer which mark the sides of the original PNB film. An SEM image of the sample following decomposition at 375°C is shown in Figure 47 (b). Un-decomposed PNB is seen in the corners of the air-gap structure. However, if the decomposition reached completion, the overcoat parylene-N would also have collapsed in as in Figure 47 (a). A major difference between parylene and the other polymers used as overcoat materials is the CTE. Parylene-N has a CTE value of 690 ppm/°C [55]. The CTE of the other polymers and glasses, in comparison, range from 0.5 to 42 ppm/°C. A 300°C temperature difference would cause a 70 µm wide overcoat membrane to expand over 14 µm. A material with a CTE of 42 ppm/°C would only expand ~0.9 µm over a 300°C temperature change. Similar to the other materials, the parylene-N may soften slightly and be pulled down by surface tension forces during the decomposition. However, unlike the other materials, the membrane at elevated temperature is much longer than the underlying space on the substrate. The membrane begins to touch the substrate at the center. As it decomposes, it folds at the corners, which are the last areas to decompose. Since the decomposition is near the T_g, the membrane may permanently retain some of its length. Upon cooling, the corners of the elongated membrane remain folded instead of collapsing directly to the substrate.

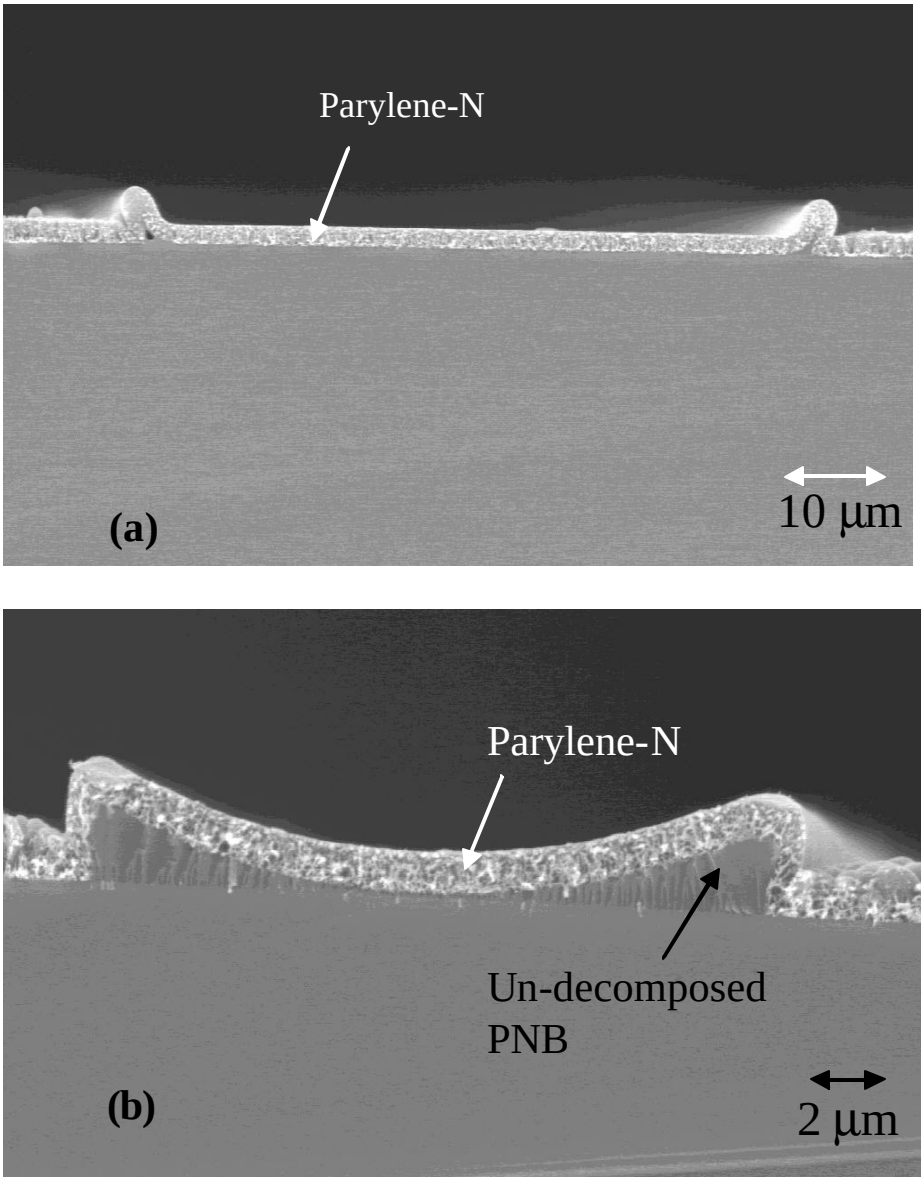

Figure 47: SEM images following the completion of the air-gap fabrication process with 2 μm thick Parylene-N overcoat material. (a) Cross-sectional view showing an area with original PNB film 70 μm wide and 3.6 μm thick following a 1.5 hour decomposition at 400^{o}C. (b) Cross-sectional view showing an area with original PNB film 15 μm wide and 3.6 μm thick following a 2 hour decomposition at 375^{o}C.

5.4.6 Discussion of polymer overcoated air-gaps

The various polymers chosen as overcoat materials for PNB sacrificial material allow a comparison of the effect polymer properties have on the air-gap fabrication process. Not all the polymers selected as candidates with PNB sacrificial material worked as expected. Air-gaps are successfully fabricated with four of the polyimide overcoat materials: Ultradel 7501, PI-2611, PI-2734, and PI-2540. The common factor between all these polyimides is a high T_g (>350^{o}C). The other polyimides, PI-2555, PI-2771, and HD4000 collapse during the decomposition, except for the 15 μm wide features. The T_g of PI-2555 is reported as >320^{o}C, the T_g of PI-2771 is 294^{o}C, and the T_g of HD4000 is reported as exactly 350^{o}C. PBO also has a low T_g of 294^{o}C. These results strongly indicate that the T_g is a property that contributes to the collapse of an overcoat polyimide.

Other properties of the polymers are directly compared, one property at a time. Ultradel 7501 is a preimidized polyimide, while PI-2611, PI-2734, and PI-2540 require a condensation curing reaction. The PI-2611 and PI-2734 are both rigid rod polyimides and structurally similar, except PI-2734 contains components for photosensitivity. Both PI-2540 and PI-2611 are non-photosensitive polyimides with a T_g over 400^{o}C. However the backbone structure of PI-2540 is semi-flexible and has a lower elastic modulus than the rigid-rod PI-2611. PI-2771 and HD4000 are photosensitive, while PI-2555 is not. These three materials also vary in elastic modulus. The CRC-8650 is a rigid-rod polymer similar to PI-2611 and PI-2734; yet, the T_g is substantially lower than the rigid-rod polyimides. From these comparisons, the results indicate that the condensation curing reaction, photosensitivity, and elastic modulus do not cause the air-gap structures to

collapse. The type of polymer backbone structure is not a necessary criteria in an overcoat material. However, the thermal properties of a polymer are often related to the backbone structure. Other properties of the overcoat polymer to consider are the CTE and degree of planarization. The results from FLARE and Parylene-N show that these properties are an element of air-gap failure.

The sizes and geometries of air-gaps with polymer overcoats vary with the overcoat material. As with the glasses, the minimum feature size depends on the ability to lithographically produce small features. Another factor to consider with the polymer overcoats is the viscosity and gap-fill ability of the overcoat polymer into or around small features. The overcoat thickness is limited by the maximum thickness which is still reasonably permeable to the decomposition products. In this research, successful air-gaps were formed with 30 μm thick Ultradel 7501. A thin overcoat compromises the mechanical strength of the film spanning the cavity. Air-gaps were not successfully fabricated with overcoat thicknesses of <1 μm of Ultradel 7501 and <2 μm of FLARE.

Larger dimension air-gaps are possible with the polymer overcoated air-gaps than with glasses. Lower stresses in the films allow the overcoat to span a larger area without cracking. In addition, dome-shaped air-gaps are often much taller in the center than the original PNB film. Dome-shaped structures were fabricated >60 μm in height at the center. Deposition of a glass by PECVD over even a 10 μm tall feature, with good step coverage, is extremely difficult. The final air-gap shape depends on pressure in the cavity, but is also a complex function of the overcoat material, the air-gap geometry, and the decomposition profile. Dome-shaped cavities are not seen when the PNB volume is

very small. As height or width of the air-channel increases (i.e. more PNB present), larger arching of the polymer overcoat is seen.

The length of the unsupported span of the air-gap is a key aspect to consider. 15 µm wide air-gaps were fabricated with the overcoats PI-2771, PI-2555, and HD4000. The simplest case is to describe the unsupported overcoat polymer in two dimensions as a membrane fixed on the sides. The deflection at the center of a membrane when fixed on the ends can be simply described in the x-z direction by equation (5.1) [95]:

$$d_{max} = \frac{5pL^3}{32Et^3} \qquad \text{(Eq. 5.1)}$$

where d_{max} is the maximum deflection at the center of the beam, p is line pressure (pressure/width), L is the width of the beam, E is the elastic modulus, and t is the thickness. This equation assumes that the beam does not stretch and lose thickness when it deflects.

Two different membranes are considered which are identical in modulus and thickness, but differ in width: L_1 and L_2 where $L_2 > L_1$. Equation 5.1 is used to compare the pressure required to deflect the membranes the same distance, d_{max}. The result is $p_1 >> p_2$, or much more force would be required to deflect the shorter membrane, L_1, than the longer membrane, L_2. Considering the dimensions of the samples overcoated with PI-2771 shown in Figure 42, deflection of the polymer spanning the 15 µm wide channel would require 13x the force required to deflect the polymer spanning the 35 µm wide channel the same distance. Even more force would be required in comparison to the 70 and 140 µm wide channels. This may result in the success of forming 15 µm wide air-gaps, while the other dimension air-cavities collapse. The smaller span across the

channel possibly increases the resistance to surface tension forces during the decomposition.

The various results show that limitations on polymer encapsulated air-gaps will vary from one overcoat material to another. Regardless, the overcoat must meet certain general criteria in order to work successfully in the fabrication process. The polymer must withstand the decomposition temperature of the sacrificial material. Therefore, the T_g of the material must be at or above the decomposition temperature of the sacrificial material. If the overcoat material softens or flows during the decomposition, the air-channel becomes severely distorted. If the T_g of the overcoat material is lower than the temperature at which decomposition begins ($<350^oC$), the entire membrane is already softened and is in contact with the PNB when decomposition begins. As the PNB decomposes, it passes through a liquid-like stage. The overcoat material has already lost mechanical stability, is attracted to the PNB by surface tension, and follows the shape as the material decomposes. The change in properties at the T_g may also render the film more permeable to the decomposition products. This reduces the pressure opposing the force of surface tension. However, the overcoat materials that form dome-shaped structures also may pass through their T_g. In this case, the decomposition would begin at a temperature lower than the T_g of the overcoat material. If temperature is ramped slowly ($\sim 1^oC$/min), much of the decomposition may occur before the T_g of the overcoat polymer is reached. The overcoat membrane would not entirely be in contact with the PNB and thus not overcome by surface tension forces. Gaseous decomposition products would fill the space between the overcoat and remaining PNB, and pressure may build. In this case, once the T_g is reached, the polymer softens while suspended over a gas. The pressure in

the cavity allows the softened membrane to deform in the upward dome-shaped position. The air-gap overcoat then freezes in this position when cooled from the decomposition temperature.

The CTE of the overcoat is also important to prevent collapse. As with Parylene-N, the increase in length of the membrane during the decomposition can easily allow the overcoat to fold or be pulled into the channel. As with the SiO_2 and SiN_x overcoats, the polymer must have adequate permeability, and mechanical strength to span the air-channel without sagging, collapsing or rupturing during the polymer decomposition. None of the polymers applied in this research ruptured during the decomposition. However, brittle or non-permeable materials, such as metals, may not withstand pressure build-up inside the cavity and crack during the decomposition. A very soft material is highly susceptible to the surface tension forces from the PNB.

5.5 Overcoming Thermal and Mechanical Problems With Overcoat Materials

The reason several of the previously described overcoat materials fail has been attributed to a loss in mechanical properties or flow of the polymer when the overcoat polymer passes through the T_g. In the softened stage, the polymer is easily overcome by surface tension forces. One hypothesized approach to eliminate this problem is to add a thin layer of SiO_2 as a rigid support layer either between the sacrificial and overcoat polymers, or on top of the overcoat polymer layer. In the previous section, PI-2771, PI-2555, HD4000, and PBO CRC-8650 overcoat materials were shown collapse into the air-channels. These same materials were used to investigate the fabrication of air-gaps with a glass support layer.

5.5.1 Experimental details relevant to Section 5.5

The samples contained 5.03 to 5.49 μm thick PNB layers patterned into 140 μm, 70 μm, 35 μm, and 15 μm wide features. The overcoat materials were: (i) polymer only; (ii) 5000 Å of SiO_2 + polymer; (iii) polymer + 5000 Å SiO_2; and (iv) polymer + 2 μm of SiO_2. SiO_2 was deposited at a temperature of 200 ^oC, using the Plasmatherm PECVD conditions previously described in Table 15 (pg. 105). The overcoat polymer in sample sets (iii) and (iv), with SiO_2 on top of the polymer, was first cured in a Lindberg tube furnace before deposition of the glass. The cure schedules recommended by the polymer manufacturers were followed. Samples containing polyimides PI-2771, PI-2555, and HD4000 were decomposed using decomposition program A, listed in Table 16 (page 105). Decompositions with PBO as the overcoat material were performed using program E in Table 16 (page 105). The samples were cross-sectioned and examined with the SEM.

5.5.2 Results of air-gaps with two-layer overcoats

A summary of the results for the various sized air-gap structures and overcoat combinations is given in Table 19. The overcoat polyimides PI-2771 and PI-2555 without a glass layer collapsed in every case, except for the 15 μm wide features. When a 5000 Å layer of SiO_2 was deposited between the PNB sacrificial material and these overcoat polyimides, the problem with the overcoat collapsing was corrected. Figure 48 (a) through (d) show SEM images of the various sized structures overcoated with SiO_2 and PI-2771. Some of resulting air-cavities were dome-shaped, as seen with the other polyimides, PI-2611, PI-2734, and Ultradel 7501. The amount of the overcoat deformation and the height of the resulting channel increased with increasing channel

width. The results for PI-2555 were similar to those for PI-2771, except the structures with SiO_2 and PI-2555 deformed less. Many of the air-channels were rectangular. Figure 49 shows a 35 µm wide air-channel overcoated with SiO_2 and PI-2555. The two layers of overcoat material are clearly differentiated in this image. Delaminating of the polyimide from the substrate occurs from cross-sectioning. However, the glass layer is visibly intact.

A 5000 Å layer of SiO_2 deposited between the PNB sacrificial material and PBO CRC-8650 also allows the formation of air-gaps. Figure 50 (a) and (b) show SEM images of air-gaps overcoated with 5000 Å SiO_2 and 10 µm of PBO CRC-8650. Cracks occur along the top surface of some of the channels, as shown in Figure 50 (b). This is attributed to the CTE mismatch (SiO_2 = 0.5 ppm/^oC, PBO = 51 ppm/^oC) between the glass and the polymer overcoat layer.

Table 19: Summary of results for air-gaps fabricated using SiO_2 as a mechanical support layer with overcoat materials PI-2771, PI-2555, HD4000, and PBO CRC-8650. (Thin refers to a SiO_2 layer ~5000 Å and thick refers to a SiO_2 layer ~2 μm thick).

Overcoat Layer(s)	**PNB (μm)**	**Glass (Å)**	**Overcoat polymer (μm)**	**Worked?**			
				15 μm	**35 μm**	**70 μm**	**140 μm**
PI-2771 only	5.46	N/A	9	Yes	No	No	No
SiO_2+ PI-2771	5.46	5360	9	Yes	Yes	Yes	Yes
PI-2771 + thin SiO_2	5.49	5360	9	Yes	Yes	Yes	Yes
PI-2771 + thick SiO_2	5.49	17000	9	Yes	Yes	Yes	Yes
PI-2555 only	5.46	N/A	5	Yes	No	No	Some
SiO_2+ PI-2555	5.46	5360	5	Yes	Yes	Yes	Some
PI-2555 + thin SiO_2	5.46	5360	5	Yes	Yes	Yes	Yes
PI-2555 + thick SiO_2	5.46	17000	5	Yes	Yes	Yes	Yes
HD4000 only	5.23	N/A	15	No	No	No	No
HD 4000 + thin SiO_2	5.23	5360	15	Some	Yes	Yes	Some
HD 4000 + thick SiO_2	5.23	17000	15	Yes	Yes	Yes	Yes
PBO CRC-8650 only	5.46	N/A	10	No	No	No	No
SiO_2 + PBO CRC-8650	5.49	5360	10	Yes	Yes	Yes	Yes
PBO CRC-8650 + thick SiO_2	5.03	17000	10	Yes	Yes	Yes	Some

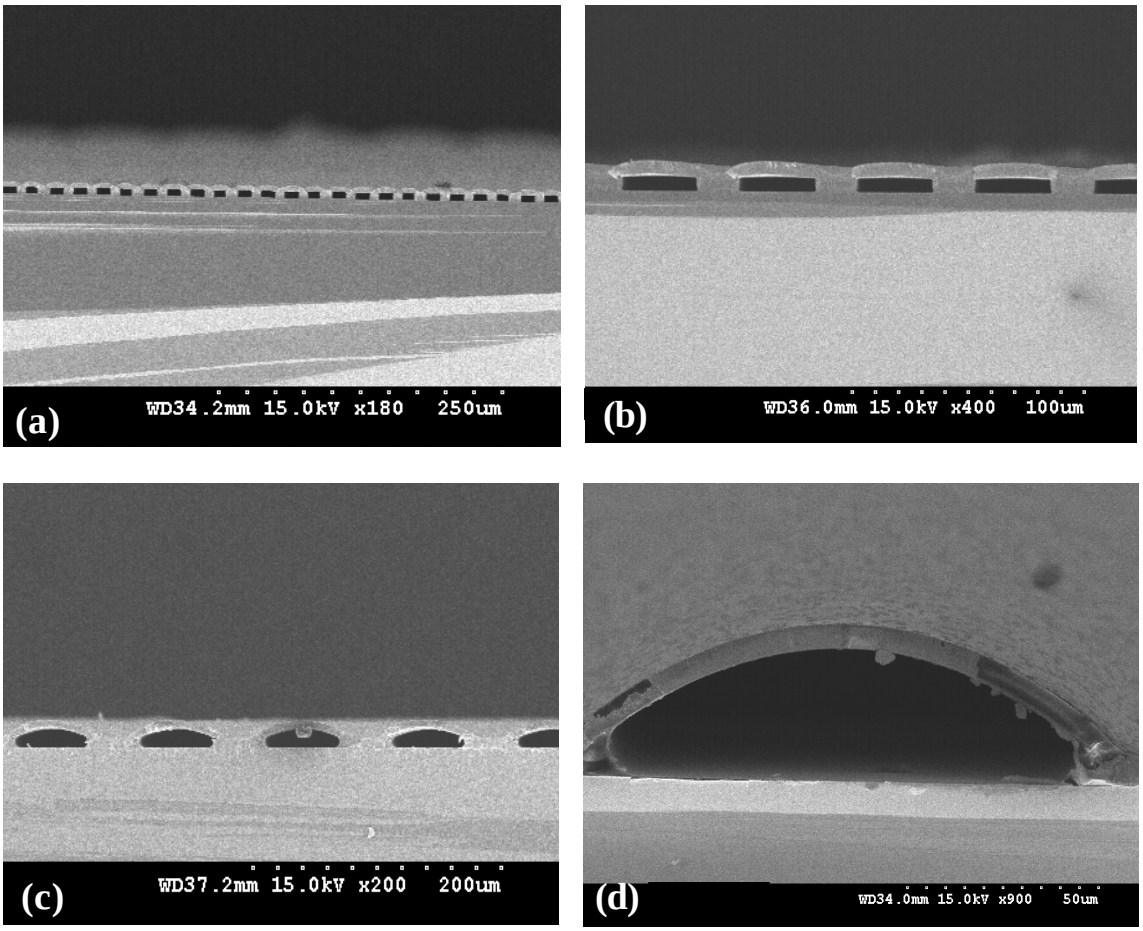

Figure 48: SEM images of air-gaps overcoated with 5000 Å SiO_2 and 9 µm PI-2771. The with of the air-gaps shown are: (a) 15 µm; (b) 35 µm; (c) 70 µm; and (d) 140 µm.

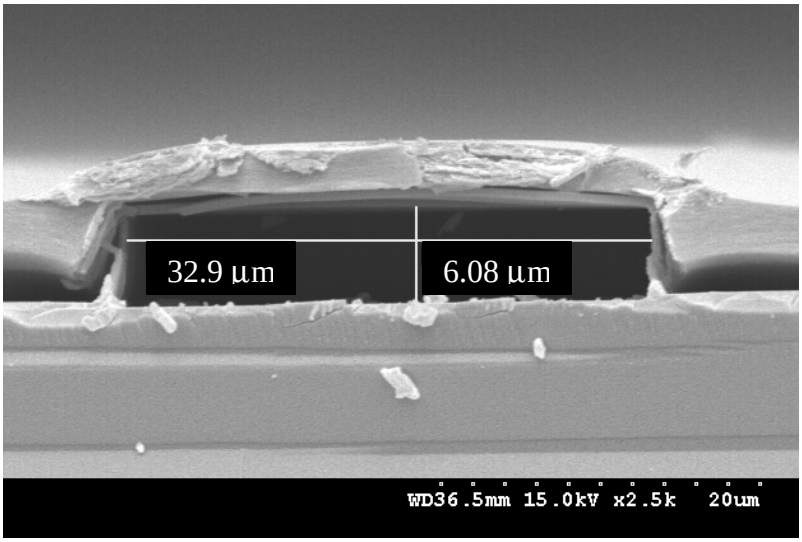

Figure 49: SEM cross-sectional image of a 35 µm air-gap overcoated with 5000 Å SiO_2 and 4 µm PI-2555.

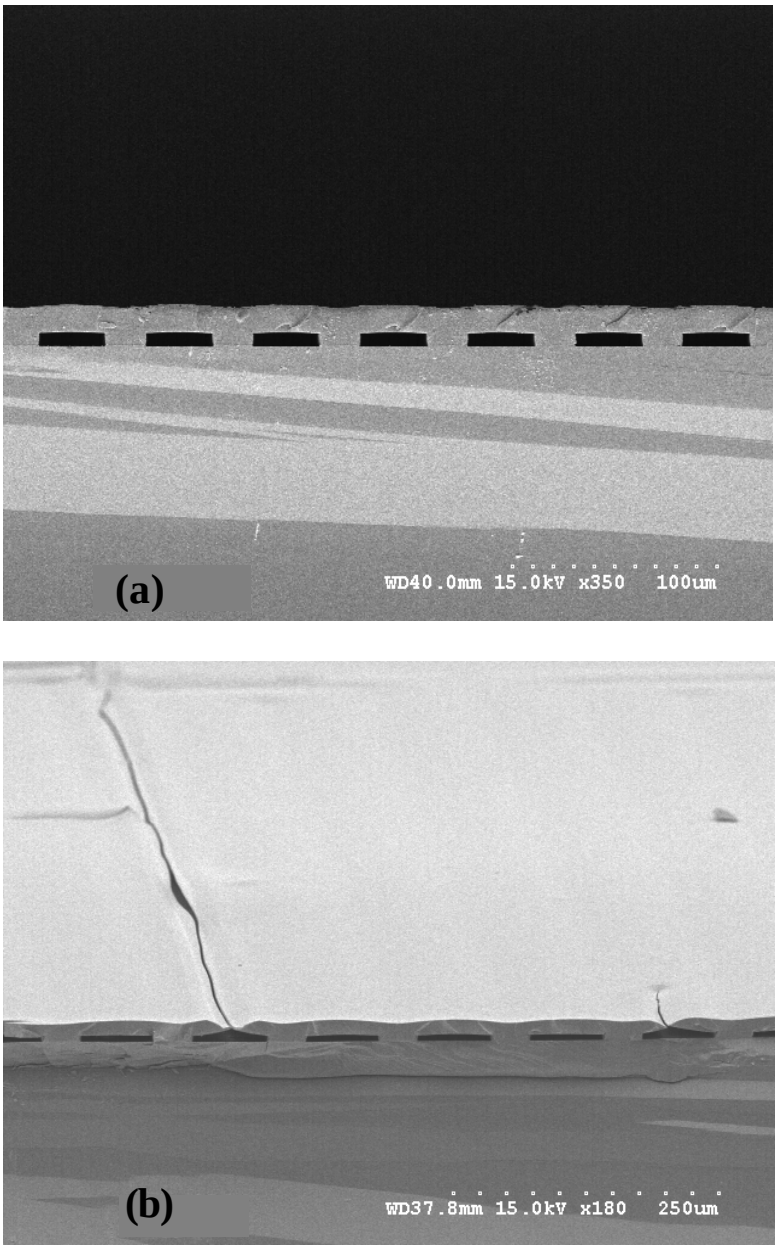

Figure 50: SEM images of air-gaps (a) 35 µm wide, and (b) 70 µm wide, overcoated with 5000 Å SiO_2 and 10 µm PBO-8650.

Two different thicknesses of glass (~5000 Å, ~2 μm) were also deposited on the top surface of the polymer (sample sets iii, iv). One advantage to this approach is the glass can be removed after the decomposition with a plasma or wet-chemical etch. Figures 51 (a) and (b) are SEM images of air-gaps overcoated with cured PI-2771 and 5000 Å of glass over the cured polymer. The overcoat membrane slightly sags into the channel near the center, but the final structure is improved compared to those overcoated with only PI-2771. Figures 51 (c) and (d) are SEM images of air-gaps overcoated with cured PI-2771 then approximately 2 μm of SiO_2. The thicker glass layer improves the final shape of the structures. Both thicknesses of the SiO_2 layer improved the structures overcoated with PI-2555 and HD4000 when deposited on the top surface. The addition of glass on top of PBO overcoated structures showed a great improvement for the smaller feature sizes, but many of the larger features still collapsed. Figure 52 shows two air-channels overcoated with cured PBO CRC-8650 and 2 μm of SiO_2. Figure 52 (a) shows a typical collapsed channel. Figure 52 (b) shows a good air-channel produced with the glass layer as a mechanical support. The top glass surface on each of the four polymers is cracked following the decomposition. The channels may collapse if the glass cracks at a temperature above the T_g of the overcoat, before decomposition is complete. This is attributed to stress developed from the CTE mismatch between the polymers (~30-50 ppm/^oC) and the SiO_2 (~0.5 ppm/^oC) when cooling to room temperature. Once cooled, the cracks do not have a bearing on the air-gaps because the glass is a sacrificial layer. When the glass is removed, the overcoat material is not affected and the air-gap retains its original shape.

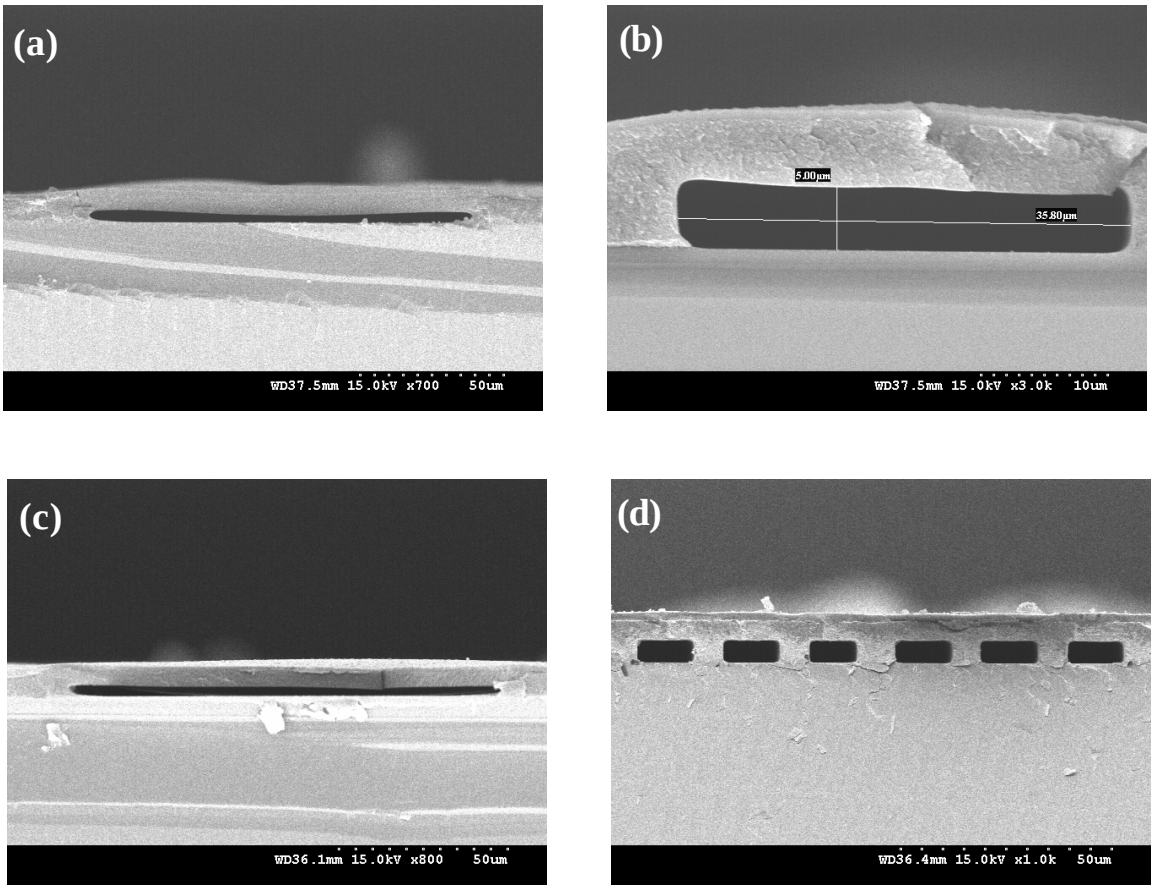

Figure 51: SEM cross-sectional images of air-gaps overcoated with PI-2771 and SiO_2. Dimensions are: (a) width: 140 µm, overcoat: 9 µm PI-2771 and 5000 Å SiO_2; (b) width: 35 µm, overcoat:9 µm PI-2771 and 5000 Å SiO_2; (c) width: 140 µm, overcoat: 9 µm PI-2771 and 2 µm SiO_2; and (d) width: 15 µm, overcoat:9 µm PI-2771 and 2 µm SiO_2.

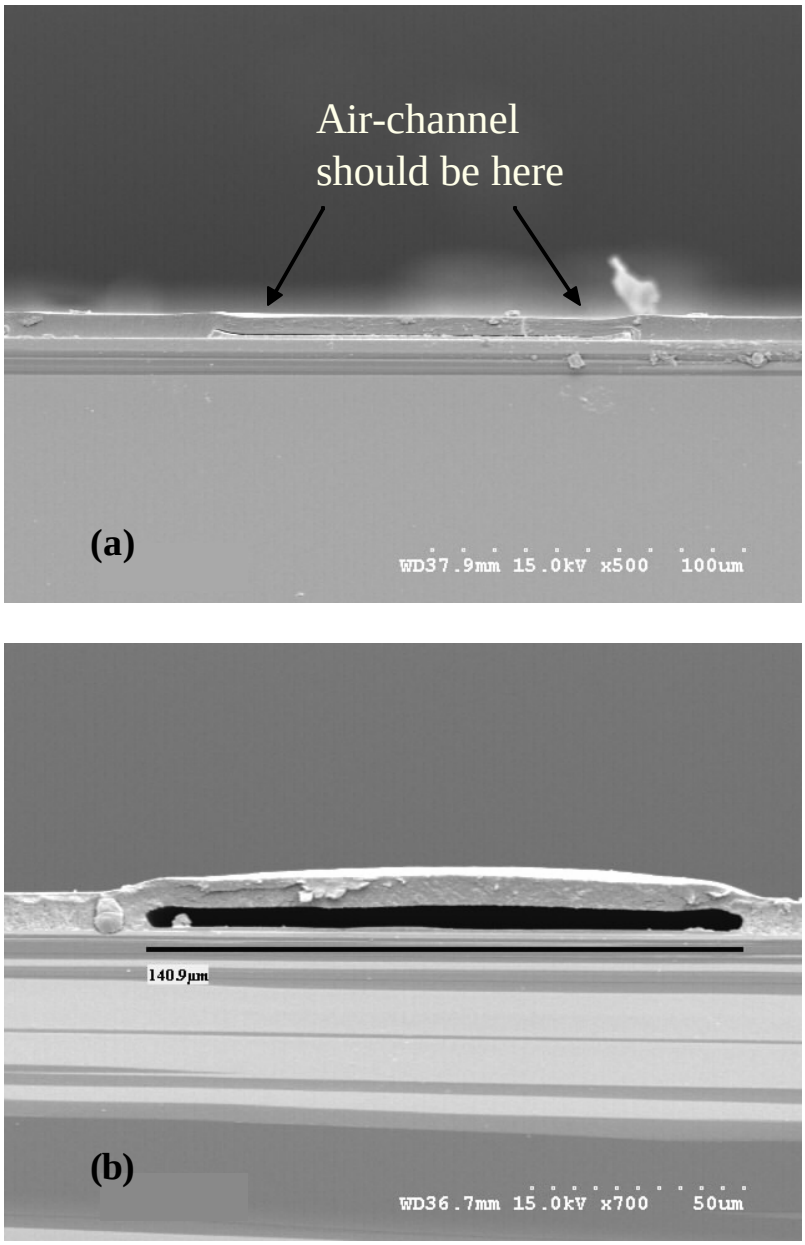

Figure 52: SEM cross-sectional images of a 140 µm wide (a) collapsed channel and (b) air-gap, overcoated with 10 µm PBO CRC-8650 and 2 µm SiO_2.

5.5.3 Discussion of two-layer overcoated air-gaps

The addition of a glass layer underneath or on top of the overcoat polymer provides a means to use polymers that collapse when overcoated alone. The glass offers a mechanical support to the polymer whether it is above or below the overcoat polymer layer. When the glass is deposited below the overcoat polymer, it provides a rigid barrier between the two softened polymers at temperatures above the T_g of the overcoat. The glass does not lose its rigidity at the 425^{o}C decomposition temperature and maintains the structure. When the glass is above the overcoat polymer, the additional support helps the softened overcoat polymer withstand the pull-down force from surface tension between the overcoat polymer and the decomposing PNB. Dome-shaped air-cavities only occur when the glass is underneath the polymer layer. If small cracks occur in the thin glass layer, pressure may deform the softened polymer. If the glass remains intact, a rectangular structure will form. When the glass is deposited over the polymer, the surface tension still may act on the softened polymer since it is in contact with the PNB when decomposition begins. The mechanical support of the glass prevents the structure from collapse or expansion.

The glass layers either below or above the overcoat polymer provide some additional benefits. Glass can act as a solubility barrier layer underneath the overcoat. If the overcoat polymer contains components or solvents PNB is also soluble in, the PNB can be dissolved, distorted, or the decomposition reaction may be affected. A microfluidic channel containing an organic liquid can be lined with SiO_2 to prevent interaction between the fluid and the overcoat polymer. The glass above the overcoat polymer provides the advantage that it can be removed following decomposition.

The additional glass layers affect the mechanical flexibility of the air-gap. The mechanical performance is an important factor to consider for many MEMS applications and SoL compliant wafer level packaging. SiO_2 has an elastic modulus of 73 GPa and will increase the effective modulus, E_{eff}, of the two-layer overcoat. The simplest case is to again treat the overcoat material as a membrane fixed at the ends. The glass and polymer are modeled as two layers in series, with thicknesses L_1 and L_2, and elastic moduli E_1 and E_2. The total height thickness of the stack with no force applied is L_0. A force, F, is applied to the top of the stack, assuming that both layers will see the same amount of force.

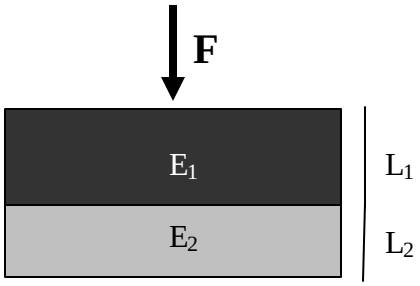

The volume fraction of each material is:

$$f_1 = L_1/L_0 \ , \quad f_2 = L_2/L_0 \qquad \text{(Eq. 5.2)}$$

Hooke's law defines the elastic modulus is equivalent to stress divided by the strain:

$$E = \sigma/\varepsilon \qquad \text{(Eq. 5.3)}$$

Where $\sigma = F/\text{Area}$, $\varepsilon_1 = \Delta L/L_o$, and $\varepsilon_2 = \Delta L_2/L_o$

Using the simple mixing rules, the strain on the total stack, ε_{total} is:

$$\varepsilon_{total} = \sigma\{f_1/E_1 + f_2/E_2\} = \sigma/E_{eff} \qquad \text{(Eq. 5.4)}$$

Therefore the effective elastic modulus can be calculated from Eq. 5.5.

$$\frac{1}{E_{eff}} = \frac{f_1}{E_1} + \frac{f_2}{E_2} \qquad \text{(Eq. 5.5)}$$

Table 20 shows the effective modulus for various SiO_2 and polymer thicknesses of PI-2555 and HD4000. The modulus of PI-2771 falls in between the moduli of these two polymers. A 0.25 μm SiO_2 layer with a 10 μm polymer layer only results in a 2.4% increase in modulus. However, as the ratio of SiO_2 thickness:polymer thickness increases, the modulus increases dramatically. Depending on the dimensions of the structure, the compliance can be severely compromised by the SiO_2 layer.

5.6 Air-gaps Integrated With Metal Features

The use of air-channels as a low-*k* intralevel dielectric in ICs as well as in microfluidic devices integrated with electrical components requires the incorporation of metals into the structures. A method was developed to demonstrate the integration of copper into the air-gap structure. The encapsulants SiO_2 and polyimide, are two preferred interlevel dielectric materials in the IC industry. The structures were fabricated with air as an intralevel dielectric and the encapsulants as the interlevel dielectric. To form the structures, the PNB was spin-coated and patterned on top of a Ti/Cu/Ti seed layer, so as to allow subsequent electroplating of Cu between the patterned PNB features. The time duration of electrodeposition and current were controlled to achieve the same thickness of Cu as the PNB. The overcoat was applied across the top surface, and decomposition was performed. Figure 53 is an SEM image showing a Cu metal line fabricated between two air-channels and overcoated with polyimide Ultradel 7501. In this case, the overcoat is planar across the top surface because the metal and PNB are uniform in height when the overcoat is applied.

Table 20: Effective Modulus for two-layer overcoats of SiO_2 and polymer. The modulus for SiO_2 is 73 GPa.

PI-2555 E = 2.4 GPa				HD4000 E = 3.5 GPa			
SiO_2 Thickness (μm)	Polymer Thickness (μm)	E_{eff} (GPa)	% change	SiO_2 Thickness (μm)	Polymer Thickness (μm)	E_{eff} (GPa)	% change
0.25	10	2.46	2.4	0.25	10	3.58	2.4
0.5	10	2.52	4.8	0.5	10	3.67	4.7
1	10	2.63	9.6	1	10	3.83	9.5
2	10	2.86	19.2	2	10	4.16	18.9
5	10	3.54	47.6	5	10	5.13	46.5
10	10	4.65	93.6	10	10	6.68	90.8
0.25	5	2.52	4.8	0.25	5	3.67	4.7
0.5	5	2.63	9.6	0.5	5	3.83	9.5
1	5	2.86	19.2	1	5	4.16	18.9
2	5	3.32	38.2	2	5	4.81	37.4
5	5	4.65	93.6	5	5	6.68	90.8
10	5	6.76	181.5	10	5	9.58	173.8
0.25	2	2.69	12.0	0.25	2	3.91	11.8
0.5	2	2.98	24.0	0.5	2	4.32	23.5
1	2	3.54	47.6	1	2	5.13	46.5
2	2	4.65	93.6	2	2	6.68	90.8
5	2	7.76	223.4	5	2	10.94	212.5
10	2	12.37	415.3	10	2	16.94	384.0

Although the metal lines are electrically interconnected through the bottom metallic layer in this particular case, these structures are intended to serve as test vehicles for demonstrating the feasibility of fabrication of such metal/air-channel/polymer structures. Alternate routes for fabricating the metal/PNB structures are also possible. For example, metal can be blanket coated on patterned PNB followed by chemical mechanical polishing (CMP). Alternately, the metal can be first inlaid and patterned by additive, semi-additive, or subtractive means, followed by blanket coating the PNB and planarizing the surface by either CMP or etching using RIE.

Insulated Cu channels were also fabricated with Ultradel 7501 overcoat as shown in Figure 54. After electroplating the copper slightly beyond the thickness of patterned PNB, the copper was etched back using nitric acid. This isotropic etch removes copper from the top and side surfaces of the Cu channels, leaving a small space between the Cu and PNB features. The Ultradel 7501 polyimide overcoat has excellent gap-fill capabilities and fills-in the small space etched between the PNB and Cu. Upon decomposition, the air-channel formed, leaving a Cu metal feature overcoated with polymer and a thin insulating layer of polymer on the sides. One benefit of this type of structure is for microfluidic devices with integrated electrical components. If the side of the channel is metal, it can be corroded by fluids inside the channel. The thin polyimide layer protects the metal surface from this corrosion.

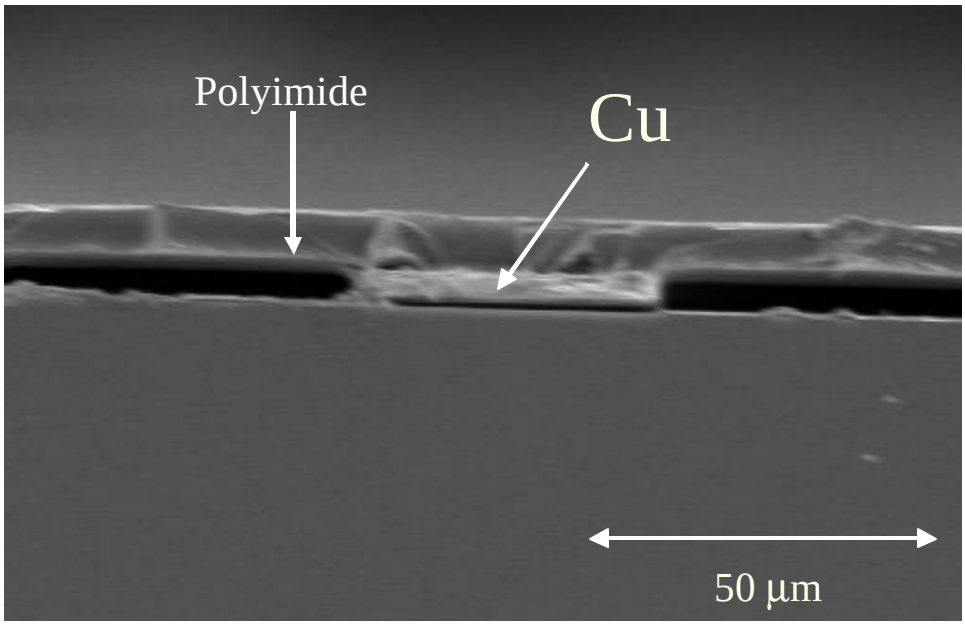

Figure 53: SEM image of two air-gaps 4 μm in height and 70 μm in width with an electroplated Cu line between them and overcoated with Ultradel 7501 polyimide.

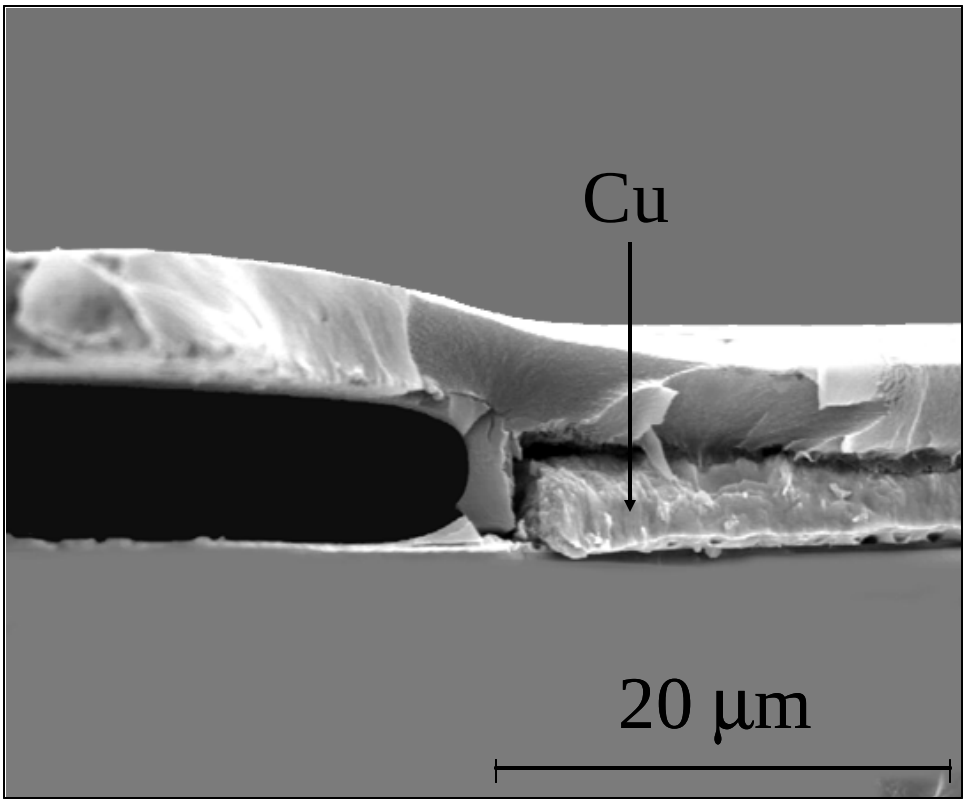

Figure 54: Air-channels fabricated between copper lines that are insulated from the air-channel and overcoated with Ultradel 7501 Polyimide

5.7 Air-gaps Fabricated With Other Composition PNB

A valuable feature of polynorbornene polymers is the ability to influence properties of the sacrificial material through the addition or alteration of the attached functional groups. Although many of the compositions of PNB sacrificial material do not decompose as cleanly as the 90/10 butyl/triethoxysilyl polynorbornene, other properties of these materials make them desirable for certain applications. As described previously, triethoxysilyl (TES) groups are included to increase adhesion to various substrate materials. Cyclolacrylate groups included in the polymer render the polymer photosensitive when combined with a photosensitive free-radical generator [96]. Norbornenes containing some functional groups display lower CTE values, such as methyl acetate polynorbornene. This section discusses the fabrication of air-gaps with alternate polynorbornene compositions to determine the impact various functional groups have on the fabrication process.

5.7.1 Polynorbornenes with varying CTE values

Section 5.3 discussed the fabrication of air-gaps with glass encapsulating materials. The results showed that one of the limitations for glass encapsulated air-gaps fabricated with the 90/10 butyl/TES PNB was the temperature for PECVD oxide or nitride deposition. Above a certain temperature, the overcoat glass cracked upon cooling from the PECVD. The maximum temperature for glass deposition without cracking was $200^{o}C$ for SiO_2 deposition, and $230^{o}C$ for SiN_x deposition. The predominant cause of this cracking was determined to be stress from CTE mismatch between the polymer and the glass upon cooling. One goal of these experiments with other PNB compositions was to determine if a polynorbornene with a lower CTE could withstand a higher temperature

PECVD deposition, yet still display a reasonably clean decomposition. The higher glass deposition temperature produces a better quality glass as a dielectric, which is a requirement from industry. The CTE for the 90/10 butyl/TES PNB is 127 ppm/^{o}C [74]. A lower CTE polymer would generate less stress from thermal mismatch at the glass/PNB interface. The methyl acetate homopolymer (PNB-5 in Table 2, page 30) and the 50/50 norbornene/triethoxysilyl norbornene co-polymer (PNB-7 in Table 2, page 30) were investigated for this purpose. The methyl acetate polymer has a CTE of approximately 75 ppm/^{o}C and the 50/50 butyl/TES copolymer has a CTE of approximately 80 ppm/^{o}C [74]. The copolymers of methyl acetate/triethoxysilyl polynorbornene were not used for fabrication, due to high residue levels seen with TGA, and also because they showed poor film quality when spin-coated.

Higher temperature glass deposition was investigated using solutions PNB-5-S2 (methyl acetate polynorbornene) and PNB-7-S1 (norbornene/triethoxysilyl norbornene copolymer), described in Table 13 (page 99). The solutions were used to spin-coat sacrificial polymer films 5 μm in thickness. Aluminum was used as a hard mask for both materials, identical to the process using the 90/10 butyl/TES PNB. However, the aluminum hard mask on PNB-5-S2 had to be patterned with RIE, as the methyl acetate polymer was soluble in the wet-chemical aluminum etchant. The polymer RIE etching was performed using the same etch program as the other polymers, PNB-ETCH2. Following etching, the features fabricated from the methyl acetate PNB delaminated in many areas and the polymer surface appeared wrinkled. The commercially available adhesion promoter A8000 (Dow) helped alleviate the delaminating, but not the wrinkling. The patterned polymer films were overcoated with approximately 2 μm of SiO_2, using

two different PECVD tools and 3 deposition temperatures: 275°C, 300°C, and 325°C. The Plasmatherm PECVD and the STS PECVD were used to compare oxide deposited under different stress conditions. The decomposition was not performed on all samples, but rather the samples were examined after SiO_2 deposition, to observe cracks. No cracking was seen in the glass deposited at 275 °C on both polymers with either PECVD tool. At 300°C, the glass deposited onto the 50/50 norbornene/butyl norbornene copolymer appeared opaque, but no cracks were observed. The glass deposited onto methyl acetate PNB at 300°C from the STS PECVD was also not cracked in any areas. However, the glass deposited onto methyl acetate PNB at 300°C using the Plasmatherm PECVD appeared cracked, but only in areas with a large amount of polymer, such as a alignment marks. The glass covering the line/space patterned features was not cracked. At 325°C, all samples cracked, mostly in the areas of large features, and at stress points, such as the corners of the features. It was concluded that these two polymers are capable of extending the glass deposition process to temperatures of 300°C. The lower CTE of these materials enables the higher temperature deposition. A CTE of 75 ppm/°C compared to a CTE of 127 ppm/°C reduces mismatch in length expansion between the polymer and the glass by 40%.

Figure 55 shows a 70 μm wide air-gap fabricated with PNB-7 (50/50 norbornene/TES norbornene copolymer) and overcoated with SiO_2 deposited at 275°C. The overcoat layer on these air-gaps is intact, with no cracks or wrinkles. Figure 56 shows air-gaps fabricated with PNB-5 (methyl acetate homopolymer) and overcoated with SiO_2 deposited at 300°C. In this case, the air-gaps are not perfectly rectangular and the glass appears wrinkled on the top surface. This is from wrinkles and roughness of the

polymer features after patterning, and not caused by the PECVD deposition. Without any adhesive groups, the methyl acetate polymer does not adhere to the surface, and easily lifts off and wrinkles when rinsed in water. Despite high residue content remaining in the TGA, the air-channels appear clean with no visible residue.

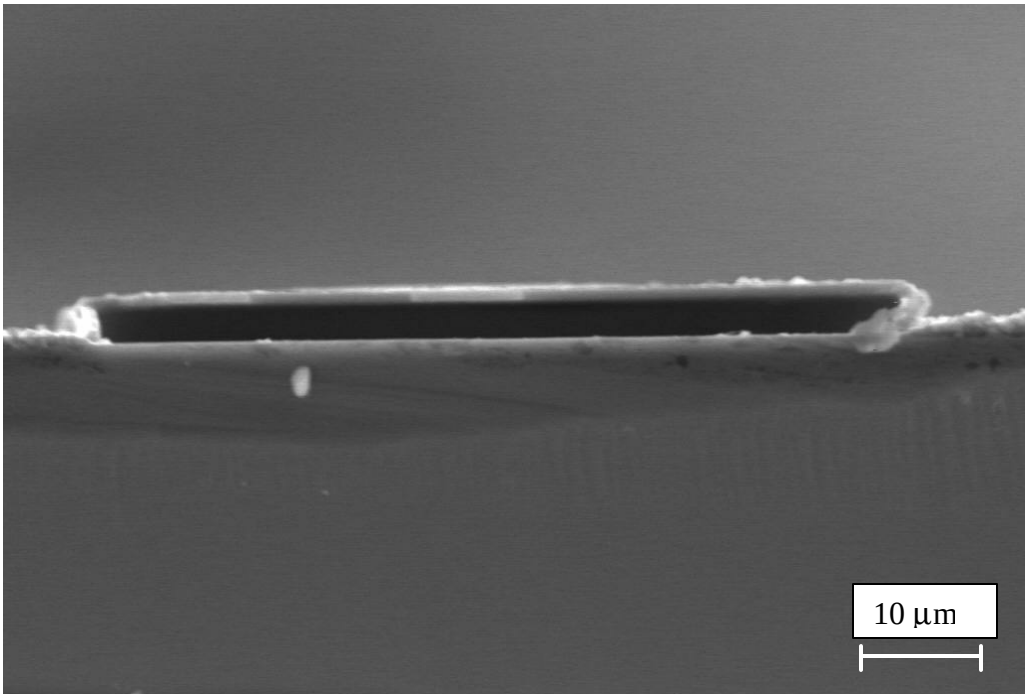

Figure 55: SEM image of a 70 µm wide air-channel fabricated with PNB-8 (norbornene/triethoxysilyl norbornene copolymer) and overcoated with PECVD SiO_2 deposited at 275^{o}C.

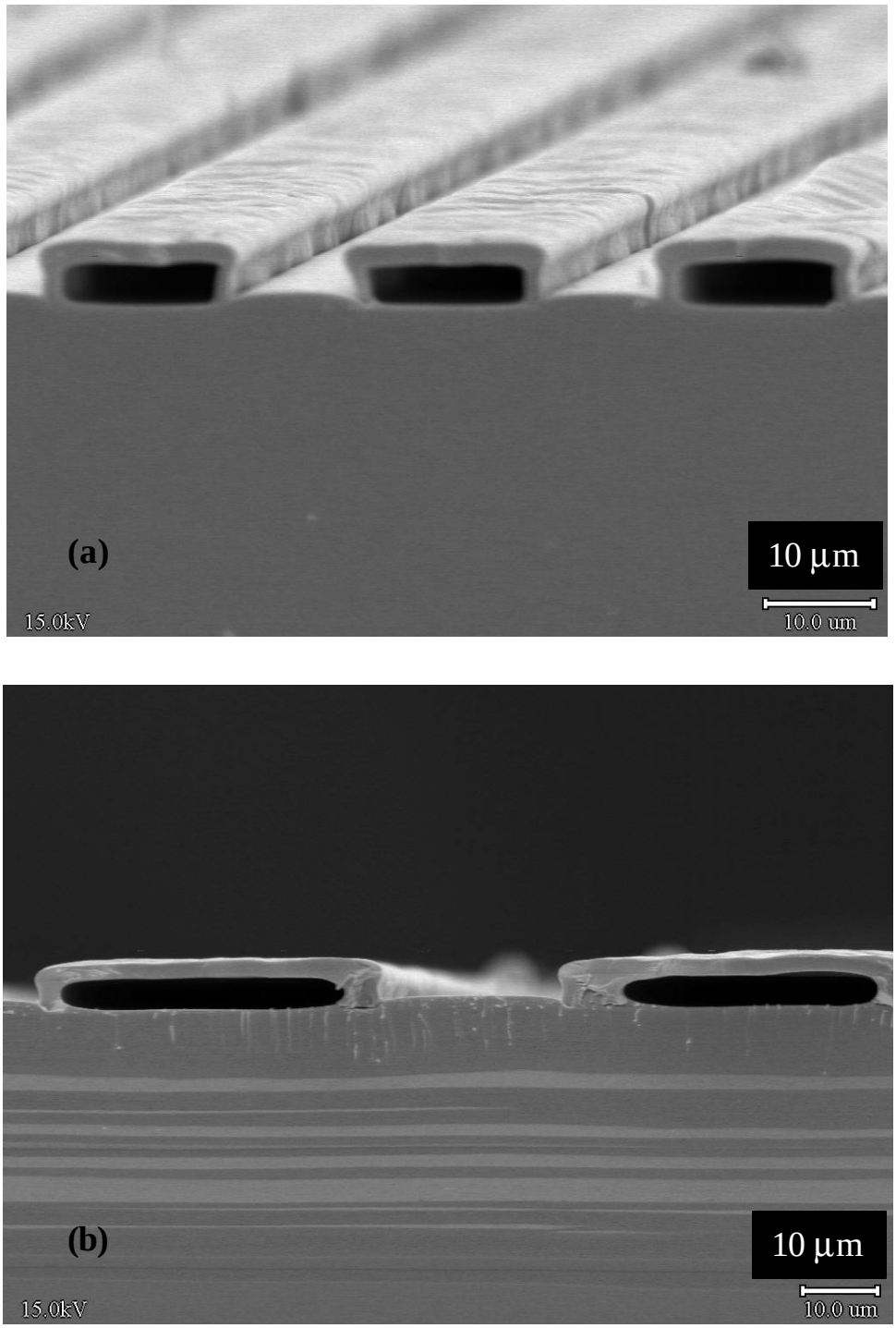

Figure 56: SEM images of 4 µm tall air-gaps and (a) 15 µm wide, and (b) 35 µm wide, fabricated with methyl acetate polynorbornene (PNB-5) and overcoated with SiO_2 deposited at 300^{o}C.

5.7.2 Photosensitive polynorbornene

A photosensitive version of the sacrificial polymers has two distinct advantages: (1) the number of processing steps required to produce the patterned polymer structures is significantly reduced and (2) the photosensitive polymers provide the opportunity to use "gray scale" lithographic masks and methods to produce channels that have structure in the direction normal to the substrate (i.e. non-uniform channel heights). Photosensitive materials are obtained by synthesizing PNB polymers containing cross-linkable cyclolacrylate functional groups and formulating these polymers with photosensitive free-radical initiators. Optimization of composition and lithographic characteristics of these materials has been studied and reported by Wu et al. [96], and is beyond the scope of this work. The goal of this work was to compare the fabrication of air-gaps using the photosensitive material to the 90/10 butyl/TES PNB processing. The photosensitive PNB was patterned both directly through photosensitivity, and also with the standard hard mask and dry etch patterning method.

Solution PNB-8-S2 (90/10 butyl/cyclolacrylate norbornene with 4 wt% benzoin ethyl ether photoinitiator), and the overcoat materials SiO_2 and Ultradel 7501, were used for the fabrication of air-gaps from the photosensitive formulation. The main component of this polymer contains butyl substituents, so the polymer was expected to behave similarly to the 90/10 butyl/TES composition. Therefore, identical fabrication procedures were followed to pattern the material by dry-etching. PNB-8-S2 was spin-coated onto silicon wafers and softbaked, patterned with and Al hard mask, and etched into patterns using the RIE process PNB-ETCH2. No differences in the processing occurred, except the deionized water rinse following RIE etching. The patterned features have poor adhesion with the substrate and many peeled off while rinsing the sample. The patterned

film was overcoated with either SiO_2 deposited at 200°C, or Ultradel 7501 polyimide, and decomposed.

Figure 57 shows 15 μm wide and 4 μm tall air-gaps fabricated with this polymer and overcoated with a 9 μm thick layer of Ultradel 7501 polyimide. No visual differences occur in the air-gaps fabricated with the photosensitive material, and those fabricated with the 90/10 butyl/TES composition.

The same polymer formulation was used to fabricate air-gaps by patterning the polymer using its inherent photosensitivity. The details of the photopatterning of the PNB are described by Wu et. al [96]. The PNB is directly exposed to UV light (365 nm) through a mask, post-exposure baked, and developed with xylene. The overcoat is applied and the structure is decomposed. Figure 58 is an SEM image of a 105 μm air-gap formed via the photosensitive processing and overcoated with 2 μm SiO_2. The air-gap formed has no visible residue. However, the photo-patterning produces a difference in the shape of the air-gap. The feature on the mask was 120 μm. However, the resulting air-gap is only 105 μm. Material is lost from the sides of the structures during the development process. In addition, the sides of the air-gap are sloped. The solvent developing results in features without 90° sidewall angles.

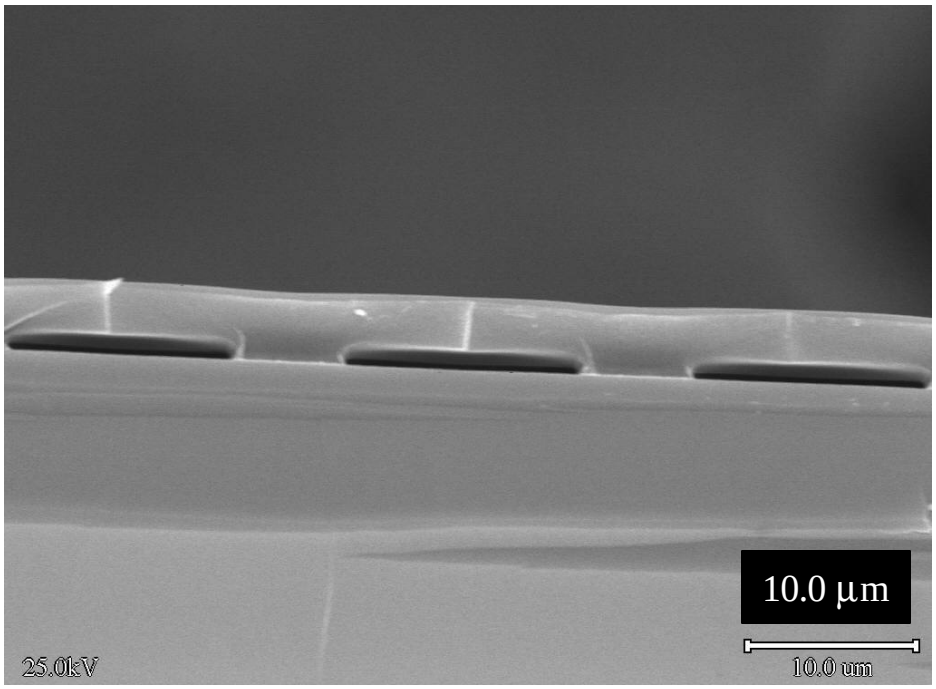

Figure 57: SEM image of 15 µm wide air-channels fabricated from solution PNB- 8-S2 (90/10 butyl/cyclolacrylate norbornene copolymer with photoinitiator) and overcoated with 9 µm Ultradel 7501 polyimide. The PNB features were patterned via non-photosensitive processing.

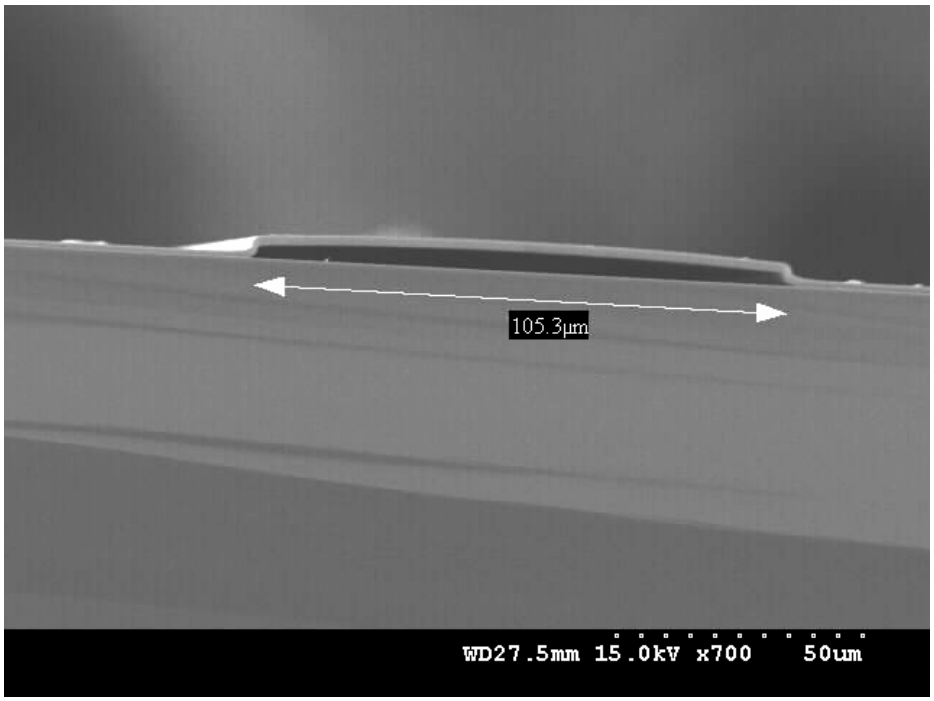

Figure 58: SEM image of a 105 µm wide air-channel fabricated from solution PNB- 8-S2 (90/10 butyl/cyclolacrylate norbornene copolymer with photo-initiator) and overcoated with 2 µm PECVD SiO_2. The PNB features were patterned photosensitive processing.

5.8 Summary of Conclusions on the Fabrication of Air-gaps With PNB Sacrificial Material

The previous sections have clearly demonstrated that PNB sacrificial material is capable of successfully forming air-gaps with several different structures, overcoat materials, and decomposition conditions. The SEM images and data presented are a small representation of the various structures fabricated and processes tested throughout this research. The processes described in sections 5.1 and 5.2 are those determined to produce optimum results. The fabrication of many other size structures led to the conclusions on the limitations with glass and polymer overcoat materials.

The one requirement for the use of PNB sacrificial material to form air-gaps, is all elements of the structure must withstand the 425^{o}C decomposition temperature of the PNB. Devices buried in the substrate and passivation layers may have a maximum temperature exposure limit. The 90/10 butyl/TES PNB processes well, has good adhesion to substrates, is compatible with several overcoat materials and metals, and decomposes to less than 1% residue However, the results from section 5.6 reveal that there is some freedom in the choice of PNB material, depending on the specific application. Some applications may tolerate a small amount of residue, and another polymer may be used, such as the butyl/cyclolacrylate polymer for photosensitivity.

SiO_2, SiN_x, and the polyimides Ultradel 7501, PI-2611, PI-2734, and PI-2540 are self-standing functional overcoat materials that work well in the fabrication process. Each of these materials has a T_g above the onset temperature for decomposition of PNB. However, the fabrication process can be altered (i.e. a thin layer of SiO_2) to allow the use of other overcoat materials in the final structures. The air-gaps fabricated with various overcoat materials can be dome shaped, rectangular, rigid, compliant, large, or small;

there is a wide variety in the shapes and sizes produced. Understanding the effects that properties of the overcoat material have on the process, allows control of the air-gaps produced. The process can therefore be altered to pinpoint the materials and processing for a specific application. For example, if large rectangular air-gaps are desired with a polyimide overcoat, a vent hole may be added to the design in order to produce the desired shape. The effective modulus of an overcoat material may also be altered by adding a specific amount of glass.

The results indicate that photosensitivity, elastic modulus, tensile strength, and backbone structure of the overcoat material do not cause an air-gap to collapse. The T_g of the material is the most important factor to consider. If the T_g is below the onset temperature for decomposition ($< 350^oC$), the material will likely fail. The CTE of the polymer also provides an indication in how much stress will build between adjacent layers during the decomposition process. Therefore, if a new overcoat material is available, the thermal properties (T_g, T_d, curing temperature) can indicate whether the material will successfully form air-gaps.

CHAPTER 6

POLYCARBONATE AIR-GAP FABRICATION AND RESULTS

The details and results of air-gap fabrication using polycarbonate (PC) sacrificial materials are discussed in this chapter. Polycarbonate sacrificial materials which decompose at modest temperatures enable the use of a wide range of dielectric materials and substrates with different thermal stabilities and properties. Silicon dioxide is one overcoat material that is potentially compatible with many various decomposition temperature sacrificial materials. SiO_2 is selected as an overcoat material with PC to allow a comparison between the polynorbornene and polycarbonate fabrication results. Other materials chosen as encapsulants with PC polymers cannot be used with polynorbornene sacrificial materials due to their thermal properties. These include a thermoplastic polymer: Avatrel 2000P Dielectric Polymer (Promerus LLC., Brecksville, OH); and two thermoset polymers: bisbenzocyclobutene (BCB) Cyclotene 3022-57 (Dow, Midland, MI), and LMB-7801 epoxy (Ciba-Geigy Chemical, New York) In addition, materials which fail under certain conditions as overcoats with PNB sacrificial polymer may potentially be used as overcoats with PC, including polyimide PI-2771, and polybenzoxazole (PBO). This chapter presents the process details and results using each of these overcoat materials to form air-gaps via PC sacrificial materials.

The fabrication process using polycarbonate sacrificial materials follows the same process sequence for air-gap fabrication with PNB, originally introduced in Figure 6 (Chapter 3, page 21). However, many of the processing steps and methods utilized with

PNB need to be re-optimized for a new set of materials with different chemical properties and thermal stability. The experimental details of the optimum fabrication process with non-photosensitive and photosensitive polycarbonates are presented in Section 6.1. Section 6.2 discusses SiO_2 as an overcoat material with non-photosensitive PC sacrificial materials. The results and discussion of air-gaps fabricated with non-photosensitive PC sacrificial materials encapsulated in polymer is included in Section 6.3. Section 6.4 then provides results and discussion of the fabrication of air-gaps using photosensitive versions of the polycarbonates. A discussion of the results of the PC process and how it compares and contrasts to the PNB process is provided in Section 6.5.

6.1 Experimental Details Relevant to Air-gap Fabrication With PC Sacrificial Material

6.1.1 Deposition of PC sacrificial materials

The air-gap fabrication with polycarbonates begins with deposition of the PC sacrificial material onto the substrate. Each of the four polycarbonate sacrificial materials are dry solid polymers: poly(ethylene carbonate) (PEC); poly(propylene carbonate) (PPC); poly(cyclohexene carbonate) (PCC); and poly(norbornene carbonate) (PNC). The dry polymers are dissolved into an organic solvent, and filtered through 0.2 µm Teflon syringe filter discs. Photosensitive sacrificial polycarbonate solutions also contain a photoacid generator (PAG), based as a percentage of the dry polymer weight only. The compositions of the various photosensitive and non-photosensitive PC solutions are shown in Table 21. The polycarbonate solutions were spin-coated onto 4" <100> silicon wafers using a CEE 100CB spin-coater. Spin-speed curves and processing details for each of these solutions are provided in Appendix B. The thickness of the resulting films ranges from 4 to 20 µm.

Table 21: Compositions of the various polycarbonate sacrificial polymer solutions.

Solution	**Polycarbonate/PAG**	**Solvent**	**Wt. polymer/ Wt. solution**
PEC-S1	PEC	N-methyl-2-pyrrolidone	18%
PPC-S1	PPC	N-methyl-2-pyrrolidone	19%
PPC-S2	PPC	γ-butyrolactone	12%
PPC-S3	PPC	γ-butyrolactone	20%
PCC-S1	PCC	Anisole	28%
PNC-S1	PNC	Cyclohexanone	40%
PPC-PS1	PPC/5 wt% DPI-TPFPB*	Anisole	12%
PPC-PS2	PPC/5 wt% DPI-TPFPB*	Anisole	20%
PCC-PS1	PCC/5 wt% DPI-TPFPB*	Anisole	20%

* See Figure 24, Page 88 for chemical structure

6.1.2 Patterning of non-photosensitive polycarbonate sacrificial materials

Non-photosensitive PC sacrificial polymers (no PAG in the solution) are patterned through the deposition and patterning of a hard mask, followed by dry etching of the polymer film. A metal hard mask (Ti, Al, Ti/Au, or Cr) was sputter deposited or electron-beam evaporated onto the polycarbonate film. The metal thicknesses are as follows: Ti = 700-2000Å; Al = 1000-2000Å; Ti/Au = 200Å/1000Å; and Cr = 700Å. The photolithography method to pattern the hard mask was identical to the polynorbornene sacrificial material process using positive photoresist (Shipley Microposit 1813 or 1827) and MF319 developer. Wet chemical etching is used to etch Ti (6:1 HF/H_2O), Au (40:4:1 $H_2O/KI/I_2$), and Cr (Mantek Co. CR-7S Chromium etchant). RIE etching is used to pattern Al (40 sccm BCl_3, 10 sccm Cl_2, 3 sccm $CHCl_3$, power = 125 W, pressure = 30

mTorr, T = 35°C). Aluminum PAN wet-etch can not be used to remove aluminum on PC because the polycarbonates are soluble in acetic acid, one component of the PAN etch. Once the metal is patterned, the exposed polycarbonate areas are etched using a Plasmatherm RIE. The RIE conditions are as follows: gas flow rates = 15 sccm Ar; 40 sccm O_2; power = 400 W; pressure = 250 mTorr; and T = 35°C. The average etch rates of the polycarbonates in this chemistry are 0.30 μm/min for PEC and PPC, 0.87 μm/min for PCC, and 0.54 μm/min for PNC. Fluorine-containing gases fluorinate the polycarbonate surface and deposit a "Teflon-like" material everywhere on the sample which cannot be removed. Therefore, fluorine gases must be removed from the etch chemistry. Following the removal of the exposed polycarbonate areas by RIE, the remaining hard mask is stripped by the same etchants used for metal patterning. The non-photosensitive polycarbonates were patterned into air-gaps using the mask containing microchannels 140 μm wide with 60 μm spaces, 70 μm wide with 30 μm spaces, 35 μm wide with 15 μm spaces and 15 μm wide with 5 μm spaces.

The two straight-chain aliphatic polycarbonates, PEC and PPC, have glass transition temperatures of 25°C and 40°C, respectively [97]. The low glass transition temperatures introduce problems with hard mask deposition, glass overcoat deposition, and feature formation. The metal hard mask films which are deposited on PEC and PPC crack when removed from either metal deposition tool. The low T_g of the PEC and PPC may induce the cracking when the PC softens or expand during the metal deposition. Since the PC is above its T_g during metal deposition, stress also builds from the large CTE difference between the polymer and metal as the sample cools from the metal deposition temperature. PCC and PNC have a much higher thermal stability with a T_g

over 110°C. Metal cracking is not present on PCC or PNC. In addition, PEC, PPC, and PCC are soluble in solvents including acetone and acetic acid, creating compatibility problems with the chemicals used for lithography and etching. Any remaining photoresist was removed by RIE. Figure 59 shows an optical microscope image of PEC features patterned with a sputter deposited Ti/Au hard mask, following RIE etching and hard mask removal. The cracks first seen in the metal after hard mask deposition have transferred into the top surface of the polymer material. However, the cracks do not affect the final air-gap structure when the sacrificial material is removed. Figures 60 (a) and (b) show the top-surface and a cross-section of a PPC film patterned with a Ti sputter-deposited hard mask, following RIE etching and hard mask removal. Although the cracks are present in these features, the cross-sectional image shown in Figure 60 (b) reveals that most of the top surface of the patterned polymer is flat and uniform. The rough side edges of the features result from undercutting of the polymer and flow of the polymer during processing. Figures 61 (a) and (b) contain SEM images of a similar PPC film patterned with a sputter deposited Cr hard mask. More cracks and wrinkles occured in the PPC features patterned with Cr due to the high stress properties of the metal. In addition, holes form in the features where cracks in the mask do not protect areas during the etch process. Therefore, Ti or Ti-Au is a better hard mask material for PEC or PPC. Figure 62 and Figure 63 show images of features patterned into a 6.8 μm thick PNC film patterned with an Al hard mask. Following mask removal, the PNC features wrinkle and delaminate due to poor adhesion. The mask pattern contains a regular pattern of straight lines. However, as seen in Figure 62, the pattern becomes irregular when the features lose adhesion with the substrate, and eventually re-stick in another location. This occurs

during a rinsing step following RIE etching. PCC does not have any of the adhesion problems seen with PNC, nor does it crack as with PEC and PPC.

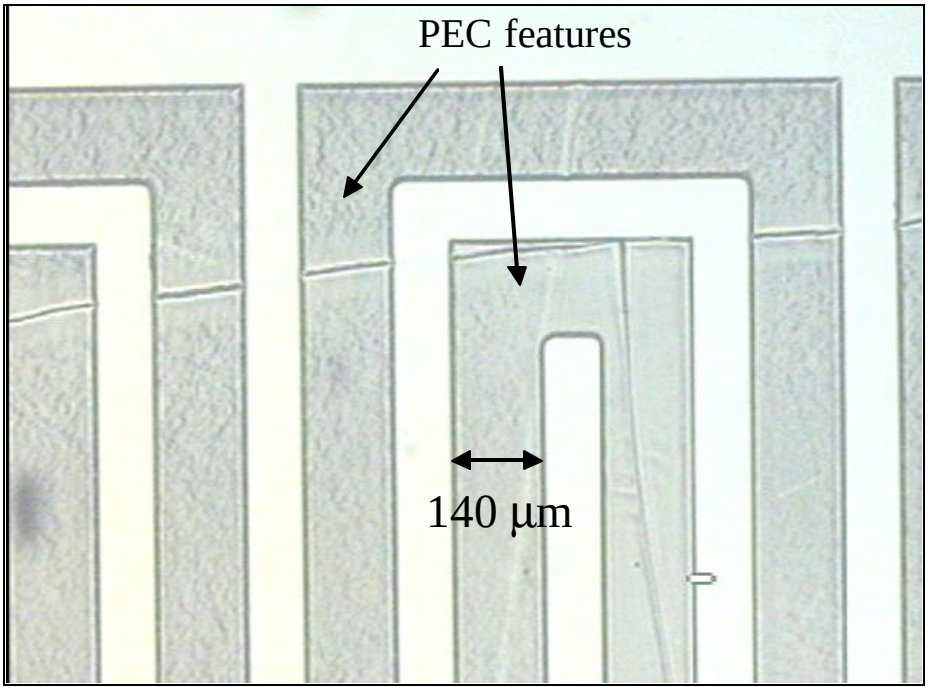

Figure 59: Optical microscope image showing the top surface of 140 μm wide PEC features following RIE etching and Ti/Au hard mask removal.

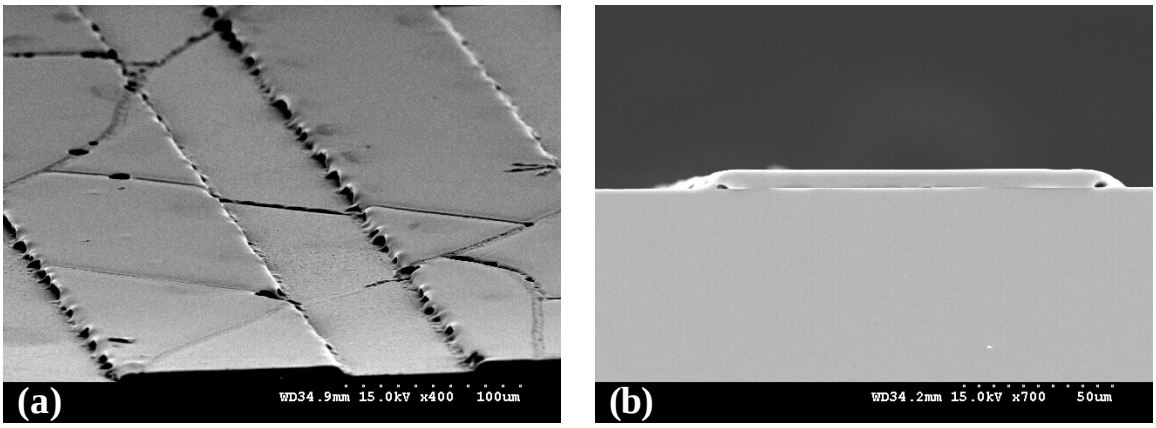

Figure 60: (a) Top-surface and (b) cross-sectional SEM images of patterns formed in a 5.4 µm thick PPC sacrificial layer, following RIE etching and Ti hard mask removal.

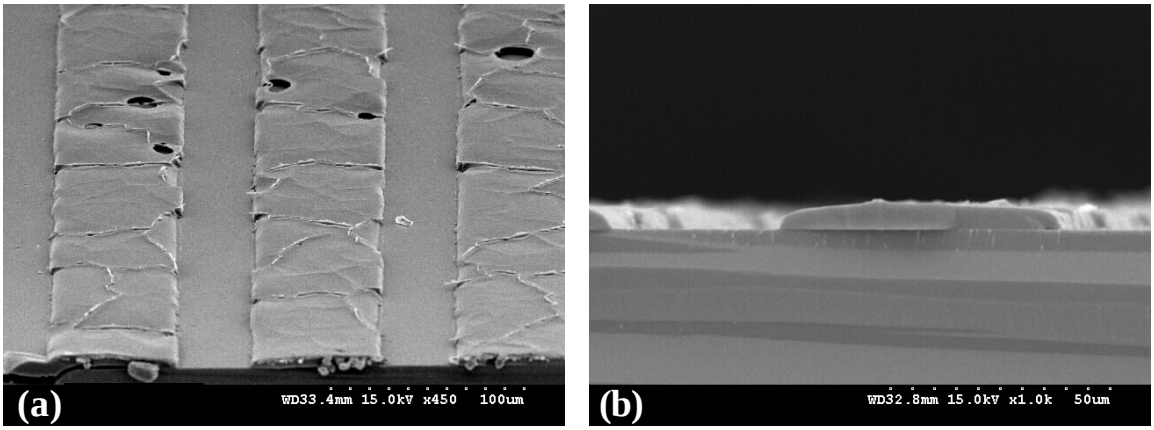

Figure 61: (a) Top-surface and (b) cross-sectional SEM images of patterns formed in a 5.3 µm thick PPC sacrificial layer, following RIE etching and Cr hard mask removal.

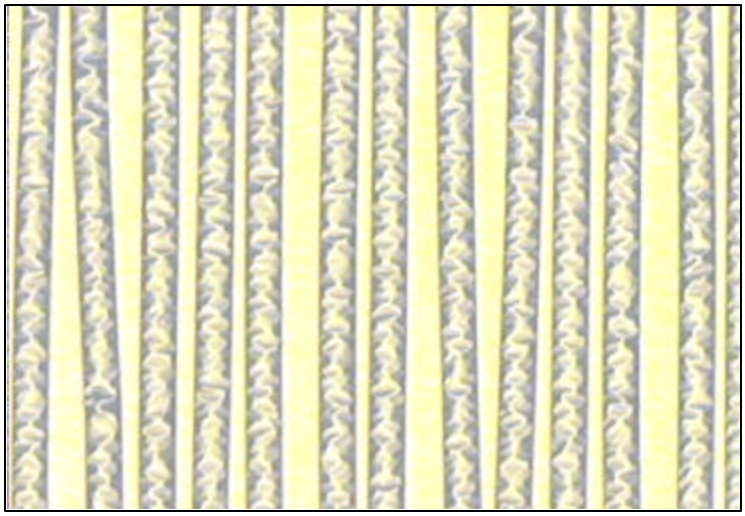

Figure 62: Optical microscope image of 70 µm wide PNC features following RIE etching and Al hard mask removal. Poor adhesion results in an irregular pattern and wrinkling of the features.

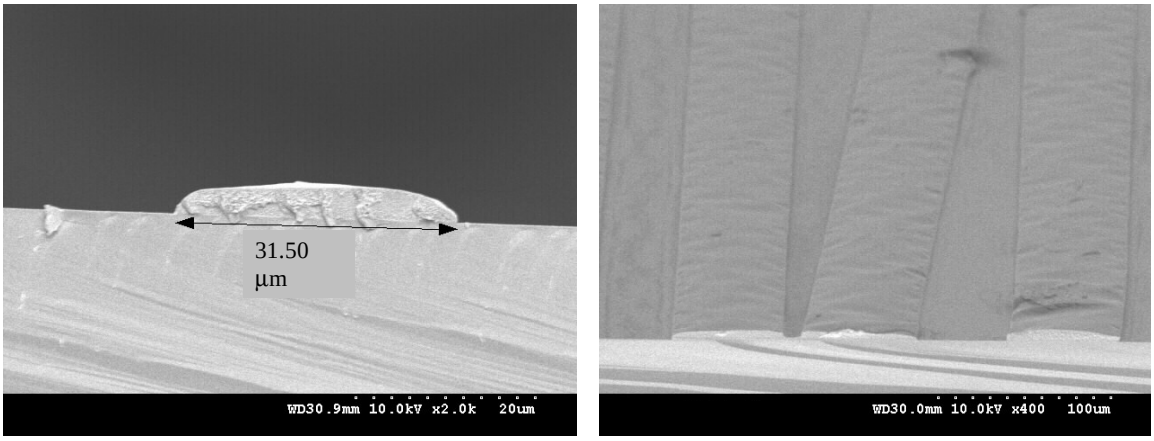

Figure 63: (a) Cross-sectional and (b) top-surface SEM images of features patterned into a 6.8 µm thick PNC film following RIE etching and Al hard mask removal.

6.1.3 Patterning of photosensitive polycarbonate sacrificial materials

Chapter 4 described modification of the decomposition temperature of the sacrificial polycarbonates through addition of a photoacid generator (PAG) to the polymer. In all cases, the photo-initiated acid catalyzed (PIAD) decomposition occurs at a lower temperature than the thermal-initiated acid catalyzed decomposition (TIAD). Therefore, selective decomposition of areas across a sample may be possible by exposing only the areas to be removed and baking at a temperature between the PIAD and the TIAD temperatures. The fabrication sequence to form air-gaps using a photosensitive material is shown in Figure 64. The process flow is similar to the non-photosensitive method, except the sacrificial layer patterning is done through direct exposure and bake-development instead of a hard mask and RIE.

The ability to photopattern the PCs is demonstrated using PPC. A typical process for patterning photosensitive PPC includes five steps. First, the photosensitive PC solution was spin-coated onto silicon and soft-baked on a hotplate at 110°C for 10 min. Next, the film was UV irradiated through a clear-field quartz mask with a typical dose of 1 J/cm2 (240 nm). The exposure was followed by dry bake-developing at 110°C on a hotplate for 1 to 10 min. At 110°C, the UV generated acid induces the decomposition of the PPC and the exposed areas were removed. Following development, a "descum" in an oxygen plasma for 30 s is performed to remove any remaining residual material on the surface. Figure 65 shows a pattern obtained using the photosensitive PPC solution PPC-PS1. The colored lines in the figure are the areas in which the polycarbonate sacrificial material remains. The corners of the features are slightly rounded in comparison to the pattern formed using RIE etching, shown in Figure 59.

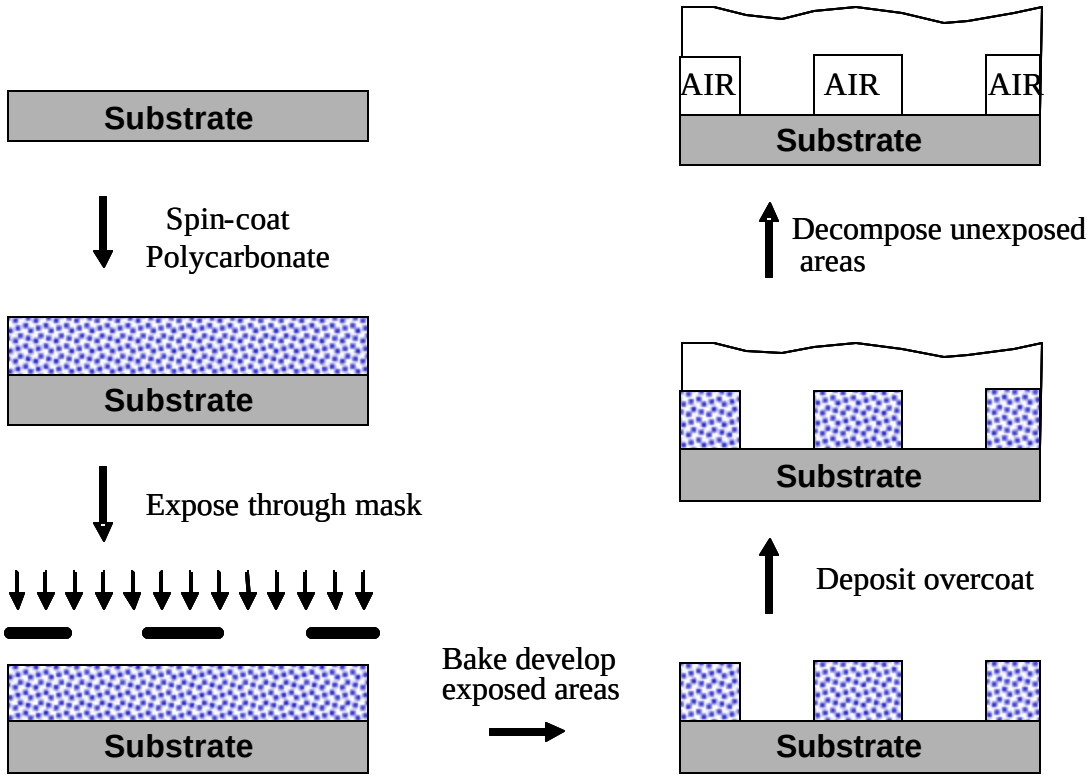

Figure 64: Fabrication process flow for the fabrication of air-gaps using photosensitive polycarbonate sacrificial materials.

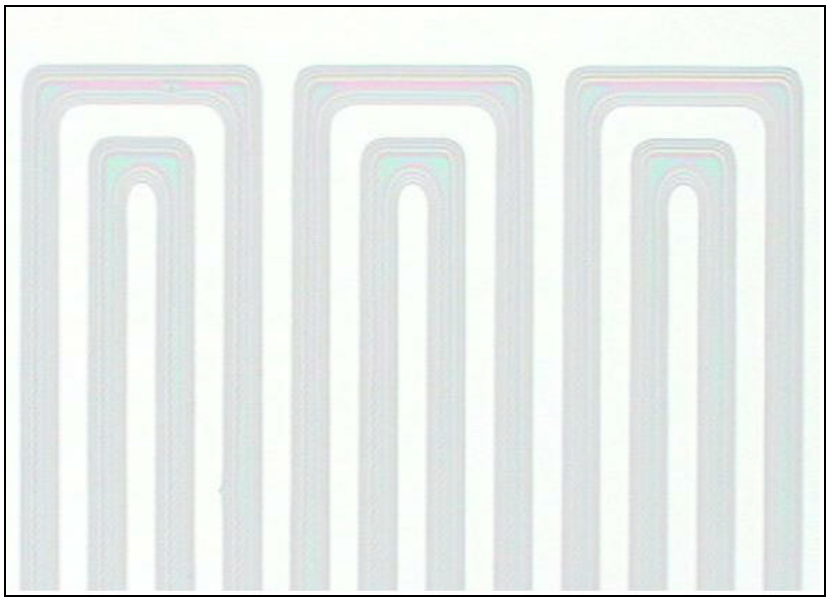

Figure 65: Optical microscope image of a pattern formed from a solution of 12 wt% PPC in anisole with 5 wt% DPI-TPFPB based on dry polymer. Mask dimensions are lines = 70 µm, and spaces = 35 µm.

6.1.4 Deposition of encapsulating material and decomposition

A complete list of all encapsulating materials used in this research was provided previously as Table 3 (Chapter 3, Section 3.3, page 36). The encapsulating materials selected for use with the PC sacrificial materials were chosen based on their solvent compatibility with the PC sacrificial material, and their thermal properties, including curing temperature and T_g. A specific PC with an appropriate decomposition temperature was then chosen based on the encapsulating material properties. Three types of encapsulating materials are included: an inorganic glass, a thermoset polymer, and a thermoplastic polymer. In addition, a few of the encapsulating materials which are not completely successful in producing air-gaps using PNB were tried with the PC's. The overcoat materials include: PECVD deposited SiO_2; Avatrel 2000P Dielectric Polymer; LMB-7081 Epoxy; Cyclotene bis-benzocyclobutene; Pyralin polyimide PI-2771; and polybenzoxazole (PBO) CRC-8650.

The encapsulating material is deposited following either photo-patterning of the PC, or RIE etching and hard mask removal. Portions of one large sample for each PC were used to fabricate air-gaps with the various overcoat materials. Therefore, the resulting shapes of the air-gaps with different overcoat materials can be directly compared to one another. SiO_2 is deposited using a Plasmatherm PECVD at 200^{o}C, using the deposition parameters in Table 15 (Chapter 5, page 105). Spin-speed curves and processing details for the polymeric overcoat materials are provided in Appendix C. Following encapsulation of the patterned PCs, decomposition was carried out in a Lindberg horizontal tube furnace in either air or nitrogen. The decomposition conditions varied with each sacrificial and overcoat material combination, and are listed in Table 22.

Table 22: Decomposition conditions for various polycarbonate/encapsulant combinations.

Program	**Sacrificial Material**	**Encapsulating Material**	**Decomposition Conditions**
1	PEC	SiO_2	5^oC/min to 230^oC, hold for 2 hours
2	PPC	SiO_2	5^oC/min to 280^oC, hold for 2 hours
3	PCC or PNC	SiO_2	5^oC/min to 250^oC, no hold 1^oC/min to 320^oC, hold 1 hour
4	PEC	Avatrel	3^oC/min to 200^oC, hold 1 hour 1^oC/min to 230^oC, hold 2 hours
5	PPC	Cyclotene BCB	10^oC/min to 250^oC, hold 1 hour 1^oC/min to 285^oC, hold 2 hours
6	PEC	LMB 7081 Epoxy	10^oC/min to 165^oC, hold 1 hour 1^oC/min to 230^oC, hold 1 hour in AIR
7	PPC	PI-2771	5^oC/min to 250^oC, hold 1 hour 1^oC/min to 350^oC, hold 1 hour
8	PCC	PBO CRC-8650	3^oC/min to 170^oC, hold 1 hour 3^oC/min to 250^oC, hold 0.5 hour 1^oC/min to 280^oC, hold 0.5 hour
9	Photosensitive PPC	SiO_2	1^oC/min to 170^oC, hold 1 hour
10	Photosensitive PCC	SiO_2	1^oC/min to 180^oC, hold 1 hour
11	Photosensitive PPC	Avatrel 2000P	1^oC/min to 180^oC, hold 1 hour

6.2 Air-gap Fabrication With Non-photosensitive PC and SiO_2 Encapsulation

6.2.1 Results of air-gaps fabricated with PC encapsulated in SiO2

This section presents the results of microchannels fabricated specifically with non-photosensitive PC sacrificial materials encapsulated in an inorganic glass. A demonstration with each of the four polycarbonate sacrificial materials was performed using SiO_2 as the encapsulating material. Section 5.3, discussing air-gaps fabricated with PNB encapsulated by SiO_2, indicated that the limiting factors using SiO_2 are the temperature for glass deposition, step-coverage of the glass over the sacrificial materi features, and the length of the unsupported glass spanning the cavity. These limits were also regarded as applicable to the PC sacrificial material process, and it was speculated that a set of conditions within these limits should not cause the process to fail. Therefore, the same feature sizes and patterns were used with the PC sacrificial polymers. Figure 66 shows cross-sectional SEM images of microchannels fabricated from 4.8 μm thick sacrificial PEC patterned using mask features (a) 35 μm wide and (b) 140 μm wide. The features are encapsulated by 1 μm thick silicon dioxide. The resulting microchannels in Figure 66 (a) are approximately 5 μm in height and 25 μm in width. The decrease in width of the microchannel from the dimensions on the mask is a result of undercutting during the RIE etching of the PC. In addition, the RIE process is performed at 35°C, which is above the glass transition temperature of PEC. Curved sidewalls result from undercutting and some flow of the material during the etching and PECVD deposition processes. Wrinkling of the oxide is present on all size features fabricated with PEC, as shown on the top-surface of the channel in Figure 66 (b). Figure 59 shows that the PEC sacrificial material is smooth on the top surface, with a few cracks, following RIE etching

and metal hard mask removal. The wrinkling appears after the PECVD process step as a result of intrinsic stress in the glass from CTE mismatch between the oxide and polymer upon cooling from the glass deposition temperature of 200°C. Deposition of the oxide occurs above the glass transition temperature of the polymer, which also results in some deformation of the sacrificial material shape during the oxide deposition. In Figure 66 (b), the SiO_2 appears to be sagging into the center of the channel. This shape is only seen in the large channels, and is similar to the results for PNB. As the width of the channel increases, the glass can no longer maintain a rigid span across the channel. However, the microchannels appear clean with no visible residue, indicating that the decomposition products are able to permeate the overcoat material and successfully form an air-channel. The results for PPC are identical to those for PEC sacrificial material.

SiO_2 was also used as an encapsulating material to provide a demonstration with non-photosensitive PCC and PNC. Figures 67 (a) to (d) show SEM images of four different sized air-channels fabricated from a 8 μm thick film of PCC overcoated with SiO_2. Figures 68 (a) and (b) are SEM images of air-channels fabricated with a 6.8 μm thick film of PNC overcoated with SiO_2. The SiO_2 overcoat thickness in both figures is 6 μm. The SiO_2 overcoat appears slightly wrinkled immediately following deposition on both PCC and PNC, although not as severe as on PEC and PPC. Similar to PEC and PPC, the resulting air-channels are about 10 μm narrower in width than the original mask pattern. The wavy channels fabricated from PNC shown in Figure 68 (b) result from the irregular pattern formed due to poor adhesion after etching the PNC. However, the air-channels form in the exact pattern of the PNC material before glass deposition. With both PNC and PCC, the air-channels appear clean with no cracks or ruptures in the

overcoat material, indicating the decomposition occurs in the channels and the products are able to permeate out through the SiO_2. The decomposition temperatures of PNC and PCC are approximately the same. However, due to the adhesion and processing problems seen with the PNC material, PCC was selected as the better alternative for a 300°C decomposition temperature material.

6.2.2 Discussion of SiO2 encapsulated air-gaps

The results of air-channels formed using SiO_2 as an overcoat demonstrate the ability to form air-gaps with each of the four PC materials at modest temperatures between 230°C and 320°C. Similar to structures formed with PNB sacrificial material, the use of SiO_2 is limited to feature sizes that can be achieved with available lithography techniques, and also allow good step-coverage of the encapsulating glass. The maximum feature width is dependent on the length of the unsupported span across the cavity. As the width increases, the SiO_2 may begin to collapse into the channel, as seen in Figure 66 (b). The same width constraint is also observed for air-gaps fabricated with PNB sacrificial material encapsulated in SiO_2.

The lower decomposition temperature of the polycarbonates introduces limitations and processing issues with SiO_2 overcoat in addition to those seen with PNB sacrificial materials. These include the temperature for glass deposition, the roughness of the SiO_2 surfaces, and the resulting shape of the air-gaps. Each of these factors is a result of the thermal properties of the PC materials. The glass transition temperature for each of the PC materials is lower than the glass deposition temperature of 200°C. Therefore, the polymer features easily distort during the glass deposition. Figure 66 through Figure 68 show that the PC sacrificial polymers produce air-gap cross-sections with rounded

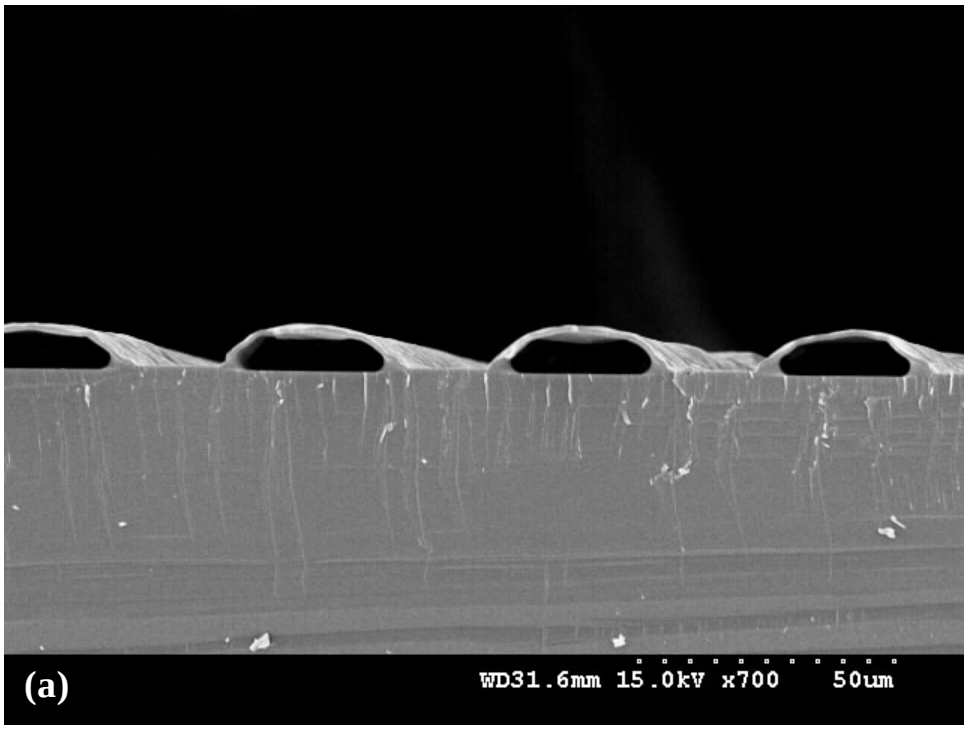

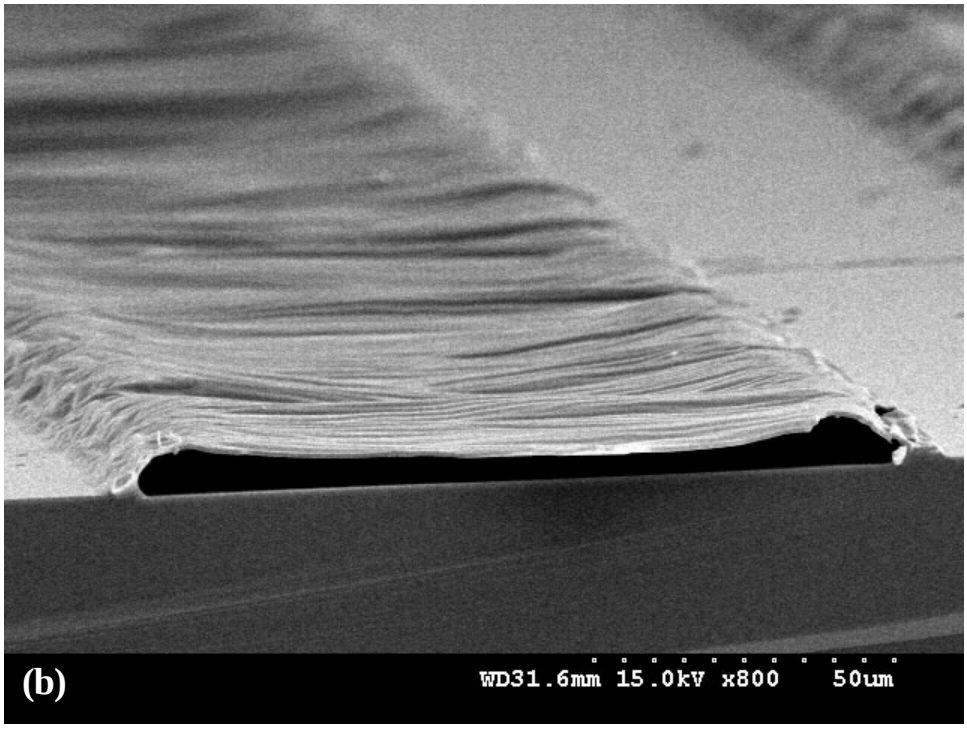

Figure 66: SEM images of (a) 25 μm wide and (b) 130 μm wide air-channels fabricated from a 4.8 μm thick PEC sacrificial layer and overcoated with PECVD SiO_2 deposited at 200°C. The original mask dimensions are 35 μm and 140 μm.

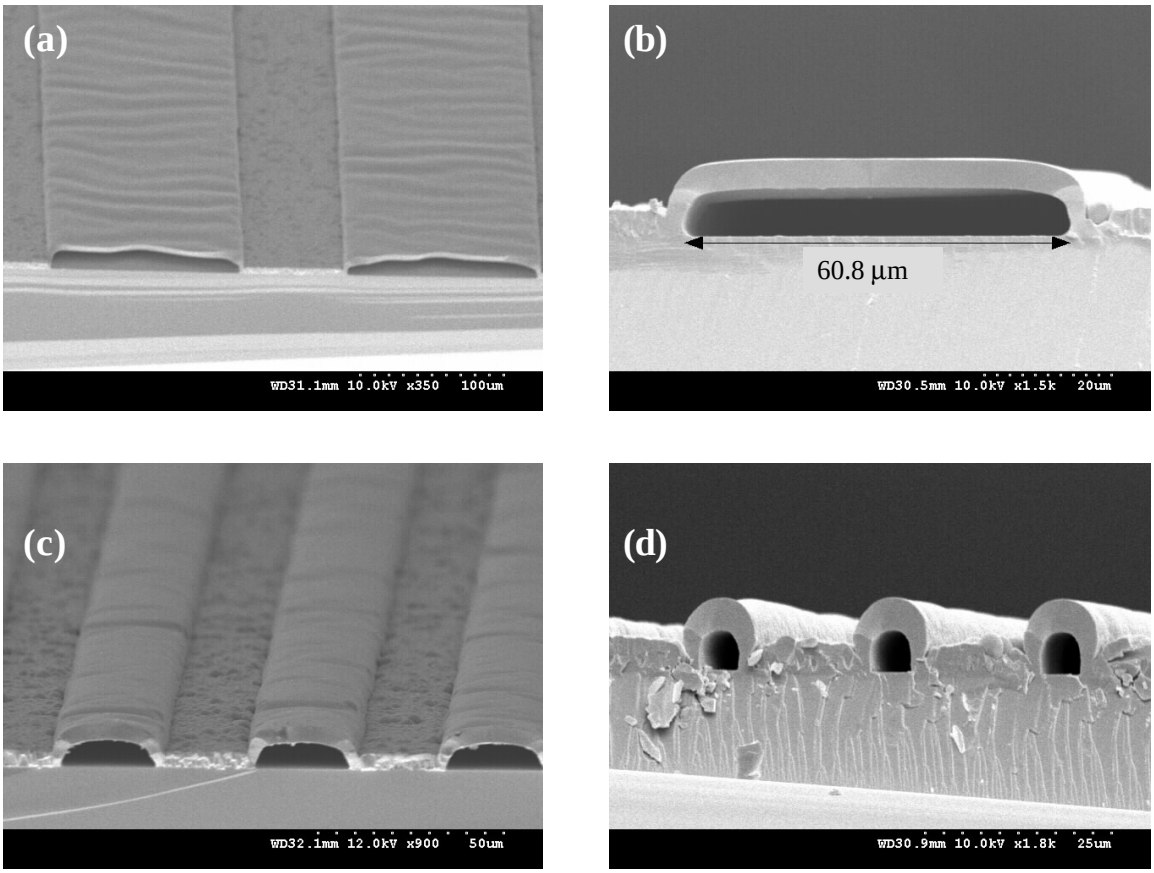

Figure 67: SEM images of air-channels fabricated from an 8.0 µm thick PCC overcoated with PECVD SiO_2 deposited at 200 ^{o}C. The features on the mask had width dimensions of: (a) 140 µm; (b) 70 µm; (c) 35 µm; and (d) 15 µm. The resulting channels are about 10 µm less in width from undercutting during RIE etching.

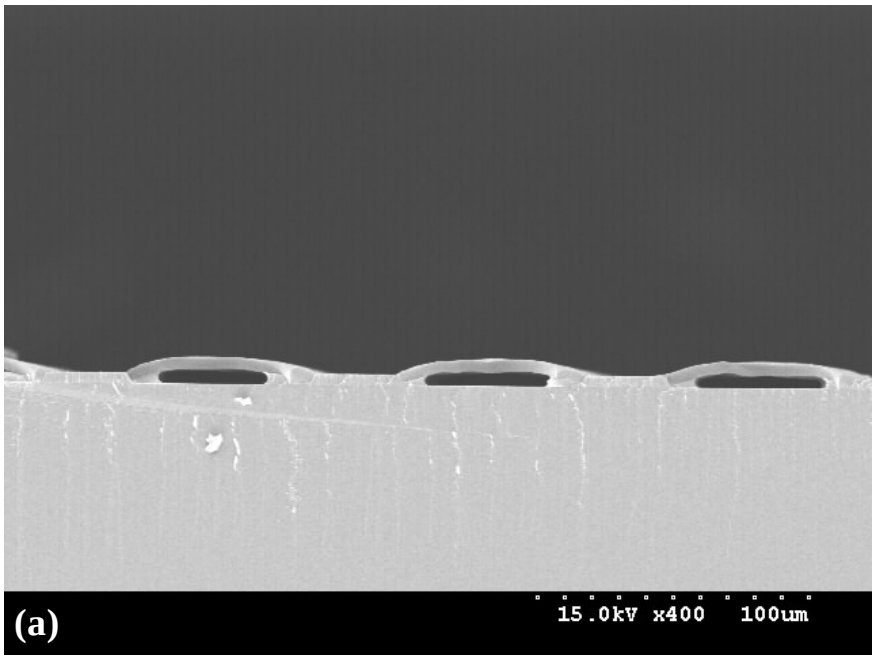

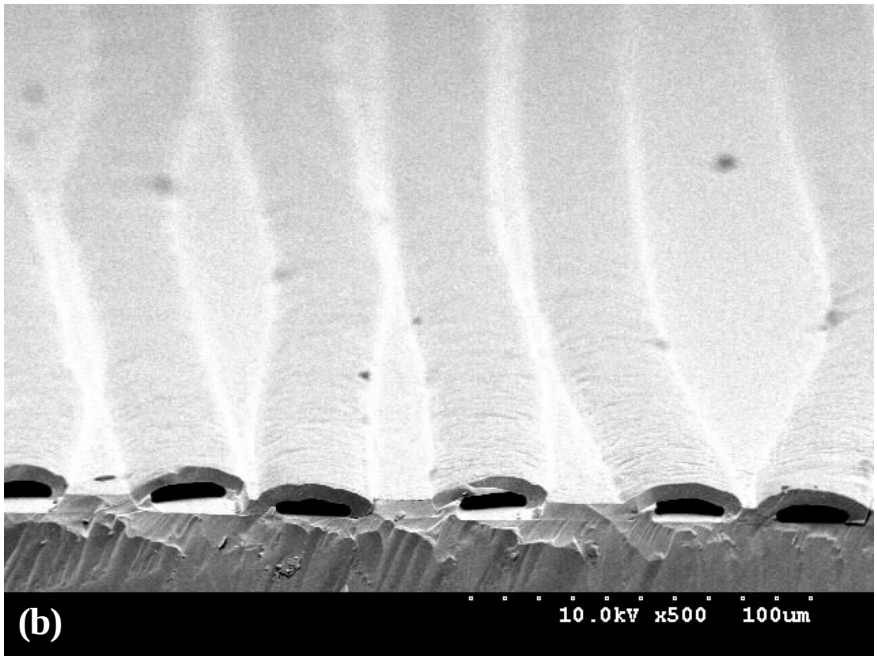

Figure 68: SEM images of air-channels fabricated from a 6.8 μm thick PNC sacrificial layer and overcoated with PECVD SiO_2 deposited at 200°C. The features on the mask had width dimensions of: (a) 70 μm; and (b) 35 μm. The resulting dimensions are smaller from undercutting during RIE etching.

corners. In addition, the air-channels fabricated with PEC and PPC do not maintain a flat top surface, but rather have irregular cross-sectional shapes with non-uniformities. The SiO_2 is a conformal coating material which is thermally stable and maintains rigidity during decomposition of the sacrificial polymer. The final shape of the channel is determined during SiO_2 deposition, and should not be affected by decomposition of the PC. The corner and sidewall shape is a result from both undercutting of the polymer during RIE etching, and flow of the polymer during glass deposition. The irregular shapes fabricated from PEC and PPC result from some decomposition of the sacrificial material during the initial portion of the glass deposition process. The dynamic TGA data presented in Chapter 4 indicated the onset for decomposition of PEC and PPC at a heating rate of 10^oC/min occurred at 203^oC and 234^oC, respectively. The onset temperature for PPC shifts to 177^oC/min at a heating rate of 0.5^oC/min, and PEC would begin to decompose at even a lower temperature. Therefore, at 200^oC, both of these polymers will begin to decompose. At 200^oC, the PCC and PNC are above their T_g, but have not reached the onset temperature for decomposition. Some softening of the polymer may occur as the SiO_2 is deposited, but the top surface maintains its flat shape.

The thermal properties of the PC sacrificial materials also contribute to the roughness and wrinkling of the encapsulating SiO_2. The wrinkling is present only on the top surface of the fabricated air-channels, shown in Figure 66 through Figure 68. In addition, the roughness of the SiO_2 is more prevalent on the channels fabricated with PEC, shown in Figure 66. The CTE of a polymer is greater at temperatures above the T_g in comparison to temperatures below the T_g [98]. Since the glass is deposited above the T_g of each PC, a large change in volume occurs as the sample cools from above the T_g,

passes through the T_g, and continues to cool to room temperature. The CTE difference between the polymer and the glass creates stress in the SiO_2 layer, which causes the wrinkling seen in the glass once it is released from the substrate. The effect is increased for PEC and PPC, since the greater CTE value dominates over a larger temperature range.

The thermal properties of the sacrificial PCs thus impose limitations on shape and processing temperatures for air-gaps created via PC encapsulated in SiO_2. The maximum temperature for glass deposition without distortion of the air-gap shape is limited by the onset decomposition temperature of the PC material. PECVD SiO_2 can be deposited as low as room temperature to help alleviate glass roughness and shape nonuniformity. However, the quality of PECVD SiO_2 films decreases with deposition temperature. The final application of the air-gaps dictates the materials and processing conditions to be utilized in the fabrication process. In circumstances where the glass is present to form a channel or behave as a structural barrier, the quality may be traded for smoother geometry. If a high quality glass is required, the final application must be tolerant of the resulting geometry deformation. However, in either case, the use of the PCs presents the ability to form air-gaps in an inorganic glass at a lower decomposition temperature.

6.3 Air-gap Fabrication Using Non-Photosensitive PC and Polymer Encapsulation

6.3.1 Results of air-gaps fabricated with PC encapsulated in thermoplastic polymers

The fabrication of microchannels using non-photosensitive PC sacrificial materials with several polymeric overcoat materials is also investigated. The thermal properties of many potential polymer overcoats render them unsuitable for the higher temperature PNB sacrificial material process. These include both thermoplastic and thermoset overcoat materials with various thermal and mechanical properties. One

thermoplastic overcoat polymer is Avatrel 2000P dielectric polymer. Avatrel 2000P is a photosensitive polynorbornene-based polymer with a cure temperature of 200°C and a T_g >250°C. Avatrel has a low dielectric constant and has applications in interconnect and packaging as an interlevel dielectric or an optical material. The applications further restrict the maximum temperature exposure to approximately 250°C. PEC is chosen as the sacrificial material with Avatrel in order to decompose the sacrificial material at a temperature lower than the T_g of the overcoat material. Ideally, the Avatrel will fully cure at 200°C before significant loss of the sacrificial material occurs. Figure 69 (a) is an SEM image of 5 μm tall and 25 μm wide microchannels overcoated with 11.6 μm thick Avatrel 2000P. The cross-sectional air-gap shape includes a flat top surface and rounded corners, similar to the cross-sectional shape of the PEC in Figure 60. The bottom air-gap corners (between the substrate and Avatrel sidewall) do show a slight difference from the shape of the unencapsulated PEC. The rounded corners of the air-gaps may result from slight flow of the Avatrel under the undercut edge of the PEC film during the overcoat polymer deposition. A flat overcoat top surface results from the excellent planarizibility of the Avatrel encapsulating polymer. Figure 69 (b) shows that the Avatrel 2000P overcoat material collapses into the channel for 140 μm wide features. The resulting air-channel in Figure 69 (b) is similar to the 140 μm air-channels fabricated with PNB and the overcoat polyimides PI-2771 and PI-2555. The PEC undergoes glass transition and passes through a liquid form during decomposition. The large surface tension force between the overcoat and the decomposing PC keeps the two materials in contact throughout the decomposition, and pulls the overcoat into the channel. In addition, Figure 69 shows air-gaps in Avatrel have a significantly different cross sectional shape

than those with SiO_2 overcoat in Figure 60. The resulting air-channels in Figure 69 (a) represent the same shape as the patterned PEC before encapsulation, shown in Figure 60 (b). However, the air-gaps formed with the two overcoat samples are derived from the same patterned PC film. The result indicates that deformation in the oxide-encapsulated microchannels (Figure 66) is taking place during the PECVD deposition process.

6.3.2 Results of air-gaps fabricated with PC encapsulated by thermoset polymers

Microchannels have been fabricated using PC overcoated with two thermoset polymers: LMB-7081 epoxy (Ciba Geigy) and Cyclotene 3022-57 BCB (Dow). Both of these materials typically are used for board-level applications, due to their properties and low curing temperatures. LMB-7081 epoxy requires a 1 hour cure at 165^{o}C in air, and BCB 3022-57 requires a one hour cure at 250^{o}C in nitrogen. Based on the required cure temperatures, PEC is chosen as the sacrificial material to use with LMB-7081 epoxy, and PPC is chosen as the sacrificial polymer with BCB 3022-57. The processing conditions of these overcoat polymers are included in Appendix C. The PC choices should allow the overcoat material to reach full cure with minimal loss of the sacrificial material. Figure 71 is an SEM image of a 140 μm wide air-channel formed in LMB-7081 epoxy from a 1.5 μm thick film of PEC sacrificial material. The small aspect ratio (height:width) of this feature makes it difficult to observe the cleanliness of the channel in the figure. However, an increase in magnification shows the air-channel to be free of residue following the decomposition in air. Figure 70 shows SEM images of microchannels encapsulated in BCB and fabricated from a 5.3 μm thick PPC sacrificial layer patterned into microchannels (a) 140 μm wide and (b) 70 μm wide. The BCB planarizes the PPC very well, resulting in a flat-top surface, similar to the Avatrel overcoated air-channels.

The rounded corners are seen in the PPC patterned film following removal of the titanium hard mask as a result of undercut during the RIE etching. The resulting cross-sectional shape of the channels in Figure 70 is identical to the shape of patterned PPC before the overcoat is applied, shown in Figure 60. The air-gaps produced with both the thermoset overcoat polymers are free from residual material. In addition, the air-channels formed in LMB 7081 epoxy and BCB demonstrate the decomposition can be performed in either nitrogen or air environments.

6.3.3 Results of air-gaps fabricated with PC encapsulated in higher-cure temperature polymers

Select polymers investigated as overcoat materials for air-gaps fabricated from PNB sacrificial material were also used with PC sacrificial materials. These include polyimide PI-2771, and polybenzoxazole (PBO). The thermal stabilities of both PBO and PI-2771 are not entirely compatible with the 425^{o}C decomposition temperature required for PNB sacrificial material. However, the cure temperature of these materials is above the onset of decomposition for all four PC sacrificial materials. Polyimide PI-2771 requires 1 hour at 350^{o}C and PBO requires a maximum temperature of at 320^{o}C in order to reach a fully cured state. Again, the ideal air-gap fabrication process uses a sacrificial material with a decomposition temperature that allows the overcoat to fully cure before decomposition begins. However, if most of the curing reaction can be performed before decomposition begins, the film may develop thermal and mechanical properties similar to the fully cured film by the onset of decomposition. The negative photosensitivity of PI-2771 enables it as a potential overcoat polymer for use with PC sacrificial materials. The photoexposure and cross-linking of the polyimide occurs at

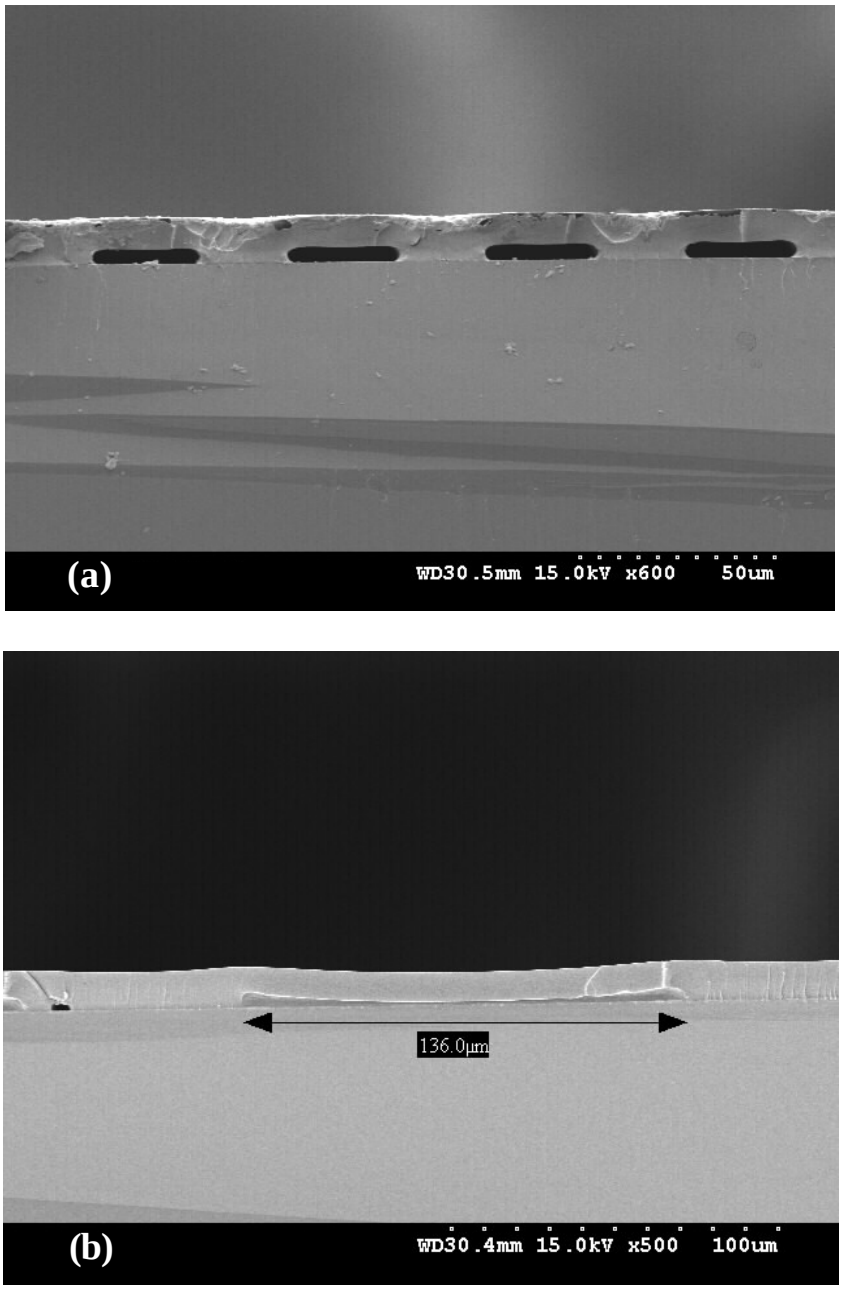

Figure 69: SEM images of air-channels fabricated from a 4.9 µm thick PEC sacrificial layer overcoated with Avatrel 2000P dielectric polymer. The width of the air-channels on the mask are: (a) 35 µm; and (b) 140 µm wide. The overcoat collapsed into the channel in (b).

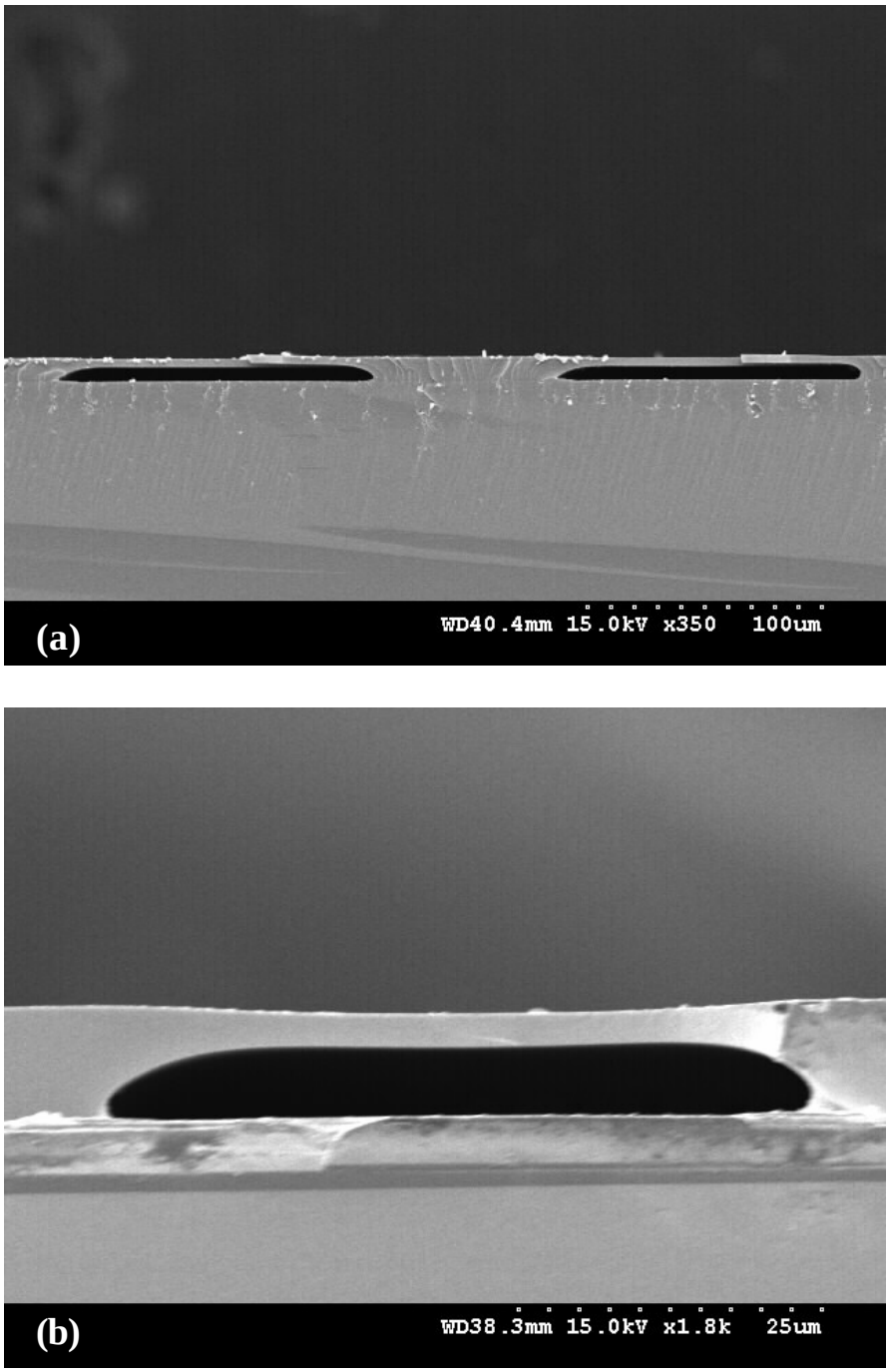

Figure 70: SEM images of air-channels fabricated from a 5.3 μm thick PPC sacrificial layer and overcoated with Cyclotene 3022-57 BCB. Air-channels were fabricated from PPC patterned into channels using a mask with features (a) 140 μm wide and (b) 70 μm wide.

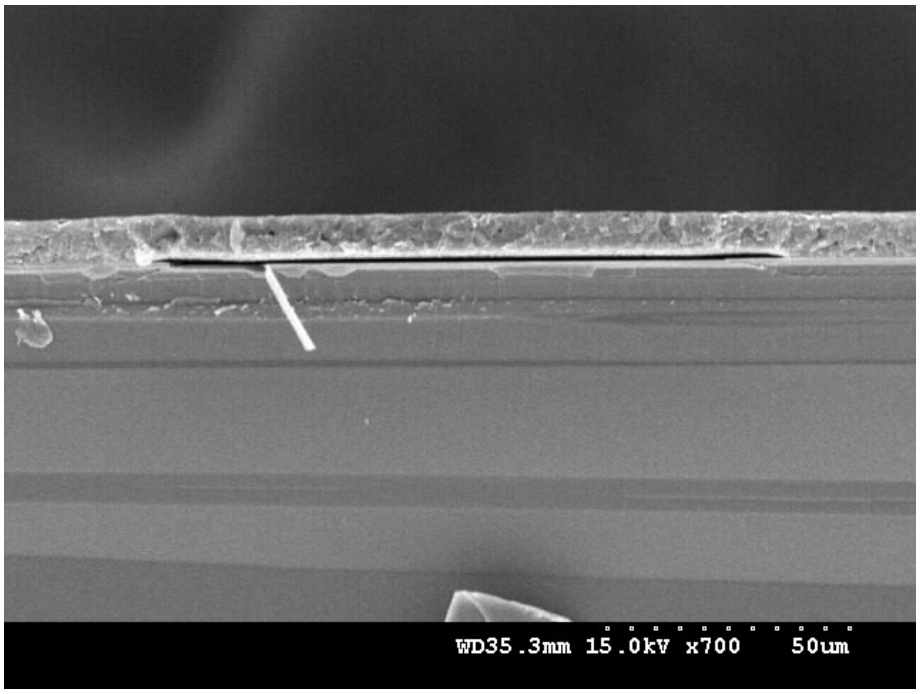

Figure 71: SEM image of a 140 μm wide microchannel fabricated from a 1.5 μm thick layer of PEC sacrificial material and overcoated with LMB-7081 epoxy.

room temperature; and may allow the polymer to exist in a fairly rigid form before the final cure. PBO is a potential material for use with PC sacrificial materials based on the manufacturer's recommended cure schedule. The recommended temperature cycle for curing in nitrogen is: a 3°C/min ramp to 150°C, hold 30 min., a 3°C/min to 250°C, hold 20 min, and a 3°C/min to 320°C, hold 30 min. The first two ramp and hold steps are below the decomposition temperature of PCC. Therefore, a substantial portion of the cure reaction is expected to occur even before the final curing step at 320°C. The overcoat polymer may be able to retain shape of the air-channels as the final cure is performed.

PCC sacrificial material is selected as the PC to use with the two polymeric overcoat materials. Figures 72 (a) and (b), and Figure 73 are SEM images of the resulting

structures formed from 5.3 μm tall PCC features overcoated with 10 μm thick PI-2771. Figures 72 (a) and (b) show two images of features formed from 35 μm wide PCC patterns. Two different resulting structures are observed to form from the same dimension PPC patterns. In Figure 72 (a), the overcoat polymer has completely filled into the space where the air-channel should be present. Only a small hole or air-gap remains where the corner or side-wall of one of the air-channels should exist. The image in Figure 72 (b) shows that some irregular shaped air-channels have formed. The measured height of these air-channels is less than the original 5.3 μm thick PPC film. Also, the air-channels do not form with a straight edge across the top of the channel, but rather the PI-2771 sags into the channel in the center of the air-gap. Figure 73 shows the resulting structure formed from the decomposition of 140 μm wide PCC channels encapsulated in PI-2771. The cross-section of the larger dimension channels reveals similar results to the features shown in Figure 72 (a). However, small bubbles or holes are observed on the top surface of the PI-2771 following decomposition of the sacrificial material. The variation in the structures in Figure 72 and Figure 73 is a result of solvent incompatibility between the PCC sacrificial material and the solvent in the PI-2771, n-methyl-pyrrolidone (NMP). The sacrificial material is highly soluble in the organic solvent of the overcoat material. As the overcoat polymer is dispensed and spin-coated onto the PCC patterned features, the features begin to dissolve. The PI-2771 is puddle dispensed into the center of the sample and remains there for several seconds until the spin process begins. The features in Figure 72 (a) and Figure 73 are obtained from the center of the PCC sample, or the dispensing location the overcoat polymer. Most of the PCC is removed by the overcoat solvent before the decomposition ever begins. A

profilometer scan of the sample surface reveals a similar profile both before and after the cure/decomposition heat treatment. The small holes and bubbles are formed from small areas of PCC which are not completely removed by the solvent. The features in Figure 72 (b) are fabricated from PCC features closer to the sample edge. The solvent exposure of the PCC features at the edge of the sample is minimal. A loss in thickness, or height of the air-channel occurs; yet the features are not completely removed by the solvent.

Figure 74 and Figure 75 are SEM images of features formed from 5.3 μm thick PCC overcoated with 8.8 μm thick PBO CRC-8650. The mask dimensions used to form the features in Figure 74 and Figure 75 are 140 μm and 70μm, respectively. Several large bubbles form in the overcoat material, which reach several hundreds of microns in height and interconnect many individual air-channels. As shown in Figure 75, successful air-gaps form only where a large intact bubble is interconnected to the feature. A complex combination of the material properties of PBO, the feature dimensions, and the temperature profile for decomposition contribute to the feature formation. The dynamic TGA at a heating rate of 1^{o}C/min shows that PCC decomposition reaction reaches 50% conversion around 270^{o}C. Therefore, in the air-gap fabrication process most of the PCC has already decomposed during the 20 min. hold at 250^{o}C, and the ramp up to the final curing temperature of 320^{o}C. Throughout the decomposition reaction, the PBO is not yet in the fully cured state. The mechanical properties of the uncured film are typically lower than the fully cured film due to residual solvent and remaining photo-active compounds [54]. In addition, the large bubble formation clearly indicates a pressure force acting on the overcoat material from inside the air-channel. The bubbles must form in areas with weak adhesion to the substrate because they delaminate the entire film from the substrate

to interconnect several features. The large pressure force acting on the inside surface of the air-channel prevents the PBO from being pulled into the air-channel by the decomposing PPC. No successful air-gaps form in the areas of the sample with no bubble or a large ruptured bubble. The pressure due to the volume of the PCC and high conversion of the decomposition reaction combined with the easily plastically deformed uncured PBO film produces the resulting structure. The large elongation to break value of PBO compared to each of the other overcoat polymers allows it to form a large bubble without rupture. However, the pressure must remain in the air-channel during the curing reaction to allow the PBO to solidify into position.

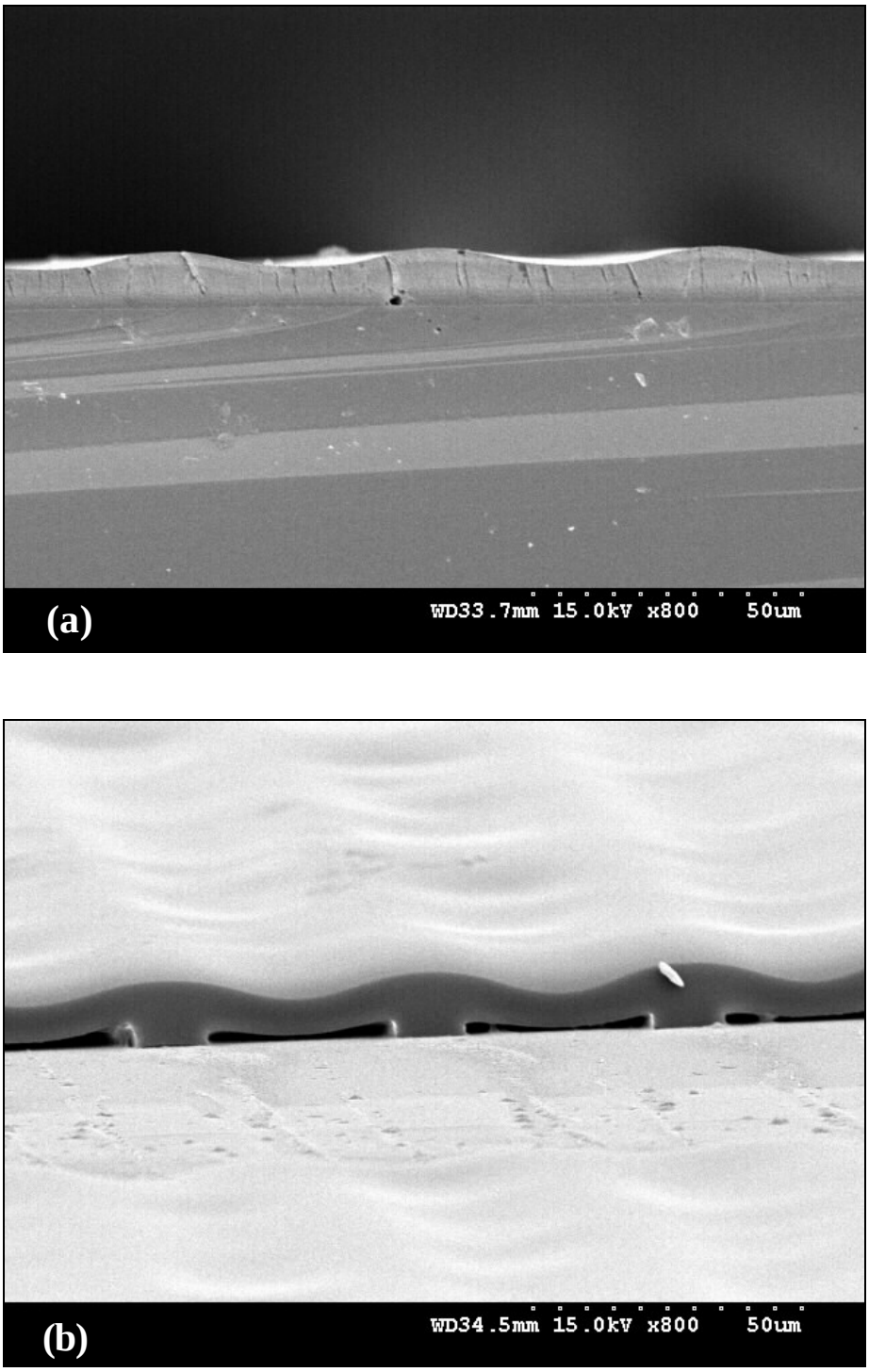

Figure 72: SEM images showing the resulting structures from the decomposition of 5.3 µm thick PCC patterned into 35 µm wide air-channels and overcoated with polyimide PI-2771.

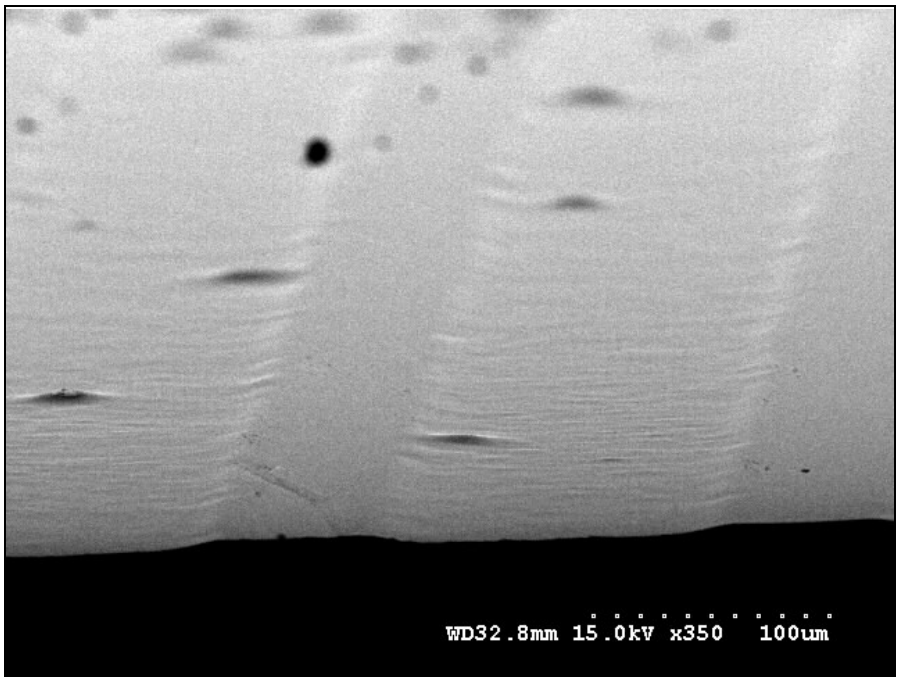

Figure 73: SEM image showing the resulting structures from the decomposition of 5.3 μm thick PCC patterned into 140 μm wide air-channels and overcoated with polyimide PI-2771.

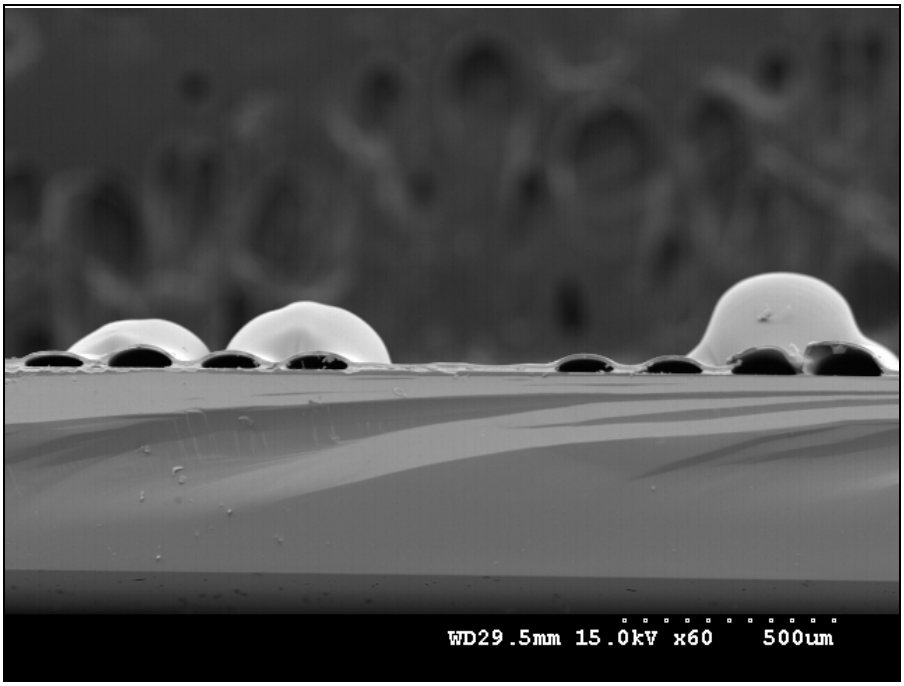

Figure 74: Cross-sectional SEM image showing the resulting structures from the decomposition of 5.3 μm thick PCC patterned into 140 μm wide air-channels and overcoated with PBO CRC-8250.

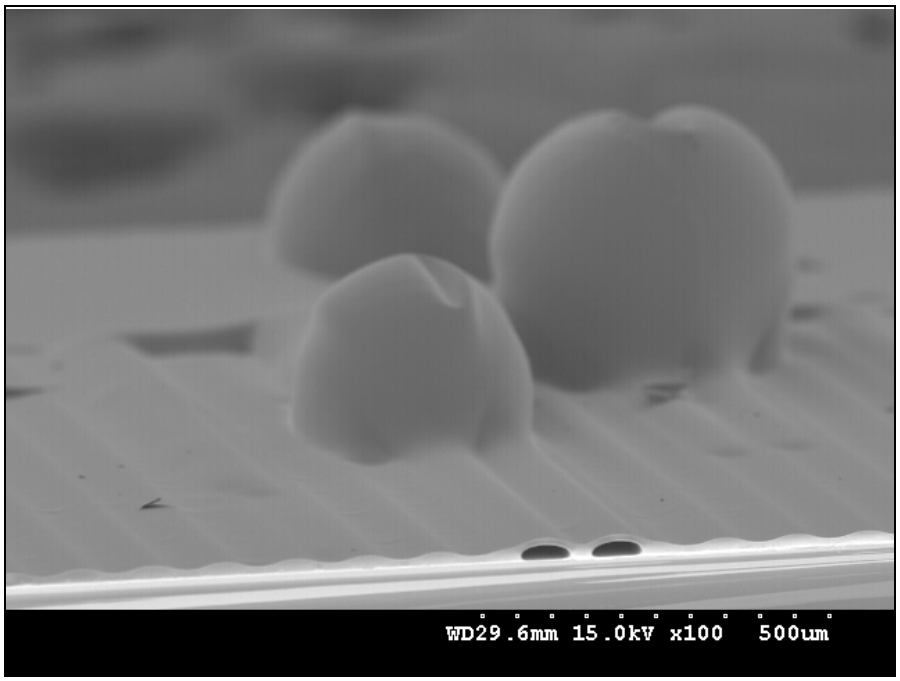

Figure 75: SEM image showing the resulting structures from the decomposition of 5.3 μm thick PCC patterned into 70 μm wide air-channels and overcoated with PBO CRC-8650.

6.3.4 Discussion of air-gaps fabricated from non-photosensitive PC encapsulated in polymer

Microchannel formation in the four polymeric overcoat materials used in this study demonstrates that the aliphatic polycarbonates PEC and PPC can be used as thermally decomposable sacrificial materials for lower-temperature air-gap formation in both air and nitrogen atmospheres. The encapsulating materials demonstrated each differ in their thermal and mechanical properties. Avatrel 2000P, LMB 7081 epoxy, and BCB all have the thermal stability and rigidity to span the microchannels, and sufficient permeability to allow air-cavity formation. A key similarity between these materials is that these materials can be deposited or cured at or below 250^{o}C, allowing cure of the

overcoat before polycarbonate decomposition. The materials which require a curing temperature above the decomposition temperature of the PC do not work as well in the process. PI-2771 illustrates another important concern in selecting an overcoat material is the compatibility of the solvent system of the sacrificial polymer and the overcoat polymer. PBO shows potential as an overcoat, but would require precise optimization of the feature dimensions and the cure/decomposition temperature program in order to produce reliable results.

The TGA data in Chapter 4 revealed that PPC decomposes cleanly in both air and nitrogen environments. Due to the chemical similarity, the decomposition of PEC is assumed to also decompose cleanly in both environments. The formation of air-channels overcoated with LMB-7081, which requires an air environment during the decomposition, demonstrates that PEC can be used for the fabrication of air-gaps in both air and nitrogen atmospheres.

6.4 Air-gaps Fabricated With Photosensitive Polycarbonates

Air-gap fabrication was also performed using photosensitive versions of the polycarbonates. As described in Section 6.1, the polymer and solvent composition of the photosensitive PC solutions are identical to the non-photosensitive versions, except the photosensitive solutions contain a PAG. Chapter 4 demonstrated that the PAG can be photolytically or thermally activated, resulting in acid catalyzation of the PC decomposition, and a decrease in the decomposition temperature from the thermal T_d of the PC. The TGA data of the photosensitive polycarbonates indicates a possible

extension of the formation of air-cavities to temperatures as low as 110°C. However, verification is needed that the photopatterned PC decomposes cleanly at lower temperature without significant differences in the processing or resulting air-gaps.

SiO_2 and Avatrel 2000P dielectric polymer were used as encapsulating materials with photosensitive PPC and PCC in order to compare the results to the non-photosensitive methodology. The photosensitive PPC and PCC are photo-patterned following the process description in Section 6.1, and the final decomposition is performed in a Lindberg tube furnace at 180°C for 1 hour under nitrogen. Figure 76 and Figure 77 show SEM images of 70 µm wide air-channels fabricated from 5 µm thick photo-patterned PPC (solution PPC-PS2) overcoated with 7800 Å PECVD SiO_2 deposited at 100°C, and 8 µm Avatrel 2000P dielectric polymer, respectively. The mask pattern used to fabricate the air-gaps in Figure 76 and Figure 77 contains 100 µm wide channel features. Significant loss in feature width occurs from the photopatterning process. The acid produced upon photoexposure may migrate into the unexposed areas of the polymer film during the bake develop step, resulting in a loss of material from the edges of the features. In addition, the photopatterning of PPC results in features with sloped or curved sidewalls. The shape of the air-gap overcoated with Avatrel in Figure 77 is the shape of the PPC feature after photo-patterning. The bake develop step is performed at 100°C, well over the T_g of the PPC. Therefore, flow of the PPC occurs during the bake develop and results in the sloped sidewalls of the feature. The rounded corners of the air-gap in Figure 76 result from flow of the PPC above its T_g both during the bake develop, and during the PECVD glass deposition at 100°C. The combination of photopatterned PPC sacrificial material and the overcoats (Avatrel or SiO_2) are

compatible with each other (no solvent interference or structural deformation), and demonstrate favorable results from air-channel fabrication. Both overcoat materials form clean air-channels free from visible debris. The results indicate complete decomposition of the PPC occurs at lower temperature, and the overcoats are permeable to volatiles from both the polymer and the PAG. Figure 78 is an SEM image of two air-channels fabricated from 8 μm thick photopatterned PCC overcoated with 5 μm PECVD SiO_2. The air-channels formed with photopatterned PCC also are smaller in width than the mask feature dimensions. Sloped sidewalls also occur with PCC as a result of the photopatterning process. The SiO_2 encapsulating the air-gaps in Figure 78 is wrinkled upon removal from the PECVD. Again, the wrinkling is a result of stress formed in the glass from the difference in CTE between the PCC patterns and the SiO_2 as the sample cools from the glass deposition temperature. The air-gaps formed with photosensitive PCC sacrificial material also appear clean with no visible residue from either the polymer or the PAG following decomposition. Avatrel dielectric polymer is not suitable as an overcoat material with PCC sacrificial material due to solvent incompatibility between the Avatrel solvent, anisole, and the PCC sacrificial polymer.

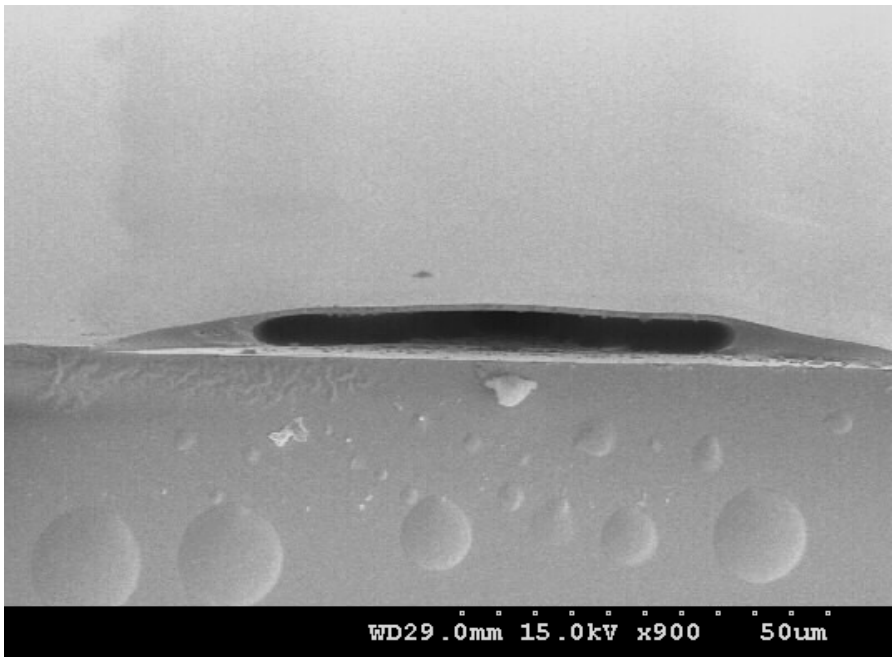

Figure 76: Micrograph of a 70 μm wide air-channel fabricated from 5 μm photo-patterned PPC overcoated with 7800 Å PECVD SiO_2 deposited at 100°C.

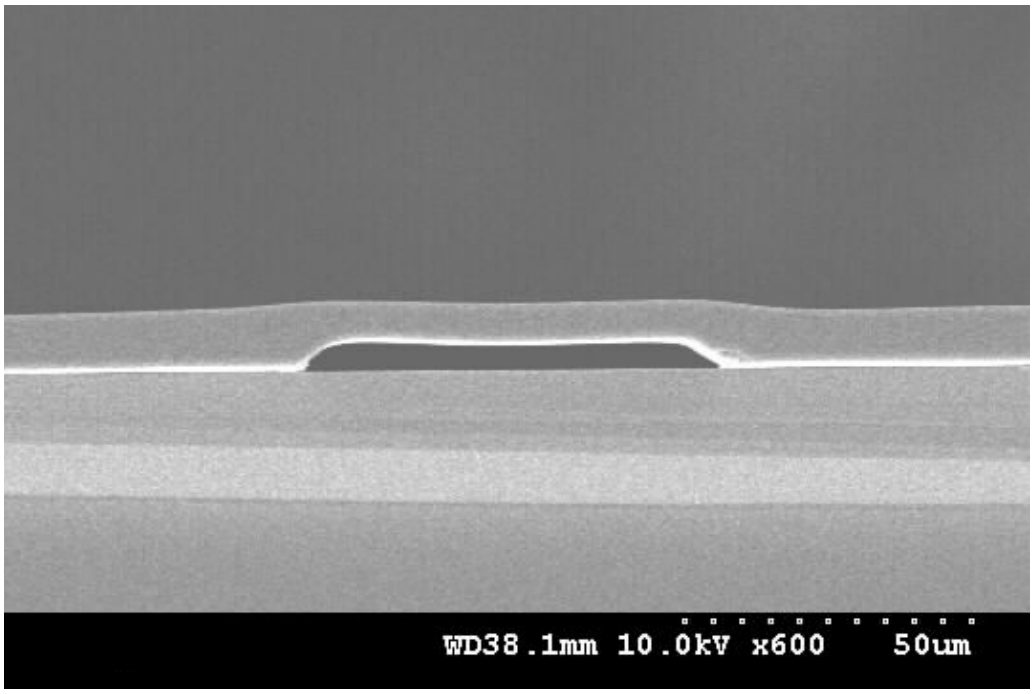

Figure 77: SEM image of a 70 μm wide air-channel fabricated using a 5.45 μm thick photo-patterned PPC encapsulated in 8 μm Avatrel 2000P dielectric polymer.

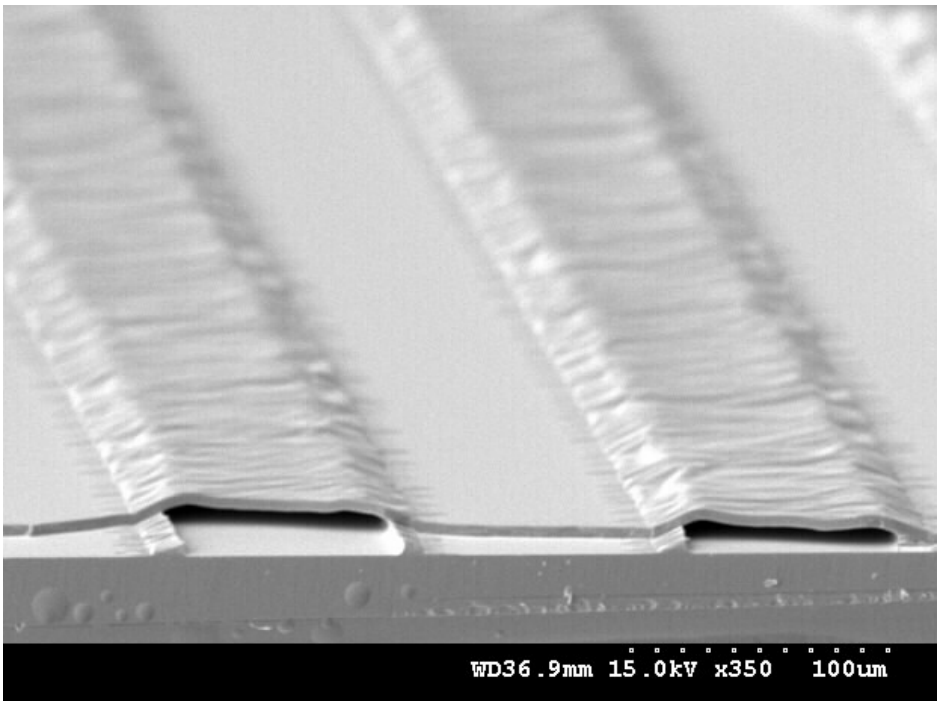

Figure 78: SEM micrograph showing two air-channels fabricated with photosensitive PCC sacrificial material and overcoated with PECVD SiO_2.

6.5 Discussion of Air-gaps Fabricated Using Polycarbonate Sacrificial Materials

The results of air-gaps fabricated with polycarbonate sacrificial materials demonstrate that PC sacrificial materials lead to the formation of air-cavities at modest temperatures, in a variety of encapsulating materials with different properties. Several acceptable combinations of sacrificial materials and overcoat materials have been found, but the approach is not universal. The PC sacrificial materials are much more sensitive to processing conditions and require optimization for each specific application.

PC sacrificial materials do possess certain advantages over PNB sacrificial materials. The most important advantage of PC sacrificial materials is the lower decomposition temperature in comparison to PNB sacrificial material. The lower

decomposition temperature greatly expands the number and type of overcoat materials and substrates that may be used in the air-gap fabrication process. In addition to the lower temperature, the decomposition temperature of the PC can be further modified through the choice of the PC and the inclusion of photoactive components. Temperature modification creates the ability to tailor the fabrication process for each different application and encapsulating material. The objective of selecting a decomposition temperature is the ability to completely cure or deposit the overcoat material below the onset temperature for decomposition of the PC. Another advantage of the PC process is the processing itself. The photosensitive process requires no metals, harsh acid etches, or large quantities of solvents. The process therefore may be more cost effective and more environmentally benign. PC sacrificial materials also may be decomposed in both nitrogen and air environments. The TGA data in Chapter 4, and the fabrication results using LMB 7081 epoxy as an overcoat material demonstrate the successful decomposition of PC in an oxygen containing environment. The decomposition of PNB is limited to oxygen depleted environments in order to prevent char of the polymer and the formation of large amounts of residue.

PC sacrificial materials are, however, subject to many of the limitations established for PNB sacrificial materials. A similar set of limitations are found for the use of SiO_2 as an encapsulant on PC and PNB sacrificial materials. The feature dimensions are limited by lithography and patterning techniques, the ability to deposit SiO_2 with adequate step coverage, and the ability of the overcoat to span the air-cavity without collapsing. In addition, the maximum temperature for glass deposition is restricted by the thermal properties of both PNB and PC sacrificial materials. The

maximum glass deposition temperature for PNB is limited by the CTE of the polymer. At a temperature above approximately 230^{o}C, the glass cracks from stress developed between the glass and the PNB as the sample cools from the deposition temperature. The glass deposited onto PC sacrificial materials wrinkles due to the CTE difference between PC and SiO_2, but remains intact without crack formation. However, the maximum temperature is controlled by the T_g and T_d of the polycarbonate material. Glass deposition above the T_g results in enhanced stress in the encapsulating SiO_2. Deposition above the T_d results in severe distortion of the air-gap shape due to material loss during the glass deposition cycle. In general, PNB sacrificial material is superior to PC sacrificial materials for the fabrication of air-gap structures with SiO_2. Although the PNB process is also constrained by the glass deposition temperature, the PNB is much more thermally stable at the glass deposition temperature, resulting in less deformed features and less stress in the glass. Similar to PNB, the limitations on polymer encapsulated air-gaps vary from one overcoat to another. In some cases the overcoat material softens or loses mechanical strength at the decomposition temperature and sags or flows into the cavity, or permanently deforms (e.g. expands) from pressure build-up inside the cavity.

The PC air-gap fabrication process is also restricted by factors not applicable to the PNB processing. The main disadvantage to the PC process is the thermal properties of the sacrificial materials severely constrain the possible feature shapes and dimensions. The low T_g of PEC and PPC create difficulty with processing. One of the issues is cracking of the hard mask used for PC patterning, and the transfer of the cracks into the top surface of the PC film. Although the PC material is sacrificial and eventually removed, the cracks may not be tolerated in circumstances which require planarity of the

top surface or severe critical dimension control. The deposition technique, deposition rate of the metal, and softbake time of the film do not correct the problem. In addition, many other mask materials cannot be used due to solvent compatibility. For example, a thick photoresist film may not be used because the solvent removal of the photoresist also removes the PC features. Another critical issue with PC processing is the adhesion of the polymer to Si and other substrate materials. The PNB inherently contains TES groups to chemically react with and promote adhesion to substrate materials. The adhesion of PC to a substrate is by physical means only. Therefore, any physical force applied to the film (such as a water rinse) can easily cause delamination of the features from the substrate. In addition, if a liquid has an affinity for the substrate material, it easily may creep underneath the film from an edge or a defect and move along the PC/substrate interface, causing severe delamination of the PC features. PNC sacrificial material displays the poorest adhesion of the polycarbonate sacrificial materials, and a method to achieve successful non-photosensitive patterning of the material has not been established.

The dimensional control and shape of PC patterns, whether formed by hard mask and dry etching or photopatterning, is another critical issue with PC sacrificial materials. Both techniques result in features with narrower dimensions than the original mask pattern. Therefore, structures which require extreme dimensional control may not be possible using polycarbonate sacrificial materials. The features on the mask may be increased in size to account for the loss of material. However, if many different size structures exist across a single mask, the processing may become extremely complex. It also may be possible to optimize the plasma etch program to result in little or no undercut and the formation of straight sidewalls, but is beyond the scope of this work. In addition,

rectangular features are not possible from photopatterning due to the lithographic contrast of the PC materials and flow of the sacrificial polymer during the bake development step. Therefore the types and shapes of structures produced using PC sacrificial materials has some limitations. Another critical issue with PC sacrificial materials is the solubility of the sacrificial polymer in the overcoat polymer solvent. For example, Avatrel 2000P, can be used with PPC sacrificial material but not with PCC sacrificial material. The Avatrel is spin-coated in the solvent anisole, which is also a good solvent for PCC sacrificial material.

Thus, complex materials processing and design rules for PC sacrificial materials have evolved. In order to accommodate a wider variety of overcoat polymers, the patterned sacrificial material should be resistant to *any* solvent used to cast the overcoat polymer (where the solvent may lead to the dissolution of the sacrificial material). Also, the polymer overcoat must provide excellent mechanical strength to span the eventual air-gap during and after fabrication without sagging or expanding. This is especially critical at the highest temperature used in the process (e.g. the decomposition temperature of the sacrificial material) because the overcoat polymer may be near or above its glass transition temperature and the sacrificial polymer may exist in liquid form. Also, the application of the air-channels must be tolerant to the shape and sizes of the air-gaps produced.

CHAPTER 7

IN-SITU DECOMPOSITION OF POLYNORBORNENE IN AIR-GAPS

This chapter includes the results and discussion of investigations into the decomposition of polynorbornene sacrificial material while encapsulated in a dielectric material. While the decomposition of unencapsulated polynorbornene has previously been investigated [69] and discussed in Chapter 4, it cannot be assumed that the decomposition of the material will occur similarly in the encapsulated state. The air-gap fabrication results with PNB sacrificial material reveal a pressure build up inside a completely closed cavity during the decomposition process. The pressure may significantly affect the reaction rate of the overall decomposition and the remaining residual material. Thermogravimetric analysis (TGA), x-ray photoelectron spectroscopy (XPS) and goniometry are used to study the thermal decomposition of PNB sacrificial material in two environments: (1) encapsulated in a dielectric material and (2) open to an ambient N_2 environment. Section 7.1 of this chapter describes the experimental details relevant to the studies in this chapter. Section 7.2 discusses the results of TGA experiments on unencapsulated PNB and PNB encapsulated in polyimide. Section 7.3 uses the TGA data to investigate the kinetic parameters of the decomposition reaction in both environments. Analysis of the residual surfaces using XPS and goniometry to detect differences between encapsulated and unencapsulated decomposition of PNB is included in Section 7.4. Discussion of the encapsulated decomposition process and optimization using the kinetic parameters is discussed in Section 7.5

7.1 Experimental Details Relevant to Chapter 7

7.1.1 TGA sample preparation and procedure

The copolymer of 90/10 butyl/TES PNB (PNB-2, Table 2, page 30) was used to study the decomposition of PNB in an encapsulated state and open to a nitrogen-purged environment. This PNB composition was used extensively for air-gap fabrication, discussed in Chapter 5, based on its desirable decomposition and processing characteristics. The sacrificial polymer solution used in the unencapsulated and encapsulated TGA experiments is PNB-2-S1 (30.8 wt% 90/10 Butyl/TES PNB in mesitylene). The procedure for the preparation of samples and operation of the TGA was briefly described in Chapter 3. Specific details of sample preparation for this set of studies are as follows:

1. The weight of an empty Al TGA sample pan is determined using the balance mechanism on the TGA;
2. The PNB solution is dispensed dropwise into the pan via a syringe, followed by a softbake for 5 min. on a 120^{o}C hotplate. A total of 1-5 drops is used for each sample to attain a uncured PNB weight of 2-20 mg;
3. The PNB is cured in a nitrogen-purged Lindberg horizontal tube furnace ramped 5^{o}C/min to 275^{o}C, and held for 1 hour;
4. The weight of cured PNB is measured using the TGA balance mechanism;
5. Select samples are encapsulated by syringe dispensing Pyralin PI-2611 polyimide (DuPont) on top of the PNB sacrificial material.

Encapsulation with Polyimide PI-2611 was performed by dispensing the polyimide solution drop-wise into the sample pan, following each dispense with a

hotplate softbake at 100°C for 20 min. to remove the solvent. A total of 5 drops were added to each sample, and the syringe needle was used to spread the polymer so that the entire drop of sacrificial material was completely covered. The cure of PI-2611 was performed in the TGA by ramping 5°C/min to 350°C and holding for 1 hour. The cure was immediately followed by the dynamic or isothermal TGA program conditions for decomposition of the sacrificial material.

Dynamic and isothermal TGA experiments were performed on both the encapsulated and unencapsulated PNB samples, and PI-2611 alone. Table 23 through Table 25 show the polymer masses added to each TGA pan, and the respective TGA programs. The sample numbers in the tables can be interpreted as follows: S = sacrificial PNB; P = polyimide; D* = dynamic TGA at *°C/min, or CD* = polyimide cure followed by dynamic TGA at *°C/min; CI# = polyimide cure followed by isothermal TGA at #°C. For example, SP-CD3-1 is sacrificial PNB encapsulated with PI-2611, cured in the TGA, and followed by a 3°C/min constant ramp to 530°C. Dynamic TGA was also performed on unencapsulated PNB sacrificial material in various coated sample pans to determine if specific metals provide a catalytic effect to the decomposition reaction. These include a standard Al pan, a Pt pan, a SiO_2-coated Al pan, and a Cu-coated Al pan (samples S-D10-1, SPt-D10-1, SOx-D10-1, and S-DCu-D10-1).

Comparison of the decomposition of PNB in the encapsulated and unencapsulated state requires subtraction of the encapsulant mass from each data point in the encapsulated PNB sample results. The mass of the Al pan remains constant throughout the TGA experiment and is subtracted from each data point. Baseline dynamic and isothermal runs with empty Al pans in the TGA showed a maximum change of ±30 µg.

Table 23: Dynamic TGA samples containing unencapsulated PNB sacrificial material and PNB encapsulated in polyimide PI-2611

Sample	**Materials Added**	**PNB Mass (mg)**	**Encapsulant Mass (mg)**	**TGA Program**
S-CD10-1	PNB	2.601	--	Polyimide cure; Dynamic 10^{o}C/min
P-CD10-1	PI-2611	--	9.488	Polyimide cure; Dynamic 10^{o}C/min
SP-CD10-1	PNB + PI-2611	3.285	7.920	Polyimide cure; Dynamic 10^{o}C/min
S-CD3-1	PNB	2.036	--	Polyimide cure; Dynamic 3^{o}C/min
S-CD3-2	PNB	2.208	--	Polyimide cure; Dynamic 3^{o}C/min
S-CD3-3	PNB	3.865	--	Polyimide cure; Dynamic 3^{o}C/min
P-CD3-1	PI-2611	--	9.147	Polyimide cure; Dynamic 3^{o}C/min
P-CD3-2	PI-2611	--	15.774	Polyimide cure; Dynamic 3^{o}C/min
P-CD3-3	PI-2611	--	9.491	Polyimide cure; Dynamic 3^{o}C/min
P-CD3-4	PI-2611	--	12.441	Polyimide cure; Dynamic 3^{o}C/min
SP-CD3-1	PNB + PI-2611	1.961	13.057	Polyimide cure; Dynamic 3^{o}C/min
SP-CD3-2	PNB + PI-2611	2.882	11.342	Polyimide cure; Dynamic 3^{o}C/min
SP-CD3-3	PNB + PI-2611	2.569	7.186	Polyimide cure; Dynamic 3^{o}C/min
S-CD1-1	PNB	3.462	--	Polyimide cure; Dynamic 1^{o}C/min
P-CD1-1	PI-2611	--	8.646	Polyimide cure; Dynamic 1^{o}C/min
SP-CD1-1	PNB + PI-2611	2.547	6.712	Polyimide cure; Dynamic 1^{o}C/min

Table 24: Dynamic TGA samples containing unencapsulated PNB sacrificial material on various TGA pan surfaces.

Sample	Materials Added	PNB Mass (mg)	Encapsulant Mass (mg)	TGA Program
S-D3-1	PNB on Al pan	1.921	--	Dynamic 3^{o}C/min
S-D10-1	PNB on Al pan	2.378	--	Dynamic 10^{o}C/min
SPt-D10-1	PNB on Pt coated Al pan	1.562	--	Dynamic 10^{o}C/min
SOx-D10-1	PNB on SiO_2 coated Al pan	2.812	--	Dynamic 10^{o}C/min
SCu-D10-11	PNB on Cu coated Al pan	2.127	--	Dynamic 10^{o}C/min

Table 25: Isothermal TGA samples containing unencapsulated PNB sacrificial material and PNB encapsulated in polyimide PI-2611.

Sample	Materials Added	PNB Mass (mg)	Encapsulant Mass (mg)	TGA Program
S-CI400-1	PNB	2.552	--	Polyimide cure; Isothermal 400^{o}C
P-CI400-1	PI-2611	N/A	7.311	Polyimide cure; Isothermal 400^{o}C
SP-CI400-1	PNB + PI-2611	2.066	6.813	Polyimide cure; Isothermal 400^{o}C
S-CI425-1	PNB	3.943	N/A	Polyimide cure; Isothermal 425^{o}C
P-CI425-1	PI-2611	--	9.184	Polyimide cure; Isothermal 425^{o}C
SP-CI425-1	PNB + PI-2611	3.306	6.708	Polyimide cure; Isothermal 425^{o}C

The mass of encapsulant PI-2611 listed in Table 23 and Table 25 is the mass of the polymer in the softbaked (uncured) state. Mass is lost from the polyimide PI-2611 during the ramp and hold at 350°C due to the condensation curing reaction of the polymer, and removal of residual solvent. Unencapsulated PNB also lose mass during a ramp and hold at 350°C. The unencapsulated PNB samples show 86.83% ± 0.78% (95% confidence) and 1.13% (1σ) of the original mass remaining after the polyimide cure temperature program of a 5°C/min ramp to 350°C and holding for 1 hour. The samples containing only uncured PI-2611 show 63.45% ± 1.56% (95% confidence) and 2.39% (1σ) of the polyimide mass remains after the ramp hold at 350°C. However, the two individual components do not additively combine when decomposed together. If the mass lost during the cure reaction from the PI-2611 is assumed to be the same whether PNB is present or not, the calculations result in a PNB mass following the cure that is larger than the original amount. Therefore, the mass of each component when combined and following a cure for 1 hour at 350°C was determined from a set of equations with two unknowns, equation 7.1 and equation 7.2.

$$y = \frac{\frac{T_2}{P_2} - \frac{T_1}{P_1}}{\frac{W_2}{P_2} - \frac{W_1}{P_1}} \qquad \text{Eq. (7.1)}$$

$$x = \frac{T_1}{P_1} - \frac{W_1}{P_1} y \qquad \text{Eq. (7.2)}$$

x = weight percentage PNB remaining after 350°C for 1 hour;

y = weight percentage PI-2611 remaining after 350°C for 1 hour;

P_x = weight of PNB in sample X initially;

W_x = Weight of PI-2611 in sample X initially;

T_x = total weight of both polymers remaining after cure.

Any pair of data (P_1, W_1, T_1, and P_2, W_2, T_2) may be used in order to solve for x and y as long as the initial weights, W_1 and W_2, and P_1 and P_2, are significantly different to obtain a real solution. Eighteen significantly different data pair combinations from ten samples were used to solve for x and y. The average result is 66.65% with a 95% confidence interval of ± 3.32% PI-2611 and 99.6% with a 95% confidence interval of 4.42% PNB remains after curing when the sample contains PNB encapsulated in PI-2611. The remaining weight of PI-2611 has a smaller confidence interval and is similar to the weight lost from PI-2611 alone. Therefore, the percentage and limits of PI-2611 mass is used as the basis for calculation of the mass of PNB throughout the TGA experiments containing both polymers. The average weight of sacrificial PNB remaining after the 1 hour hold at 350^{o}C was calculated by subtracting 66.65% of the original PI-2611 mass from the total sample mass. A lower 95% confidence limit of PNB weight is calculated by subtracting (66.65 + 3.32)% of the initial PI-2611 mass from the total. The upper 95% confidence interval of the remaining percentage of PI-2611 again results in more PNB than originally contained in the sample. Therefore the upper limit on PNB weight remaining after cure is the condition where 100% of the initial PNB remains. The PI-2611 continues to show a gradual weight loss during the remainder of each of the TGA programs. Therefore, the PNB temperature and time decomposition profile is found by subtraction of the amount of the PI-2611 remaining as a function of time and temperature, as determined from the samples containing PI-2611 alone. From the dynamic TGA thermograms, the temperature for 5% weight loss is determined as the

onset temperature for decomposition and the temperature for 50% weight loss as the decomposition temperature (T_d). The percent weight remaining at 500°C is used as a comparison for residual weight from the decomposition. The temperature range for decomposition (10-90% conversion) and the temperature of the maximum rate of decomposition also serve as a comparison between samples. Isothermal TGA experiments were performed by ramping quickly to temperatures of either 400°C or 425°C, and holding for 300 min. The time for 5% weight loss, the time for 50% weight loss, the time for 10-90% conversion, and residuals after 1, 2, and 3 hours at the hold temperature were used as comparisons between each decomposition environment.

7.1.2 XPS sample preparation and procedure

Samples for XPS analysis were prepared using Ti/Au sputtered 4" Si wafers as a substrate. The Au surface provides a zero-reference for the elements O and Si. PNB solution PNB1-S1 (22.0 wt% 90/10 Butyl/TES PNB in mesitylene) was spin-coated onto each Au-coated substrate, softbaked on a hotplate at 120°C for 5 min, and cured in a Lindberg tube furnace ramped 5°C/min to 275°C, and held for 1 hour in nitrogen. The spin-coating conditions resulted in three film thicknesses: 2.69, 8.66, and 20.1 µm. The films were patterned into large circles and squares of widths or radii from 2mm-1cm using 2000 Å of Al as a hard mask, and RIE etching using PNB-ETCH3. Each wafer was broken into individual pieces. Three of the pieces (one of each PNB film thickness) received no overcoat. One of each thickness was spin-coated with VM-652 adhesion promoter and 8 µm polyimide PI-2611. The three remaining pieces were coated with 100 Å of sputtered Ti, followed by 4.66 µm of PECVD SiO_2, using a STS PECVD at the

conditions described previously in Table 15 (Chapter 5, page 105). The Ti was necessary to act as an adhesion promoter between the Au and the SiO_2 surface. All samples were decomposed under the same conditions in a nitrogen-purged horizontal Lindberg tube furnace ramped 3°C/min to 350°C, held for 1 hour, ramped 1°C/min to 405°C, held for 1 hour, ramped 1°C/min to 425°C, and held for 1 hour, followed by cooling to room temperature. The glass and PI-2611 encapsulants were removed by cellophane tape attached to the encapsulant and peeling the film from the wafer. The overcoat material is not attached to the substrate in the areas containing the air-gaps and is easily removed. After removal of the overcoat, the samples were stored in a nitrogen-purged dry-box and only exposed to an ambient atmosphere only upon loading into the vacuum chamber of the XPS. Portions of the same samples were also used for contact angle measurements.

7.1.3 Air-gap fabrication details of samples for the decomposition of PNB at a constant rate of conversion

This section contains the experimental details of the fabrication of air-gaps for the decomposition of PNB at a constant rate of conversion, discussed in Section 7.5. Solutions PNB-1-S1 and PNB-2-S2 (Chapter 5, Table 13, page 99) were used to create sacrificial PNB films on 4" Si wafers with thicknesses of approximately 10 μm, 20 μm, and 30 μm. The thicknesses of the sacrificial layers measured using a Tencor Alphastep contact profilometer are 11.3 μm, 21.8 μm, and 31.3 μm. The sacrificial layers were patterned into channels 100 μm wide and 900 μm in length. Polyimide PI-2611 was used as the overcoat material with a thickness of about 8 μm after curing. The samples were then divided into several pieces to be decomposed with various decomposition programs. One piece of each thickness was decomposed using the experimental constant rate of

conversion programs for 0.1, 0.5, 1, 2 and 5 % conversion/min, described in Section 7.5. The heights of the resulting air-channel structures were analyzed using two methods. The Tencor Alphastep contact profilometer was used to measure the channel height and uniformity of the channels following decomposition. Cross-sections of the samples were examined by SEM to determine the channel height and the completeness of the decomposition. Some difficulty was encountered in cross-sectioning the samples, due to the high elongation of the PI-2611. The samples were submerged in liquid nitrogen for several minutes and cleaved across the channels. However, in many cases, the polymer overcoat did not break cleanly, deformed, peeled back, or delaminated. Therefore, results using SEM were not able to be determined for select samples.

7.2 Thermogravimetric Analysis Results for Unencapsulated and Encapsulated PNB

7.2.1 Dynamic TGA results of unencapsulated PNB in the presence of metals

Dynamic thermograms showing weight percentage as a function of temperature for unencapsulated PNB sacrificial polymer decomposed in a variety of coated Al TGA pans are shown in Figure 79. Each of the curves shows a single drop in weight with an increase in temperature. All four curves have a similar slope during the main reaction occurring between 10 to 90 percent conversion. A comparison of the curves at various points in the decomposition reaction is provided in Table 26**.** The onset of decomposition (indicated by the temperature for 5% weight loss), the T_d, the temperature at which maximum weight loss occurs, and the temperature range of 10-90% conversion show insignificant differences (< 9^oC) between the various pan materials. The small temperature differences between each of the four samples at points during the decomposition reaction show no consistent pattern and are not due to a catalytic effect.

Ideally, the TGA provides an identical steady ramp rate during each experiment. However, at a fast heating rate of 10^{o}C/min, differences in the ramp rate occur in the experiment due to nitrogen flow, or lag in the control system from differences in the thermal conductivity of the samples. In addition, the weight of the sample pan is subtracted from the data. The outcome of these two effects is the curve shifts slightly on the x-axis at points during the reaction, leading to small temperature gradients from sample to sample. A catalytic effect would change the shape of the curve, or significantly affect the slope of the TG curve, indicating a variation in the rate of reaction. Slight errors are also introduced in the weight remaining at 500^{o}C from subtraction of the sample pan weight from each data point. The mass of the PNB sacrificial material in these experiments is about 2 mg. Therefore, approximately a 3% error in weight occurs due to the resolution of the tool for these small sample sizes.

7.2.2 Dynamic TGA results of unencapsulated PNB and PNB encapsulated by PI-2611

This section presents the results from dynamic TGA experiments performed on unencapsulated PNB sacrificial material (samples S-CD10-1, S-CD3-1 through 3, S-CD1-1); DuPont Pyralin PI-2611 polyimide alone (samples P-CD10-1, P-CD3-1 through 4, P-CD1-1); and PNB encapsulated in PI-2611 polyimide (SP-CD10-1, SP-CD-1 through 3, SP-CD1-1). Each of these samples was exposed to the temperature program required for the PI-2611 cure (350^{o}C for 1 hour), followed by a constant heating rate ramp to 530^{o}C. Figure 80 compares PNB decomposition at a heating rate of 3^{o}C/min for unencapsulated PNB with and without the one hour hold at 350^{o}C. The curve for the sample held at 350^{o}C was normalized to 100 percent weight immediately following the hold period to account for mass lost during the cure. Unencapsulated PNB held at 350^{o}C

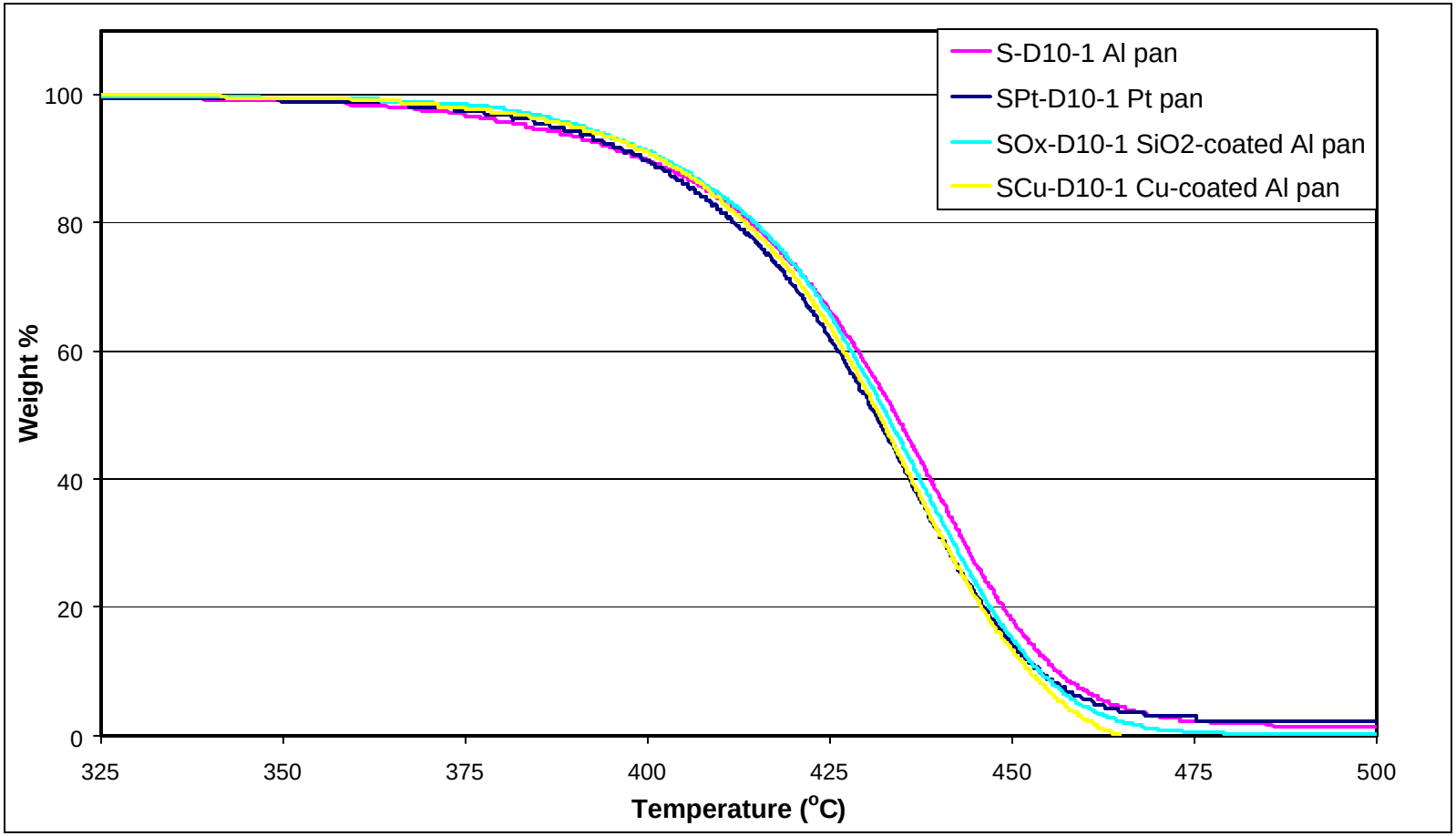

Figure 79: Dynamic thermograms for the decomposition of unencapsulated PNB sacrificial material using TGA sample pans coated with various materials at a heating rate of 10°C/min in nitrogen.

Table 26: Dynamic TGA characteristics for the decomposition of PNB using various sample pans at a heating rate of 10^{o}C/min in nitrogen.

Sample	**PAN Material**	**T for 5% weight loss (^{o}C)**	**T_d (^{o}C)**	**T for 10-90% remaining weight (^{o}C)**	**T for maximum rate of weight loss (^{o}C)**	**Weight at 500 ^{o}C (%)**
S-D10-1	Al	383.3	434.1	399.9-456.2	442.6	1.47%
SPt-D10-1	Pt	386.7	431.3	398.5-453.8	434.8	2.30%
SOx-D10-1	SiO_2-coated Al	391.3	432.8	402.1-453.9	437.1	0.18%
SCu-D10-1	Cu-coated Al	389.6	431.8	400.5-452.6	438.7	-3.06%

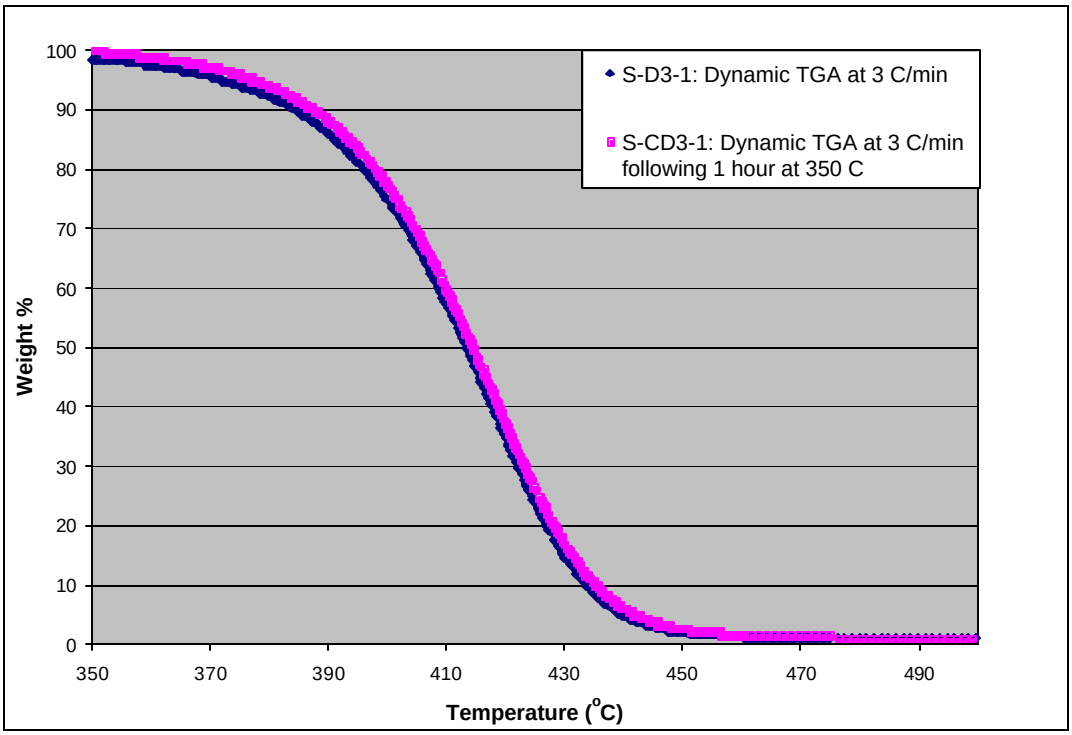

Figure 80: Dynamic TGA at a heating rate of 3°C/min for unencapsulated PNB with and without a 1 hour hold at 350°C.

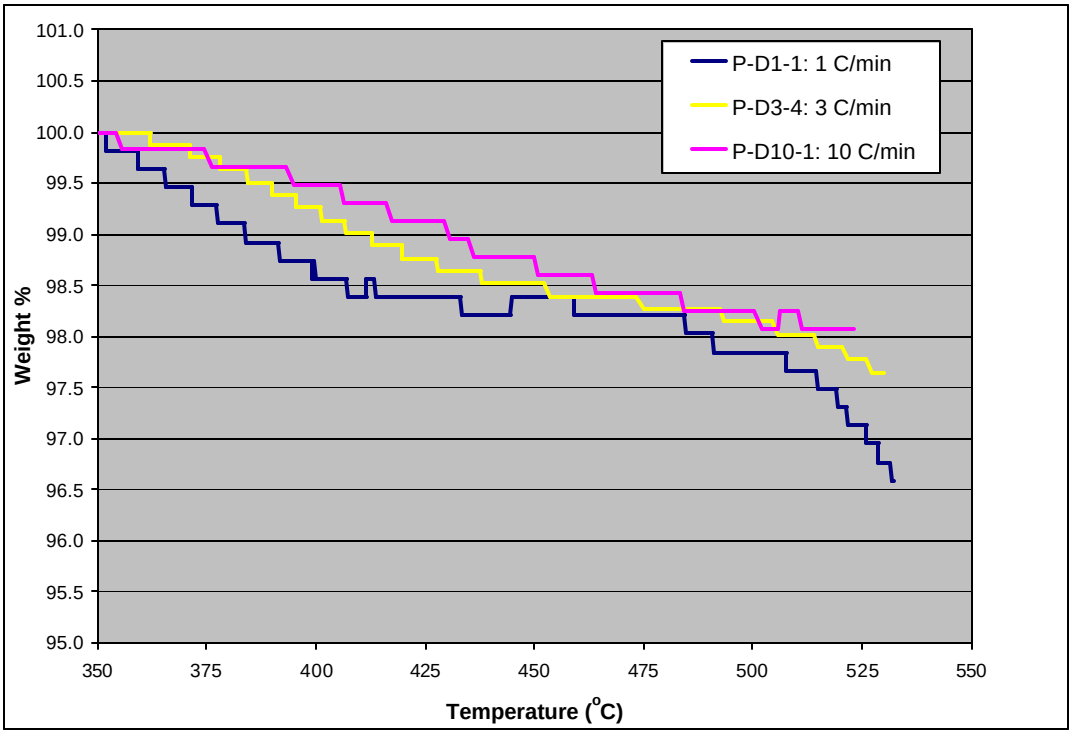

Figure 81: Dynamic TGA at heating rates of 1, 3, and 10°C/min for polyimide PI-2611 following a 1 hour cure at 350°C.

for 1 hour shows a slightly higher temperature for 5% weight loss than the unencapsulated PNB which is not exposed to the temperature hold period. For example, the 5% weight loss temperatures for the data in Figure 80 are 371.8^{o}C for S-D3-1 (no hold), and 377.0^{o}C for S-CD3-1 (with the hold). However, there is no difference between T_d of the two samples and the temperature where 90% conversion is reached. Sample S-D3-1 has a T_d of 413.3^{o}C and S-CD3-1 has a T_d of 414.0^{o}C. Thus, despite the mass lost during the 1 hour hold at 350^{o}C, a higher temperature is required in order to initiate the full overall decomposition reaction.

The weight percentage of PI-2611 polyimide as a function of temperature following a cure at 350^{o}C for 1 hour is shown in Figure 81. The three curves in Figure 81 represent three constant heating rates of 1, 3, and 10^{o}C/min. The sensitivity of the TGA compared to the polymer sample size creates the step pattern seen in the data. The amount of weight lost by the polyimide at each heating rate is <3% during the heating from 350^{o}C to a temperature of 500^{o}C. This small amount of weight loss is assumed to occur whether the PI-2611 is heating alone, or while encapsulating PNB. Therefore, the mass of PNB encapsulated in PI-2611 as a function of temperature was determined by subtracting the initial mass of PI-2611 at 350^{o}C multiplied by the percentage remaining according to the appropriate curve in Figure 81.

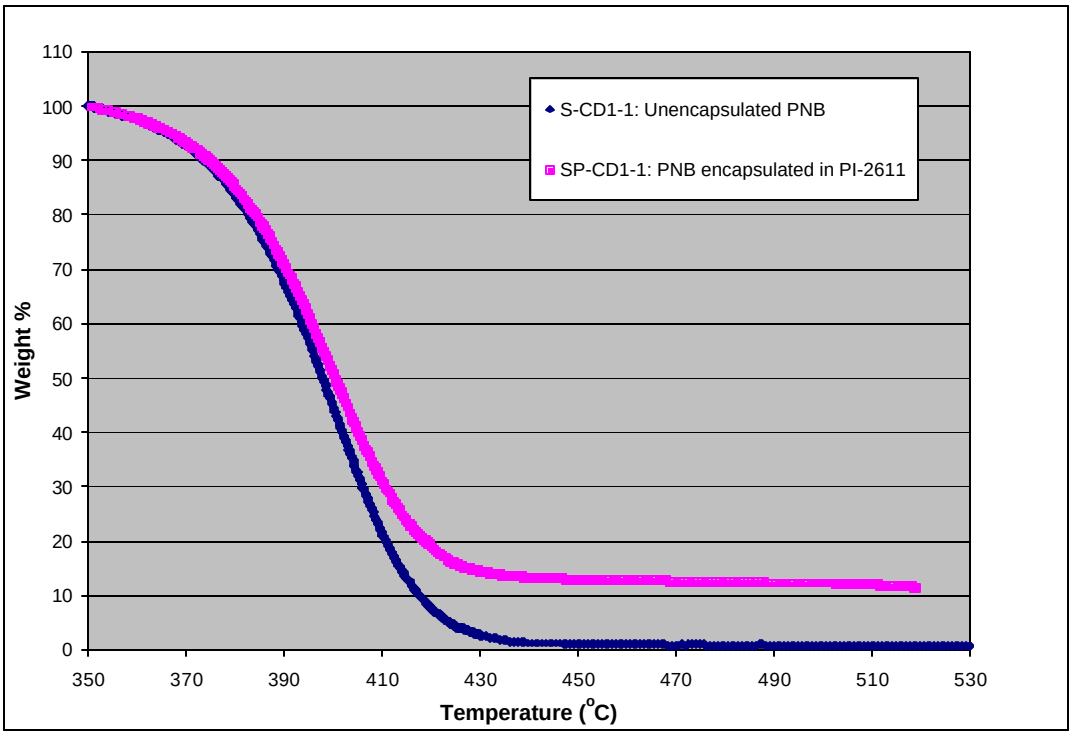

Figure 82: Dynamic thermogram obtained at a heating rate of 1°C/min for unencapsulated PNB and PNB encapsulated in PI-2611, following 1 hour at 350°C.

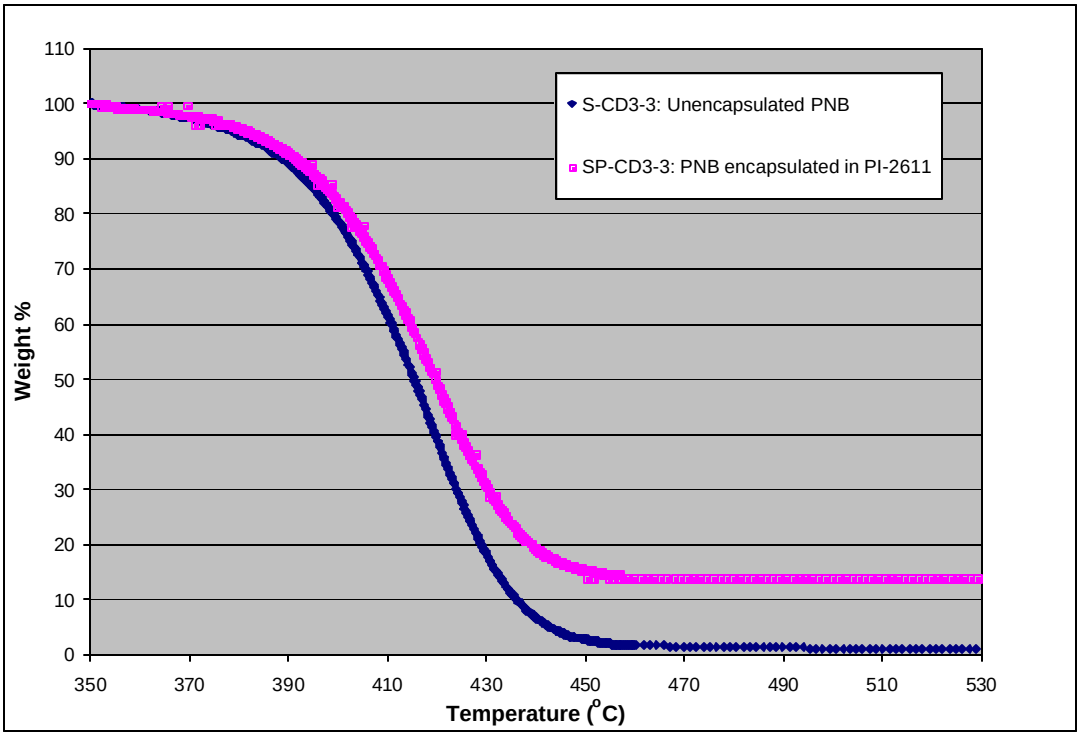

Figure 83: Dynamic thermogram obtained at a heating rate of 3°C/min for unencapsulated PNB and PNB encapsulated in PI-2611, following 1 hour at 350°C.

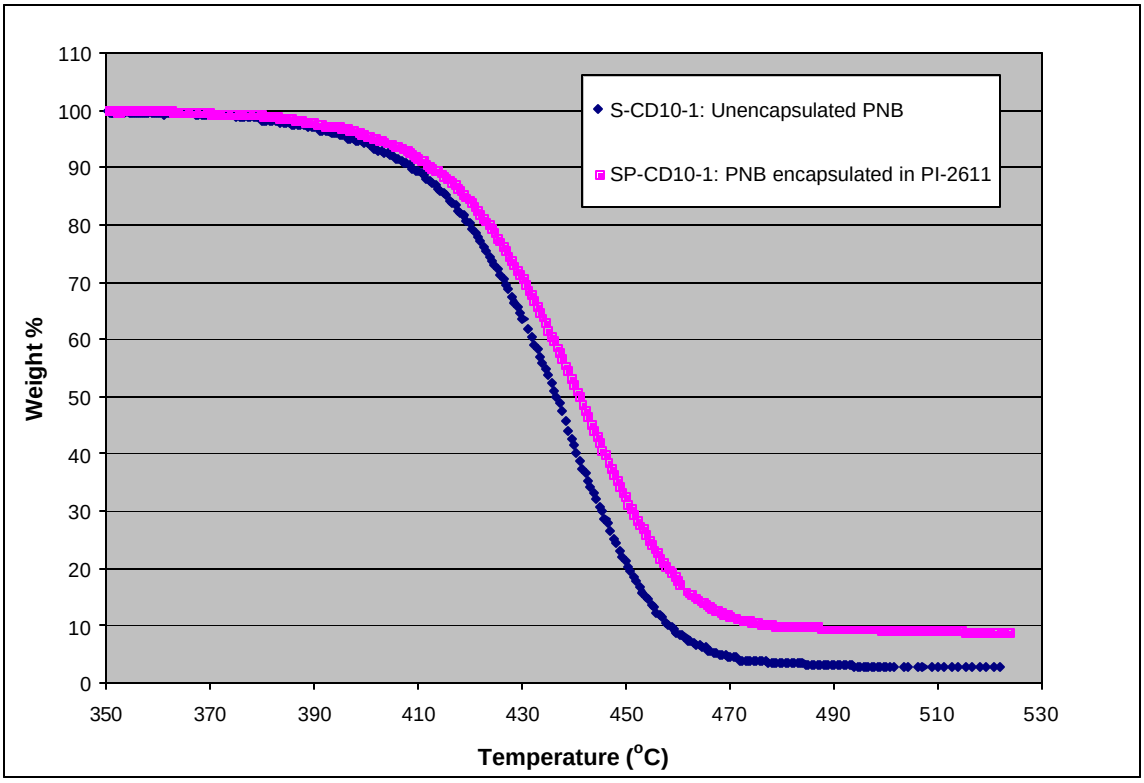

Figure 84: Dynamic thermogram obtained at a heating rate of 10°C/min for unencapsulated PNB and PNB encapsulated in PI-2611, following 1 hour at 350°C.

Table 27: Comparison of the dynamic TGA at various points in the decomposition reaction for unencapsulated PNB and PNB encapsulated in polyimide PI-2611

SAMPLE	MATERIALS ADDED	RAMP RATE (^{o}C/ min)	T FOR 5% WEIGHT LOSS (^{o}C)	T_d (^{o}C)	T FOR 10-90% REMAINING WEIGHT (^{o}C)	T FOR MAXIMUM RATE OF WEIGHT LOSS (^{o}C)	WEIGHT AT 500^{o}C (%)
S-CD3-1	PNB	3	377.0	414.4	387.6 -435.5	418.4	1.02%
S-CD3-2	PNB	3	376.9	413.3	386.3 – 432.7	417.5	-2.12% (-40 μg)
S-CD3-3	PNB	3	379.1	415.6	388.9 - 436.2	420.3	1.06%
SP-CD3-1	PNB + PI-2611	3	387.1 ± 1.1	424.3 ± 2.9	393.9 – 500*	421.9	15.11± 9.67%
SP-CD3-2	PNB + PI-2611	3	382.2 ± 1.1	418.4 ± 1.7	392.2 – 500*	422.8	8.46 ± 5.64%
SP-CD3-3	PNB + PI-2611	3	384.3 ± 0.9	424.7 ± 1.3	394.1 – 500*	419.6	28.10 ± 2.87%
S-CD10-1	PNB	10	397.7	436.6	408.8 - 458.4	438.3	2.73%
SP-CD10-1	PNB + PI-2611	10	404.0 ± 0.7	444.2 ± 0.5	414.6 -500*	441.0	18.37 ± 3.24%
S-CD1-1	PNB	1	366.2	397.9	373.7 – 417.7	403.9	0.62%
SP-CD1-1	PNB + PI-2611	1	368.9 ± 0.4	403.8 ± 1.4	376.8 – 500*	420.6	21.49 ± 3.15%

*Weight did not reach 10% or less remaining by 500 ^{o}C

The dynamic TGA results showing weight percentage as a function of temperature for unencapsulated PNB and PNB encapsulated in PI-2611 are shown in Figure 82, Figure 83, and Figure 84. A comparison of the unencapsulated and encapsulated PNB decomposition data at various points in the reaction is provided as Table 27. The data from samples containing only PNB or only PI-2611 are single temperature and weight values since the exact weight and temperature relationship is known. The temperature and residual weight values for the samples containing PNB encapsulated in PI-2611 (SP-CD1-1, SPCD3-1, SP-CD3-2, SP-CD3-3, and SP-CD10) are given as 95% confidence intervals. The range in these values derives from the 95% confidence interval of the weight of PI-2611 remaining after cure. The temperature range for a given conversion of PNB decomposition is then determined from the upper and lower limits of the PNB weight. The dynamic experiments at 3^{o}C/min were run in triplicate to verify the repeatability of results. The temperature data shows consistent results between the three experiments. However, the samples containing both PNB and PI-2611 show a large amount of variation in the values for weight remaining when the constant temperature ramp reaches 500^{o}C. The difference in the total remaining sample mass and the estimation of PI-2611 mass introduces a large error due to the larger amount of PI-2611 to Unity 400 in the sample. However, clear trends are observed from the data in Table 27. At each of the three ramp rates (1, 3, and 10^{o}C/min) the encapsulated PNB samples have higher temperatures for 5% weight loss, and T_d, ranging from 2.7 to 10.2^{o}C over the unencapsulated PNB temperature values. Figure 82, Figure 83, and Figure 84 show this effect by the x-axis shift of the encapsulated PNB TG curve to higher temperatures in comparison to the unencapsulated PNB TG curve. As the heating rate is

increased from 1°C/min to 3°C/min to 10°C/min, a the x-axis shift in the encapsulated curve begins at a lower extent of conversion. At a slow ramp rate of 1°C/min shown in Figure 82, the two curves overlap one another until approximately 30% weight loss. At 3°C/min and at 10°C/min, the curves overlap until 10% weight loss and 5% weight loss, respectively. In addition, at all three heating rates, the slope of the encapsulated PNB TG curve between 10-90% conversion of the PNB decomposition reaction is slightly less than the slope of the unencapsulated PNB TG curve. These changes in the data indicate the overall decomposition reaction is occurring at a slower rate in the encapsulated state. At a faster heating rate, the difference in decomposition rate is amplified. The rate may be slowed by effects such as differences in PNB heating when it is in encapsulated in PI-2611, or pressure build-up inside the air-cavity. Another difference between the encapsulated and unencapsulated samples is the weight remaining at when the temperature reaches 500°C. Although significant error limits occur in the remaining weight percentage of PNB due to error in the PI-2611 weight, the weight remaining in the encapsulated samples is higher than in the unencapsulated samples by as much as 25%. This clearly indicates a difference is occurring between the reactions in the two systems. The amount of weight remaining in the dynamic TGA can only be used as a comparison between the unencapsulated and encapsulated decomposition. If the reaction is progressing more slowly in the encapsulated state, time may be the factor contributing to more weight remaining in the encapsulated samples. The cross-sectional images of fabricated air-cavities show very little visual residue in the cavity after decomposition in the encapsulated state. However, in air-cavity fabrication, the PNB is decomposed using a constant temperature hold at 425°C. Therefore, Isothermal TGA was also performed on

the encapsulated and unencapsulated PNB to investigate the decomposition in more detail.

7.2.3 Isothermal TGA results of unencapsulated PNB and PNB encapsulated in PI-2611

Isothermal TGA was performed on unencapsulated PNB and PNB encapsulated in polyimide PI-2611 at hold temperatures of 400°C and 425°C. Figure 85 compares the isothermal TGA at 400°C of unencapsulated PNB following a hold at 350°C for 1 hour, to the TGA of unencapsulated PNB ramped immediately to 400°C. The hold at 350°C decreases the time required for the decomposition reaction of the PNB. The mass loss from the PNB during the 350°C hold indicates that the reaction has initiated at 350°C. Initiation of the reaction and bond breakage changes the extent of reaction when the TGA reaches the isothermal temperature of 400°C. On the other hand, the decomposition of PNB without the hold at 350°C must still initiate when the TGA reaches 400°C. The difference in the starting point of the reaction at 400°C accelerates the reaction time for PNB held at 350°C. The unencapsulated samples with the hold at 350°C were used as the comparison to the samples encapsulated in PI-2611. Figure 86 shows the isothermal thermograms at 400°C and 425°C for PI-2611, following a cure at 350°C for 1 hour. The polymer loses less than 2% weight at each hold temperature over a period of 5 hours. The PNB weight in the samples containing both polymers was determined by subtracting the PI-2611 weight as a function of time according to Figure 86. The fast ramp rate from 350°C to the isothermal temperature creates a difficulty in determining the exact point where the cure period ends, and the isothermal hold begins. Therefore, although the weight is known throughout the isothermal TGA experiments on unencapsulated PNB, upper and lower error limits of the PNB weight were determined using 86.83 ± 0.78% of

the initial mass of PNB. TGA thermograms of weight percentage as a function of time for unencapsulated PNB and PNB encapsulated in PI-2611 are shown in Figure 87 for (a) 400°C and (b) 425°C. A comparison of the characteristics of these isothermal thermograms is shown in Table 28. Similar to the dynamic TGA experiments, significant differences are seen in the temperature at which a certain conversion is achieved, and in the weight remaining at the end of the hold period. The onset of the reaction, given by the 5% weight loss time and temperature, is the same for the encapsulated and unencapsulated samples. However, Figure 87 indicates that there is a slower reaction rate occurring in the encapsulated samples. The TGA curve shifts on the x-axis to increased time for each value of reaction conversion. In addition, the encapsulated samples show significantly higher residual weight remaining after three hours at the isothermal hold temperature. Quantification of these differences through analysis of the kinetic parameters is discussed in the following section.

7.3 Kinetic Parameters for the Decomposition of Encapsulated and Unencapsulated PNB

The dynamic and isothermal TGA results suggest that the decomposition reaction occurs at a slower rate for encapsulated PNB than unencapsulated PNB, indicated by a change in the slope of the TGA thermograms. Wedlake [69] has previously shown the thermal decomposition of unencapsulated polynorbornene in nitrogen follows first-order kinetics. The methods to extract kinetic parameters from TGA data described in Chapter 4, Section 4.1 are applied to the unencapsulated and encapsulated PNB TGA data. The goals are to: (1) confirm the unencapsulated decomposition of PNB in nitrogen follows first order kinetics; and (2) quantify any differences in the rate of reaction between encapsulated and unencapsulated PNB decomposition.

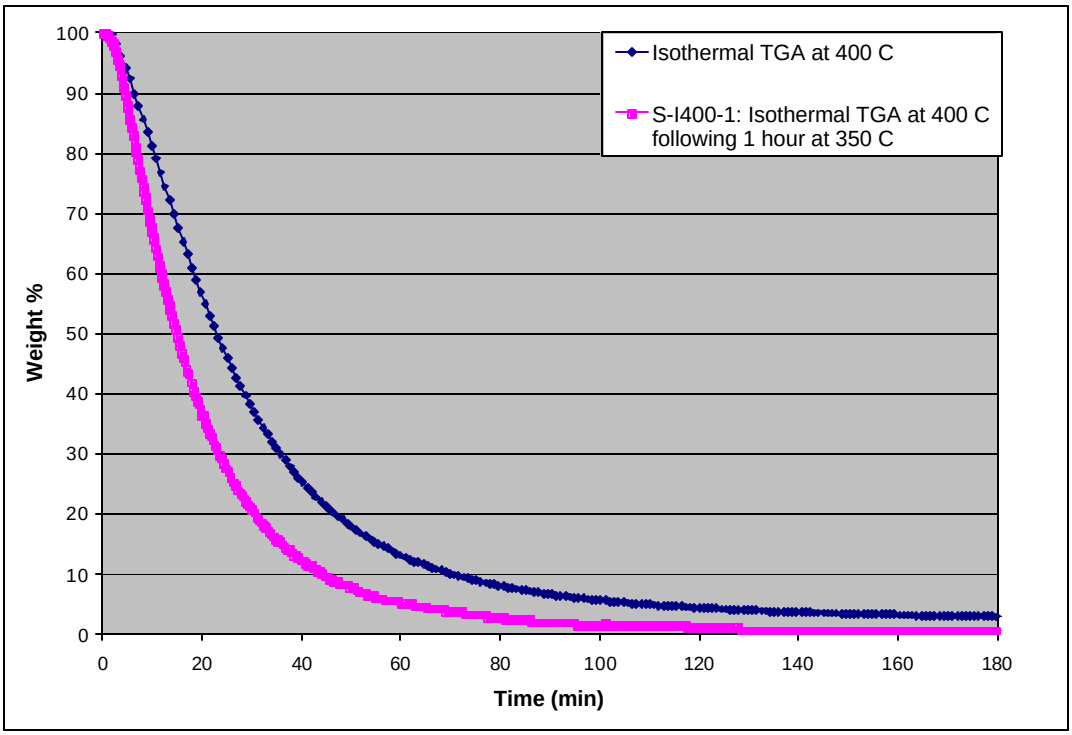

Figure 85: Thermogram from isothermal TGA at a hold temperature 400°C for unencapsulated PNB with and without a 1 hour hold at 350°C.

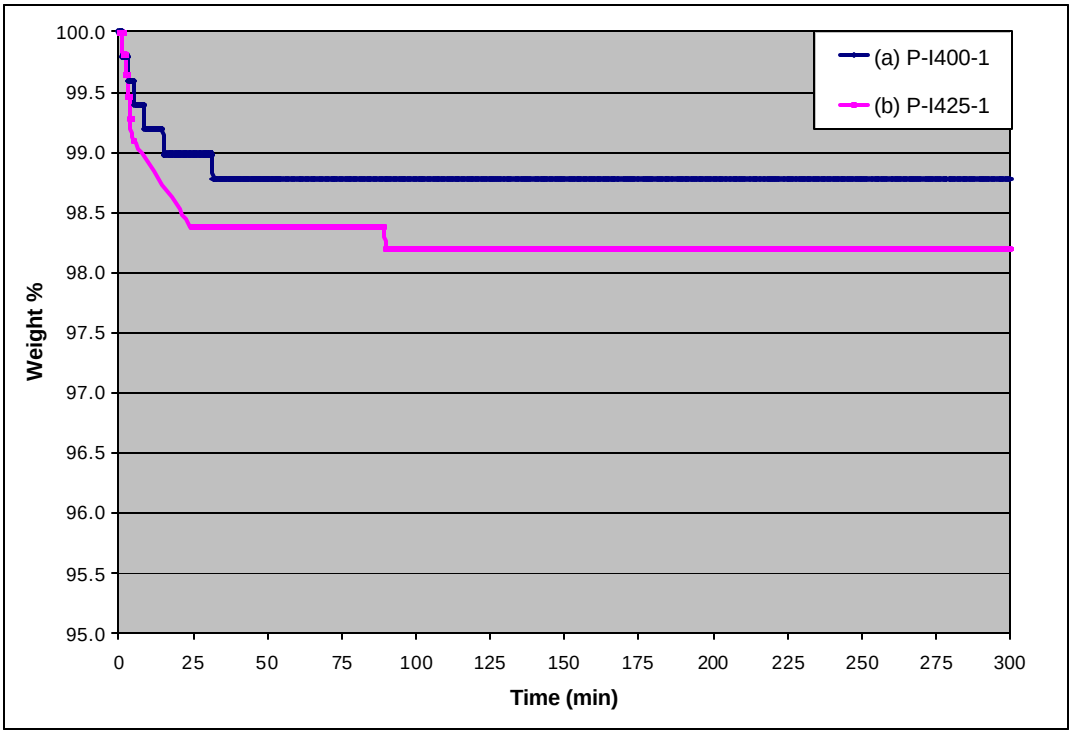

Figure 86: Weight percentage as a function of time for PI-2611 held for 300 min at (a) 400°C and (b) 425°C; PI-2611 following a 1 hour hold at 350°C.

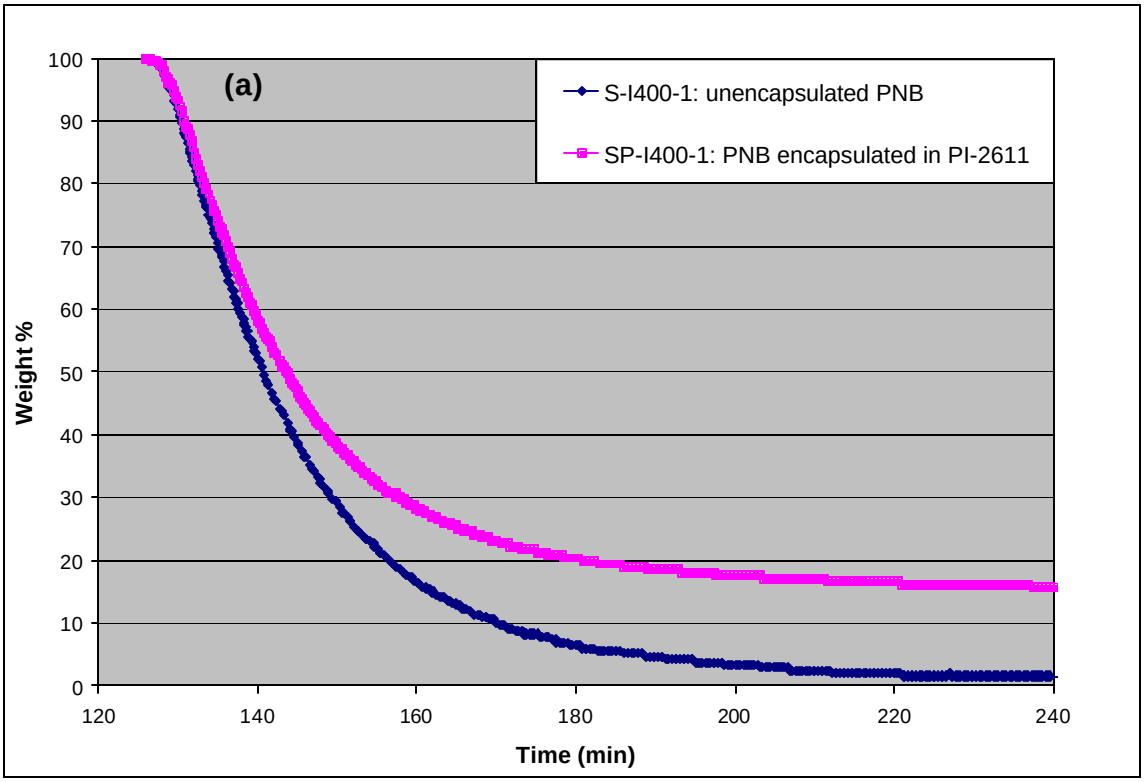

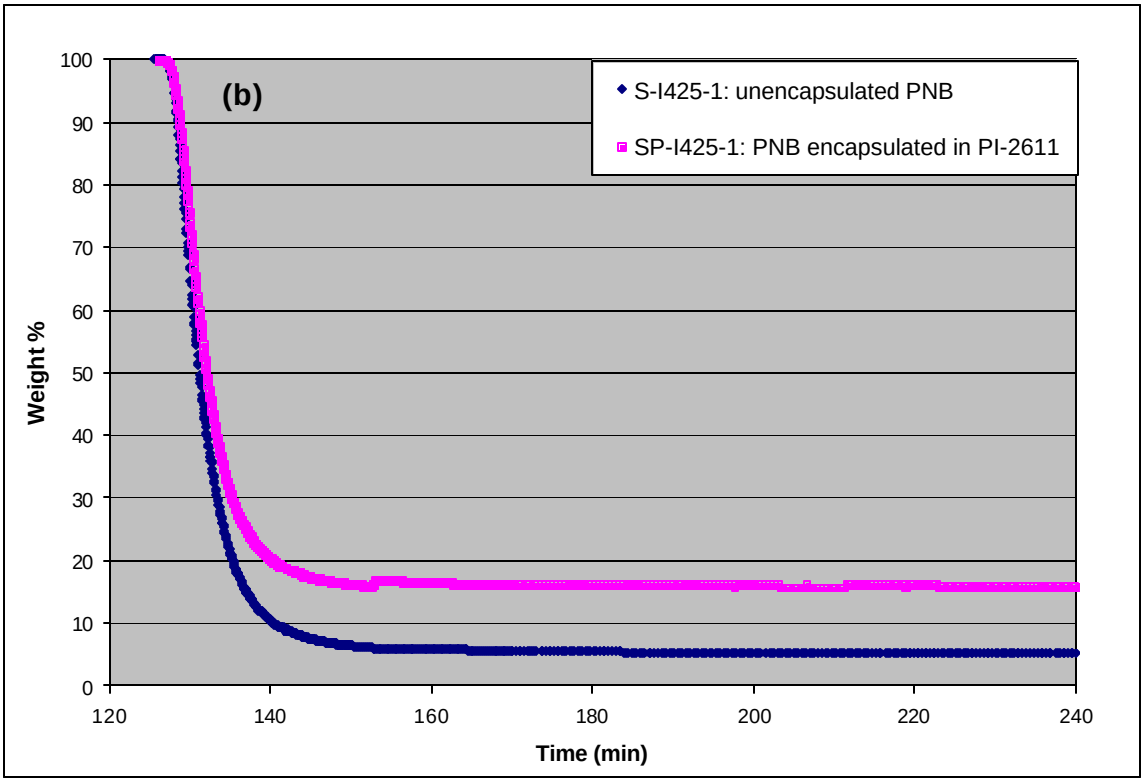

Figure 87: Isothermal thermograms of unencapsulated PNB and PNB encapsulated in polyimide PI-2611 at hold temperatures of (a) 400°C and (b) 425°C.

Table 28: Isothermal TGA characteristics for unencapsulated PNB and PNB encapsulated in polyimide PI-2611

Sample	Materials Added	Hold Temp (^oC)	5% Weight loss Time (min) & T (^oC)	50% Weight loss Time (min) & T (^oC)	Weight % at start of isothermal hold	Time for 90-10% remaining weight (min)	Weight % after hold at the isothermal temp.		
							30 min	60 min	180 min
S-I400-1	PNB	397.2	129.1 min 396.2^{o}C	140.8 min 397.9^{o}C	83.44	130.4 – 170.1	4.21	1.07	0.63
SP-I400-1	PNB + PI-2611	398.3	129.3 ± 0.1 min 396.1 ± 0.3^{o}C	143.8 ± 2.4 min 398.4 ± 0.1^{o}C	82.17 ± 1.23	131.0 - *	19.05 ± 8.51	15.79 ± 8.86	14.85 ± 8.96
S-I425-1	PNB	424.6	128.0 min 411.8^{o}C	131.2 min 423.9^{o}C	32.33	128.4 – 140.5	5.15	5.15	4.86
SP-I425-1	PNB + PI-2611	424.0	128.2 ± 0.1 min 412.6 ± 1.2^{o}C	132.4 ± 0.3 min 423.4 ± 0.1^{o}C	42.05 ± 2.62	128.8 -*	16.04 ± 5.37	15.98 ± 5.36	15.69 ± 5.38

*10% remaining weight not reached by 180 min

7.3.1 Kinetic parameters for the decomposition of unencapsulated PNB and PNB encapsulated in PI-2611 from dynamic TGA data

As described in Section 4.1.1, kinetic parameters may be determined from dynamic TGA data at several different heating rates. The mechanism of the reaction is assumed to follow n-order kinetics, represented by equation 4.8:

$$\frac{dW}{dt} = A \exp\left(\frac{-E_a}{RT}\right) W^n \qquad \text{Eq. (4.8)}$$

The Ozawa integral method uses an integrated form of equation 4.8:

$$\log \frac{b}{T^2} = -\left(\frac{E_a}{2.3RT}\right) + \text{const.} \qquad \text{Eq. (4.7)}$$

A plot of $\log(\beta/T^2)$ as the ordinate and 1/T as the abscissa is constructed from the dynamic data at conversions of 10, 20, 30, 40, 50, and 60 percent. These charts are included as Figure A.29 and Figure A.30 in Appendix A for unencapsulated PNB, and Figure A.31 and Figure A.32 in Appendix A for PNB encapsulated by PI-2611. Two values of the heating rate (β) were used in the calcuations: the average heating rate and the instantaneous heating rate. The activation energy is then calculated from slope of a straight line through each set of data at a single conversion. Once the activation energy is known, the residue factor (RF) is determined from the relationship between dW/dt and W, corrected for temperature. The details of the activation energy and the RF calculations are included in Appendix A.

Table 29 lists the calculated RF values for each dynamic TGA experiment, determined using both the instantaneous heating rate and the average heating rate. Following the determiniation of the activation energy, the reaction order and pre-exponential constant are determined from the overall rate expression. The details of the

calculations for n and A are also included in Appendix A. The kinetic parameters are determined using both the instantaneous and the average heating rates. A summary of the resulting kinetic parameters n, A, and E_a, along with the rate constant values at 400°C and 425°C from the dynamic TGA data are included in Table 31.

7.3.2 Kinetic parameters for the decomposition of unencapsulated PNB and PNB encapsulated in PI-2611 from isothermal TGA data

As described in Section 4.1.2, equation 4.8 is the governing equation for the calculation of kinetic parameters from isothermal TGA data. The natural log function is applied to both sides of the overall weight loss rate expression to yield equation 4.11.

$$\ln \frac{d\mathrm{W}}{d\mathrm{t}} = \ln k + \mathrm{n} \ln \mathrm{W} \qquad \text{Eq. (4.11)}$$

A plot of ln dW/dt as a function of ln W yields a line with a slope of n, and a y-axis intercept of ln k. These plots for the isothermal decomposition of PNB are included in Appendix A, as Figure A.67 and Figure A.71 for decomposition at 400°C and Figure A.68 and Figure A.72 for decomposition at 425°C. The 95% confidence limits are represented in these figures as the upper and lower limit curves. RF values are also determined for the isothermal data and are listed in Table 30. Details on the calculation of the RF for the isothermal data are also provided in Appendix A. The slope of each line corrected with RF gives n, the corrected reaction order of the polymer decomposition reaction. A summary of the kinetic parameters from isothermal data are also included in Table 31.

7.3.3 Discussion of the TGA results for the decomposition of unencapsulated PNB and PNB encapsulated by PI-2611

The first goal of the TGA studies on encapsulated and unencapsulated PNB decomposition is to verify that the reaction follows first-order kinetics when the PNB is unencapsulated. Wedlake [69] performed a large number of isothermal and dynamic TGA experiments to extract the values of n, A, and E_a for methyl, butyl, and hexyl polynorbornene homopolymers and the 90/10 butyl/triethoxysilyl copolymer. The values are listed only for the 90/10 butyl/triethoxysilyl PNB composition polymer in Table 32. Wedlake's data is compared to the kinetic parameters extracted from the dynamic and isothermal TGA data for unencapsulated PNB, listed in Table 31. Both sets of results confirm a first order reaction. Although the results from the dynamic TGA data yield a reaction order slightly less than the results from the isothermal TGA data, the average from the two methods yields a value of 1.0 for both sets of data. In addition, the average activation energy values from the two sets of data are almost identical. Wedlake's experiments yield an average E_a of 232.4 KJ/mol, and the experimental data on unencapsulated PNB yield an average E_a of 230.5 KJ/mol. The results from the two sets of data are consistent and verify a first order reaction.

Table 29: Residue factors from the dynamic TGA decomposition of PPC performed at various ramp rates in: (1) nitrogen; and (2) air

	Sample	Instantaneous ß Residue Factor (mg)	Average ß Residue Factor (mg)
Unencapsulated PNB in Nitrogen	S-CD10-1	72.2	64.4
	S-CD3-1	48.6	40.8
	S-CD3-2	-11.7	23.2
	S-CD3-3	89.9	75.2
	S-CD1-1	89.1	74.0
PNB Encapsulated in PI-2611	SP-CD10-1 Average W	380.0	388.3
	SP-CD10-1: Lower Limit	91.9	100.1
	SP-CD10-1: Upper Limit	386.9	396.1
	SP-CD3-1: Average W	223.9	245.2
	SP-CD3-1: Lower Limit	-236.7	-191.2
	SP-CD3-1: Upper Limit	139.1	159.3
	SP-CD3-2: Average W	53.4	67.2
	SP-CD3-2: Lower Limit	-287.8	-192.5
	SP-CD3-2: Upper Limit	174.3	248.5
	SP-CD3-3: Average W	668.0	682.8
	SP-CD3-3: Lower Limit	201.6	247.1
	SP-CD3-3: Upper Limit	249.8	292.3
	SP-CD1-1: Average W	501.7	515.4
	SP-CD1-1: Lower Limit	280.0	312.2
	SP-CD1-1: Upper Limit	306.6	336.0

Table 30: Residue factors from the isothermal TGA decomposition of PNB at 400°C and 425°C: (1) unencapsulated; and (2) encapsulated in polyimide PI-2611.

Sample & Isothermal Hold Temperature (°C)		**Residue Factor (mg)**	**Initial PNB Mass (mg)**	**RF as a Percentage of Initial Mass**
Unencapsulated PNB in Nitrogen S-I400-1 T = 397.2°C	Average W	21.1	2.234	0.94%
	Lower 95% Confidence Limit	-80.2	2.140	-3.75%
	Upper 95% Confidence Limit	30.1	2.243	1.34%
Unencapsulated PNB in Nitrogen S-I425-1 T = 424.6°C	Average W	207.9	3.458	6.01%
	Lower 95% Confidence Limit	56.8	3.030	1.87%
	Upper 95% Confidence Limit	219.9	3.466	6.34%
PNB Encapsulated in PI-2611 SP-I400-1 T = 398.3°C	Average W	364.4	2.166	16.82%
	Lower 95% Confidence Limit	140.8	1.939	7.26%
	Upper Limit	215.5	2.392	9.01%
PNB Encapsulated in PI-2611 SP-I425-1 T = 424.0°C	Average W	561.9	3.425	16.41%
	Lower 95% Confidence Limit	-154.1	3.202	-4.81%
	Upper Limit	316.7	3.647	8.68%

Table 31: Kinetic parameters for the thermal decomposition reaction of unencapsulated PNB and PNB encapsulated in PI-2611 from dynamic and isothermal TGA data.

	Activation Energy, E_a	**Reaction order, n**	**Pre-exponential Constant, A**	**Rate constant, *k* at 400°C**	**Rate constant, *k* at 425°C**
Unencapsulated PNB Dynamic TGA data Instantaneous heating rate	227.0 ± 8.5	0.988 ± 0.010	$2.774 \times 10^{16} \pm 1.482 \times 10^{15}$	0.0667	0.285
Unencapsulated PNB Dynamic TGA data Average heating rate	221.3 ± 2.5	0.987 ± 0.004	$1.022 \times 10^{16} \pm 4.901 \times 10^{14}$	0.0673	0.277
Unencapsulated PNB Isothermal TGA data	243.1	1.027 ± 0.038	4.914×10^{17}	0.0556	0.308
PNB encapsulated in PI-2611 Dynamic TGA data Instantaneous heating rate	214.3 ± 4.5	1.021 ± 0.047	$2.256 \times 10^{15} \pm 6.746 \times 10^{14}$	0.0529	0.209
PNB encapsulated in PI-2611 Dynamic TGA data Average heating rate	225.5 ± 7.1	1.011 ± 0.037	$1.719 \times 10^{16} \pm 5.328 \times 10^{15}$	0.0545	0.231
PNB encapsulated in PI-2611 Isothermal TGA data	264.7	1.022 ± 0.043	1.891×10^{19}	0.0479	0.275

The second goal of the TGA experiments is to identify differences in the decomposition of unencapsulated PNB compared to the decomposition of PNB encapsulated in a dielectric material. The kinetic parameters of the decomposition reaction of PNB encapsulated in PI-2611 in Table 31 show the encapsulated reaction is also first order. A comparison of the dynamic TGA thermograms for unencapsulated and encapsulated PNB decomposition showed the slopes of the two TG curves slightly differ, but both curves show a single drop in weight with time or temperature. The consistency in the shape of the TGA curve along with the result that both reactions follow first order kinetics indicates the mechanism of the reaction does not seem to be affected by the encapsulation. The change in slope of the TGA curves, however, indicates a change in the rate of the reaction. The kinetic parameters n, A, and E_a are used to calculate a rate constant from the Arrhenius equation at temperatures of 400^{o}C and 425^{o}C, listed in Table 31. Although the three sets of parameters (dynamic or isothermal methods) produce some variance in the rate constant values, the rate constant for the encapsulated PNB is always less than the rate constant for unencapsulated PNB. Therefore, the encapsulation does cause a slight decrease in the reaction rate.

The activation energy values for unencapsulated PNB, determined from the dynamic data using the average heating rate, and the isothermal data, are slightly smaller than for encapsulated PNB. The activation energies calculated from the dynamic TGA data and the instantaneous heating rate show the opposite effect. However, the results using the average heating rate provide a better measure of the overall reaction parameters because large fluctuations in the data due to the heating rate are minimized. A larger percentage of PNB remains after the cure at 350^{o}C for one hour when the sacrificial

polymer is encapsulated in PI-2611 (99.6% with a 95% confidence interval of 4.42% for encapsulated PNB vs. 86.83% ± 0.78% for unencapsulated PNB). The encapsulation seems to prevent the initial loss of material at a lower temperature. Since the decomposition reaction in the unencapsulated PNB samples is initiated during the 350°C hold, the apparent activation energy for the overall decomposition reaction following the hold period is slightly less than for PNB encapsulated in PI-2611. Both the isothermal and the dynamic TGA data also show that the encapsulated PNB decomposition contains more residual weight at 500°C, or after several hours. The residual weight could derive from: 1) the volatile products of the PNB decomposition reacting with or dissolving in the polyimide overcoat material and not completely leaving the system; or 2) the encapsulated PNB reaction not reaching the same extent of conversion, leaving a thicker residual material inside the air-gap. Therefore, the residual surfaces following the decomposition of unencapsulated or encapsulated PNB have been investigated and the results are discussed in the following section.

Table 32: Kinetic parameters determined by Wedlake [69] for the decomposition of 90/10 butyl/TES PNB in nitrogen.

	Value from dynamic TGA data	**Value from isothermal TGA data**
E_a, activation energy (kJ/mol)	236.7 ± 4.7	228.0 ± 6.7
n, reaction order	0.9909 ± 0.0057	1.042 ± 0.075
A, pre-exponential constant (min^{-1})	$1.087 \times 10^{17} \pm 4.9 \times 10^{15}$	$2.243 \times 10^{16} \pm 6.0 \times 10^{14}$

7.4 Analysis of Surfaces Following the Decomposition of Unencapsulated and Encapsulated PNB Sacrificial Material

7.4.1 X-ray photoelectron spectroscopy (XPS) of residual surfaces

X-ray photoelectron spectroscopy (XPS) was used to examine the chemical composition of Au surfaces exposed to the decomposition of PNB in a nitrogen environment. The PNB was decomposed while unencapsulated, encapsulated in SiO_2, and encapsulated in polyimide PI-2611. The TGA data indicate a higher weight percentage of residual material when PNB is in the encapsulated state, and exposed to the same temperature cycle as compared with unencapsulated PNB. Analysis of the elemental composition of the final surfaces can indicate possible origins of the residual material, and provide a relative thickness comparison from one sample to another.

Each residual surface was scanned through all binding energies using XPS to detect the elements present on the Au surface. High resolution scans were then performed at three locations on the sample in the binding energy ranges of the detected elements. The atomic ratio of each element is derived at each location on the sample through analysis of the area under the peaks obtained from the high resolution scans. Table 33 contains the XPS results for both the unencapsulated and encapsulated samples, and shows all elements detected on each sample as well as the atomic percentage of each element. The atomic percentages in Table 33 represent the surfaces scanned immediately after loading into the XPS chamber, and following 90 s of Ar^+ sputtering, which removes approximately 45 Å of residual material. The x-ray penetration depth is 75 Å with a detection limit of approximately 15 Å.

Table 33: Atomic composition of residual surfaces following the decomposition of unencapsulated PNB and PNB encapsulated in either PECVD deposited SiO_2 or polyimide PI-2611.

Sample	Original Film Thickness (μm)	Analysis depth	Atomic Percentage of Elements						
			C	O	Si	Al	F	Ti	Au
Unencapsulated PNB	2.69	surface	65.3	20.3	8.20	2.14	--	0.20	2.14
		90 s sputter	40.2	32.9	6.47	10.7	0.79	0.63	8.28
Unencapsulated PNB	8.66	surface	67.9	18.6	9.79	1.93	--	--	1.82
		90 s sputter	36.7	29.9	2.34	12.2	1.38	0.66	16.9
Unencapsulated PNB	20.1	surface	64.1	20.5	9.73	1.43	--	--	4.28
		90 s sputter	28.1	36.2	1.56	17.7	1.92	1.45	13.1
PNB encapsulated in Ti/SiO2	2.69	surface	82.6	14.2	2.45	--	0.51	0.17	0.06
		90 s sputter	86.0	8.21	4.26	--	--	1.01	0.52
PNB encapsulated in Ti/SiO2	8.66	surface	87.8	8.77	3.39	--	--	--	0.03
		90 s sputter	94.9	2.18	2.79	--	--	--	0.10
PNB encapsulated in Ti/SiO2	20.1	surface	88.4	8.37	3.16	--	--	--	0.05
		90 s sputter	94.3	2.40	3.20	--	--	--	0.09
PNB encapsulated in PI-2611	2.69	surface	85.8	11.1	2.81	--	0.36	--	--
		90 s sputter	93.9	3.67	2.44	--	--	--	--
PNB encapsulated in PI-2611	8.66	surface	85.5	10.4	3.90	--	--	--	--
		90 s sputter	95.2	2.53	2.29	--	--	--	--
PNB encapsulated in PI-2611	20.1	surface	87.5	9.97	2.51	--	--	--	--
		90 s sputter	95.9	2.08	1.98	--	--	--	--

The XPS results show several differences between the residual surfaces of encapsulated and unencapsulated PNB decomposition. One significant difference is the relative percentages of C and O in the unencapsulated and encapsulated PNB samples. The resulting surfaces from decomposition of three different film thicknesses of unencapsulated PNB have C atomic percentages after Ar^+ sputtering of 40.9%, 36.7%, and 28.1%, and O atomic percentages of 23.9%, 29.9%, and 36.2%. The surfaces exposed to the decomposition of PNB encapsulated in either SiO_2 or PI-2611 have a greater C content varying from 86.0 to 95.9 atomic percent, and also less O content of 2.08% to 8.21%. Carbon is often absorbed onto the sample from exposure to the environment. The Ar^+ sputtering is performed to remove this residual layer from the top surface of the residue. The atomic percentages of C on the surfaces from unencapsulated PNB decrease from Ar^+ sputtering by 25-30%, along with a small decrease in Si content. To account for the decrease of these elements, the oxygen content increases by approximately 10-15%, with simultaneous increases in Al, F, and Au percent. The surfaces from encapsulated PNB decomposition show an opposite effect. The atomic percentage of C increases after sputtering the samples from PNB encapsulated in either SiO_2 or PI-2611, and the oxygen content decreases. The Si content in the residual films from encapsulated PNB decomposition remains approximately constant.

The C content of the residual surfaces is not a function of film thickness for either unencapsulated or encapsulated decomposition. The decrease in C content after sputtering as film thickness increases for unencapsulated PNB is a result of the higher content of other elements. Only the unencapsulated PNB samples have F and Al present in the residual surface material. Both these elements may result from the hard mask and

dry-etching process. Al is used as the hard mask material, and CHF_3 is one of the process gases in the RIE etch process. The 20.1 μm thick film requires over twice the process time in the RIE chamber than the other two films, and has an Al content almost twice the other films. The atomic ratio of these elements increases when the top surface of the film is sputtered away. The amount of Al and F throughout the film actually may be constant, but the surface carbon lowers the atomic ratio at the surface. The PNB passes through its T_g around the decomposition temperature. Therefore Al and F on the top surface of the unencapsulated PNB may migrate into the film as the decomposition reaction occurs. The contamination elements are likely also present in the encapsulated PNB samples. However, if these contaminants are initially on the top surface of the undecomposed PNB, they may adhere to and be removed along with the overcoat material.

The atomic percentage of Au detected on the residual surfaces is another significant difference between the samples. A higher Au atomic percentage is a result of the XPS detection limit reaching a depth where the Au substrate is visible underneath the residual film. An accurate measurement of film thickness is not a result from the XPS analytical technique. However, the relative film thickness between samples is determined. The results show that the thickness of the residual film is dependent on the material used as the encapsulant for PNB sacrificial material. Au content of 8 to 17 atomic percent is detected by the XPS in the residual film from unencapsulated decomposition. The Au signal is barely detected by the XPS in the residual films from PNB decomposition while encapsulated in SiO_2. Au cannot be detected by the XPS in the residual films from PNB decomposition while encapsulated in PI-2611. It is possible that the residual film is present on all surfaces throughout the air-cavity and a portion of it

is removed with the overcoat material. Therefore, an exact measurement of residue thickness cannot be determined. Regardless, the XPS results clearly show that the encapsulated PNB samples clearly have thicker residual films than the unencapsulated PNB samples.

In addition to variation in thickness, the composition of the residual surfaces also indicates differences in the residue remaining from the unencapsulated and encapsulated PNB decomposition. Sources of silicon and oxygen in the residual films include the TES groups attached to the PNB backbone, attachment of SiO_2 molecules from the overcoat material, and the adhesion promoter VM-652 used with PI-2611 overcoat material (solution of 1-amino-2-propyl-triethoxysilane). Oxygen may also be present on the top surface of the film from absorption of CO_2 or water vapor in the atmosphere. The surfaces from encapsulated PNB contain much larger Si:O ratios than the unencapsulated PNB surfaces. In addition, the Si:O ratio increases when the top surface is removed by sputtering, and also increases with increasing film thickness. The Si:C ratio is the largest for the unencapsulated PNB surfaces, second largest for the surfaces from PNB encapsulated in SiO_2, and smallest for PNB encapsulated in PI-2611. In all cases the Si:C ratio decreases with increasing original film thickness. These atomic ratios indicate the remaining surfaces from the decomposition of encapsulated PNB are much more carbon-rich than the unencapsulated PNB surfaces. The encapsulation may not allow as many of the higher molecular weight products to escape during the decomposition, resulting in a lower degree of conversion, and a larger carbon content in the remaining film. Wedlake [69] showed that many of the decomposition products of unencapsulated polynorbornene are multi-ringed high MW carbon species. The diffusivity of the species

in the polyimide or SiO_2 is expected to decrease with increasing size of the molecules. The inability of the largest species to permeate out of the overcoat film could account for the higher carbon content seen in the residual material. In addition, the larger Si:O ratio in the encapsulated films indicates that many of the TES groups may still be intact, or more remain in the residual film. Intact TES groups attached to the high MW carbon-species has also been reported by Wedlake, and could account for the increase in Si:O content.

7.4.2 Goniometry results of residual surfaces

The nature of the residual surfaces following the decomposition of either unencapsulated or encapsulated PNB are further investigated using goniometry to determine the contact angle of distilled, deionized water on the residual surface. The samples used for goniometry are portions of the same samples prepared for XPS analysis. Two to four contact angle measurements are obtained from each surface after removal of the SiO_2 or PI-2611 encapsulating material. The average of these measurements and one standard deviation is reported in Table 34. No significant difference in hydrophobicity is observed in the unencapsulated and encapsulated PNB samples. All samples have a hydrophobic surface following the PNB decomposition and removal of the encapsulating layer. Exposure of the residual material to a high-temperature oxygen-rich environment may be used to alter the nature of the residue from hydrophobic to hydrophilic. To investigate if this can be done to the material in the encapsulated state, portions of the identical samples with the overcoat material intact were placed on a hotplate at 300^{o}C in ambient air for 1 hour. The encapsulating material was removed following this heat-treatment step and the contact angle was re-measured. The results of these measurements

are in Table 34. The residual surface formed from unencapsulated PNB changed from hydrophobic to hydrophilic after heat-treatment in an ambient environment. The samples encapsulated in SiO_2 also changed from hydrophobic to hydrophilic. The samples encapsulated in PI-2611 polyimide showed little or no change in the contact angle after heat treatment. It may take a longer treatment to convert these residues to a hydrophilic nature since the oxygen from the ambient must diffuse through the polyimide film and into the air-cavity.

Table 34: Contact Angle measurements of residual surfaces following the decomposition of unencapsulated PNB and PNB encapsulated in either SiO_2 or polyimide PI-2611.

		Average Contact Angle in degrees (^{o})	
Sample	**Original Thickness (μm)**	**After PNB decomposition and overcoat removal**	**After heat treatment in Air**
Unencapsulated PNB	8.66	73 ± 2	40 ± 3
Unencapsulated PNB	20.1	102 ± 2	57 ± 1
PNB Encapsulated in SiO_2	8.66	93 ± 2	56 ± 2
PNB Encapsulated in SiO_2	20.1	99 ± 4	48 ± 2
PNB Encapsulated in PI-2611	8.66	77 ± 5	80 ± 1
PNB Encapsulated in PI-2611	20.1	95 ± 2	85 ± 1

7.5 Optimization and Discussion of PNB Decomposition

The TGA thermograms, the kinetic parameters of the decomposition reaction, and XPS results all indicate differences in the decomposition of PNB when the polymer is encapsulated in a dielectric material. Various overcoat materials, however, likely affect the decomposition of the polymer to a different degree. Both PNB encapsulated in SiO_2 and PNB encapsulated in PI-2611 confirm a higher atomic percentage of carbon and a lower atomic percentage of oxygen on the residual surfaces following decomposition, compared to the surfaces from unencapsulated PNB. However, the oxygen and silicon content in the surfaces resulting from the PNB encapsulated in the two different overcoat materials varies. In addition, PNB encapsulated in PI-2611 indicates a thicker film of remaining residual material than from PNB encapsulated in SiO_2. The permeability of an overcoat material is influenced by two main factors: 1) the solubility of the volatile products in the overcoat film; and 2) the diffusion of the volatiles through the polymer film. These factors are, in turn, influenced by many variables, including the crystal structure of the overcoat, temperature, and any reaction of the volatile products with the overcoat film, i.e. hydrogen bond formation. Therefore, the kinetic parameters calculated for the decomposition reaction of PNB encapsulated in PI-2611 may only apply to that particular sacrificial polymer/overcoat material combination. The parameters are not applicable to all decompositions of encapsulated PNB. However, the kinetic parameters for unencapsulated PNB decomposition and the decomposition of PNB encapsulated in PI-2611 are used in this section to re-optimize the decomposition based on the change observed in the reaction rate.

7.5.1 Analysis of the time of decomposition from the reaction kinetic parameters

In many applications, including as an intralevel dielectric, air-gaps must be fabricated on top of substrates containing active devices. High-temperature steps may degrade or warp the substrate, and induce the diffusion of metals or dopants into unwanted areas. Many materials and devices have strict thermal budgets. Therefore, the decomposition must be understood and optimized to reduce the thermal exposure of elements and materials on the substrate.

The overall decomposition of polynorbornene was represented by the following n^{th}-order kinetic rate expression described previously in Chapter 4, equation 4.8. The reaction order for either encapsulated or unencapsulated PNB has been shown to be first order, which simplifies the integration of equation 4.8. Assuming n = 1 and integrating over the limits of time from 0 to t and weight from W_o to W, equation 4.8 becomes:

$$t = \frac{\ln \frac{W_o}{W}}{k} \qquad \text{Eq. (7.3)}$$

If the initial polymer weight of PNB, either unencapsulated or inside an air-cavity, is known, a time for decomposition of the polymer to reach a given conversion can be calculated using equation 7.3. Table 35 lists the geometries and dimensions of some air-gap designs on a lithography mask designed for mechanical testing. Air-gaps with these dimensions have been fabricated and mechanically tested, and are discussed in Chapter 9. The dimensions are selected based on the space limitations from the pitch of devices in the plane of the mask to 190 μm in the x-direction, and 1 cm in the y-direction. The shapes include four different diameter circles (circle 1 through circle 4), a square with sides 190 μm in length, an ellipse with a major axis 275 μm and a of minor axis of 190

μm, and two rectangles: 190 μm × 590 μm; and 190 μm × 9940 μm. A PNB film thickness of 10 μm is used for the sample calculations in the first 8 rows of Table 35. The last three rows in Table 35 are for the same geometry (an ellipse with major and minor axes of 150 μm and 120 μm), but film thicknesses of 5, 7, and 10 μm. The initial mass of PNB is determined from the geometry, film thickness, and the density of the material, about 0.95 g/cm^3. The final weight, W, corresponding to a reaction conversion of 95% or 99% is shown in the last two columns of Table 35. The averages of the values of n, A, and E_a in Table 31, and equation 7.2, are used to calculate time for decomposition of unencapsulated PNB and PNB encapsulated in PI-2611 at isothermal temperatures of 400^{o}C and 425^{o}C. The results are shown in Table 36. The results are for decomposition at isothermal temperatures of 400^{o}C and 425^{o}C, where *k* is a constant at each temperature. The time to reach a specific conversion is independent of the area and thickness of the PNB sacrificial material. However, a larger weight of PNB remains at constant conversion as the volume of the air-gap is increased. Table 36 shows that the times for decomposition of either unencapsulated or encapsulated PNB at 400^{o}C are over 4 times longer than the time required for decomposition at 425^{o}C. Therefore, if a sample can withstand a temperature of 425^{o}C, or even higher, the throughput and time savings dramatically increase when the decomposition is performed at the higher temperature. The time for decomposition of PNB encapsulated in PI-2611 to a given conversion is about 1.2 times the time required for the decomposition of unencapsulated PNB. Any encapsulating which slows the decomposition reaction rate increases the time necessary for decomposition.

Table 35: Geometries and initial and final weight values for various PNB structures decomposed to 95 and 99 percent conversion.

Air-gap geometry				**PNB Volume** thickness = 10 μm	**Initial PNB Mass, W_o** Density = 0.95 g/cm^3	**Fractional Conversion**	
Shape	**Radius or Width (mm)**	**Length (mm)**	**Area (mm^2)**	**(cm^3)**	**(mg)**	**0.95 W (mg)**	**0.99 W (mg)**
Circle 1	190	--	28353	2.84E-07	0.27	0.0135	0.0027
Circle 2	130	--	13273	1.33E-07	0.13	0.0063	0.0013
Circle 3	110	--	9503	9.50E-08	0.09	0.0045	0.0009
Circle 4	90	--	6362	6.36E-08	0.06	0.0030	0.0006
Square	190	190	36100	3.61E-07	0.34	0.0171	0.0034
Ellipse 1	190	275	41037	4.10E-07	0.39	0.0195	0.0039
Rectangle 1	190	590	112100	1.12E-06	1.06	0.0532	0.0106
Rectangle 2	190	9940	1888600	1.89E-05	17.94	0.897	0.197
Ellipses							
Ellipse 2, 5 μm thick	120	150	14137	7.07E-08	0.07	0.0034	0.00067
Ellipse 2, 7 μm thick	120	150	14137	9.90E-08	0.09	0.0047	0.00094
Ellipse 2, 10 μm thick	120	150	14137	1.41E-07	0.13	0.0067	0.0013

Table 36: Estimated time of reaction for the thermal decomposition of unencapsulated PNB and PNB encapsulated in PI-2611.

	Time to reach a conversion of:			
	95% conversion		**99% conversion**	
	T = 400 °C	**T = 425 °C**	**T = 400 °C**	**T = 425 °C**
Unencapsulated PNB	47.4 min.	10.3 min.	72.9 min	15.9 min.
PNB encapsulated in PI-2611	57.9 min.	12.6 min.	89.0 min	19.3 min.

The time calculations are on the basis of conversion, assuming a theoretical reaction conversion of 95% or 99%. An approximation of residual thickness based on the remaining weight in each of the geometries, assuming the density of any residue was 1 g/cm^3 gives about 0.5 μm for 95% conversion and 0.1 μm for 99% conversion. The initial mass of PNB in the each of the air-gap geometries described in Table 35 is 10^2 to 10^4 times smaller than the mass of a TGA sample. Therefore, the residual weight shown by the TGA for the decomposition of encapsulated PNB would be very difficult to visually detect. In practical application, a tolerable amount of residual material would be identified either by weight or by thickness, and then the time for decomposition would be chosen based on the conversion required to reduce the polymer weight to the chosen amount. In the case of a non-isothermal decomposition, the temperature and time relationship of the decomposition profile is known. Substitution of this relationship into the Arrhenius expression for *k* in equation 4.8 allows a subsequent solution for the total time required for the decomposition at non-isothermal conditions.

7.6 The Effect of Area, Volume, and Rate of Decomposition on Air-gap Formation

The preceding section discussed the calculation of the time required for isothermal decomposition of PNB. However, a fast decomposition at an isothermal temperature may not always be the best process technique to use for air-gap fabrication. Chapter 5 described dome-shaped air-gaps which result from pressure accumulation inside the air-cavity during decomposition, combined with a softening of the overcoat polyimide. The maximum pressure would be achieved under the following conditions: 1) all the sacrificial polymer decomposes to monomer units inside the air-gap; 2) the permeation rate out of the air-cavity is zero; 3) the maximum volume of the air-gap is the

volume of the solid PNB (no overcoat expansion); and 4) the decomposition reaches 100% conversion. A course approximation of the maximum pressure is determined using the ideal gas law. The decomposition of any thickness of sacrificial PNB at an isothermal temperature of 400^{o}C would equate to a pressure inside the air-gap of 325 atm! A pressure of this magnitude would never form under real conditions. However, if the production rate of volatile species from decomposition is greater than the permeation rate of volatiles out through the encapsulating material, a net positive pressure builds inside the air-cavity. The accumulated amount of pressure is examined by a mass balance on the volatiles in an air-cavity represented by the following expression:

mass accumulated volatiles = mass produced by reaction – mass lost to permeation

The mass balance is represented as the change in total mass per unit time by equation 7.5:

$$\frac{dm_{TOTAL}}{dt} = \frac{dm_{RXN}}{dt} - \frac{dm_{PERM}}{dt} \qquad \text{Eq. (7.4)}$$

The mass of volatile gases inside the air-cavity is the source of any accumulated pressure inside the air-cavity. The mass of volatiles produced by the decomposition reaction is equivalent to the mass lost from the initial weight of PNB. Therefore, the rate of production of volatiles from the reaction is equivalent to the rate of loss of solid PNB. The rate of production of volatiles at any point in the reaction is represented by the first-order kinetic rate equation for the decomposition of PNB, equation 7.5. To simplify the mass balance, the rate of production of volatiles from the reaction is considered independent of pressure.

$$\frac{\mathrm{dm}_{\mathrm{RXN}}}{\mathrm{dt}} = -\frac{d(W_o - W)}{dt} - \frac{dW}{dt} = kW \qquad \text{Eq. (7.5)}$$

The rate of volatile mass lost from permeation through the overcoat material is a function of the pressure inside the air-cavity. The transmission of a gas through a membrane is represented as a function of time and the partial pressure drop of the gas across the membrane, equation 7.6 [99]:

$$\frac{\Delta m_{gas}}{\Delta t} = P_e \frac{A\Delta p}{l} \qquad \text{Eq. (7.6)}$$

P_e is the permeability coefficient of the gas through the membrane material; $\Delta m_{gas}/\Delta t$ is the flux of volatiles out of through the overcoat membrane in time interval Δt; A is the area of the membrane; l is the thickness of the membrane; and Δp is the partial pressure difference across the membrane. In the air-gap decomposition process, Δp is a function of time. The partial pressure of the products from decomposition of the PNB outside the air-gap is zero. The nitrogen purge, operating throughout the decomposition, would flush the decomposition products away from the sample as they permeate out the air-cavity overcoat material. Therefore, Δp is equivalent to p, or the pressure inside the air-cavity. Equation 7.7 represents the rate of change in mass due to permeation of volatiles out of the air-cavity.

$$\frac{dm_{PERM}}{dt} = P_e \frac{l}{A} p \qquad \text{Eq. (7.7)}$$

The change in total mass of volatiles inside the air-cavity is a function of *both* time and pressure. The ideal gas law is used to determine the relationship between the rate of change in the total mass of volatiles inside the air-cavity with time, and the rate of change in pressure:

$$\frac{dm_{TOTAL}}{dt} = \frac{V \cdot MW}{RT}\frac{dp}{dt} \qquad \text{Eq. (7.8)}$$

The expressions for all three mass rate terms in the mass balance are replaced with functions of time and pressure to obtain equation 7.9

$$\frac{V \cdot MW}{RT}\frac{dp}{dt} = kW - P_e \frac{A}{l} p \qquad \text{Eq. (7.9)}$$

Equation 7.9 describes the relationship between the pressure formed inside the air-cavity, based on the decomposition conditions and properties of the sacrificial and encapsulating materials.

7.6.1 Pressure inside the air-gap during isothermal decomposition

Equation 7.9 is used to consider the pressure formed inside an air-gap during an isothermal decomposition at temperature, *T*. The volume of gaseous space inside the air-cavity is a function of the time of decomposition, and increases as the solid sacrificial material converts to volatile products. If the encapsulating polymer does not deform, the volume filled by the volatile products is equivalent to the mass lost from the solid PNB, multiplied by the volume that mass occupied as a solid. The volume is represented by Equation 7.10.

$$V = (W_o - W)\frac{1}{r_{solid}} = \frac{W_o}{r_{solid}}(1 - e^{-kt}) \qquad \text{Eq. (7.10)}$$

In equation 7.10, r_{solid} is the density of the solid PNB polymer. The expression for *V* given in equation 7.10 replaces *V* in equation 7.9 to yield a first-order linear differential equation. A differential equation of the form of equation 7.10 is solved using the

integrating factor technique, where each term in equation 7.9 is multiplied by the integrating factor. The form of the integrating factor specific to equation 7.9 is shown in equation 7.11. The group of constants in the integrating factor equation, and in equation 7.11, is represented by a general constant, C_1. The relationship for W as a function of time is determined by integration of the first-order kinetic equation to obtain $W = W_o e^{-kt}$. This substitution is made for W and each side of equation 7.9 is multiplied by the integrating factor to yield equation 7.12.

$$integrating\ \ factor = e\wedge(\int P_e \frac{A}{l}\frac{RT}{MW \cdot W_o}) r_{solid} \frac{1}{(1-e^{-kt})} dt = e\wedge(\int C_1 \frac{1}{(1-e^{-kt})} dt)$$

$$where\ \ C_1 = P_e \frac{A}{l}\frac{RT}{MW \cdot W_o} r_{solid}$$

Eq. (7.11)

$$\frac{dp}{dt}\exp[C_1 t + \frac{C_1}{k}\ln(1-e^{-kt})] + C_1 \frac{1}{(1-e^{-kt})}\exp[C_1 t + \frac{C_1}{k}\ln(1-e^{-kt})] p e^{C_1 t} = \frac{kRT}{MW} r_{solid}(e^{-kt})\frac{1}{(1-e^{-kt})}\exp[C_1 t + \frac{C_1}{k}\ln(1-e^{-kt})]$$

Eq. (7.12)

The subsequent integration of equation 7.12 yields equation 7.13, the solution for pressure as a function of time at an isothermal decomposition temperature (reaction rate is also constant).

$$p = \frac{RT}{MW} r_{solid} \frac{e^{(C_1 - k)t}}{(C_1 - k)(e^{C_1 t})} \frac{1}{(1-e^{-kt})^{(C_1/k)}} (Hypergeometric\ {}_2F_1[1-\frac{C_1}{k}, 1-\frac{C_1}{k}; 2-\frac{C_1}{k}; e^{-kt}])$$

Eq. (7.13)

Equation 7.14 is the series approximation solution to the Hypergeometric Function ${}_2F_1$.

$$ {}_2F_1[h, j; k; z] = 1 + \frac{hj}{1!k} z + \frac{h(h+1)\,j(j+1)}{2!k(k+1)} z^2 + \frac{h(h+1)(h+2)\,j(j+1)(j+2)}{3!k(k+1)(k+2)} z^3 + ... $$

Eq. (7.14)

Some typical values for each of the variables in equation 7.13 are given in Table 37, based on a square air-gap with dimensions of 190 × 190 μm, and an initial PNB thickness of 10 μm. The volume is considered a function of time, but any change in the volume from expansion of the air-gap beyond the original dimensions of the solid PNB is omitted. The decomposition is performed isothermally at 425°C, reaches a conversion of 95%, and the kinetics are based on the decomposition of PNB encapsulated by PI-2611. Permeability is a function specific to the overcoat material and the permeant, and is usually studied experimentally for gases diffusing through solid materials [100]. A value of about 2×10^{-13} $(cm^3(STP)\cdot cm)(Pa\cdot cm\cdot s)^{-1}$ is reported for the diffusion of CO_2 at 25°C in a polyimide with the same chemical composition as PI-2771 or PI-2540 [101]. Water vapor at the same temperature through the polyimide has a P_e value of 1900×10^{-13} in the same units. The permeability is affected by temperature, based on an Arrhenius relationship. Typical polymer permeability is reported to generally increase by 30 to 50% for each 5°C increase in temperature [99]. The larger molecular weight products of the decomposition likely diffuse at a slower rate than CO_2 due to the increase in molecular size. The 30% increase as a basis would increase the value of permeation to approximately 5×10^{-12} at 425°C.

The values listed in Table 37 are used in equation 7.13 to obtain a value of the pressure formed in a specific time period. A time of 12.57 minutes corresponds to a reaction conversion of 95% of the solid PNB to gaseous products. Using the values in

Table 37, the ${}_2F_1$ Hypergeometric Function series approximation converges to a value of 0.4581 for a time of 12.57 min., resulting in a pressure of 0.007 atm. This pressure equates to a force on the overcoat polyimide of 0.026 N. If the mechanical properties of the overcoat are not entirely degraded at the decomposition temperature, the overcoat should easily withstand a force of this magnitude. However, since the experimental results show deformation of the overcoat polymer, either the elastic modulus of the polymer has degraded or decreased due to temperature, or the pressure inside the air-gap has decreased by the time the reaction reaches 95% conversion. The same pressure calculation is performed using a time of 5 min., and results in a pressure of 7.15 atm, the equivalent of 26 mN on the overcoat polymer. A significant deflection of the overcoat material occurs under this amount of force, as to be shown in Chapter 9. When the time reaches 60 min., the pressure has decreased to 1.5×10^{-5} atm. The pressure is being generated during the initial portion of the reaction when the PNB begins to decompose and the volume of space for the gaseous products to fill is small. The permeation rate is the rate-limiting step during this portion of the decomposition and results in a net gain of pressure inside the air-cavity. The pressure decays as the volume inside the air-cavity increases and the reaction reaches high values of conversion.

The parameter, C_1, in equation 7.13 is an indicator of the permeation rate through the air-gap overcoat material. An increase in C_1 results in a decrease in the pressure at any time, t. The factors which contribute to a larger permeation rate of volatiles through the overcoat material result in an increase of the value of C_1, including an increase in P_e, an increase in T, or an increase in the area of the overcoat material. The value of C_1 decreases if the membrane thickness, l, increases or the initial mass of solid PNB

increases without a simultaneous increase in the area of the overcoat material. On the other hand, the term e^(-C_1t) decays more rapidly as the value of C_1 increases, leading to a reduction in pressure. When C_1 >> k, the Hypergeometric function and the term (1-e^{-kt})^(C_1/k) are strong functions of C_1 and result in a pressure of zero. In this case, the reaction rate is the rate limiting step and all the volatile products permeate out through the overcoat material, resulting in no pressure accumulation.

Table 37: Typical values for the variables in equation 7.13, based on a square air-gap with dimensions of 190 μm ×190 μm, formed from 10 μm thick sacrificial PNB, decomposed isothermally at 425°C to a reaction conversion of 95%.

VARIABLE	**TYPICAL VALUE**
Temperature, T	698 K
Overcoat Area, A	36100 μm^2
Overcoat thickness, l	8 μm
Air-gap volume, V	3.61×10^{-7} cm^2
Rate constant, k, at 425 °C	0.238 $(min)^{-1}$
Universal Gas Constant, R	82.057 atm·cm^3(mol·
MW	161 g/mol (average wt.-all monomer)
W_o	0.34 μg
P_e	~2×10^{-13} cm^3(STP)·cm(cm^2·Pa·s)$^{-1}$ for CO_2 in PI-2771/PI-2540 at 25°C
time	12.57 min (95% conversion at 425°C)

7.6.2 Air-gaps with identical overcoat area and thickness, but different PNB thickness

In order to evaluate the effect of PNB thickness on an air-gap, equation 7.13 is used to compare the pressure accumulated in air-gaps with the same overcoat area and thickness, but different initial PNB thickness. Two air-gaps are considered where one initially contains twice the PNB thickness of the other: air-gap #1: initial PNB weight = W_o, Area = A, PNB thickness = h; and air-gap #2: initial PNB weight = $2W_o$, Area = A, PNB thickness = $2h$. The only parameter in equation 7.13 that varies between the two air-gaps is C_1. The air-gap with a thickness of $2h$ has a value of C_1 equal to 1/2 the value of C_1 for the air-gap with thickness, h. A comparison of the two air-gaps results in equation 7.15, where p_1 and C_1 represent the pressure and the constant for the air-gap with a thickness of h.

$$\frac{p_1}{p_2} = \frac{(\frac{1}{2}C_1 - k)}{(C_1 - k)}(1 - e^{-kt})^{(C_1/2k)} \frac{{}_2F_1[airgap\#1]}{{}_2F_1[airgap\#2]} \qquad \text{Eq. (7.15)}$$

The ratio of the Hypergeometric Function for the two air-gaps varies according to the materials and parameters for the decomposition reaction. If k and C_1 are about the same in magnitude, or $k >> C_1$, the ratio of the two functions is one. The resulting pressure, p_1 is a fraction of p_2. If $k > C_1$, the ratio of the functions yields a number < 1, and the pressure difference between the two air-gaps increases in magnitude. The analysis verifies that thickness does have an impact on the amount of pressure formed in two air-gaps of similar area. However, equation 7.15 only represents the case of an isothermal decomposition for a controlled amount of time.

7.6.3 Constant rate of conversion decomposition

In an isothermal decomposition of PNB, the rate of volatile formation is greater when the reaction is at low conversion and much of the solid PNB mass remains. In order to control the rate formation of volatiles, a constant rate of conversion decomposition program is considered, where C_R is the rate of conversion. The rate of permeation of the gas through the overcoat material is identical to the previous case and is described by Equation 7.7. However, temperature no longer is a constant. The temperature/time relationship is determined by the substitution of C_R into the overall rate equation in terms of conversion, along with the Arrhenius expression for k, and solving for temperature to yield equation 7.16.

$$T = \frac{-E_a}{R \ln\left(\frac{C}{A(1-Ct)}\right)} \qquad \text{Eq. (7.16)}$$

The mass balance on the volatiles per unit time is now represented by equation 7.17. Substitution of equation 7.16 for temperature and $(W_o\text{-}W)r_{solid}$ for volume into equation 7.17, followed by separation of variables and integration results in equation 7.18

$$\frac{V \cdot MW}{RT}\frac{dp}{dt} = C_R(W_o - W_f) - P_e\frac{A}{l}p \qquad \text{Eq. (7.17)}$$

$$\frac{-l}{P_e A}\ln[C_R(W_o - W_f) - P_e\frac{A}{l}p] = \frac{-E_a}{MW \cdot C_R(W_o - W_f)r_{xolid}}\int\frac{1}{t}\frac{1}{\ln\left(\frac{C_R}{A(1-C_R t)}\right)}dt$$

Eq. (7.18)

The right side of equation 7.18 requires numerical integration to find a solution for pressure. However, the equation is simplified for the case of two air-gaps that vary only in initial PNB thickness, decomposed at the same rate of conversion. To further simplify, the residual mass at the end of the reaction, W_f, is assumed to be zero. The value of the integral in equation 7.17 is equivalent for both air-gaps and a ratio of the equations reduces to equation 7.19

$$\frac{(2C_R W_O - P_e \frac{A}{l} p_2)^{2W_o}}{(C_R W_o - P_e \frac{A}{l} p_1)^{W_o}} = 1 \qquad \text{Eq. (7.19)}$$

Equation 7.19 yields a solution of $p_2 > p_1$ for positive values of C_R, W_o, P_e, A, and l. The term $C_R W_o$ represents the amount of mass produced by the reaction per unit time and $P_e(A/l)p$ is indicative of the permeation rate of volatiles leaving the system through the overcoat material. At small values of C_R, the permeation term dominates, and at large values of C_R, the reaction term dominates. Therefore, either process may be rate limiting, depending on the rate of conversion during the decomposition.

7.6.4 Results of air-gaps fabricated at a constant rate of conversion

Air-gaps are fabricated according to the temperature-time profiles for a constant rate of conversion. The average kinetic parameters for the decomposition of PNB encapsulated by PI-2611 and equation 7.16 are used to build a temperature-time relationship at values of C_R equal to 0.1, 0.5, 1, 2, and 5% conversion/min. The temperature-time relationships are plotted as the dotted or gray curves in Figure 88 through Figure 92. Experimental decomposition conditions are created to follow the

calculated temperature-time profile at each constant rate of conversion. The controller for the furnace used for the decomposition of samples requires a program with a maximum of 8 steps, each consisting of a ramp rate, a temperature level, and a dwell time. Temperature set-point control is in whole degrees Celsius, temperature heating rates to the nearest ^{o}C/min with a minimum of 1^{o}C/min, and dwell time control is in increments of 0.1 hour. The experimental temperature-time profiles are designed to follow the curves determined from the temperature-time relationship equation. However, the limitations of the temperature controller mandate a step-wise temperature program to best mimic the calculated curve. The experimental temperature-time conditions are plotted as the solid black curves in Figure 88 through Figure 92. In addition, the temperature profiles are described by individual steps in Table 38. The calculated temperature/time curves approach infinity as time increases. In order to perform the experiments in real conditions, all experimental curves followed the calculated curves to a maximum temperature of 425^{o}C, followed by a 0.5 hour hold at 425^{o}C to complete the decomposition process.

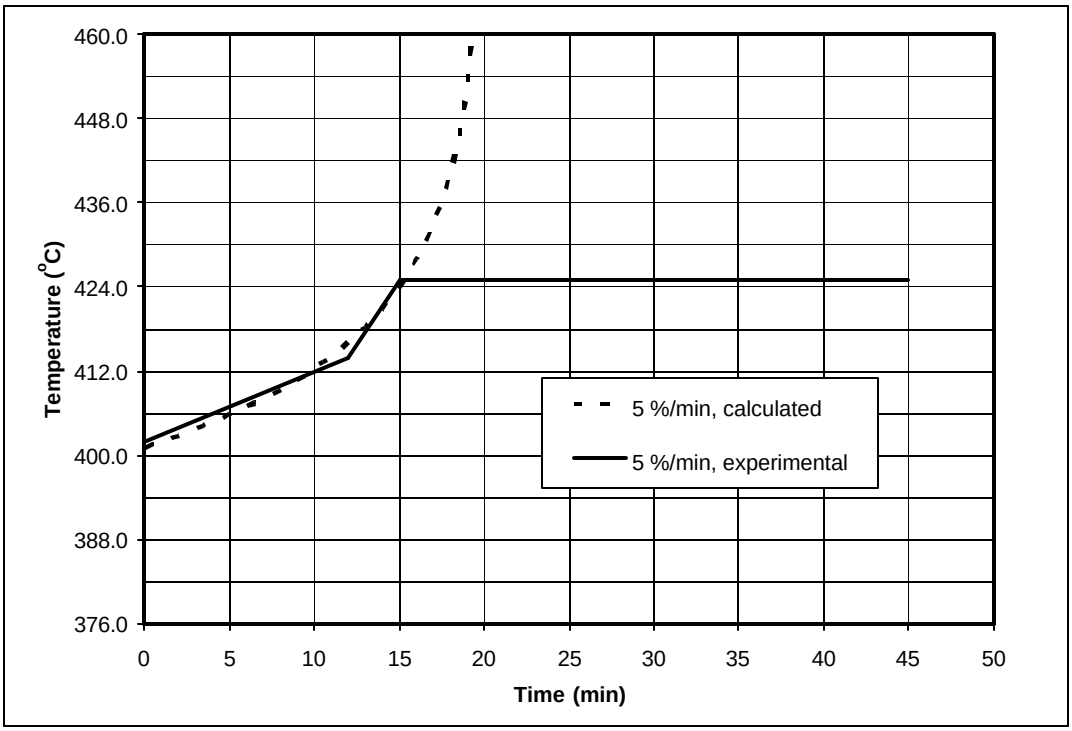

Figure 88: Calculated and experimental time/temperature profiles for the decomposition of PNB at a constant rate of conversion of 5 %/min.

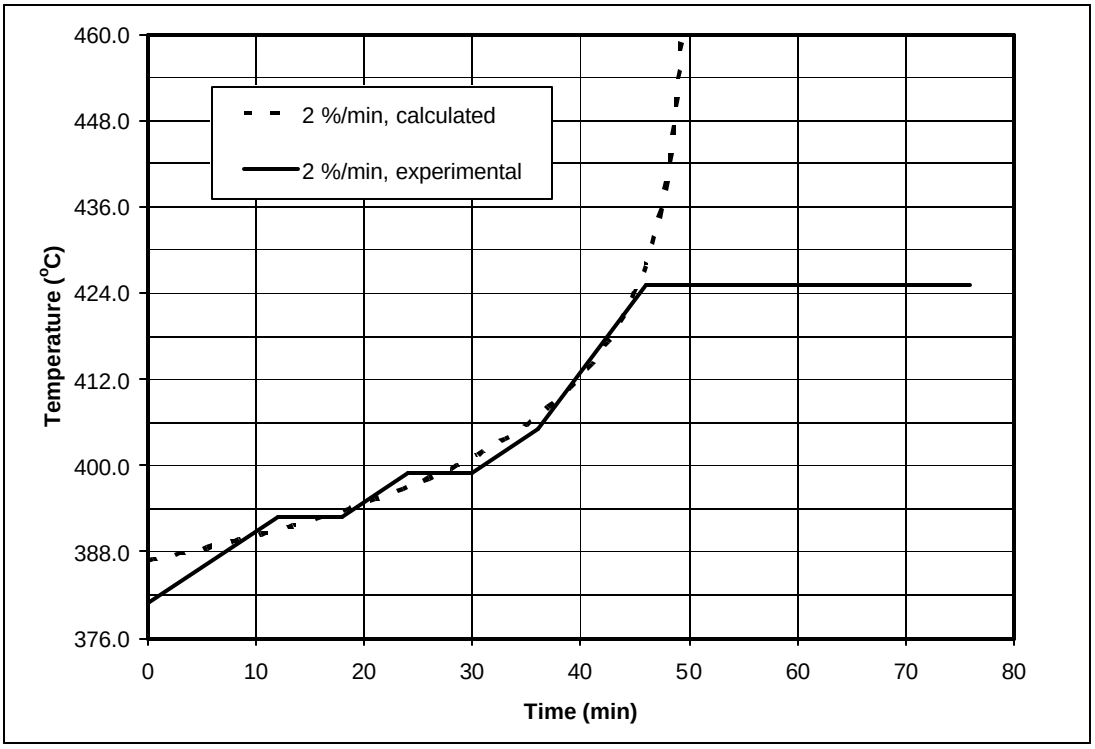

Figure 89: Calculated and experimental time/temperature profiles for the decomposition of PNB at a constant rate of conversion of 2 %/min.

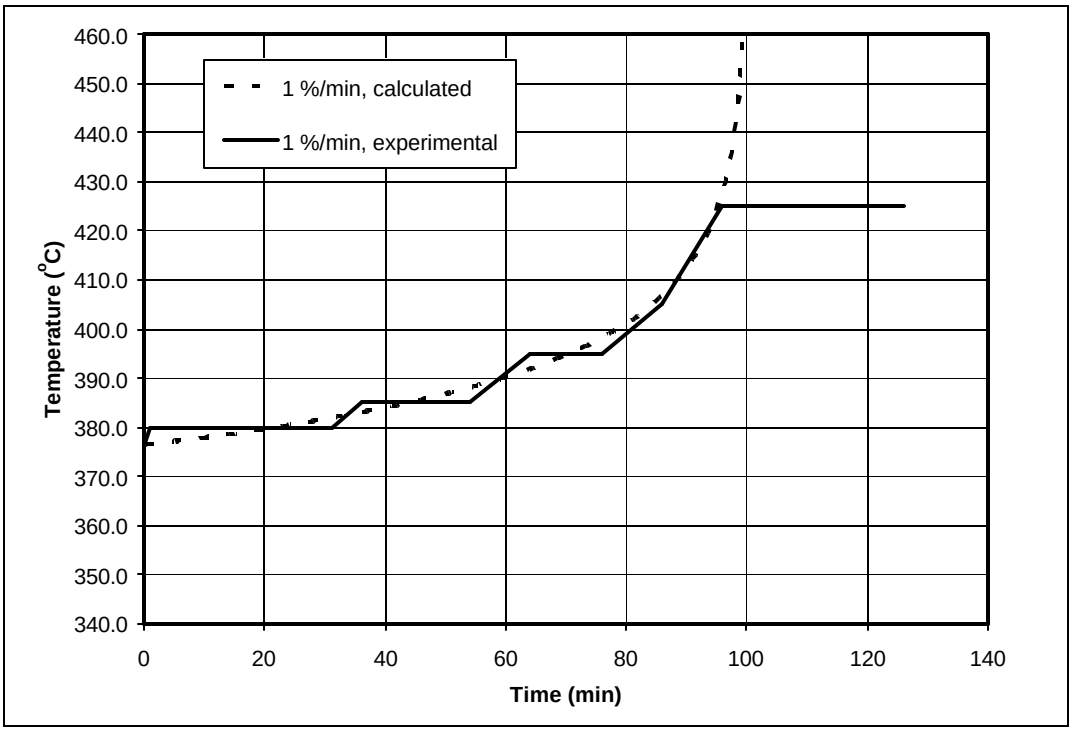

Figure 90: Calculated and experimental time/temperature profiles for the decomposition of PNB at a constant rate of conversion of 1 %/min.

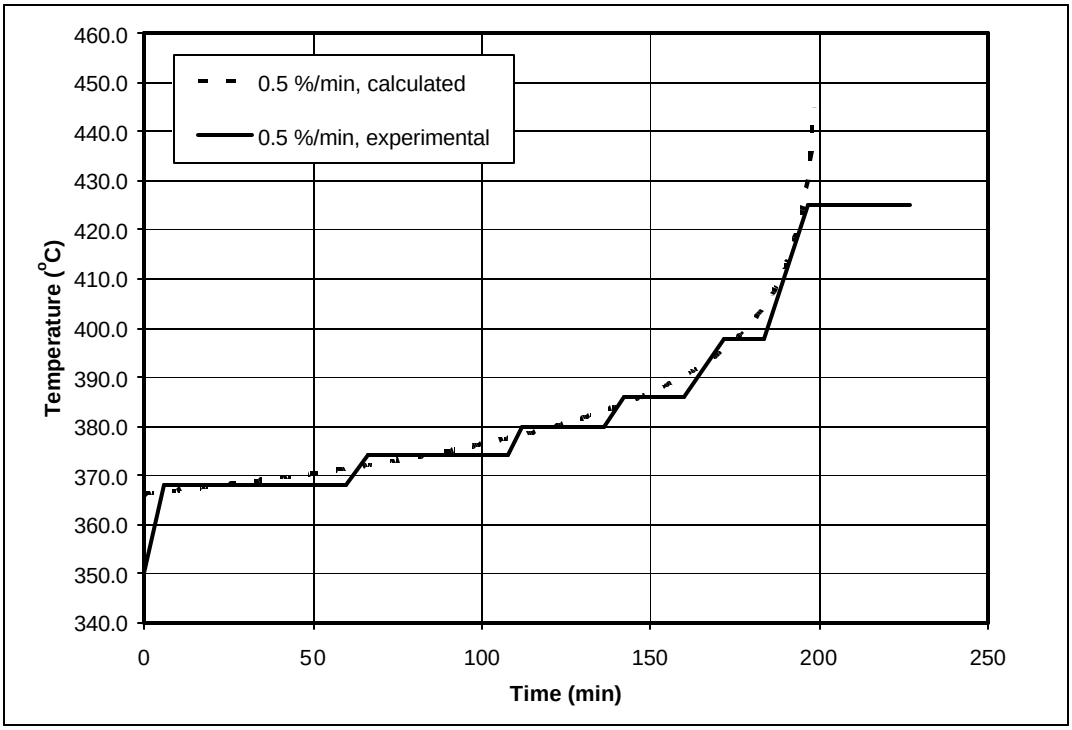

Figure 91: Calculated and experimental time/temperature profiles for the decomposition of PNB at a constant rate of conversion of 0.5 %/min.

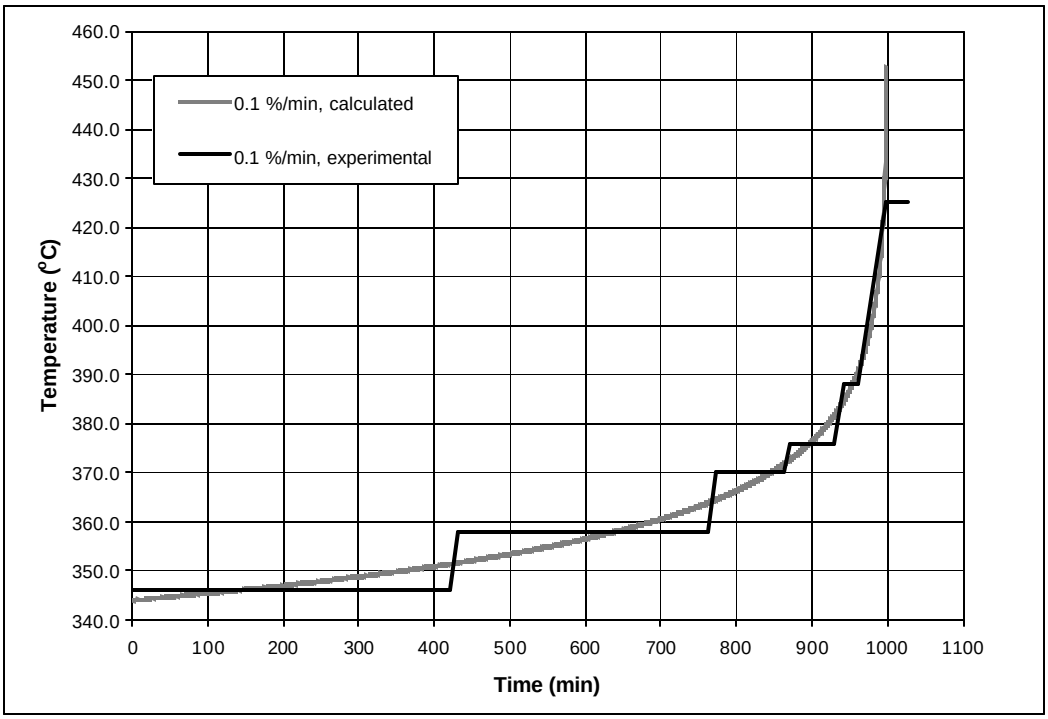

Figure 92: Calculated and experimental time/temperature profiles for the decomposition of PNB at a constant rate of conversion of 0.1 %/min.

Table 38: Experimental furnace programs for the constant rate of conversion decomposition of PNB.

	Conversion Rate				
Step	**0.1 %/min**	**0.5 %/min**	**1 %/min**	**2 %/min**	**5 %/min**
1	5 °C/min to 350 °C, hold 1.0 hr	5 °C/min to 350 °C, hold 1.0 hr	5 °C/min to 350 °C, hold 1.0 hr	5 °C/min to 350 °C, hold 1.0 hr	5 °C/min to 350 °C, hold 1.0 hr
2	1 °C/min to 346 °C, hold 7 hr	3 °C/min to 368 °C, hold 0.9 hr	5 °C/min to 380 °C, hold 0.5 hr	3 °C/min to 381 °C, no hold	5 °C/min to 402 °C, no hold
3	1 °C/min to 358 °C, hold 5.5 hr	1 °C/min to 374 °C, hold 0.7 hr	1 °C/min to 385 °C, hold 0.3 hr	1 °C/min to 393 °C, hold 0.1 hr	1 °C/min to 414 °C, no hold
4	1 °C/min to 370 °C, hold 1.5 hr	1 °C/min to 380 °C, hold 0.4 hr	1 °C/min to 395 °C, hold 0.2 hr	1 °C/min to 399 °C, hold 0.1 hr	4 °C/min to 425 °C, hold 0.5 hr
5	1 °C/min to 376 °C, hold 1.0 hr	1 °C/min to 486 °C, hold 0.3 hr	1 °C/min to 405 °C, no hold	1 °C/min to 405 °C, no hold	step to 25 °C
6	1 °C/min to 388 °C, hold 0.5 hr	1 °C/min to 398 °C, hold 0.2 hr	2 °C/min to 425 °C, hold 0.5 hr	2 °C/min to 425 °C, hold 0.5 hr	
7	1 °C/min to 425 °C, hold 0.5 hr	2 °C/min to 425 °C, hold 0.5 hr	step to 25 °C	step to 25 °C	
8	step to 25 °C	step to 25 °C			

Air-channels with initial PNB thickness of approximately 10, 20, and 30 mm were fabricated using each of the experimentally designed constant rate of conversion temperature-time profiles. Table 39 lists the resulting average height of several channels measured by profilometry and by SEM following the decomposition. SEM images of samples decomposed at 0.1, 1, and 5% conversion/min. are shown in Figure 93, Figure 94, and Figure 95. Table 39 indicates a general trend of an increase in the resulting channel height as the rate of conversion for the decomposition is increased. In addition, the pressure model for the comparison of air-gaps at an identical rate of conversion, equation 7.18, indicates the pressure formed during the decomposition is greater in an air-gap with a thicker initial PNB film. The average height of the air-channel does increase as the film thickness increases from 11.3, to 21.8, to 31.3 μm. However, even at the extremely slow decomposition rate of 0.1 %/min., an increase in channel height > 16 μm is observed for all samples. Deformation of the overcoat material indicates that at 0.1%/min., the permeation of the products must be slower than the formation of volatiles inside the cavity. The value for the initial mass of PNB, W_o, may be large enough to dominate the contribution to pressure, limiting the reaction by the permeation rate of volatiles out of the air-gap. A further decrease in C_R or W_o may attain conditions where the pressure formation is limited by the reaction rate.

A similar study was performed with Wu et al. [102] using photosensitive sacrificial polynorbornene materials containing alkyl and cyclolacrylate pendant side groups. In those experiments, a 3.5 to 4.0 μm thick PNB film (containing 4 wt% photo-initiator per weight of PNB) was spin-coated onto a silicon wafer and patterned by exposure to UV light, and spray developed with xylene to produce channel patterns. The

patterned samples were then encapsulated using different overcoat materials: either 4.5 μm thick Pyralin PI-2734, or 2 μm thick PECVD deposited SiO_2. Kinetic parameters obtained for the decomposition of photosensitive polynorbornene were used to calculate temperature-time profiles for the decomposition at constant rates of conversion. The decomposition of the encapsulated polymer patterns were performed in a similar fashion at the various conversion rates to investigate the effect of the rate on the channel structure.

At rates of conversion of 1 and 2%/min., the air-gaps maintain the size and shape of the original PNB sacrificial polymer pattern. However, at a decomposition rate of 3%/min., the air-channels distort into dome-shaped profiles. Channels with larger width clearly deformed more than channels of smaller dimensions. It also was observed that the extent of channel deformation was higher in the SiO_2 overcoated structures compared to the polyimide overcoated channels at the same nominal channel feature sizes and polymer decomposition rates. This set of experiments confirms the results expected from the analysis of pressure according to thickness and area variation. The thickness of these samples was less than 5 μm. In this case, the initial weight of PNB, W_o, and the properties affecting the permeation rate (P_e, l, A) put the samples in a regime where the rate limiting step may be either the formation or permeation of volatiles, depending on the value of C_R. Increased deformation in the SiO_2 overcoated samples could be due to differences in both the mechanical properites and the permeability of the overcoat material.

Table 39: Air-gap height following decomposition at a constant rate of conversion, as measured by profilometry and SEM.

PROFILOMETER MEASUREMENTS:			
PNB thickness before decomposition (μm)	11.3	21.8	31.3
Decomposition Rate in % conversion/min.	**Air-gap Height (mm)**		
0.1% / min	28.1	40.8	51.3
0.5 % / min	29.2	42.7	50.4
1 % / min	30.1	40.2	53.1
2 % / min	31.0	42.6	52.8
5 % / min	32.3	47.8	56.2
SEM MEASUREMENTS*:			
PNB thickness before decomposition (μm)	11.25	21.82	31.26
Decomposition Rate in % conversion/min	**Air-gap Height (mm)**		
0.1 % / min	24.7	42.0	50.2
0.5 % / min	25.4	N/A	N/A
1 % / min	27.8	41.6	52.6
2 % / min	30.4	41.8	N/A
5 % / min	30.7	42.2	52.8

*N/A –no cross sectional measurement could be obtained

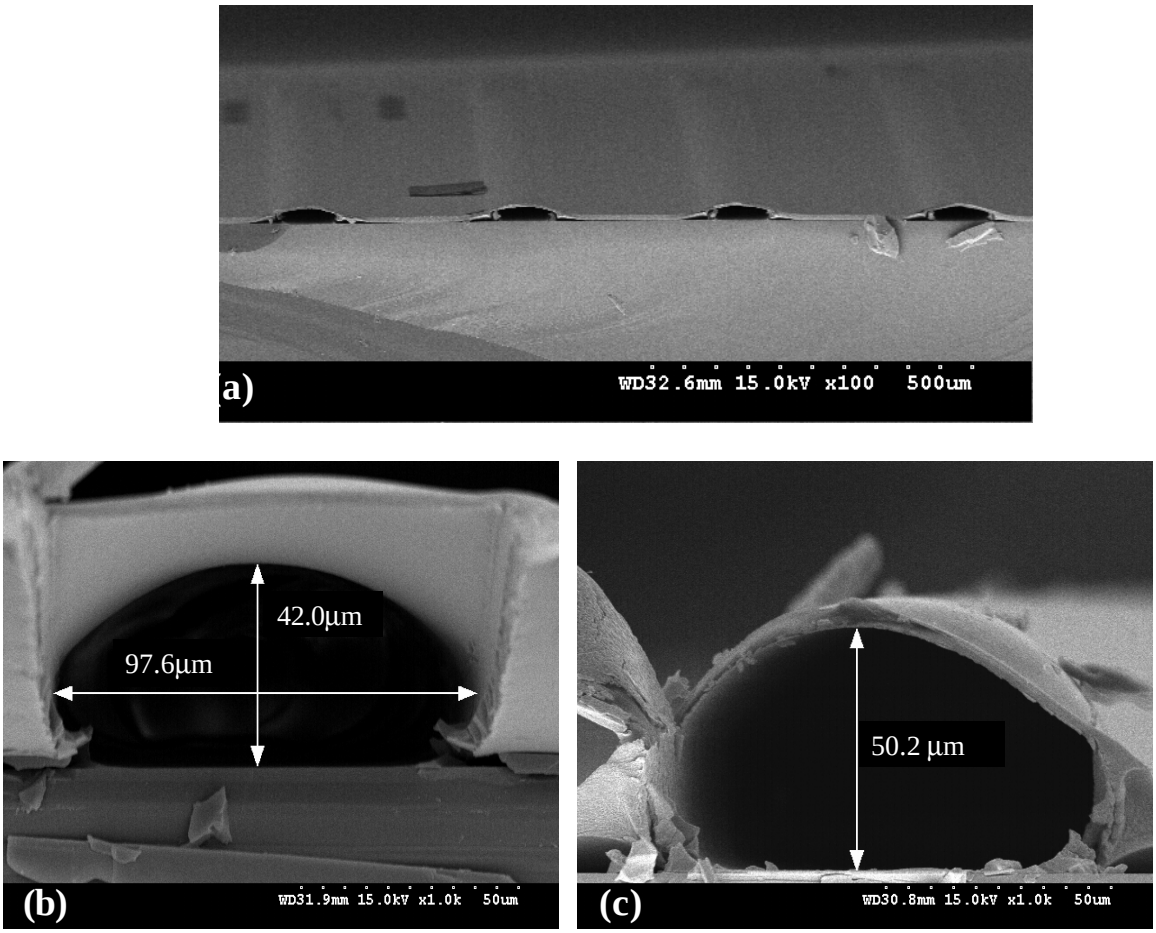

Figure 93: SEM images of air-channels decomposed at a rate of 0.1 % conversion/min from original PNB thickness of (a) 10 µm (b) 20 µm and (c) 30 µm.

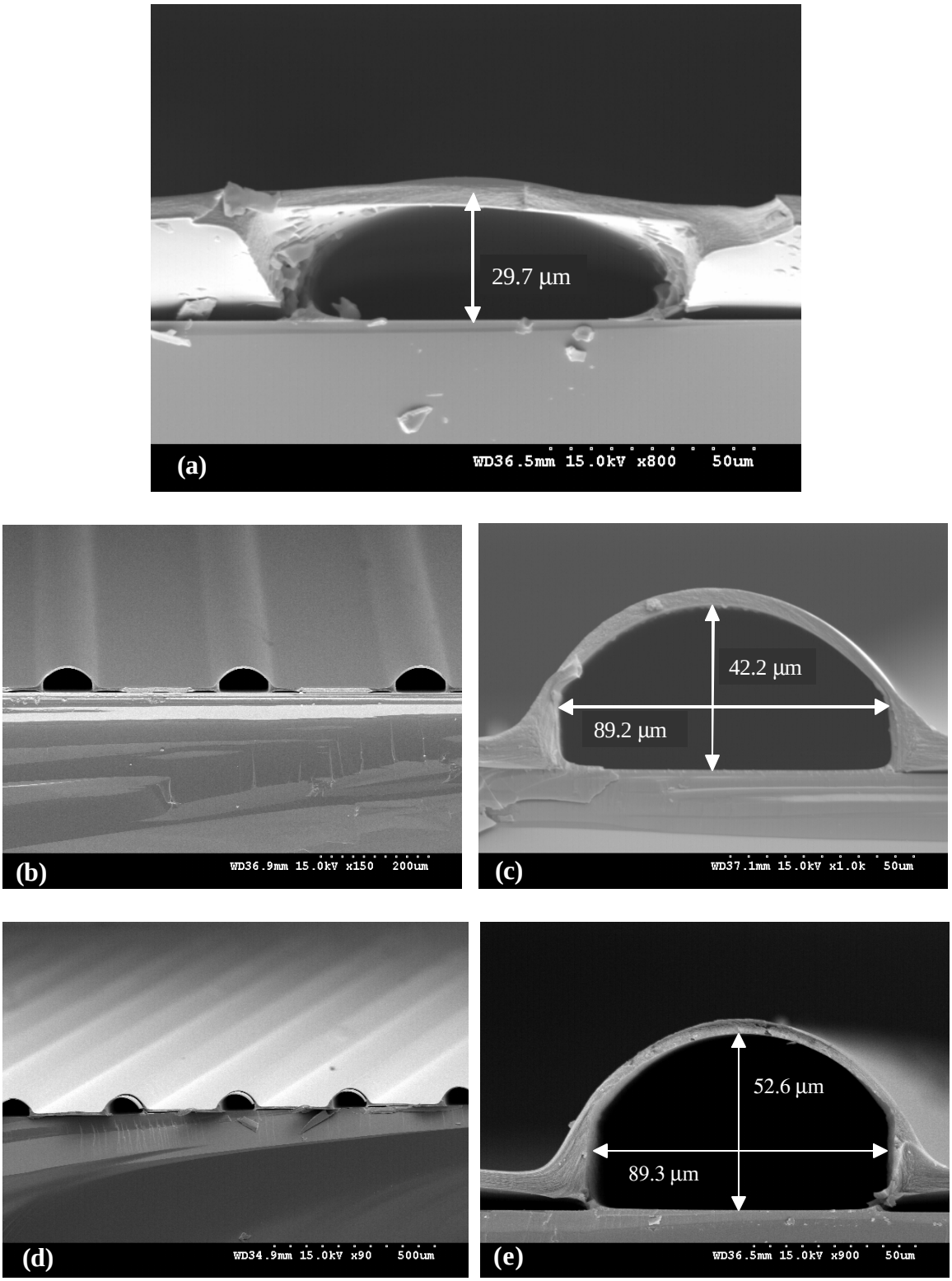

Figure 94: SEM images of air-channels decomposed at a rate of 1 % conversion/min from original PNB thickness of (a) 10 µm (b, c) 20 µm and (d, e) 30 µm.

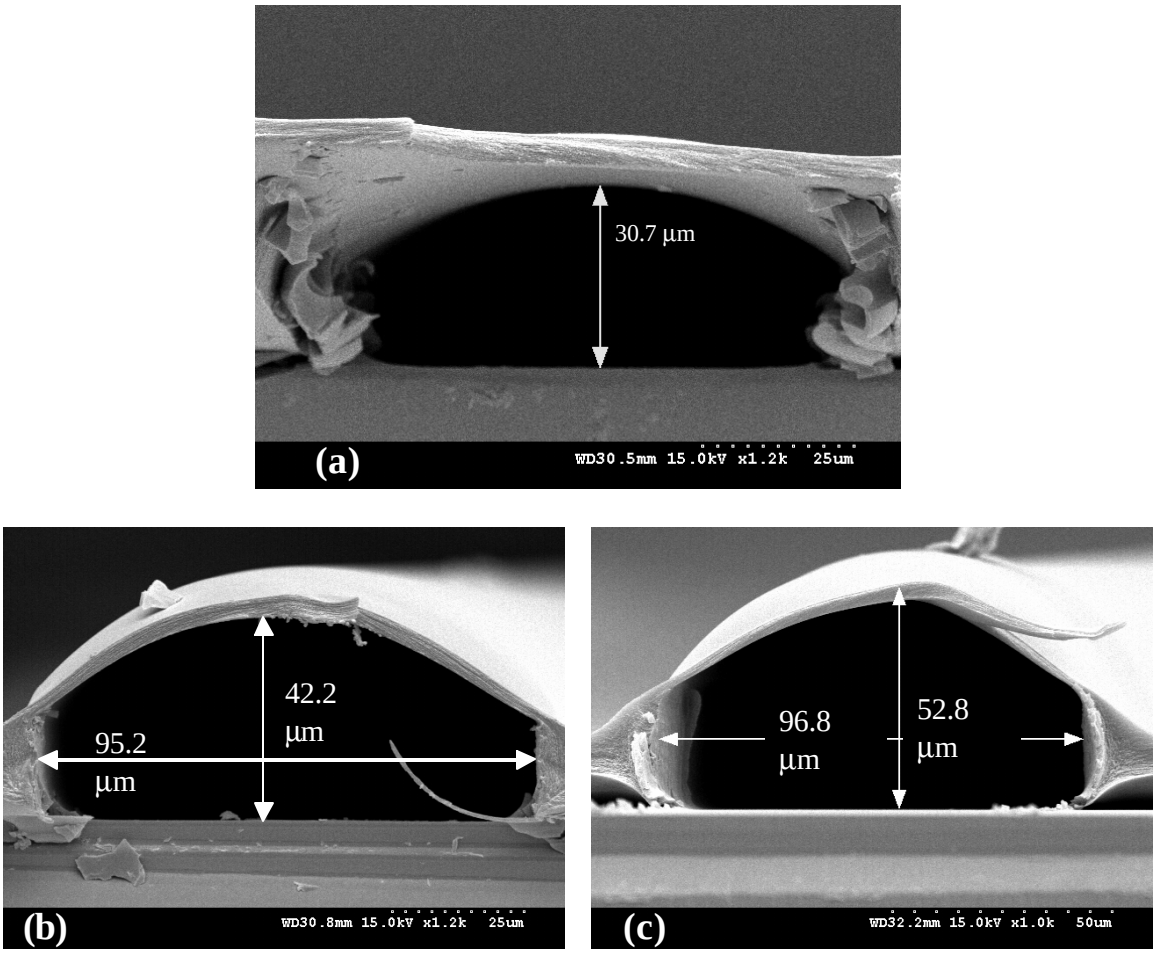

Figure 95: SEM images of air-channels decomposed at a rate of 5 % conversion/min from original PNB thickness of (a) 10 µm (b) 20 µm and (c) 30 µm.

CHAPTER 8

AIR-GAPS IN SEA OF LEADS WAFER LEVEL PACKAGING TECHNOLOGY

This chapter focuses on the integration of air-gaps into Sea of Leads (SoL) compliant wafer level packaging technology. The design concept of three-dimensionally compliant SoL packaging technology is introduced in Chapters 1 and 2. In-plane compliance of electrical I/O connections is achieved through a s-shaped flexible metal lead. A gold electroplated flexible s-shaped lead on a flat polymer surface is shown in Figure 96, demonstrating the typical shape of the lead. The shape and size of the leads, and their inherent lateral compliance, is ultimately dictated by the chip layout. Leads capable of 70 μm movements in the lateral direction have been demonstrated on a chip with 1000 leads/cm^2 [25].

Out-of-plane, or vertical compliance of leads is particularly interesting to many applications, including probe-cards for wafer-level test and burn-in [21]. The SoL out-of-plane compliance is achieved through the use of a thick compliant polymer layer underneath the lead. However, the addition of an embedded air-gap in the polymer beneath the lead may greatly enhance the out-of plane compliance. Figure 97 demonstrates how the addition of an embedded air-gap to SoL enables simultaneous contact to all I/O across a non-planar test probe card or PWB through vertical compliance. Contact is made to the eutectic solder bumps, which are approximately 50 μm in diameter and >30 μm above the surface of the silicon. The compliant interconnects physically deflect in the vertical direction, as needed, to make firm contact

to all I/Os on the wafer. Fifty micrometers of vertical deflection has been reported as the requirement for wafer-level testing and burn-in due to non-planarity across parts [103].

The thermally decomposable sacrificial polymer method of air-gap fabrication is valuable to SoL because it allows complete control over air-gap geometry, the formation of fully enclosed air-gap structures, and the embedded air-gaps may be formed at a variety of temperatures using PNB or PC sacrificial materials. Chapters 5 and 6 have demonstrated air-gaps which have been formed at various temperatures in many different low-κ encapsulating materials, with air-gap sizes ranging from 0.25 μm to 1 cm in width, and 500 nm to 50 μm in height. In addition, if the decomposition rate is high and the overcoat is flexible or can flow, a net pressure builds inside the air-gap and the resulting air-gap is dome-shaped. The dome-shaped air-gap is a possible benefit to the SoL structures. This concept is demonstrated in Figure 98. Figure 98 is a schematic showing the top view and side view of a SoL interconnection. The lead is positioned so that it begins in the via next to the air-gap, and ends on top of the air-gap at the maximum height. A dome-shaped air-gap may be favorable to avoid corners and bends in the lead. Section 8.1 of this chapter describes the SoL fabrication process developed in order to integrate air-gaps into the compliant package. The critical issues resulting from the addition of air-gaps into the process are then discussed. The mechanical properties and achievable compliance using both methods: (1) a thick compliant polymer layer, and (2) an air-gap embedded in polymer, are discussed in Chapter 9.

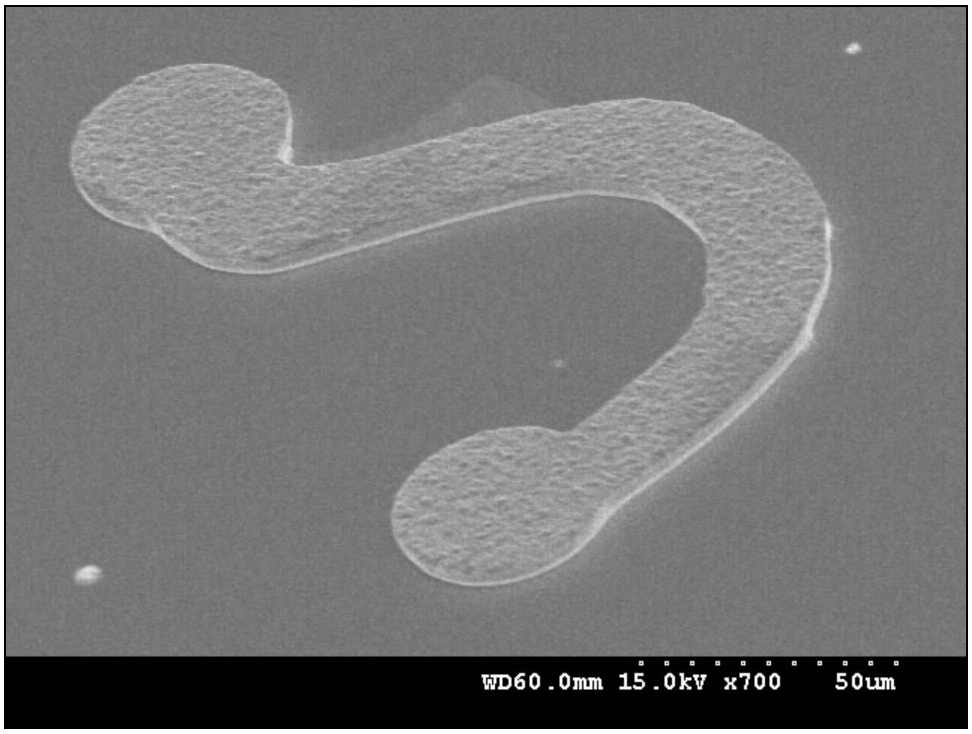

Figure 96: SEM image demonstrating the s-shape of an Au electroplated lead designed for lateral compliance in SoL packaging technology.

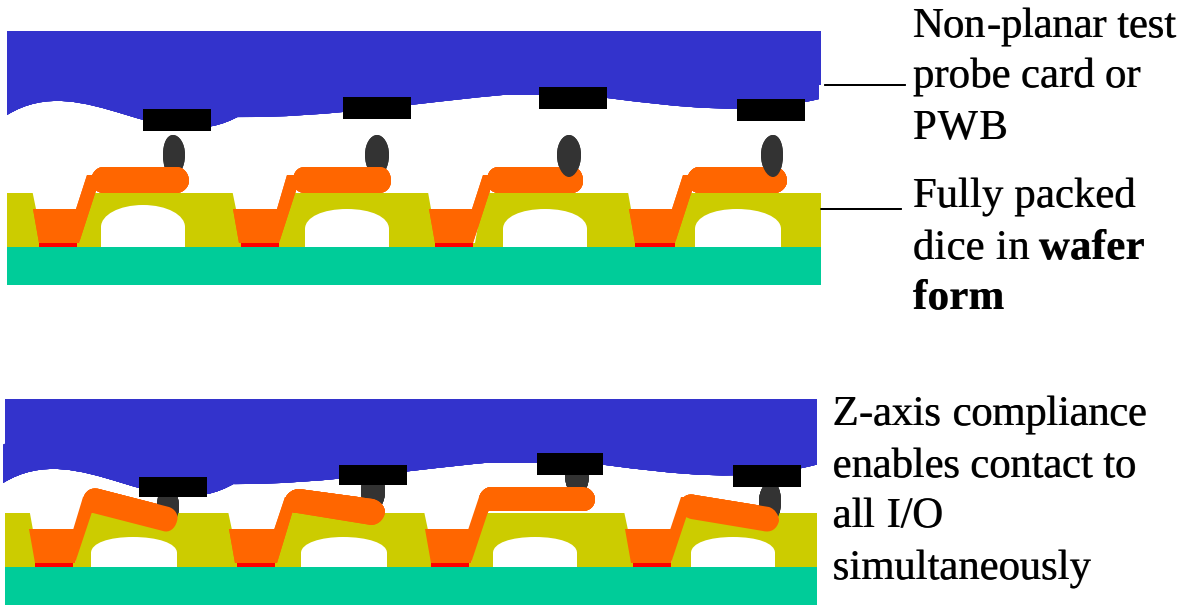

Figure 97: Diagram demonstrating how SoL CWLP allows simultaneous contact to all I/O across a wafer through z-axis (out-of-plane) compliance.

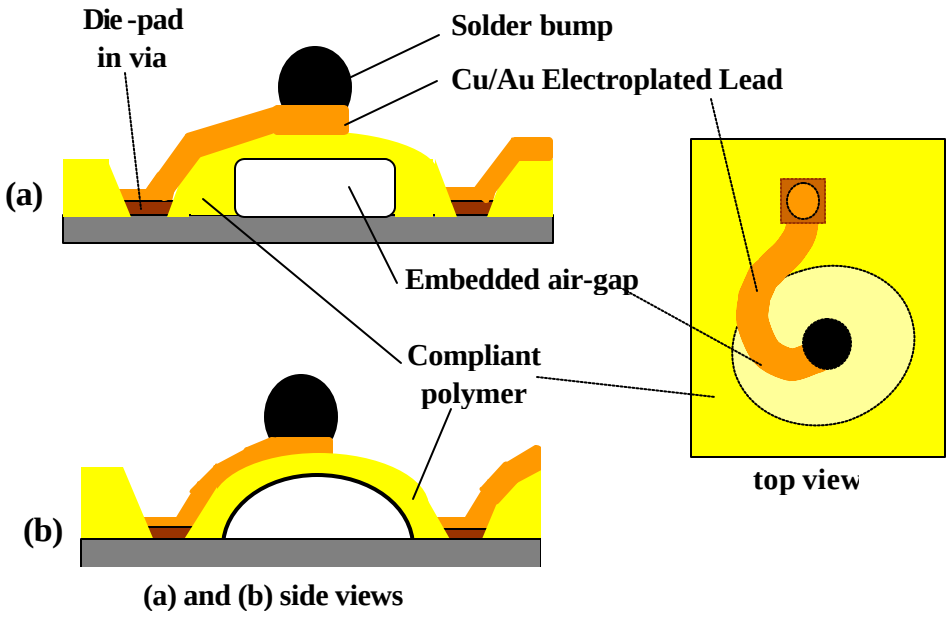

Figure 98: Schematic showing the top view and side view of a SoL interconnect with (a) a rectangular air-gap and (b) a dome-shaped air-gap.

8.1 Experimental Process Details for SoL Fabrication With Embedded Air-gaps

Figure 4 (Chapter 2, Section 2.2, page 19) depicted the SoL chip I/O fabrication process without an embedded air-gap. The entire SoL fabrication process described in Figure 4 consists of three lithography masking steps: (1) patterning and etching of vias in the compliant polymer layer to expose the metal contact pads on the wafer; (2) lead formation; and (3) solder ball placement on the end of the compliant leads. The fabrication of SoL without embedded air gaps uses a low elastic modulus polymer, Avatrel 2000P dielectric polymer (E = 0.5 GPa), as a thick compliant polymer layer underneath electroplated leads. The details of the fabrication process for SoL without embedded air-gaps are described elsewhere [23].

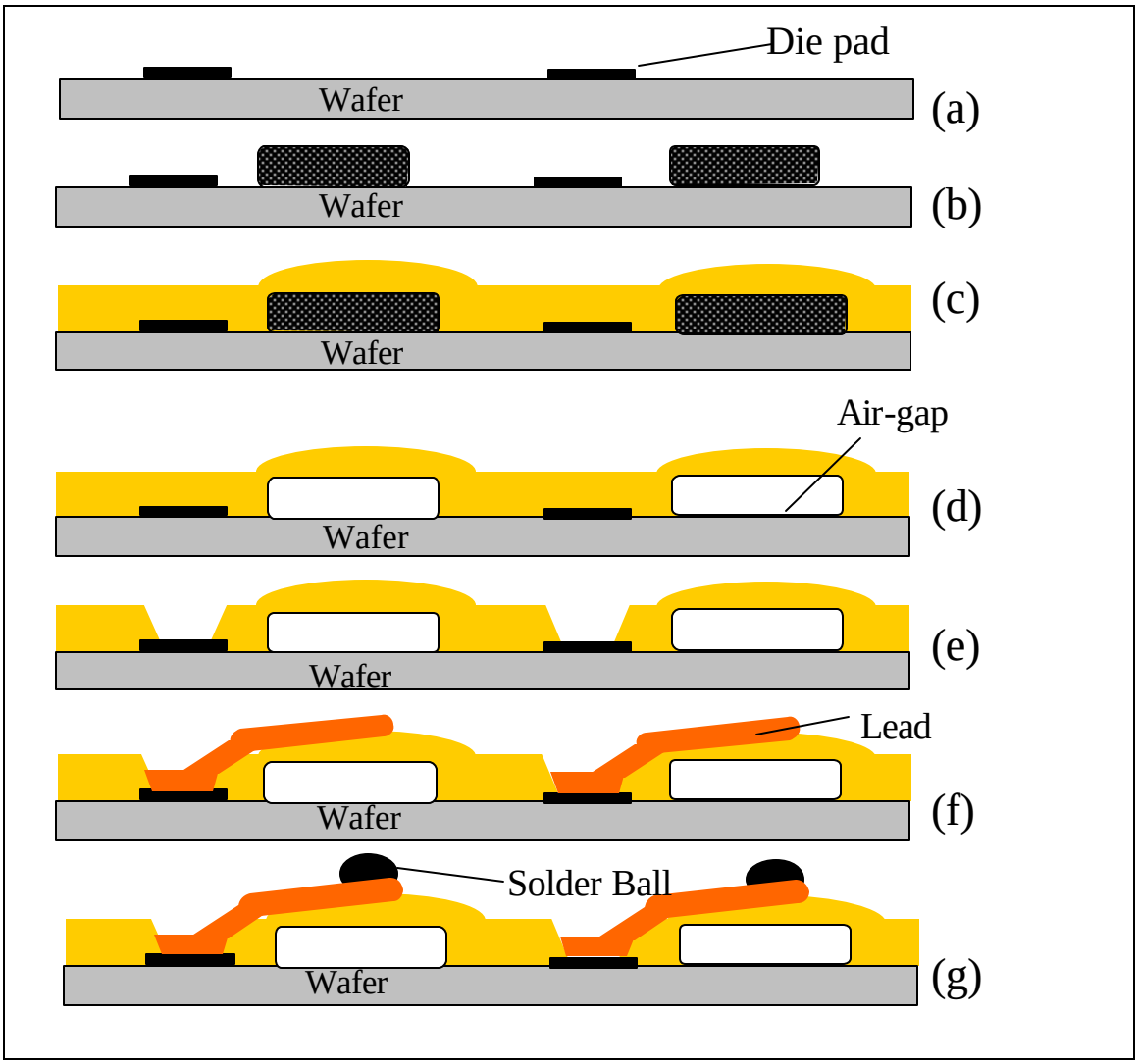

Figure 99: Schematic of the fabrication process sequence for SoL with an embedded air-gap: (a) chip fabrication is complete; the die-pads are exposed; (b) the sacrificial polymer film is applied and patterned; (c) the overcoat polymer is deposited and encapsulates the sacrificial polymer layer; (d) the sacrificial material is thermally decomposed to form air-gaps; (e) vias are etched in the overcoat polymer to expose the die pads; (f) the compliant leads are electroplated; (g) the chip solder bumps are fabricated.

A schematic of the process sequence developed for SoL with the addition of embedded air-gaps is depicted in Figure 99. The addition of air-gaps into the SoL structure adds only one additional lithography processing step. The first masking step of the process becomes the patterning of a sacrificial polymer material, which will later form the embedded air gaps. The following lithography steps remain the same. However, the integration of air-gaps into SoL requires re-optimization of the entire fabrication process to ensure compatibility of the process with a new set of materials, including the use of PNB sacrificial material. Polyimides, including Ultradel 7501, Pyralin PI-2611, and Pyralin PI-2734, are considered as overcoat polymers in SoL fabrication with elastic moduli of 3.5 GPa, 4.7 GPa, and 8.5 GPa, respectively. It is desirable for the encapsulating polymer to have a low elastic modulus to allow the compliant leads to deflect as needed during wafer-level testing and burn-in and during thermal cycling. Although the elastic moduli of these polyimides are greater than the elastic modulus of Avatrel 2000P, these three polyimides are capable of forming vertically compliant structures. Dome-shaped air-cavities have been fabricated up to 50 µm in height with the overcoat polyimides. A larger structure is capable of more total displacement in the vertical direction. The next paragraphs describe the processing details for the optimized SoL fabrication process with embedded air-gaps, using 90/10 butyl/TES PNB sacrificial material and polyimides Ultradel 7501, PI-2734, and PI-2611 as encapsulating polymers.

Mask 1: Fabrication of air-gaps

The SoL process begins on a completed wafer with exposed die pads and bond pad openings as shown in Figure 99 (a). The PNB sacrificial polymer is applied by spin-

coating, and softbaking, followed by curing at 275°C for one hour in nitrogen. PNB sacrificial polymer solutions PNB-1-S1 (22.0 wt % 90/10 Butyl/TES PNB in mesitylene) and PNB-2-S1 (30.8 wt % 90/10 Butyl/TES PNB in mesitylene) were used to create sacrificial films ranging from 5 to 30 μm. The processing method described in Chapter 5 for the patterning of non-photosensitive PNB with an Al hard mask was used to pattern the sacrificial polymer film, as shown in Figure 99 (b). The encapsulating polymer is then blanket coated onto the wafer as in Figure 99 (c). The overcoat polyimides, Ultradel 7501, PI-2611, and PI-2734, are processed according to the conditions described in Appendix B. Following encapsulation, the overcoat material is cured and the sacrificial polymer is thermally decomposed by holding the wafer at the decomposition temperature in a nitrogen-purged horizontal tube furnace (Figure 99 (d)). The overcoat polymer, its permeability properties, and the decomposition conditions, determine whether the resulting embedded air gap is dome shaped or flat. The decomposition occurs before the fabrication of the compliant leads in order to prevent stress or distortion of the leads that may occur during the decomposition process. The resulting structure at the end of the sacrificial polymer decomposition is shown schematically in Figure 99 (d). SEM images of both flat and dome-shaped air-gaps fabricated using mask patterns designed for integration into SoL packaging technology are shown in Figure 100.

Mask 2: Via patterning in overcoat polyimide

The second masking step (Figure 99 (e)) defines via holes in the overcoat polymer, to expose the underlying die-pads and allow electrical interconnection to the chip. The vias are etched in the encapsulating polymer using plasma etching. An Al metal hard mask with a thickness of 2000 to 3000 Å is used to protect the overcoat

polyimide while the openings are etched. Standard processing recipes for Futurrex NR9-8000 negative photoresist and Futurrex RD-6 developer solution are used to form the via pattern in 5 μm thick photoresist on top of the Al hard mask [104]. The Al is patterned using a Plasmatherm RIE with the following process conditions: Pressure = 280 mTorr; gas flow rates = 45 sccm O_2, and 5 sccm CHF_3; Temperature = 35°C; and Power = 300 W. Figure 101 shows SEM images of (a) the top surface and (b) a cross section of a via etched into 10 μm thick PI-2611 overcoat polymer layer. The resulting sidewalls of the via are sloped, as shown in Figure 101 (b). This sidewall profile is desirable because it enhances plating uniformity (i.e., increases thickness) at the via sidewalls (especially at the via's neck). In addition, the sloped sidewall aids in continuity of seed-layer metals for electroplating. The deposition of a metal seed-layer is more difficult on a surface perpendicular to the metal source. Any discontinuity in the seed-layer can result in delamination of the leads when the seed layer is removed.

Mask 3: Lead fabrication

Once the vias are fabricated to expose the die pads, SoL leads are electroplated across the wafer using photoresist as an electroplating mold (Figure 99 (f)). A metal seed layer such as Ti/Au, or Au, is sputter deposited across the entire wafer. Futurrex NR9-8000 resist is spin-coated, exposed, and developed according to the instructions provided by the manufacturer, in order to produce a 10-20 μm thick patterned film. Since the leads are typically 10 μm thick and must be resilient to oxidization, gold is an effective metallization. Not only does the lead thickness influence the force-displacement behavior of the lead, but it also influences the electrical performance of the leads. In addition, the adhesion of the lead to the polymer overcoat also affects the mechanical

behavior of the lead. The displacement of the lead in the in-plane direction is increased if the lead is "slippery" and non-adherent to the polymer surface. Two methods are used to control the adhesion of the lead to the overcoat polymer [19-25]. Strong adhesion to the overcoat polymer is achieved by using a sputter deposited titanium/gold (Ti/Au) seed layer, where the Ti provides excellent adhesion between the Au and the overcoat polymer. For poor adhesion (slippery leads), Au alone can be sputter deposited on the wafer. However, in order to anchor the leads at the die pad end and leave the remainder of the lead free to move, electroless nickel (Ni) is plated on only the Cu die pads as an adhesion promoter and diffusion barrier before the sputtering of the Au seed layer. Thus, the leads plated on the seed layer have good adhesion to the die pads but adhere poorly to the overcoat polymer. Another method of fabricating slippery leads is to plate the leads on a seed layer that is selectively etched when the leads are ready to be released from the surface. For example, a Ti/Cu seed layer may be used to electroplate Au leads. Following the fabrication of the leads and solder bumps, the Cu seed layer is first selectively etched with a dilute nitric acid solution and the Ti seed layer is etched using buffered oxide etchant (BOE). Neither of the wet-chemical etchants removes Au.

Mask 4: Tin/lead solder ball fabrication

The fourth masking step for SoL with embedded air-gaps is the formation of solder bumps on the metal pads residing on top of the air-gap at the end of the leads. Eutectic solder alloy (67% tin)/(33% lead) is electroplated on the tail end of the lead. Lead-free solder alloys are also process compatible with SoL. Details of solder bump plating are reported elsewhere [23].

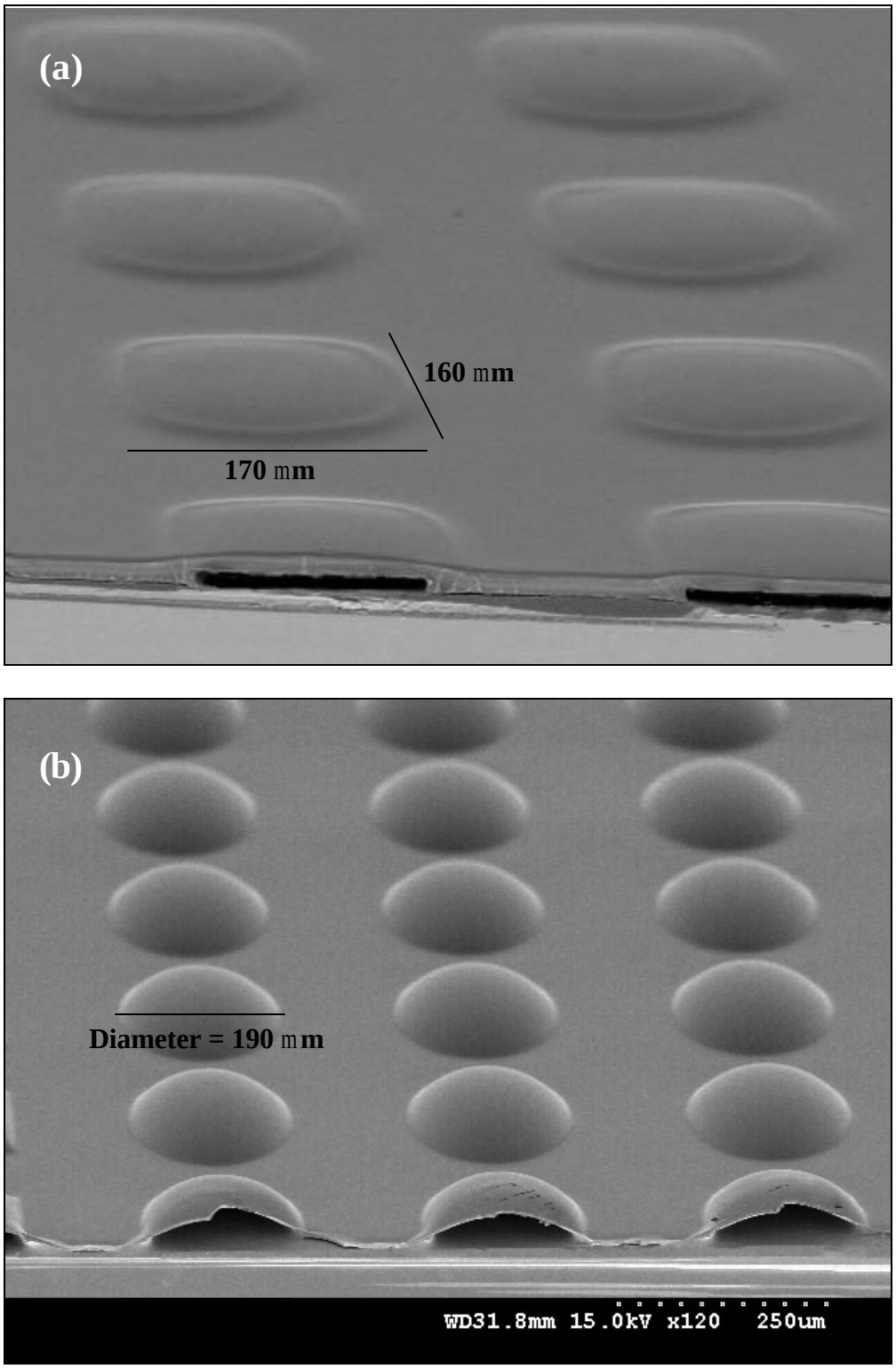

Figure 100: SEM images of (a) flat and (b) dome-shaped air-gaps for SoL, following decomposition of the sacrificial polymer (step (d) in Figure 99).

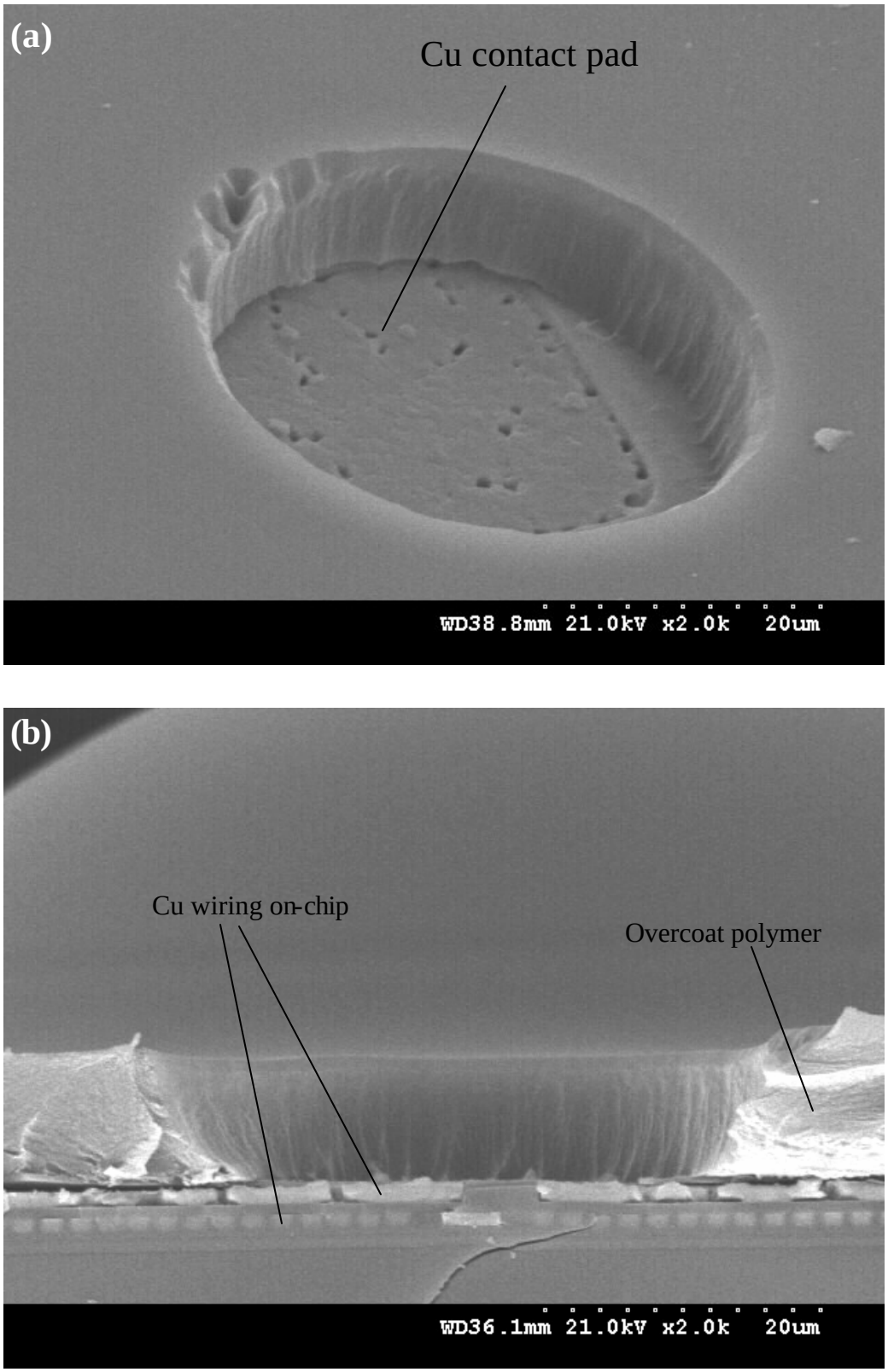

Figure 101: SEM images of (a) the top surface and (b) a cross-section of vias etched into 10 µm thick PI-2611 overcoat polyimide layer.

The complete SoL compliant package with embedded air-gaps is demonstrated through the fabrication of a prototype package with a density of 1,000 leads/cm^2. A SEM image of the prototype is shown in Figure 102. The air-gaps are 170μm × 160 μm polygons designed to fit underneath the leads. The air-gap thickness for the prototype is 10 μm, the overcoat polyimide is 15 μm thick Ultradel 7501, and the leads are electroplated copper leads 10 μm thick and 250 μm in length. Solder balls were not electroplated onto this prototype. The SoL I/O are arranged in an area array on the chip with a pitch from center to center of 325 μm. A single SoL structure from this prototype is shown in Figure 103. The air-gap is flat on the top surface with a height of about 10 μm. At these dimensions, the lead effectively extends from the via to the top of the air-gap without bends or discontinuity. Ideally, the pad for the solder ball would lie directly on the center of the air-gap. However, misalignment during the air-gap lithography step resulted in a slight misplacement of the leads.

A second prototype SoL package was fabricated to demonstrate the ability to fabricate SoL with embedded air-gaps on active device chips. A set of SoL lithography masks were designed to align with the die pads on active chips, which consist of an area array density of 3000 leads/cm^2. A higher density of I/O per unit area results in shorter leads and smaller air-gaps. The air-gaps in this prototype are ellipses with major and minor axes of 150 and 120 μm, respectively. Figure 104 is an SEM image of a 3000 leads/cm^2 SoL package fabricated on a chip containing active devices. The PNB thickness of this sample was 13 μm before decomposition, overcoated with 8 μm PI-2611. The resulting air-gap structures are dome-shaped with a height of about 30 μm at the highest point. Figure 105 is a SEM image of one of the SoL I/O in the 3000

leads/cm^2 package. The lead begins at the via and extends over the air-gap to the maximum height. Although the air-gap is dome-shaped, the lead encounters a sharp bend as it extends from the flat polymer surface up the sloped air-gap. Thus, only the end portion of the lead is able to deflect when a vertical force is applied to the lead.

8.2 Discussion of Results and Critical Issues for the Integration of Air-gaps Into SoL

The prototype SoL packages demonstrate the successful integration of air-gaps into SoL compliant wafer level packaging technology. The processing methodology used in the fabrication of these packages has been developed with consideration to the compatibility between all four patterning steps in the SoL process. The process details for the prototype packages shown in Figure 102 through Figure 105 are included in Table 40, and describe the specific materials and process parameters selected throughout the fabrication. However, the SoL process steps are not limited to the exact materials and conditions in Table 40. As materials and methods continue to develop in the electronics industry, including PC sacrificial materials, a new set of conditions may be integrated into the SoL fabrication process. Regardless, there are several critical issues of SoL fabrication with embedded air-gaps that must be considered with any set of materials for successful fabrication of the entire package.

8.2.1 Metal compatibility in SoL processing

One of the critical issues in SoL processing is the use of several metals throughout the construction of the package. Several metal layers in SoL fabrication are deposited as sacrificial metals, and only necessary for patterning or electroplating, then removed.

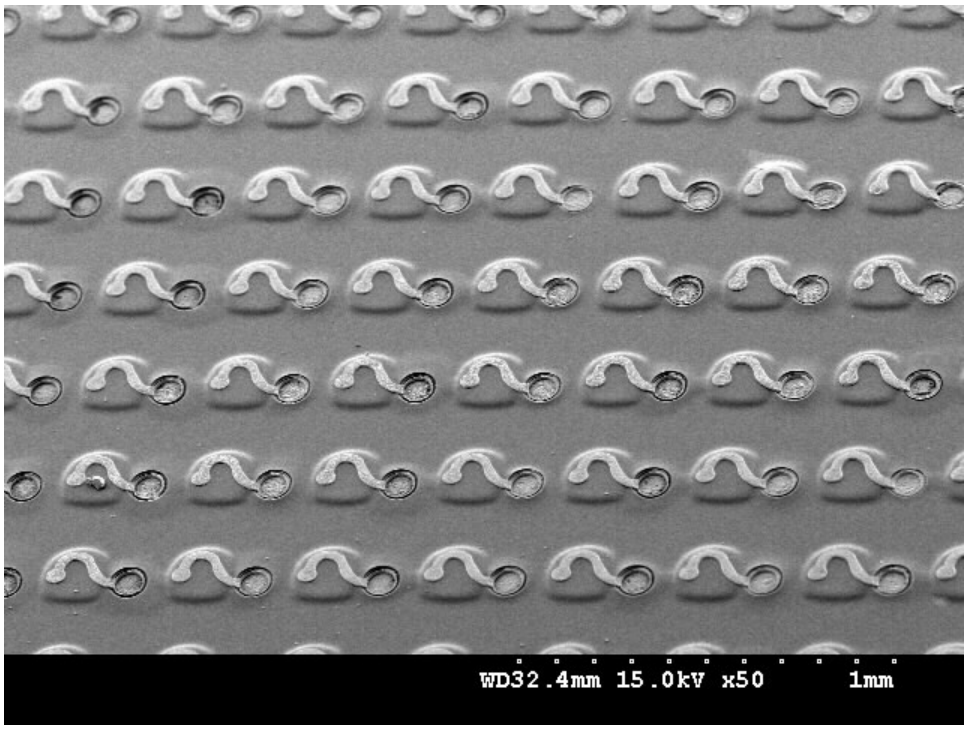

Figure 102: SEM image of a SoL package containing 1000 leads/cm^2, fabricated with Ultradel 7501 polyimide and embedded air-gaps under each lead.

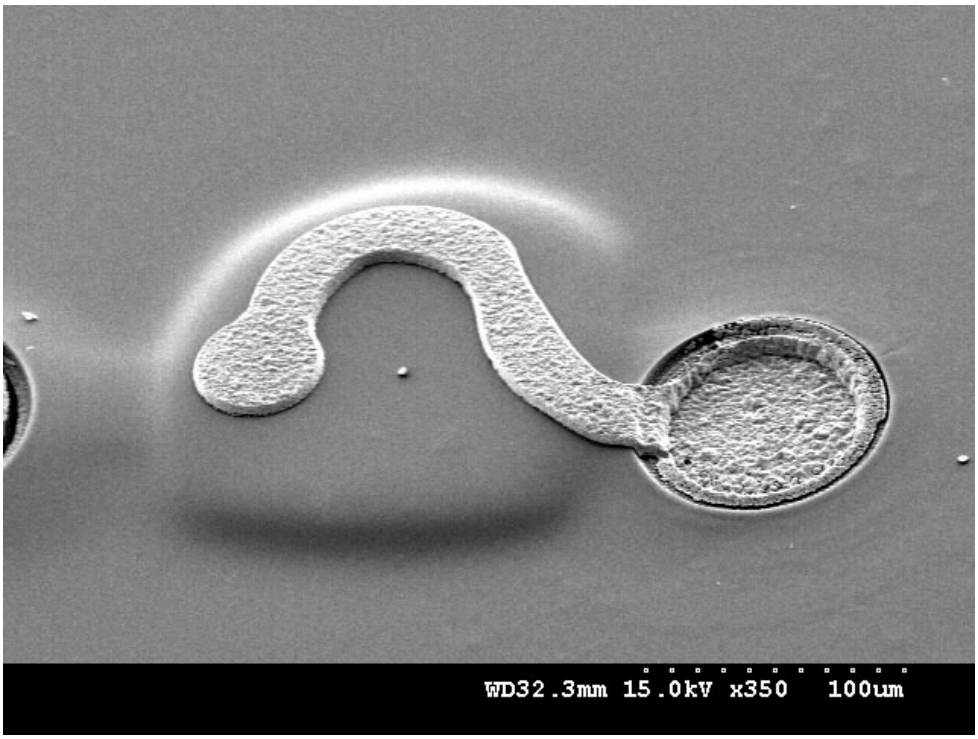

Figure 103: SEM image of a SoL I/O structure with an embedded air-gap. The structure was fabricated using PNB sacrificial polymer, Ultradel 7501 overcoat polyimide, and electroplated Cu leads.

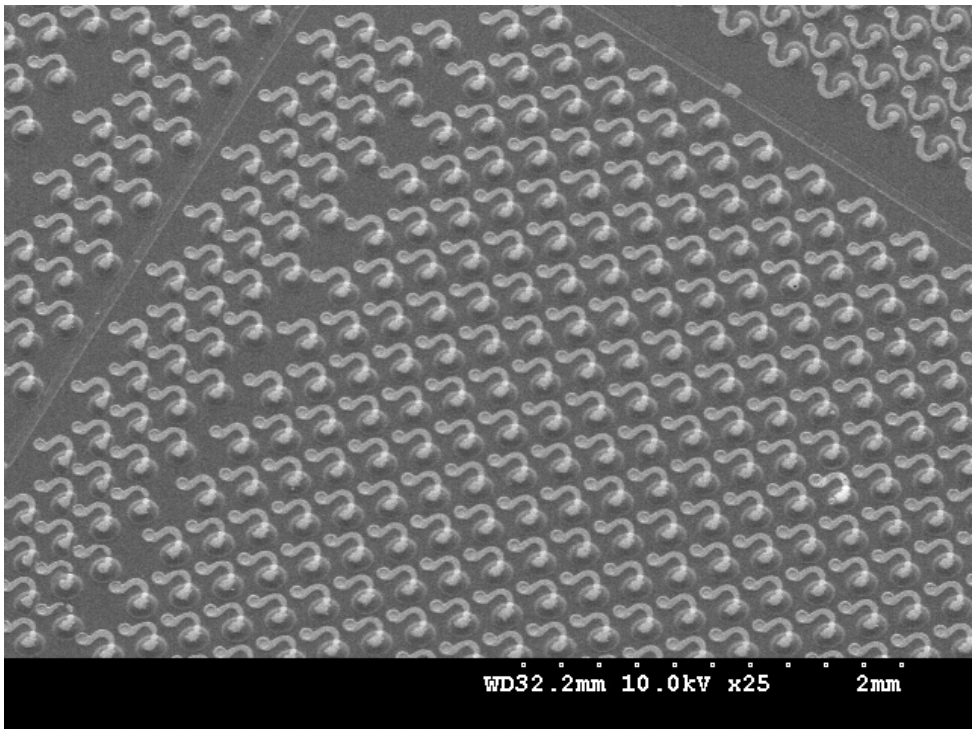

Figure 104: SEM image of a SoL package containing 3000 leads/cm^2, fabricated with polyimide PI-2611 and air-gaps under each electroplated Au lead.

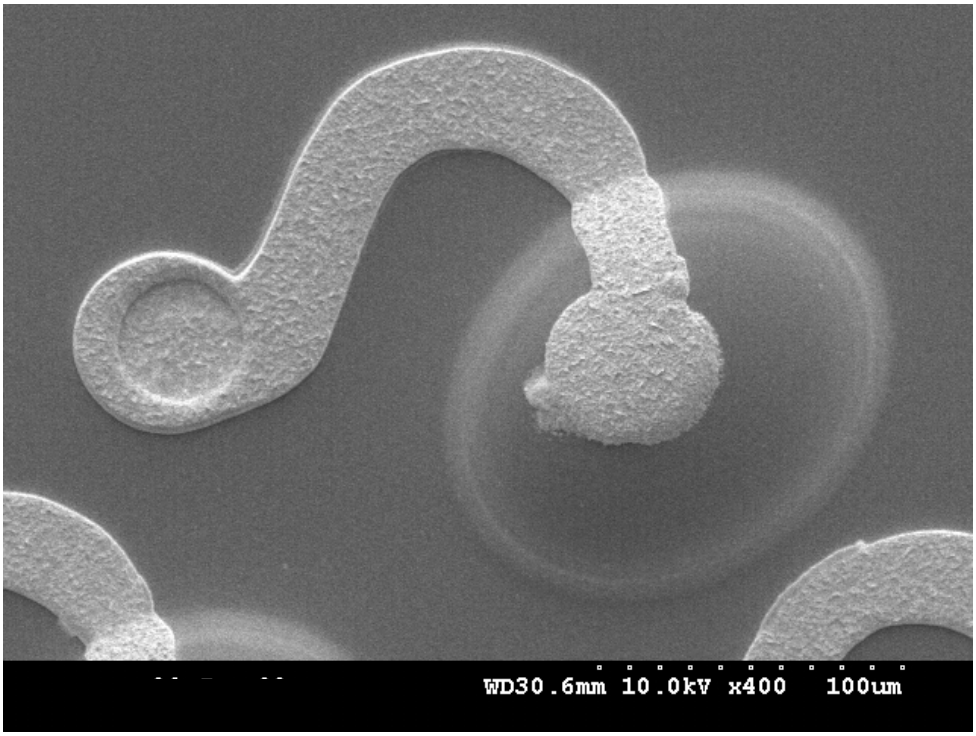

Figure 105: SEM image of a SoL I/O structure with an embedded air-gap. The structure was fabricated using PNB sacrificial polymer, overcoat polyimide PI-2611, and Au electroplated leads.

Table 40: Processing conditions for the fabrication of SoL prototype packages.

	Process Step	1000 lead/cm^2 prototype (Figure 102 and 103)	3000 lead/cm^2 prototype (Figure 104 and 105)
1	PNB polymer	10.9 μm	13.9 μm
2	PNB cure	275°C for 1 hr	275°C for 1 hr
3	Air-gap hard mask	1300 Å sputtered Al	1600 Å sputtered Al
4	Air-gap mask: photoresist/developer	Shipley 1827, dose = 100 mJ/cm^2 (365 nm) Shipley MF319 develop, 30 s	Shipley 1813, dose = 150 mJ/cm^2 Shipley MF319 develop, 45 s
5	Air-gap hard mask etch	PAN wet etch, 20 s	RIE Al etch 2 min
6	Air-gap PNB etching Program: PNB ETCH-2 (see pg. 103)	RIE, 33 min	RIE, 42 min
7	Air-gap mask removal	RIE, 2 min	RIE, 2 min
8	Overcoat material	Ultradel 7501 polyimide	Pyralin PI-2611 polyimide
9	Overcoat thickness (after curing)	10 μm	10 μm
10	Decomposition (nitrogen environment)	10°C/min to 200°C, hold 1 hr, 10°C/min to 350°C, hold ½ hr, 1°C/min to 425°C, hold 2 hr	3°C/min to 350°C, hold 1 hr, 1°C/min to 405°C, hold ½ hr, 1°C/min to 425°C, hold 1 hr
11	Via hard mask	2000Å sputtered Al	2300Å sputtered Al
12	Via lithography	Futurrex NR9-8000 Softbake 100°C, 2 min Dose = 150 mJ/cm^2 PEB 100°C, 2 min RD6 develop, 10 s	Futurrex NR9-8000 Softbake 100°C, 2 min Dose =190 mJ/cm^2 PEB 100°C, 2 min, RD6 develop, 60 s
13	Via hard mask etching	PAN wet etch, 20 s	PAN wet etch, 20 s
14	Via polyimide etching	12 min	22 min
15	Lead seed layer	Sputtered Ti/Au/Ti 300Å/2000Å/300Å	Sputtered Ti/Au/Ti 300Å/2000Å/300Å
16	Lead photolithography	Futurrex NR9-8000 Softbake: ramp 70-100°C, hold 2 min dose = 150 mJ/cm^2, RD6 develop, 60 s	Futurrex NR9-8000 Softbake: ramp 70-100°C, hold 2 min dose = 190 mJ/cm^2, RD6 develop, 6 min
17	Lead electroplating	Cu	Au, 30 mA, 40 min

Not only do the metals introduce possible contamination, but the processes used deposition and removal may also contribute to device or feature degradation. Many of the possible etchants for the removal of one metal attack other metals and materials throughout the sample.

Even before fabrication of SoL begins, a key factor is the cleanliness of the exposed metal contact pads on the completed wafer. The contact pads must be free from debris that may remain from the etching of the final chip passivation layer to expose the contact pads. Once SoL processing begins, the metal contact pads are exposed to several additional deposition and etching processes. The sacrificial polymer is applied and etched from the pads, followed by a second encasement of the pads with the encapsulating polymer, and second plasma etch step to re-expose the metal contacts. Each of these process steps may leave residual polymeric material on the metal or cause damage to the contact pads from ion bombardment during the plasma etch processes. Any non-conductive residual material on the pad may result in poor adhesion of the lead to the contact pad, or degrade the electrical performance of the leads. Therefore, the process steps must be optimized to ensure the cleanliness of the pads, or an additional cleaning step may be added to the process before seed layer deposition and electroplating of the leads. In addition, the metal contact pads are typically constructed of Cu, which oxidizes when exposed to an ambient atmosphere. The oxide is non-conductive and must be removed, as it also can contribute to poor adhesion of the leads at the via, or degradation in electrical performance.

Several approaches are possible in order to ensure cleanliness of the metal contact pads and good adhesion of the lead to the contact pad in the via. One approach is to

deposit a metal layer designed to protect the pads during the air-gap and via fabrication steps in SoL. The Cu pads are cleaned with a dilute nitric acid solution to remove copper oxide from the surface, followed by immediate sputter deposition of a metal across the entire wafer. The metal is then patterned to remain only in the contact pad areas. Once the air-gap and via fabrication steps are complete, the secondary metal may be removed, re-exposing the clean Cu contact surfaces. Au is one metal option since it does not oxidize when exposed to either ambient or the oxygen-containing plasma etch processes. Therefore, any degradation due to oxide formation is eliminated. However, an attempt to remove the Au with a KI/I_2 etch solution and re-expose the clean Cu surface before lead seed-layer deposition, results in etching of both metals from the contact pad surface. Therefore, the Au must remain in place before seed layer deposition. Slight over-etching during the via plasma etch step may help clean the Au surface before seed layer deposition. A second option is deposition of a thin Ti layer on the clean Cu pad surfaces. Once the SoL via etch process in the encapsulating polymer is complete, the Ti may be removed with a dilute buffered oxide etch (BOE) solution, followed by removal of any Cu oxide with dilute nitric acid. The removal of the Ti should lift-off any polymer contamination from the contact pad surface. Although protection of the contact pads introduces an additional masking step, it potentially eliminates other problems down the line with processing and reliability.

Another important issue regarding metals in the SoL process sequence is the use of Al hard masks to protect the both PNB and the encapsulating polymer during plasma etch processes. Al is chosen as a hard mask material for the polymers due to the high selectivity of the polymer plasma etch between polymer and aluminum. An Al layer with

a thickness of a few thousand angstroms can be used to protect over 30 μm of polymer during etching. The polymer etch chemistry has lower selectivity to other possible mask materials, such as photoresist or silicon dioxide. Several microns of these materials are required to protect the polymer. However, the wet-chemical PAN etch (phosphoric acid, acetic acid, nitric acid) for the removal of aluminum also etches copper due to the nitric acid component. Therefore, PAN etch cannot be used for any Al removal when Cu elements are exposed on the surface. A dry Al etch process using RIE is selective to Cu, and resolves this issue. However, the incompatibility between Al wet etch and Cu demonstrates how each individual component of the SoL fabrication must be thoughtfully considered to ensure compatibility of the process steps.

8.2.2 Lithography on non-planar surfaces

The lithographic process steps in SoL fabrication are another critical component of the entire SoL fabrication process. The thick polymer layers and opaque metals used to construct the SoL I/O interconnections complicate the mask alignment and lithographic processing. The complications limit the structures and dimensions which can be fabricated using currently available lithographic materials and techniques. The first SoL lithographic mask (air-gap patterning) is designed to align to marks and patterns on the completed die. The alignment marks on the surface of the completed die are often only a few microns or less in height, while the thickness of the sacrificial layer may be 5 to 30 μm. Although the thick PNB sacrificial polymer film planarizes the features and alignment marks on the die surface, the alignment marks are visible through the transparent sacrificial polymer film. However, once Al is sputter coated across the entire surface as a hard mask, the alignment marks are no longer visible. One possible solution

is to cover the alignment marks on the wafer edges with tape or photoresist during the aluminum sputter deposition, then subsequently remove the aluminum by a lift-off process. However, die at the edge of the wafer are often sacrificed.

Another lithography concern occurs during the second masking step of SoL (via etching) when the fabricated air-gaps have a large height dimension (20 μm or greater) in comparison to the surrounding polymer film. The air-gap decomposition occurs before via etching or lead fabrication to avoid distortion of the vias or leads as the air-gaps increase in size. Following decomposition, Al is deposited as a hard mask across the entire wafer surface to protect the encapsulating polymer during via etching. The vias are located between the air-gaps and rest below the highest point of the surface. If the mask alignment is performed using contact printing, contact between the mask and wafer results in compression of the air-gaps, which induces cracking in the Al mask. As the vias are etched, a whole forms in the overcoat polymer of the air-gap from loss of etch protection by the Al. The alternative is proximity printing, where the mask and wafer are separated by a small distance during alignment and exposure. The Al hard mask covering the air-gaps remains intact using this technique. However, the dimensions and shape of the vias do not transfer exactly from the mask pattern.

The most critical lithography processing issue in SoL with embedded air-gaps is the formation of the photoresist electroplating mold for lead fabrication. A thick (10-20 μm) photoresist layer is spin-coated across the entire surface of the wafer, exposed, and removed in the areas for formation of the leads. The surface topography due to air-gaps and vias on the wafer surface increases the difficulty of patterning. The photoresist coats features on the wafer non-conformally, resulting in a thicker photoresist film between the

air-gaps in comparison to the film on the top surface of the air-gaps. The resist must be processed according to exposure and development times necessary for the thickest portion of the resist, in order to entirely clear the resist from those areas. However, process control is important because if the resist is over-developed, a loss of the photoresist occurs on top of the air-gap. Figure 106 shows an image of a photoresist mold for lead electroplating on an air-gap 30 μm in height, following exposure and development of the photoresist. On the top surface of the air-gap, the mold is only approximately 2-3 μm in depth. Figure 107 shows Au leads that were fabricated from a photoresist mold similar to Figure 106. Once the Au completely fills the mold on the top of the air-gap, overplating occurs. Enlarged contact pads on the top of the air-gaps form due to Au electroplating outside the photoresist mold. The enlarged contact pads may decrease the in-plane compliance of the leads as well as change the electrical performance.

In order to fabricate a photoresist mold with more depth on top of the air-gap, the photoresist film must be coated greater than 30 μm thick. A 30 μm film of the negative resist currently used for lead electroplating, Futurrex NR9-8000, cannot be clearly developed to the wafer surface. In fact, a 20 μm thick photoresist film requires a descum for 30 s in an oxygen plasma following development, to clear residual photoresist from the structure. Figure 108 is an SEM image of poorly formed leads due to residual photoresist remaining in the electroplating mold. The Au does not electroplate where residual material remains in the transitional area between the flat surface and the air-gap. Other thick-film photoresists may be used to form the lead electroplating mold.

However, in addition to clear patterning development of the features, the resist must be resilient to the Au or Cu electroplating bath for the entire duration of plating.

8.2.3 Yield and uniformity of air-gaps in SoL

The yield and uniformity of SoL structures is critical to the mechanical performance of the entire package. The leads are designed to move in the out-of-plane direction to account for non-planarity on chips and boards, and for test probe contact. In order to form a reliable contact between all components, the leads must be able to contact each of the pads on the opposing substrate. If one air-gap fails to form, the surrounding contacts may be tens of microns higher off the substrate. Each of these surrounding contacts would have to deflect almost 100% before any contact is made to the failed structure. Polyimide PI-2611 produces air-gaps with the highest yield and uniformity. Figure 109 shows an optical microscope view of the top surface of an array of air-gaps fabricated from 12 μm PNB sacrificial material overcoated with 8 μm thick polyimide PI-2611. The elliptical shapes of the air-gaps appear uniform. In addition, the color and focus of each of the air-gaps is similar for the entire array. The focus and color indicate uniform height of each of the structures. The red arrow in Figure 109 indicates the path for a profilometry scan across the center of a row of air-gaps. Figure 110 shows a 5000 μm long surface profile of a row of air-gaps obtained using a stylus tip at a rate 50 μm/s with 1 mg force. Each of the air-gaps has a height between 31 and 35 μm with regular spacing in between the structures. The space in Figure 110 between 3000 and 3500 μm on the x-axis is the area where the scan crosses a scribe line to the next die. The uniformity of the air-gaps is <10% of the total height and is sufficient to enable contact to

each I/O. Any future processes and materials used for fabrication of SoL packages must produce similar uniformity and yield in order to be successful.

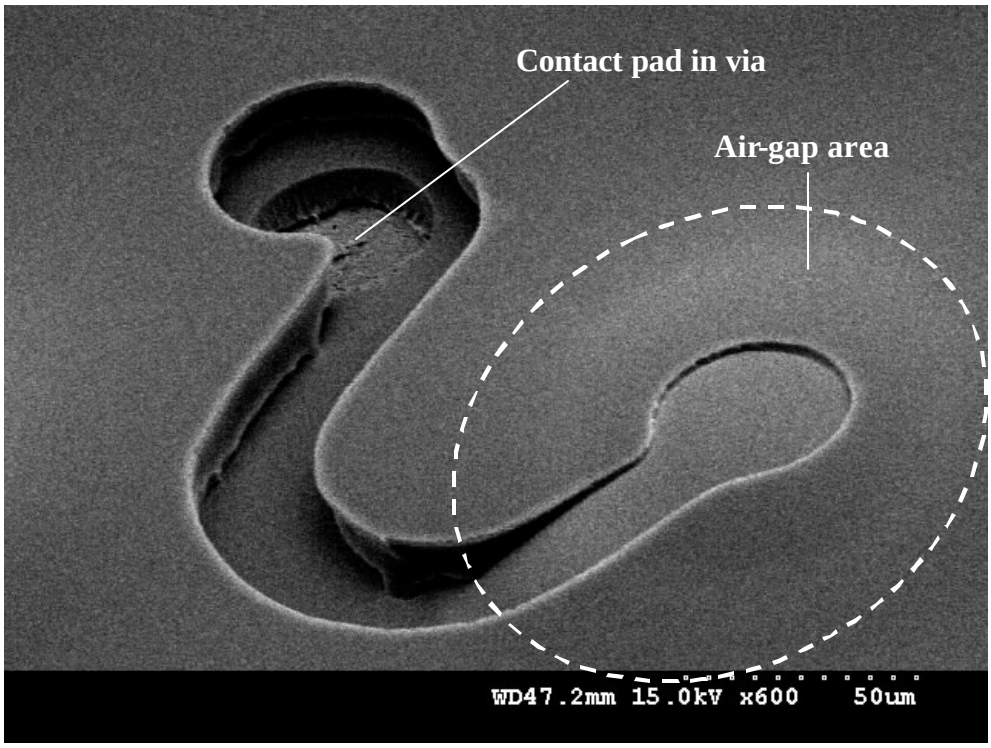

Figure 106: Photoresist electroplating mold for SoL lead fabrication on an air-gap with a maximum height of 30 μm.

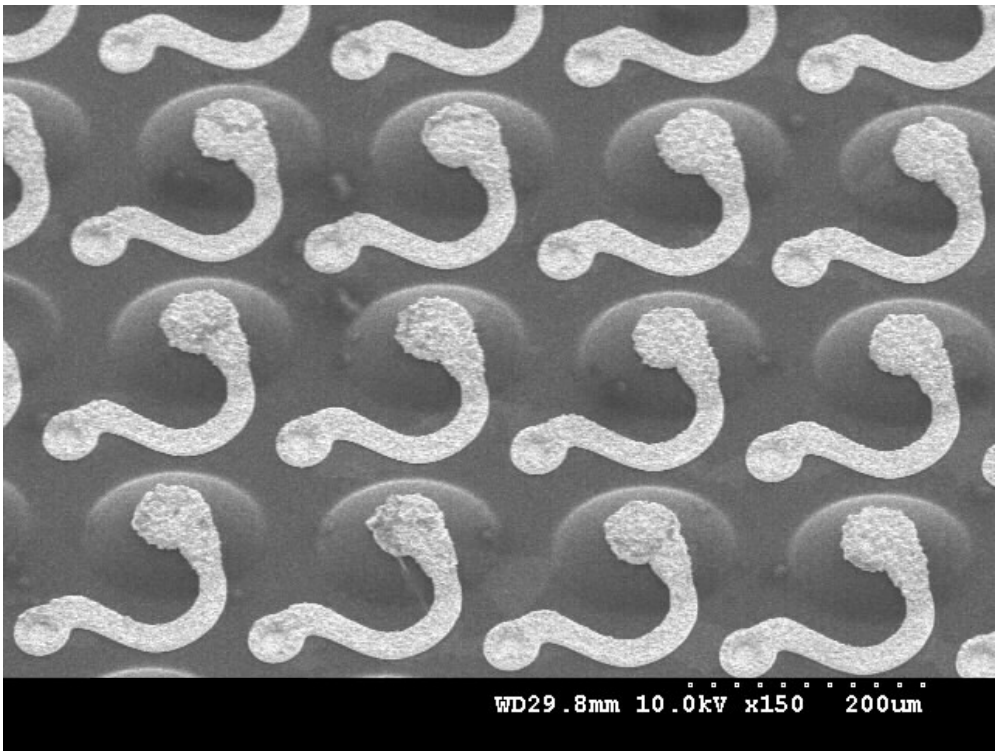

Figure 107: Leads with enlarged contact pads due to overplating of Au in the photoresist mold for lead electroplating.

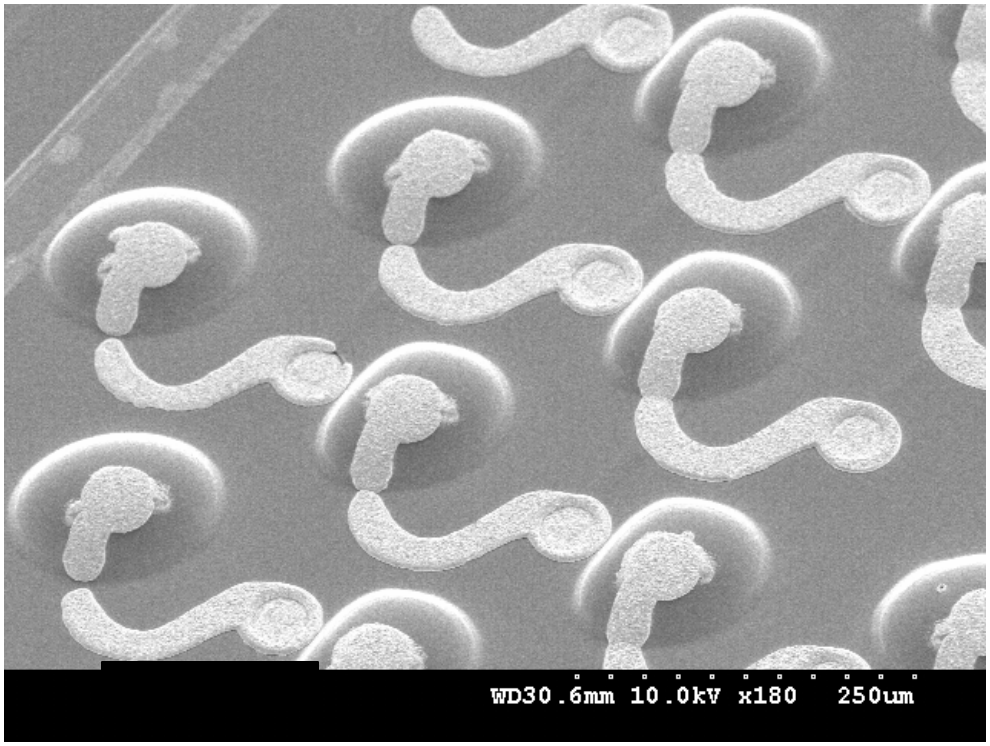

Figure 108: Poorly formed leads on air-gaps due to incomplete development of the photoresist mold for lead electroplating.

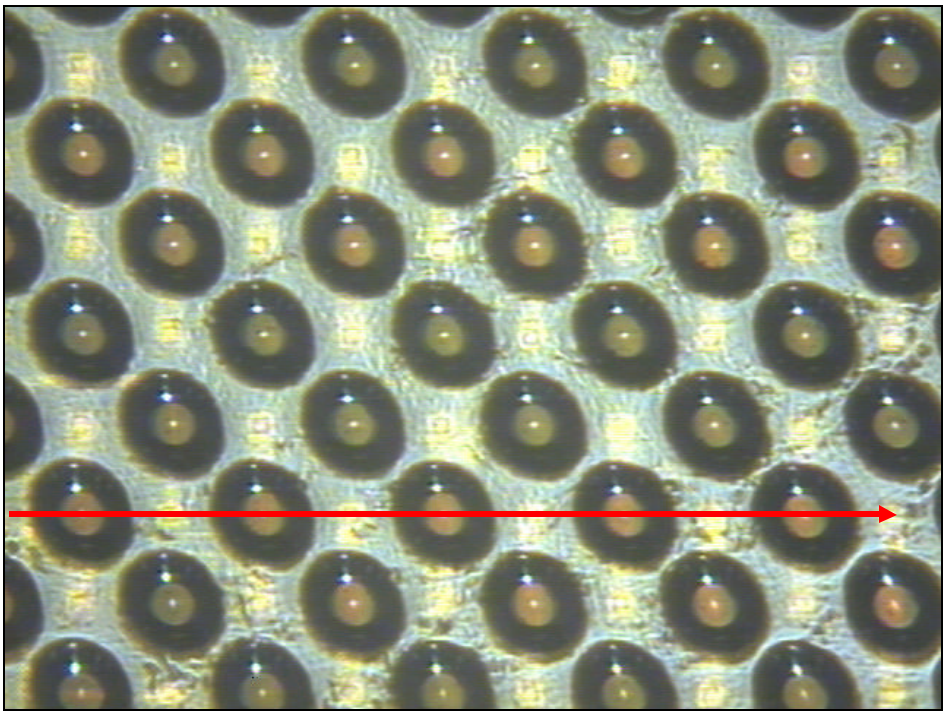

Figure 109: Optical microscope photograph of the top surface of air-gaps for SoL. The red arrow indicates the path for a profilometry scan across the center of a row of air-gaps.

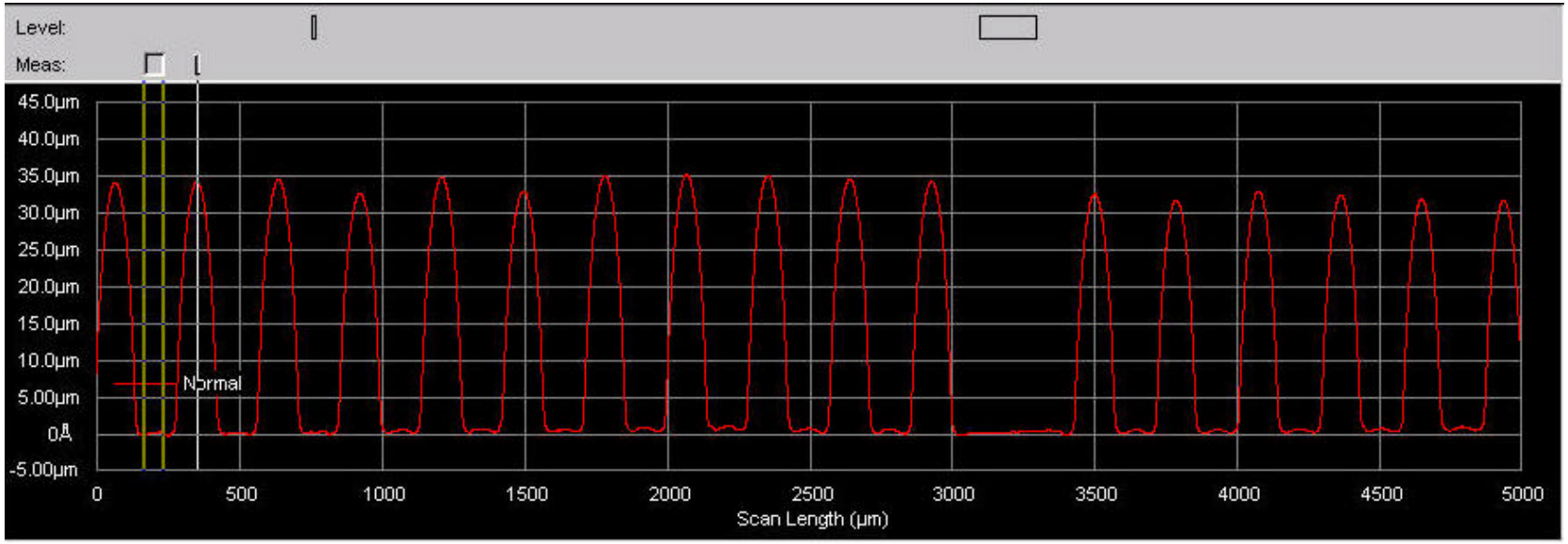

Figure 110: Profilometry scan performed across the center of a row of air-gaps to measure height uniformity.

CHAPTER 9

MECHANICAL PERFORMANCE OF AIR-GAPS

The out-of-plane (z-axis) mechanical performance of air-gaps is a crucial aspect of SoL CWLP. The addition of embedded air-gaps in a low-modulus polymer underneath each SoL I/O interconnection may enhance the vertical compliance of the structures in comparison to a solid polymer film. Mechanical performance studies were designed to: (1) evaluate factors influencing the z-axis mechanical performance of the air-gaps; and (2) determine the feasibility of achieving the necessary z-axis compliance through the incorporation of air-gaps in SoL packaging technology. The experimental force-displacement characteristics of various size and shape air-gaps, with different overcoat thicknesses and materials, have been determined using nanoindentation. The air-gap mechanical deflections are described with an analytical model using CoventorWare^{TM} (Coventor Inc., Cray, NC). The model calculations combined with the known limitations of fabrication are applied to provide a design space for maximum out-of place mechanical movement and compliance of the air-gaps.

9.1 Experimental Methods Specific to Chapter 9

9.1.1 Fabrication details of air-gaps for mechanical testing

Air-gaps were fabricated specifically for mechanical analysis using the non-photosensitive PNB air-gap fabrication process described in Chapter 5 and Chapter 8. Three variables were selected to be investigated for their influence on z-axis mechanical

performance: (1) overcoat mechanical properties, i.e. elastic modulus and elongation; (2) overcoat material thickness; and (3) air-gap geometry, including area and height. A set of samples was designed and prepared in order to provide a direct comparison of the effect on compliance from each single variable. A summary of the samples, labeled MECH-1 through MECH-4, and the process details and conditions for the fabrication of the samples, is given in Table 41. Each fabrication processing step has been previously described in detail in Chapter 5 and Chapter 8.

Two polyimides were selected as overcoat materials from those proven to work well in the air-gap fabrication process: Dupont Pyralin PI-2611 and PI-2734. A large variety of air-gaps sizes, both flat and dome-shaped, are achievable using these two polyimide overcoat materials. A comparison of the thermal and mechanical properties of the two polyimides was provided previously in Table 18 (Chapter 5, Section 5.4, page 123). PI-2611 and PI-2734 are both rigid-rod backbone polyimides based on BPDA/ODA chemistry and have similar thermal properties. However, PI-2611 has an elastic modulus of 8.3 GPa, which is 1.8 times greater than the elastic modulus of PI-2734. PI-2611 also has an elongation and a tensile strength about twice that of PI-2734. Samples MECH-1 and MECH-2 were fabricated from a 10 μm thick sacrificial PNB layer overcoated with 2.4 and 7.4 μm thick layers of PI-2734, respectively. These two samples provide a direct comparison for the effect of overcoat thickness on mechanical performance. Samples MECH-2 and MECH-3 vary only in air-gap height and are both overcoated with 7.4 μm thick PI-2734. Samples MECH-2 and MECH-4 were both fabricated from a 10 μm thick PNB sacrificial layer overcoated with approximately 7.5μm of overcoat polyimide. The difference between MECH-2 and MECH-4 is

Table 41: Processing details for the fabrication of samples for mechanical analysis.

Sample # / Process	MECH-1	MECH-2	MECH-3	MECH-4
Substrate	Si with native SiO_2	Si with native SiO_2	Si with native SiO_2	Si with native SiO_2
Sacrificial Polymer Solution (Table 13, page 99)	PNB-1-S1	PNB-1-S1	PNB-2-S1	PNB-1-S1
Hotplate softbake	120°C, 5 min.	120°C, 5 min.	120°C, 5 min.	120°C, 5 min.
Polymer cure	5°C/min to 250°C, dwell 1 hr.	5°C/min to 250°C, dwell 1 hr.	5°C/min to 250°C, dwell 1 hr.	5°C/min to 250°C, dwell 1 hr.
Sacrificial Polymer Thickness	9.7 μm	9.7 μm	29.5 μm	10.6 μm
Hard Mask	0.18 μm Al	0.18 μm Al	0.16 μm Al	0.16 μm Al
Photoresist/ Developer	Shipley 1813 / Shipley MF319	Shipley 1813 / Shipley MF319	Shipley 1813 / Shipley MF319	Shipley 1813 / Shipley MF319
Hard Mask Etchant	PAN etch at 50°C	PAN etch at 50°C	PAN etch at 50°C	PAN etch at 50°C
RIE Conditions (Table 14, page 103)	PNB-ETCH2, 23 min.	PNB-ETCH2, 23 min.	PNB-ETCH3, 56 min.	PNB-ETCH2, 26 min
Overcoat	PI-2734	PI-2734	PI-2734	PI-2611
Overcoat Polymer Thickness (after cure)	2.4 μm	7.4 μm	7.4 μm	7.8 μm
Decomposition (Table 16, page 105)	Program D	Program D	Program E	1 °C/min to 405°C, hold 0.5 hr., 1 °C/min to 425°C, hold 0.5 hr

MECH-2 is overcoated with PI-2734, and MECH-4 is overcoated with PI-2611. These two samples provide a direct comparison of the influence of the overcoat material mechanical properties on the air-gap mechanical performance.

The patterning of the air-gaps was performed using contact-printing and a standard processing recipe for Shipley Microposit 1813 photoresist. A lithography mask with several die containing various size and shape air-gap patterns was designed to investigate the effect of air-gap shape on z-axis mechanical performance. A summary of the shapes and dimensions of the patterns on the lithography mask is provided in Table 42. All four samples, MECH-1 through MECH-4, were fabricated using the various shapes mask for the lithography. Once the air-gap fabrication was complete, the shape and size of the structures were analyzed using SEM and profilometry, following the procedures described in Chapter 3.

Table 42: Air-gap geometries and dimensions for mechanical performance analysis.

	NAME	**DIMENSIONS on Mask**
1	Rectangle1	Rectangle 190 x 590 μm
2	Rectangle 2	Rectangle 190 x 9940 μm
3	Ellipse1	275 μm major axis, 190 μm minor axis
4	Square1	190 x 190 μm
5	Circle 1	190 μm diameter
6	Circle 2	130 μm diameter
7	Circle 3	110 μm diameter
8	Circle 4	90 μm diameter

The resulting air-gaps on samples MECH-1 through MECH-4 are completely enclosed air-gap structures. However, a hole or a vent in the air-cavity may affect the mechanical performance of the structure. Therefore, sample MECH-4 was broken into two pieces following complete fabrication of the air-cavities. Small vent holes were etched into the air-gaps on one of the two pieces. A mask containing 50 μm diameter holes at the same pitch of the air-cavities was used to form the holes. The mask was intentionally mis-aligned to form the hole near the side of each air-gap.

In order to fabricate the holes, a 3000 Å thick Al layer was deposited by DC sputtering as a hard mask material. Futurrex NR9-8000 negative resist and RD-6 developer was used to perform lithography on the hard mask. The pattern was transferred from the resist into the Al hard mask layer using PAN aluminum etchant at 50 ^{o}C, followed by stripping of the photoresist with acetone, methanol, isopropanol, and deionized water. The holes were defined in the polyimide overcoat layer using a Plasmatherm RIE under the following conditions: Pressure = 280 mTorr; Power = 300 W; gas flow rates: 45 sccm CHF_3 and 5 sccm O_2; Temperature = 35^{o}C. The total etch time was 16 min. The remaining Al mask layer was removed with the PAN wet chemical etch.

9.1.2 Experimental details of nanoindentation

Nanoindentation was performed using a Hysitron Triboindenter nanoindentation tool. The general sample mounting and data collection process is described in Chapter 3, Section 3.4.7. The Triboindenter is capable of operation with two load heads: a low-force head with load application capability up to 9 mN of applied force and displacement

of about 10 μm; and a high-force head with load application capability up to 1 N of applied force and displacement up to 100 μm. The high-force load head is used in all nanoindentation experiments performed on air-gaps. Several nanoindenter diamond-tips of various shape and size are available for use with the Triboindenter. Large radii spherical or conical tips were used on the air-gap samples in order to reduce penetration of the tip into the overcoat polymer film. Each sample, MECH-1 through MECH-4, was tested with two different nanoindenter tips: samples MECH-1 and MECH-2 were indented with a 50 μm conical tip and a 200 μm radius spherical tip; sample MECH-3 was indented with a 50 μm conical tip and a 20 μm radius conical tip; and sample MECH-4 was indented with a 20 μm radius conical tip and a 200 μm spherical tip. Both the 20 μm and 50 μm conical tips have a 60^{o} included angle.

The Triboindenter can be operated in two modes: load control mode; and displacement control mode. The total height of the air-gaps is known prior to indentation, from profilometry of the surface following completion of air-gap fabrication. Therefore, displacement control mode was applied to the indents in order to control the compression ratio of the air-gaps. Each indent consists of three set parameters: a maximum displacement, a rate of displacement, and a hold time at the maximum displacement. When operating the Triboindenter with the high force head, only single indentations can be performed. Therefore, repeat displacements of air-gaps are manually performed by successively indenting the air-gap in approximately the identical position with the same set parameters as the previous indentation.

9.2 Mechanical Properties From Nanoindentation

Micro- or nano-indentation has rapidly become a dominant method for measuring the mechanical properties of thin film materials [105-114]. A hard diamond-tip indenter is contacted to and pressed into the thin film while using high-resolution electronics to continuously measure the applied force and the displacement of the indenter tip. The most common reason indentation is performed is to extract mechanical properties from a thin film, including the elastic modulus (*E*) and the hardness (H). A commonly used method of analysis is that described by Oliver and Pharr [107] which relates the load (P) and the vertical displacement (*h*), along with the contact area (A) and the contact stiffness, S = dP/d*h*, to the elastic modulus and hardness of the indented material. This methodology has been well documented in the literature using sharp pyramidal indenters such as a Berkovich tip (three-sided pyramid), a Vickers tip (four-sided pyramid), and various radii conical tips [105-109, 111-115].

The Oliver and Pharr analysis method treats the unloading of the indenter tip as a purely elastic deformation and begins by describing the load-displacement relationship for nanoindentation unloading as a power-function [105, 107, 109, 111]:

$$P = \alpha (h - h_f)^m \qquad \text{Eq. (9.1)}$$

P is the load, h is the displacement, h_f is the final displacement after complete unloading, and α and m are constants for various tip geometries and indented materials: generally, m = 1 for a flat punch indenter, m = 2 for cones, and m = 1.2-1.6 for Berkovich indenters and spheres.

The elastic modulus of the material (*E*) (or the ratio of the tensile stress to the tensile strain in the material) is described through equation 9.2 [107],

$$\frac{1}{E_r} = \frac{(1-\nu^2)}{E} + \frac{(1-\nu_i^2)}{E_i} \qquad \text{(Eq. 9.2)}$$

where ν is the Poisson's ratio and E is the elastic modulus for the indented material, E_i and ν_i are the elastic modulus and Poisson's ratio for the indenter (diamond: E_i = 1141 GPa; ν_i =0.07), and E_r is the reduced modulus obtained from the Sneddon stiffness equation given by equation 9.3 [107, 111].

$$E_r = \frac{S\sqrt{p}}{2\sqrt{A}} \qquad \text{(Eq. 9.3)}$$

In equation 9.3, S is the contact stiffness, and A is the area of contact between the indenter and the sample.

The projected area of elastic contact, *A*, in equation 9.3 is determined by an area function describing the indenter geometry. The indenter itself is assumed to not deform. The contact area can be determined empirically, or from an ideal area function based on the tip geometry. An empirical area function may be determined by indenting to various contact depths in a low-hardness and known modulus material, such as aluminum. However, the calculations of modulus in these studies were performed using the ideal tip area function. For a conical indenter with a radius of r, the ideal contact area as a function of contact depth is described by equation 9.4.

$$A = -ph_c^{\,2} + 2prh_c \qquad \text{(Eq. 9.4)}$$

The ideal contact area as a function of contact depth for a spherical indenter with radius, *r*, is:

$$A = 2\pi r h_c \qquad \text{(Eq. 9.5)}$$

The contact depth (h_c) in equations 9.4 and 9.5 is not the total measured displacement (h), but the total displacement minus the distance the surface is displaced at the perimeter of the contact. The contact depth (h_c) is calculated from the following equation:

$$h_c = h_{\max} - \varepsilon \frac{P_{\max}}{S} \qquad \text{(Eq. 9.6)}$$

where ε is a constant dependent on tip geometry. Equation 9.6 relates the total measured depth to the displacement of the surface at the perimeter of the contact (ε is 0.72 for conical indenters and ε is 0.75 for a spherical indenter) [107].

The quality of the analysis of nanoindentation data depends on how well equations 9.1 and 9.3 model a real situation. Pharr, Oliver, and Brotzen [112] have shown that equation 9.3 applies to the unloading curve from any indenter which can be described as a smooth body of revolution. King [116] used the finite element method to show that equation 9.3 also holds true for flat-ended punches with square (Vickers-like) and triangular (Berkovich-like) cross-sections. However, finite element simulations of indentation with a rigid cone have shown that this equation leads to an overestimate in the elastic modulus [106]. The source of the error stems from the deformed area not being perfectly conical, but rather some complicated geometry. Hay et al. [106] suggest a correction factor, γ, to the Sneddon stiffness equation for indentation by a cone:

$$S = g\frac{2}{\sqrt{p}}E_r\sqrt{A} \qquad \text{(Eq. 9.7)}$$

The correction factor, γ, is usually small; reported values vary from 1.04-1.25 [106,111] The correction factor can be approximated from the following equation [106]:

$$g = p\frac{\frac{p}{4} + 0.15483073\cot f\frac{(1-2\nu)}{4(1-\nu)}}{(\frac{p}{2} - 0.83119312\cot f\frac{(1-2\nu)}{4(1-\nu)})^2} \qquad \text{(Eq. 9.8)}$$

where φ is the half angle of the conical indenter and ν is Poisson's ratio of the material being indented. For a 20 or 50 μm radius conical tip with a 60^o included angle indented into a material with ν = 0.3, equation 9.8 yields a correction factor of γ = 1.11.

In the Oliver and Pharr [107] analysis method, the film is loaded and unloaded three times to 10% of the maximum load, followed by a fourth loading, a hold, and a final complete unloading. This load/unload cycle allows the final unloading curve is to be mostly elastic. The last unload curve is then used in the analysis for the film mechanical properties. However, when operated with the high-force load head, the Hysitron Triboindenter nanoindentation tool only allows a trapezoidal load function to be applied to the sample, consisting of a single load, hold, and unload. Oliver and Pharr [107] have shown that when a power-law fit is applied to the data from the first and last load cycles, the difference in the calculated contact stiffness is minimal.

In order to carry out the analysis to determine the elastic modulus, the unloading curve of the indentation data is first fit to a power law function, described by equation 9.1. The constants α, m, and h_f are extracted from the fitting equation. The next step is to evaluate the contact stiffness, S, at the initial part of the unloading curve, or at h_{max}.

Equation 9.1 is differentiated with respect to h, and the expression evaluated at $h_{max.}$ Once S is known, h_c and A(h_c) are evaluated with the equations relevant to the tip geometry (spherical or conical). Equation 9.7 along with the correction factor, γ, if a conical tip was used, are then used to find the reduced modulus, E_r. The elastic modulus is finally calculated by using equation 9.2.

The same indentation data can be utilized in order to determine the hardness, H, of the indented material. The ideal area function, given by either equation 9.4 or 9.5 depending on tip geometry, is first used to find the projected area of contact under peak load, or at h_c. The hardness is defined as the mean pressure the material will support under load. Hardness is calculated using equation 9.9:

$$H = \frac{P_{max}}{A} \qquad \text{(Eq. 9.9)}$$

9.3 Nanoindentation Results for Polyimide Overcoat Films

In order to verify the accuracy of the nanoindentation technique and the analysis method described in section 9.3, indents were performed on samples MECH-1, MECH-2, and MECH-4 in the areas where no air-gaps were present. The unloading portion of the force-displacement curves obtained from the single indents was used to calculate the elastic modulus. Table 43 shows the experimental parameters for the indents, the power-law fit parameters to the unloading curve, and the resulting calculated elastic modulus values. The correction factor, γ, was applied only to sample MECH-2b, indented with the 50 μm conical tip. The value of γ for this tip with a 60^o included angle is 1.11.

The values of elastic modulus as reported by the polymer manufacturer for PI-2734 and PI-2611 are 4.7 GPa and 8.5 GPa, respectively. The calculated modulus values vary in error from these literature values from 12-80%. In all indents performed with the 200 μm spherical indenter tip, the power-law exponent, *m*, falls within the reported range of 1.2-1.6 for a spherical tip [107]. However, the power-law exponent for the sample MECH-2b indented with the 50 μm conical tip is 1.45, which is below the typical value of 2 for cones. The large radius of this tip may cause it to behave more as a spherical tip than a cone. When a conical power-law fit is performed on this data set, setting $m = 2$, the modulus value increases from 5.3 to 9.0. This is an increase in percent error from 12 to 90%.

Error may be introduced in all indents simply from using the ideal area function in the calculations. Any overestimate in the actual contact area of the tip would lead to a lower calculated elastic modulus value. With such large radius tips, there is a good chance that the tip does not perfectly follow the ideal geometry. However, even with the assumptions that the tip follows ideal geometry and the single indent is perfectly elastic, this method of analysis still yields a correct order of magnitude elastic modulus value.

9.4 Mechanical Performance Sample Fabrication Results

Images of MECH-1 through MECH-4 were obtained using SEM prior to nanoindentation in order to verify complete decomposition and observe the shape of the resulting air-cavities. Figure 111 through Figure 114 show representative SEM images of various shaped air-cavities from each of the four samples. No visible residue was observed in all cross-sectioned air-cavities, indicating complete decomposition. All the

Table 43: Indentations and elastic modulus calculation results from polymer overcoat films containing no air-gaps.

			Indent Parameters			Power-law Fit Parameters				
Sample	**Overcoat Polymer**	**Tip**	**Displace-ment**	**Ramp Rate**	**Hold Time**	**A**	**h_f (nm)**	**m**	**R^2**	**Elastic Modulus (GPa)**
MECH-1	PI-2734	200 μm spherical	1 μm	500 nm/s	5 s	4.032	836.1	1.3507	0.9453	0.971
MECH-2a	PI-2734	200 μm spherical	5 μm	1000 nm/s	5 s	0.9949	701.9	1.6081	0.9860	3.45
MECH-2b	PI-2734	50 μm conical	5 μm	500 nm/s	5 s	4.216	1573	1.4513	0.9973	5.28
MECH-4a	PI-2611	200 μm spherical	5 μm	1000 nm/s	5 s	0.5466	236.9	1.4403	0.9919	4.61
MECH-4b	PI-2611	200 μm spherical	5 μm	1000 nm/s	5 s	2.251	187.7	1.4466	0.9982	2.04

resulting air-cavities on each sample were somewhat dome-shaped, despite the use of slow decomposition profiles.

Measurements of the resulting maximum in air-cavity height and the overcoat polymer thickness were performed using a KLA/Tencor P-15 contact profilometer. Table 44 lists the average measured air-cavity heights and the standard deviation in height for the various shapes and samples. The reported values are the averages of 10+ measurements taken from at least 3 different die across the wafer. 3-D surface plots of the air-gaps were also obtained using the Tencor P-15 profilometer. Scans were taken at 20 μm intervals to form a 3-D image. Figure 115 through Figure 118 show 3-D surface plots of the 190 μm diameter circle air-gaps from each of the 4 samples.

Although the air-gaps vary in height by shape and sample, the height is fairly uniform across air-gaps of similar shape on a single sample. The height uniformity increases when the overcoat thickness to sacrificial material thickness ratio is greater. The air-gaps on sample MECH-1 display a slightly different profile than the other three samples. The overcoat polyimide, PI-2734, collapses to the silicon surface near the edge of the air-gap, resulting in a ridge of overcoat polymer surrounding a dome-shaped air-cavity. This shape is clearly demonstrated in Figure 115. A similar but less pronounced result is seen in the other samples fabricated with PI-2734 overcoat polyimide. Both MECH-2 and MECH-3 contain flatter areas near the corners and edges of the air-gaps.

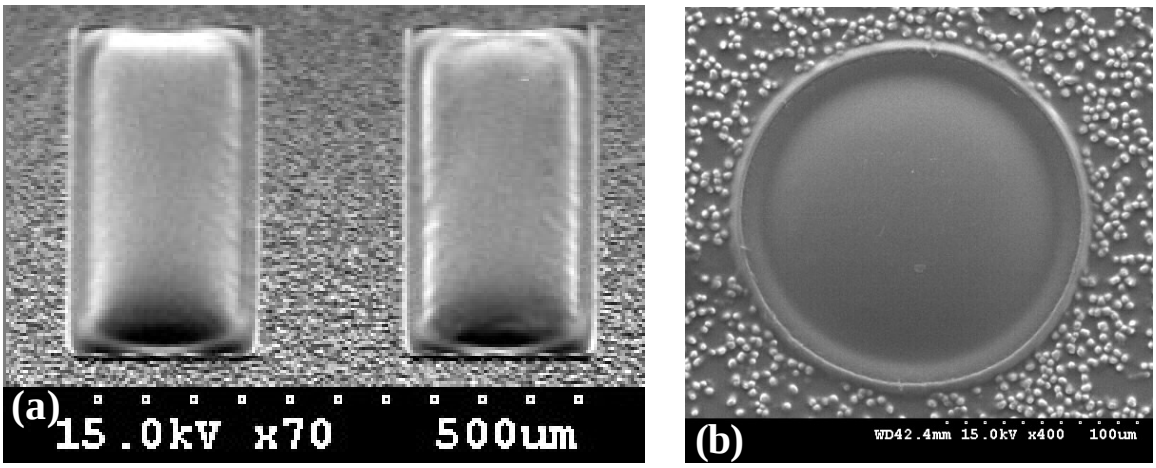

Figure 111: SEM images of various shape air-gaps from sample MECH-1 overcoated with 2.4 μm thick PI-2734. The various shapes shown are: (a) rectangle1: 190 x 590 μm and (b) circle 1: 190 μm diameter.

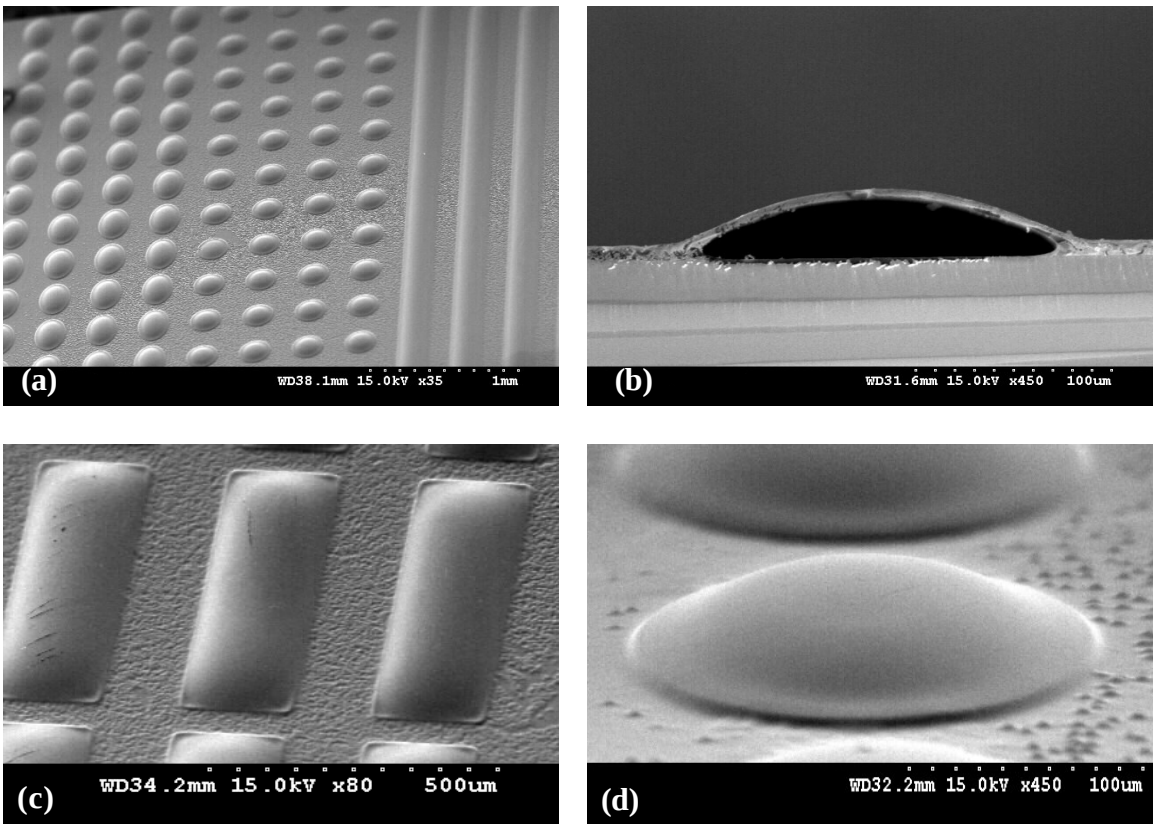

Figure 112: SEM images of various shape air-gaps from sample MECH-2 overcoated with 7.4 μm thick PI-2734. The various shapes shown are: (a) circle 1:190 μm diameter; ellipse1 190 × 225 μm; and rectangle 2: 190 × 9940 μm; (b) a cross sectional image of rectangle 1: 190 × 590 μm; (c) rectangle 1: 190 × 590 μm; and (d) circle 1: 190 μm diameter.

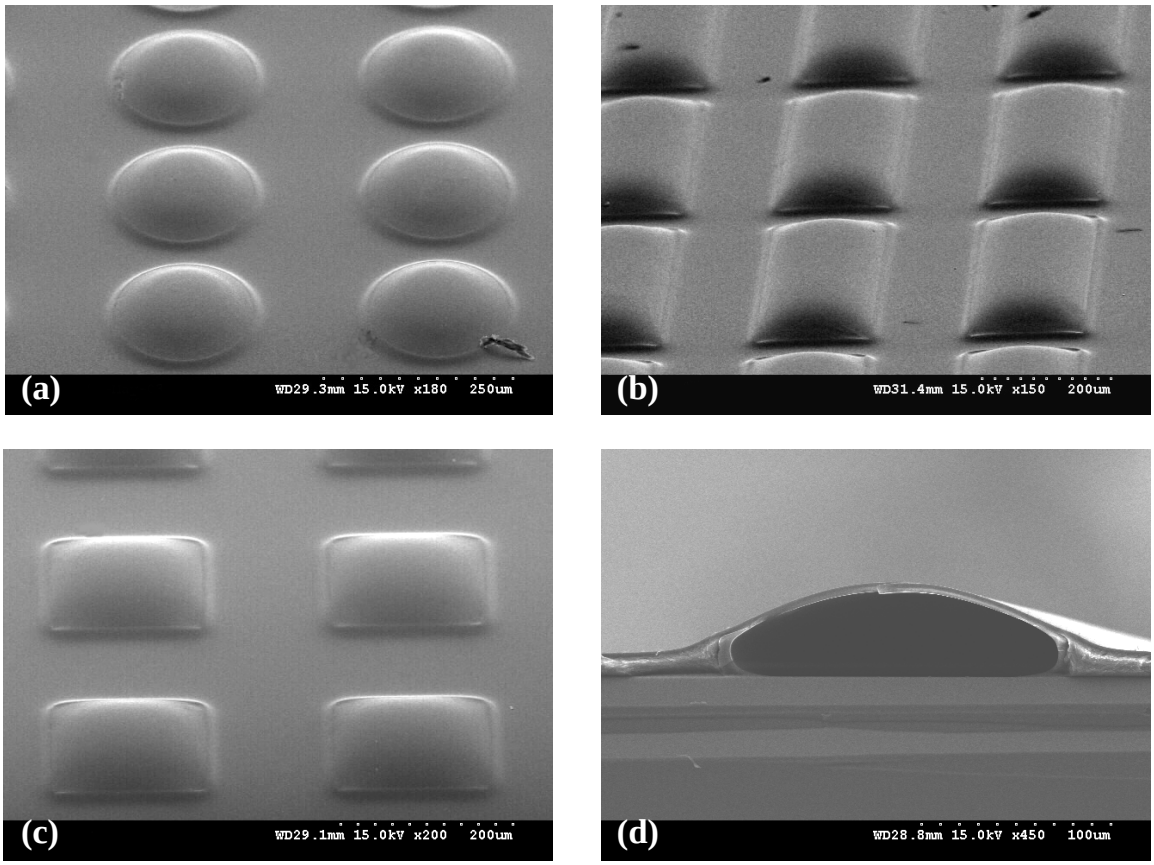

Figure 113: SEM images of the various shape air-gaps from sample MECH-3 overcoated with 7.4 µm thick PI-2734. The various shapes include: (a) circle 1: 190 µm diameter; (b) rectangle 1: 190 × 590 µm; (c) square 1: 190 × 190 µm; and (d) a cross sectional image of rectangle 2: 190 × 9940 µm.

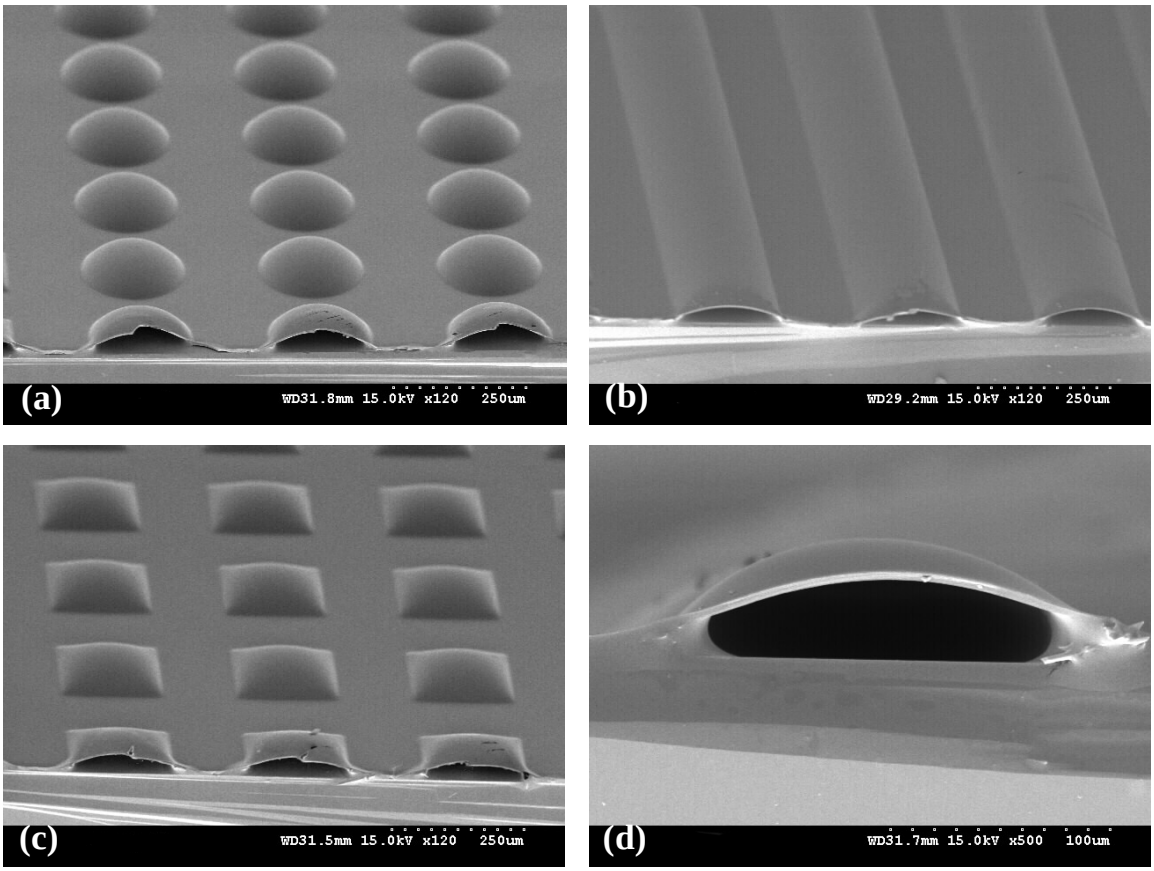

Figure 114: SEM images of the various shape air-gaps from sample MECH-4 overcoated with PI-2611. The various shapes include: (a) circle 1: 190 μm diameter; (b) rectangle 2: 190 × 9940 μm; (c) square 1: 190 × 190 μm; and (d) a cross sectional image of rectangle 1: 190 ×590 μm.

Table 44: Air-gap height for air-gaps on samples MECH-1 through MECH-4, measured by contact profilometry.

	Air-gap Height (μm)			
Geometry	**MECH-1**	**MECH-2**	**MECH-3**	**MECH-4**
Rectangle-1	25.85 ± 2.91	31.44 ± 0.43	45.46 ± 2.43	54.53 ± 1.29
Rectangle-2	24.94 ± 5.75	32.52 ± 0.53	33.67 ± 3.21	53.60 ± 1.48
Ellipse-1	21.80 ± 1.73	25.64 ± 0.22	37.09 ± 2.51	43.81 ± 0.61
Square-1	15.09 ± 3.29	22.92 ± 0.08	33.17 ± 1.56	39.98 ± 0.72
Circle-1	14.00 ± 3.05	21.61 ± 0.87	32.55 ± 1.77	47.69 ± 0.81

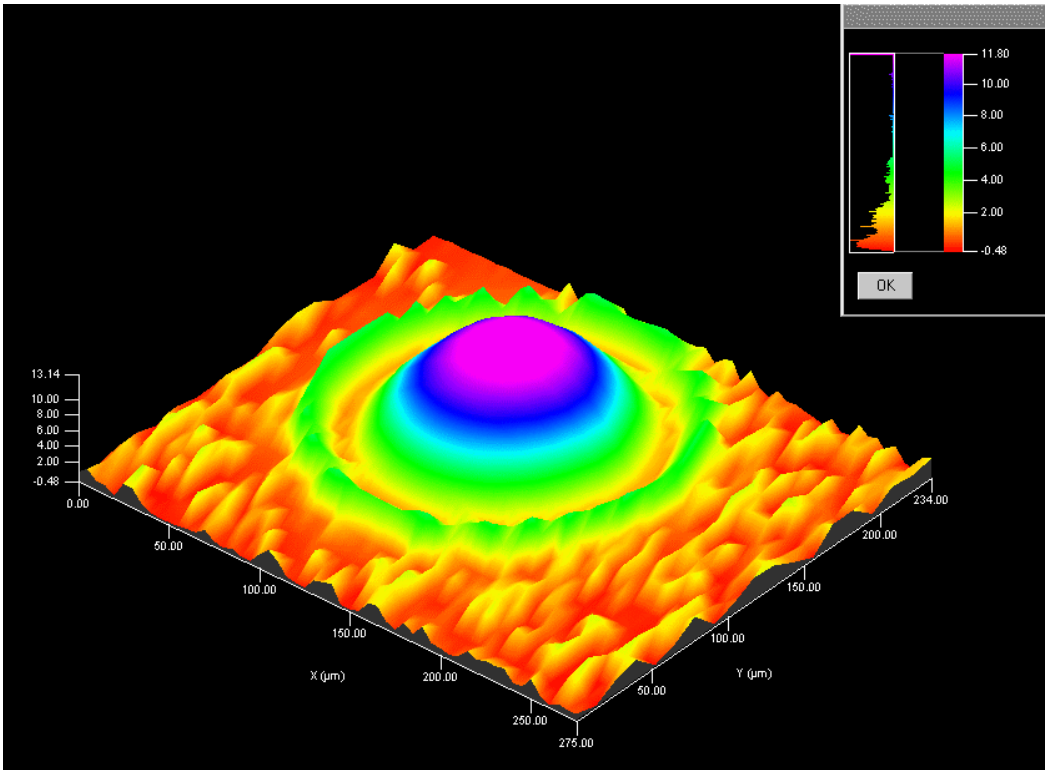

Figure 115: 3-D surface profile of a 190 µm dia. circular air-gap on sample MECH-1.

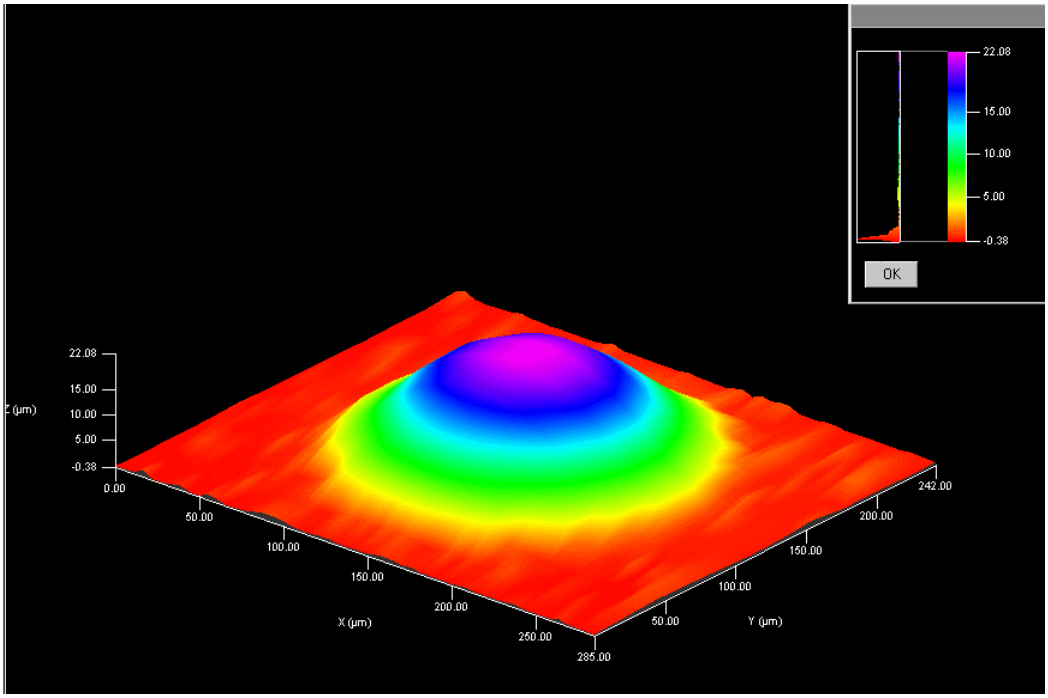

Figure 116: 3-D surface profile of a 190 µm dia. circular air-gap on sample MECH-2.

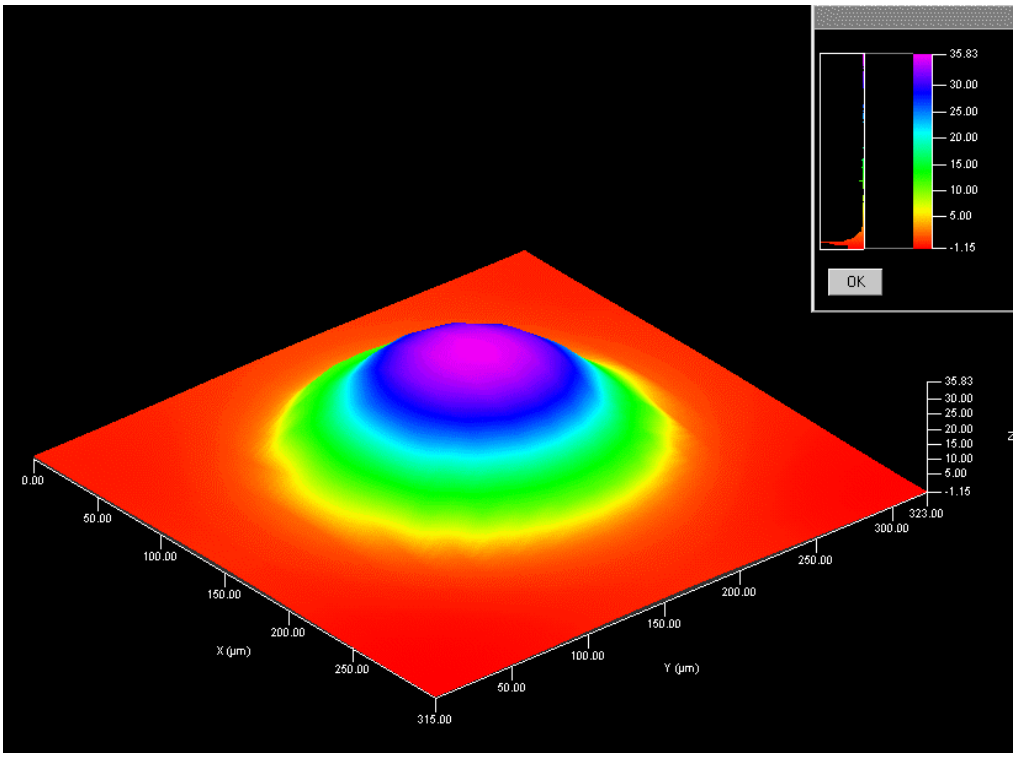

Figure 117: 3-D surface profile of a 190 µm dia. circular air-gap on sample MECH-3.

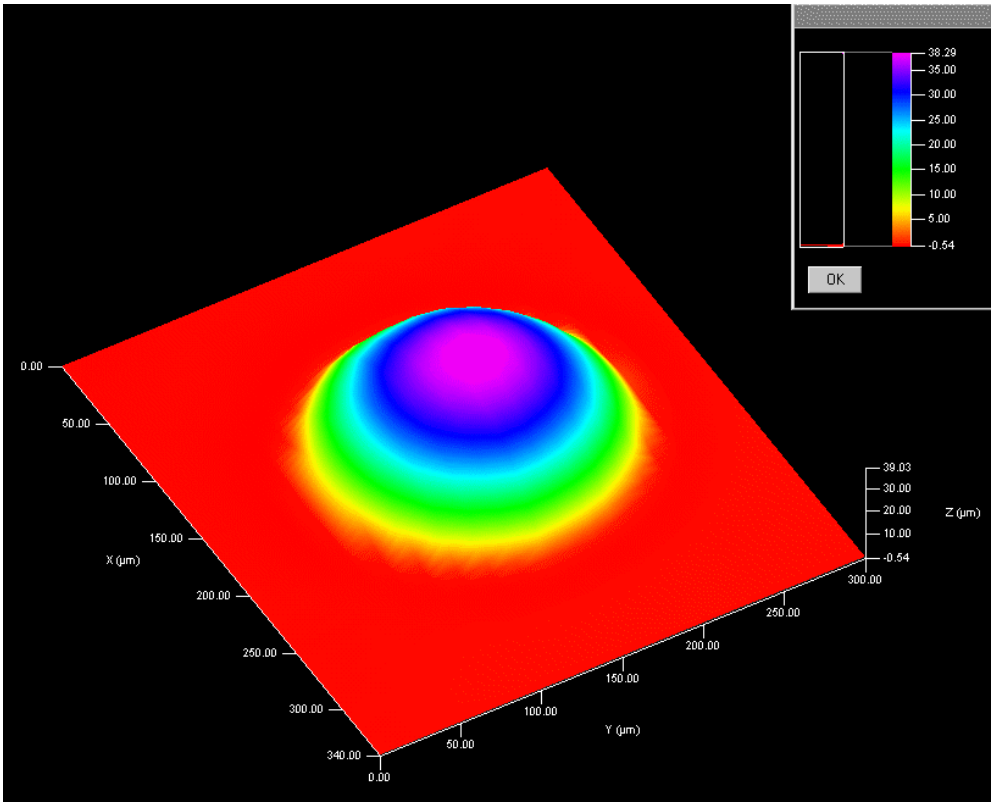

Figure 118: 3-D surface profile of a 190 µm dia. circular air-gap on sample MECH-4.

9.5 Air-gap Indentation Results and Discussion

A series of indentations were performed on the various shaped air-gaps on all four samples fabricated for mechanical tests. The results from the indentations are presented and discussed in this section. The variation in the force-displacement characteristics between air-gaps of identical geometry on a single sample, and the effect of the experimental conditions are discussed in Sections 9.5.1 and 9.5.2. The experimental conditions include indenter tip geometry, maximum displacement, displacement rate, and hold time at the maximum displacement. The force-displacement characteristics between the air-gaps on the four samples are then discussed in Sections 9.5.3 and 9.5.4.

The force-displacement curves from air-gap indentations are not used to determine the elastic modulus of air-gaps; rather, the entire force-displacement curves are analyzed for the indentation behavior. If the air-gap is behaving as an elastic material, the compliance (inverse of the elastic modulus, or $1/E$) is determined to indicate the amount of vertical movement that occurs under a given load. A material has perfectly elastic behavior if it obeys Hooke's Law, which states the strain (ε) in a material is directly proportional to the stress (σ) applied. The common form of Hooke's law is presented as equation 9.10

$$E = \frac{\sigma}{\varepsilon} \qquad \text{(Eq. 9.10)}$$

The proportionally constant in equation 9.10 is the elastic modulus (E). In the indentation of an air-gap, the stress is proportional to the force of the indenter tip and the strain is proportional to the tip displacement. Therefore, if an air-gap is behaving perfectly elastically, the force-displacement curve is a straight line with a slope of E.

Figure 119 is the result of an indent performed on a rectangular air-gap on sample MECH-2 with a 200 µm radius spherical tip. The load/unload function is a typical trapezoidal load function: a 10 s displacement increase at a rate of 2000 nm/s; a 5 s hold at the 20 µm maximum displacement; and a 10 s displacement decrease at the same rate of 2000 nm/s. The top portion of the curve in Figure 119 is created as the displacement is increased, with a resulting increase in the load. Once the maximum displacement is reached, a 5 s hold is performed. The vertical portion at the extreme right of the curve is created during this 5 s hold. The load decreases during the 5 s hold as the tip sinks into

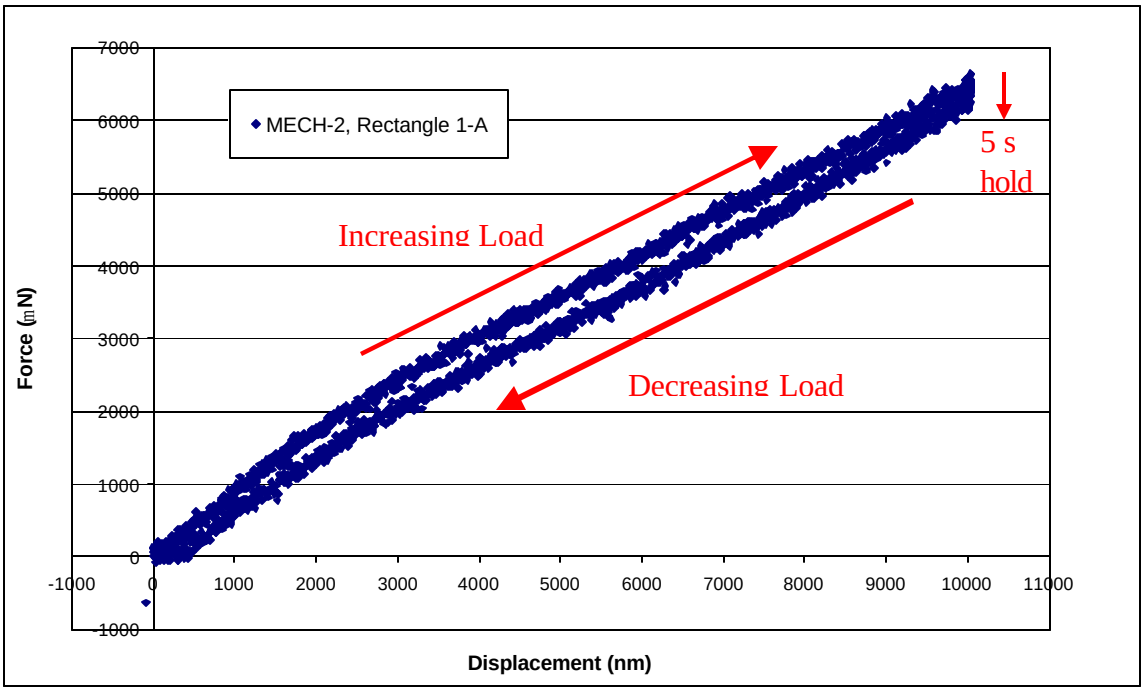

Figure 119: Linear force-displacement curve for an air-gap on MECH-2 with dimensions of Rectangle-1 (190 × 590 µm). The indent was performed with a 200 µm tip at a rate of 2000 nm/s, and a 5 s hold at maximum displacement.

the polymer surface. The bottom portion of the curve is then formed as the tip is unloaded from the air-gap. A perfectly elastic air-gap shows no hysterisis between the loading and unloading curves, and they lie directly on top of one another. Any hysterisis or deviation from linearity indicates plastic deformation in the sample. The curve in Figure 119 has very little hysterisis and is at a displacement of only 140 nm when the force returns to zero. Therefore the air-gap is returning to its original height before indentation. A small change in slope occurs in Figure 119 around a displacement of 2000 nm. The higher slope indicates more stiffness in the sample. This initial higher slope portion of the curve is a result of the tip indenting the overcoat film at the beginning of the indentation, followed by pure compression of the air-gap only. However, the air-gap indentation in Figure 119 represents an almost ideal case and is considered an elastic deformation.

9.5.1 Repeatability of the force-displacement behavior of air-gaps

This section presents the force-displacement results from indents of similar size and shape air-gaps on a single sample. The results are examined to determine the repeatability of air-gaps indented under identical conditions. Figure 120, Figure 121, and Figure 122 are representative force-displacement curves resulting from the indentation of three sets of air-gaps of similar geometry. Figure 120 shows the results of 20 μm displacement-controlled indents performed on rectangular air-gaps on sample MECH-1 with a 50 μm radius conical tip. The experimental conditions for the indents in Figure 120 are a ramp rate of 2000 nm/s with a 5 s hold at maximum displacement. Figure 121 contains the force-displacement results for 10 μm indents performed on rectangular air-

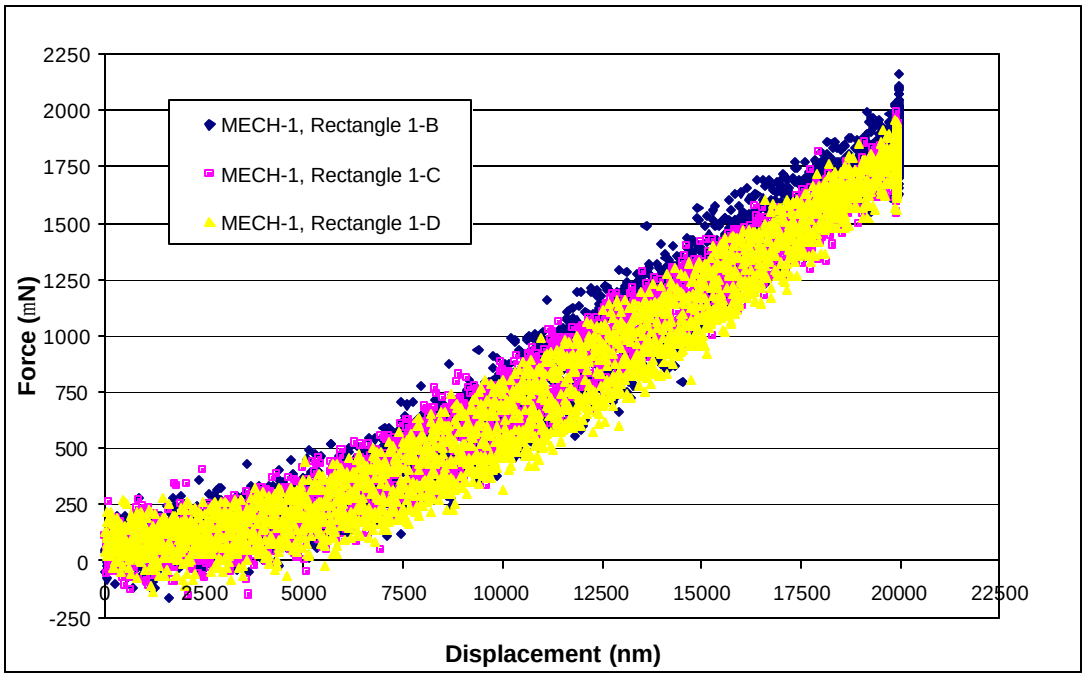

Figure 120: Force-displacement curves for three MECH-1 air-gaps with dimensions of Rectangle 1 (190 × 590 µm) indented with a 50 µm conical tip to a depth of 20 µm at a displacement rate of 2000 nm/s and a 5 s hold at maximum displacement.

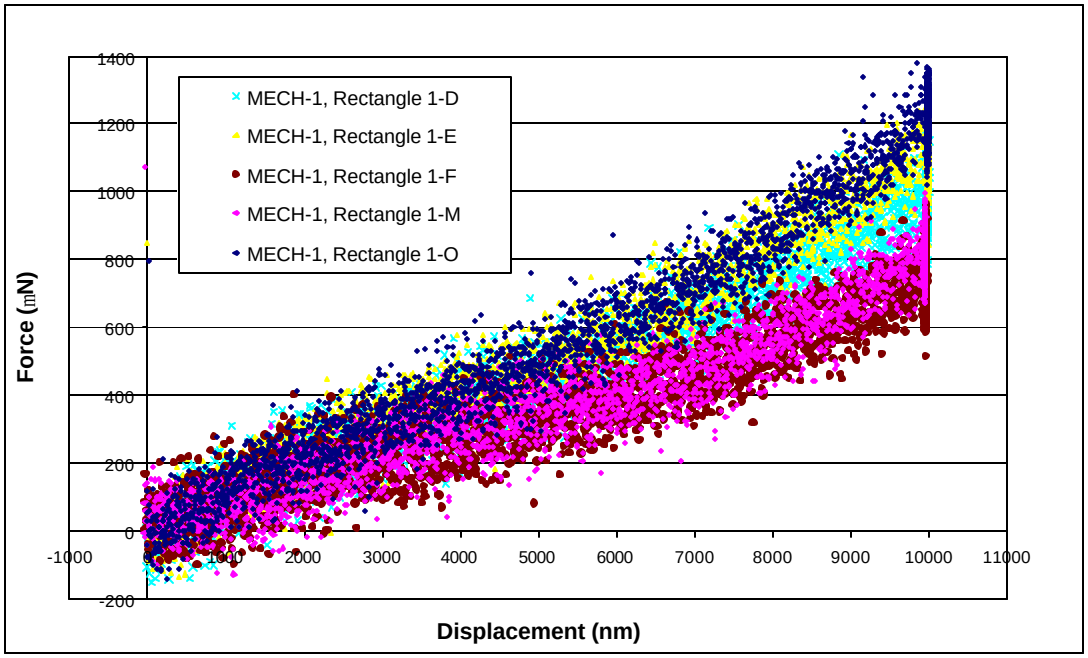

Figure 121: Force-displacement curves for five MECH-1 air-gaps with dimensions of Rectangle 1 (190 × 590 µm) indented with a 200 µm spherical tip to a depth of 10 µm at a displacement rate of 1000 nm/s and a 5 s hold at maximum displacement.

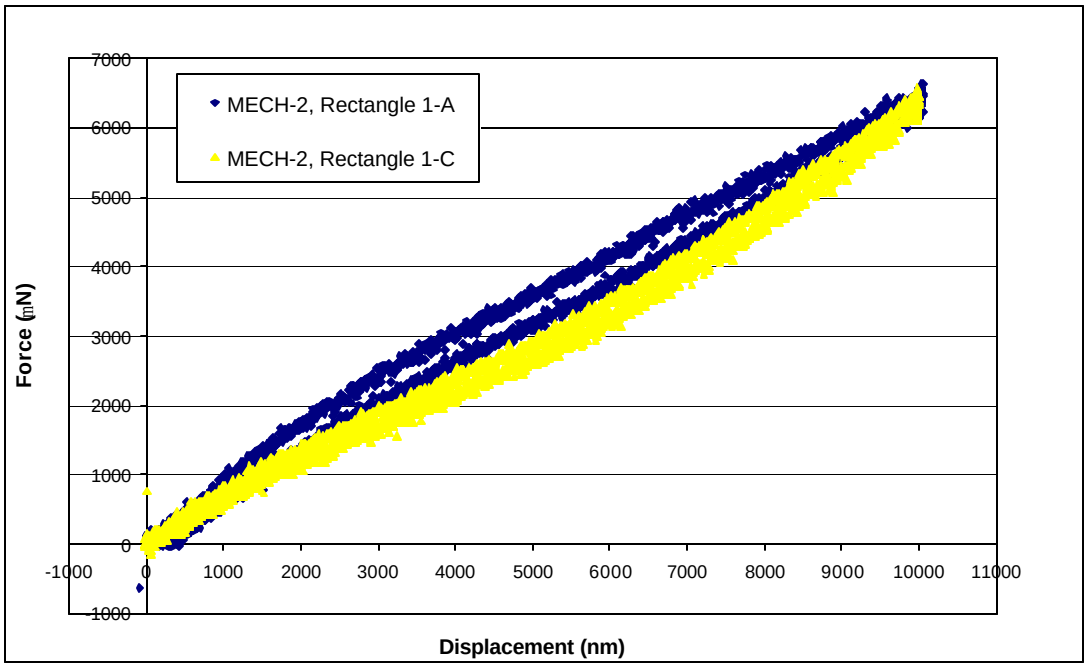

Figure 122: Force-displacement curves for two MECH-2 air-gaps with dimensions of Rectangle 1 (190 × 590 μm) indented with a 200 μm spherical tip to a depth of 10 μm at a displacement rate of 1000 nm/s and a 5 s hold at maximum displacement.

gaps on sample MECH-1 with a 200 μm radius spherical tip. The conditions for the indents in Figure 121 are a displacement rate of 1000 nm/s and a hold of 5 s at maximum displacement. Figure 122 shows force-displacement curves for the indentation of rectangular air-gaps on sample MECH-2 with a 200 μm radius spherical tip. The indents in Figure 122 were performed to a depth of 10 μm at a displacement rate of 1000 nm/s, and a 5 s hold at maximum displacement. The three figures show results typical to other samples and other air-gap shapes. Slight variations are observed in either the shape of the curves, or the maximum load at maximum displacement. The force-displacement curves in Figure 120 and Figure 121 feature consistent force-displacement curve shape between the different air-gaps of identical geometry. However, there is some deviation in the

amount of force required to reach maximum displacement between the different air-gaps. The force at maximum displacement (based on the average of 20 data points at maximum) for the curves in Figure 120 is 1847 ± 33 μN. The force at maximum displacement for the curves in Figure 121 is 995 ± 194 μN. The percentage of deviation from the average load increases as the depth of the indentation is decreased. Therefore, indents to 10 μm, such as the curves in Figure 121, have more variability in the forces required. Figure 122, on the other hand, is an example of typical variation in the shape of the curves. Although one air-gap gives a slightly concave force-displacement curve, the force required at maximum displacement is approximately equal. The small differences in the shape of the curve or forces required for indentation, as seen in these figures, occur between air-gaps which are considered identical. The small deviations result from some variation of the overcoat thickness between air-gaps, or the position of the indenter tip on the air-gap. Differences with a magnitude similar to the results in Figure 120 through Figure 122 are not considered in the subsequent sections as effects from significant changes in air-gap materials or geometry.

9.5.2 The effect of experimental parameters on air-gap force-displacement curves.

Three parameters are experimentally set for each indentation: 1) maximum displacement; 2) displacement rate; and 3) hold time at maximum displacement. Air-gaps were indented with variation in these three parameters in order to understand the effect of the indentation conditions on the force-displacement behavior. Figure 123 is an example of force-displacement curves obtained at various displacement rates. The curves in Figure 123 are from 20 μm deep indents on MECH-4 air-gaps with dimensions of Rectangle 1 (190 × 590 μm), performed with a 20 μm radius conical tip at displacement

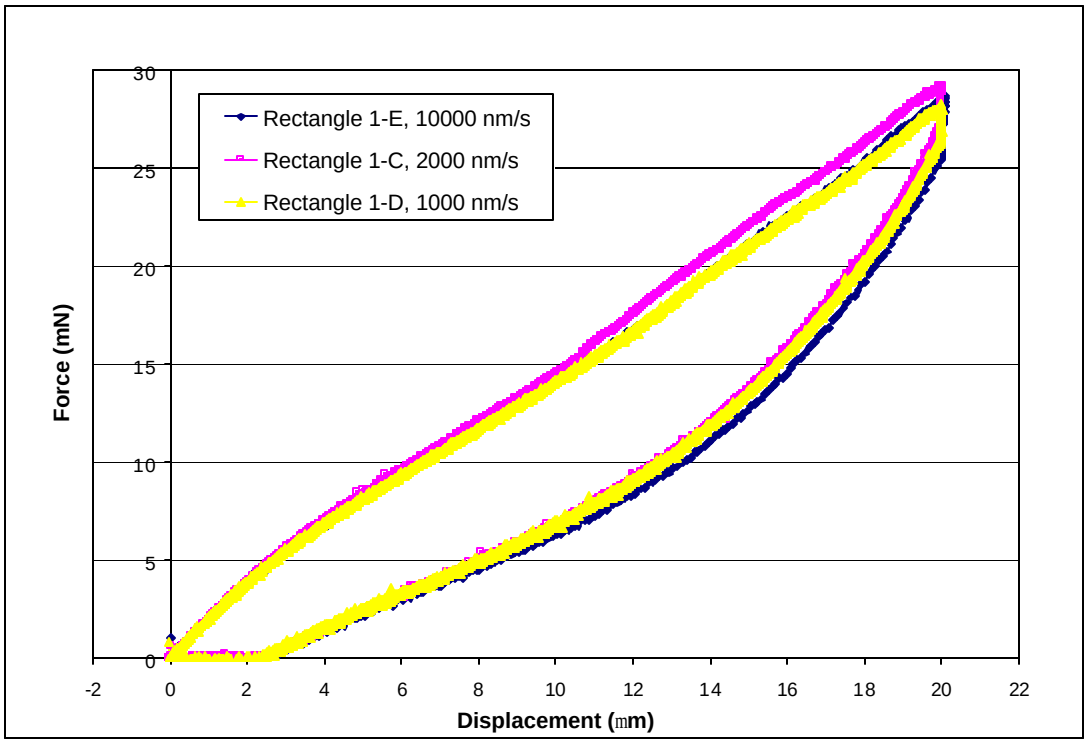

Figure 123: Force-displacement curves for MECH-4 air-gaps with dimensions of Rectangle 1 (190 × 590 µm) indented 20 µm with a 20 µm radius conical tip at displacement rates of 10000, 2000, and 1000 nm/s.

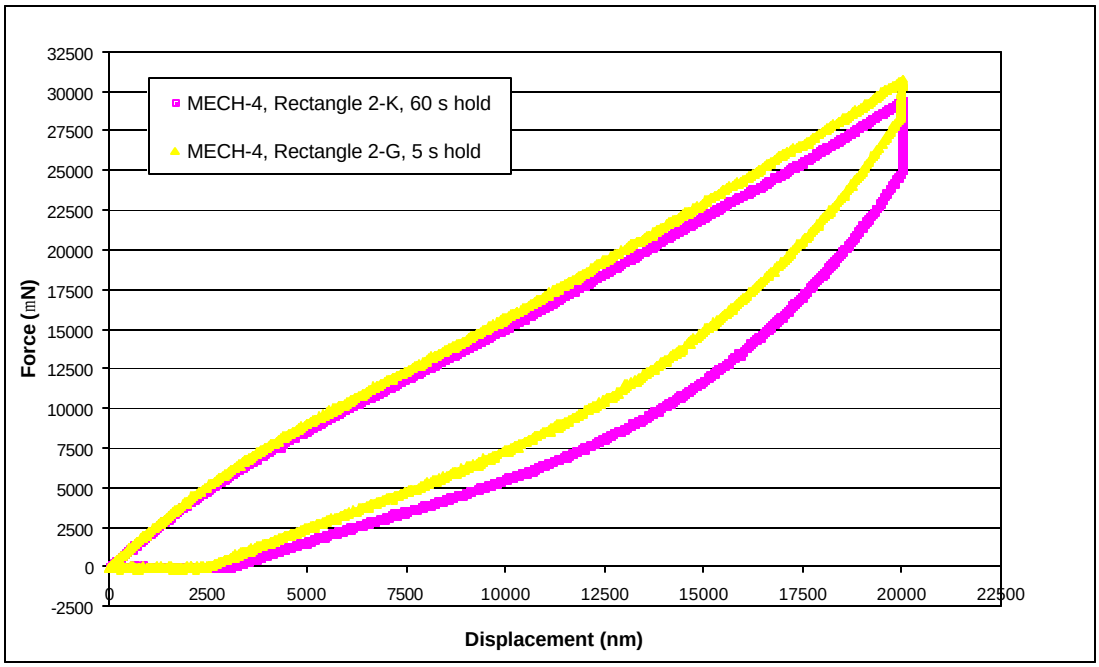

Figure 124: Force-displacement curves for MECH-4 air-gaps with dimensions of Rectangle 2 (190 × 9940 µm) indented 20 µm with a 20 µm radius conical tip at a displacement rates of 2000 nm/s. Hold times at maximum displacement were 5 and 60 s.

rates of 10000, 2000, and 1000 nm/s. A displacement rate of 30 nm/s was also considered. The displacement rate in the range of the indentation experiments shows no influence on the resulting shape of the force-displacement curve.

Figure 124 contains two force-displacement curves obtained from 20 μm indents on MECH-4 air-gaps, with hold times at maximum displacement of 5 s and 60 s. The indents were performed on air-gaps with dimensions of Rectangle 2 (190 × 9940 μm) with a 20 μm radius conical tip at a displacement rate of 2000 nm/s. The variation in the force at maximum displacement of about 1200 μN is not an effect from the hold time. The difference in forces observed in the loading curves occurs before the onset of the hold period at maximum deflection, and is of the magnitude seen between identical air-gaps. The hold time, however, does affect the amount of hysterisis between the loading and unloading portions of the curves. The nanoindenter tip continues to sink into the polymer film during the longer hold period of 60 s, compared to 5 s. Therefore, the unloading begins at a lower force for the air-gap held for 60 s (pink curve in Figure 124), and the entire unloading curve is shifted to a larger displacement on the x-axis. The larger remaining displacement at zero force may be recovered over time due to the viscoelastic behavior of the overcoat material.

Indents were performed to various depths on the air-gaps in order to investigate the change in force-displacement behavior with compression ratio. Figure 125, Figure 126, and Figure 127 demonstrate the relationship of indentation depth to the force-displacement characteristics of the air-gaps. Each of the figures shows the force displacement curves for indents performed on a single air-gap sample and shape to a depth of 10, 20, and 30 μm. The displacement rate varies for each depth in order to

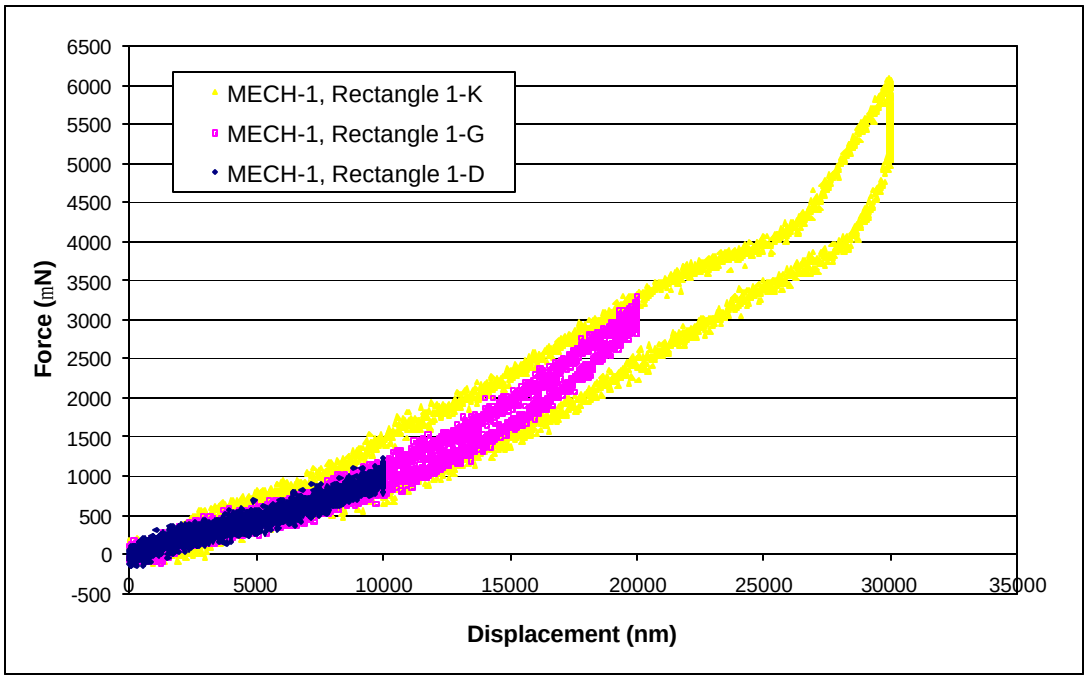

Figure 125: Force-displacement curves for MECH-1 air-gaps with dimensions of Rectangle 1 (190 × 590 μm) indented with a 200 μm radius spherical tip to maximum displacements of 10, 20, and 30 μm. The displacement rate varies to create a 10 s load and unload, with a 5 s hold at maximum displacement.

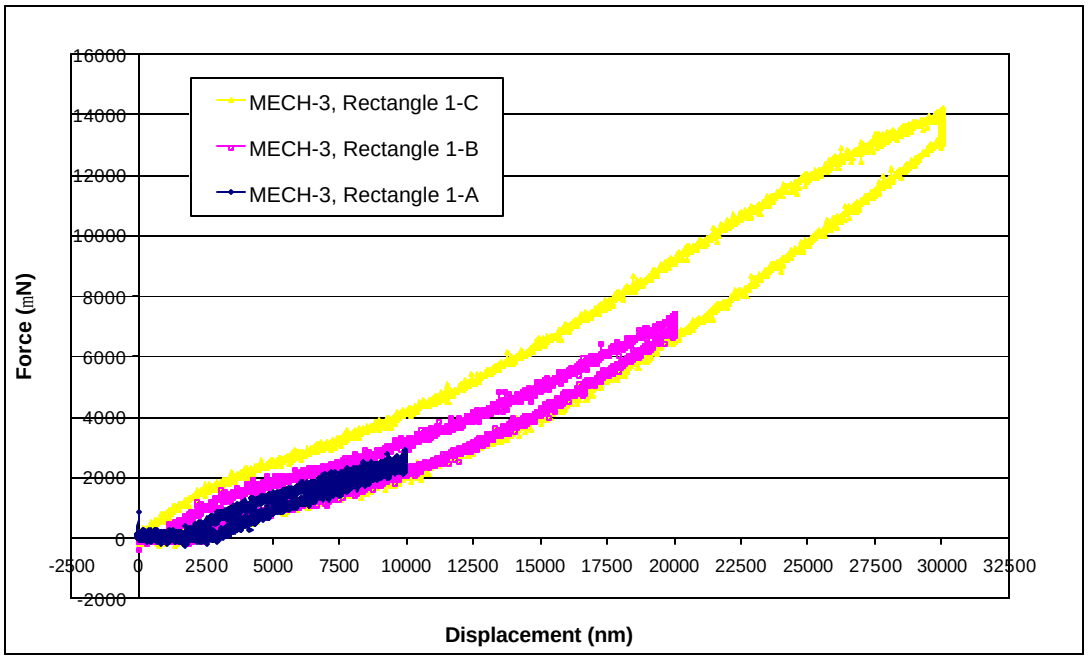

Figure 126: Force-displacement curves for MECH-3 air-gaps with dimensions of Rectangle 1 (190 × 590 μm) indented with a 50 μm radius conical tip to maximum displacements of 10, 20, and 30 μm. The displacement rate varies to create a 10 s load and unload, with a 5 s hold at maximum displacement.

create a 10 s load and unload, with a 5 s hold at maximum displacement. Figure 125 shows the force-displacement curves for MECH-1 air-gaps with dimensions of Rectangle 1 (190 × 590 μm) indented with a 200 μm radius spherical tip. Figure 126 contains the force-displacement curves for MECH-3 air-gaps with dimensions of Rectangle 1 (190 × 590 μm) indented with a 50 μm radius conical tip. In these two figures, the indents generally lie on top of one another as the indentation depth is increased. The loading curves show variation in force typical to those seen between identical indentations. The 10 μm indent in Figure 126 is slightly offset in depth, but aligns with the loading portion of the other two curves when a correction is performed for the offset. The 10 μm indentations occur elastically and produce linear relationships with little hysterisis between the loading and unloading portions of the curve. As the depth of the indent increases, the indents begin to drift further from elastic behavior. The forces in the air-gap overcoat polymer counteracting the applied force will change with the compression ratio of the air-gap. Pure compression of the air-gap will occur to a certain depth, followed by an increase in resistance as the tension in the overcoat polymer film increases. The 20-30 μm depth force-displacement curves show a small change in the contact stiffness (slope) approximately between the 10-15 μm depth, or when the compression ratio reaches approximately 30-50%. This change in slope indicates a small change in the resistance of the air-gap beyond compression of ~30%.

Figure 127 shows the force-displacement curves for MECH-4 air-gaps with dimensions of Rectangle 1 (190 × 590 μm) indented with a 20 μm conical tip to maximum displacements of 10, 20, and 30 μm. In this case, the air-gap is behaving non-elastically at each penetration depth. The loading portions of the force-displacement

relationships are fairly linear and remain constant with changes in the compression ratio applied to the air-gap. However, the force-displacement curves demonstrate extremely non-elastic unloading with plastic deformation remaining when the force returns to zero. Figure 128 shows optical images of a MECH-1, Rectangle-1 air-gap before and after a 30 μm indentation. The force-displacement curve for this indentation is relatively linear (Figure 125), and the image of the air-gap shows no changes after indentation. Figure 129 shows optical images of a MECH-4, Rectangle-1 air-gap before and after a 30 μm indentation. The overcoat polymer on MECH-4 (PI-2611) is stiffer than the overcoat polymer on MECH-1 (PI-2734). Flattening is seen in the center portion of the MECH-4 air-gap image in Figure 129 (b). The flattening is represented by the plastic deformation on the force-displacement curve, but may be eventually recovered.

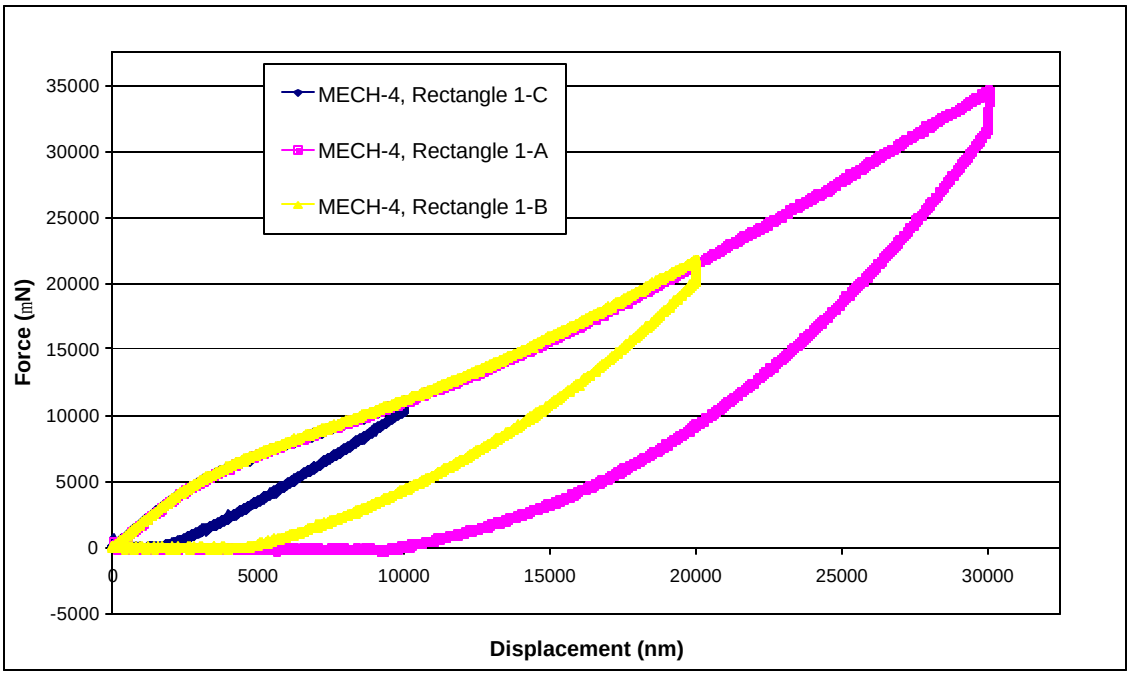

Figure 127: Force-displacement curves for MECH-4 air-gaps with dimensions of Rectangle 1 (190 × 590 μm) indented with a 20 μm conical tip to maximum displacements of 10, 20, and 30 μm. The displacement rate varied to create a 10 s load and unload, with a 5 s hold at maximum displacement.

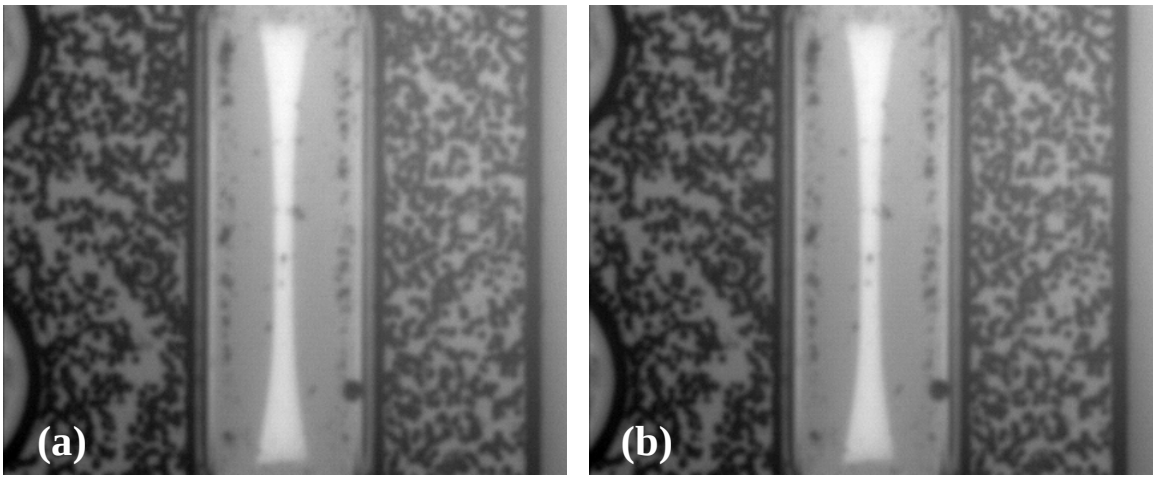

Figure 128: Optical images of a MECH-1, Rectangle-1 air-gap (190 × 590 μm) (a) before indentation, and (b) after a 30 μm indentation with a 200 μm spherical tip.

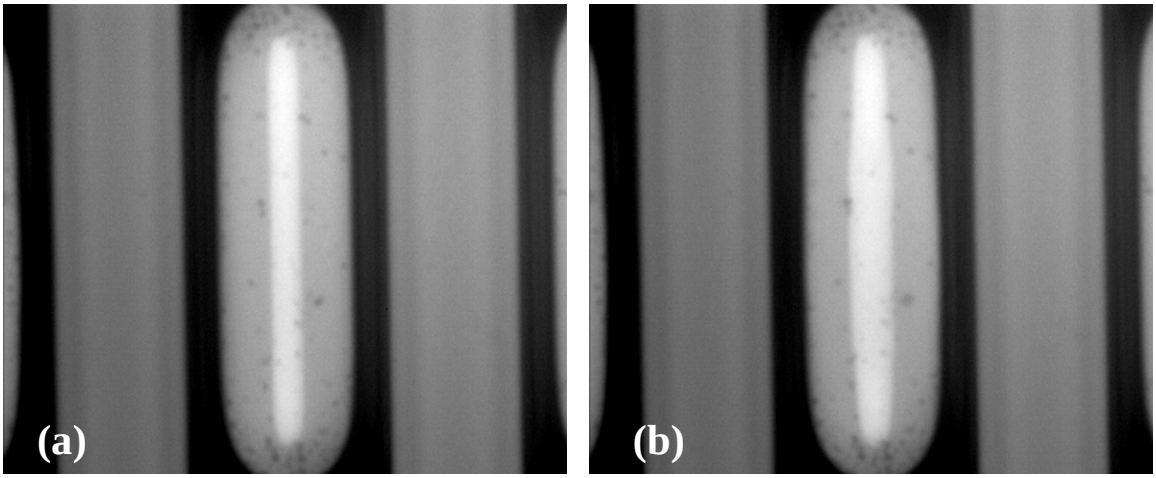

Figure 129: Optical images of a MECH-4, Rectangle-1 air-gap (190 × 590 μm) (a) before indentation, and (b) after a 30 μm indentation with a 200 μm spherical tip.

9.5.3 The effect of nanoindenter tip geometry on air-gap force-displacement results

Each mechanical test air-gap sample was indented with two different diamond-tip geometries to determine the effect of the tip on the deflection of the air-gap. If the air-gap is compressing without any effect of the tip on the overcoat polymer, the force-displacement curves are independent of tip geometry. Figure 131 through Figure 135 provide comparisons of force-displacement curves generated with varying indenter tip geometries. The force-displacement curves are independent of tip geometry only for Figure 130 and Figure 131. These figures represent small deflections (10 μm) on air-gaps with a large area (190 × 590 μm). However, Figure 132 through Figure 135 indicate that the displacement mechanism of air-gaps is generally influenced by the method of load application. Figure 132 presents the force-displacement curves for larger indents (30 μm) on MECH-1 air-gaps with the same area as Figure 130 and Figure 131. In this case, the 200 μm spherical tip requires more force to reach the same indentation depth as the 50 μm radius conical tip. An indent with a larger contact area with the polymer overcoat requires a larger force than an indent with less contact area, in order to maintain the same displacement. Therefore, the 200 μm spherical tip is in contact with a greater portion of the overcoat polymer area at large displacements than the 50 μm spherical tip. The shape of the air-gap explains these results. The overcoat polymer of the rectangular is a curved (or dome-shaped) surface along the short-axis (190 μm), but the surface is flat along the long-axis (590 μm). During the indent, the rectangular air-gap can compress to a limited depth where the force in the center can be counter-acted by the end areas which are not underneath the indenter tip. Eventually, the tip then begins to contact a larger area of polymer film as the depth increases. The increased area provides more resistance

to the indentation, and thus a larger force is required. A similar result is observed when the area of the air-gap is small. Figure 134 and Figure 135 show the force-displacement curves generated from 10 μm indents performed on air-gaps with Square-1 geometry (190 × 190 μm). An indent performed on a square air-gap with the 200 μm radius spherical tip requires additional force than either the 50 or 20 μm radius conical tip. The dome-shape of the air-gap causes more contact area to be made to the larger tip at the same penetration depth, resulting in the need for additional force to be applied. The results indicate that the compliance of the air-gaps is a function of the area in which the force is applied. Therefore, the results must include two pieces of data in order to be meaningful: (1) the compliance of the air-gap (force/depth); and (2) the method of application of the force.

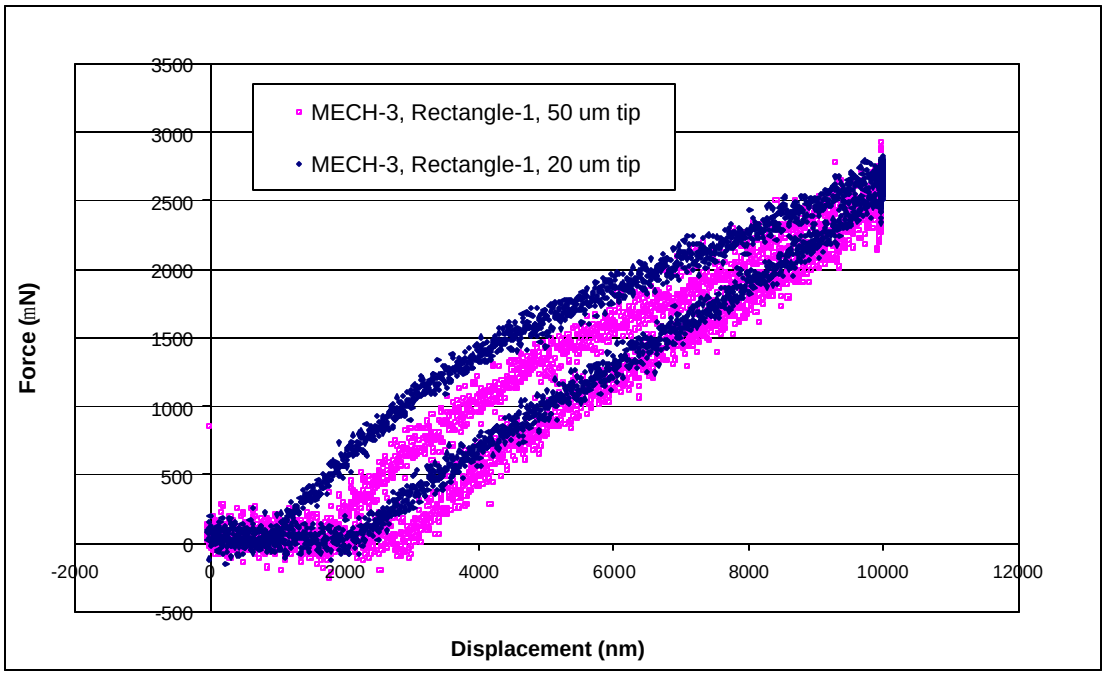

Figure 130: Force-displacement curves for MECH-3 air-gaps with dimensions of Rectangle-1 indented with a 20 µm conical tip and a 50 µm conical tip. The displacement rate is 1000 nm/s to a maximum displacement of 10 µm and a 5 s hold at maximum displacement.

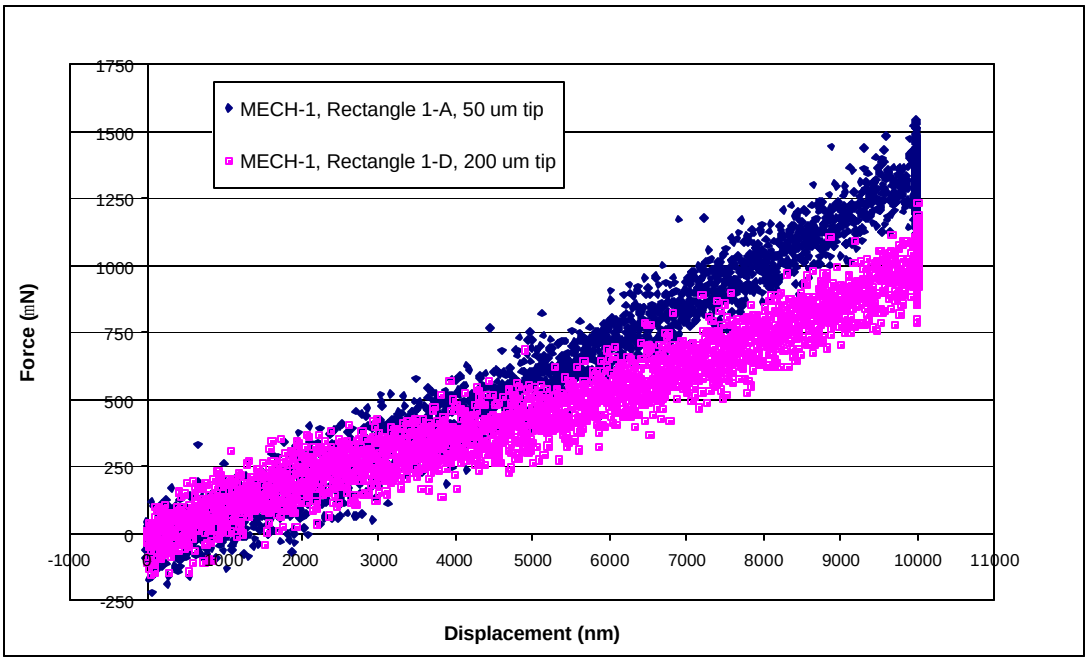

Figure 131: Force-displacement curves for MECH-1 air-gaps with dimensions of Rectangle-1 indented with a 50 µm radius conical tip and a 200 µm spherical tip. The displacement rate is 1000 nm/s to a maximum displacement of 10 µm and a 5 s hold at maximum displacement.

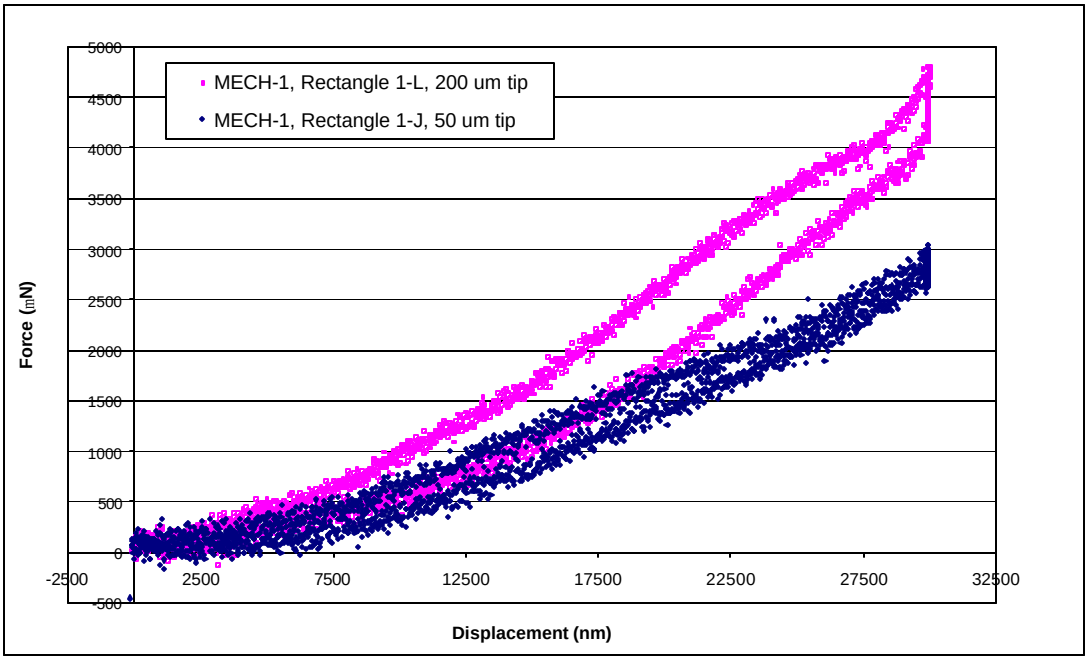

Figure 132: Force-displacement curves for MECH-1 air-gaps with dimensions of Rectangle-1 indented with a 50 µm radius conical tip and a 200 µm spherical tip. The displacement rate is 3000 nm/s to a maximum displacement of 30 µm and a 5 s hold at maximum displacement.

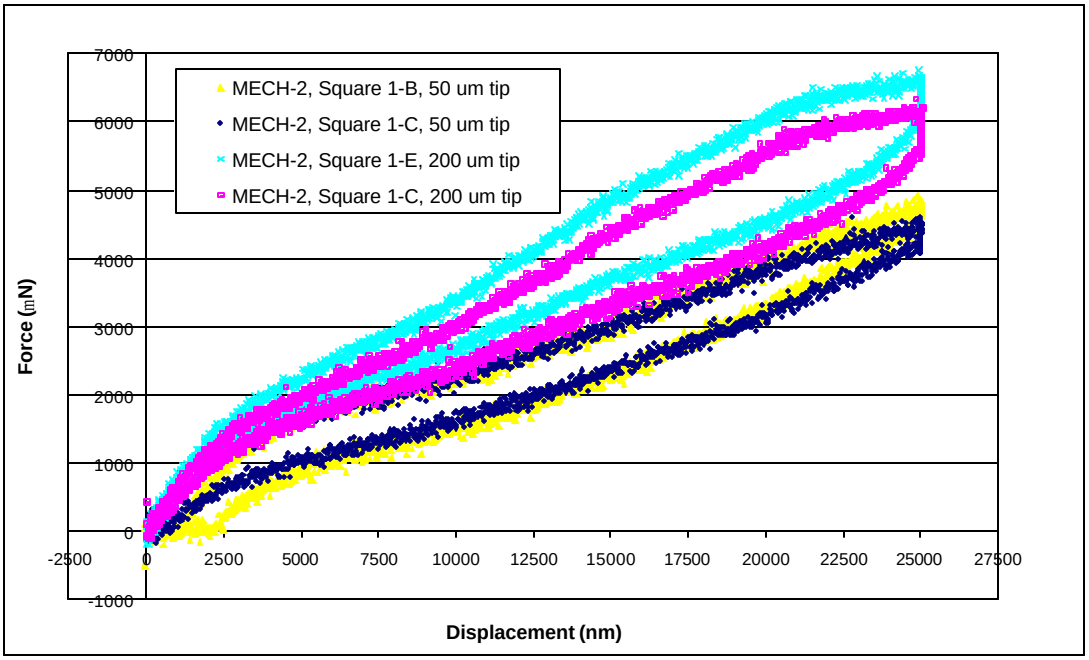

Figure 133: Force-displacement curves for MECH-2 air-gaps with dimensions of Square-1 indented with a 50 µm conical tip and a 200 µm spherical tip. The displacement rate is 2500 nm/s to a maximum displacement of 25 µm and a 5 s hold at maximum displacement.

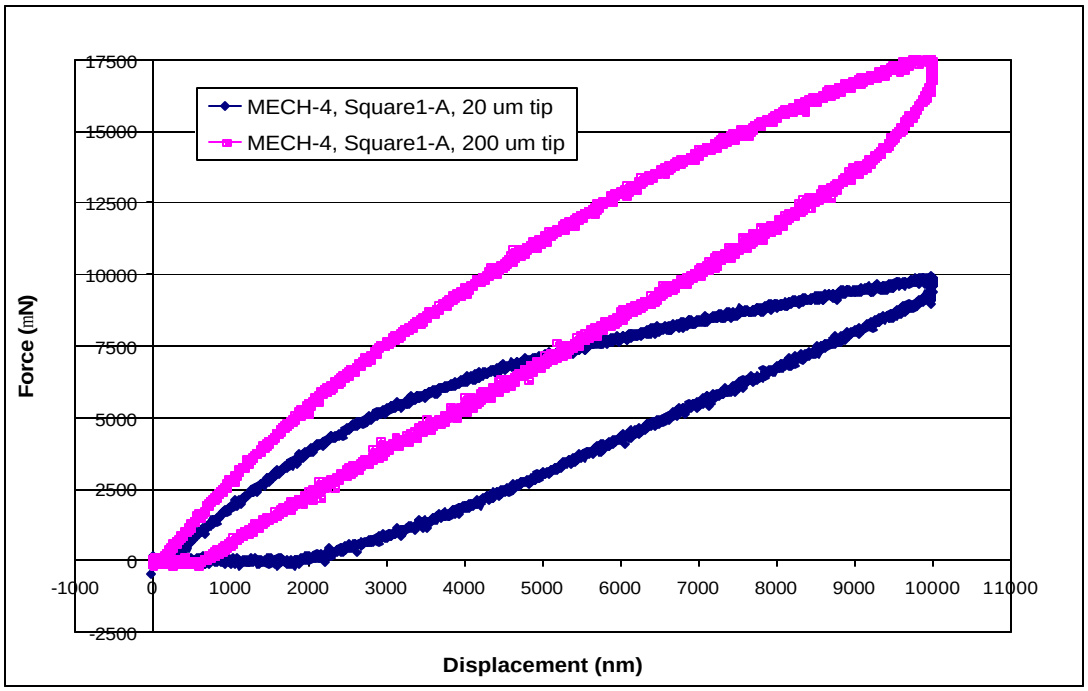

Figure 134: Force-displacement curves for MECH-4 air-gaps with dimensions of Square-1 indented with a 20 µm conical tip and a 200 µm spherical tip. The displacement rate is 1000 nm/s to a maximum displacement of 10 µm and a 5 s hold at maximum displacement.

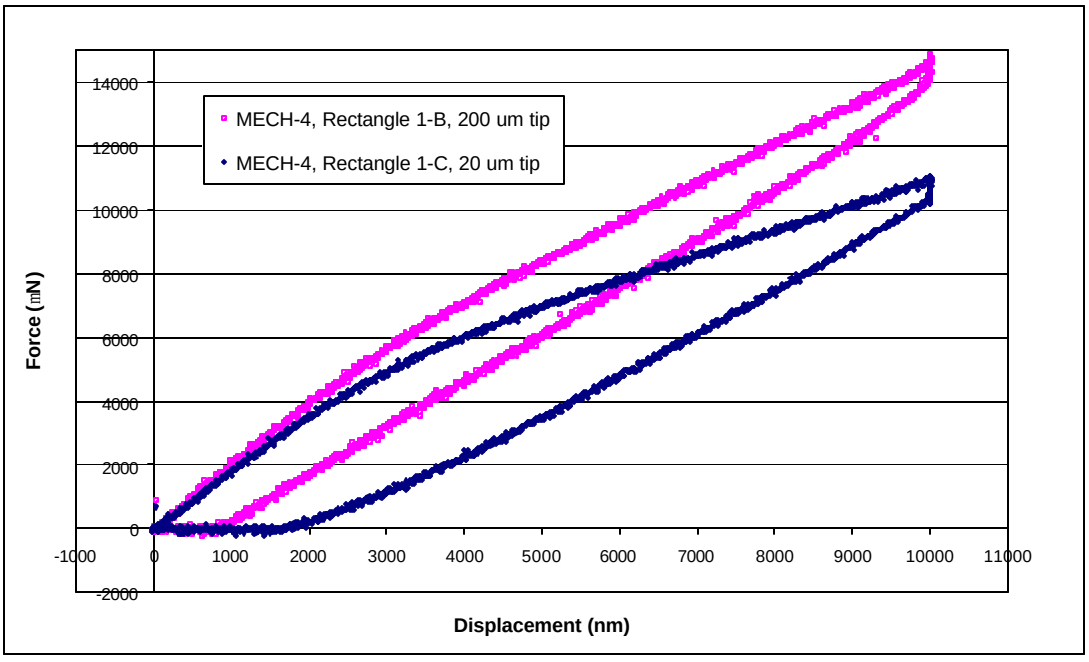

Figure 135: Force-displacement curves from MECH-2 air-gaps with dimensions of Square-1 indented with a 50 µm conical tip and a 200 µm spherical tip. The displacement rate is 2500 nm/s to a maximum displacement of 25 µm and a 5 s hold at maximum displacement.

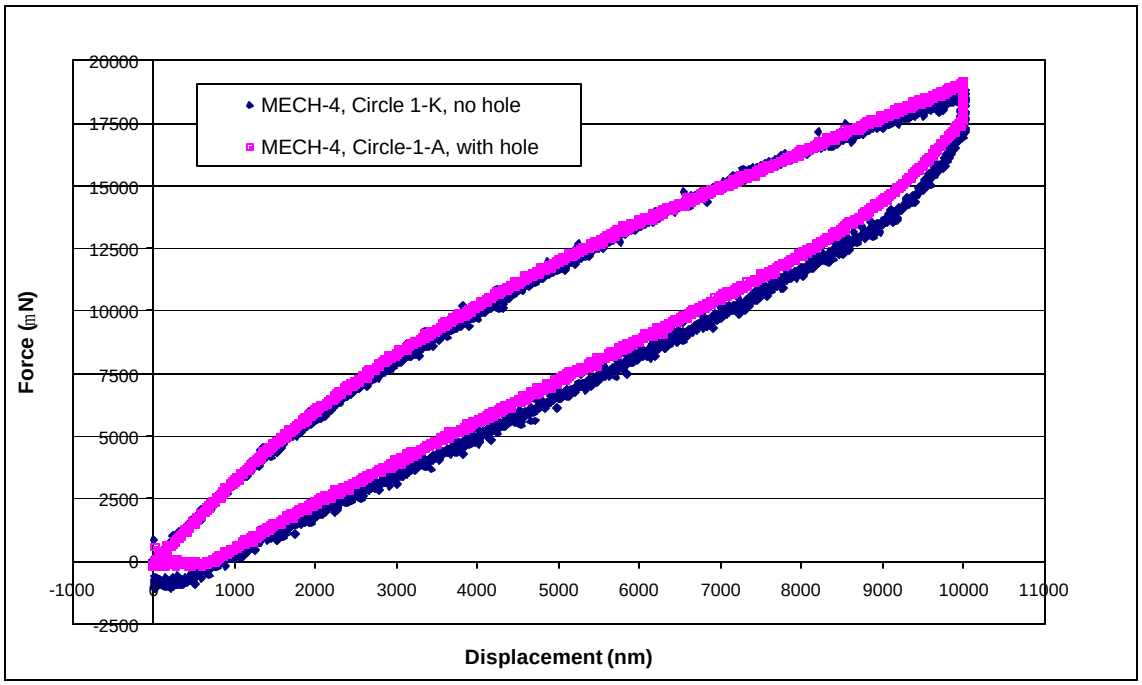

Figure 136: Comparison of force-displacement curves for MECH-4 air-gaps with and without a hole. The air-gaps have dimensions of Circle-1 (190 μm dia.). The indentation is performed with a 200 μm spherical tip, a displacement rate of 1000 nm/s to a maximum displacement of 10 μm, and a 5 s hold at maximum displacement.

9.5.4 The effect of air-gap and overcoat geometry and properties on air-gap force-displacement results

This section discusses the three variables selected for investigation of their influence on z-axis mechanical performance: (1) overcoat mechanical properties, i.e. elastic modulus and elongation; (2) overcoat material thickness; and (3) air-gap geometry, including area and height. The comparisons between air-gaps with varying geometry and properties are performed using air-gaps indented under the same experimental conditions with the same indenter diamond-tip. Figure 137 is a side-by-side plot of the force-displacement curves for Rectangle-1 air-gaps (190 × 590 μm) which vary in PI-2734 overcoat thickness. Sample MECH-1 has an overcoat thickness of 2.4 mm, and MECH-2 has an overcoat thickness of 7.4 μm. The indentation is performed with a 200 μm radius spherical tip, a displacement rate of 1000 nm/s to a maximum displacement of 10 μm, and a 5 s hold at maximum displacement. Both air-gaps show almost perfectly elastic behavior under these conditions. However, the a linear fit to each set of data yields a compliance of 10.0 mm/N for the rectangular air-gap on MECH-1, and 1.59 mm/N for the air-gap on MECH-2. Figure 138 compares the force-displacement curves for air-gaps with different overcoat material properties from samples MECH-2 and MECH-4. The overcoat material for the rectangle-1 air-gap (190 × 590 μm) on MECH-2 is 7.4 μm PI-2734, and 7.8 μm PI-2611 for MECH-4. The indentations were performed on each sample with a 200 μm radius spherical tip, a displacement rate of 1000 nm/s to a maximum displacement of 10 μm, and a 5 s hold at maximum displacement. A linear fit to the unloading portion of the curves yields a compliance of 0.63 for MECH-2, and 1.63 for MECH-4. Figure 139 compares the force-displacement curves for 10 μm indents performed on various-shaped air-gaps on sample MECH-4 with

a 200 μm radius spherical tip. The shape of the air-gap does not produce a large effect on the compliance of the air-gaps. The calculated compliance for the air-gaps in Figure 139 ranges from 0.55 to 0.70 mm/N. The overcoat material properties and thickness produce a more drastic change in the compliance with a change in the parameters. Table 45 lists some experimental compliance numbers for various geometry air-gaps indented with each of the different geometry indenter tips.

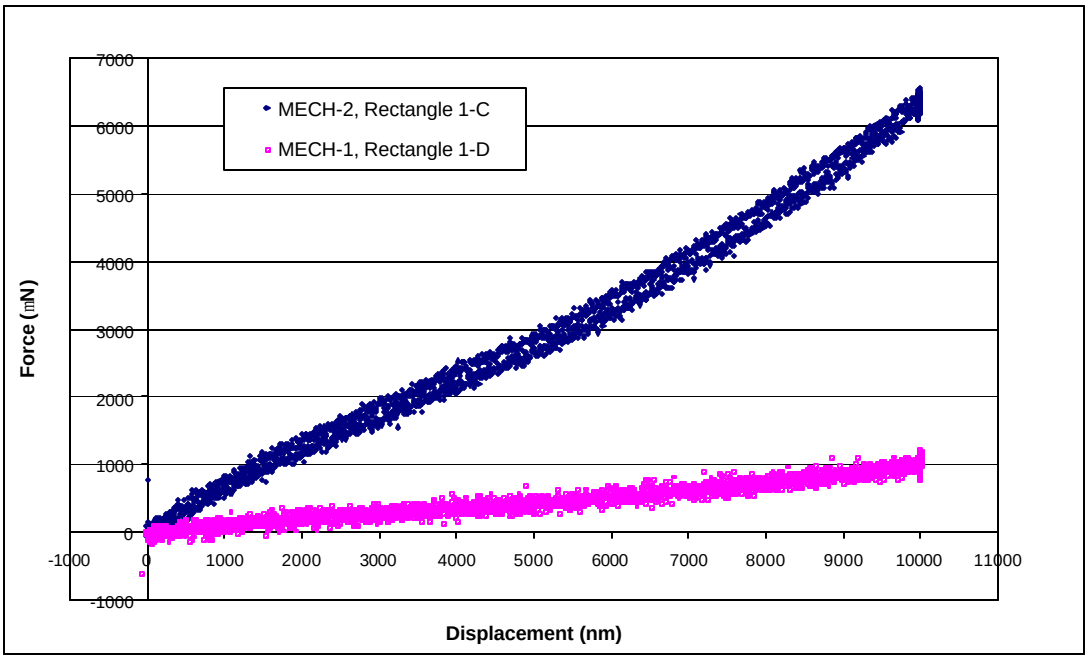

Figure 137: Comparison of force-displacement curves for Rectangle-1 air-gaps (190 × 590 μm) which vary in PI-2734 overcoat thickness. The indentation is performed with a 200 μm radius spherical tip, a displacement rate of 1000 nm/s to a maximum displacement of 10 μm, and a 5 s hold at maximum displacement.

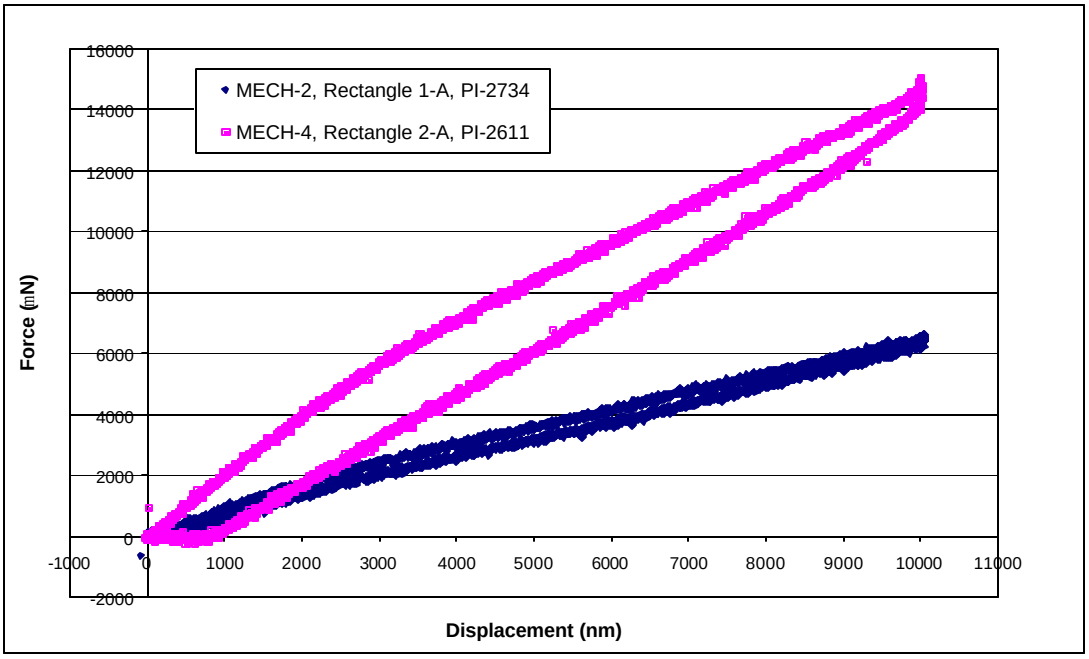

Figure 138: Comparison of force-displacement curves for air-gaps with different overcoat material properties. The Rectangle-1 air-gaps (190 × 590 μm) are from samples MECH-2 and MECH-4.

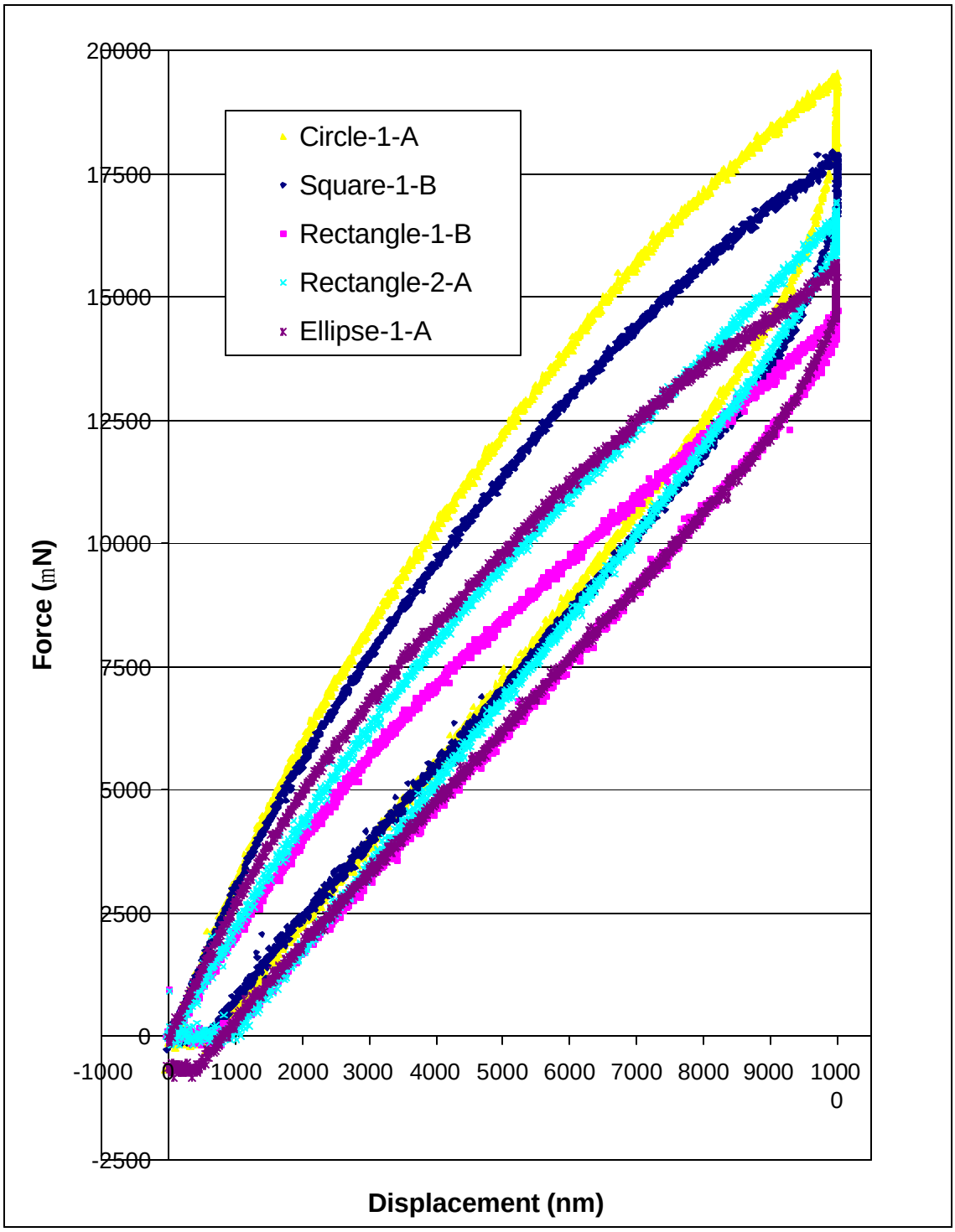

Figure 139: Comparison of force-displacement curves for differently shaped air-gaps from sample MECH-4, indented to 10 µm with a 200 µm radius spherical tip. The indentation parameters are a displacement rate of 1000 nm/s, and a 5 s hold at maximum displacement.

Table 45: Compliance for selected geometry air-gaps from various depth indentations.

SAMPLE	AIR-GAP GEOMETRY/ ID LETTER	NANOINDENTER TIP GEOMETRY	INDENT DEPTH (μm)	COMPLIANCE (mm/N)
MECH-1	No air-gap	200 μm spherical	1	
MECH-1	Rectangle 1-D	200 μm spherical	10	10
MECH-1	Rectangle 1-L	200 μm spherical	30	6.33
MECH-1	Rectangle 2-A	200 μm spherical	20	7.32
MECH-1	No air-gap	50 μm conical	1	
MECH-1	Rectangle 1-A	50 μm conical	10	7.04
MECH-1	Rectangle 1-E	50 μm conical	30	10.3
MECH-1	Rectangle 2-B	50 μm conical	25	7.14
MECH-2	No air-gap	200 μm spherical	5	
MECH-2	Rectangle 1-C	200 μm spherical	10	1.59
MECH-2	Rectangle 1-D	200 μm spherical	30	1.39
MECH-2	Rectangle 2-A	200 μm spherical	30	0.97
MECH-2	Circle 1-D	200 μm spherical	20	4.35
MECH-2	No air-gap	50 μm conical	5	
MECH-2	Rectangle 1-A	50 μm conical	30	2.36
MECH-2	Rectangle 2-B	50 μm conical	35	2.23
MECH-2	Square 1-C	50 μm conical	25	6.48
MECH-3	Rectangle 1-A	20 μm conical	30	2.86
MECH-3	Rectangle 1-D	20 μm conical	10	3.62
MECH-3	Rectangle 2-A	20 μm conical	30	2.39
MECH-3	Circle 1-B	20 μm conical	10	2.32
MECH-3	Square 1-A	20 μm conical	10	3.14
MECH-3	Rectangle 1-A	50 μm conical	10	3.58
MECH-3	Rectangle 1-C	50 μm conical	30	2.19
MECH-4	Rectangle 1-A	20 μm conical	30	0.87
MECH-4	Rectangle 1-C	20 μm conical	10	0.93
MECH-4	Square 1-A	20 μm conical	10	1.06
MECH-4	Circle 1-B	20 μm conical	10	1.05
MECH-4	No air-gap	200 μm spherical	5	
MECH-4	Rectangle 1-A	200 μm spherical	10	0.64
MECH-4	Rectangle 1-G	200 μm spherical	30	0.67
MECH-4	Rectangle 2-A	200 μm spherical	10	0.59
MECH-4	Circle 1-C	200 μm spherical	20	0.59
MECH-4	Square 1-E	200 μm spherical	20	0.67

9.6 Modeling of Air-gap z-axis Mechanical Movement With CoventorWare

CoventorWare is a software program designed to model MEMS and other devices typically fabricated with standard IC processing techniques. The CoventorWare model of a device or structure is constructed through the input of process steps similar to those used in the actual fabrication process, including mask patterning, deposition, and etching. The various materials in the structure are either described in the model by selection from a database of common materials, or the properties of a select layer are input directly. However, the model is designed only to consider elastic properties of the materials, and provides no indication of failure mechanisms or limits.

A CoventorWare air-gap model was designed to mimic the experimental conditions of nanoindentation as closely as possible. The first step in creation of the model was to imput the formation of a base silicon layer with a thickness of 50.0 μm as the substrate. Next, a deposition step of a sacrificial polymer layer of a given thickness was performed in the model. The mechanical properties of this layer are arbitrary, since the entire layer is sacrificial and is eventually removed from the model. The shape of the air-gap is determined by the creation of a “mask” in the model. For example, a 190 μm × 190 μm square mask is created to match the dimensions of the square air-gaps fabricated on the samples MECH-1 through MECH-4. The third step in the model-building process is a 15 μm thick etch step using the square air-gap mask pattern to "etch" through all 15 μm of sacrificial polymer. The result following this step is a silicon base with a three-dimensional box on the surface with length 190 μm, width 190 μm, and height 15 μm. A second model deposition step is performed, choosing a planar coating layer with a thickness of 25 μm. Therefore, a 10 μm thick film remains on the top of the air-cavity

and a 25 μm thick layer surrounds the air-cavity. The properties of the overcoat material are input in order to describe the polymer overcoat layer. For example, an overcoat of PI-2734 is described with an elastic modulus of 4.7 GPa, a Poisson's ratio of 0.3, and a density of 1.62×10^{-15} kg/μm^3. The last step to complete the model is a second etch step applied to the sacrificial polymer layer, resulting in removal of the entire area. Figure 140 shows a bottom view of the square air-gap model created in CoventorWare in the absence of the silicon substrate. The green area represents the boundaries of the air-gap and the blue is the overcoat material.

The force application was designed to represent the indentation of an air-gap with a small conical or spherical tip. Therefore, force is applied to the air-gap model as a pressure on a 20 × 20 μm square area in the center of the air-gap. The bottom surface and outside vertical perimeter walls of the overcoat material are described as rigidly fixed surfaces. A mesh was applied to the model, and the deflection and stress was computed as a function of position. Figure 141 shows a top view of the displacement magnitude as a function of position for a 140 MPa force applied to a 20 × 20 μm square area at the center of a 190 × 190 μm square air-gap. The defined height of the air-gap is 15 μm. However, the model computes a vertical deflection of 29.5 μm at the center of the air-gap, since no failure limits can be input into the program. The model treats the air-gap as essentially a thin square membrane which is suspended over a cavity and fixed at the edges. Figure 142 shows the mises stresses (MPa) in the overcoat polymer film as a function of position when the 140 MPa stress is applied to the center of the air-gap.

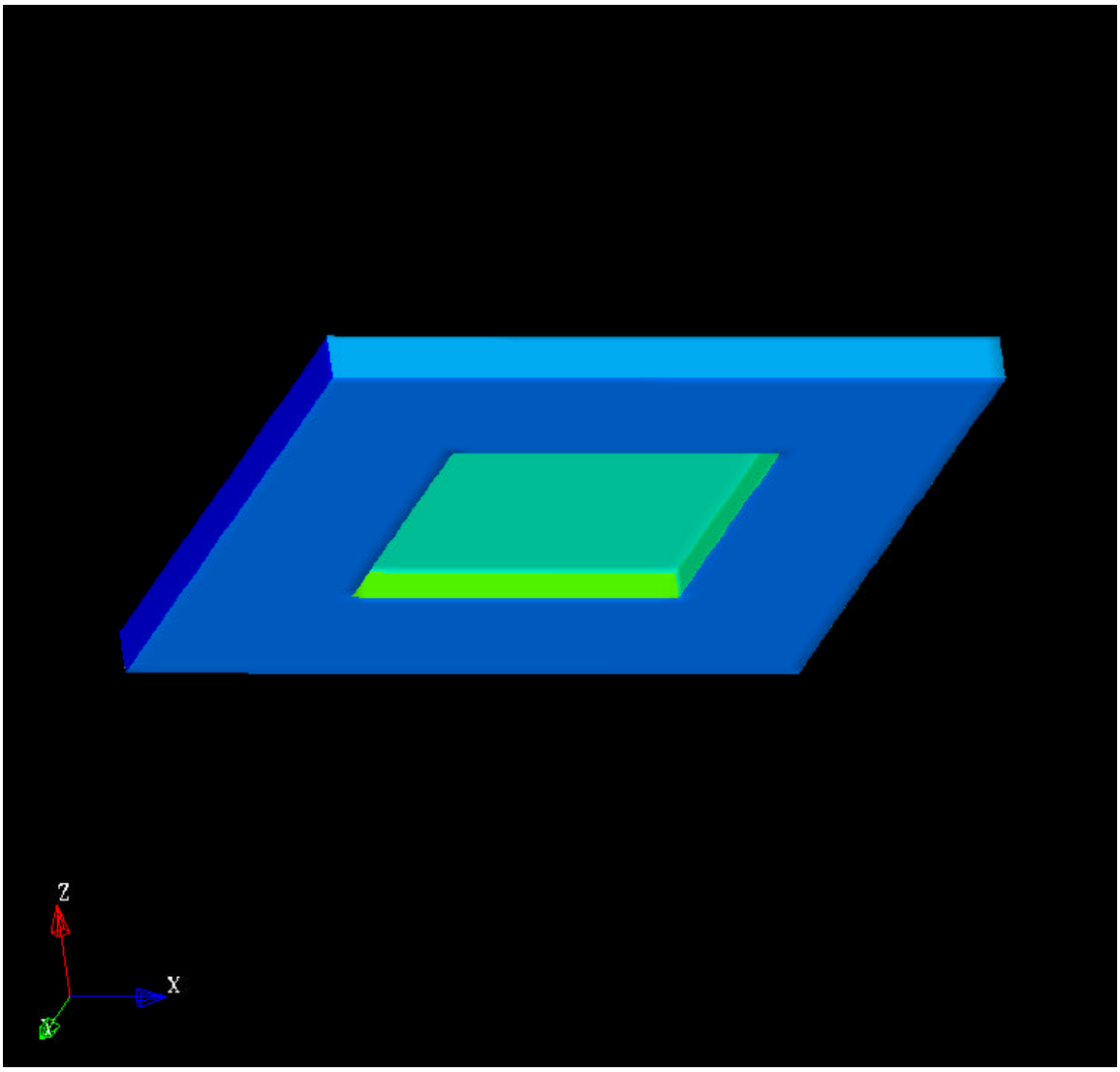

Figure 140: Bottom view of a 190 × 190 μm square air-gap model created using CoventorWare.

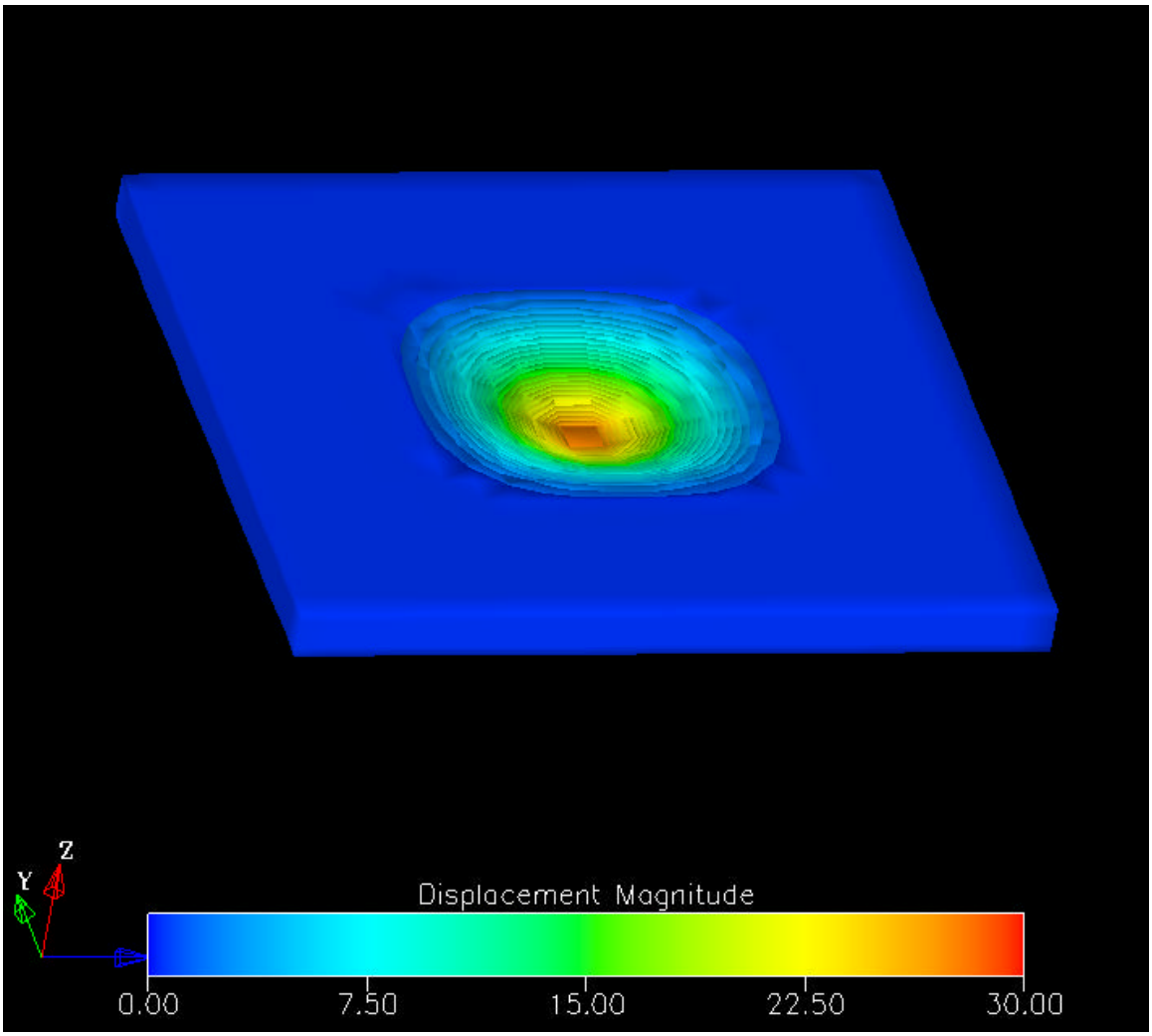

Figure 141: Top view of the displacement magnitude as a function of position for a 140 MPa pressure force applied to a 20 × 20 µm square area in the center of a 190 × 190 µm square air-gap.

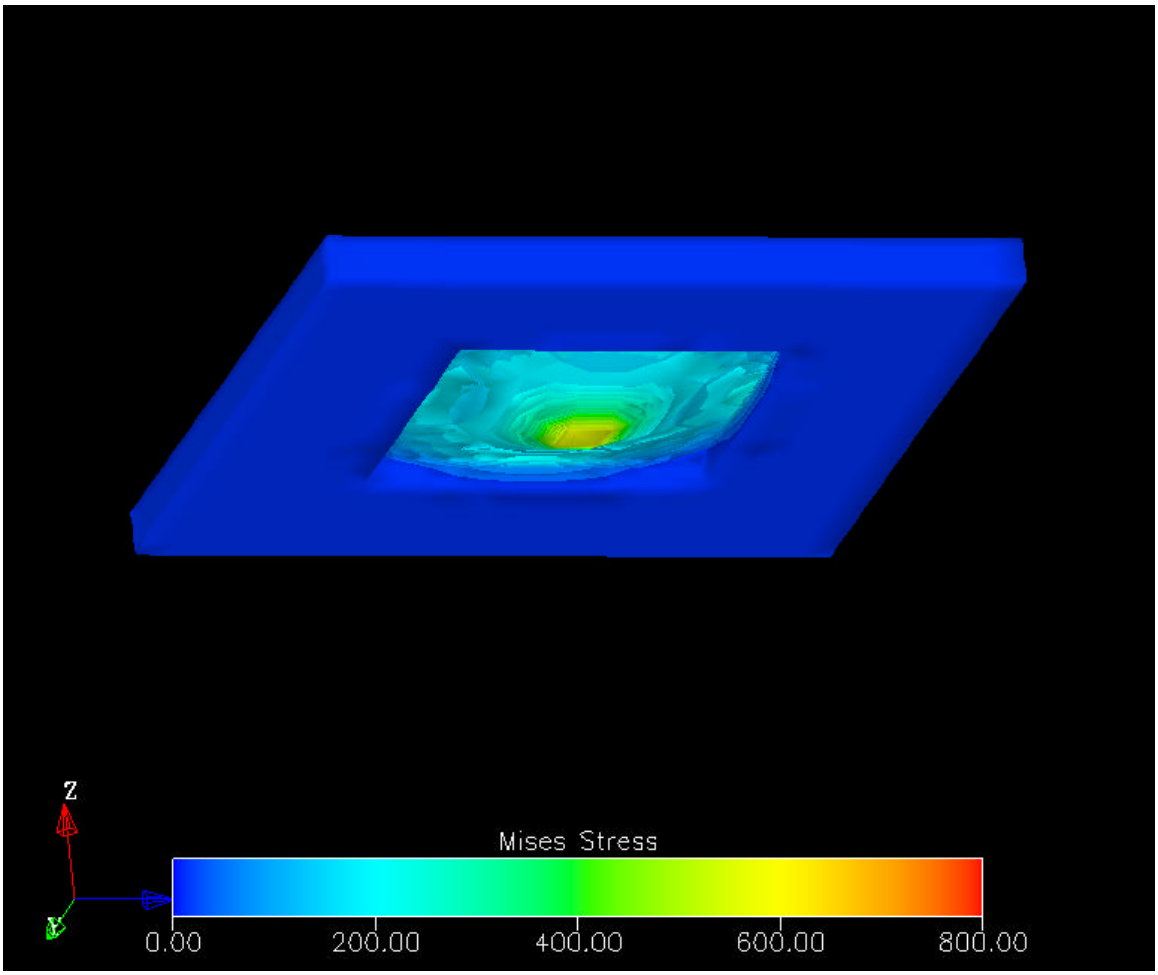

Figure 142: Bottom view of mises stress as a function of position for a 140 MPa pressure force applied to a 20 × 20 µm square area in the center of a 190 × 190 µm square air-gap

Table 46: Maximum stress and displacements predicted by CoventorWare for a 190 × 190 μm square air-gap or 190 μm diameter circular air-gap with various overcoat properties.

Air-gap Shape	Applied Pressure (MPa)	Elastic Modulus (GPa)	Air-gap Thickness (μm)	Overcoat Thickness (μm)	Maximum z-axis Displacement (μm)	Maximum x-y Displacement (μm)	Maximum Stress at Corner (MPa)
Square	140	4.7	100	10	29.3	2.05	
Square	140	4.7	15	10	29.5		557
Square	140	4.7	15	5	211	7.86	2480
Square	140	4.7	15	7.5	65.6	3.56	1050
Square	140	4.7	15	2.5	1605	30.7	10000
Square	140	4.7	15	20	4.58	0.53	77
Square	140	2.35	15	20	9.17		
Square	910	4.7	15	20	29.8		502
Circle	140	4.7	15	10	25.2	1.86	
Circle	140	4.7	15	20	4.18	0.5	
Circle	140	4.7	15	5	175	7.1	

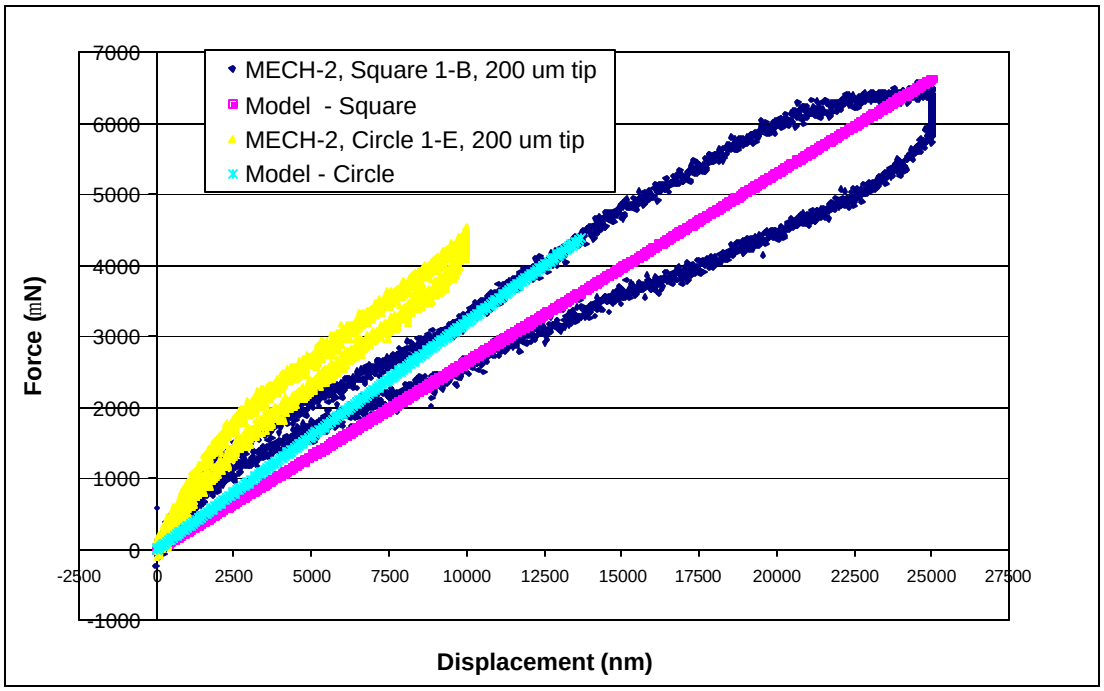

Figure 143: Comparison between experimental data and the CoventorWare model results for square and circular air-gaps from sample MECH-2.

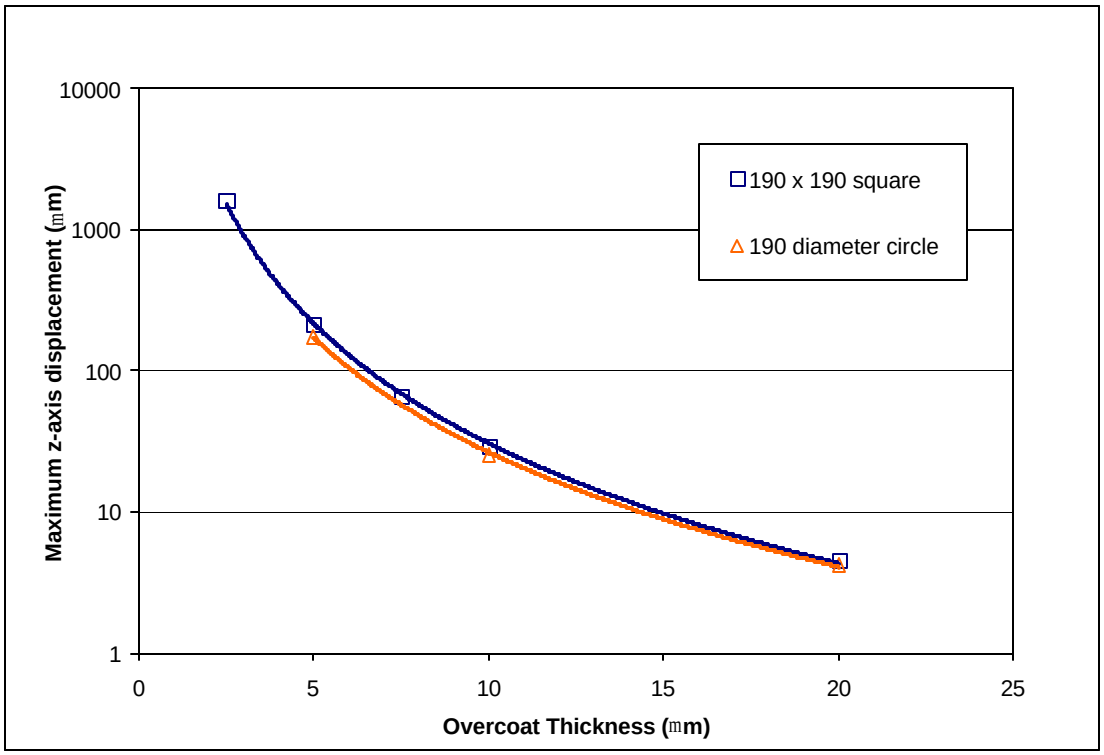

Figure 144: Maximum z-axis displacement as a function of overcoat thickness for a 140 MPa pressure force applied to a 20 × 20 µm square at the center of a 190 × 190 µm square or a 190 µm diameter circle air-gap.

The CoventorWare model correlates well to the experimental data for elastic deformations. Figure 143 directly associates the linear CoventorWare elastic model results with experimental data. The geometry and properties of the CoventorWare model results shown in Figure 143 include an elastic modulus of 4.7 GPa, a poisson's ratio of 0.3, an overcoat film thickness of 7.5 μm, and two geometries: a circular air-gap with a 190 μm diameter, and a square air-gap 190 × 190 μm. The experimental data was obtained with the 200 μm spherical indenter tip and the model data was calculated from an applied 140 mN force to a 20 × 20 μm square at the center of the air-gap. The experimental results correlate well with the elastic model of the air-gaps. Therefore, the experimental parameters in the parameters were altered in the model to characterize the effects of the air-gap and overcoat material geometry and properties on the compliance of the structures. Figure 144 demonstrates the CoventorWare model results for the z-axis displacement as a function of overcoat thickness and air-gap geometry for a 140 MPa pressure applied to a 20 × 20 μm square at the center of the air-gap. The compliance of the air-gap increases by a factor of 10 when the thickness of the overcoat polymer is reduced from 20 to 10 μm, or again from 10 μm to 5 μm. On the other hand, the change in geometry of the air-gap produces little change in the compliance of the structure. The next section discusses application of the model to the design of air-gaps for out-of-plane compliance.

9.7 Design Considerations for Air-gap Out-of-plane Compliance

The design procedure for out-of-plane compliance in SoL differs from the design procedure for in-plane compliance. This can be understood by noting that the motivation

for each is different: in-plane compliance compensates for the CTE mismatch between the chip and the PWB while out-of-plane compliance provides the ability for two non-planar structures to make reliable electrical contact, as required during wafer-level testing and burn-in as well as during assembly. Wafer-level testing and burn-in requires approximately 50 µm of z-axis deflection [27]. A set of experiments was conducted to compare the compliance of polymer films with embedded air gaps to the out-of-plane compliance of solid polymer films without embedded air gaps. The CoventorWare model was then used to predict the maximum compliance and displacement achieveable based on the limitations of fabrication.

Two wafers were spin coated with different thicknesses of a polynorbornene polymer that has a manufacturer specified tensile modulus of ~0.5 GPa. Following curing, the first wafer had an 18 µm thick layer of the polymer while the second wafer had a 35 µm thick layer. Using the Hysitron TriboIndenter, the force-displacement properties of the two polymer films were tested. For this measurement, a 10 µm wide conical tip with a 60° included angle was used. A trapezoidal force load function was applied with a 10 second ramp to 8 mN followed by a 30 second hold and finally a 10 second downward ramp to zero force. The maximum recorded displacement of the 35 µm thick polymer film at 8 mN was approximately 2.8 µm. A similar measurement was made for the wafer with the 18 µm thick polymer film, and the recorded maximum displacement at 8 mN was approximately 1.6 µm. In both samples, there were no visible permanent indents on the polymer's surface indicating elastic deformation during the measurements. Based on these measurements, if we restrict the elastic region to 10% strain for this polymer (1.6 µm displacement for 18 µm thick polymer film), then the

polymer film must be approximately 500 µm thick to provide 50 µm of compliance at 8 mN. A polymer layer that thick would complicate the fabrication of SoL, especially for the via etching, lithography, and alignment.

Similar indentations were performed on 30 µm tall air gaps with a 5 µm thick PI-2734 polyimide overcoat layer (with an approximate modulus of 4.7 GPa). The patterned air-gap geometry on the wafer was the 190 µm x 190 µm square. The force-displacement characteristics of the structure (similar to the figures presented previously) showed a 30 µm displacement at 55 mN. At forces beyond 55 mN, the tip made contact with the substrate (Si). A comparison of the compliance achievable by the thick, low-modulus polymer film and the air-gap illustrates that polymer films with embedded air gaps provide substantially higher values of compliance as well as larger compression ratios.

The ultimate goal was to determine the possible amount of compliance and deflection achievable through the integration of air-gaps into the polymer film. Chapter 5 discussed the known limits of fabrication of air-gaps with polymer overcoat materials. An polyimide overcoat layer of < 1 µm collapsed into the channel during decomposition. Therefore, the compliance is limited the overcoat thickness limits of fabrication. In addition, the maximum displacement possible is dictated by the total height of the air-gap. Chapter 8 also described limits on air-gap size based on the layout and pitch of the chip I/O. Larger air-gaps may provide enhanced compliance, but at the sacrifice of chip real-estate. The limits of fabrication were imput into the CoventorWare model to assess the possible compliance achieveable if the air-gap behaved in a completely elastic way, The design space for air-gap compliance and maximum displacement is illustrated in Figure 145. Both the area and the height of the air-gap dictate the compliance and the

maximum deflection (based on 100% compression). However, using the current air-gap fabrication techniques, the largest aspect ratio (height:width) structures fabricated to-date have approximately a 1:4 aspect ratio. Therefore, the compliance and displacement achievable is also a function of pitch, or the number of air-gaps per unit area. Air-gaps up to 35 μm in height with a compliance of and 15 mm/N may be produced, but only when the area of the air-gaps is large enough for the air-gaps to be producible. Therefore, as the pitch decreases, the air-gaps must be smaller to fit into the space boundaries, at the sacrifice of height and some compliance.

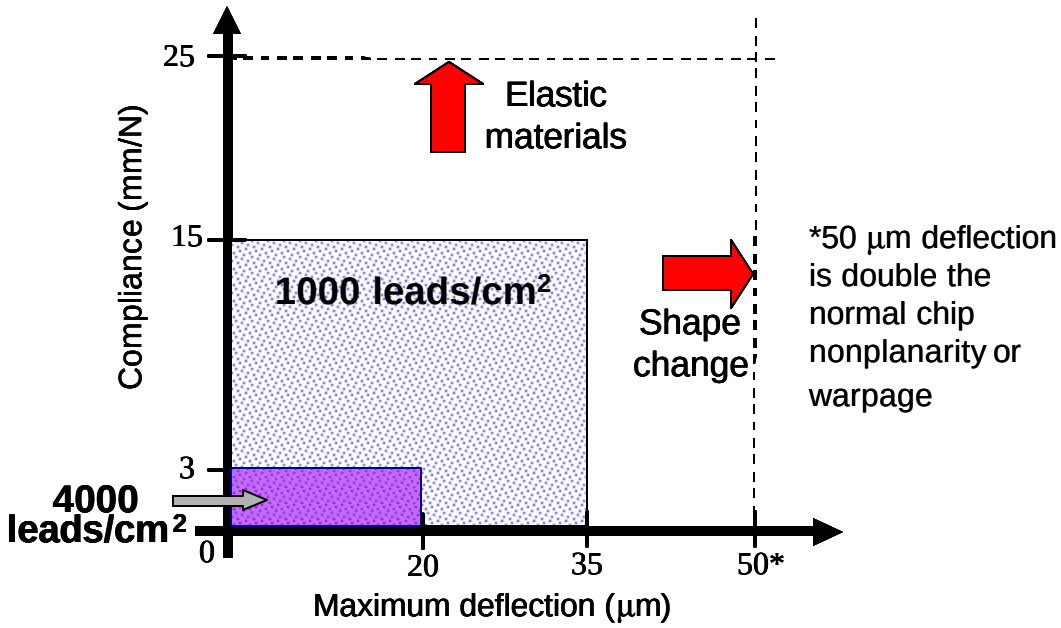

Figure 145: Design space for maximum compliance and maximum deflection of air-gaps, limited by fabrication capability.

APPENDIX A

SUPPORTING DATA FOR THE CALCULATION OF KINETIC PARAMETERS FROM TGA DATA

This appendix contains data and equations that support the calculation of kinetic parameters from experimental TGA data. Section A.1 contains supporting information for Chapter 4, Section 4.5.3, covering the decomposition of polypropylene carbonate (PPC) in air and nitrogen environments. Both dynamic and isothermal TGA data in each environment are used for calculation of the kinetic parameters. Section A.2 supports Chapter 7, Section 7.3 for the decomposition of 90/10 butyl/triethoxysilyl polynorbornene (PNB) while encapsulated in polyimide PI-2611 and unencapsulated in a nitrogen environment.

The following calculations follow the procedures outlined in Chapter 4, Section 4.1. The overall decomposition reaction is modeled by a n^{th} order reaction with an Arrhenius rate coefficient as follows:

$$\frac{dW}{dt} = A\exp\left(\frac{-E_a}{RT}\right)W^n \qquad \text{Eq. (A.1)}$$

The kinetic parameters are determined from dynamic TGA data using the Ozawa method described in Section 4.2.1. Eqation A.1 is integrated and rearranged to the form of equation A.2

$$\log\frac{b}{T^2} = -\left(\frac{E_a}{2.3RT}\right) + \text{const.} \qquad \text{Eq. (A.2)}$$

Equation A.2 describes a line with an x-axis of (1/T) and a y-axis of $\log(\beta/(T^2))$. At each heating rate (β), there exists a single value of conversion at any specific temperature. A least squares method is used to find the equation for the best fit line to the data points from each heating rate, at each conversion. β can either be the instantaneous heating rate at each value of conversion, or the average heating rate across all conversions. The activation energy at each conversion is then calculated from the slope (m) of the line using Equation A.3. The units of the gas constant (R) determine the units of E_a. The value of R used in the calculations is 8.314 J/(mol*K).

$$E_a = 2.3mR \qquad \text{Eq. (A.3)}$$

Once the activation energy value is known, it is used to determine the residue factor, RF. The residue factor is the remaining weight of non-decomposable material in the sample, based on the governing kinetics of the reaction. In order to find RF, first the relationship between dW/dt and W is determined. A plot is constructed of (dW/dt) as a function of W at each heating rate. The relationship of dW/dt vs. W is corrected for temperature by dividing the ordinate data by $\exp(-E_a/RT)$. The determinination of the RF is simplified by using data in the range where dW/dt and W has a linear relationship. The RF is the x-intercept of the least squares best fit line to the linear portion of the data at high conversion. The RF indicates the amount of non-reactable weight remaining in the sample when dW/dt reaches zero, based on the activation energy.

Equation A.1 is rearranged and the natural log function is applied to both sides of to yield Equation A.4.

$$\ln \frac{-\frac{dW}{dt}}{\exp(\frac{-E_a}{RT})} = n \ln W + \ln A \qquad \text{Eq. (A.4)}$$

A new plot is constructed of (ln((-*d*W/*d*t)/exp(-E_a/RT))) as a function of ln(W) to find the uncorrected reaction order (slope) and the pre-exponential constant (inverse natural log of the y-intercept). The abscissa is changed to ln(W-RF) to find the reaction order and pre-exponential constant corrected with RF.

The kinetic parameters are determined from isothermal TGA data using the method described in Section 4.2.2. The rate constant, *k*, replacers the Arrhenius function and the natural log function is applied to both sides of Equation A.1 to give equation A.5.

$$\ln(\frac{-dW}{dt}) = n * \ln W + \ln k \qquad \text{Eq. (A.5)}$$

A plot of the left side of Equation A.4 as the ordinate and lnW as the abscissa yields a linear function with a slope of n and a y-intercept of ln *k*. For isothermal experiments, RF can be determined directly from a plot of *d*W/*d*t vs. W. There is no need for a temperature correction since temperature throughout the experiment is constant. The RF is determined from the x-intercept of the best fit line through the data which shows a linear relationship near the endpoint of the reaction. The corrected reaction order and rate constant is determined by replacing W with (W-RF) in Equation A.5.

A.1 Kinetic Parameters From Dynamic and Isothermal TGA Data for PPC Decomposed in Air and Nitrogen

Dynamic TGA data of the decomposition of PPC was obtained at five different heating rates in both air and nitrogen. The $-\log(\beta/T^2)$ as a function 1/T for various

conversion values at each heating rate are included as Figure A.1 for PPC decomposed in nitrogen and Figure A.2 for PPC decomposed in air. The overall average heating rate is used in the determination of $-\log(\beta/T^2)$ to correct for any small inconsistencies in the heating rate due to the temperature control system. The equations describing the least squares best fit line at each conversion are also shown in the figures. The resulting activation energy values at each conversion, the average E_a, and one standard deviation in nitrogen and air are listed in Table A.1. Figure A.3 and Figure A.4 show the relationship of dW/dt as a function of W and Figure A.5 and Figure A.6 show the relationship corrected for temperature. The relationship in each environment is linear near the end of the reaction from about 80% conversion to completion. The data points between 85 to 95% conversion were used for the calculation of RF at each heating rate for PPC in air. The range of conversion between 85% to 91% was used for PPC in nitrogen, to avoid data from the "foot"seen in the dynamic TG curves (Figure 21, Section 4.3.2, page 74). The plots and equations to determine the residue factor at each heating rate in nitrogen and air are included as Figure A.7 and Figure A.8. The residue factors are listed in Table 9, Section 4.3.3, page 83. Figure A.9 thru Figure A.18 contain the plots used in the determination of n and A from the dynamic TGA at each heating rate. The uncorrected data, and the data corrected by RF and their respective equations are included in these figures. The data between 40 and 90 percent conversion, where the governing kinetics are prevalent, were used to determine n and A for both environments. A summary of the parameters n and A from the dynamic TGA data in nitrogen and air are included as Table A.2.

The functions to calculate the parameters n and *k* from the isothermal data are included as Figure A.19 and Figure A.20. The data in the range of 60 to 90 percent conversion was used to construct the plot from the isothermal decomposition data of PPC in air. The data from 70 to 95% conversion was used to construct the plot for PPC in nitrogen, due to limited data points between 60 to 90 percent. However, similar to the dynamic data, the isothermal data must be adjusted with the correction factor, RF. The relationship of dW/dt as a function of W for PPC decomposed isothermally in nitrogen and air is shown in Figure A.21 and Figure A.22. PPC decomposition in either air or nitrogen shows a linear relationship between dW/dt and W when the reaction reaches approximately 70 percent conversion. However, a significant change in the slope occurs during approximately the last 5% conversion of the reaction in nitrogen. The data between 70 and 95% conversion were used for the calculation of RF in air. Due to limited data, the values between 70 to 95% were used for decomposition in nitrogen at temperatures of 292.4 and 265.7°C. The data between 90 to 95% conversion were used to calculate the RF at the temperatures of 248.6, 302.8, 324.0, and 346.3°C. The plots to determine RF are included as Figure A.23 for PPC in nitrogen and Figure A.24 for PPC in air. The residue factors are listed in Table 9, Section 4.3.3, pg. 83. The corrected weight data were used to determine n and *k* at each isothermal temperature as shown in Figure A.25 and Figure A. 26, which are shown in Table A.3. Finally, plots are constructed of ln *k* as a function of 1/T as shown in Figure A.27 for PPC in nitrogen and Figure A.28 for PPC in air. The best fit line to the data gives a slope of (E_a/R) and a y-axis intercept of ln A. A summary of all the calculated kinetic parameters for PPC decomposition in air and nitrogen is given in Table 10, section 4.3.3, pg. 84.

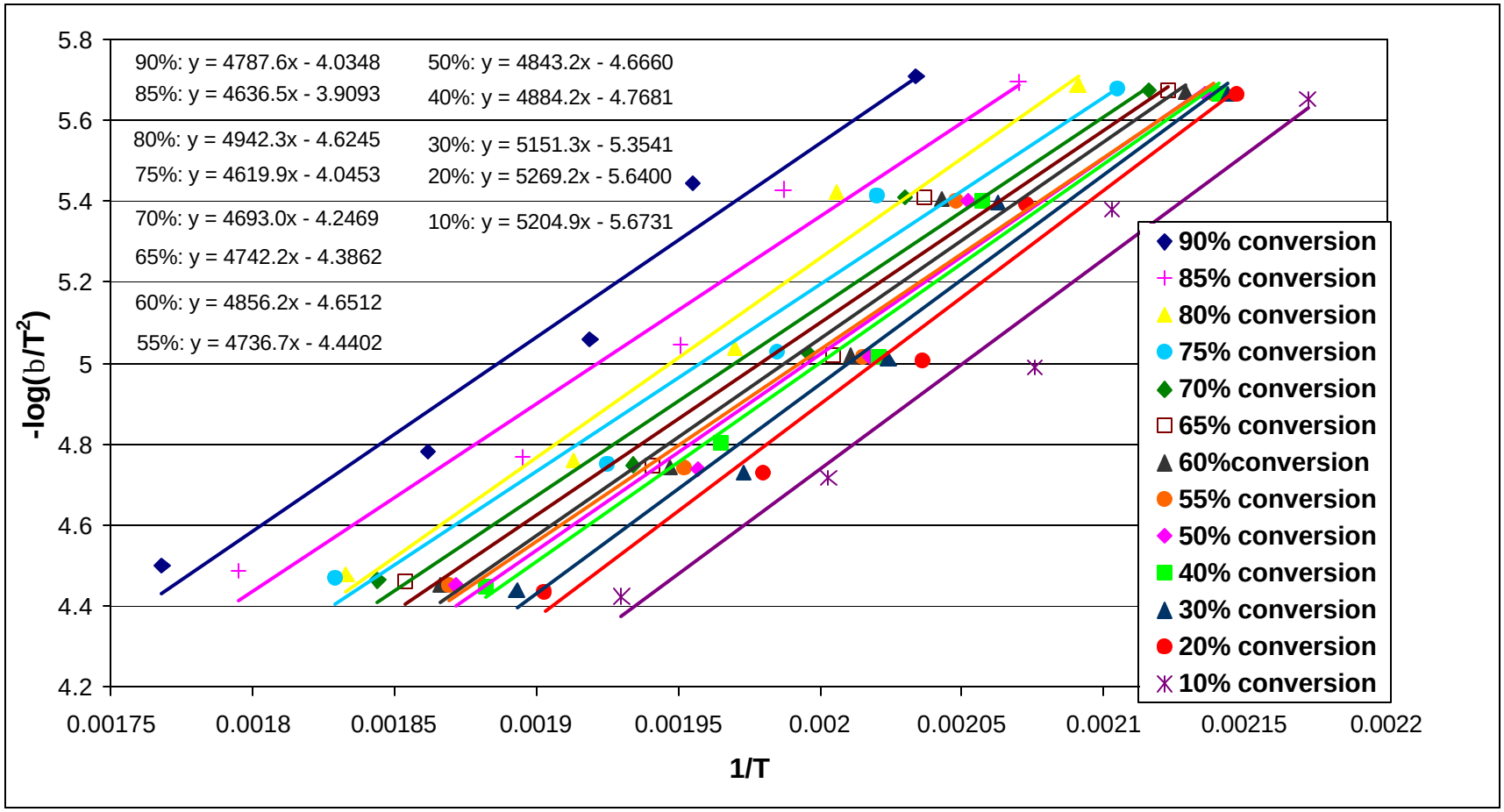

Figure A.1: Analysis plot to determine the activation energy for the decomposition of PPC in nitrogen from dynamic TGA.

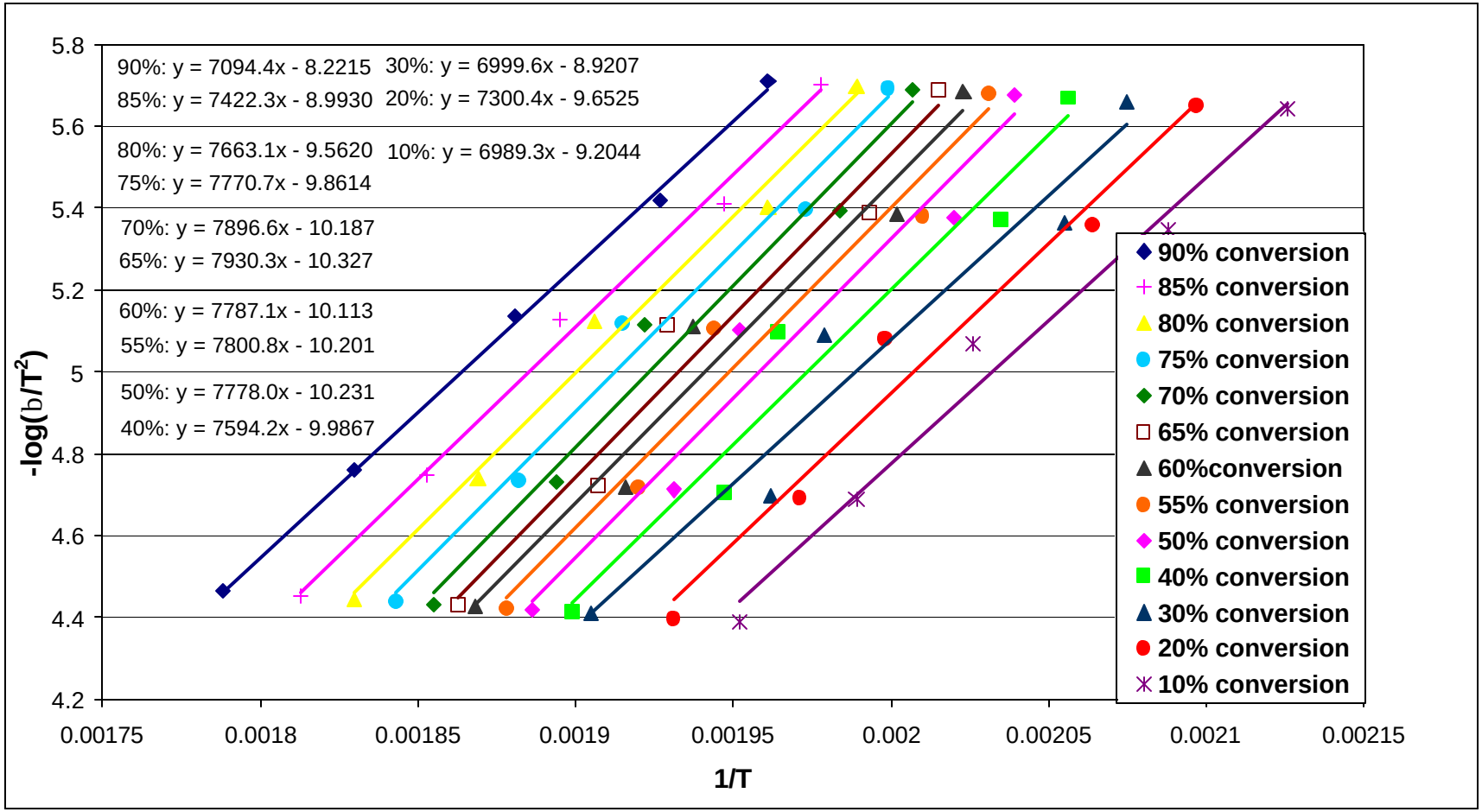

Figure A.2: Analysis plot to determine the activation energy for the decomposition of PPC in air from dynamic TGA.

Table A.1: Activation Energy (kJ/mol) at various values of conversion for the decomposition of PPC in nitrogen and air.

	PPC in Nitrogen	**PPC in Air**
Conversion (%)	**Activation Energy, E_a (kJ/mol)**	**Activation Energy, E_a (kJ/mol)**
10	99.53	133.65
20	100.76	139.60
30	98.50	133.85
40	93.40	145.22
50	92.61	148.73
55	90.58	149.17
60	92.86	148.91
65	90.68	151.65
70	89.74	151.00
75	88.34	148.59
80	94.51	146.54
85	88.66	141.93
90	91.55	135.66
Average/ Standard Deviation	93.21 ± 2.08	114.2 ± 6.5

Table A.2: The reaction order and pre-exponential constant for the decomposition of PPC in nitrogen and air at various heating rates.

	PPC in Nitrogen			PPC in Air		
Heating Rate (^{o}C/min)	**Uncorrected Reaction Order, n**	**Corrected Reaction Order, n**	**Pre-exponential Constant, A (min^{-1})**	**Uncorrected Reaction Order, n**	**Corrected Reaction Order, n**	**Pre-exponential constant, A (min^{-1})**
0.5	2.655	1.382	6.116×10^{7}	1.435	1.086	3.166×10^{13}
1	2.331	1.308	7.790×10^{7}	1.727	1.239	1.119×10^{13}
2	2.513	1.404	7.049×10^{7}	1.372	1.092	2.780×10^{13}
5	2.096	1.219	2.668×10^{8}	1.976	1.162	2.443×10^{13}
10	1.816	1.170	2.090×10^{8}	2.073	1.161	2.738×10^{13}
Average/Std. Deviation	--	1.297 ± 0.101	$1.371 \times 10^{8} \pm 9.448 \times 10^{7}$	--	1.148 ± 0.063	$2.449 \times 10^{13} \pm 7.868 \times 10^{12}$

Table A.3: The reaction order and reaction constant for the decomposition of PPC in nitrogen and air at various isothermal temperatures.

PPC in Nitrogen				PPC in Air			
Isothermal Temperature (^{o}C)	**Uncorrected Reaction Order, n**	**Corrected Reaction Order, n**	**Reaction Constant, *k***	**Isothermal Temperature (^{o}C)**	**Uncorrected Reaction Order, n**	**Corrected Reaction Order, n**	**Reaction Constant, *k***
248.6	4.070	1.612	0.00430	219.4	3.125	1.720	0.000281
265.7	3.665	1.358	0.0539	239.4	1.114	1.012	0.113
292.4	3.133	1.498	0.0392	271.3	1.734	1.171	0.147
302.8	2.237	1.411	0.0756	292.5	1.377	1.145	0.351
324.0	1.695	1.306	0.197	313.8	1.305	1.092	0.848
346.3	1.927	1.231	0.510	335.4	1.145	1.050	1.62
Average/Std. Deviation	--	1.297 ± 0.101	--	Average/Std. Deviation	--	1.198 ± 0.262	--

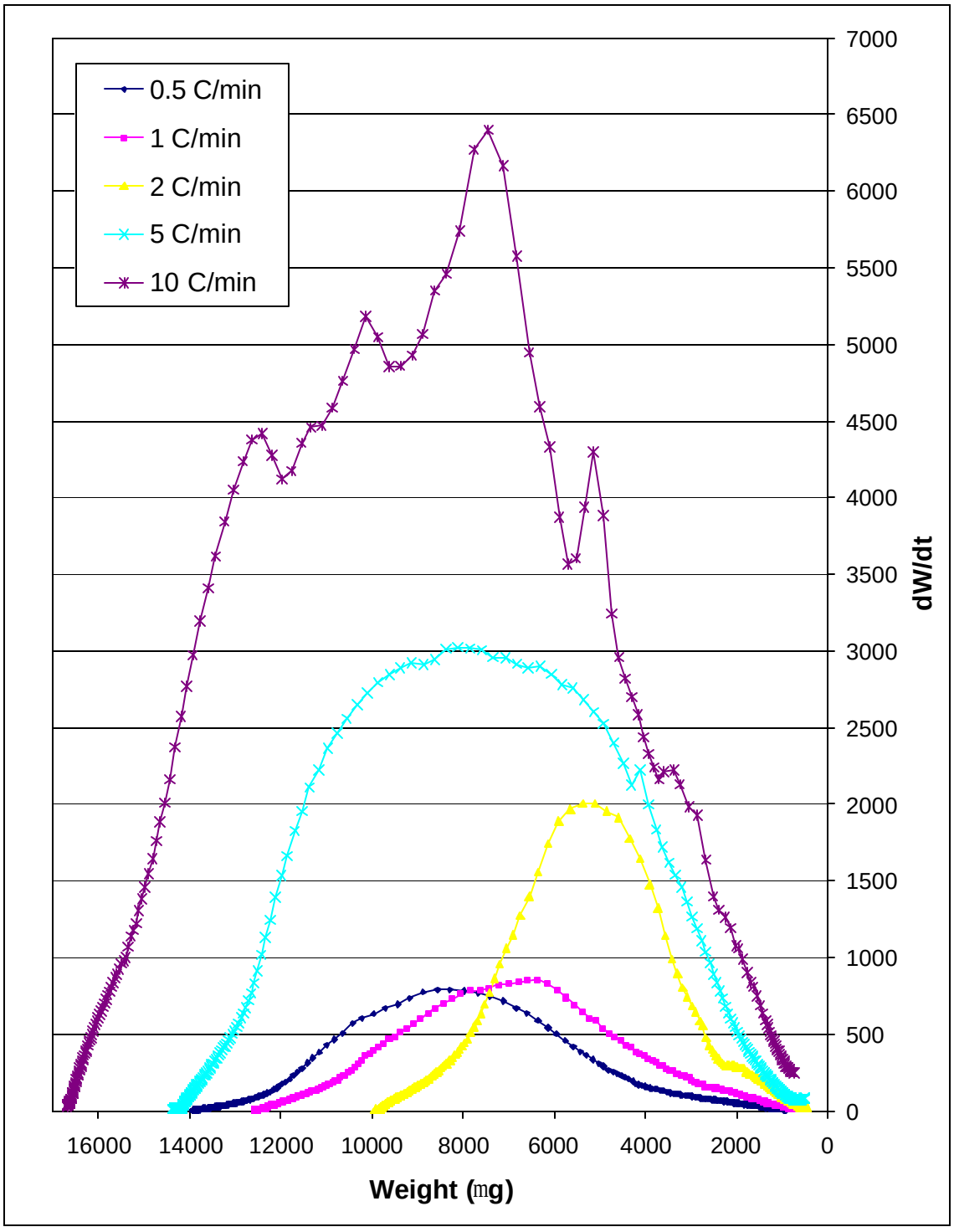

Figure A.3: *d*W/*d*t as a function of W for the decomposition of PPC in nitrogen at various heating rates.

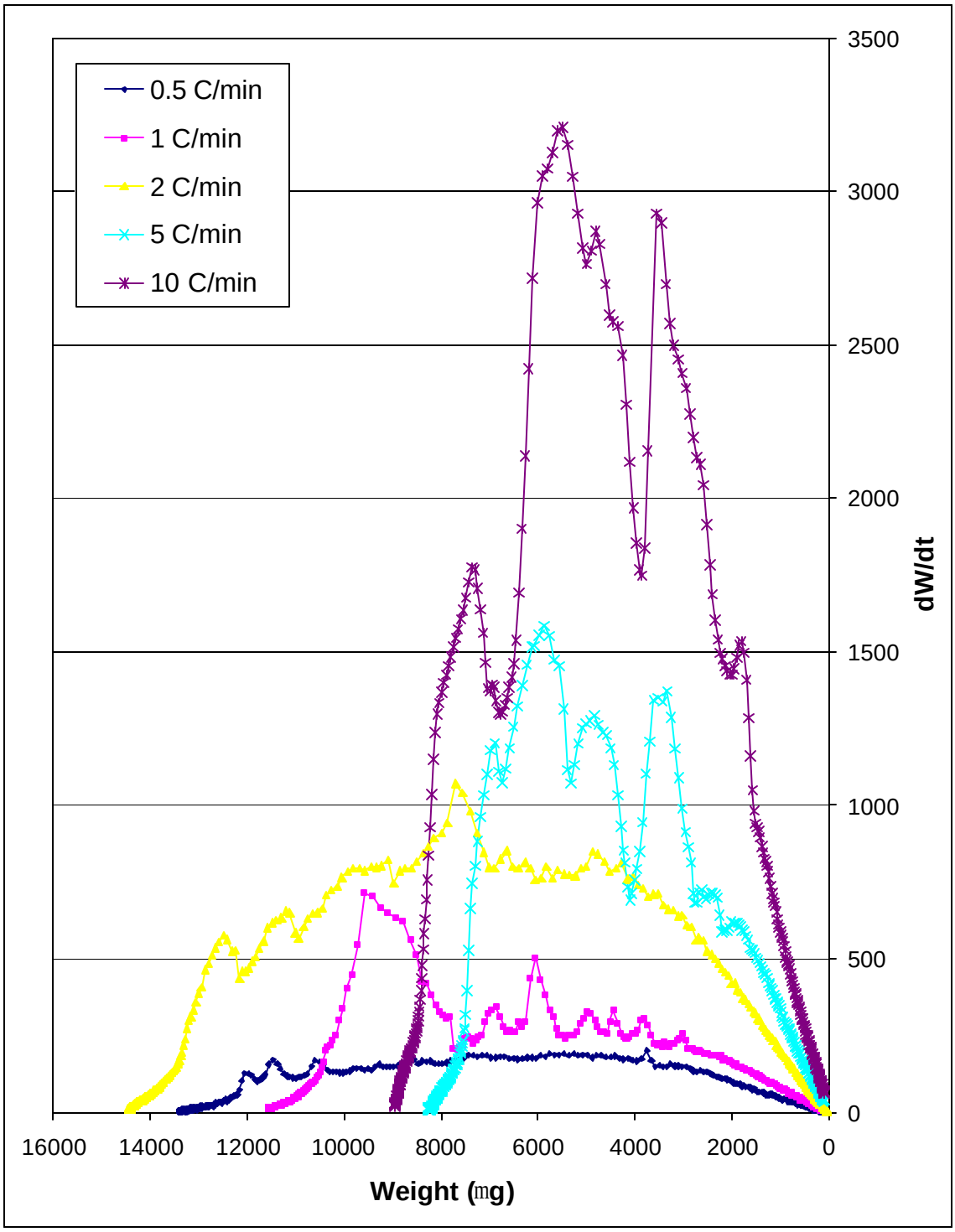

Figure A.4: *d*W/*d*t as a function of W for the decomposition of PPC in air at various heating rates.

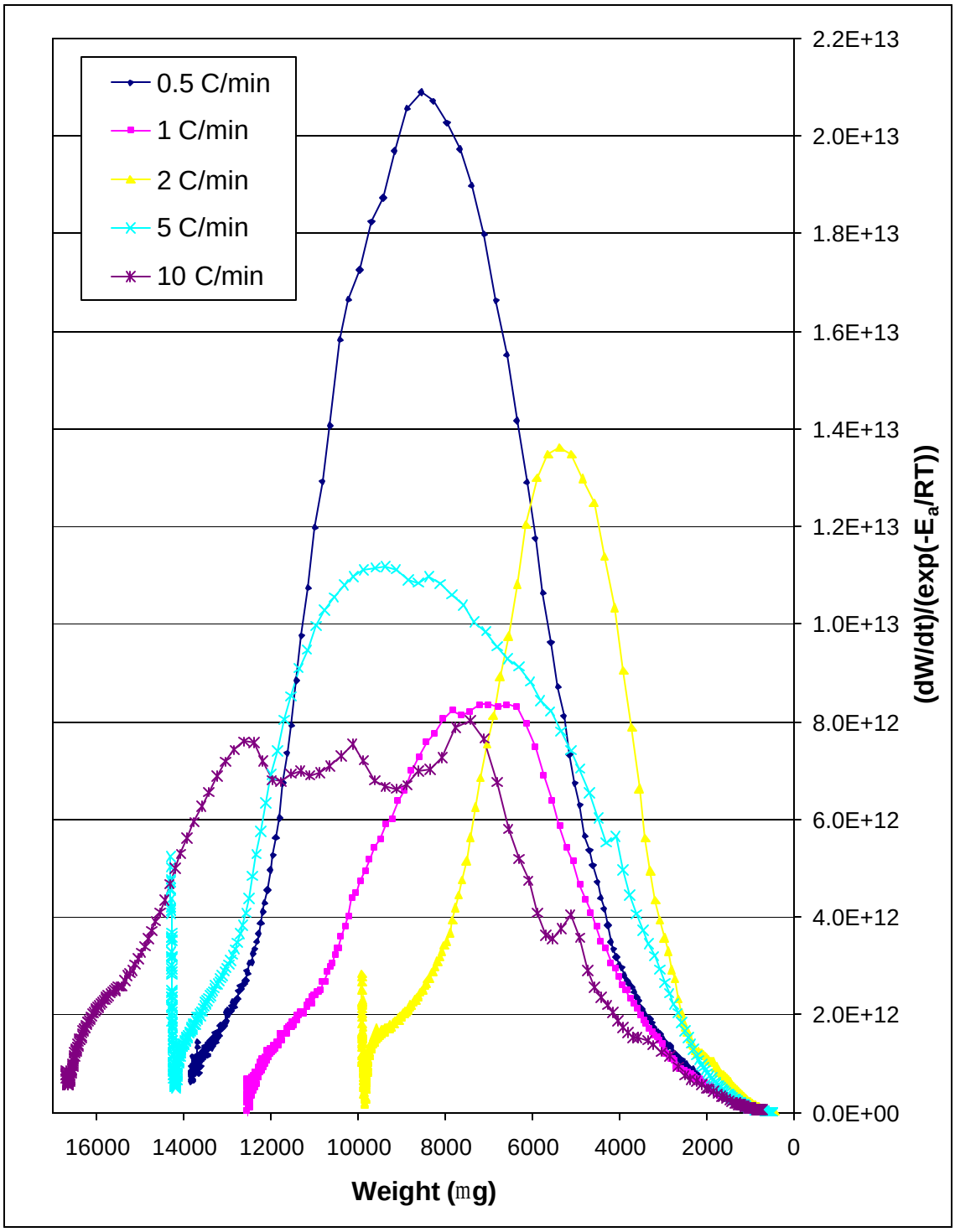

Figure A.5: *d*W/*d*t corrected for temperature as a function of W for the decomposition of PPC in nitrogen at various heating rates.

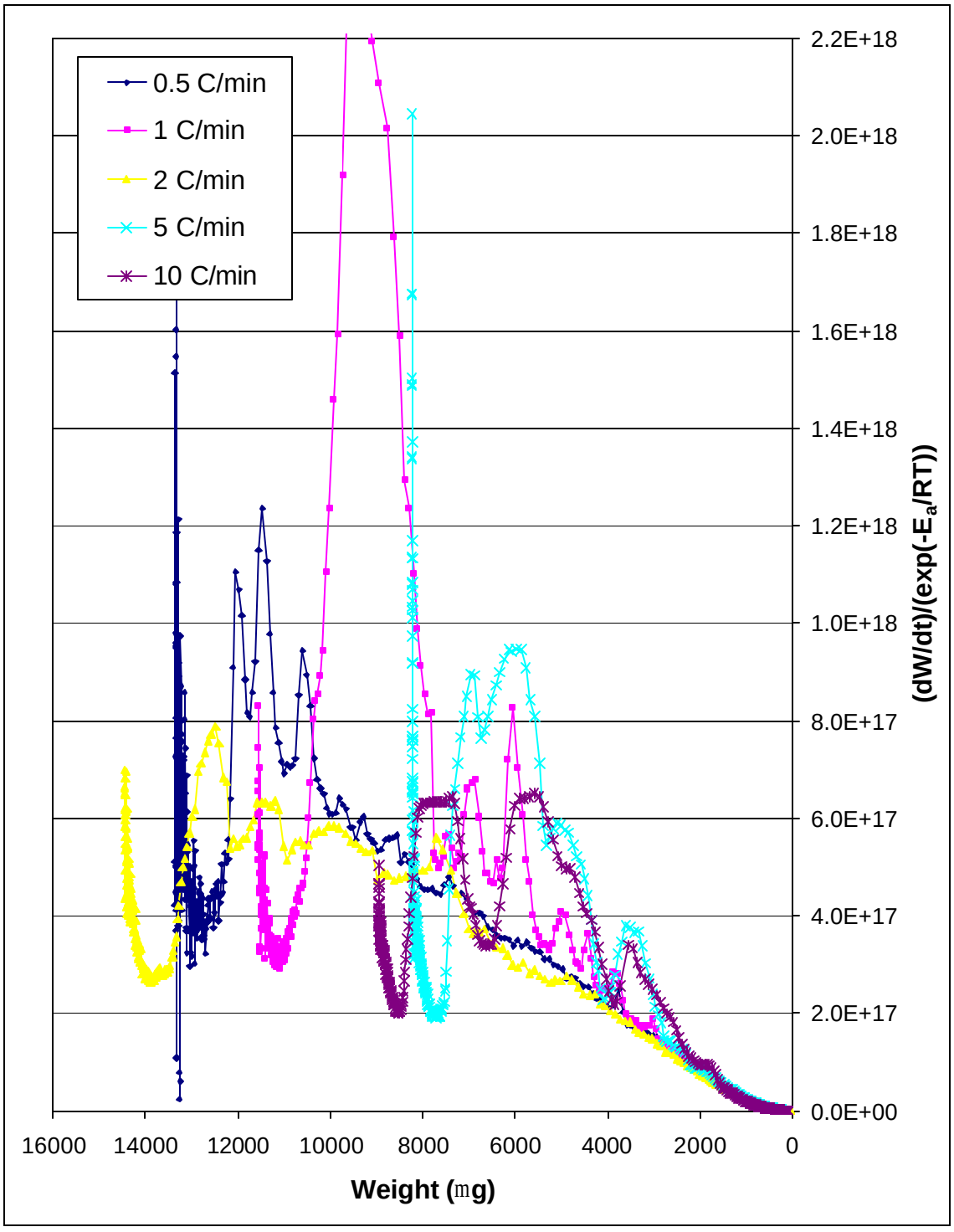

Figure A.6: *d*W/*d*t corrected for temperature as a function of W for the decomposition of PPC in air at various heating rates.

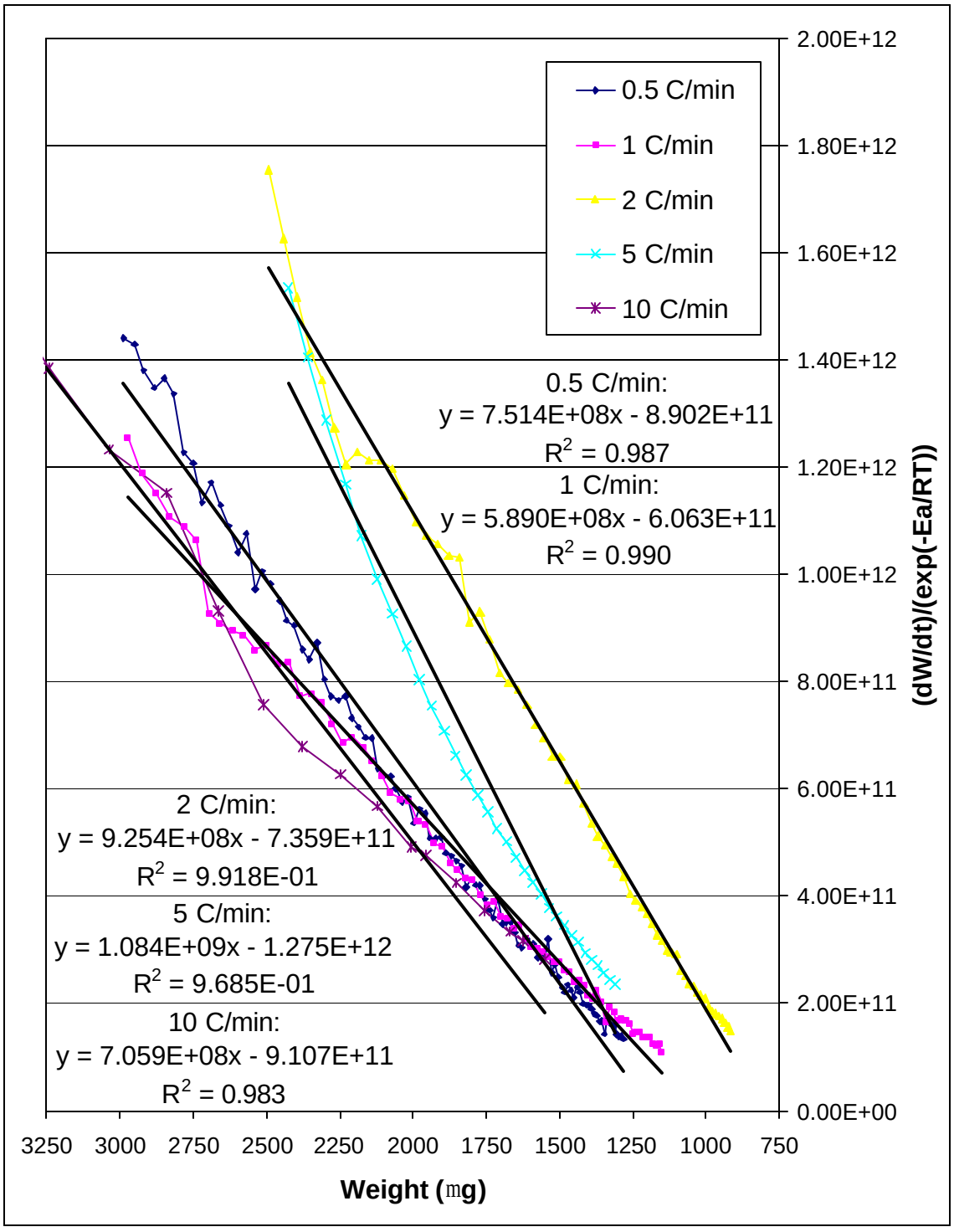

Figure A.7: The determination of RF for the decomposition of PPC in nitrogen at constant heating rates of 0.5, 1, 2, 5, and 10°C/min.

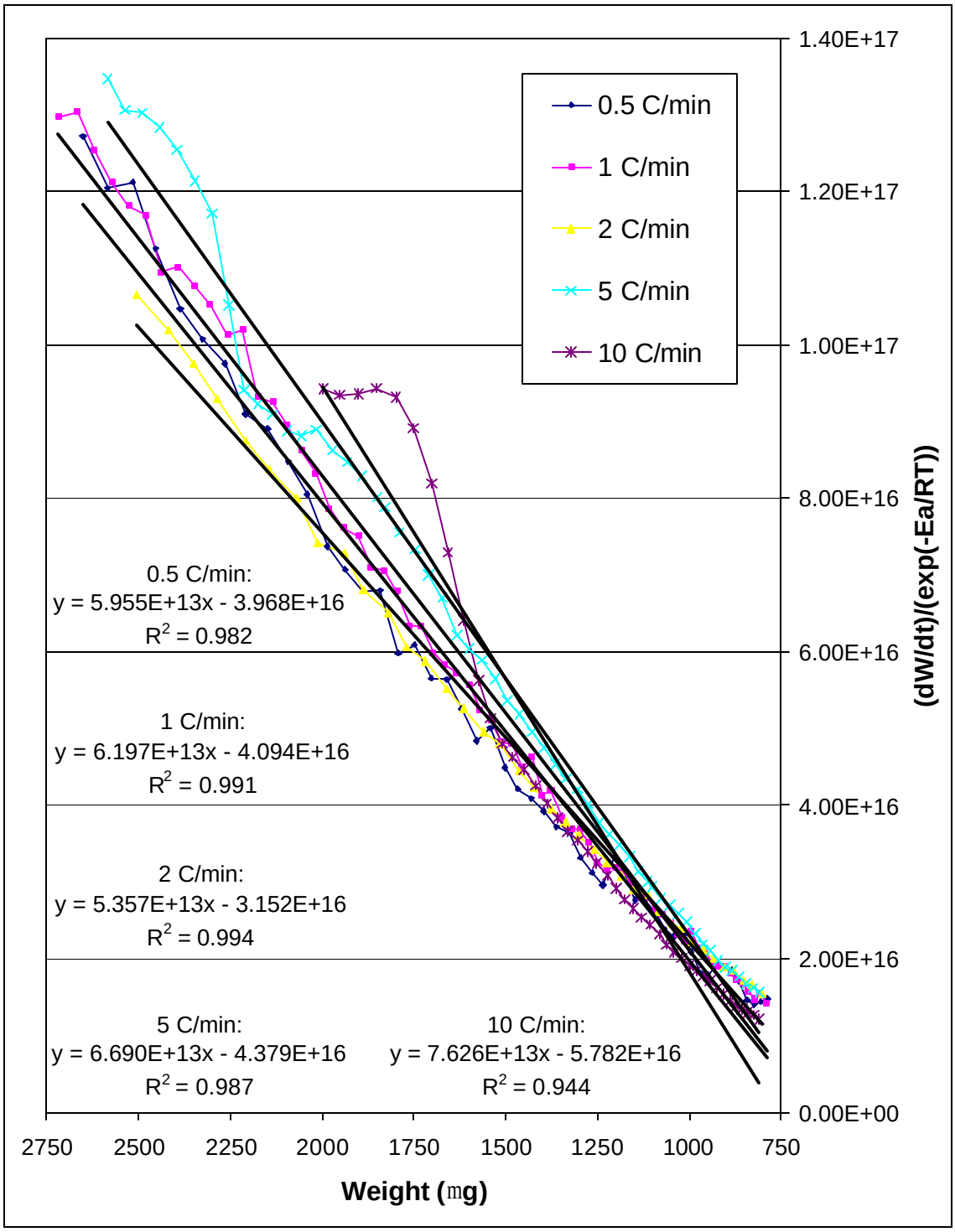

Figure A.8: The determination of RF for the decomposition of PPC in air at constant heating rates of 0.5, 1, 2, 5, and 10^{o}C/min.

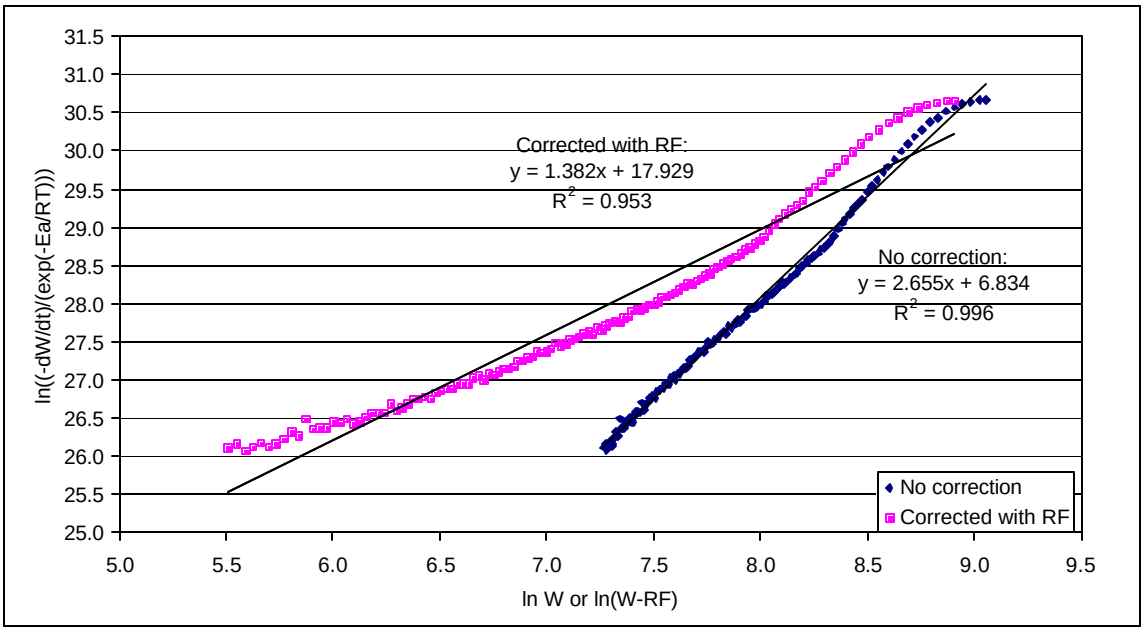

Figure A.9: The determination of n and A from dynamic TGA at 0.5°C/min for the decomposition of PPC in nitrogen

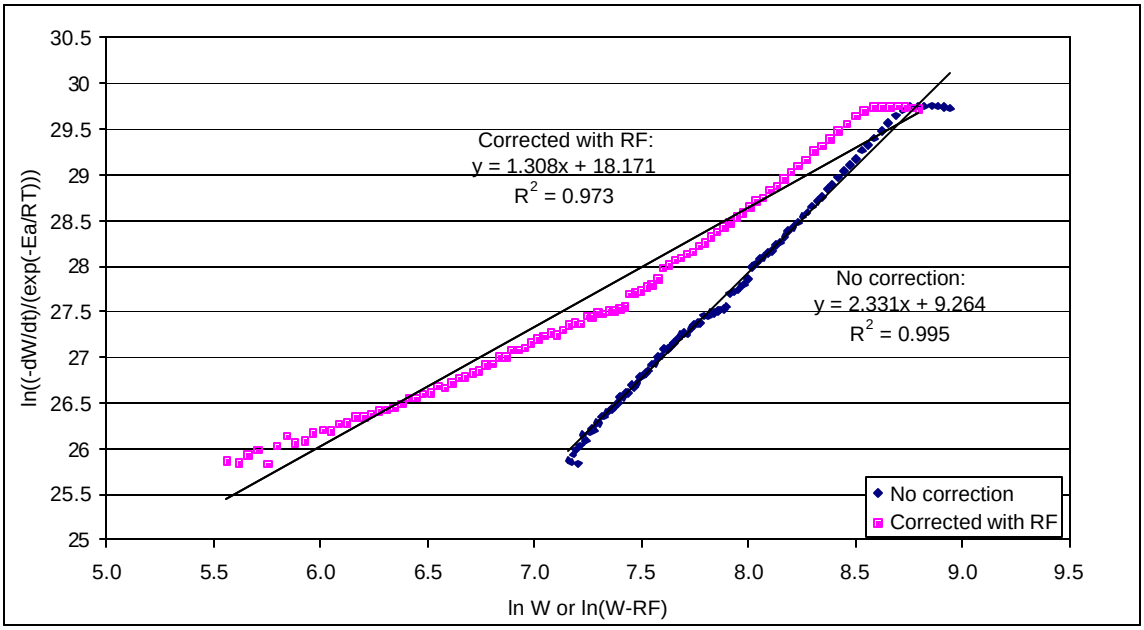

Figure A.10: The determination of n and A from dynamic TGA at 1°C/min for the decomposition of PPC in nitrogen

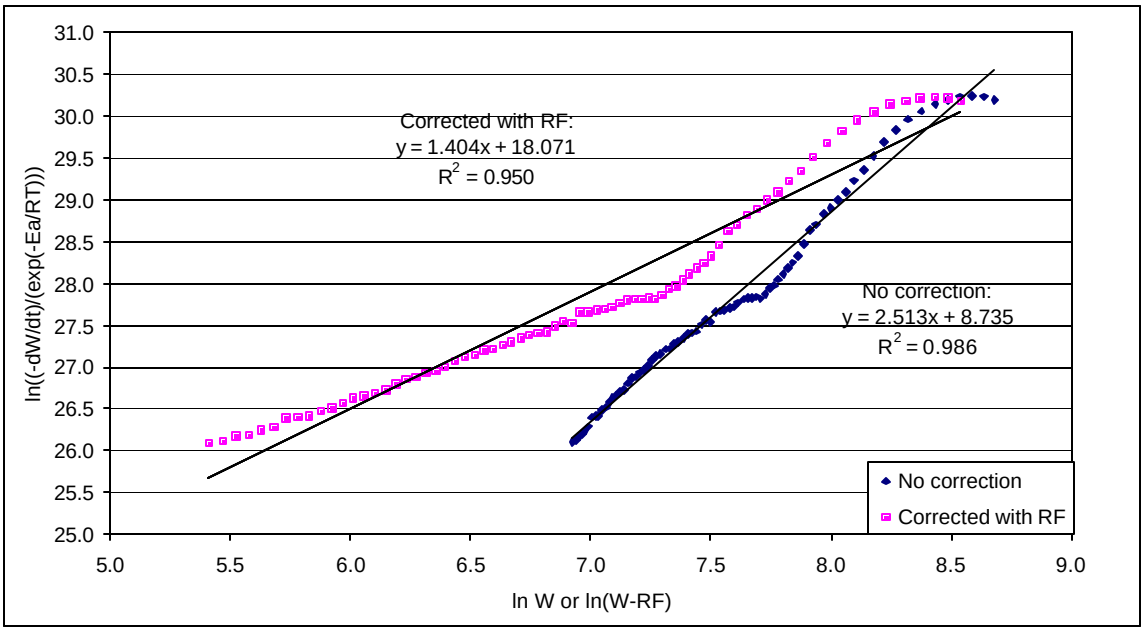

Figure A.11: The determination of n and A from dynamic TGA at 2°C/min for the decomposition of PPC in nitrogen.

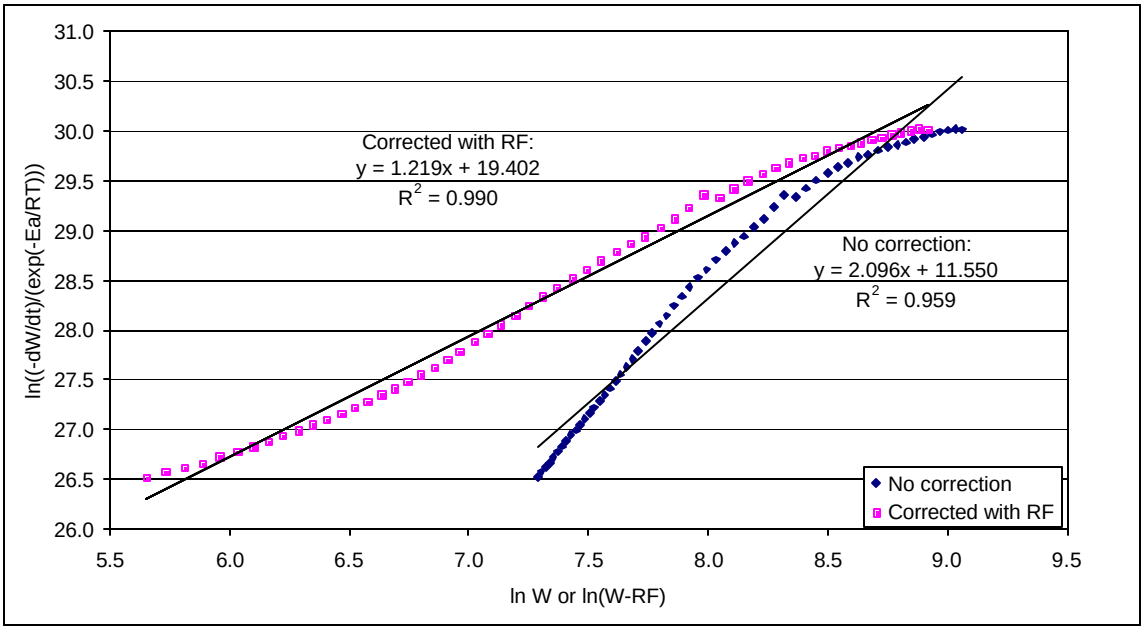

Figure A.12: The determination of n and A from dynamic TGA at 5°C/min for the decomposition of PPC in nitrogen.

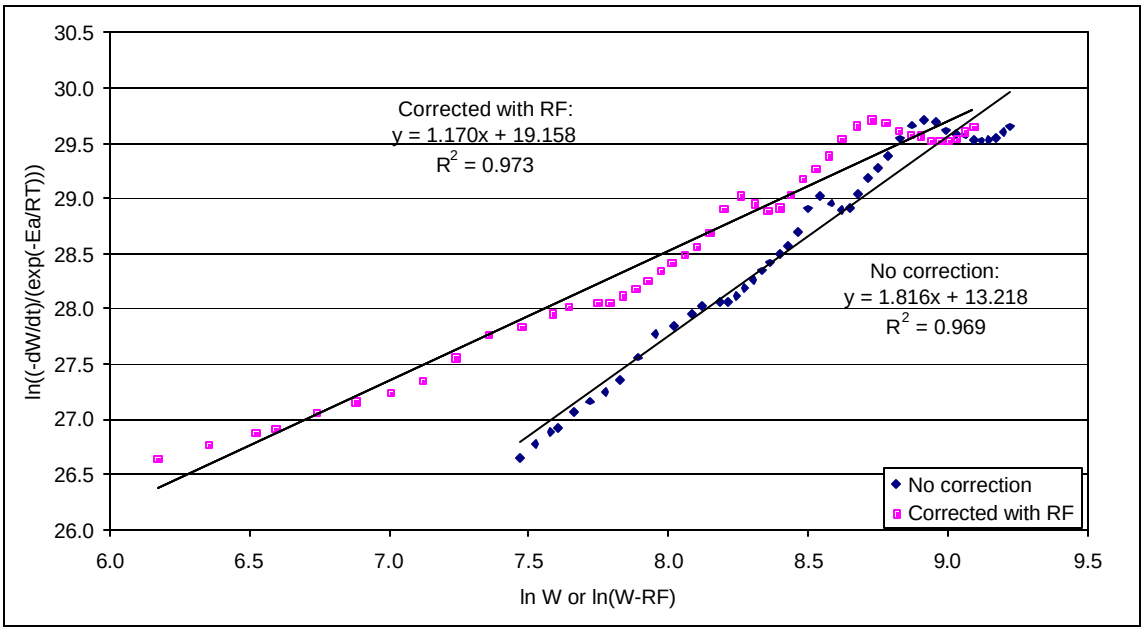

Figure A.13: The determination of n and A from dynamic TGA at 10°C/min for the decomposition of PPC in nitrogen.

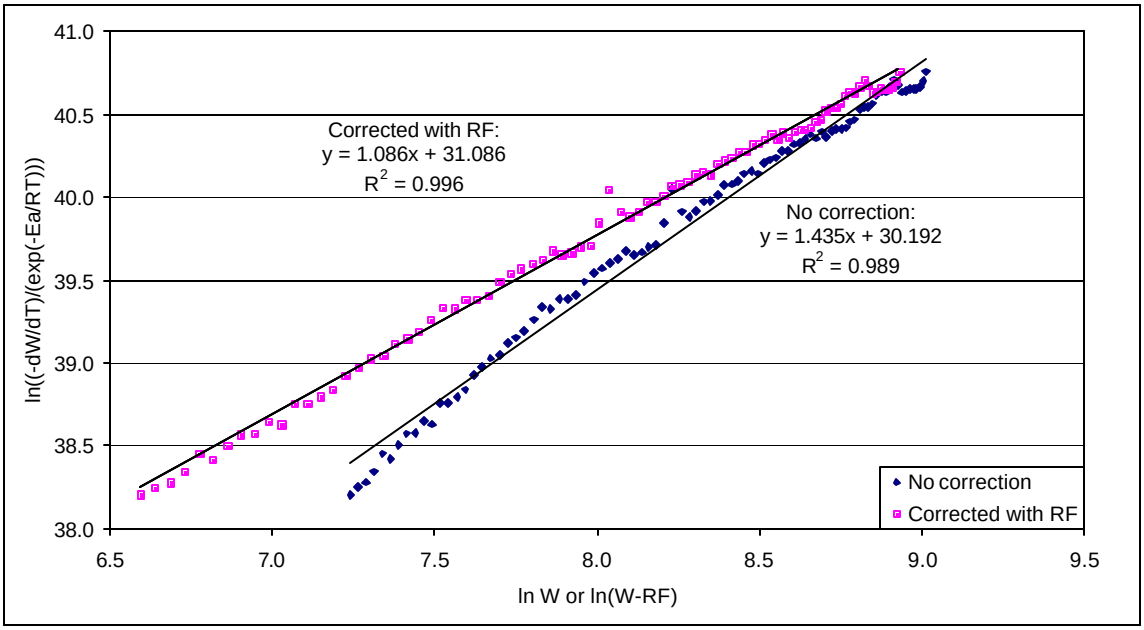

Figure A.14: The determination of n and A from dynamic TGA at 0.5°C/min for the decomposition of PPC in air.

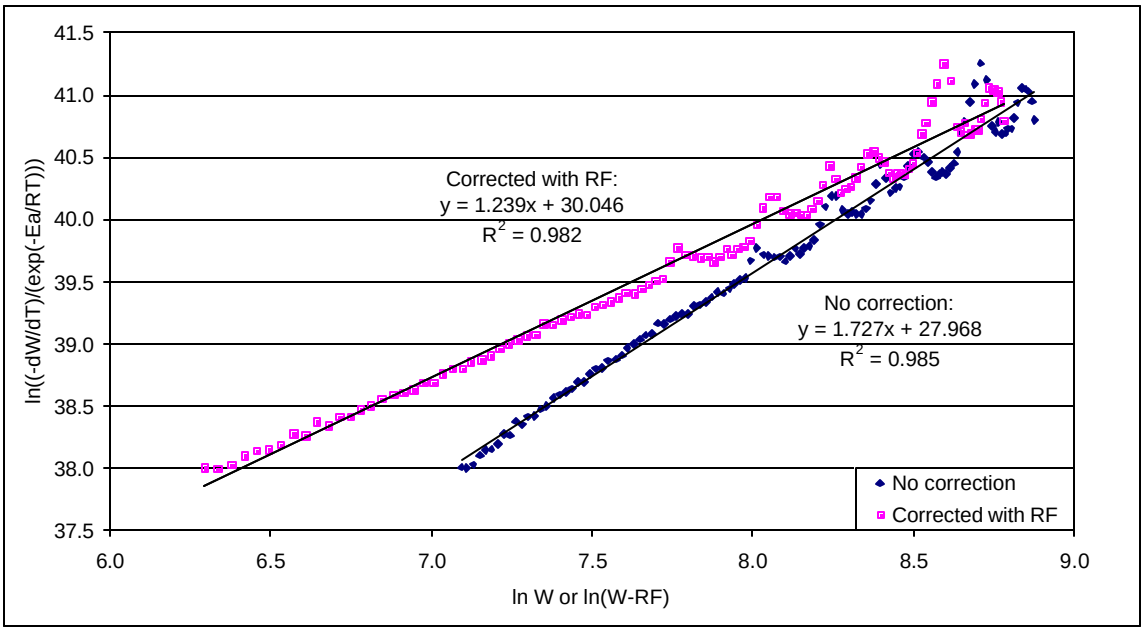

Figure A.15: The determination of n and A from dynamic TGA at 1°C/min for the decomposition of PPC in air.

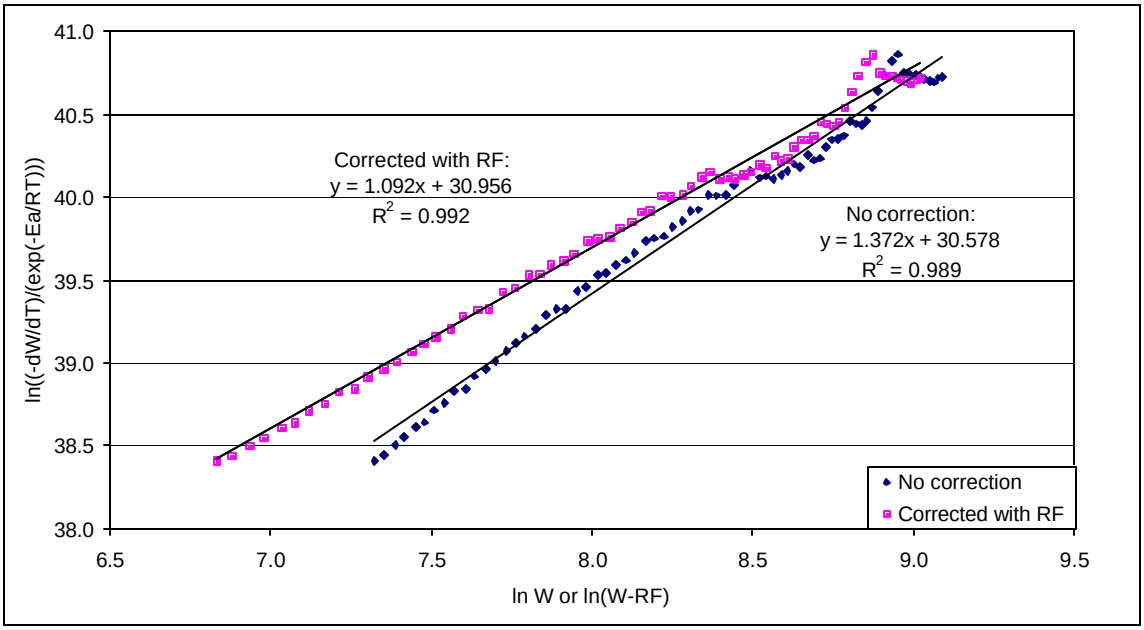

Figure A.16: The determination of n and A from dynamic TGA at 2°C/min for the decomposition of PPC in air.

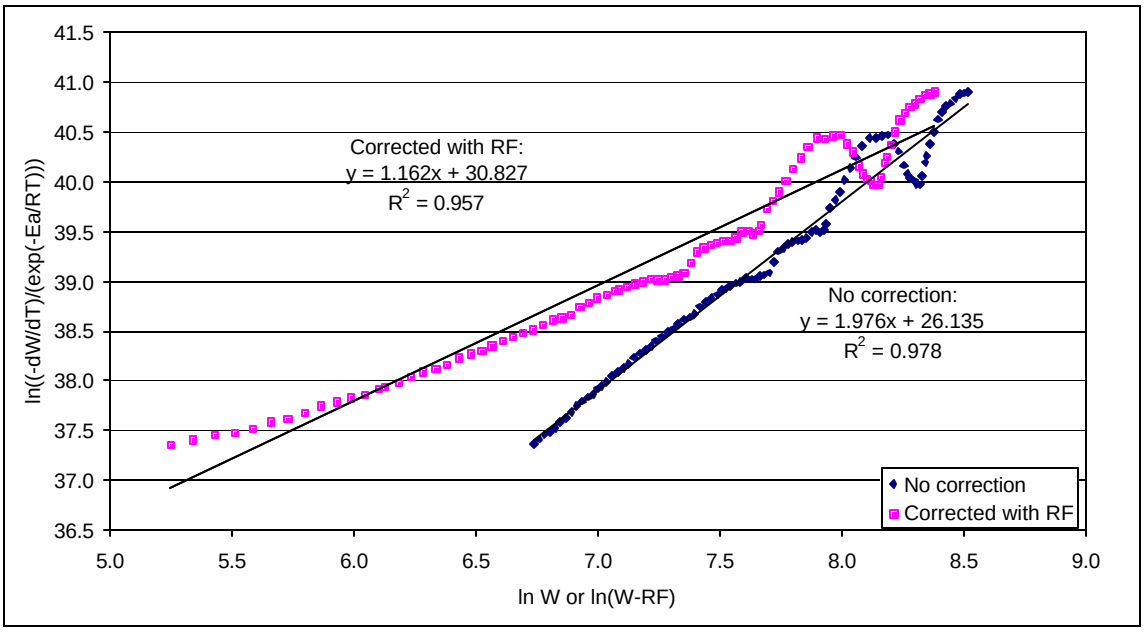

Figure A.17: The determination of n and A from dynamic TGA at 5°C/min for the decomposition of PPC in air.

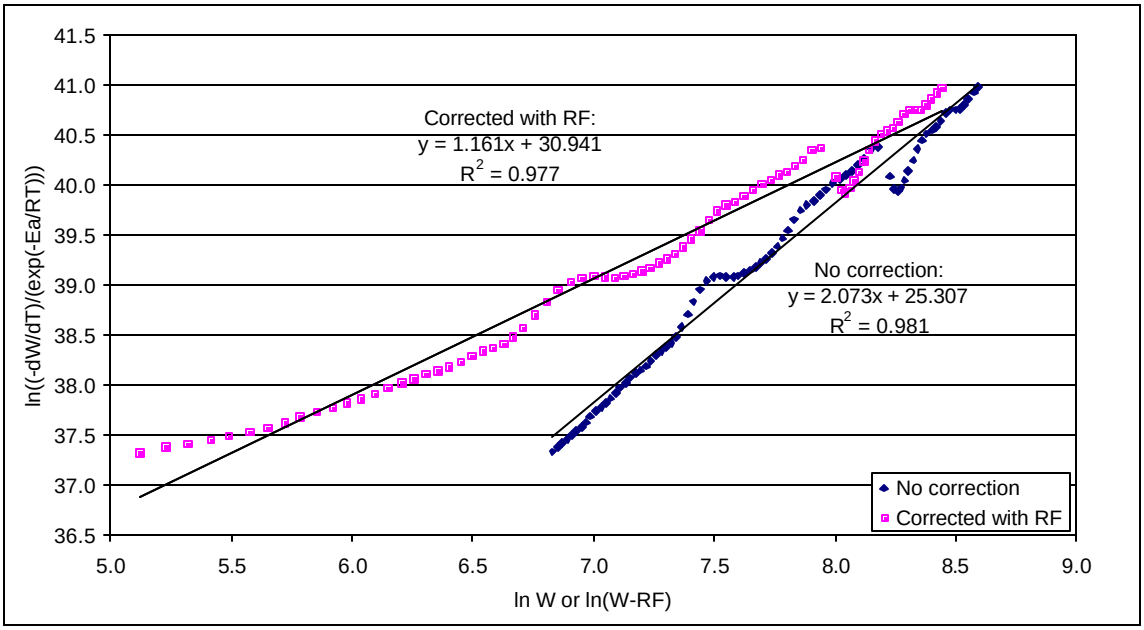

Figure A.18: The determination of n and A from dynamic TGA at 10°C/min for the decomposition of PPC in air.

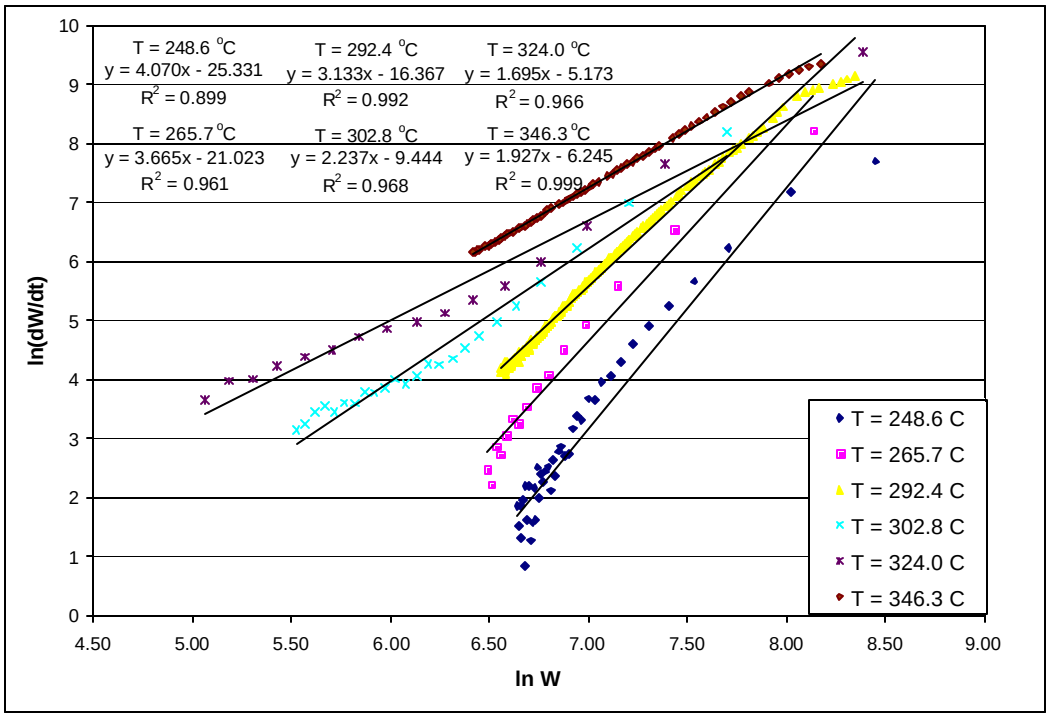

Figure A.19: Plot of ln(dW/dt) as a function of ln(W) to determine the uncorrected reaction order for the decomposition of PPC in nitrogen at various isothermal temperatures.

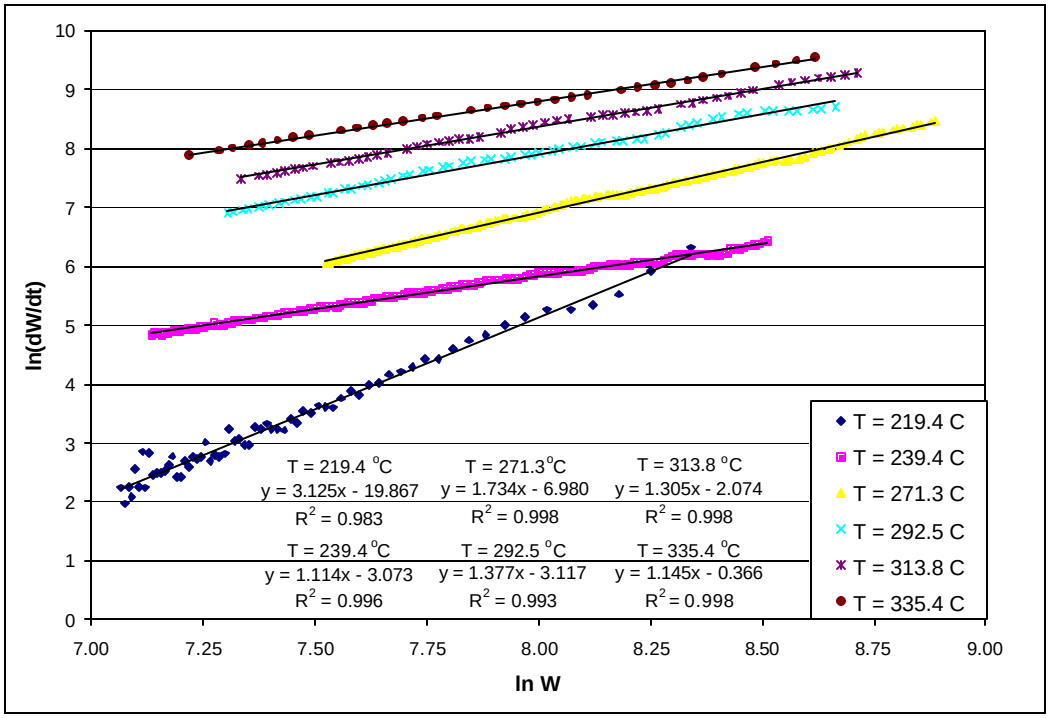

Figure A.20 Plot of ln(dW/dt) as a function of ln(W) to determine the uncorrected reaction order for the decomposition of PPC in air at various isothermal temperatures.

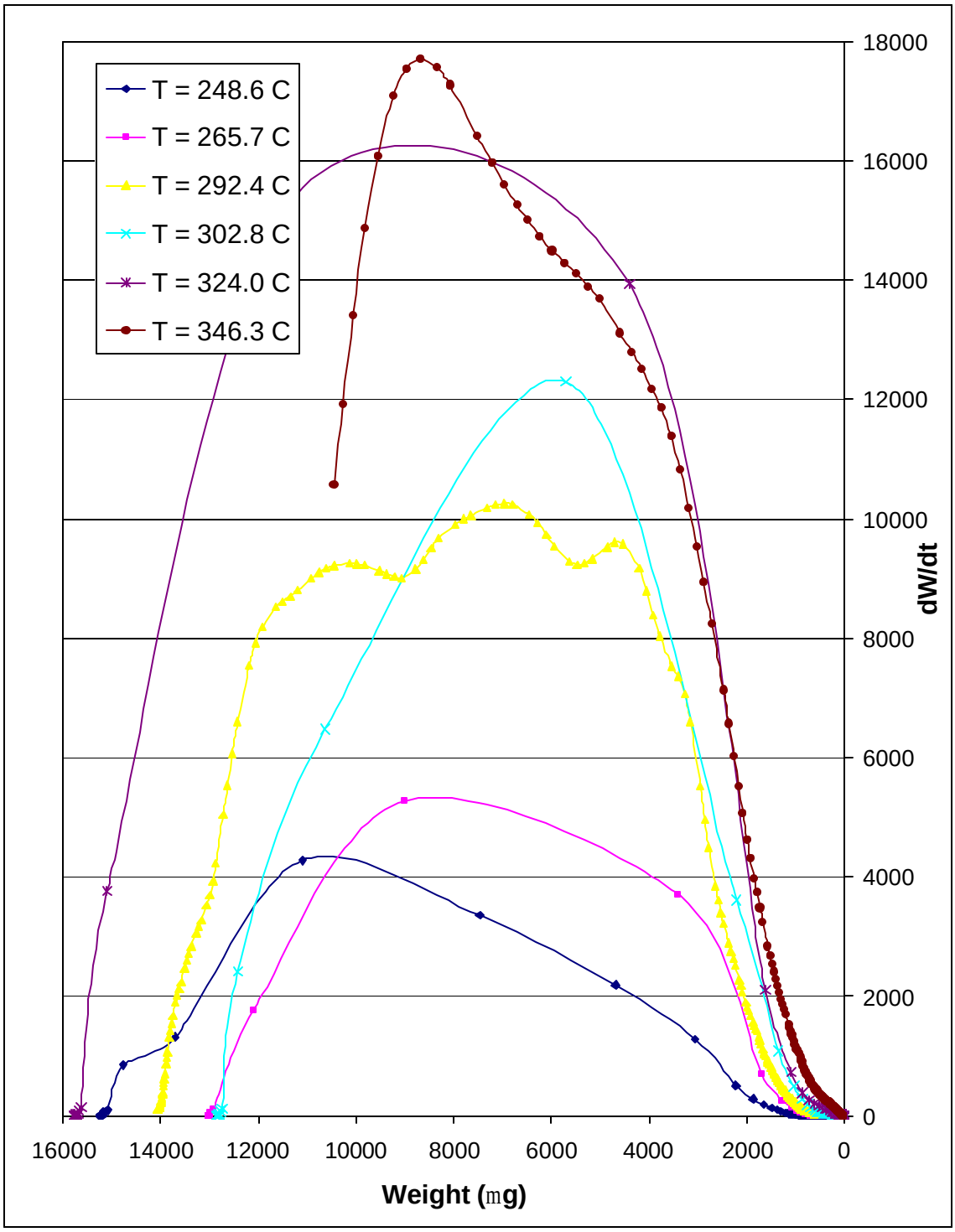

Figure A.21: *d*W/*d*t as a function of W for the decomposition of PPC in nitrogen at various isothermal temperatures

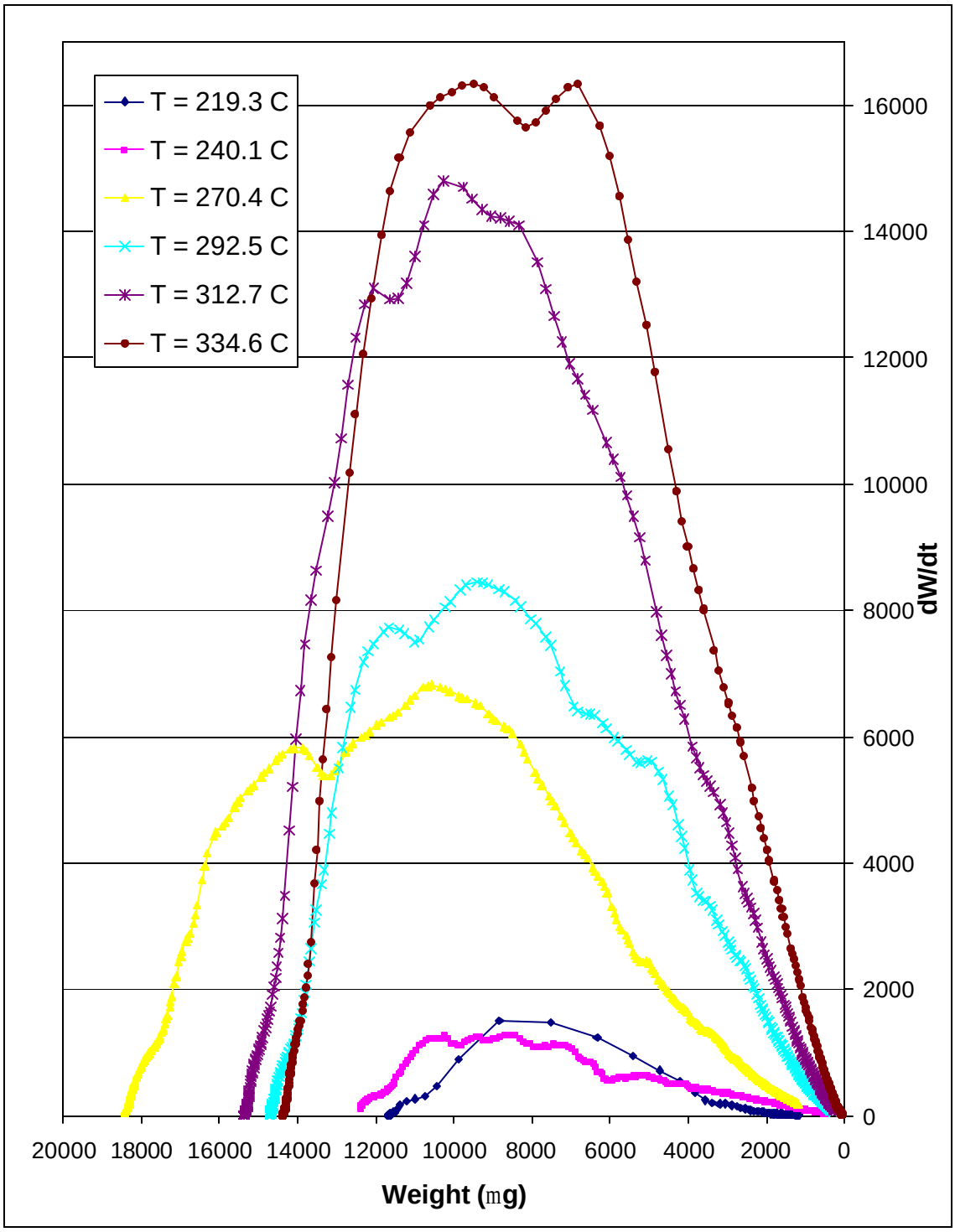

Figure A.22: *d*W/*d*t as a function of W for the decomposition of PPC in air at various isothermal temperatures.

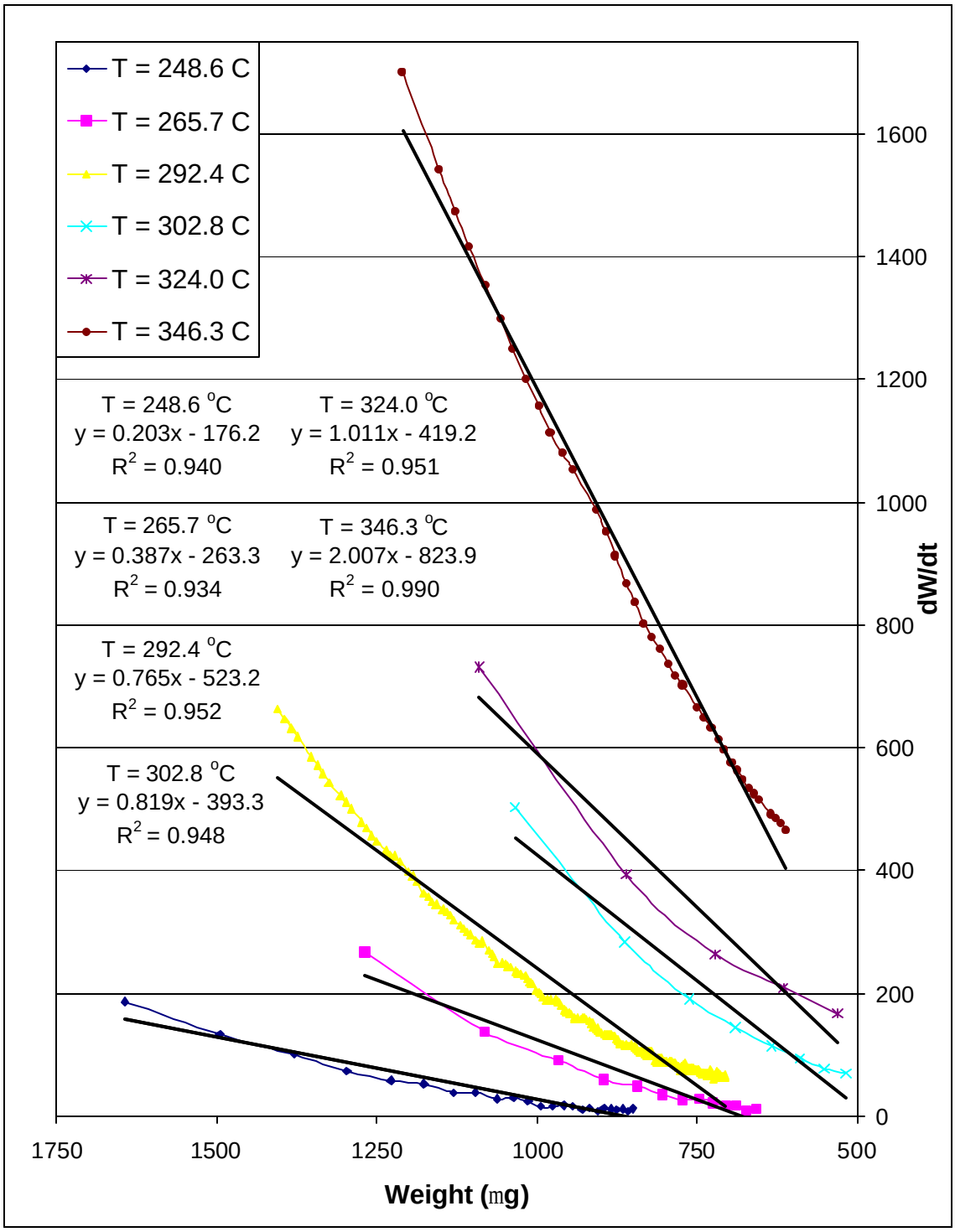

Figure A.23: The determination of RF for the decomposition of PPC in nitrogen at isothermal temperatures.

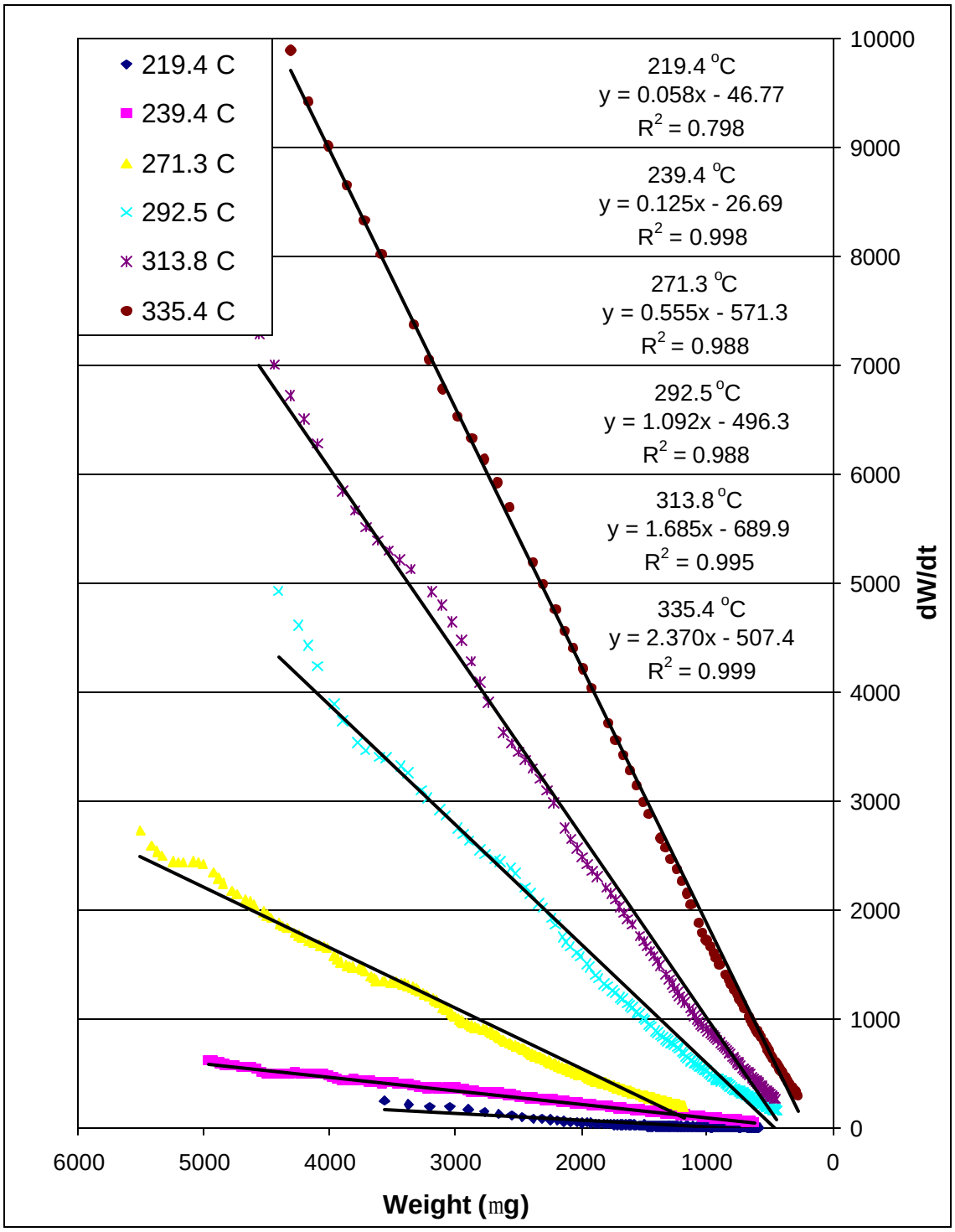

Figure A.24: The determination of RF for the decomposition of PPC in air at isothermal temperatures.

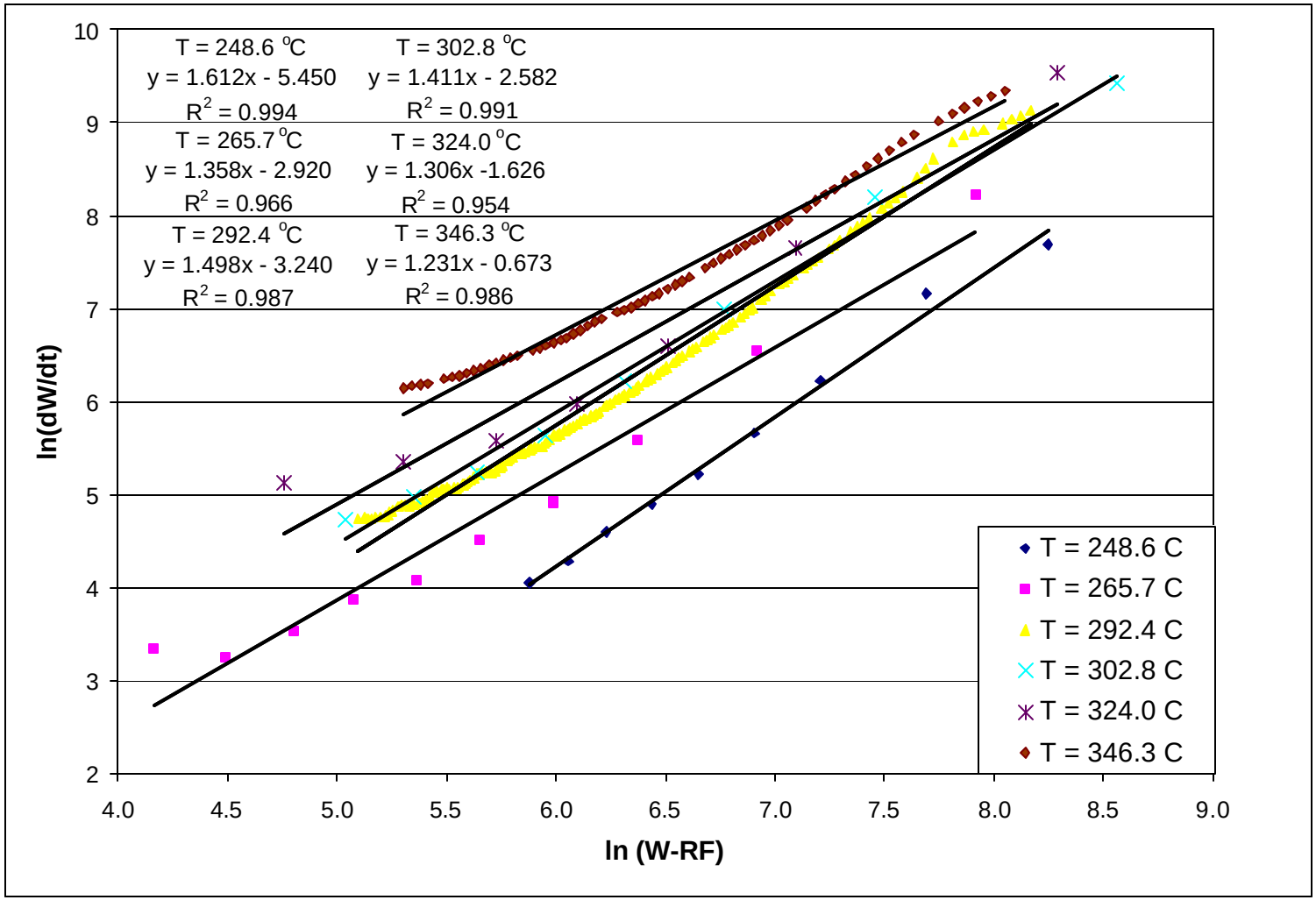

Figure A.25: Plot of ln(dW/dt) as a function of ln(W-RF) to determine the reaction order and the reaction rate constant corrected with RF, for the decomposition of PPC in nitrogen at various isothermal temperatures.

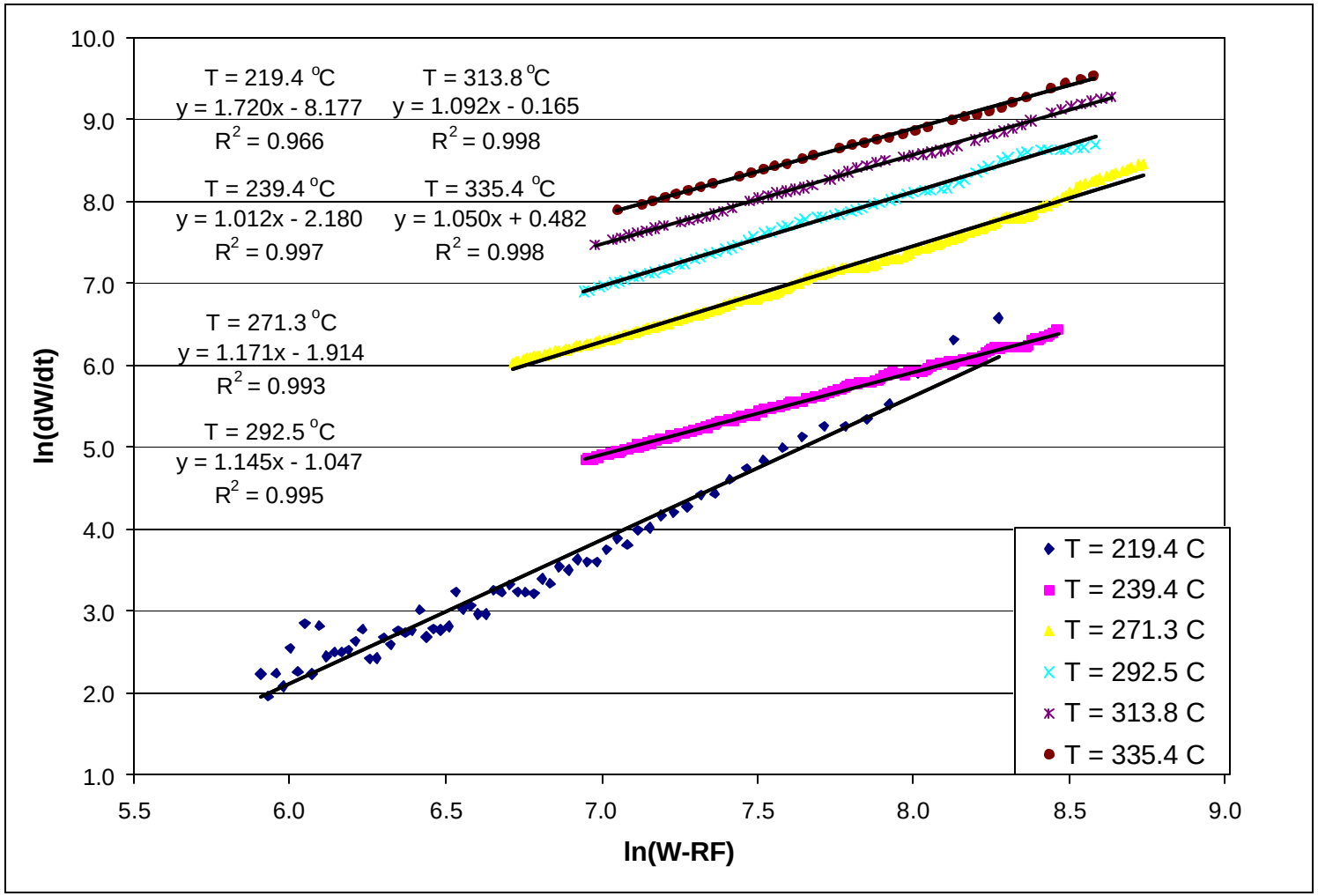

Figure A. 26: Plot of ln(*d*W/*d*t) as a function of ln(W-RF) to determine the reaction order and reaction rate constant corrected with RF, for the decomposition of PPC in air at various isothermal temperatures.

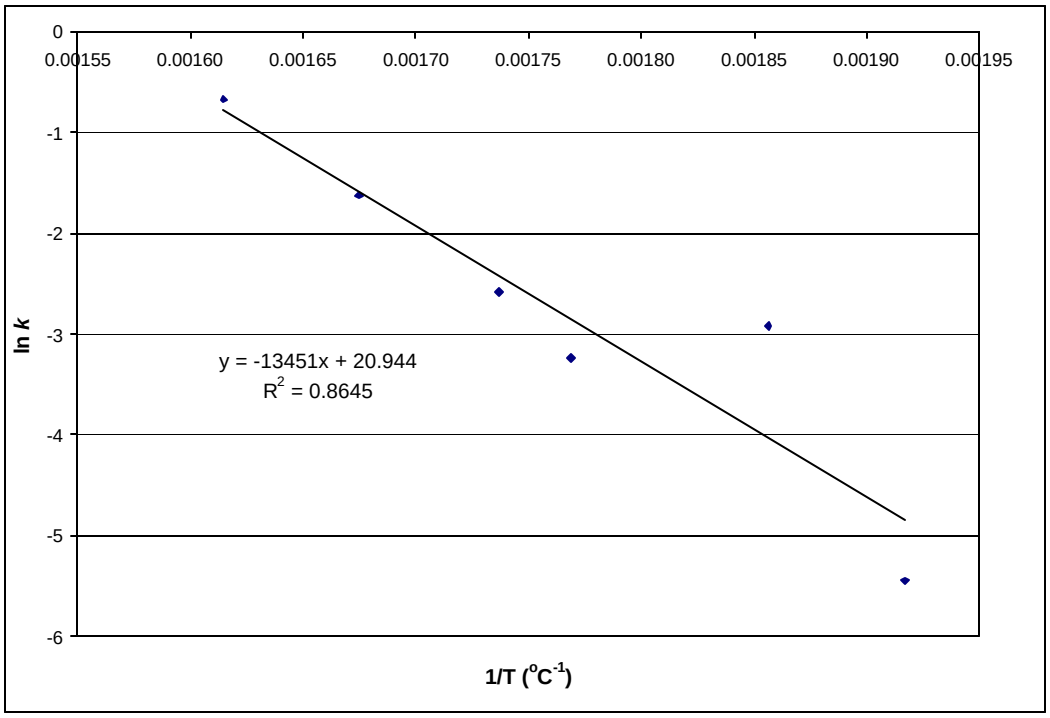

Figure A.27: The determination of E_a and A from isothermal TGA data of the decomposition of PPC at various temperatures in nitrogen.

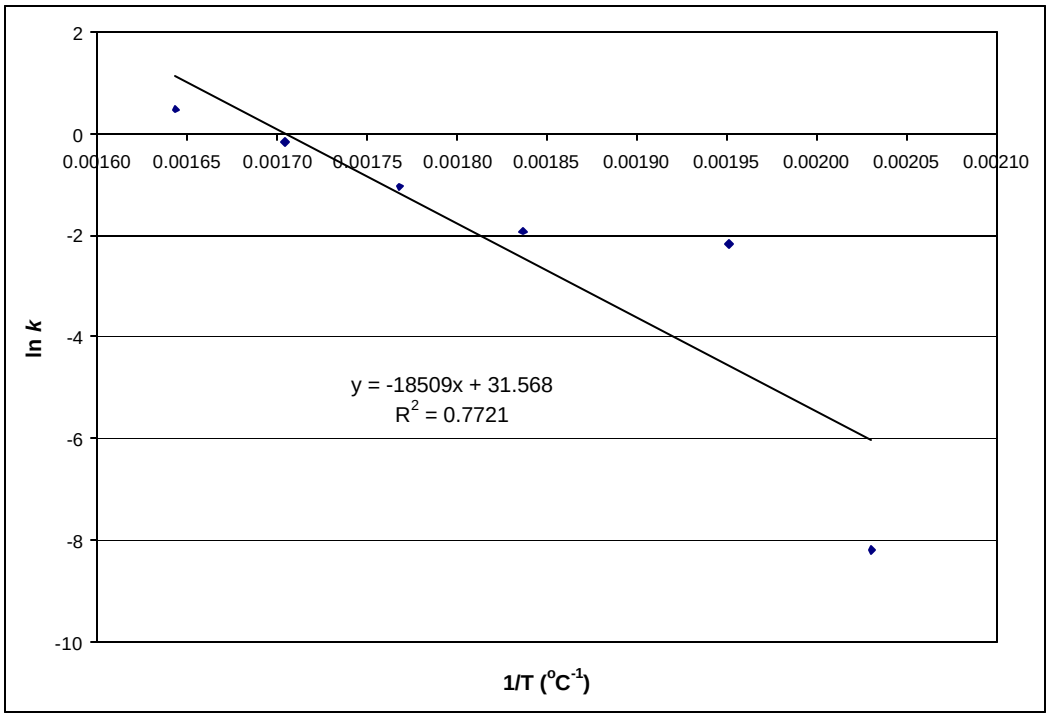

Figure A.28: The determination of E_a and A from isothermal TGA data of the decomposition of PPC at various temperatures in air.

A.2 Kinetic Parameters From Dynamic and Isothermal TGA Data in Nitrogen for Unencapsulated and PNB Encapsulated by PI-2611

Dynamic TGA data of the decomposition of unencapsulated PNB and PNB encapsulated in PI-2611 was obtained at heating rates of 1, 3, and 10°C/min in nitrogen. The $-\log(ß/T^2)$ as a function 1/T for various conversion values at each heating rate are included as Figure A.29 thru Figure A.32. The data in Figure A.29 and Figure A.31 was calculated using the instantaneous heating rate at each value of conversion. The data in Figure A.30 and Figure A.32 was calculated using the overall average heating rate found from the average of the instantaneous heating rate values across all points of the reaction. The equations describing the least squares best fit lines to the data are also shown in the figures. The resulting activation energy values at each conversion, the average E_a, and one standard deviation in nitrogen and air are listed inTable A.4 for unencapsulated PNB and Table A.5 for PNB encapsulated in PI-2611. Figure A.33 and Figure A.34 show the relationship of dW/dt as a function of W for unencapsulated PNB and PNB encapsulated in PI-2611, respectively. When the relationship between dW/dt and W is corrected for temperature by the Arrhenius equation as shown in Figure A.35 and Figure A.36, the relationship is directly proportional from approximately 20% weight loss to completion of the reaction. The data points between 20 to 90% conversion were used for the calculation of RF for unencapsulated PNB decomposition at each dynamic heating rate. The data between 30% to the point were dW/dt reaches zero was used for the calculation of RF for PNB encapsulated in PI-2611. The RF was also determined using both the average and instantaneous heating rate values. Figure A.37 and Figure A.38 show the plots and equations to determine the residue factors for unencapsulated PNB at each

dynamic heating rate using the instantaneous heating rate and the average heating rate, respectively. Figure A.39 thru Figure A.42 are the plots used in the determination of RF for PNB encapsulated in PI-2611. Figure A.39 and Figure A.40 are formed using the instantaneous heating rate values. Figure A.41 and Figure A.42 are formed using the overall average heating rate. The linear equations representing the best-fit lines to the encapsulated PNB data in Figure A.39 thru Figure A.42 are provided in Table A.6. The calculated residue factors are included in Section 7.3.3 as Table 29, pg. 247.

Following calculation of the RF, n and A are determined from the dynamic TGA at each heating rate. $\ln(dW/dt)$ as a function of the uncorrected W, and W corrected by RF, and the respective best-fit linear equations to the data are included in Figure A.43 thru Figure A.62. The data between 20 and 90% conversion is used to calculate the reaction order and pre-exponential coefficient for unencapsulated PNB. The range of 30 to 80% conversion is used for PNB encapsulated in PI-2611. A smaller range of data is used for the encapsulated samples to help eliminate error from the limits on the weight of PNB. Between 30 and 80% conversion, the governing kinetics of the reaction are prevalent. A summary of the parameters n and A from the dynamic TGA data for unencapsulated PNB is presented as Table A.7. The parameters n and A for the decomposition of PNB encapsulated in PI-2611 from dynamic TGA are summarized in Table A.8.

Isothermal TGA performed at $400^{o}C$ and $425^{o}C$ is also used to determine the kinetic parameters for the decomposition of unencapsulated PNB and PNB encapsulated in PI-2611. The relationship of dW/dt as a function of W for isothermal decomposition is shown in Figure A.63 for unencapsulated PNB and Figure A.64 for PNB encapsulated in

PI-2611. The relationship between dW/dt and W is linear from approximately 30 percent conversion to the endpoint of the reaction. Figure A.65 and Figure A.66 are the plots used to calculate RF for each isothermal experiment. The data in the range of 30 to 95 percent decomposition was used to construct the RF plot for isothermal decomposition of encapsulated PNB. A summary of the RF values for isothermal decomposition is included in Section 7.3.3, Table 30, page 248. Following calculation of RF, the reaction order and rate constant are determined from a plot of $\ln(dW/dt)$ as a function of ln(W). The data between 20 and 80 percent conversion is used to find n and k. The initial portion of the data is excluded because the system has not yet reached the isothermal temperature. The portion of the data and the end of the reaction is excluded to avoid the large residue amounts in the encapsulated samples. The determination of the uncorrected and corrected n and k is shown in Figure A.71 for unencapsulated PNB and Figure A.72 for PNB encapsulated PI-2611. The results are summarized in Table A.9. Finally, a plot is constructed of ln k as a function of 1/T as shown in Figure A.73. The best fit line to the data gives a slope of (E_a/R) and a y-axis intercept of ln A. A summary of all the calculated kinetic parameters for the decomposition of unencapsulated PNB and PNB encapsulated in PI-2611 in nitrogen is given in Section 7.3.3, Table 31, page 249.

Table A.4: Activation energy (kJ/mol) at various values of conversion for the decomposition of unencapsulated PNB, based on instantaneous and average dynamic heating rates.

	Instantaneous Heating Rate	**Average Heating Rate**
Conversion (%)	**Activation Energy, E_a (kJ/mol)**	**Activation Energy, E_a (kJ/mol)**
10	225.4	225.0
20	213.8	219.0
30	221.1	219.3
40	231.4	220.0
50	234.8	220.6
60	235.3	223.8
Average/ Standard Deviation	227.0 ± 8.5	221.3 ± 2.5

Table A.5: Activation energy (kJ/mol) at various values of conversion for the decomposition of PNB encapsulated by PI-2611 in nitrogen, based on instantaneous and average dynamic heating rates.

	Instantaneous Heating Rate	**Average Heating Rate**
Conversion (%)	**Activation Energy, E_a (kJ/mol)**	**Activation Energy, E_a (kJ/mol)**
10	210.0	219.5
20	214.26	219.2
30	211.9	221.7
40	222.9	224.8
50	213.2	230.3
60	213.5	237.4
Average/ Standard Deviation	514.3 ± 4.5	225.5 ± 7.1

Table A.6: Linear coefficients and the best fit parameter, R^2, for the linear function used to determine RF.

A, B represent constants in an equation of the form y = Ax+B			
SAMPLE	**A**	**B**	**R^2**
Instantaneous Heating Rate			
SP-CD10-1: Average	2.579E+15	-9.800E+17	0.997
SP-CD10-1: Lower limit	2.506E+15	-2.304E+17	0.996
SP-CD10-1: Upper limit	2.535E+15	-9.807E+17	0.997
SP-CD3-1: Average	2.344E+15	-5.248E+17	0.999
SP-CD3-1: Lower limit	2.227E+15	5.271E+17	0.992
SP-CD3-1: Upper limit	2.202E+15	-3.063E+17	0.997
SP-CD3-2: Average	2.316E+15	-1.236E+17	0.994
SP-CD3-2: Lower limit	2.468E+15	7.104E+17	0.953
SP-CD3-2: Upper limit	2.214E+15	-3.860E+17	0.981
SP-CD3-3: Average	2.684E+15	-1.793E+18	0.985
SP-CD3-3: Lower limit	2.558E+15	-5.156E+17	0.972
SP-CD3-3: Upper limit	2.510E+15	-6.269E+17	0.978
SP-CD1-1: Average	2.667E+15	-1.338E+18	0.991
SP-CD1-1: Lower limit	2.654E+15	-7.430E+17	0.992
SP-CD1-1: Upper limit	2.610E+15	-8.001E+17	0.992
Average Heating Rate			
SP-CD10-1: Average	1.725E+16	-6.699E+18	0.998
SP-CD10-1: Lower limit	1.681E+16	-1.682E+18	0.997
SP-CD10-1: Upper limit	1.697E+16	-6.721E+18	0.998
SP-CD3-1: Average	1.691E+16	-4.147E+18	0.998
SP-CD3-1: Lower limit	1.658E+16	3.170E+18	0.996
SP-CD3-1: Upper limit	1.588E+16	-2.530E+18	0.998
SP-CD3-2: Average	1.972E+16	-1.325E+18	0.995
SP-CD3-2: Lower limit	2.249E+16	4.329E+18	0.898
SP-CD3-2: Upper limit	1.974E+16	-4.906E+18	0.994
SP-CD3-3: Average	1.917E+16	-1.309E+19	0.986
SP-CD3-3: Lower limit	1.890E+16	-4.670E+18	0.989
SP-CD3-3: Upper limit	1.848E+16	-5.402E+18	0.989
SP-CD1-1: Average	2.014E+16	-1.308E+19	0.992
SP-CD1-1: Lower limit	2.050E+16	-6.401E+18	0.990
SP-CD1-1: Upper limit	2.009E+16	-6.751E+18	0.990

Table A.7: Reaction orders and pre-exponential constants calculated from dynamic TGA for unencapsulated PNB.

Sample	**Average ß n, uncorrected**	**Average ß n, corrected**	**Instant ß n, uncorrected**	**Instant ß n, corrected**	**Average ß Pre-exponential Constant, A (min^{-1})**	**Instant ß Pre-exponential Constant, A (min^{-1})**
S-CD10-1	1.095	0.983	1.119	0.990	1.080×10^{16}	2.739×10^{16}
S-CD3-1	1.084	0.994	1.109	0.998	9.887×10^{15}	2.648×10^{16}
S-CD3-2	0.945	0.985	0.969	0.990	1.068×10^{16}	2.840×10^{16}
S-CD3-3	1.070	0.987	1.094	0.992	1.004×10^{16}	2.645×10^{16}
S-CD1-1	1.079	0.986	1.103	0.972	9.701×10^{15}	2.997×10^{16}

Table A.8: Reaction orders and pre-exponential constants calculated from dynamic TGA for PNB encapsulated by PI-2611.

Sample	**Average ß n, uncorrected**	**Average ß n, corrected**	**Instant ß n, uncorrected**	**Instant ß n, corrected**	**Average ß Pre-exponential Constant, A (min^{-1})**	**Instant ß Pre-exponential Constant, A (min^{-1})**
SP-CD10-1: Average W	1.559	1.018	1.501	0.993	1.524×10^{16}	2.738×10^{15}
SP-CD10-1: Lower Limit	1.203	1.062	1.164	1.035	1.083×10^{16}	1.976×10^{15}
SP-CD10-1: Upper Limit	1.393	0.998	1.328	0.961	1.722×10^{16}	3.364×10^{15}
SP-CD3-1: Average W	1.618	0.980	1.499	0.997	1.924×10^{16}	2.392×10^{15}
SP-CD3-1: Lower Limit	0.734	0.980	0.668	0.971	1.907×10^{16}	2.722×10^{15}
SP-CD3-1: Upper Limit	1.316	1.025	1.258	1.024	1.343×10^{16}	1.889×10^{15}
SP-CD3-2: Average W	1.183	1.068	1.137	1.050	1.055×10^{16}	1.677×10^{15}
SP-CD3-2: Lower Limit	0.694	0.923	0.658	0.975	3.256×10^{16}	2.939×10^{15}
SP-CD3-2: Upper Limit	1.458	1.064	1.933	1.142	1.093×10^{16}	8.247×10^{14}
SP-CD3-3: Average W	2.966	0.991	2.883	1.035	2.023×10^{16}	2.130×10^{15}
SP-CD3-3: Lower Limit	1.396	1.005	1.340	1.037	1.831×10^{16}	1.982×10^{15}
SP-CD3-3: Upper Limit	1.486	1.011	1.427	1.043	1.717×10^{16}	1.874×10^{15}
SP-CD1-1: Average W	1.393	0.998	1.328	0.961	1.722×10^{16}	3.364×10^{15}
SP-CD1-1: Lower Limit	1.602	1.017	1.543	1.044	1.825×10^{16}	1.968×10^{15}
SP-CD1-1: Upper Limit	1.633	1.020	1.572	1.040	1.761×10^{16}	1.996×10^{15}

Table A.9: Reaction orders and rate constants for the decomposition of unencapsulated PNB and PNB encapsulated by PI-2611 from isothermal TGA.

Sample		**Data used in Analysis (% conversion)**	**n, uncorrected**	**n, corrected**	**rate constant, *k* (min^{-1})**
S-I400-1	Average W	20-80%	1.021	1.007	0.0568
	Lower 95% Confidence Limit	20-80%	0.921	1.016	0.0531
	Upper 95% Confidence Limit	20-80%	1.043	1.007	0.0568
S-I425-1	Average W	40-80%	1.205	0.985	0.305
	Lower 95% Confidence Limit	40-80%	0.957	1.072	0.309
	Upper 95% Confidence Limit	40-80%	1.091	1.076	0.310
SP-I400-1	Average W	20-75%	2.061	1.098	0.0346
	Lower 95% Confidence Limit	20-75%	1.177	1.012	0.0608
	Upper Limit	20-75%	1.465	1.041	0.0484
SP-I425-1	Average W	30-70%	1.717	0.993	0.288
	Lower 95% Confidence Limit	30-70%	1.616	1.015	0.217
	Upper Limit	30-70%	0.789	0.974	0.321

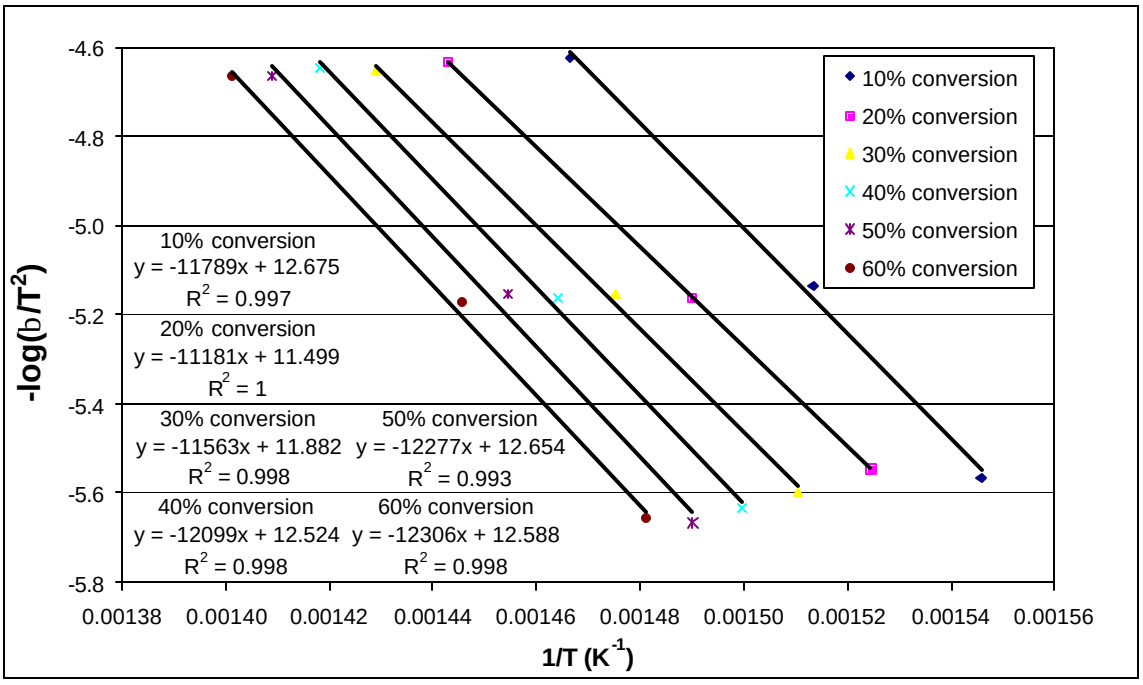

Figure A.29: Analysis plot to determine the activation energy for the decomposition of unencapsulated PNB in nitrogen, using instantantaneous heating rate values.

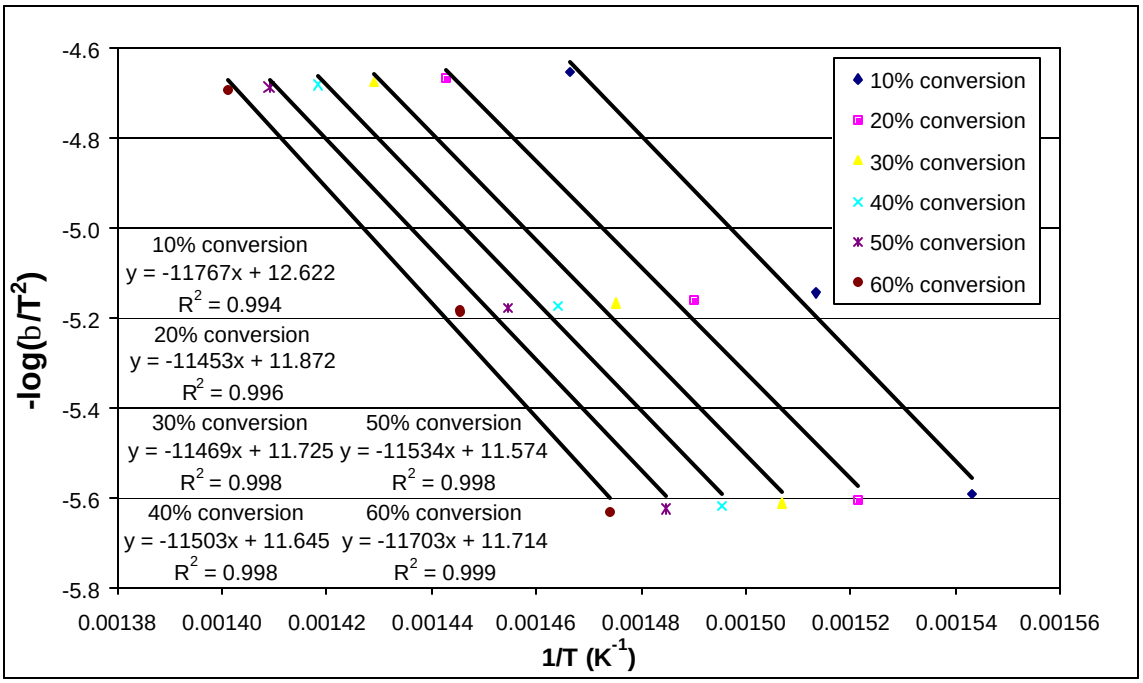

Figure A.30: Analysis plot to determine the activation energy for the decomposition of unencapsulated PNB in nitrogen, using the overall average heating rate values.

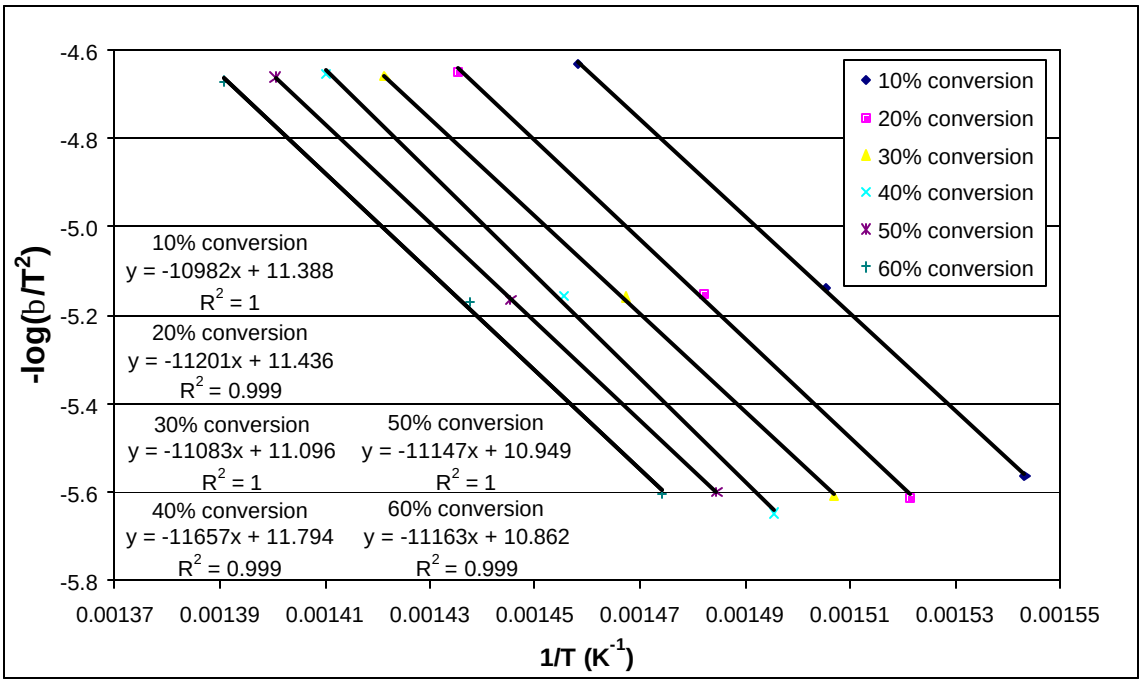

Figure A.31: Analysis plot to determine the activation energy for the decomposition of PNB encapsulated by polyimide PI-2611 in nitrogen, using instantaneous heating rate values.

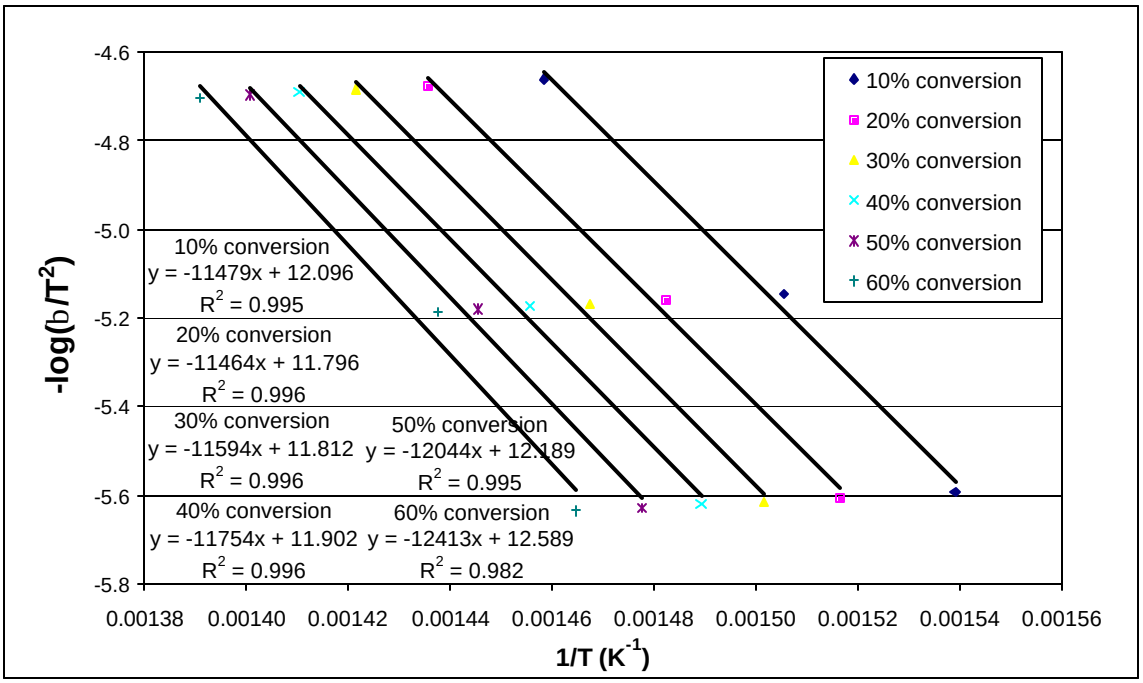

Figure A.32: Analysis plot to determine the activation energy for the decomposition of PNB encapsulated by polyimide PI-2611 in nitrogen, using the overall average heating rate values.

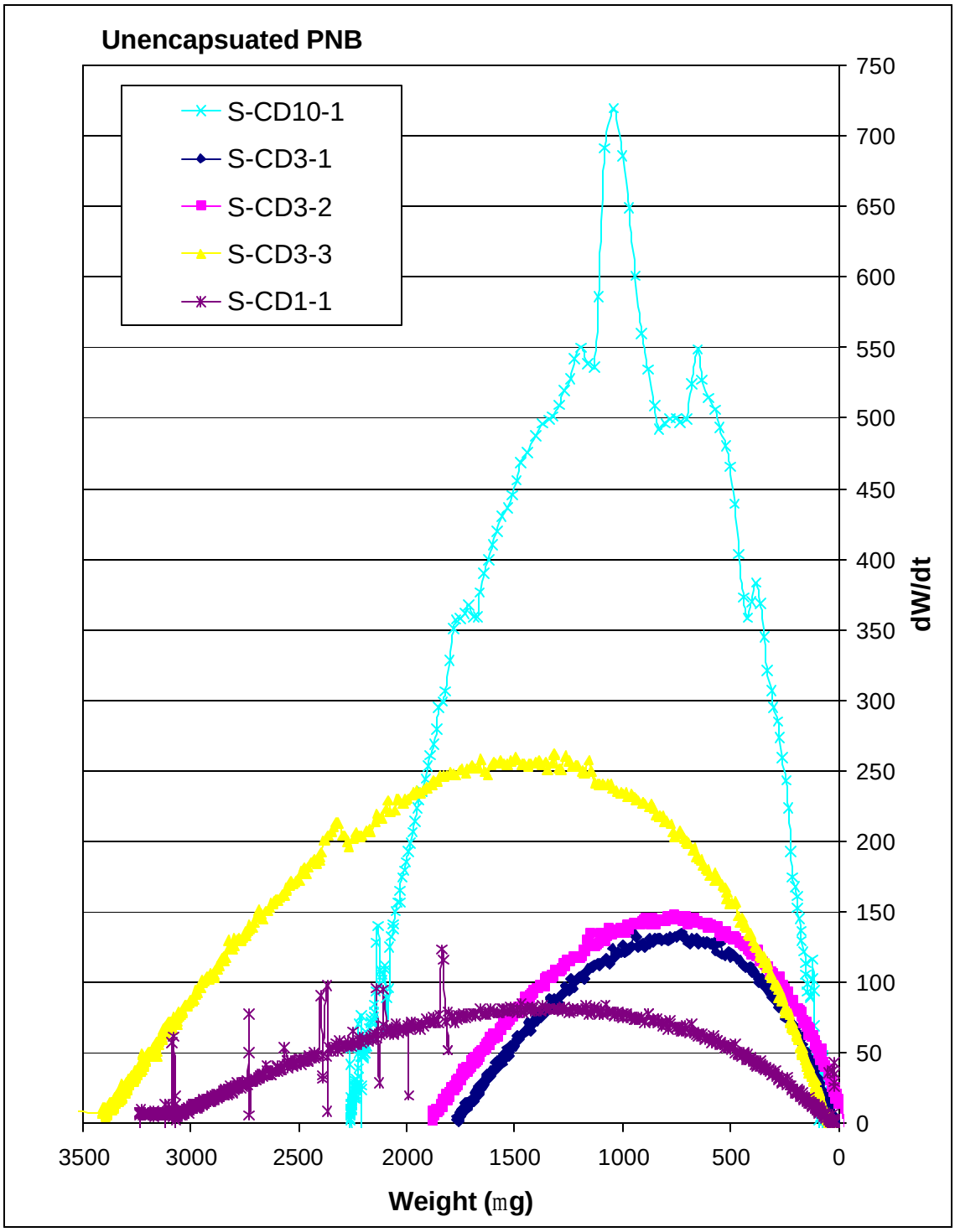

Figure A.33: *d*W/*d*t as a function of W for the decomposition of unencapsulated PNB in a nitrogen atmosphere at heating rates of 1, 3, and 10°C/min.

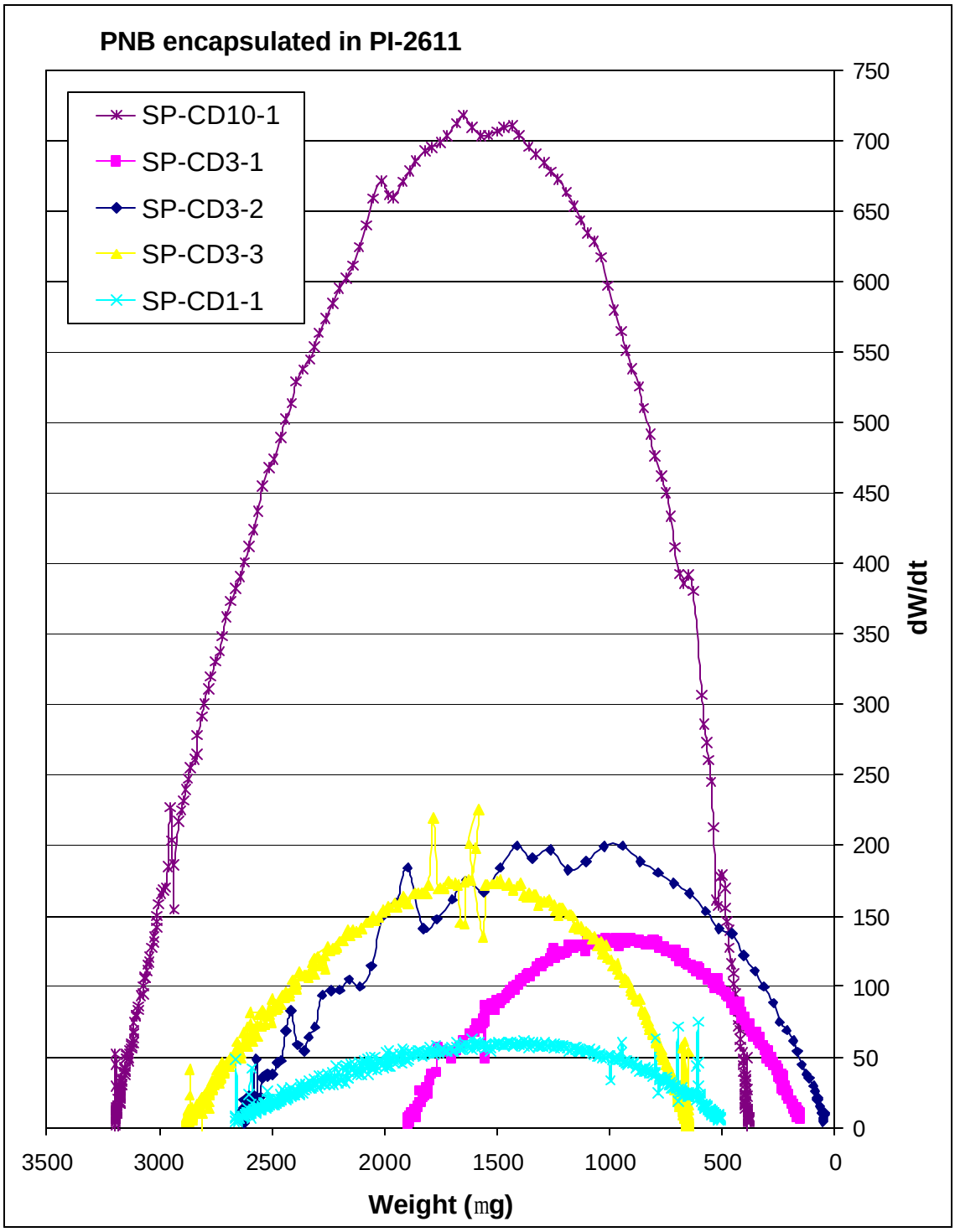

Figure A.34: dW/dt as a function of W for the decomposition of PNB encapsulated by PI-2611 and in a nitrogen atmosphere at heating rates of 1, 3, and 10°C/min.

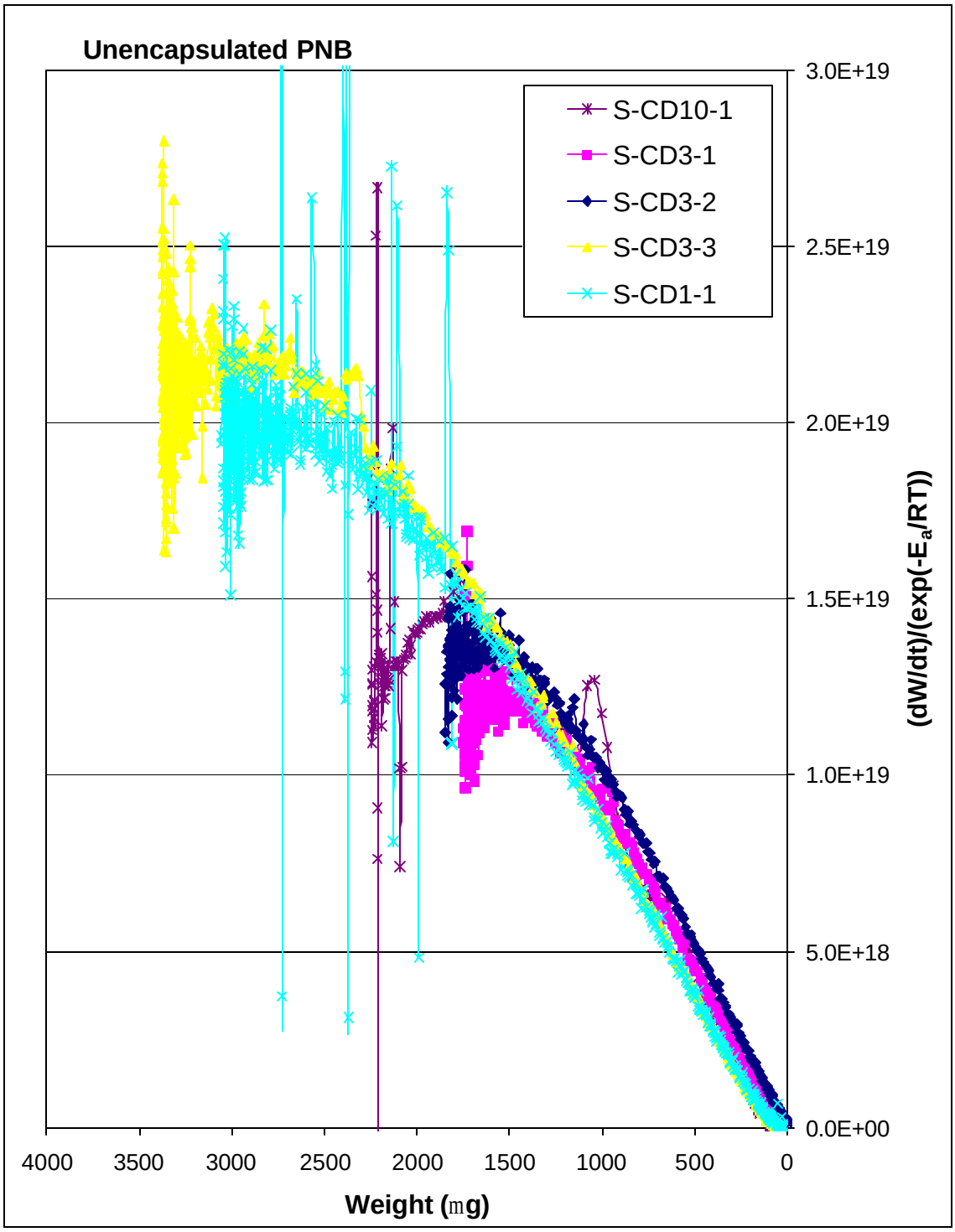

Figure A.35: *d*W/*d*t corrected for temperature as a function of W for the decomposition of unencapsulated PNB in a nitrogen atmosphere at heating rates of 1, 3, and 10°C/min.

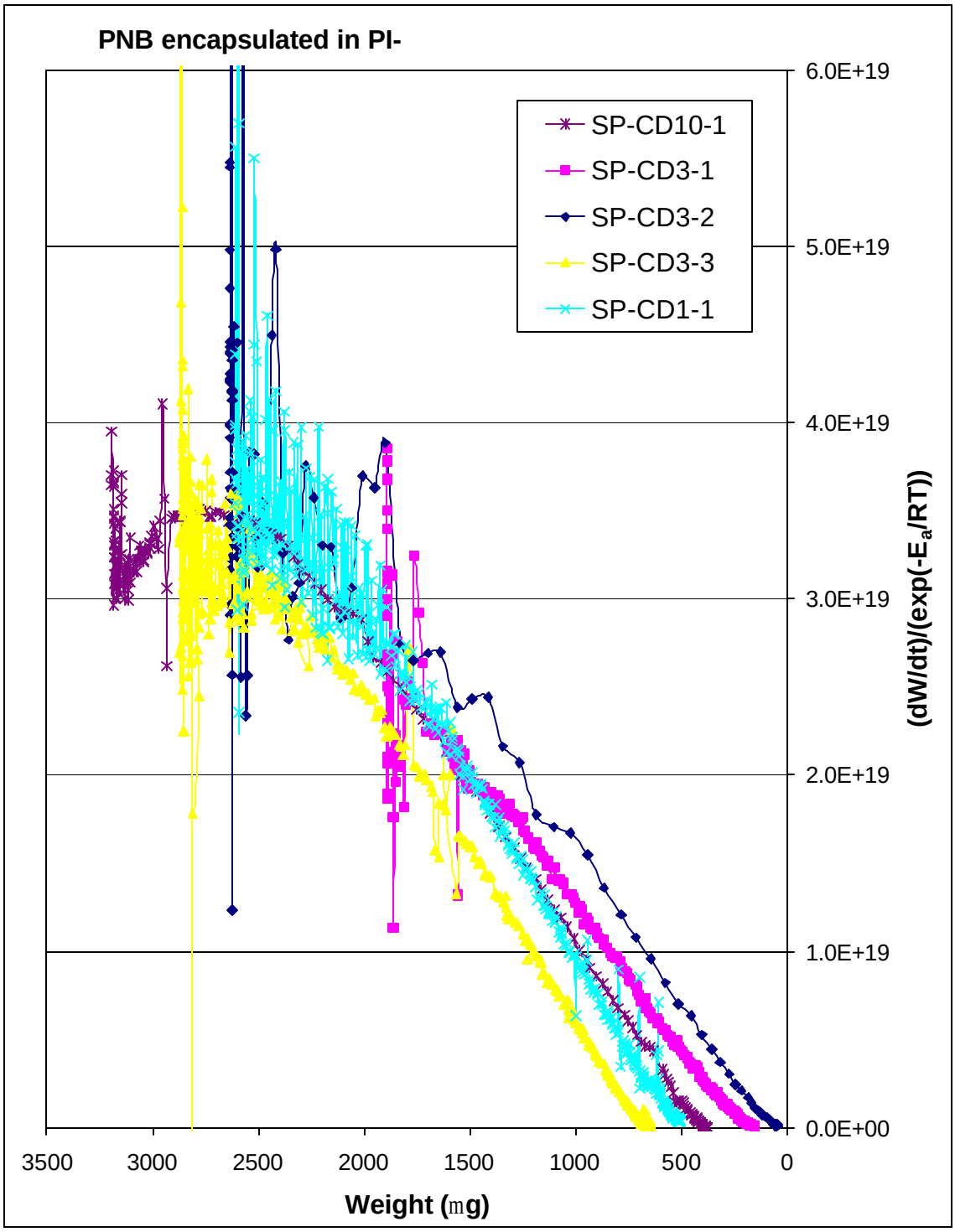

Figure A.36: *d*W/*d*t corrected for temperature as a function of W for the decomposition of PNB encapsulated by PI-2611 and decomposed in a nitrogen atmosphere at heating rates of 1, 3, and 10°C/min.

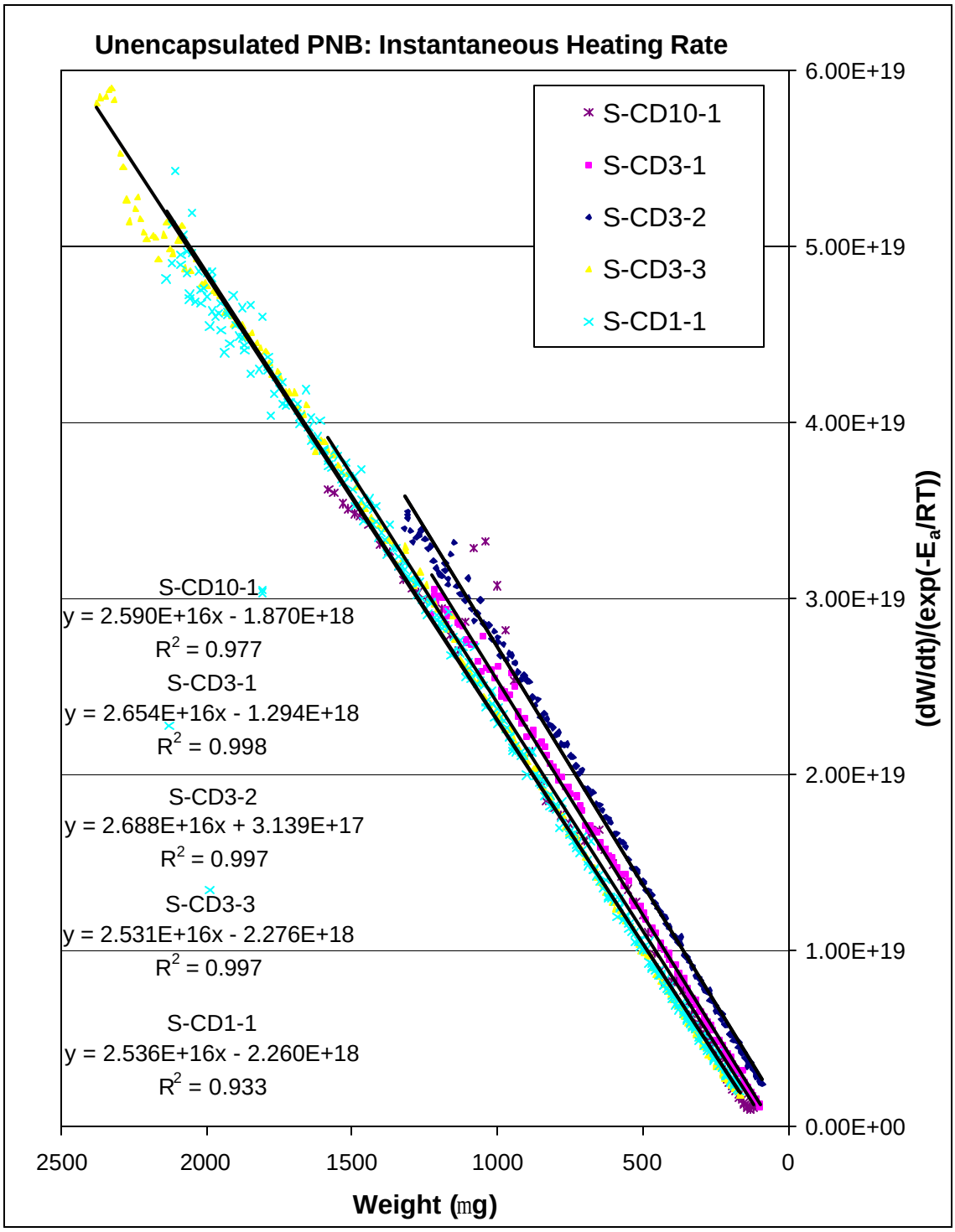

Figure A.37: The determination of RF for the constant heating rate decomposition of unencapsulated PNB in nitrogen using instantaneous heating rate values.

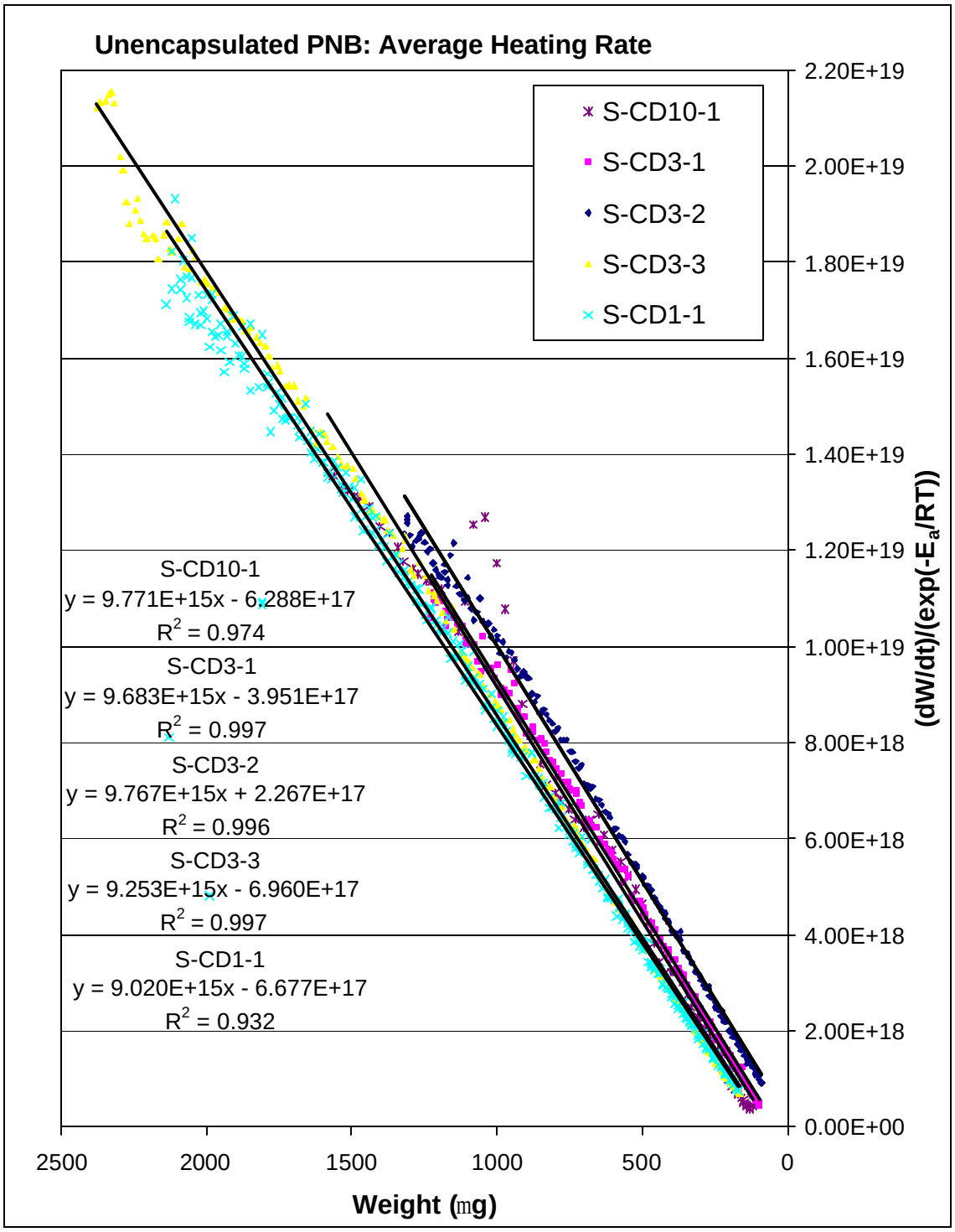

Figure A.38: The determination of RF for the constant heating rate decomposition of PNB encapsulated by PI-2611 using overall average heating rate values.

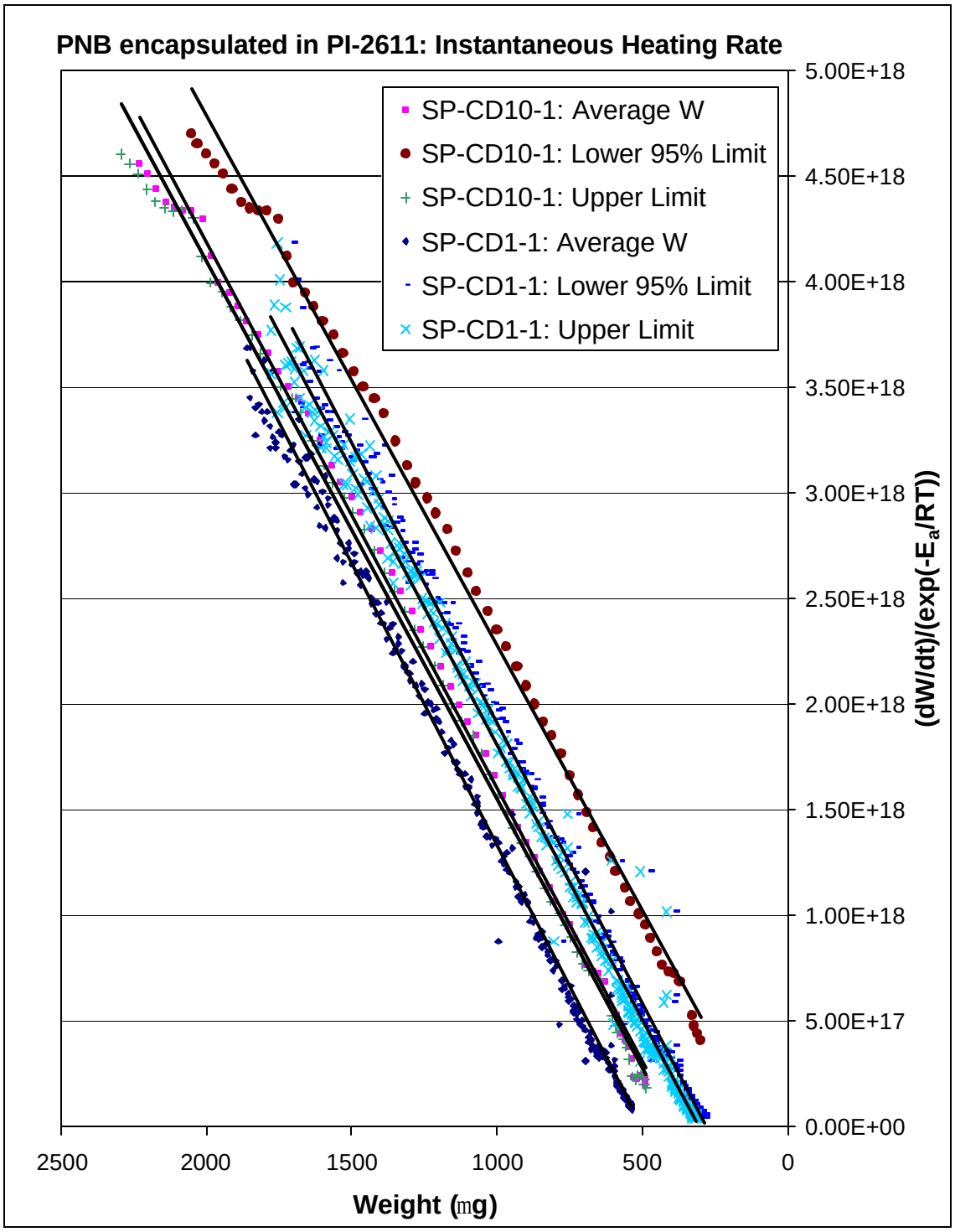

Figure A.39: The determination of RF for the constant heating rate decomposition at 1 and 10°C/min of PNB encapsulated by PI-2611 using instantaneous heating rate values.

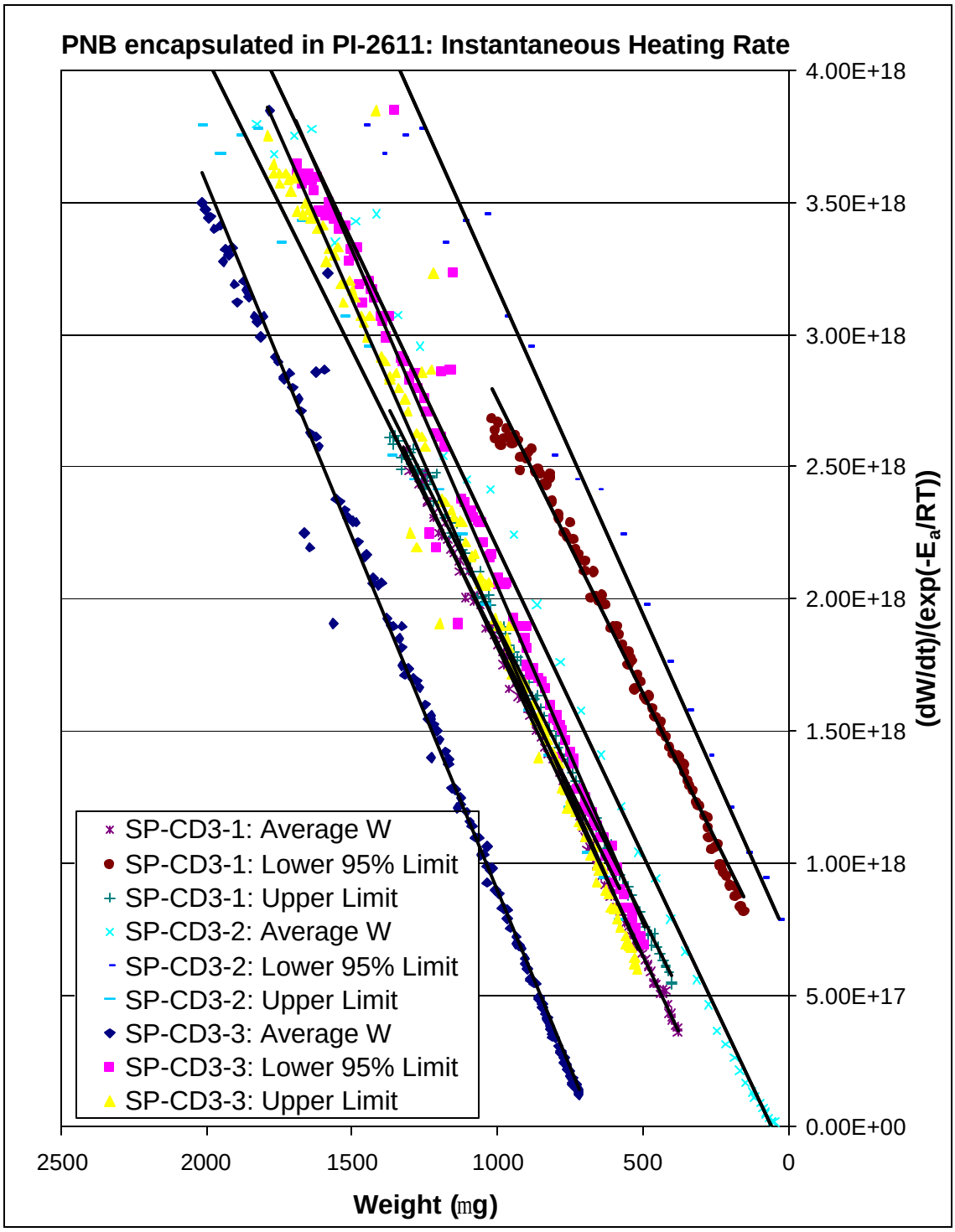

Figure A.40: The determination of RF for the constant heating rate decomposition at 3°C/min of PNB encapsulated by PI-2611 using instantaneous heating rate values.

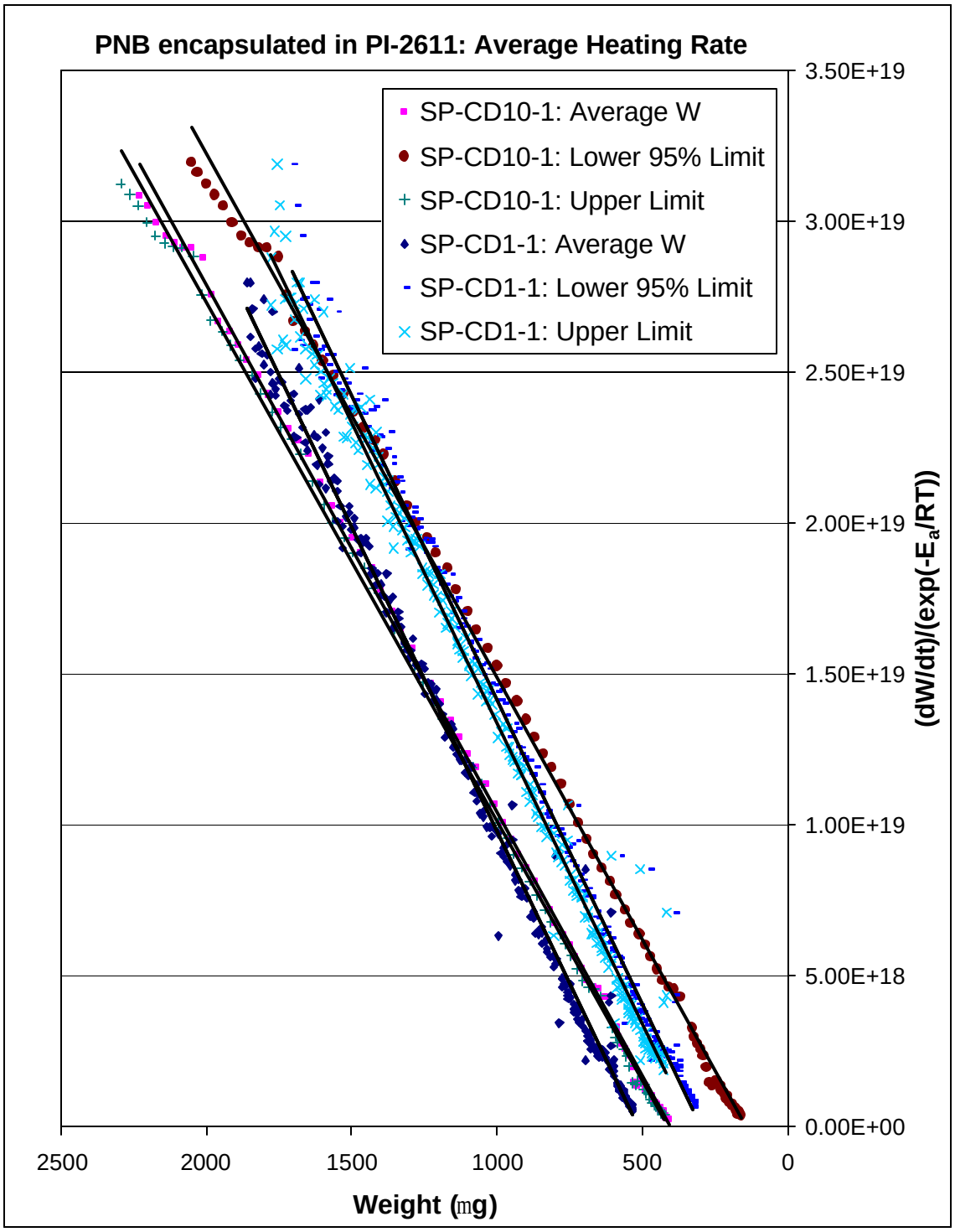

Figure A.41: The determination of RF for the constant heating rate decomposition at 1 and 10^{o}C/min of PNB encapsulated by PI-2611 using overall average heating rate values.

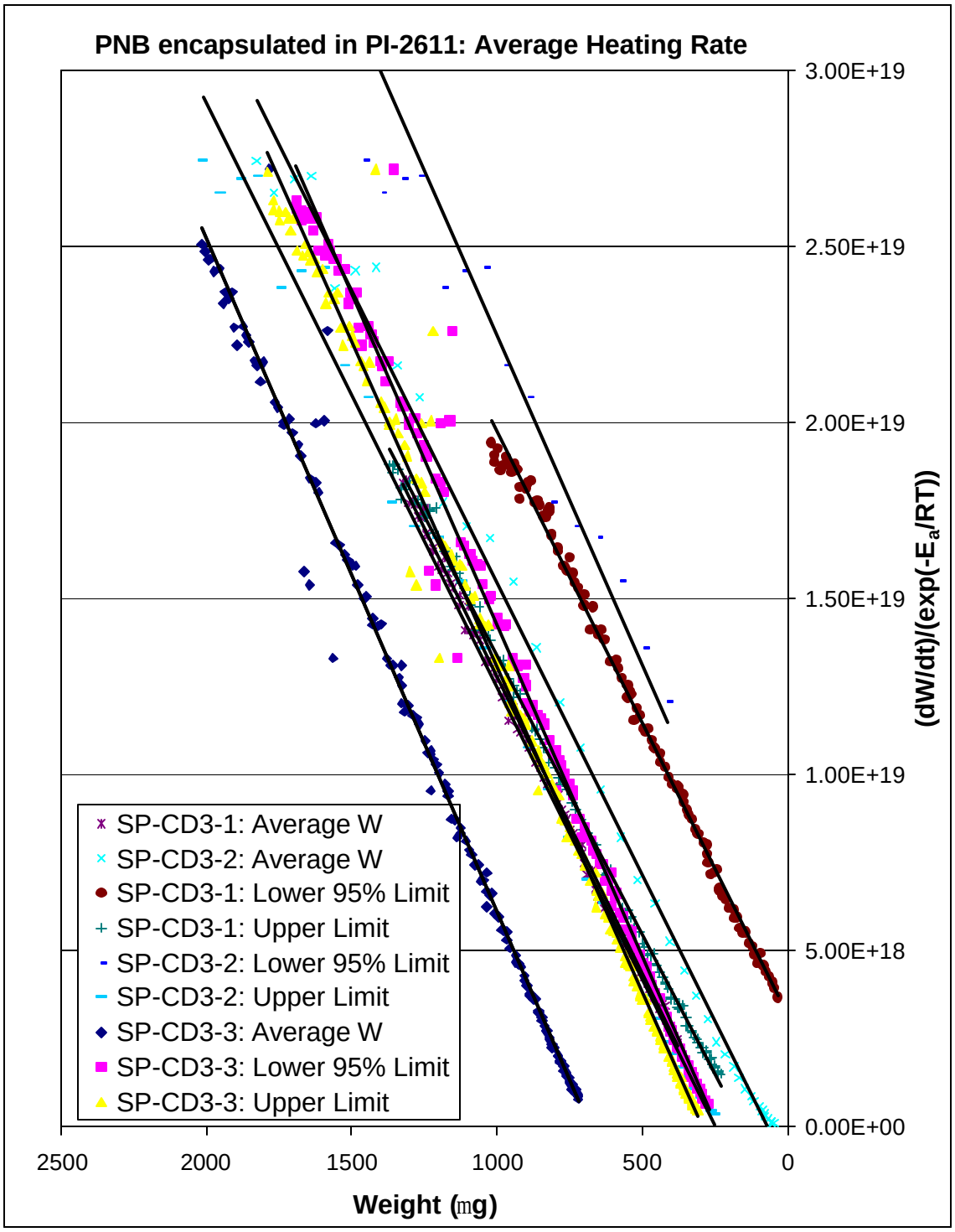

Figure A.42: The determination of RF for the constant heating rate decomposition at 3°C/min of PNB encapsulated by PI-2611 using overall average heating rate values.

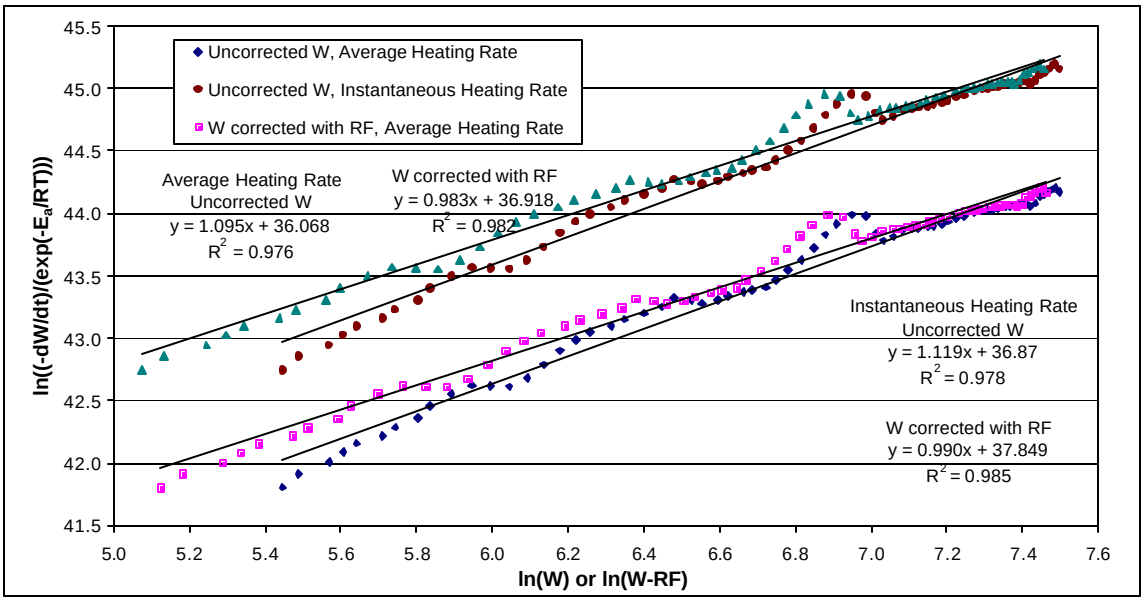

Figure A.43: The determination of n and A from sample S-CD10-1, dynamic TGA of unencapsulated PNB at a constant heating rate of 10°C/min in nitrogen.

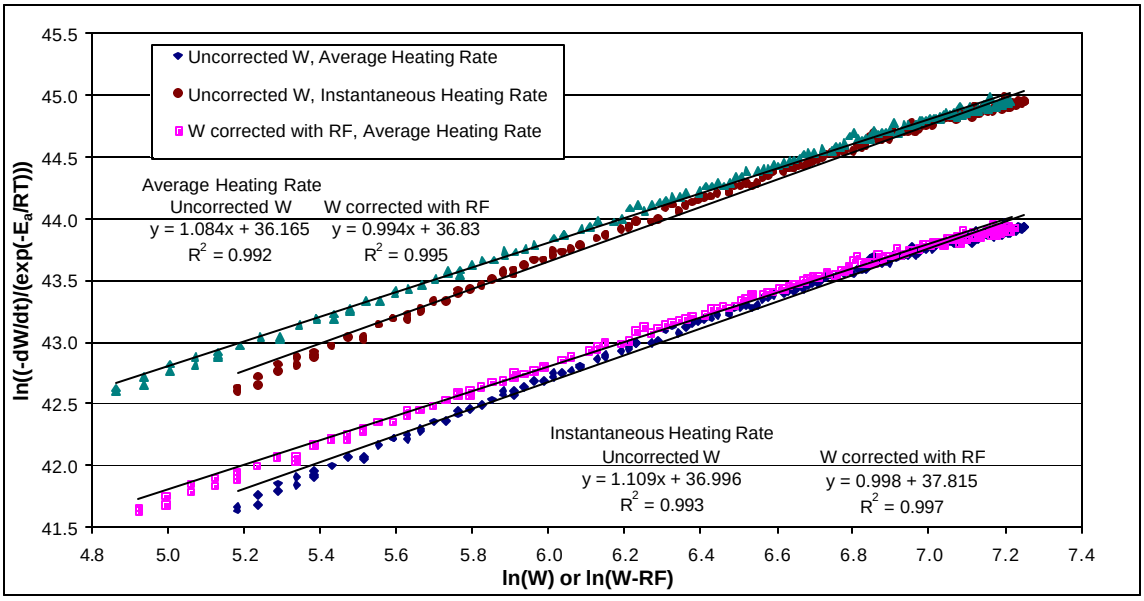

Figure A.44: The determination of n and A from sample S-CD3-1, dynamic TGA of unencapsulated PNB at a constant heating rate of 3°C/min in nitrogen.

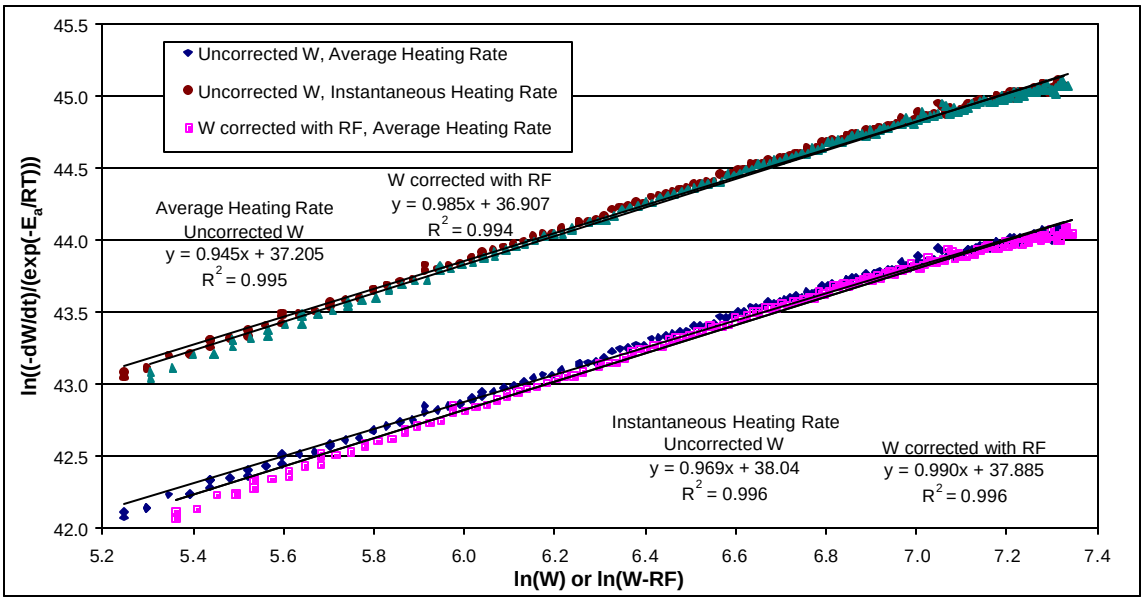

Figure A.45: The determination of n and A from sample S-CD3-2, dynamic TGA of unencapsulated PNB at a constant heating rate of 3°C/min in nitrogen.

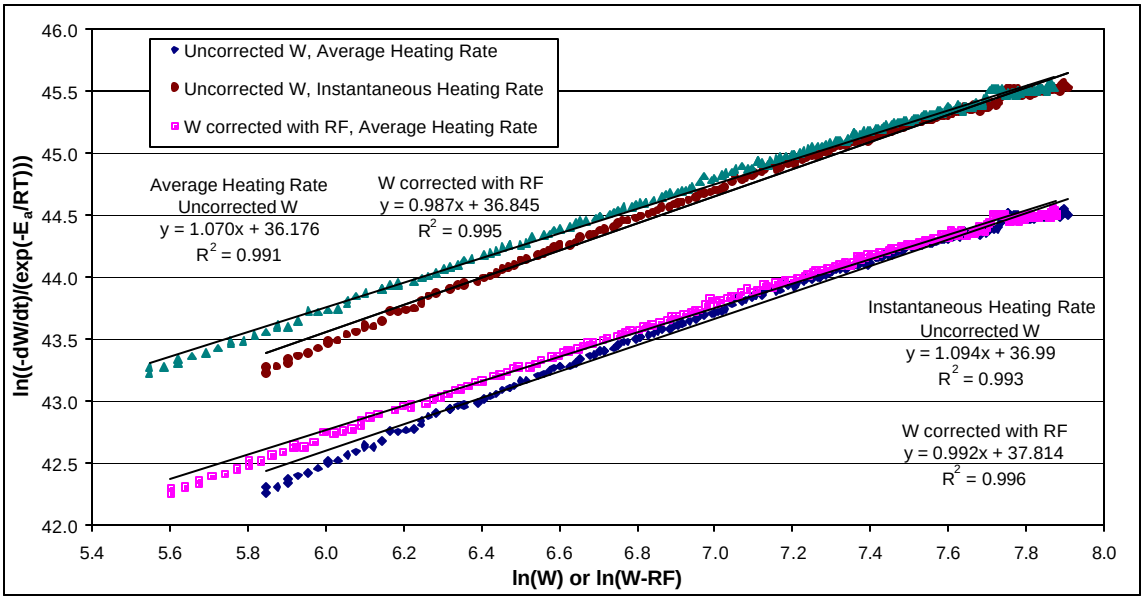

Figure A.46: The determination of n and A from sample S-CD3-3, dynamic TGA of unencapsulated PNB at a constant heating rate of 3°C/min in nitrogen.

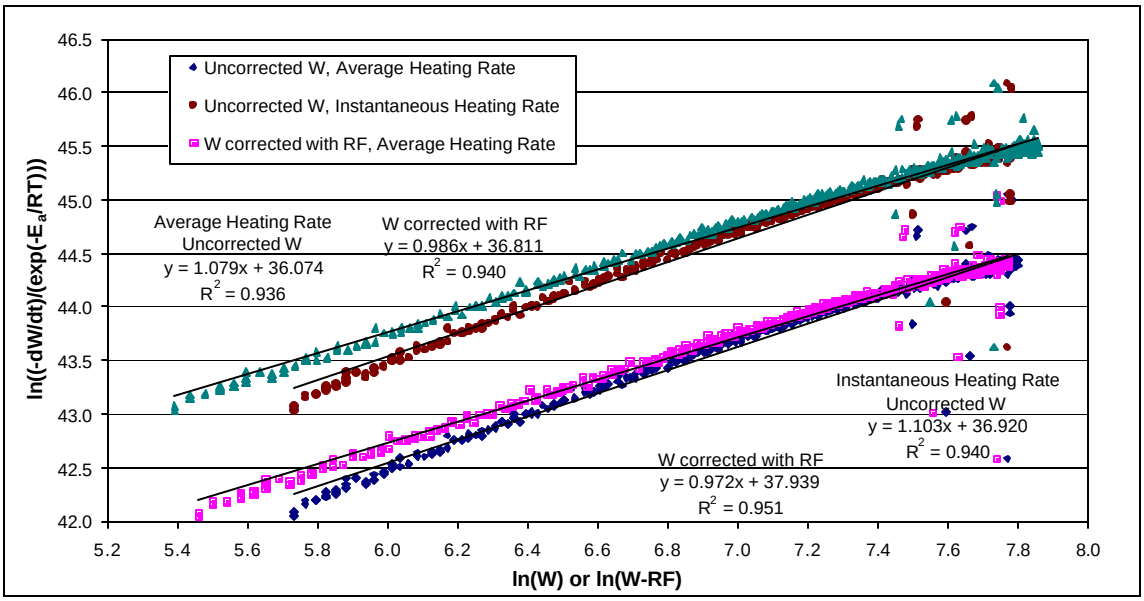

Figure A.47: The determination of n and A from sample S-CD1-1, dynamic TGA of unencapsulated PNB at a constant heating rate of 1°C/min in nitrogen.

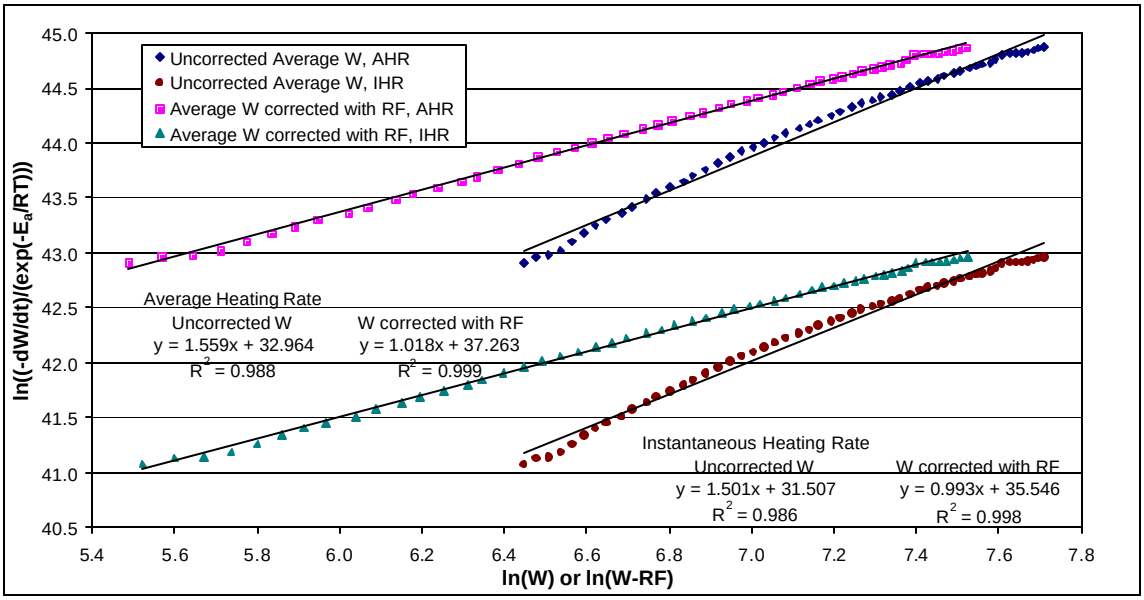

Figure A.48: The determination of n and *k* from the average PNB weight of sample SP-CD10-1, dynamic TGA of PNB encapsulated by PI-2611 at a constant heating rate of 10°C/min in nitrogen.

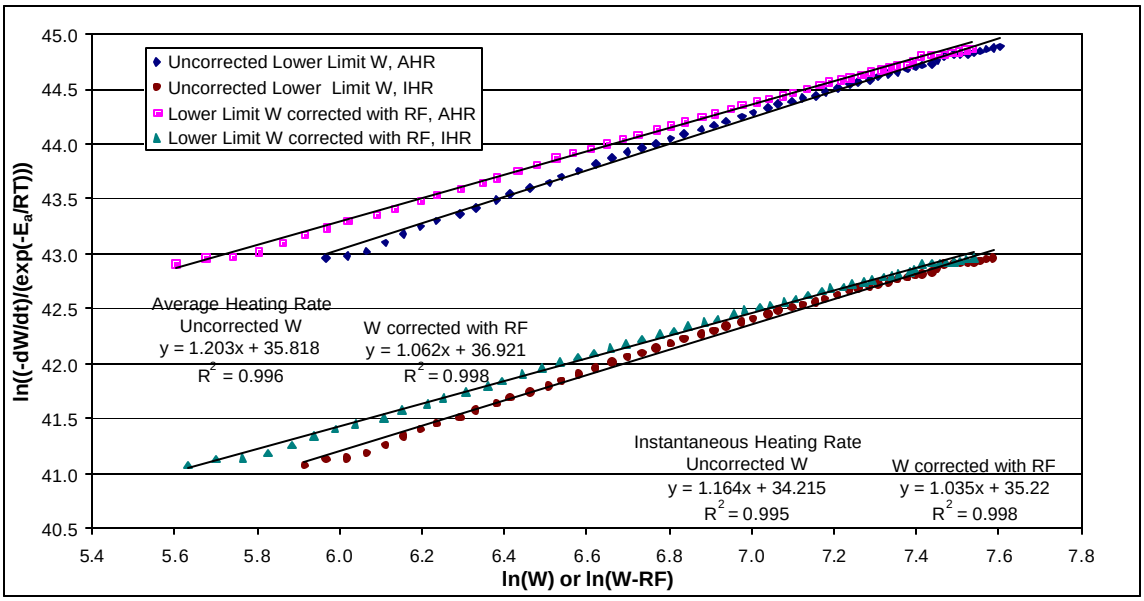

Figure A.49: The determination of n and *k* from the lower limit on PNB weight of sample SP-CD10-1, dynamic TGA of PNB encapsulated in PI-2611 at a constant heating rate of 10°C/min in nitrogen.

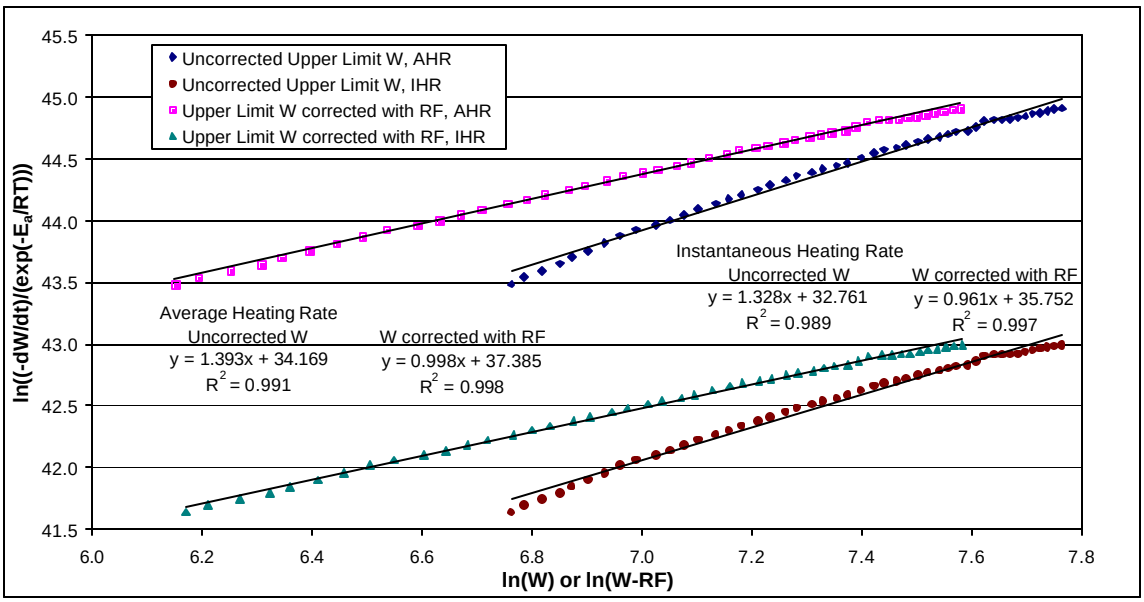

Figure A.50: The determination of n and *k* from the upper limit on PNB weight of sample SP-CD10-1, dynamic TGA of PNB encapsulated by PI-2611 at a constant heating rate of 10°C/min in nitrogen.

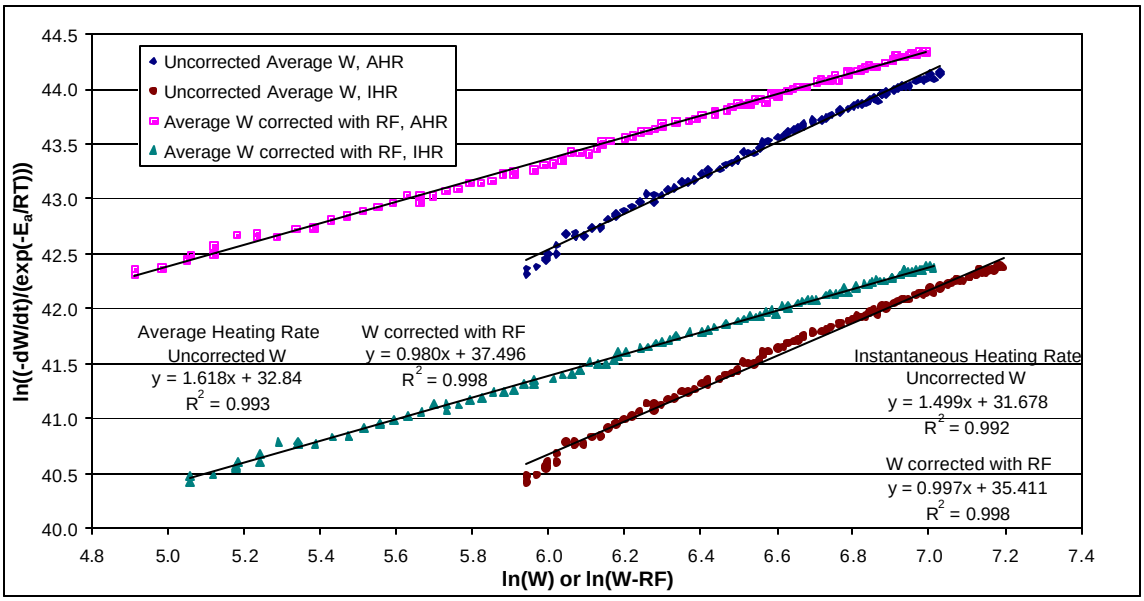

Figure A.51: The determination of n and *k* from the average PNB weight of sample SP-CD3-1, dynamic TGA of PNB encapsulated by PI-2611 at a constant heating rate of 3°C/min in nitrogen.

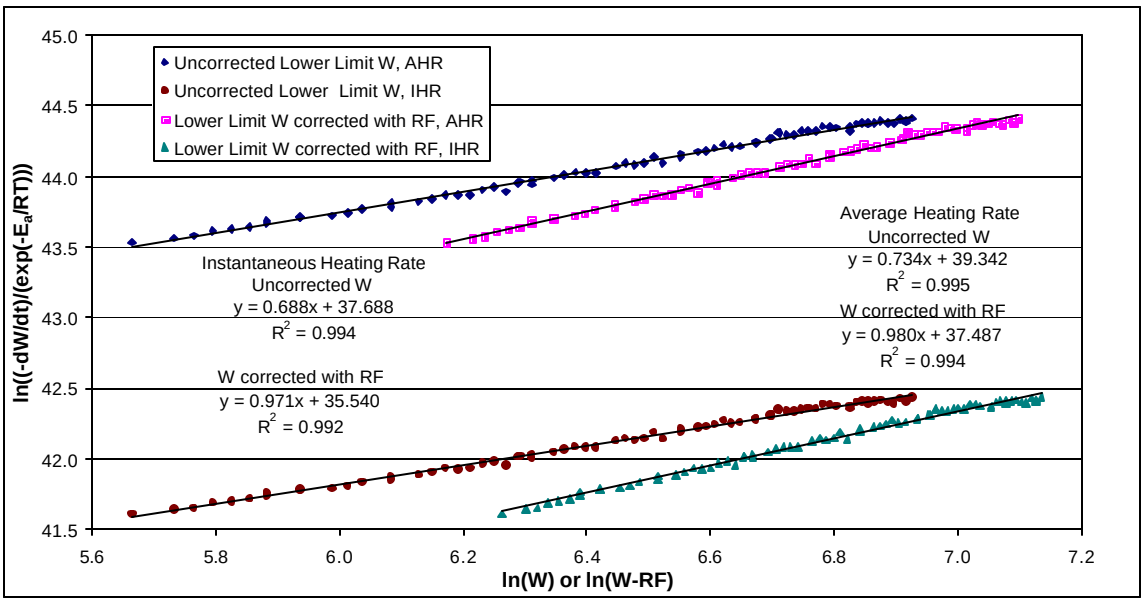

Figure A.52: The determination of n and *k* from the lower limit on PNB weight of sample SP-CD3-1, dynamic TGA of PNB encapsulated by PI-2611 at a constant heating rate of 3°C/min in nitrogen.

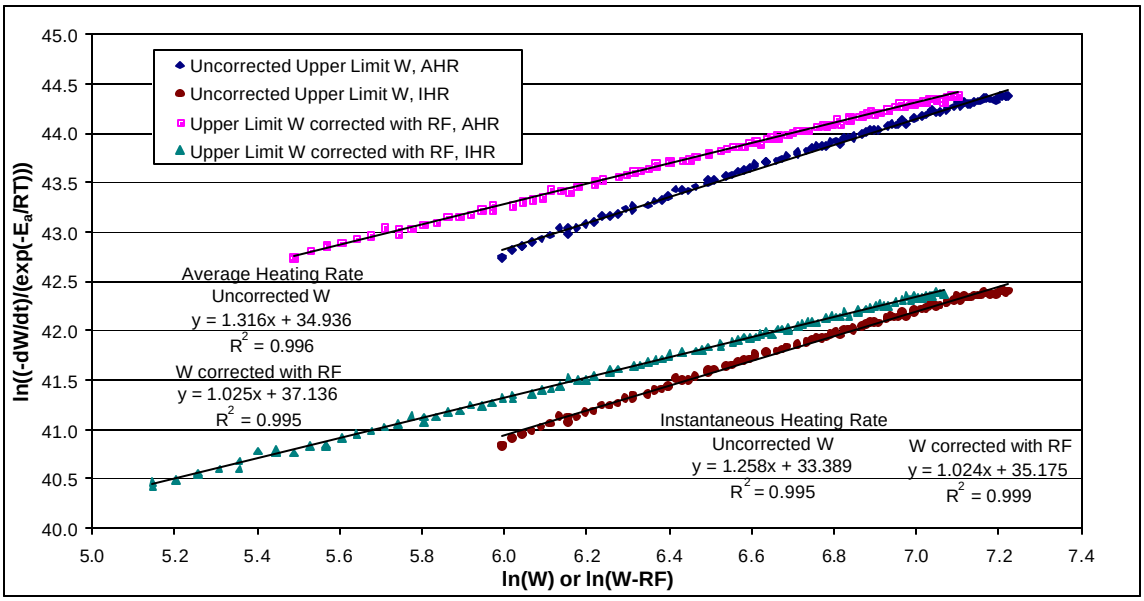

Figure A.53: The determination of n and *k* from the upper limit on PNB weight of sample SP-CD3-1, dynamic TGA of PNB encapsulated by PI-2611 at a constant heating rate of 3°C/min in nitrogen.

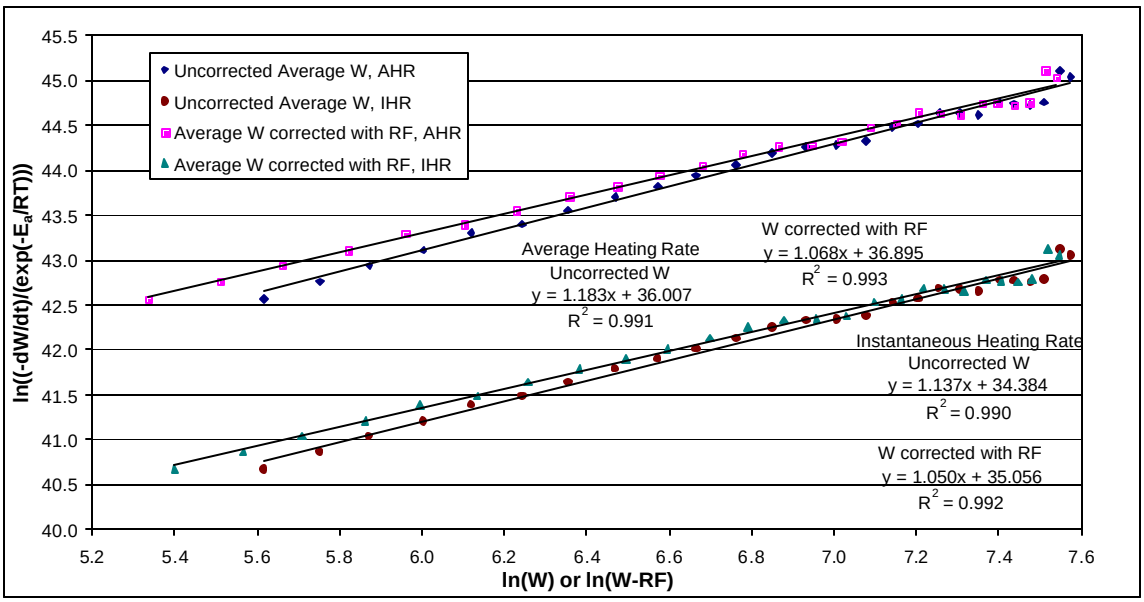

Figure A.54: The determination of n and *k* from the average PNB weight of sample SP-CD3-2, dynamic TGA of PNB encapsulated by PI-2611 at a constant heating rate of 3°C/min in nitrogen.

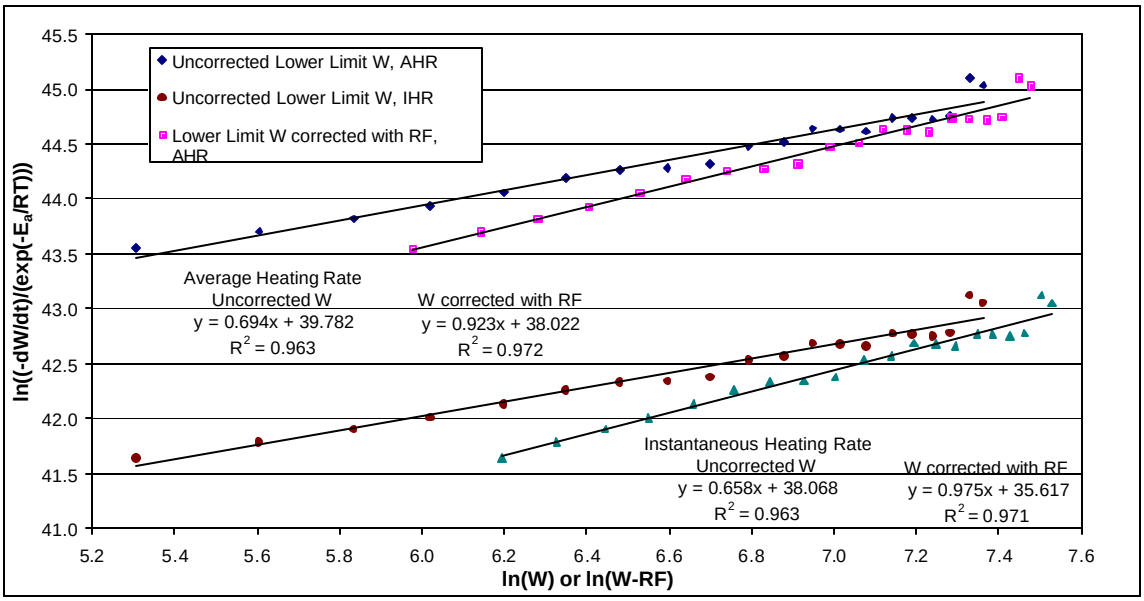

Figure A.55: The determination of n and *k* from the lower limit on PNB weight of sample SP-CD3-2, dynamic TGA of PNB encapsulated by PI-2611 at a constant heating rate of 3°C/min in nitrogen.

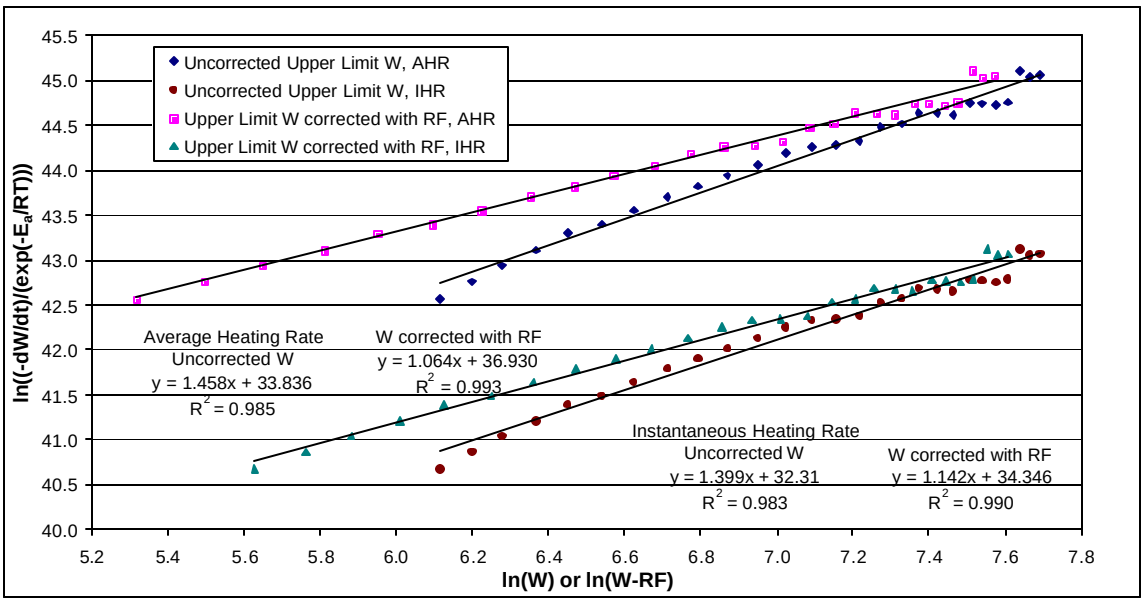

Figure A.56: The determination of n and *k* from the upper limit on PNB weight of sample SP-CD3-2, dynamic TGA of PNB encapsulated PI-2611 at a constant heating rate of 3°C/min in nitrogen.

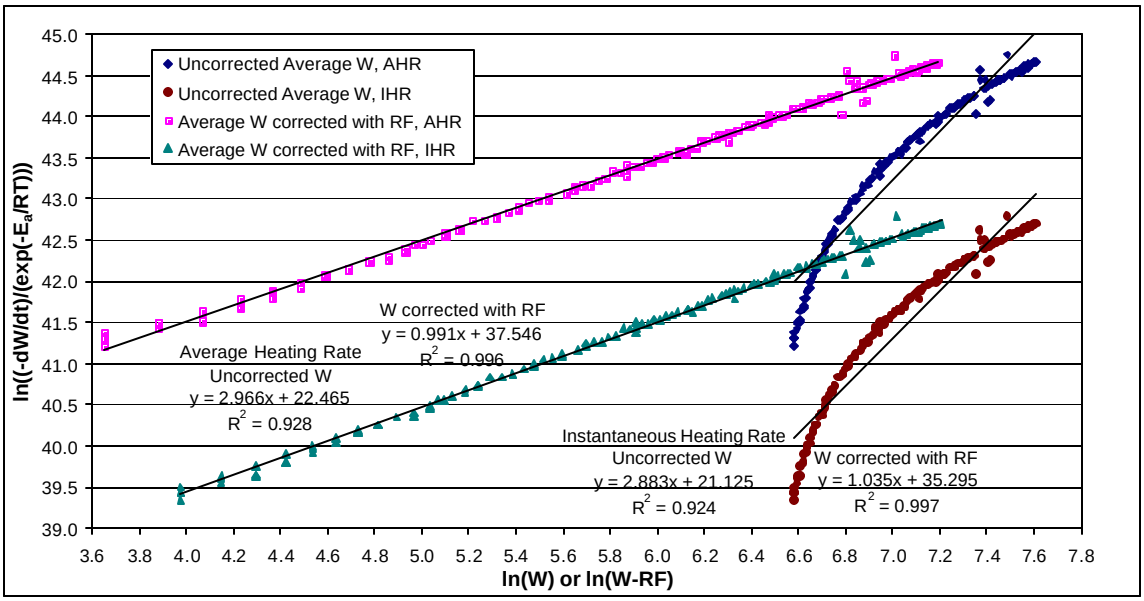

Figure A.57: The determination of n and *k* from the average PNB weight of sample SP-CD3-3, dynamic TGA of PNB encapsulated by PI-2611 at a constant heating rate of 3°C/min in nitrogen.

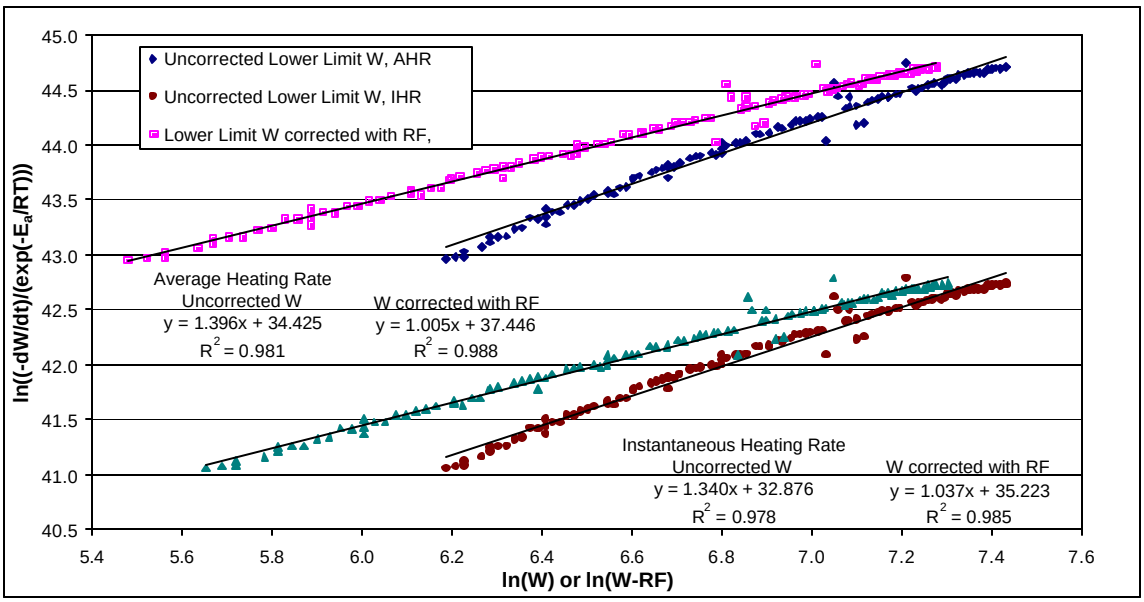

Figure A.58: The determination of n and *k* from the lower limit on PNB weight of sample SP-CD3-3, dynamic TGA of PNB encapsulated by PI-2611 at a constant heating rate of 3°C/min in nitrogen.

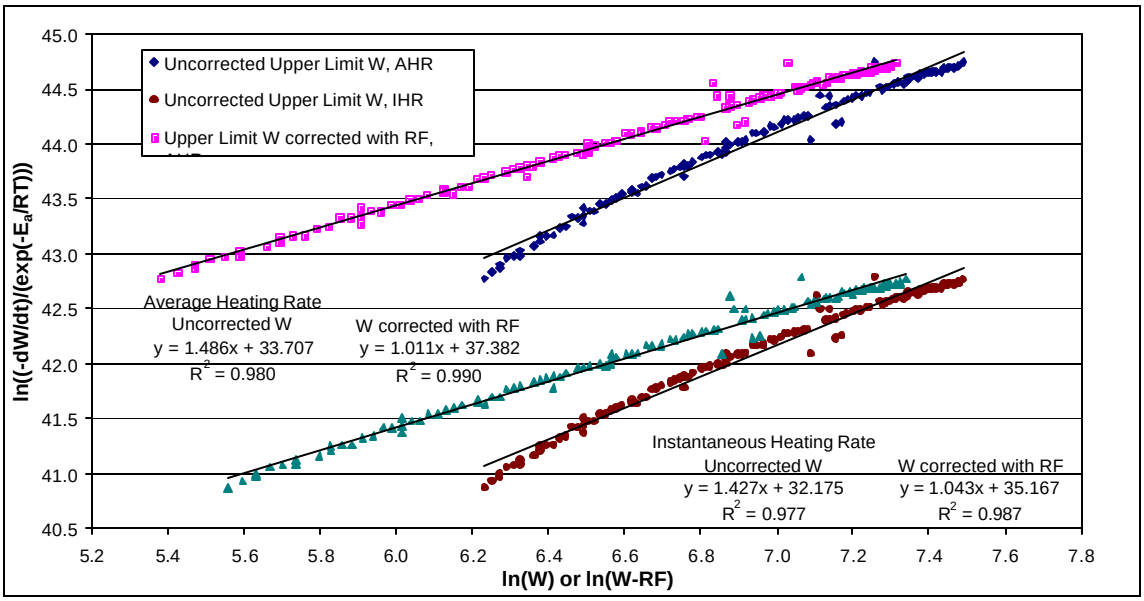

Figure A.59: The determination of n and *k* from the upper limit on PNB weight of sample SP-CD3-3, dynamic TGA of PNB encapsulated by PI-2611 at a constant heating rate of 3°C/min in nitrogen.

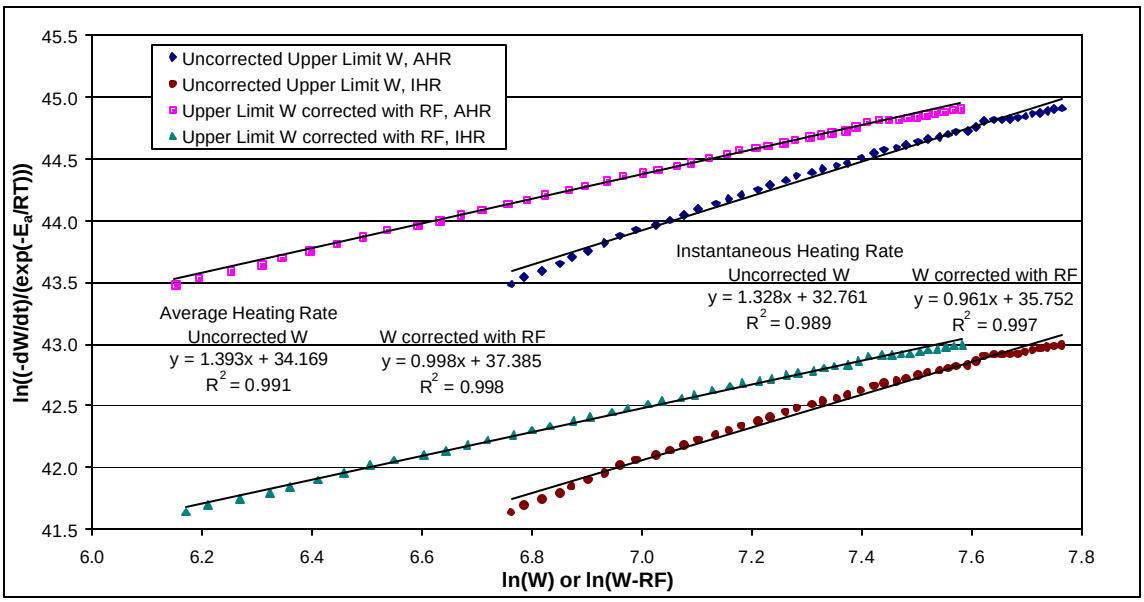

Figure A.60: The determination of n and *k* from the average PNB weight of sample SP-CD1-1, dynamic TGA of PNB encapsulated by PI-2611 at a constant heating rate of 1°C/min in nitrogen.

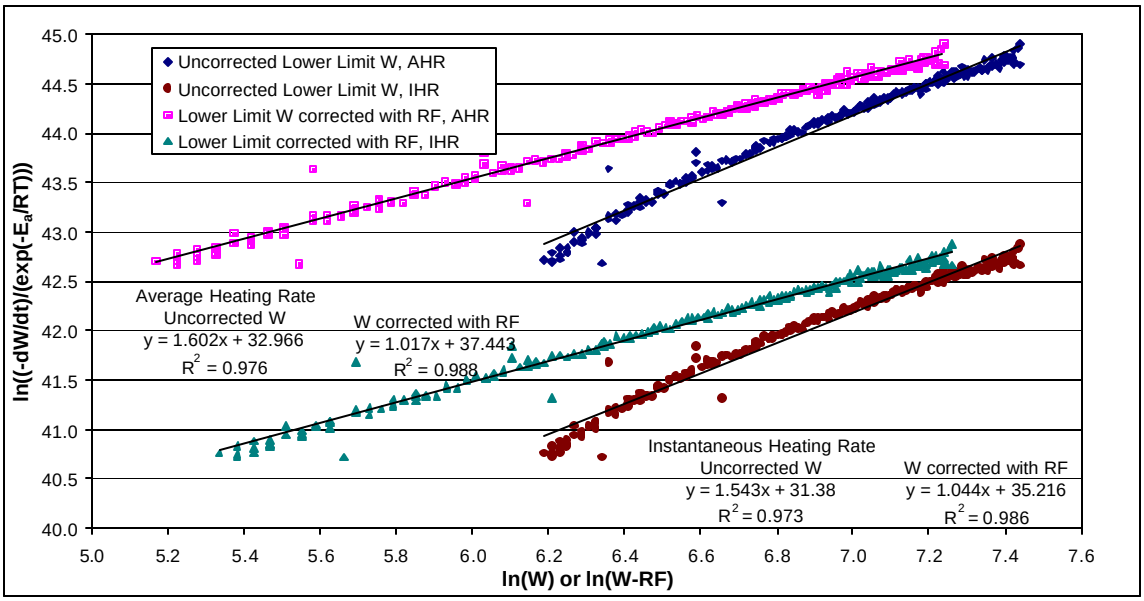

Figure A.61: The determination of n and *k* from the lower limit on PNB weight of sample SP-CD1-1, dynamic TGA of PNB encapsulated by PI-2611 at a constant heating rate of 1°C/min in nitrogen.

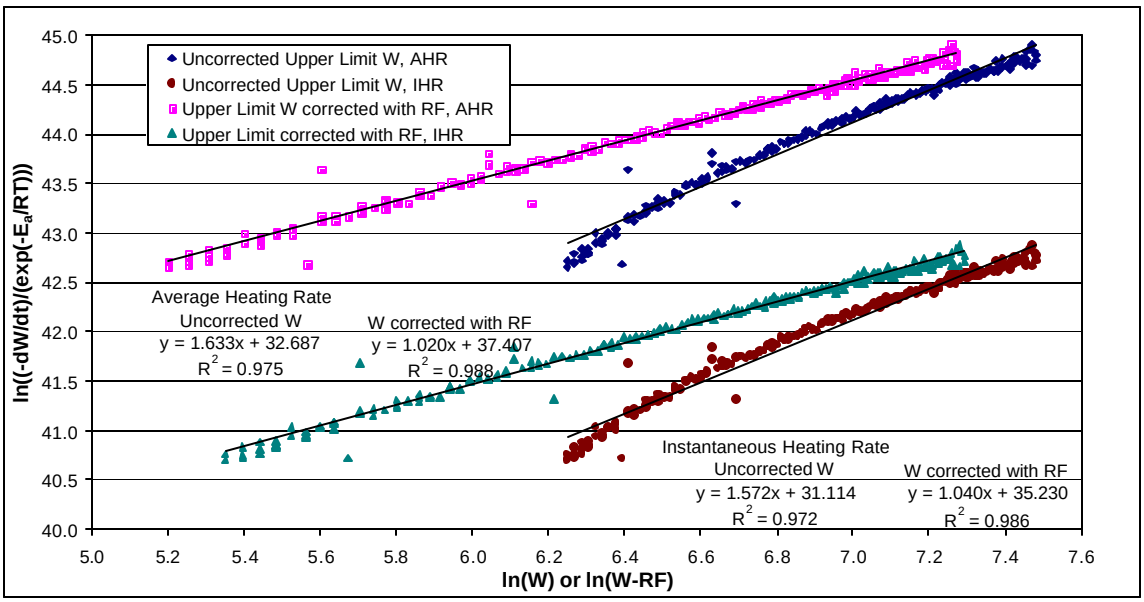

Figure A.62: The determination of n and *k* from the upper limit on PNB weight of sample SP-CD1-1, dynamic TGA of PNB encapsulated by PI-2611 at a constant heating rate of 1°C/min in nitrogen.

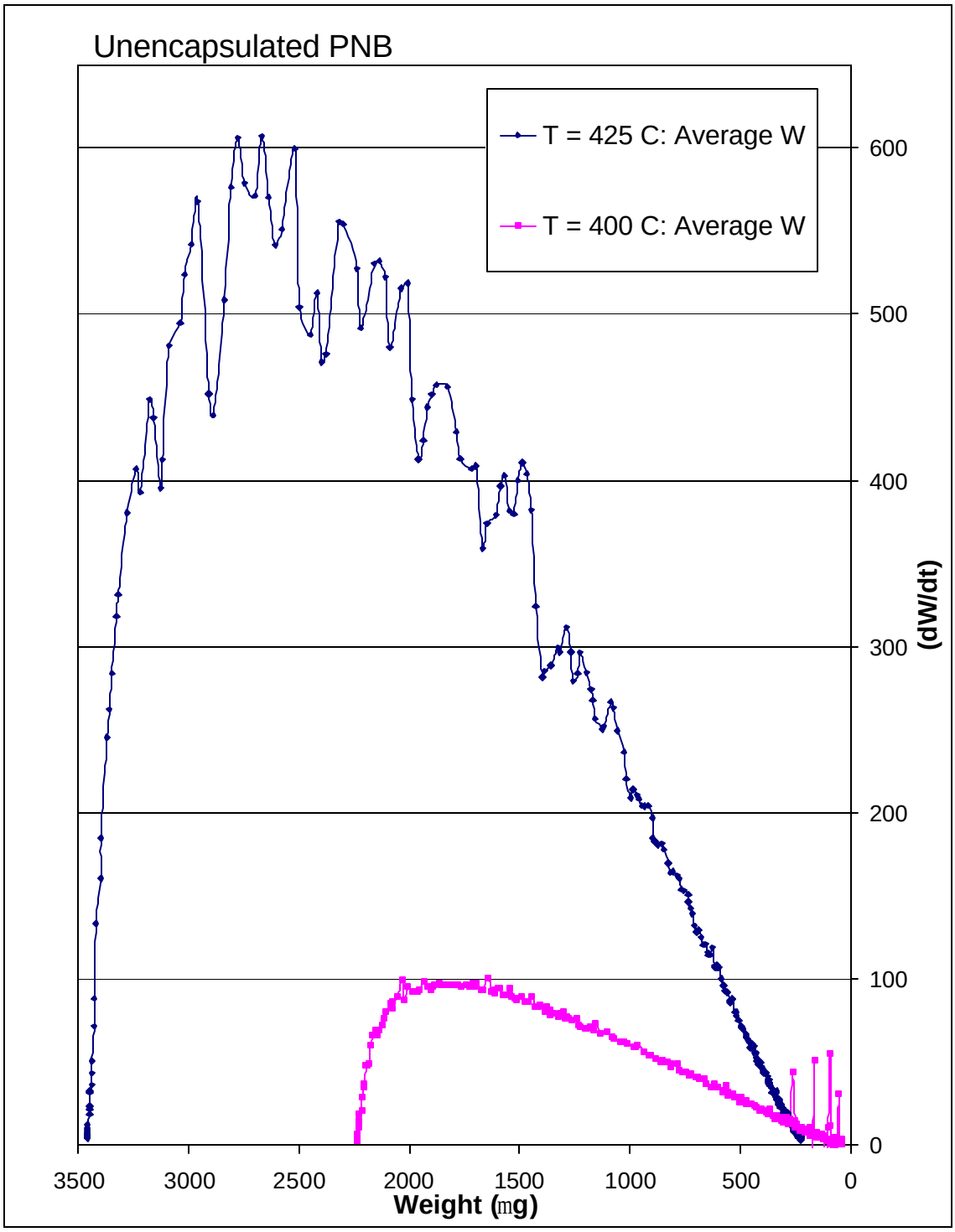

Figure A.63: *d*W/*d*t as a function of W for the decomposition of unencapsulated PNB in a nitrogen atmosphere at isothermal temperatures of 400°C and 425°C.

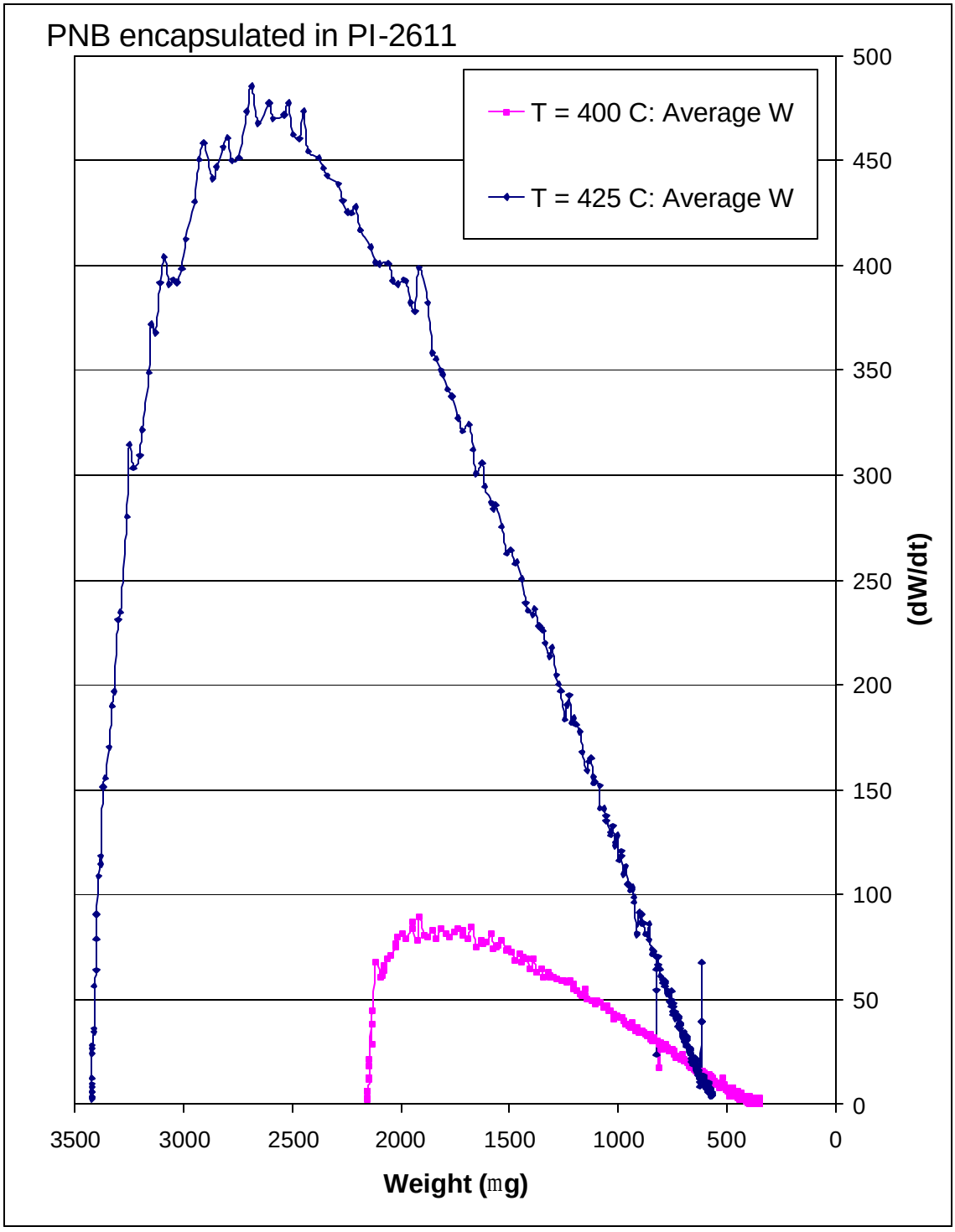

Figure A.64: dW/dt as a function of W for the decomposition of PNB encapsulated by polyimide PI-2611 at isothermal temperatures of 400°C and 425°C.

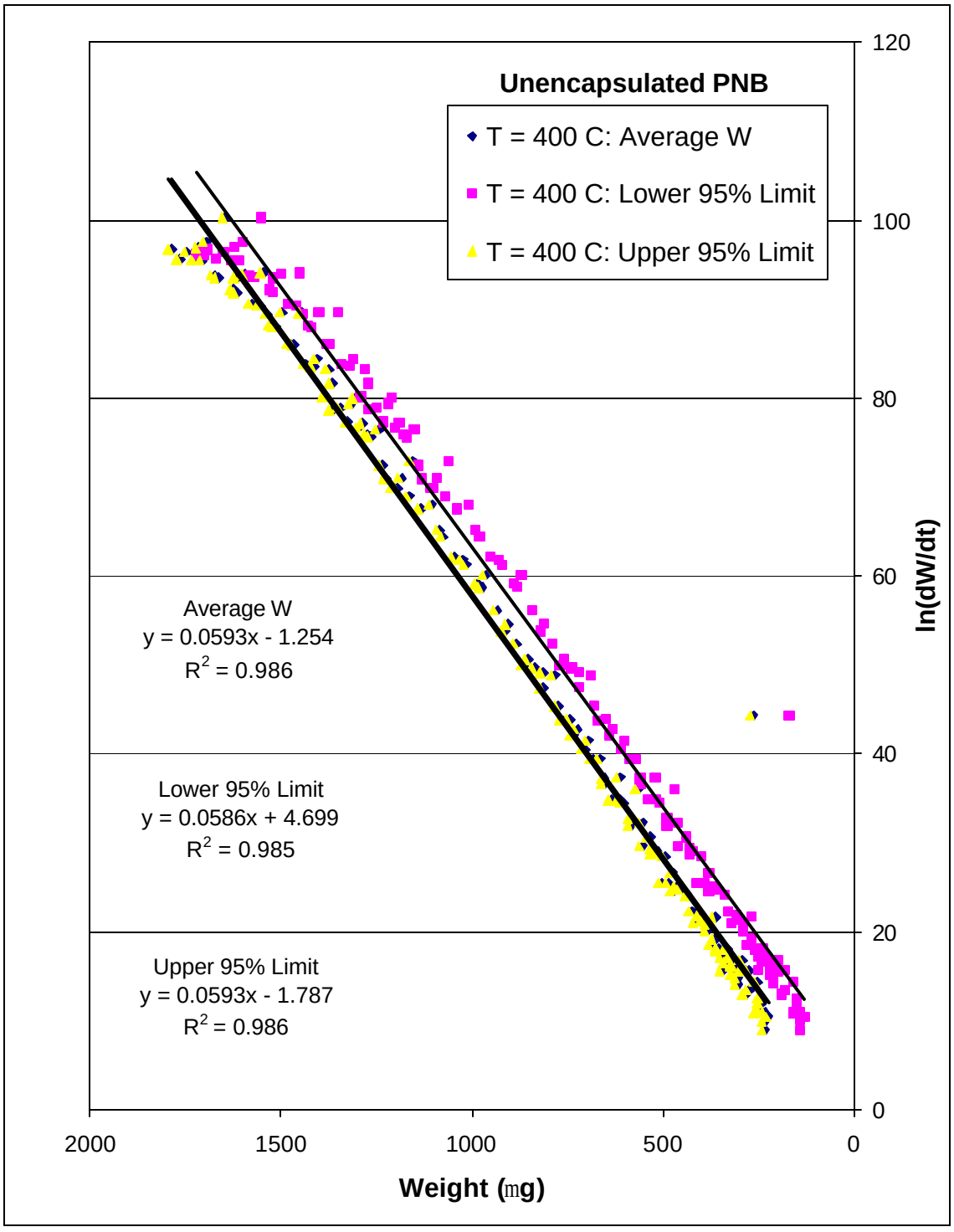

Figure A.65: The determination of RF for the decomposition of unencapsulated PNB in nitrogen at an isothermal temperature of 400°C.

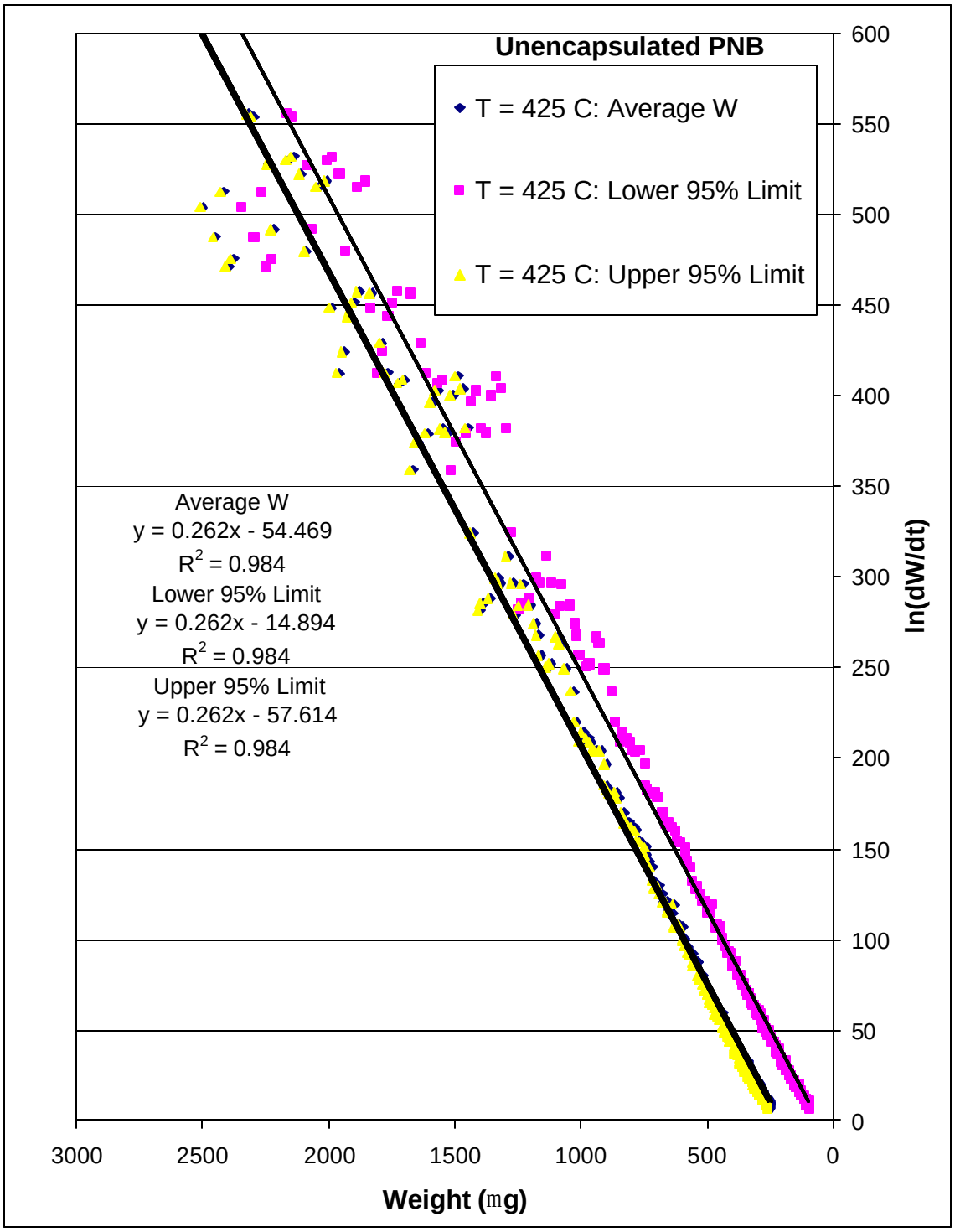

Figure A.66: The determination of RF for the decomposition of unencapsulated PNB in nitrogen at an isothermal temperature of 425°C.

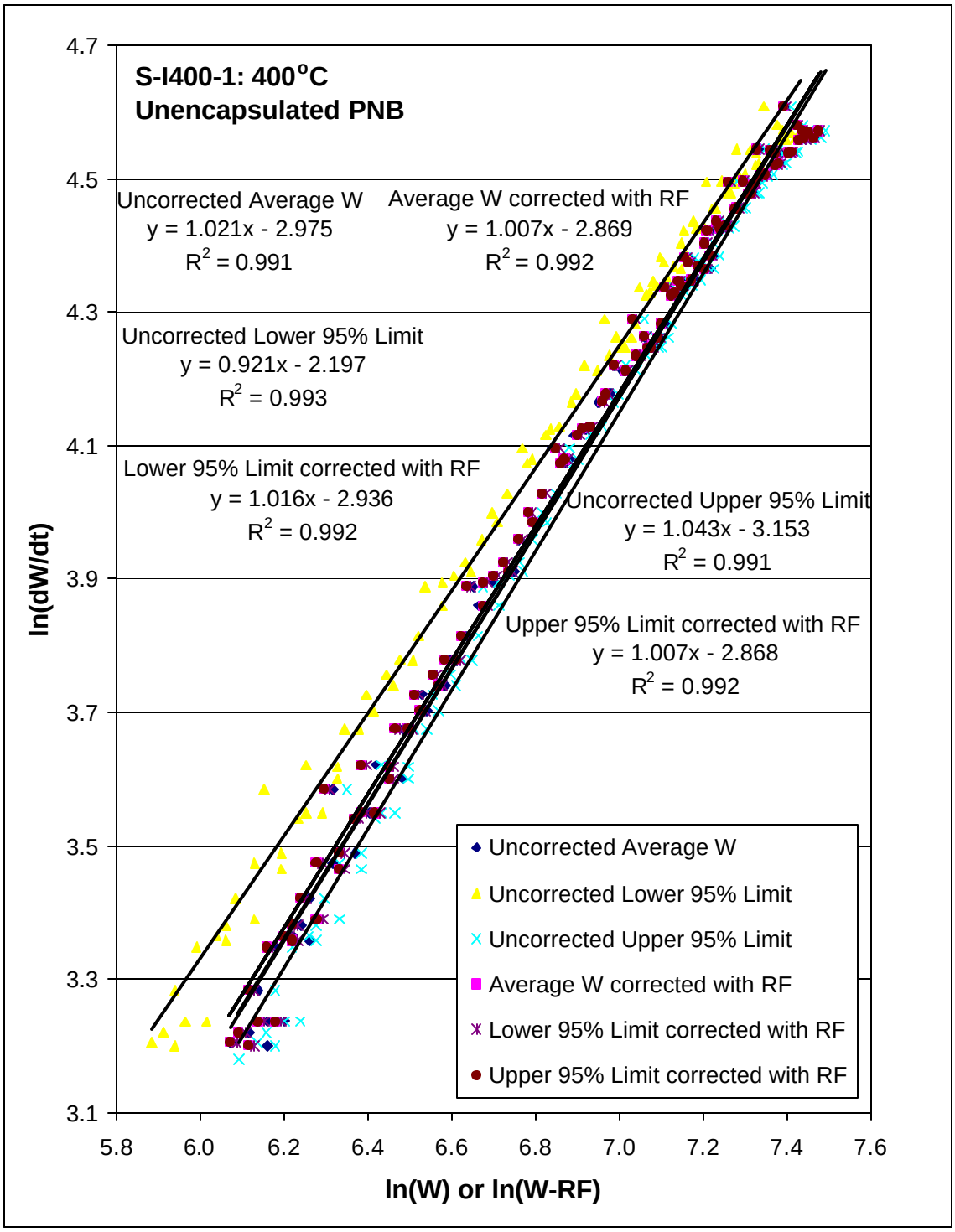

Figure A.67: Plot of ln(dW/dt) as a function of ln(W) or ln(W-RF) to determine the reaction order and reaction rate constant for the isothermal decomposition of unencapsulated PNB in nitrogen at 400°C.

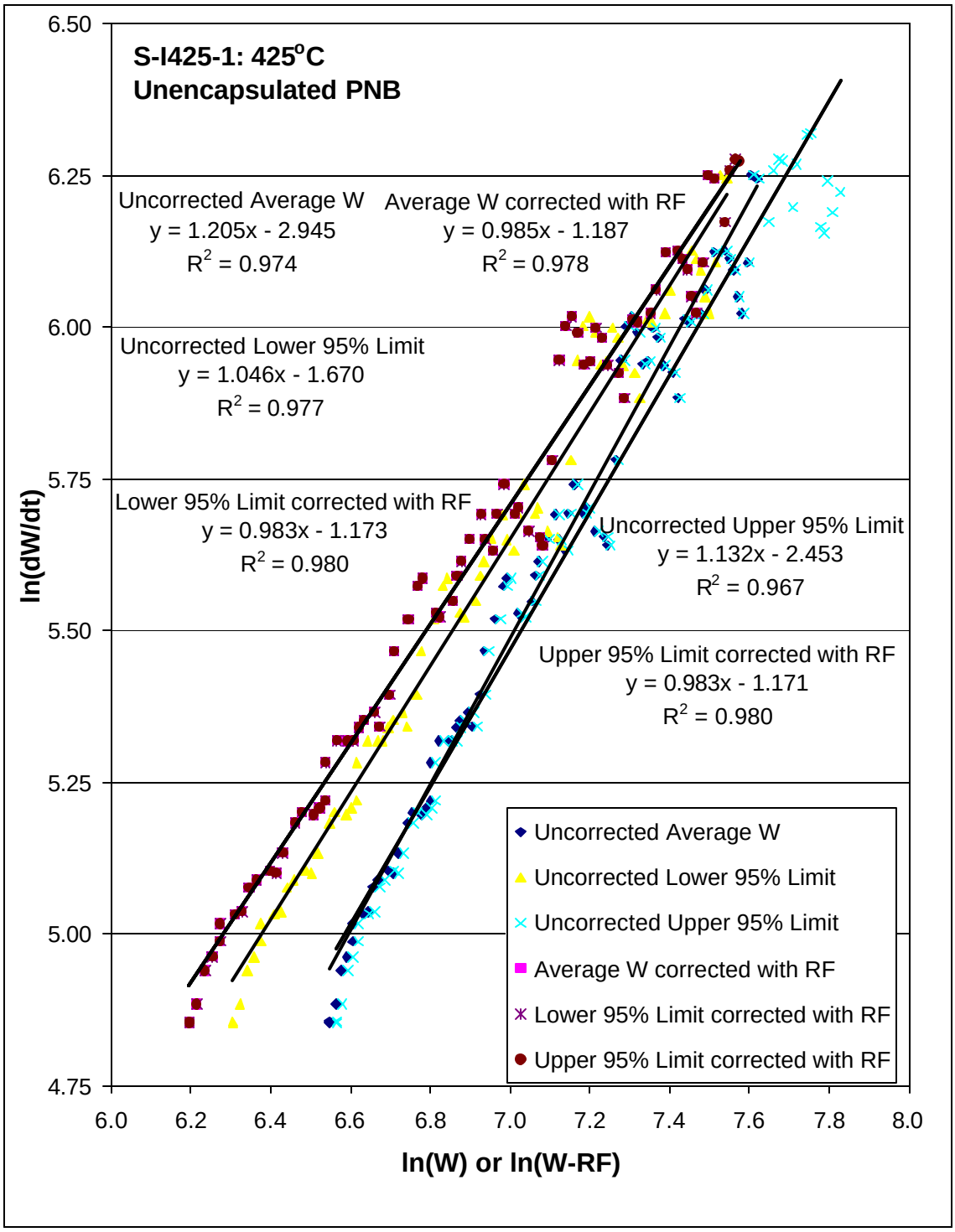

Figure A.68: Plot of ln(dW/dt) as a function of h(W) or ln(W-RF) to determine the reaction order and reaction rate constant for the isothermal decomposition of unencapsulated PNB in nitrogen at 425°C.

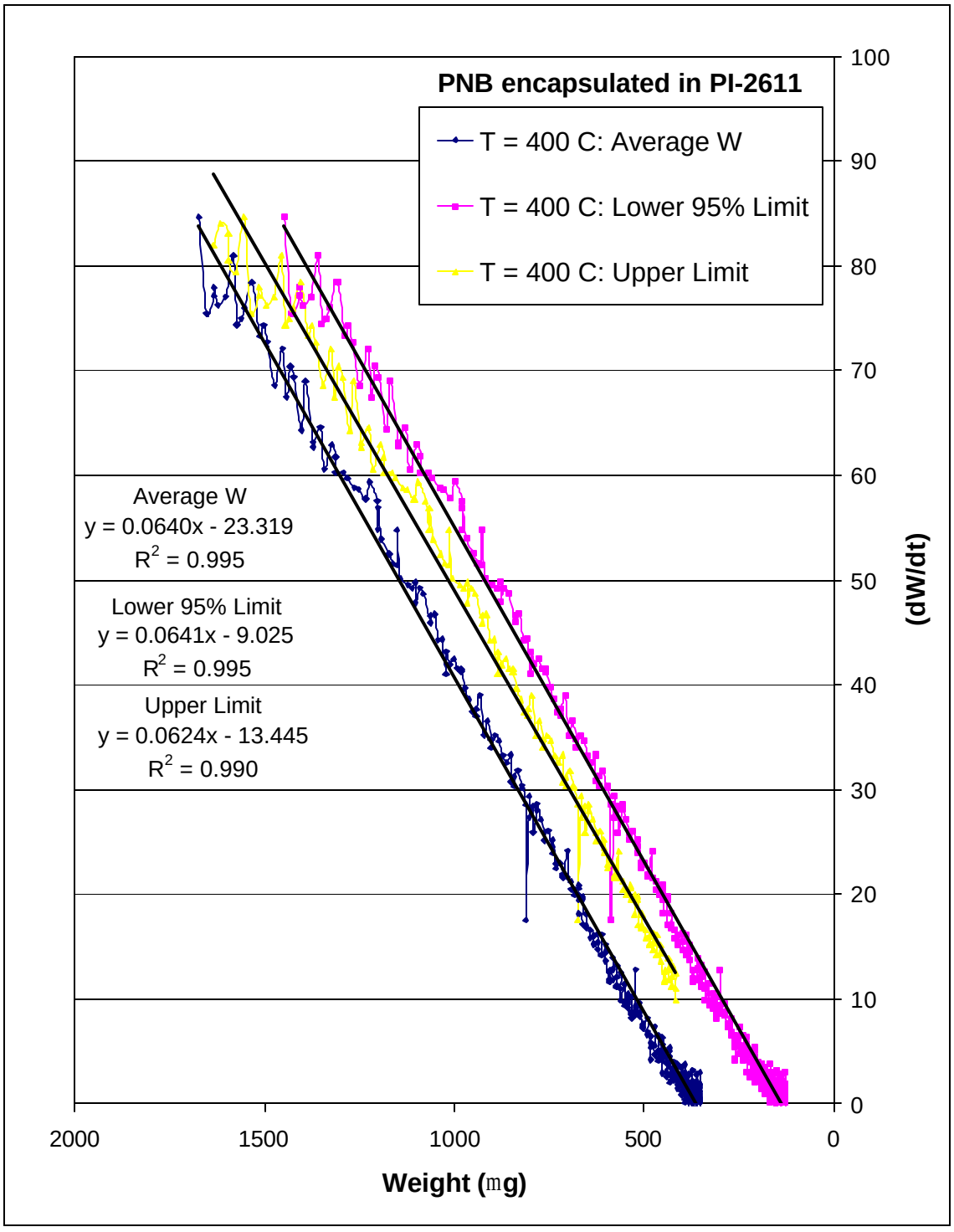

Figure A.69: The determination of RF for the decomposition of PNB encapsulated by PI-2611 in nitrogen at a constant temperature of 400^{o}C.

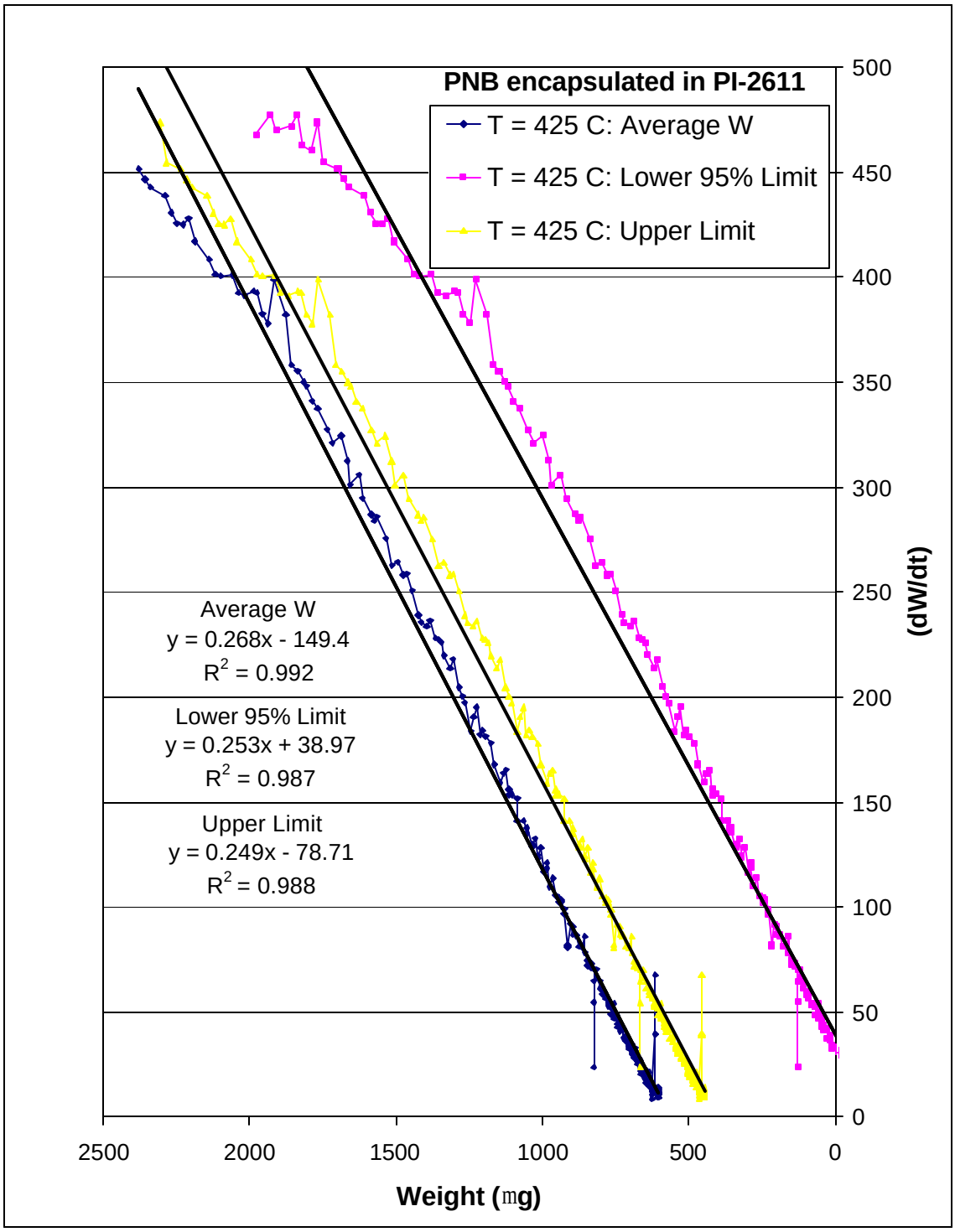

Figure A.70: The determination of RF for the decomposition of PNB encapsulated by PI-2611 in nitrogen at a constant temperature of 425°C.

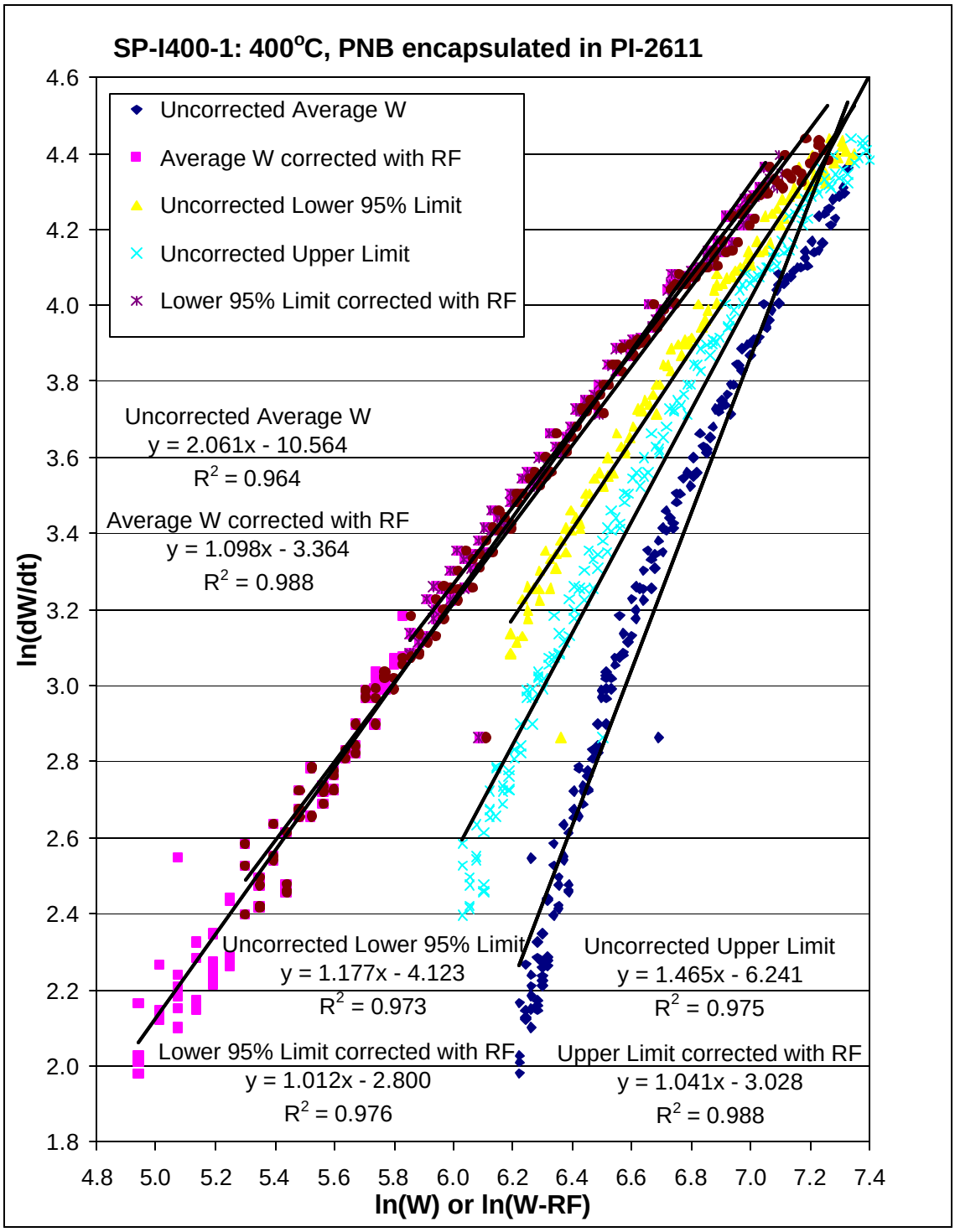

Figure A.71: Plot of ln(dW/dt) as a function of ln(W) or ln(W-RF) to determine the reaction order and reaction rate constant for the isothermal decomposition of PNB encapsulated by PI-2611 in nitrogen at 400°C.

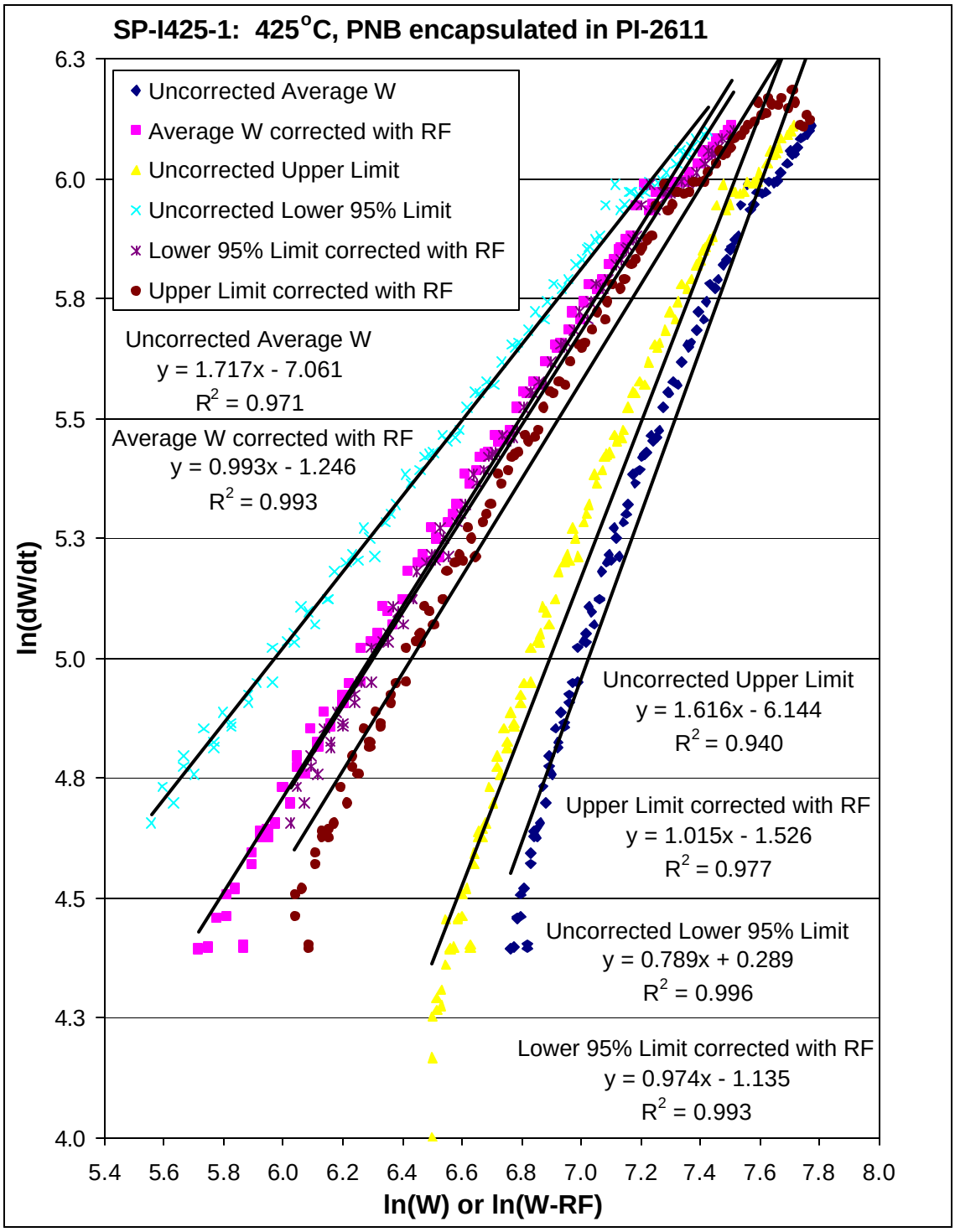

Figure A.72: Plot of ln(dW/dt) as a function of ln(W) or ln(W-RF) to determine the reaction order and reaction rate constant for the isothermal decomposition of PNB encapsulated by PI-2611 in nitrogen at 425°C.

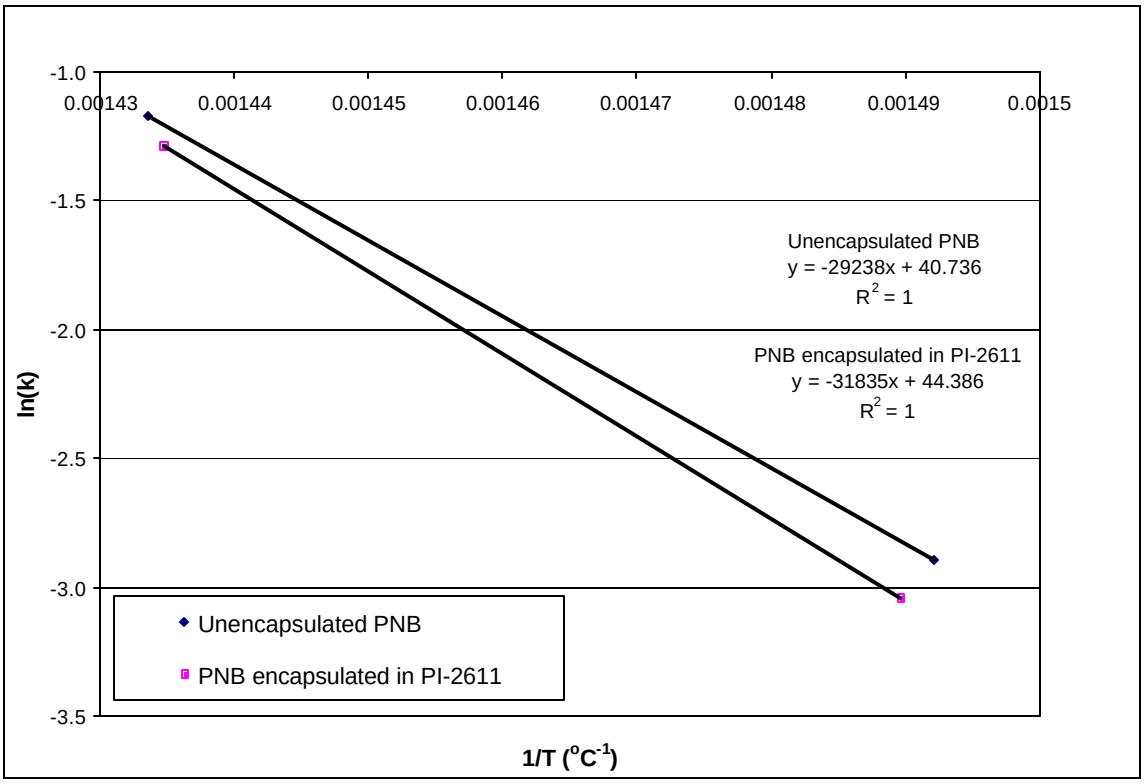

Figure A.73: The determination of E_a and A from isothermal TGA data of the decomposition of (1) unencapsulated PNB and (2) PNB encapsulated by PI-2611 at temperatures of 400°C and 425°C.

APPENDIX B

SPIN-SPEED CURVES FOR SACRIFICIAL POLYMERS

This appendix contains experimental spin-speed curve data for the various polynorbornene (PNB) and polycarbonate (PC) sacrificial polymer solutions. The compositions of the polynorbornene solutions are listed in Table 13 (Section 5.1.1, page 100). The compositions of the polycarbonate solutions are listed in Table 21 (Section 6.1.1, page 179). Each polymer solution was spin-coated onto Si wafers or wafer pieces using a CEE model 100CB spin-coater. The solution was dispensed into the center of the sample, spread at 500 RPM for 5 s and spun at the final speed for 30 s. The PNB films were softbaked on a hotplate at 100 to 120^{o}C for 3-5 min. The PC films were softbaked either on a hotplate or in an isothermal oven at a temperature between 80 and 120^{o}C. Exact softbaking conditions are given in the caption of each figure. The film thicknesses were determined by removing a portion of the polymer film with a razor blade then using a Tencor Alphastep profilometer to measure the height difference. All reported thicknesses are for softbaked films only. A power-law fit is used to fit and/or extrapolate the data to a larger range of spin-speeds. A spin-speed curve for PNB solution PNB-1-S2 is not included; this solution was spin-coated at a speed of 650 RPM and softbaked on a hotplate at 100^{o}C for 5 min. to yield a thickness of 400 nm. Spin-speed curves are not included for the polycarbonates PCC-S1, PPC-PS2, and PCC-PS1, all 20 wt% polymer in anisole. Each solution was spin-coated at a speed of 800 RPM and softbaked on a hotplate at 90^{o}C for 3 min to result in a film with a thickness of approximately 5.5 μm.

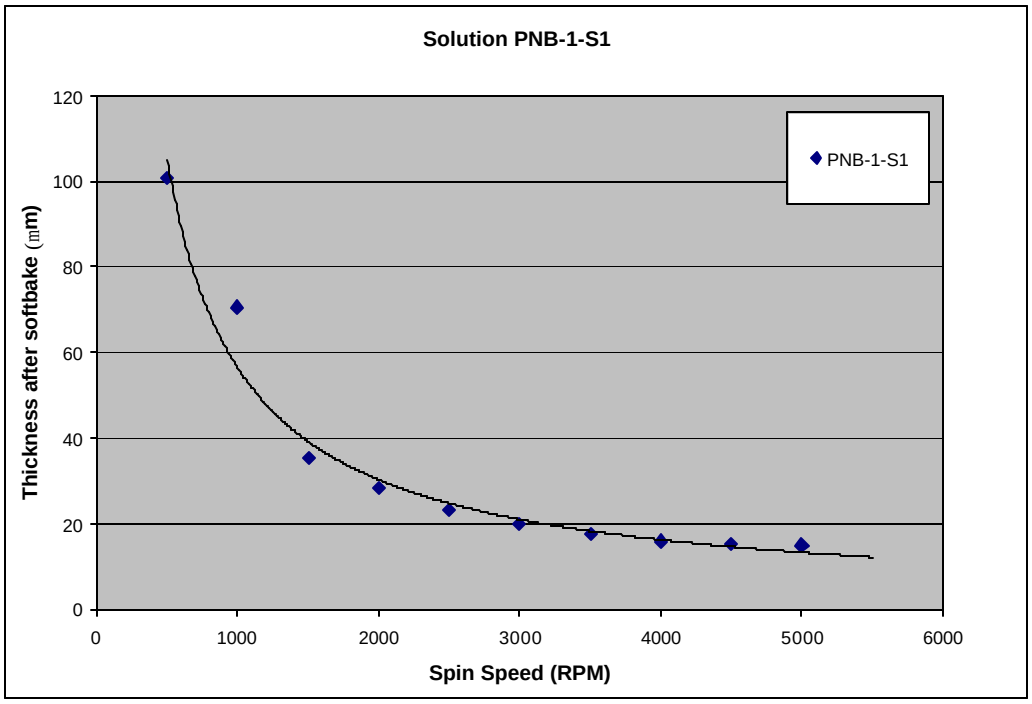

Figure B.1: Spin-speed curve for solution PNB-1-S1: 22.04 wt% 90/10 butyl/ triethoxysilyl polynorbornene (MW = 283K) in mesitylene. Softbaking conditions are a 120°C hotplate bake for 5 min.

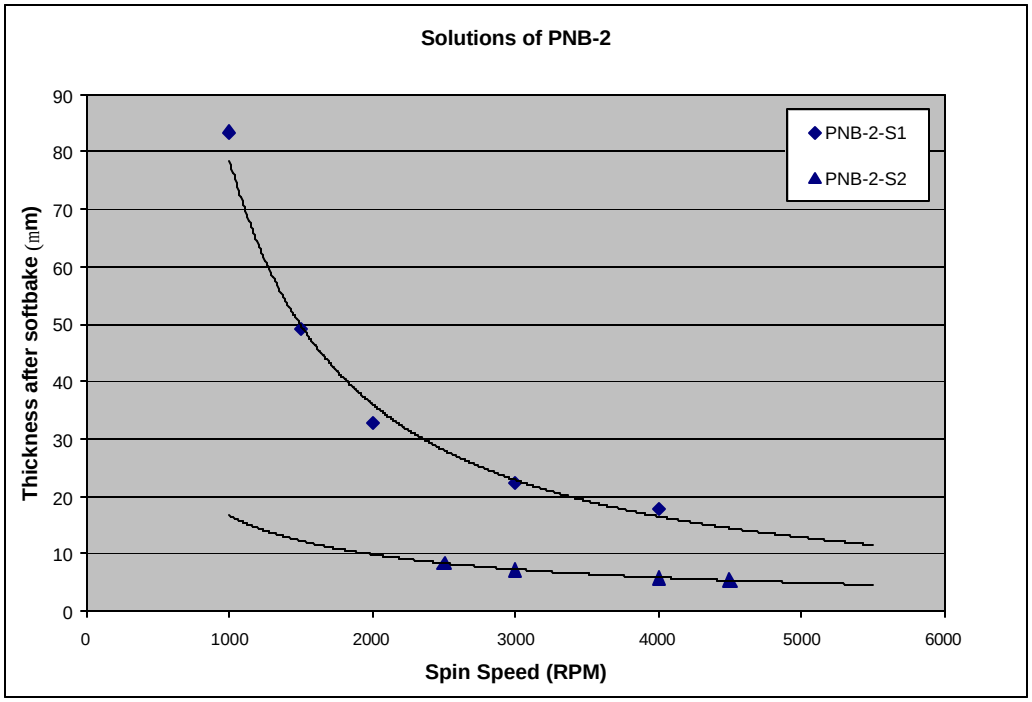

Figure B.2: Spin-speed curves for solutions of PNB-2: 90/10 butyl/triethoxysilyl polynorbornene (MW = 182K) in mesitylene. PNB-2-S1 is 30.80 wt% polymer and solution PNB-2-S2 is 20.0 wt% polymer. Softbaking conditions are a 120°C hotplate bake for 5 min.

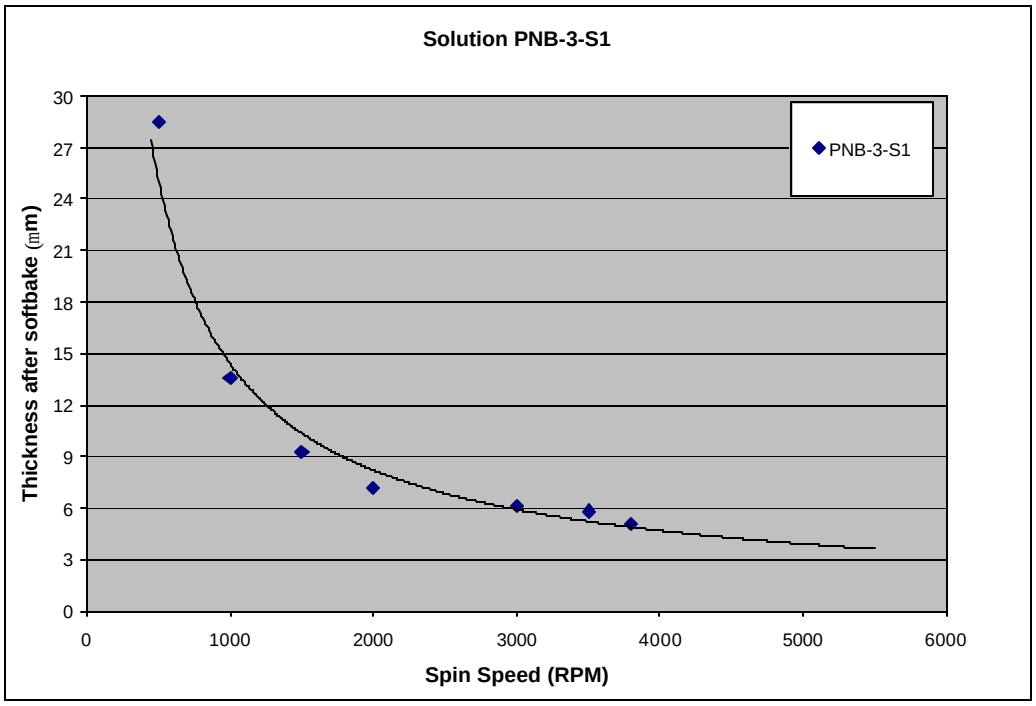

Figure B.3: Spin-speed curve for solution PNB-3-S1: 21.40 wt% 90/10 butyl/ triethoxysilyl polynorbornene (MW = 355K) in mesitylene. Softbaking conditions are a 120°C hotplate bake for 5 min.

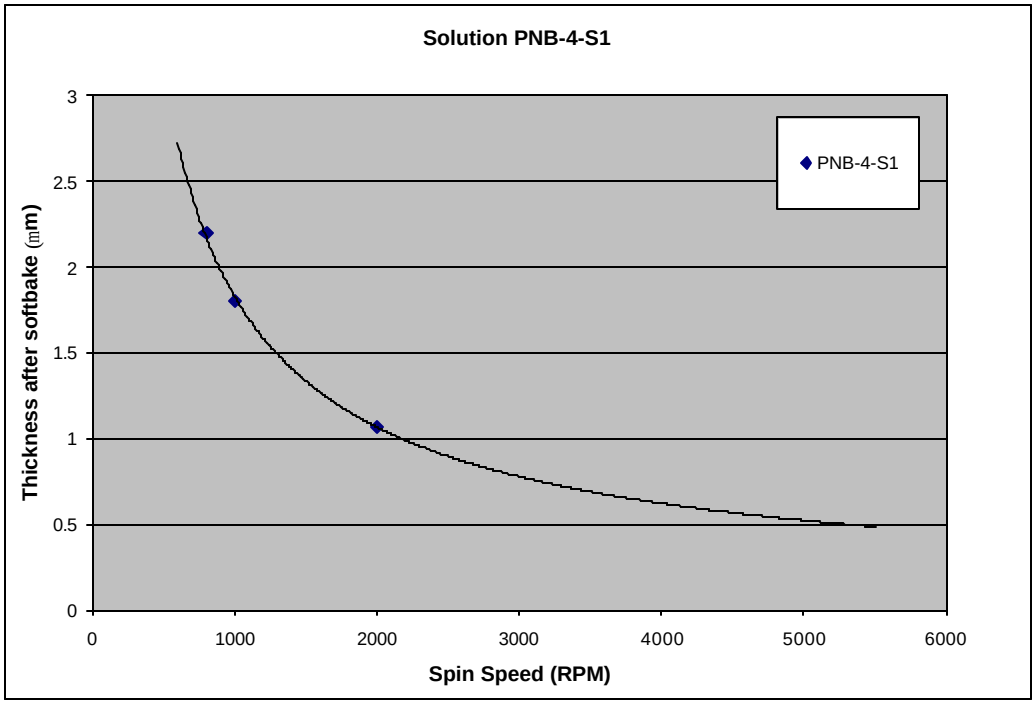

Figure B.4: Spin-speed curve for solution PNB-4-S1: 9.80 wt% methyl acetate polynorbornene (MW = 261K) in anisole. Softbaking conditions are a 100°C hotplate bake for 3 min.

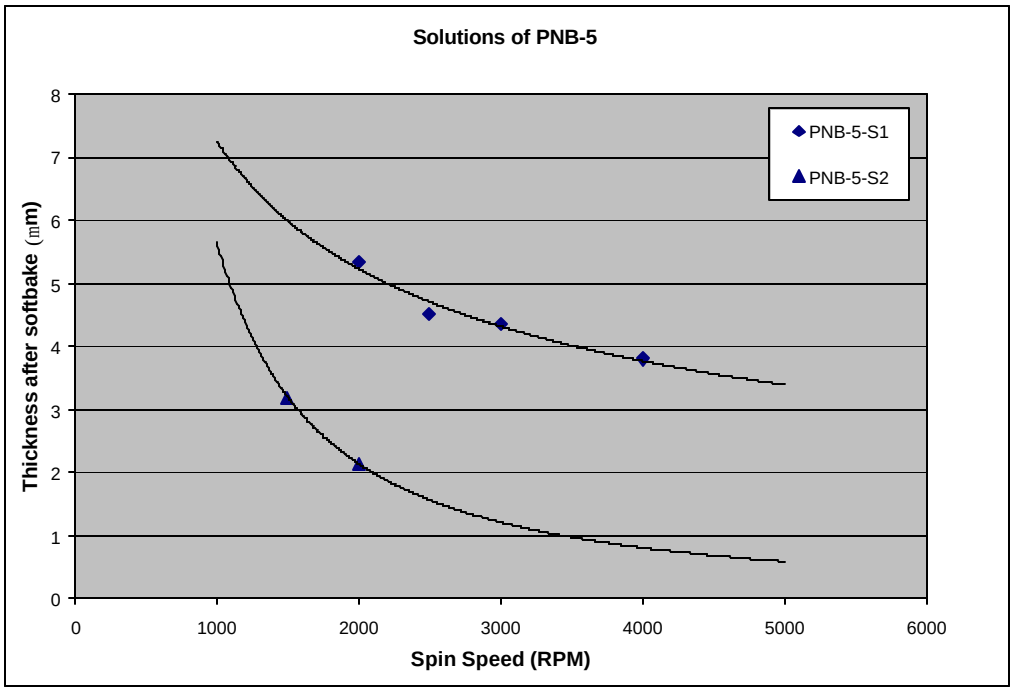

Figure B.5: Spin-speed curves for solutions of PNB-5: methylacetate polynorbornene (MW = 325K). PNB-5-S1 is 14.93 wt% polymer in anisole and solution PNB-5-S2 is 9.85 wt% polymer in toluene. Softbaking conditions are a 100°C hotplate bake for 3 min.

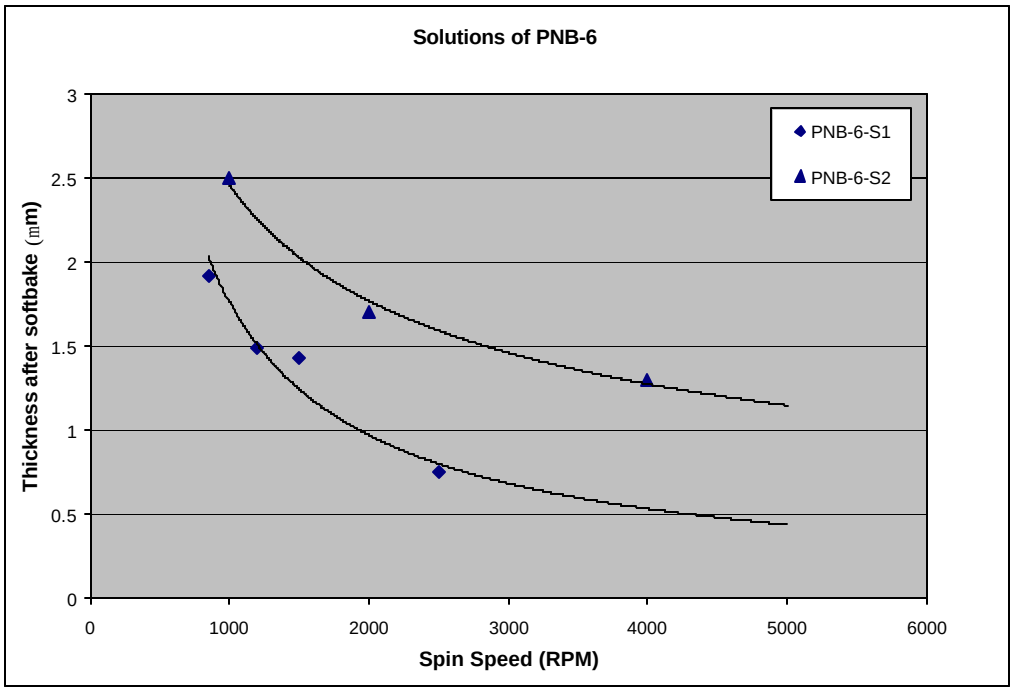

Figure B.6: Spin-speed curves for solutions of PNB-6: 90/10 methyl acetate/ triethoxysilyl polynorbornene (MW = 183K). PNB-6-S1 is 9.95 wt% polymer in anisole and solution PNB-6-S2 is 14.93 wt% polymer in toluene. Softbaking conditions are a100°C hotplate bake for 3 min.

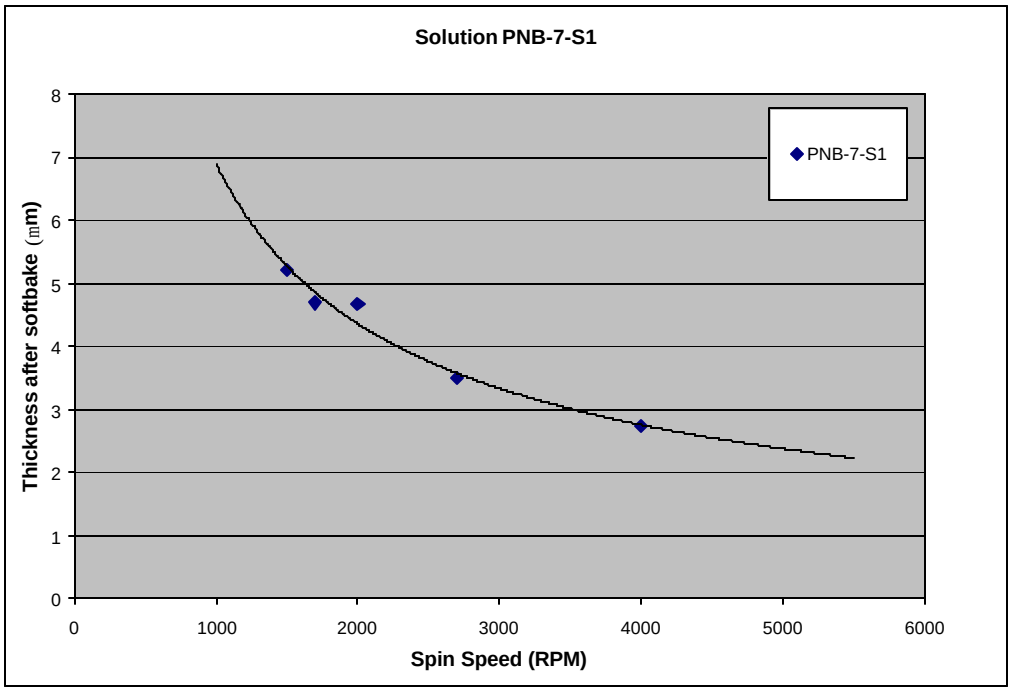

Figure B.7: Spin-speed curve for solution PNB-7-S1: 9.80 wt% 50/50 polynorbornene/triethoxysilyl polynorbornene (MW = 412K) in mesitylene. Softbaking conditions are a 120°C hotplate bake for 3 min.

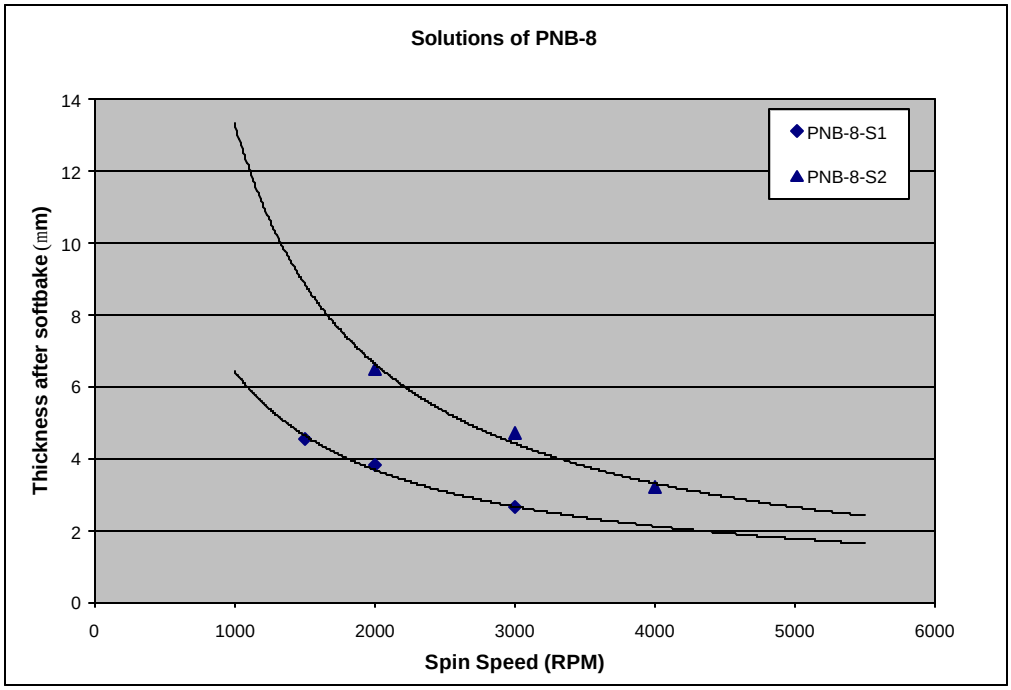

Figure B.8: Spin-speed curves for solutions of PNB-8: 90/10 butyl/cyclolacrylate polynorbornene (MW = 300K) in mesitylene. PNB-8-S1 is 9.95 wt% polymer and solution PNB-8-S2 is 15.90 wt% polymer. Softbaking conditions are a 120°C hotplate bake for 3 min.

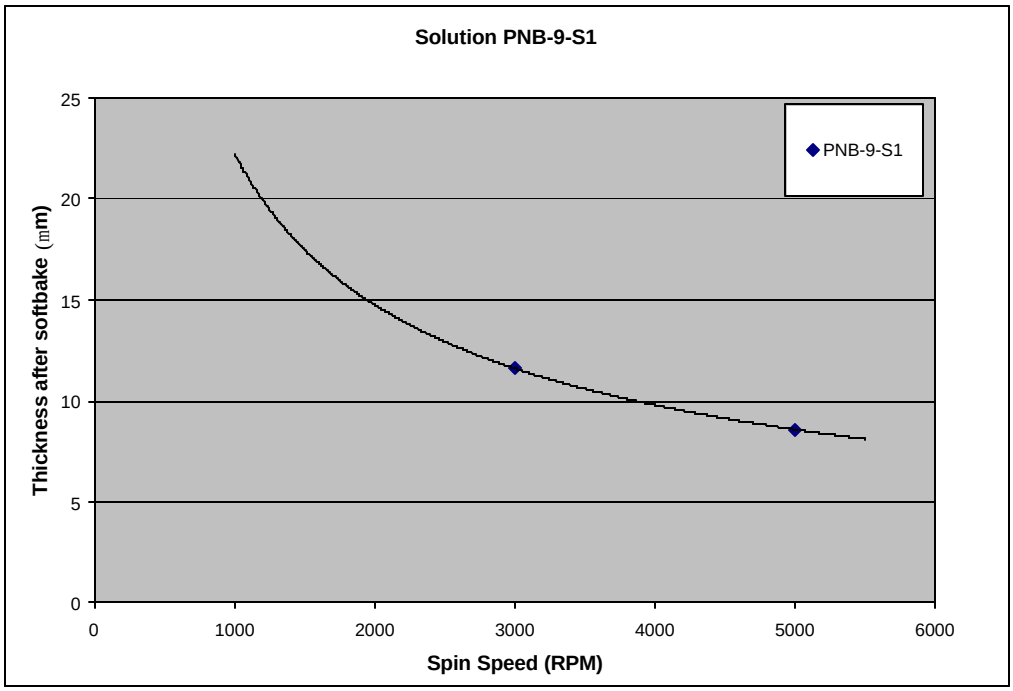

Figure B.9: Spin-speed curve for solution PNB-9-S1: 16.40 wt% 80/20 butyl/cyclolacrylate polynorbornene (MW = 213K) in trichloroethane. Softbaking conditions are a 100°C hotplate bake for 3 min.

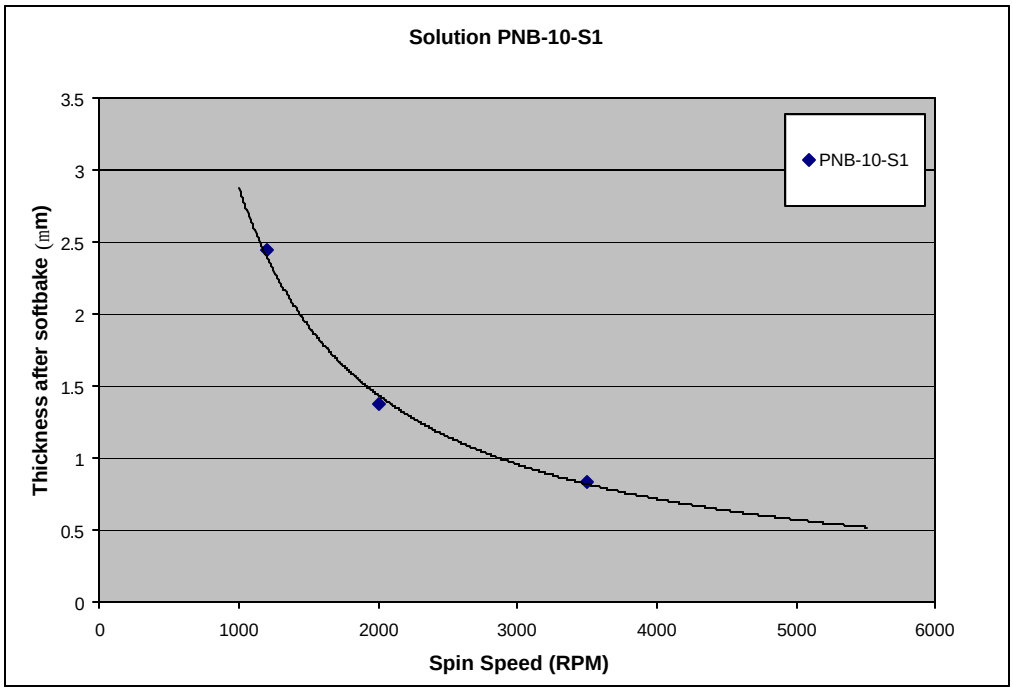

Figure B.10: Spin-speed curve for solution PNB-10-S1: 10.40 wt% 90/20 methyl acetate/cyclolacrylate polynorbornene (MW = 274K) in anisole. Softbaking conditions are a 100°C hotplate bake for 3 min.

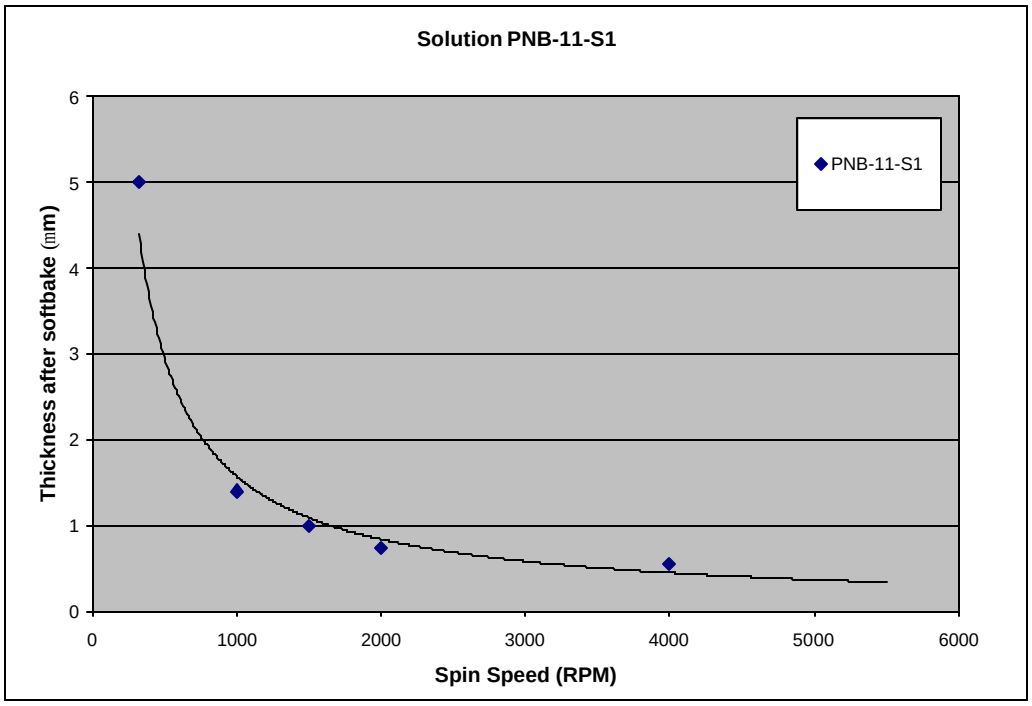

Figure B.11: Spin-speed curve for solution PNB-11-S1: 9.99 wt% 80/10/10 methyl acetate/triethoxysilyl/cyclolacrylate polynorbornene (MW = 256K) in cyclohexanone. Softbaking conditions are a 100^{o}C hotplate bake for 3 min.

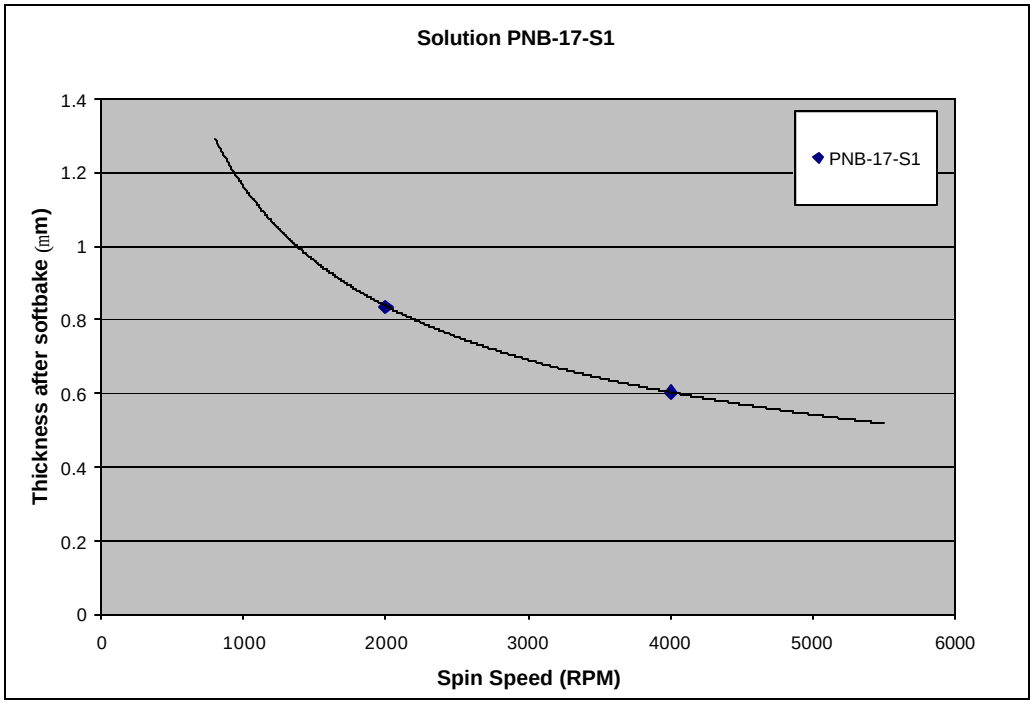

Figure B.12: Spin-speed curve for solution PNB-17-S1: 10.83 wt% 80/10/10 butyl/ triethoxysilyl/cyclolacrylate polynorbornene (MW = 213K) in mesitylene. Softbaking conditions are a 120^{o}C hotplate bake for 3 min.

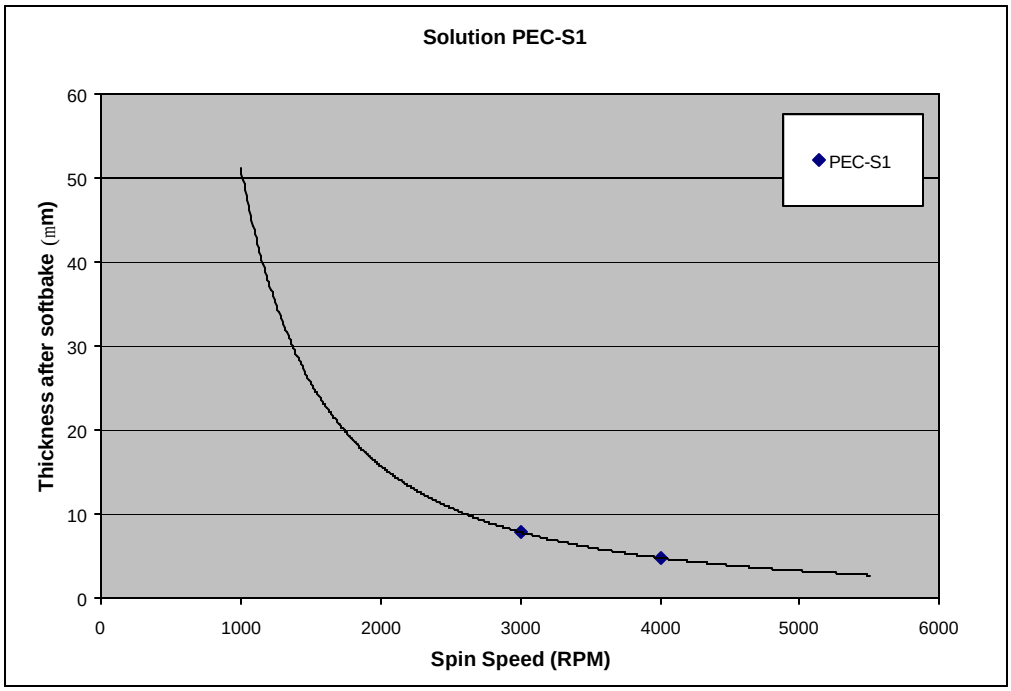

Figure B.13: Spin-speed curve for solution PEC-S1: 18 wt% poly(ethyl carbonate) in n-methyl-2-pyrrolidone. Softbaking conditions are a 95°C oven bake for 10 min.

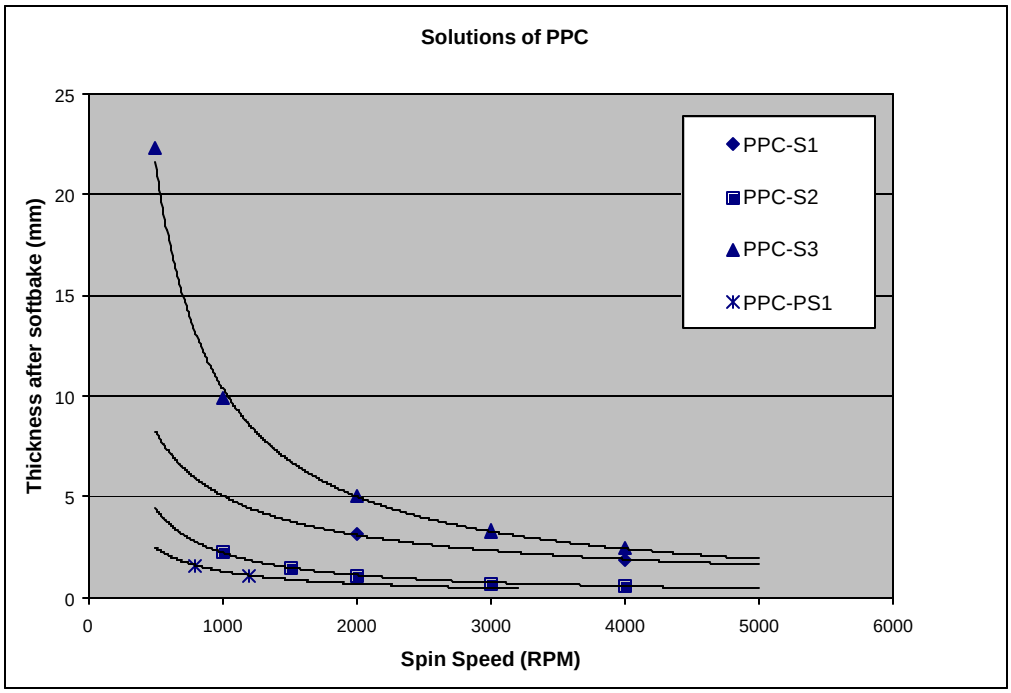

Figure B.14: Spin-speed curves for solutions of PPC: poly(propylene carbonate). PPC-S1 is 19 wt% polymer in n-methyl-2-pyrrolidone, PPC-S2 is 12 wt% polymer in ?-butyrolactone, solution PPC-S3 is 12 wt% polymer in ?-butyrolactone; solution PPC-PS1 is 12 wt% polymer in anisole. Softbaking conditions are a 95°C oven bake for 20 min.

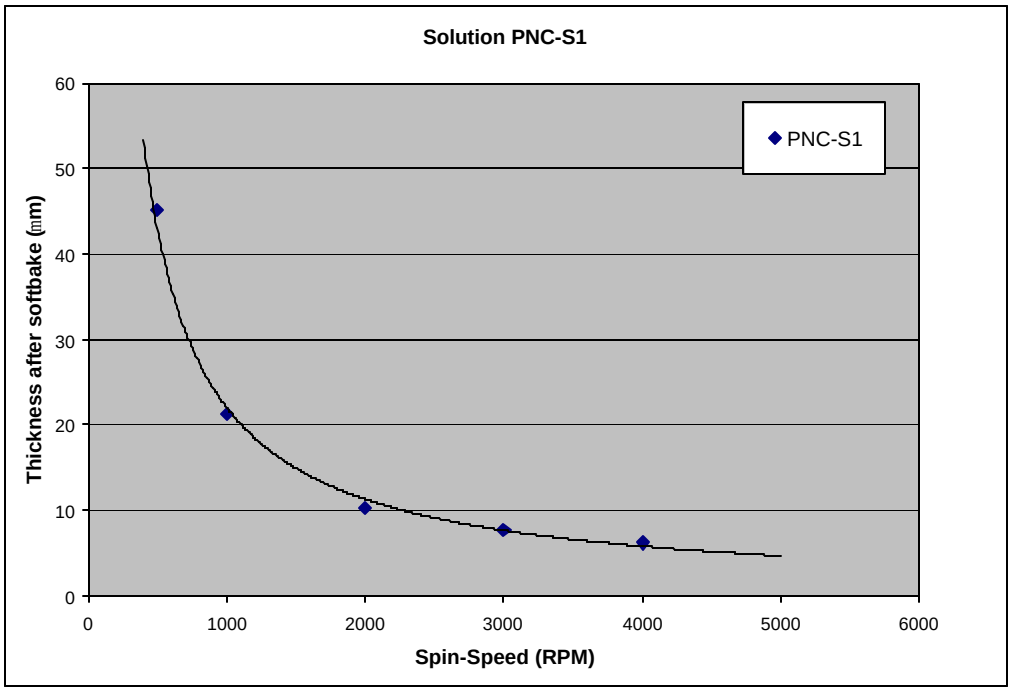

Figure B.15: Spin-speed curve for solution PNC-S1: poly(norbornene carbonate), 40 wt% polymer in cyclohexanone. Softbaking conditions are a 110^{o}C hotplate for 5 min.

APPENDIX C

SPIN-SPEED CURVES AND PROCESSING CONDITONS FOR ENCAPSULATING POLYMERS

This appendix contains experimental spin-speed curve data and describes the processing conditions used to deposit the various encapsulating polymers, listed in Table 3 (Section 3.3, page 36). All encapsulating polymers except parylene-N are commercially available liquid solutions and spin-coated onto samples using a CEE model 100CB spin-coater. Each solution was dispensed into the center of the sample, spread at 500 RPM for 5 s and spun at the final speed for 30 s. Softbaking, processing, and curing conditions for each solution are listed in Table C.1. Polymers requiring an exposure and/or post exposure bake were exposed using either an OAI or a Karl Suss MA-6 mask aligner with a broadband bulb. The exposure time was calculated based on the bulb intensity measured at 365 nm. The film thicknesses were determined by removing a portion of the film with a razor blade then using a Tencor Alphastep profilometer to measure the height difference. All reported thicknesses are for softbaked films only unless specifically stated. A power-law fit is used to fit and/or extrapolate spin-speed data to a larger range of spin-speeds.

Table C.1: Processing conditions for polymers used as overcoat materials to sacrificial polymers.

Polymer	Solvent	Adhesion Promoter (AP)	AP coat	Polymer Spin-coat	Polymer Softbake	Exposure	Post-Bake	Polymer Cure	Thick-ness
Amoco Ultradel 7501	γ-butyrolactone	Amoco A600	4000 RPM/30 s, then 100°C hotplate/30 s	500 RPM/5 s, then final speed/30 s	100°C hotplate/ 3 min.	600 mJ/cm^2 @ 365 nm	100°C oven/ 10 min	3°C/min to 350°C, hold 1 hour	See SS curve
DuPont Pyralin PI2611	NMP[#]	DuPont VM-652	3000 RPM/30 s	500 RPM /5 s, then final speed/30 s	100°C hotplate/ 5 min.	N/A	N/A	3°C/min to 350°C, hold 1 hour	See SS curve
DuPont Pyralin PI2734	NMP	DuPont VM-652	3000 RPM/30 s	500 RPM /5 s, then final speed/30 s	100°C hotplate/ 5 min.	200 mJ/cm^2 @ 365 nm	None	3°C/min to 350°C, hold 1 hour	See SS curve
DuPont Pyralin PI2731	NMP	None	N/A	500 RPM /5 s, then final speed/45 s	100°C hotplate/ 5 min.	200 mJ/cm^2	120°C oven/ 30 min	3°C/min to 350°C, hold 1 hour	See SS curve
DuPont Pyralin PI2540	NMP	DuPont VM-652	3000 RPM/30 s	500 RPM /5 s, then 4000 RPM/30 s	100°C hotplate/ 3 min	N/A	N/A	3°C/min to 350°C, hold 1 hour	5μm
DuPont Pyralin PI2771	NMP	DuPont VM-652	3000 RPM/30 s	500 RPM/5 s, then 4000 RPM/30 s	90°C hotplate/ 90 s	300 mJ/cm^2 @ 365 nm	None	3°C/min to 350°C, hold 1 hour	8 μm
Dupont Pyrlain PI2555	NMP	DuPont VM-652	3000 RPM/30 s	500 RPM/5 s, then 2500 RPM/30 s	100°C hotplate/ 3 min.	N/A	N/A	3°C/min to 350°C, hold 1 hour	8 μm
HD4000	NMP	None	N/A	500 RPM/5 s, then 3000 RPM/30 s	85°C hotplate/100 s; 95°C hotplate/ 100 s	N/A	N/A	3°C/min to 350°C, hold 1 hour	15 μm
Honeywell FLARE	cyclohexanone	None	N/A	500 RPM/5 s, then final speed/30 s	150°C hotplate/1 min; 200°C hotplate/1 min; 250°C hotplate/ 1 min	N/A	N/A	10°C/min to 250°C, hold 20 min., 5°C/min to 400°C, hold 1 hr	See SS curve

Table C.1 (cont.)

Polymer	Solvent	Adhesion Promoter (AP)	AP coat	Polymer Spin-coat	Polymer Softbake	Exposure	Post-Bake	Polymer Cure	Thick-ness
Polyimide PWDC-1000	γ-butyrolactone	None	N/A	500 RPM/5 s, then 3000 RPM/30 s	110°C hotplate/ 3 min.	None	N/A	3°C/min to 170°C, hold 30 min, 3°C/min to 250°C, hold 30 min, 3°C/min to 300°C, hold 1 hour	8 μm
PBO CRC-8650	γ-butyrolactone	None	N/A	500 RPM/5 s, then 3000 RPM/30 s	125°C hotplate/ 4 min.	None	N/A	3°C/min to 150 °C, hold 30 min, 3°C/min to 250°C, hold 30 min, 3°C/min to 320°C, hold 30 min.	10 μm
LMB-7081 Epoxy	PGMEA**	None	N/A	500 RPM/5 s, then 3000 RPM/30 s	70°C hotplate/ 15 min.	2000 mJ/cm^2 @ 365 nm	120°C oven/ 30 min	10°C/min to 165°C, hold 1 hour in AIR	7.6 μm
BCB 3022-57	mesitylene	Dow AP8000	3000 RPM/30 s	500 RPM/5 s, then final speed/30 s	120°C oven/ 5 min.	None	N/A	10°C/min to 250°C, hold 1 hour	See SS curve
Avatrel 2000P	anisole	None	N/A	500 RPM /5 s, then final speed/30 s	100°C hotplate/ 10 min	250 mJ/cm^2 @ 365 nm	100°C oven/ 10 min	3°C/min to 200°C, hold 1 hour	See SS curve

*N/A indicates not-applicable
**propylene glycol methyl ether acetate
n-methyl-2-pyrrolidone

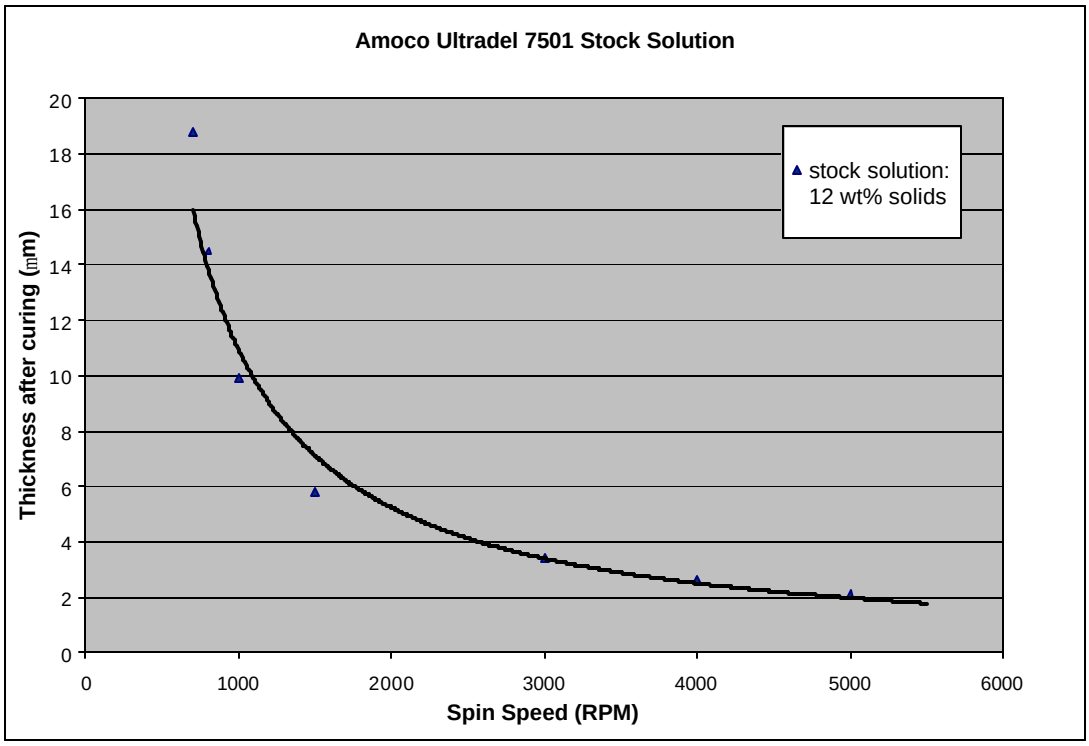

Figure C.1: Cured film thickness as a function of spin speed for Amoco Ultradel stock solution (12 wt.% solids).

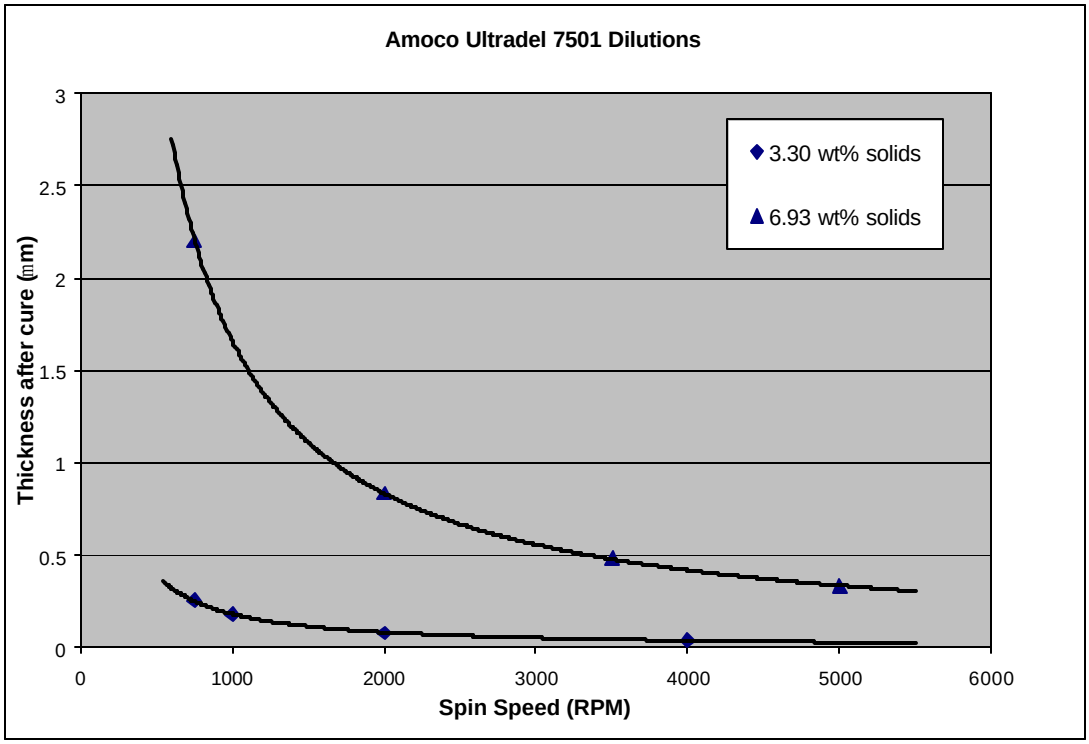

Figure C.2: Cured film thickness as a function of spin speed for dilutions of Amoco Ultradel stock solution to (a) 3.30 wt.% and (b) 6.93 wt.%.

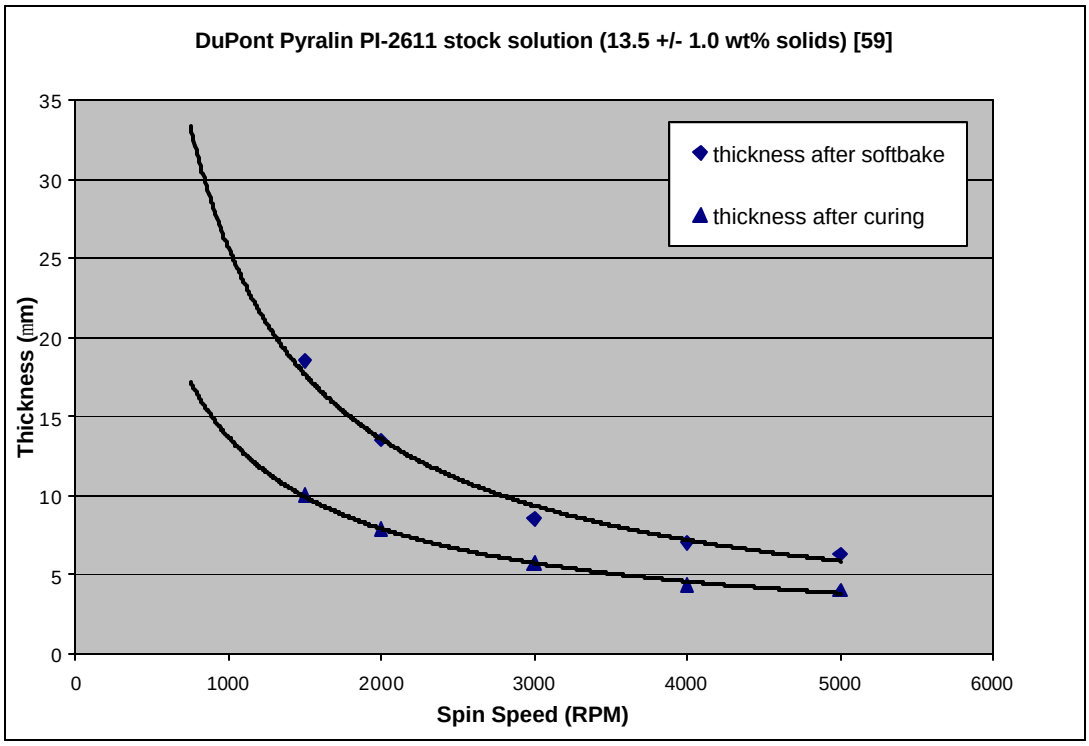

Figure C.3: Softbaked and cured film thicknesses as a function of spin speed for DuPont Pyralin PI-2611 polyimide stock solution.

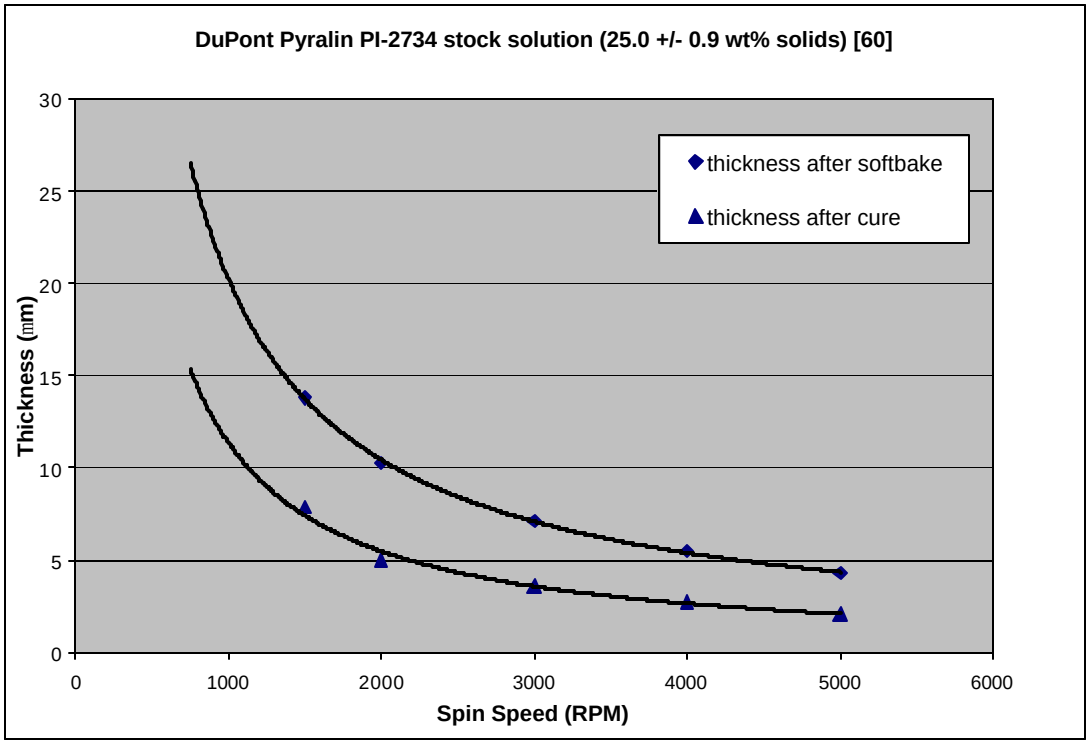

Figure C.4: Softbaked and cured film thicknesses as a function of spin speed for DuPont Pyralin PI-2734 polyimide stock solution.

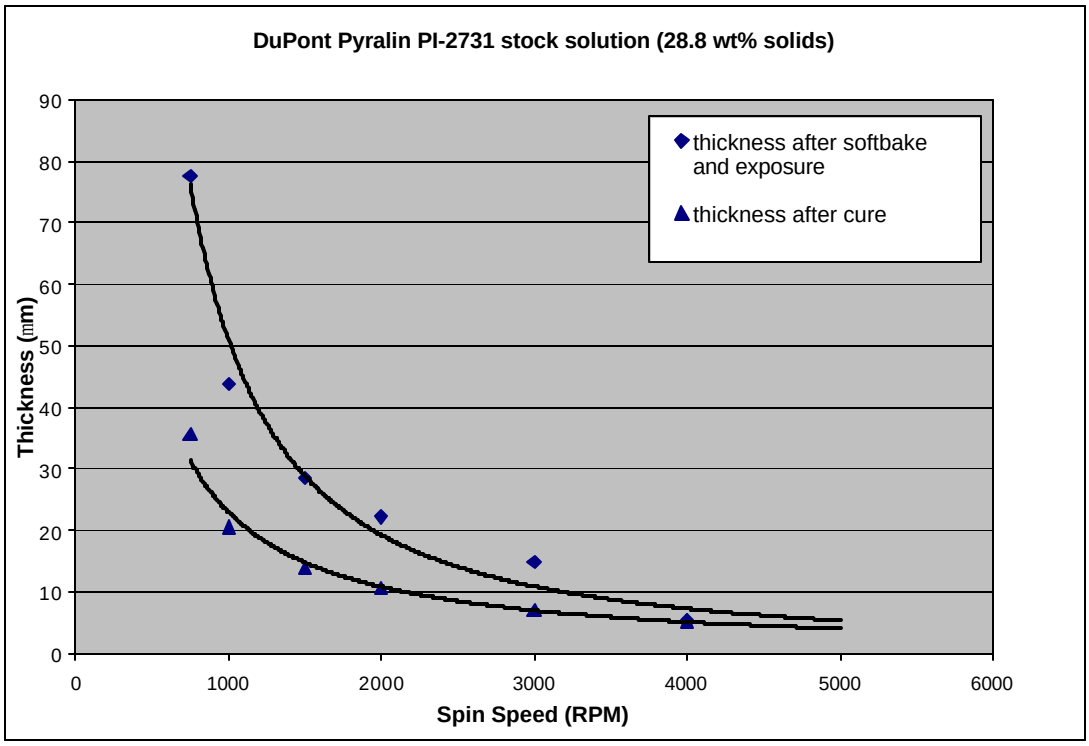

Figure C.5: Softbaked and cured film thickness as a function of spin speed for DuPont Pyralin PI-2731 polyimide stock solution.

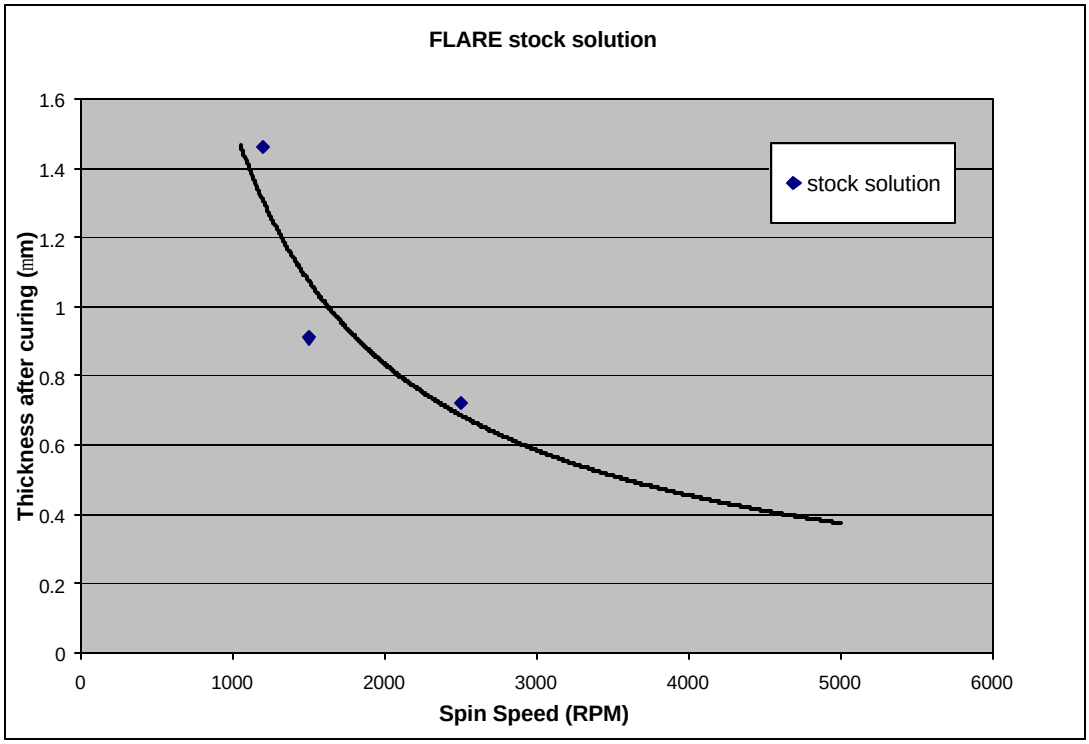

Figure C.6: Cured film thickness as a function of spin speed for Honeywell FLARE poly(arylene ether).

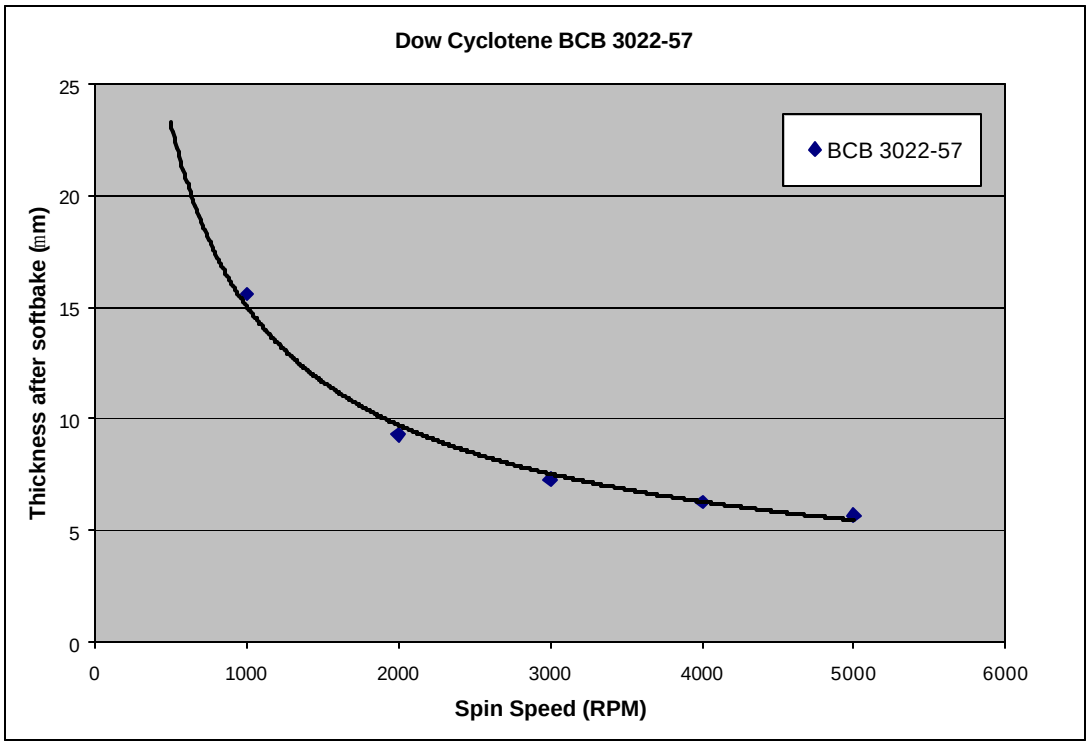

Figure C.7: Softbaked film thickness as a function of spin speed for Dow Cyclotene bisbenzocyclobutene (BCB) 3022-57.

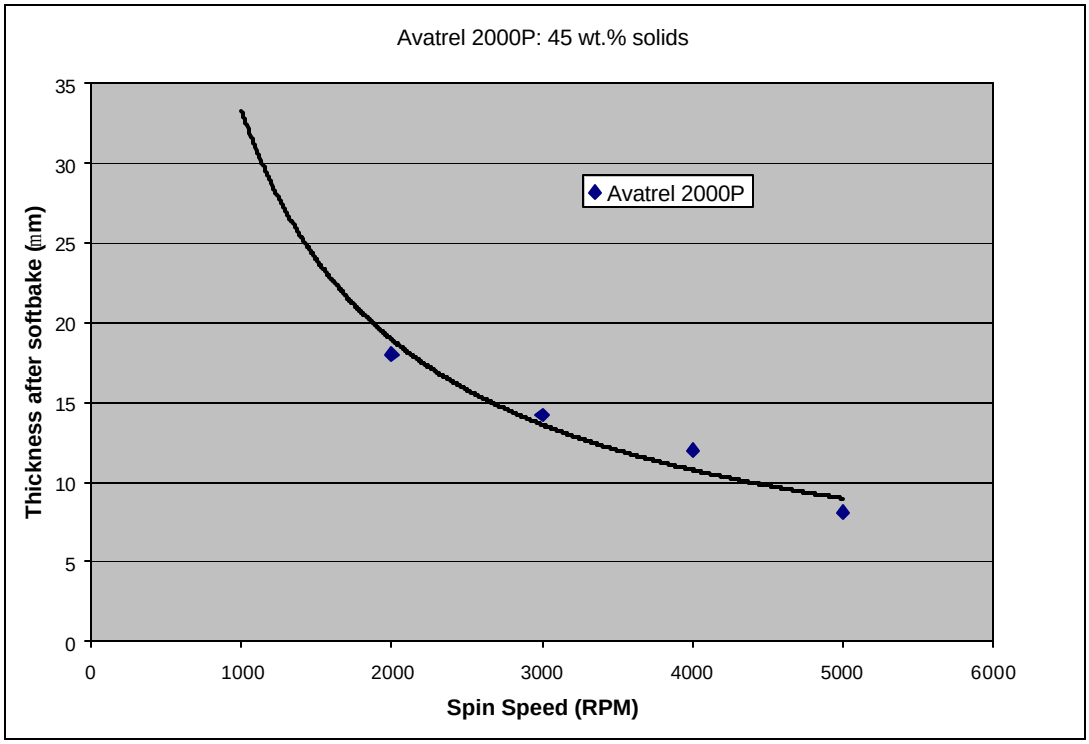

Figure C.8: Softbaked film thickness as a function of spin speed for Promerus Avatrel 2000P Dielectric Polymer (45 wt.% solids).

REFERENCES

[1] B. Shieh, K. C. Saraswat, J. P. McVittie, S. List, S. Nag, M. Islamraja, and R. H. Havemann, "Air-Gap Formation During IMD Deposition to Lower Interconnect Capacitance," *IEEE Electron Device Letters*, **19**(1), 16-18 (1998).

[2] B. Shieh, K. Saraswat, M. Deal, and J. McVittie, "Air Gaps Lower *k* of Interconnect Dielectrics," *Solid State Tech*., **42**(2), 51-58 (1999).

[3] M. B. Anand, M. Yamada, and H. Shibata, "Use of Gas as Low-*k* Interlayer Dielectric in LSI's: Demonstration of Feasibility," *IEEE Transactions on Electron Devices*, **44**(11), 1965-1971 (1997).

[4] P. Gravesen, J. Branebjerg, and O.S. Jensen, "Microfluidics – A Review," *J. Micromech. Microeng.*, **3**(4),168-182 (1993).

[5] R.F. Service, "Microchip arrays put DNS on the spot," *Science*, **282** (5388), 396-399 (1998).

[6] C. H. Mastrangelo, M. A. Burns, and D. T. Burke, "Microfabricated Devices for Genetic Diagnostics," *Proceedings of the IEEE*, **86**(8), 1769-1787 (1998).

[7] Z. Moukheiber, "A Hail of Silver Bullets," *Forbes*, **161**(2), 76 (1998).

[8] R. Srinivasan, S. L. Firebaugh, I.-M. Hsing, J. Ryley, M. P. Harold, K. F. Jensen, and M. A. Schmidt, "Chemical Performance and High Temperature Characterization of Micromachined Chemical Reactors," *Proceedings of the International Solid-State Sensors and Actuators Conference (Transducers '97),* Chicago, IL, June 16-19, 1997, 163-166.

[9] P. A. Kohl, Q. Zhao, and S. A. Bidstrup Allen, "Fabrication of a Semiconductor Device With Air Gaps for Ultra-low Capacitance Interconnections," US Patent 6,165,890, Issued December 26, 2000.

[10] P. A. Kohl, Q. Zhao, K. Patel, D. Schmidt, S. A. Bidstrup-Allen, R. Shick, and S. Jayaraman, "Air-gaps for Electrical Interconnections," *Electrochemical and Solid State Letters*, **1**(1), 49-51 (1998).

[11] D. M Bhusari, M. D. Wedlake, P. A. Kohl, C. Case, F. P. Klemens, J. Miner, B.-C. Lee, R. J. Gutmann, J. J. Lee, R. Shick, and L. Rhodes, "Fabrication of Air-gaps Between Cu Interconnects for Low Intralevel k," *Materials, Technology and Reliability for Advanced Interconnects and Low-k Dielectrics, (Materials Research*

Society Symposium Proceedings Volume 612), San Francisco, CA, April 23-27, 2000, 1-6.

[12] P. A. Kohl, D. M. Bhusari, M. Wedlake, C. Case, F. P. Klemens, J. Miner, B. Lee, R. J. Gutmann, and R. Shick, "Air-Gaps in 0.3 μm Electrical Interconnections," *IEEE Electron Device Letters*, **21**(12), 557-559 (2000).

[13] K.-M. Chang, J.-Y. Yang, L.-W. Chen, and M. H. Tseng, "A Novel Process and Thermodynamic Mechanisms of Air Gap Formation for ULSI Application," *Thin Solid Films*, **376**, 124-130 (2000).

[14] V. Arnal, J. Torres, J.-P. Reynard, P. Gayet, C. Vérove, M. Guillermet, and P. Spinelli, "Optimization of CVD Dielectric Process to Achieve Reliable Ultra Low-*k* Air Gaps," *Microelectronic Engineering*, **60**, 143-148 (2002).

[15] M. Lin, C. Y. Chang, T. Y. Huang, and M.-L. Lin, "A Multi-level Interconnect Technology with Intrametal Air Gap for High-Performance 0.25-μm-and-Beyond Devices Manufacturing," *Jpn. J. Appl. Phys.*, **38**(11), 6240-6246 (1999).

[16] D. C. Duffy, J. C. McDonald, O. J. A. Schueller, and G. M. Whitesides, "Rapid Prototyping of Microfluidic Systems in Poly(dimethylsiloxane)," *Analytical Chemistry*, **70**, 4974-4984 (1998).

[17] J. D. Meindl, J. A. Davis, P. Zarkesh-Ha, C. S. Patel, K. P. Martin, and P. A. Kohl, "Interconnect Opportunities for Gigascale Integration", *IBM Journal of Research and Development*, **46**, 245-263 (2002).

[18] J. D. Meindl, R. Venkatesan, J. A. Davis, J. Joyner, A. Naeemi, P. Zarkesh-Ha, M. S. Bakir, A. V. Mule', P. A. Kohl, and K. P. Martin, "Interconnecting Device Opportunities for Gigascale Integration (GSI)", *International Electron Devices Meeting* (IEDM) Technical Digest, Washington D.C., Dec. 2-5, 2001.

[19] M. S. Bakir, H. A. Reed, P. A. Kohl, K. P. Martin, and J. D. Meindl, "Sea of Leads Ultra High-density Compliant Wafer Level Packaging Technology," *Proceeding of the 52nd IEEE Electronic Components and Technology Conference*, San Diego, CA, May 28-31, 2002, 1087-1094.

[20] M. S. Bakir, H. A. Reed, A. V. Mule', P. A. Kohl, K. P. Martin, and J. D. Meindl, "Sea of Leads (SoL) Characterization and Design for Compatibility With Board-Level Optical Waveguide Interconnection," *Proceedings of the IEEE Custom Integrated Circuits Conf.*, Piscataway, NJ, May 12-15, 2002, 492-494.

[21] M. S. Bakir, A. V. Mule', H. D. Thacker, P. A. Kohl, K. P. Martin, and J. D. Meindl, "Sol-Compliant Wafer-Level Package Technologies," *Semiconductor International*, **25**(4), 61-64 (2002).

[22] M. S. Bakir, H. A. Reed, A. V. Mulé, J. P. Jayachandran, P. A. Kohl, K. P. Martin, T. K. Gaylord, and J. D. Meindl, "Chip-to-Module Interconnections Using "Sea of Leads" Technology," *MRS Bulletin*, **28**(1), 61-67 (2003).

[23] M. S. Bakir, "Sea of Leads Electrical-Optical Polymer Pillar Chip I/O Interconnections for Gigascale Integration," *Ph. D. Thesis*, School of Electrical and Computer Engineering, Georgia Institute of Technology, 2004.

[24] M. S. Bakir, C. S. Patel, P. A. Kohl, K. P. Martin, and J. D. Meindl, "Ultra High I/O Density Package: Sea of Leads (SoL)," *Proceedings of the HD International Conference on High-Density Interconnect and Systems Packaging*, Santa Clara, CA, April 17-20, 2001, 335-339.

[25] M. S. Bakir, H. A. Reed, H. D. Thacker, C. S. Patel, P. A. Kohl, K. P. Martin, and J. D. Meindl, "Sea of Leads (SoL) Ultrahigh Density Wafer-Level Chip Input/Output Interconnections for Gigascale Integration," *IEEE Transactions on Electron Devices*, **50**(10), 2039-2048 (2003).

[26] N.F. Raley, J.C. Davidson, and J.W. Balch, "Examination of Glass-Silicon and Glass-Glass Bonding Techniques for Microfluidic Systems," *Proceedings of the SPIE (Micromachining and Microfabrication Process Technology)*, Austin, TX, Oct 23-25, 1995, **2639**, 40-45.

[27] Y. Xia, and G. M. Whitesides, "Soft Lithography," *Agnew. Chem. Int. Ed.*, **37**, 550-575 (1998).

[28] J. R. Anderson, D. T. Chiu, R. J. Jackman, O. Cherniavskaya, J. C. McDonald, H. Wu, S. H. Whitesides, and G. M. Whitesides, "Fabrication of Topologically Complex Three-Dimensional Microfluidic Systems in PDMS by Rapid Prototyping," *Analytical Chemistry*, **72**(14), 3158-3164 (2000).

[29] W. J. Nam, S. Bae, A. K. Kalkan, and S. J. Fonash, "Nano- and Microchannel Fabrication Using Column/Void Network Deposited Silicon," *J. Vacuum Sci. and Technol. A*, **19**(4), 1229-1233 (2001).

[30] A. Maciossek, B. Löchel, H.-J. Quenzer, B. Wagner, S. Schulze, and J. Noetzel, "Galvanoplating and Sacrificial Layers for Surface Micromachining," *Microelectronic Engineering*, **27**, 503-508 (1995).

[31] J. Bühler, F.-P. Steiner, and H. Baltes, "Silicon Dioxide Sacrificial Layer Etching in Surface Micromachining," *J. Micromech. Microeng.*, **7**, R1-R13 (1997).

[32] L. S. Loo, and K. K. Gleason, "Hot Filament Chemical Vapor Deposition of Polyoxymethylene as a Sacrificial Layer for Fabricating Air Gaps," *Electrochemical and Solid-State Letters*, **4**(11), G81-G84 (2001).

[33] C. K. Harnett, G. W. Coates, and H. G. Craighead, "Heat –Depolymerizable Polycarbonates as Electron Beam Patternable Sacrificial Layers for Nanofluidics," *J. Vac. Science and Technology B*, **19**(6), 2842-2845 (2001).

[34] C. K. Harnett, K. M. Satyalakshmi, G. W. Coates, and H. G. Craighead, "Direct Electron-beam Patterning of Surface Coatings and Sacrificial Layer for Micro-Total Analysis Systems," *Journal of Photopolymer Science and Technology*, **15**(3), 493-496 (2002).

[35] H.-J. Suh, P. Bharathi, D. P. Beebe, and J. S. Moore, "Dendritic Material as a Dry-Release Sacrificial Layer," *J. of Microelectromechanical Systems*, **9**(2), 198-205 (2000).

[36] Z. Cui, and R. A. Lawes, "A New Sacrificial Layer Process for the Fabrication of Micromechanical Systems," *J. Micromech. Microeng*., **7**, 128-130 (1997).

[37] T. E. Bell, P. T. J. Gennissen, D. DeMunter, and M. Kuhl, "Porous Silicon as a Sacrificial Material," *J. Micromech. Microeng.*, **6**, 361-369 (1996).

[38] M. Boucinha, V. Chu, J. P. Alpuim, and J. P. Conde, "Micromachining of an Air-bridge Structure Using Thin-films on Glass Substrates," *Sensors and Actuators A*, **74**, 5-8 (1999).

[39] A. Bagolini, L. Pakula, T. L. M. Scholtes, H. T. M. Pham, P. J. French, and P. M. Sarro, "Polyimide Sacrificial Layer and Novel Materials for Post-processing Surface Micromachining," *J. Micromech. Microeng.*, **12**, 385-389 (2002).

[40] A. B. Frazier, C. H. Ahn, and M. G. Allen, "Development of Micromachined Devices Using Polyimide-based Processes," *Sensors and Actuators A*, **45**, 47-55 (1994).

[41] D. Memmi, V. Foglietti, E. Cianci, G. Caliano, and M. Pappalardo, "Fabrication of Capacitive Micromechanical Ultasonic Transducers by Low-Temperature Process," *Sensors and Actuators A*, **99**, 85-91 (2002).

[42] 2001 International Technology Roadmap for Semiconductors (ITRS): http://public.itrs.net/.

[43] J. Fjelstad, T. DiStefano, and A. Faraci, "Wafer level Packaging of Compliant, Chip Size ICs," *Microelectronics International*, **17**(2), 23-27 (2000).

[44] C. S. Patel, "Compliant Wafer Level Package (CWLP)," *Ph. D. Thesis*, School of Electrical and Computer Engineering, Georgia Institute of Technology, 2001.

[45] S. Inoue, T. Tsuruta, T. Takada, N. Miyazaki, M. Kambe, and T. Takaoka, "Synthesis and Thermal Degradation of Carbon Dioxide-Epoxide Copolymer," *Appl. Polymer Symp.*, **26,** 257-267 (1975).

[46] H. Yan, W. R. Cannon, and D. J. Shanefield, "Thermal Decomposition Behaviour of Poly(propylene carbonate)," *Ceramics International*, **24**, 433-439 (1998).

[47] N. R. Grove, P. A. Kohl, S. A. Bidstrup-Allen, R. A. Shick, B. L. Goodall and S. Jayaraman, "Polynorbornene for Low-k Interconnection," *Proceedings of the Materials Research Society Symposium (Low Dielectric Constant Materials III)*, San Francisco, CA, April 1-4, 1997, 3-8.

[48] R. A. Shick, B. L. Goodall, L. H. McIntosh, S. Jayaraman, P. A. Kohl, S. A. Bidstrup-Allen and N. R. Grove, "New Olefinic Interlevel Dielectric Materials for Multichip Modules," *Proceedings of the IEEE Multichip Module Conf.*, Santa Cruz, CA, Feb. 6-7, 1996, 182-187.

[49] D. A. Barnes, G. M. Benedikt, B. L. Goodall, K. Hullihen, S. Jayaraman, W. C. McDougall, L. H. McIntosh III, L. F. Rhodes, and R. A. Shick, "Advanced Materials for Electronic Applications by Polymerization of Cyclic Olefins Using Late Transition Metal Catalysts," *Proceedings of MetCon '98*, Houston, TX, June 10-11, 1998.

[50] D. J. Darensbourg, J. R. Wildeson, J. C. Yarbrough and J. H. Reibenspies, "*Bis* 2,6-difluorophenoxide Dimeric Complexes of Zinc and Cadmium and Their Phosphine Adducts: Lessons Learned Relative to Carbon Dioxide/Cyclohexene Oxide Alternating Copolymerization Processes Catalyzed by Zinc Phenoxides," *J. Amer. Chem. Soc.*, **122**(50), 12487-12496 (2000).

[51] M. Murayama, F. Sanda, T. Endo, "Anionic Ring-Opening Polymerization of a Cyclic Carbonate Having a Norbornene Structure with Amine Initiators," *Macromolecules*, **31**(3), 919-923 (1998).

[52] R. N. Manepalli, "Electron Beam Curing of Thin Film Polymer Dielectrics," *Ph. D. Thesis*, School of Chemical Engineering, Georgia Institute of Technology, 2000.

[53] Ultradel 7501 Product Information, "Ultradel 7501 Coatings, Bulletin UL-P4c," Amoco Chemical Company, 150 West Warrenville Road, Naperville, IL 60563-8460.

[54] R. T. Tummala, Ed., E. J. Rymaszewski, Ed., and A. G. Klopfenstein, Ed., Microelectronics Packaging Handbook, Semiconductor Packaging, Part II, 2nd ed., Kluwer Academic, Boston, 1999.

[55] Parylene Technical Data, available at www.paratronix.com/apps/techdata.asp, Paratronix, Inc., 129 Bank Street, Attleboro, MA 02703-1775.

[56] Dow Chemical Technical Information on Cyclotene Advanced Electronics Resins, "Processing Procedures for Dry-Etch CYCLOTENE Advanced Electronic Resins (Dry-Etch BCB)," Dow Chemical Company, 2030 Dow Center, Midland, MI, 48674, published Nov. 1997.

[57] Dow Corning/Toray Product Information, "Positive Tone Photosensitive Polyimide Coatings *Photoneese* PWDC-1000," Dow Corning Corporation, P.O. Box 994, Midland, MI, 48686-0994.

[58] HD Microsystems "Polyimides for Microelectronics: Product Selection Guide," HD Microsystems, P.O. Box 80010, Wilmington, DE 19880.

[59] HD Microsystems, "LX Series - Product Information and Process Guidelines," HD Microsystems, P.O. Box 80010, Wilmington, DE 19880, revised Dec. 1997.

[60] HD Microsystems, "Product Information and Process Guideline for Pyralin® PI 2730 Series," HD Microsystems, P.O. Box 80010, Wilmington, DE 19880, revised April 1998.

[61] HDMicrosystems, "PI-2771 Photosensitive Polyimide Process Guidelines," HD Microsystems, P.O. Box 80010, Wilmington, DE 19880, revised Nov. 1997.

[62] HD Microsystems, "Product Information on Pyralin ® PI-2800, PI-5800, PI-2540 Series Polyimides," HD Microsystems, P.O. Box 80010, Wilmington, DE 19880.

[63] HD Microsystems Product Bulletin, "Photodefinable HD-4000 Series Polyimide," HD Microsystems, P.O. Box 80010, Wilmington, DE 19880.

[64] HDMicrosystems, "Product Information on Pyralin ® PI-2525, PI-2555, PI-2575, & PI-2556," HD Microsystems, P.O. Box 80010, Wilmington, DE 19880, revised April 2001.

[65] M. E. Thomas, "Spin-on Stacked Films for Low-k_{eff} Dielectrics," *Solid State Technology*, **44**(7), 105-110 (2001).

[66] Sumitomo Bakelite product literature on PBO CRC-8650, revised Feb. 2002, obtained from http://www.sumibe.co.jp/english/products/03_06_a.html.

[67] "Processing Guidelines for Avatrel 2000P Dielectric Polymer," Promerus LLC, 9921 Brecksville Road, Cleveland, OH 44141.

[68] "Avatrel 2000P Data Sheet," Promerus LLC, 9921 Brecksville Road, Cleveland, OH 44141.

[69] M. D. Wedlake, "The Thermal Degradation of Polynorbornene," *M.S. Thesis*, School of Chemical Engineering, Georgia Institute of Technology, 2001.

[70] H. Bockhorn, A. Hornung, and U. Hornung, "Mechanisms and Kinetics of Thermal Decomposition of Plastics From Isothermal and Dynamic Measurements," *Journal of Analytical and Applied Pyrolosis*, **50**, 77-101 (1999).

[71] Flynn, Joseph H., "Thermogravimetric Analysis and Differential Thermal Analysis," In Aspects of Degradation and Stabilization of Polymers, Jellinek (Ed.), Elsevier Scientific, Amsterdam, 1978.

[72] L. Reich and S. S. Stivala, Elements of Polymer Degradation, McGraw-Hill, 1971.

[73] T. Ozawa, "A New Method of Analyzing Thermogravimetric Data," *Bulletin of the Chemical Society of Japan*, **38**(11), 1881 (1965).

[74] Correspondence with Dr. Larry Rhodes, Promerus LLC, 9921 Brecksville Road, Cleveland, OH 44141.

[75] H. Yamamoto, Y. Mi, S. A. Stern, and A. K. St. Clair, "Structure/Permeability Relationships of Polyimide Membranes. II," *J. Polymer Science: Part B: Polymer Physics*, **28**, 2291-2304 (1990).

[76] A. Shimazu, T. Miyazaki, T. Matsushita, M. Maeda, and K. Ikeda, "Relationships Between Chemical Structures and Solubility, Diffusivity, and Permselectivity of 1,3-Butadiene and *n*-butane in 6FDA-Based Polyimides," *J. of Polymer Science: Part B: Polymer Physics*, **37**, 2941-2949 (1999).

[77] R. J. Young and P. A. Lovell, Introduction to Polymers, 2nd ed., Chapman & Hall, New York 1991.

[78] I. Mita, "Effect of Structure on Degradation and Stability of Polymers," In Aspects of Degradation and Stabilization of Polymers, Jellinek (Ed.), Elsevier Scientific, Amsterdam, 1978.

[79] C. L. Beyler and M. M. Hirschler, "Thermal Decomposition of Polymers," Chapter 7 in SFPE Handbook of Fire Protection Engineering (3rd ed.), Editor-in-chief: P.J. DiNenno, NFPA, Quincy, MA, 2001.

[80] J. M. J. Fréchet, F. M. Houlihan, F. Bouchard, B. Kryczka, and C. G. Willson, "Design, Synthesis, and Study of Novel, Thermally Depolymerizable Polycarbonates," *J. Chem. Soc. - Chem. Communications*, **21**, 1514-1516 (1985).

[81] S. Inoue, "Copolymerization of Carbon Dioxide and Epoxide: Functionality of the Copolymer," *J. Macromolecular Science and Chemistry*, A**13**(5), 651-664 (1979).

[82] I. C. McNeill and A. Rincon, “Thermal Degradation of Polycarbonates: Reaction Conditions and Reaction Mechanisms,” *Polymer Degradation and Stability*, **39**, 13-19 (1993).

[83] G. Montaudo, C. Puglisi, R. Rapisardi, and F. Samperi, “Further Studies on the Thermal Decomposition Processes in Polycarbonates,” *Polymer Degradation and Stability*, **31**, 229-246 (1991).

[84] S. Inoue, “High polymers from CO2,” *Chemtech*, **6**(9), 588-594, (1976).

[85] J. M. J. Fréchet, F. Bouchard, F. M. Houlihan, B. Kryczka, E. Eichler, N. Clecak, and C. G. Willson, "New Approach to Imaging-Systems Incorporating Chemical Amplification - Synthesis and Preliminary Evaluation of Novel Resists Based on Tertiary Copolycarbonates," *Journal of Imaging Science*, **30**(2), 59-64, (1986).

[86] J. M. J. Fréchet, F. Bouchard, F. M. Houlihan, E. Eichler, B. Kryczka , and C. G. Willson, "Design and Synthesis of Novel Allylic and Benzylic Copolycarbonates Susceptible to Acidolytic or Thermolytic Depolymerization," *Makromolekulare Chemie-Rapid Communications*, **7**(3), 121-126 (1986).

[87] S. C. Narang, S. T. Attarwala, "Chemical Amplification in t-diol Polycarbonate Resists," *Abstracts of Papers of the Am. Chem. Soc*., **190**, 141 (1985).

[88] J. V. Crivello, J. H. W. Lam, "Diaryliodonium Salts - New Class of Photo-Initiators for Cationic Polymerization," *Macromolecules*, **10**(6), 1307-1315 (1977).

[89] J. P. Jayachandran, H. A. Reed, H. Zhen, L. F. Rhodes, C. L. Henderson, S. A. Bidstrup Allen, and P. A. Kohl, “Air Channel Fabrication for Microelectromechanical Systems Via Sacrificial Photosensitive Polycarbonates,” *J. Microelectromechanical Systems*, **12**(2), 147-159 (2003).

[90] Q. Zhao, and P. A. Kohl, “Reactive Ion Etching of Silicon Containing Polynorbornenes,” *J. Electrochemical Society*, **145**(4), 1257-1262 (1998).

[91] J. A. Mucha, D. W. Hess, E. S. Aydil, Larry. F. Thompson, Ed., C. Grant Willson, Ed., and Murrae J. Bowden, Ed., Introduction to Microlithography, American Chemical Society, Washington, D. C., 1994, page 427.

[92] S. W. Lim; Y. Shimogaki, Y. Nakano, K. Tada, and H. Komiyama, “Decrease in Deposition Rate and Improvement of Step Coverage by CF_4 Addition to Plasma-Enhanced Chemical Vapor Deposition of Silicon Oxide Films,” *Japanese Journal of Applied Physics, Part 1*, **39**(1), 330-336 (2000).

[93] D. J. Kovach, N. S. Amirgulyan, C.-P. Chien and M. H. Tanielian, "A Nearly Stress-free Cu/Polyimide Process for Large Format MCM Manufacturing," *Proceedings of*

[93] D. J. Kovach, N. S. Amirgulyan, C.-P. Chien and M. H. Tanielian, "A Nearly Stress-free Cu/Polyimide Process for Large Format MCM Manufacturing," *Proceedings of the 1999 symposium on Microelectronics (IMAPS)*, Chicago, IL, Oct. 26-28, 1999, 526-531.

[94] J. S. Drage, J. J. Yang, D. K. Choi, R. Katsanes, K. S. Y. Lau, S.-Q. Wang, L. Forester, P. E. Schilling and M. Ross, "Effects of Electron Beam Exposure on Poly(arylene ether) Dielectric Films," *Materials Research Society Symposium Proceedings (Low Dielectric Constant Materials III)*, San Francisco, CA, April 1-4, 1997, 121-128.

[95] www.efunda.com/formulae/solid_mechanics/beams/casestudy_display.cfm?case=simple_uniformload

[96] X. Wu, H. A. Reed, L. F. Rhodes, E. Elce, R. Ravikiran, R. A. Shick, C. L. Henderson, S. A. Bidstrup Allen, and P. A. Kohl, "Fabrication of Microchannels Using Polynorbornene Photosensitive Sacrificial Materials," *Journal of the Electrochemical Society*, **150**(9), H205-H213 (2003).

[97] QPAC polymers product information sheets on poly(ethyl carbonate) and poly (propyl carbonate).

[98] S. L. Rosen, Fundamental Principles of Polymeric Materials, 2nd Edition, John Wiley & Sons, Inc., New York, 1993.

[99] L. K. Massey, Permeability Properties of Plastics and Elastomers : A Guide to Packaging and Barrier Materials, 2nd ed., Plastics Design Library/William Andrew Pub., Norwich, NY, 2003.

[100] C. Geankopolis, Transport Processes and Unit Operations, 3rd ed., Prentice Hall, New Jersey, 1993.

[101] J. Brandrup, Ed., E. H. Immergut, Ed., E. A. Grulke, Ed., A. Abe, Assoc. Ed., and D. R. Bloche, Assoc. Ed., Polymer Handbook 4th ed., Wiley, New York, 1999.

[102] X. Wu, H. A. Reed, L. F. Rhodes, E. Elce, R. Ravikiran, R. A. Shick, C. L. Henderson, S. A. Bidstrup Allen, and P. A. Kohl, "Lithographic Characteristics and Thermal Processing of Photosensitive Sacrificial Materials," *Journal of the Electrochemical Society*, **149**(10), G555-G561 (2002).

[103] International Technology Roadmap for Semiconductors, 2002 update, available at http://public.itrs.net/.

[104] Futurrex Inc. negative resist process data sheets for NR9-8000 photoresist, Futurrex, Inc., 12 Cork Hill Road, Franklin, NJ 07416.

[105] X. Li and B. Bhushan, "A Review of Nanoindentation Continuous Stiffness Measurement Technique and its Applications," *Materials Characterization*, **48**, 11-36 (2002).

[106] J. C. Hay, A. Bolshakov, and G. M. Pharr, "A Critical Examination of the Fundamental Relations Used in the Analysis of Nanoindentation Data," *J. Materials Research*, **14**(6), 2296-2305 (1999).

[107] W. C. Oliver and G. M. Pharr, "An Improved Technique for Determining Hardness and Elastic Modulus Using Load and Displacement Sensing Indentation Experiments," *J. Materials Research*, **7**(6), 1564-1583 (1992).

[108] G. Kourtesis, G. M. Renwick, A. C. Fischer-Cripps, and M. V. Swain, "Mechanical Property Characterization of a Number of Polymers Using Uniaxial Compression and Spherical Tipped Indentation Tests," *J. Materials Science*, **32**(17), 4493-4500 (1997).

[109] G. M. Pharr and A. Bolshakov, "Understanding Nanoindentation Unloading Curves," *J. Materials Research*, **17**(10), 2660-2671 (2002).

[110] W. D. Nix, "Elastic and Plastic Properties of Thin Films on Substrates: Nanoindentation Techniques," *Materials Science and Engineering*, A234-236, 37-44 (1997).

[111] M. Martin and M. Troyon, "Fundamental Relations Used in Nanoindentation: Critical Examination Based on Experimental Measurements," *J. Materials Research*, **17**(9), 2227-2234 (2002).

[112] G. M. Pharr, W. C. Oliver, and F. R. Brotzen, "On the generality of the relationship among contact stiffness, contact area, and elastic modulus during indentation," *J. Materials Research*, **7**(3), 613-617 (1992).

[113] T. Chudoba and F. Richter, "Investigation of Creep Behaviour Under Load During Indentation Experiments and its Influence on Hardness and Modulus Results," *Surface and Coatings Technology*, **148**, 191-198 (2001).

[114] B. Taljat, T. Zacharia, and F. M. Haggag, "Analysis of Ball-Indentation Load-Depth Data: Part 1. Determining Elastic Modulus," *J. Materials Research*, **12**(4), 965-974 (1997).

[115] E. Le Bourhis and G. Patriarche, "Room-Temperature Plasticity of InAs," *Phys. Stat. Sol. (a)*, **179**, 153-158 (2000).

[116]R. B. King, "Elastic analysis of some punch problems for a layered medium," *International Journal of Solids and Structures*, **23**, 1657 (1987).